The climate-change signal in natural disasters: Supplementary material

Stefan Lange[1], Jan Volkholz[1], Tobias Geiger[1], Fang Zhao[1], Iliusi Vega del Valle[1], Ted Veldkamp[2,3], Christopher P.O. Reyer[1], Lila Warszawski[1], Veronika Huber[1], Jonas Jägermeyr[1], Jacob Schewe[1], David N. Bresch[4,5], Matthias Büchner[1], Jinfeng Chang[6], Philippe Ciais[4], Marie Dury[7], Kerry Emanuel[8], Christian Folberth[9], Dieter Gerten[1,18], Simon Gosling[10], Naota Hanasaki[13], Alexandra-Jane Henrot[7], Thomas Hickler[11,15], Yasushi Honda[12], Akihito Ito[13], Nikolay Khabarov[9], Wenfeng Liu[14], Christoph Müller[1], Kazuya Nishina[11], Sebastian Ostberg[1,18], Hannes Müller Schmied[11,15], Tobias Stacke[16], Jörg Steinkamp[9], Yoshihide Wada[3], Hong Yang[14,17], Minoru Yoshikawa[12], Katja Frieler[1]

[1] Potsdam Institute for Climate Impact Research, Germany; [2] Institute for Environmental Studies, VU Amsterdam, the Netherlands; [3] International Institute for Applied Systems Analysis, Laxenburg, Austria; [4] Institute for Environmental Decisions, ETH Zurich, Switzerland; [5] Federal Office of Meteorology and Climatology MeteoSwiss, Switzerland; [6] Laboratoire des Sciences du Climat et de l'Environnement, CEA CNRS UVSQ, Institut Pierre Simon Laplace, Gif sur Yvette, France; [7] Unit for Modelling of Climate and Biogeochemical Cycles, University of Liege, Belgium; [8] Massachusetts Institute of Technology, USA; [9] International Institute for Applied Systems Analysis (IIASA), Austria; [10] University of Nottingham, UK; [11] Senckenberg Biodiversity and Climate Research Centre (BiK-F), Germany; [12] University of Tsukuba, Japan; [13] National Institute for Environmental Studies, Japan; [14] Swiss Federal Institute of Aquatic Science and Technology (Eawag), Switzerland; [15] Institute of Physical Geography, Goethe-University Frankfurt, Germany; [16] Max Planck Institute for Meteorology, Germany; [17] Department of Environmental Sciences, University of Basel, Switzerland; [18] Geography Department, Humboldt-Universität zu Berlin, Berlin, Germany

Contents

Table S1: GCM-specific number of simulation years per global warming level bin of 1 °C width centered at different global warming levels ΔT.

	GFDL-ESM2M	IPSL-CM5A-LR	MIROC5
$\Delta T = 1.0\,°\mathrm{C}$	157	56	279
$\Delta T = 1.5\,°\mathrm{C}$	139	143	324
$\Delta T = 2.0\,°\mathrm{C}$	44	322	115
$\Delta T = 3.0\,°\mathrm{C}$	0	43	8

1 Calculation of impacts in terms of global mean temperature change

To quantify the change in the areas affected by extreme events, the number of people exposed to extreme events, or the changes in the frequency of extreme events in terms of global mean temperature change, averages of affected areas, people exposed or the frequency of extremes are calculated from all annual scenario data (historical period, RCP2.6, and RCP6.0) falling into a ±0.5 °C range of global mean temperatures around global mean warming levels increasing from 0 °C to 4 °C in steps of 0.5 °C. To quantify the pure effect of climate change the associated averages or frequencies of the same years under pre-industrial climate conditions are subtracted from the scenario data. Table 1 provides the number of simulation years included in the global warming level bins around 1 °C, 1.5 °C, 2 °C and 3 °C.

1.1 Separation of pure effect of climate change from direct human influences

The considered "scenario simulations" accounting for historical and future climate change partly also account for the historical evolution of direct human influences on the considered impact indicators (histsoc simulations, 1861–2005, according to the ISIMIP2b protocol [22]. Direct human influences comprise the effect of land use changes, fire prevention or increased ignitions, water withdrawal for irrigation or domestic and industrial consumption, dam construction, and fertilizer application. Before 1860 and after 2005 these direct human influences are held constant at 1860 (1860soc) and 2005 levels (2005soc), respectively. In addition, the calculation of exposed people accounts for historical changes (1860–2005) in population patterns [38]. The "reference simulations" (and the associated calculation of people exposed) are based on the same socio-economic development but the impact simulations are forced by pre-industrial climate conditions. Subtracting the "reference simulations" from the parallel "scenario simulations" allows for a separation of the pure climate effect from the additional effect of socio-economic development in the historical part of the "scenario simulations". The sector specific components of the SI (floods in Sect. 2, tropical cyclones in Sect. 3, crop failures in Sect. 4, wildfires in Sect. 5, droughts in Sect. 6 and heatwaves in Sect. 7) document the derivation of the pure climate effect for each individual impact model.

1.2 Scenario dependence of the global mean temperature relationship

The considered approach of estimating the pure effect of climate change at different levels of global warming is based on the assumption that the relationship between global mean temperature change and the considered impact indicator does not depend of the underlying emission scenario. In the category-specific components of the SI, the relationships are shown for RCP2.6 and RCP6.0. Generally the figures demonstrate that the scenario dependence is a minor component of the overall spread introduced by the different climate and climate-impact models.

1.3 Occurrence probability at grid scale at different levels of global warming

Probabilities of occurrence of the different categories of annual extreme events at the grid scale as defined in the main text are computed at three different global warming levels for every impact model-GCM combination. For the global warming level of $\Delta T = 0.0\,°\mathrm{C}$, the probabilities of occurrence are

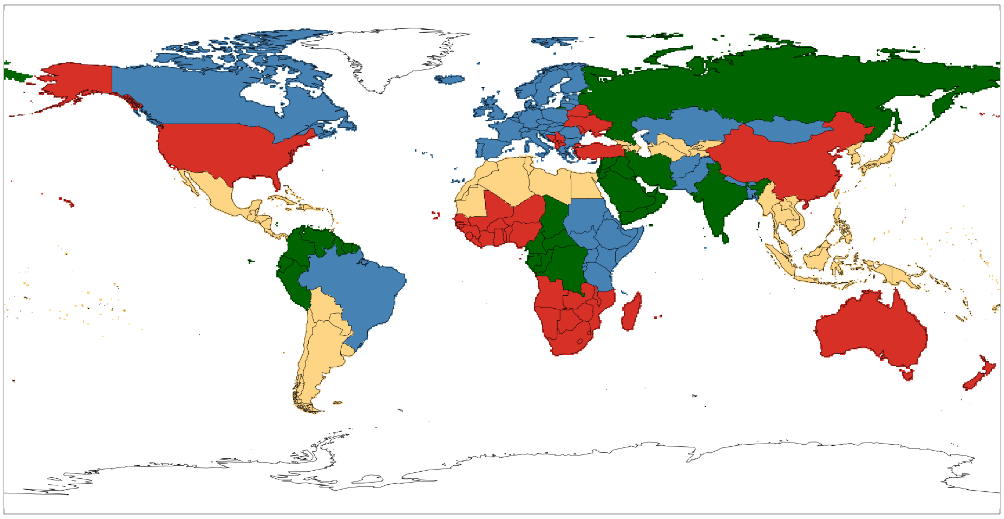

Figure S1: The 22 regions of the world. Their labels are *Canada* (blue), *USA* (red), *Brazil* (blue), *Russia* (green), *China* (red), *IND+LKA* (green), *AUS+NZ* (red), *KAZ+MNG* (blue), *N-Africa* (yellow), *W-Africa* (red), *C-Africa* (green), *E-Africa* (blue), *S-Africa* (red), *Middle-East* (green), *S-Asia-* (blue), *C-Asia* (yellow), *E-Asia* (yellow), *E-Europe* (red), *EU28+* (blue), *C-America* (yellow), *S-Latin* (yellow) and *N-Latin* (green).

derived from the impact model simulations driven by pre-industrial climate and 2005 socio-economic input data. For the global warming levels of $\Delta T = 1.5\,^\circ\mathrm{C}$ and $\Delta T = 2.0\,^\circ\mathrm{C}$, the probabilities of occurrence are derived from the impact model simulations driven by historical, RCP2.6 and RCP6.0 climate input data, using the simulation output from years whose corresponding GCM-specific global mean temperature difference to the pre-industrial mean differs by less than $0.5\,^\circ\mathrm{C}$ from ΔT. The number of simulation years that fall into these global warming level bins is given in Table 1. For every global warming level, impact model-GCM combination and grid cell, the probability of occurrence is then calculated as the number of simulation extreme years in the respective sample divided by the total number of simulation years in the sample.

1.4 Detection levels

For every impact model-GCM combination, we compute the level of global warming at which a global 1-in-50-years event under pre-industrial climate and fixed 2005 socio-economic conditions becomes a global 1-in-5-years event under changing climate and fixed2005 socio-economic conditions. This global warming level is then referred to as the detection level of the respective extreme event category. We compute two versions of detection levels, one based on the global land area fraction affected (LAFA) and the other based on the global population fraction exposed (PFE). Technically, the calculation is done as follows. First, we compute P_{98}, the 98th percentile of the annual global LAFA/PFE under pre-industrial climate and fixed 2005 socio-economic conditions. Then, using linear quantile regression, we determine $P_{80}(\Delta T)$, the 80th percentile of the annual global LAFA/PFE under historical/RCP2.6/RCP6.0 climate and fixed 2005 socio-economic conditions at different levels of global warming ΔT. Finally, we compute the detection level as the global warming level ΔT at which $P_{80}(\Delta T) = P_{98}$.

1.5 World regions

In addition to the global analyses we also investigate impacts on the regional level. For this we have divided the world into 22 regions. These are shown in Figure S1.

Table S2: Absolute changes in areas [10^6 ha] affected by different categories or aggregated types of extreme events. Changes are expressed in comparison to pre-industrial reference conditions.

	$\Delta T = 0\,°\mathrm{C}$		$\Delta T = 1\,°\mathrm{C}$		$\Delta T = 1.5\,°\mathrm{C}$		$\Delta T = 2\,°\mathrm{C}$	
floods	3.18	0.65	9.84	3.09	16.58	0.98	26.77	3.10
tropical cyclones	2.88	0.12	17.75	0.15	19.27	0.15	14.93	0.16
crop failure	4.29	1.22	6.56	3.39	11.55	5.80	16.56	4.99
wildfires	3.36	0.87	4.10	1.81	5.57	2.15	7.96	3.14
droughts	71.56	9.64	123.38	29.59	212.54	65.41	314.69	67.65
heatwaves	34.29	13.48	331.66	71.59	590.58	61.81	991.97	99.46
max/confined events	16.49	2.50	48.82	13.25	71.54	11.65	102.98	15.45
max/extensive events	96.93	9.73	439.78	49.73	773.57	99.15	1254.40	50.07

Table S3: Absolute changes in people [10^6 people] exposed to different categories or aggregated types of extreme events. Changes are expressed in comparison to pre-industrial reference conditions populations patterns corresponding to the year 2005.

	$\Delta T = 0\,°\mathrm{C}$		$\Delta T = 1\,°\mathrm{C}$		$\Delta T = 1.5\,°\mathrm{C}$		$\Delta T = 2\,°\mathrm{C}$	
floods	3.2	0.6	6.7	3.9	10.5	3.2	16.0	4.5
tropical cyclones	5.3	0.2	22.0	0.3	24.7	0.3	20.0	0.3
crop failure	11.7	3.1	12.4	9.6	27.3	17.9	43.2	15.6
wildfires	2.3	0.7	3.0	1.4	4.0	1.6	5.6	2.1
droughts	26.4	5.3	20.9	5.4	31.7	8.7	51.9	10.4
heatwaves	30.9	17.5	226.9	27.5	428.4	75.4	742.7	30.6
max/confined events	13.3	7.5	43.5	10.0	67.0	28.6	94.6	14.7
max/extensive events	48.5	12.6	243.6	20.9	454.6	79.5	780.6	26.3

1.6 Estimating expected changes in areas affected by and people exposed to extreme conditions across all climate model – impact model combinations

We use the annual data behind Figure 1 and 2 of the main text to estimate the expected change in areas affected and people exposed and the associated standard errors for different levels of global mean temperature change (see Table S2). As the data are grouped according to 1) the climate model that has been used to force the impact simulations (level 1) and 2) the impact model (for individual categories of events) or impact model combination (for types of events comprising different categories) (level 2) we apply a random effects model to adjust the estimation of the standard error according for the internal clustering of the data. The average changes reported in Table S2 correspond to the fixed effects and their standard error estimated by a linear mixed model (lmer, R Package lme4, [7]) allowing for climate model specific random deviations from these common fixed effects and impact model specific deviations from the climate model specific effects. As the projection of changes in areas affected by and the population exposed to heatwaves or tropical cyclones is directly derived from the climate model output, the estimates only consider the first level of grouping.

The uncertainty of the tropical cyclone component is not considered in the estimation of the standard error associated with the changes in the confined events.

2 Calculation of area affected by and people exposed to flood events

Flooded areas are derived from seven Global Hydrological Models (GHM) (see Table S4. All models are forced by bias-corrected daily climate data provided within ISIMIP2b [22]. They assume fixed socioeconomic conditions (e.g. changes in land-use patterns) before 1860 (1860soc for 1661–1860 according to the ISIMIP2b protocol), and if possible account for varying socio-economic drivers during the historical period (indicated with “histsoc” for 1861–2005 according to the ISIMIP2b protocol, Table S4). After 2005 socio-economic conditions are held constant at present-day levels (2005soc for 2005–2099 or 2005–2299, respectively, according to the ISIMIP2b protocol).

Table S4: Main characteristics of the Global Hydrological Models (GHMs)

Global Hydrological Model	Energy balance	Soil scheme	Evaporation scheme	Runoff scheme	Snow scheme	Direct Human influences
H08 [30]	yes	One soil layer with a depth of 1 m	Bulk formula	Saturation excess, non-linear	Energy balance	**2005soc**,fixed 2005 land use, irrigation, domestic, industrial water use, reservoir operation
JULES-W1 [8, 3]	yes	our layers of 10, 25, 65 and 200 cm thickness	Penman-Monteith	Hortonian infiltration excess mechanism enhanced by vegetation specific factors	Energy balance	**2005soc** no direct human influences considered, fixed 2005 land use
LPJmL [54, 58]	no	Five layers of 20, 30, 50, 100 and 100 cm thickness	Priestley-Taylor	Saturation excess	Degree Day	**histsoc** time-varying rainfed agriculture, irrigation area, irrigation, domestic, industrial water use, reservoir operation
MPI-HM [29, 67]	no	prescribed by the plant rooting depth	Penman-Monteith	Saturation excess, non-linear	Degree Day	**histsoc**, time-varying rainfed and irrigated crops, no other direct human influences considered
PCR-GLOBWB [74, 75]	no	2 soil layers up to 1.5 m depth (upper soil layer up to 0.3 m and lower soil layer up to 1.2 m)	Hamon	Saturation Excess Beta Function	Degree Day	**histsoc** time-varying rainfed agriculture, irrigation area, irrigation, livestock, domestic, industrial water use, reservoir operation
ORCHIDEE [28]	yes	11 layers in a 2 m soil	Bulk formula	Infiltration excess	Energy balance	**1860soc/2005soc** no direct human influences considered, fixed 1860/2005 land use, **histsoc** time-varying land use
WaterGAP2 [48, 4]	no	One soil layer, varying depth in dependence on land cover type (0.1 to 4 m)	Priestley Taylor with two alpha factors depending on the aridity of the grid cell	Beta function, saturation excess	Degree Day	**histsoc** time-varying irrigation area, irrigation, domestic, industrial, livestock water use, reservoir operation

2.1 Areas affected

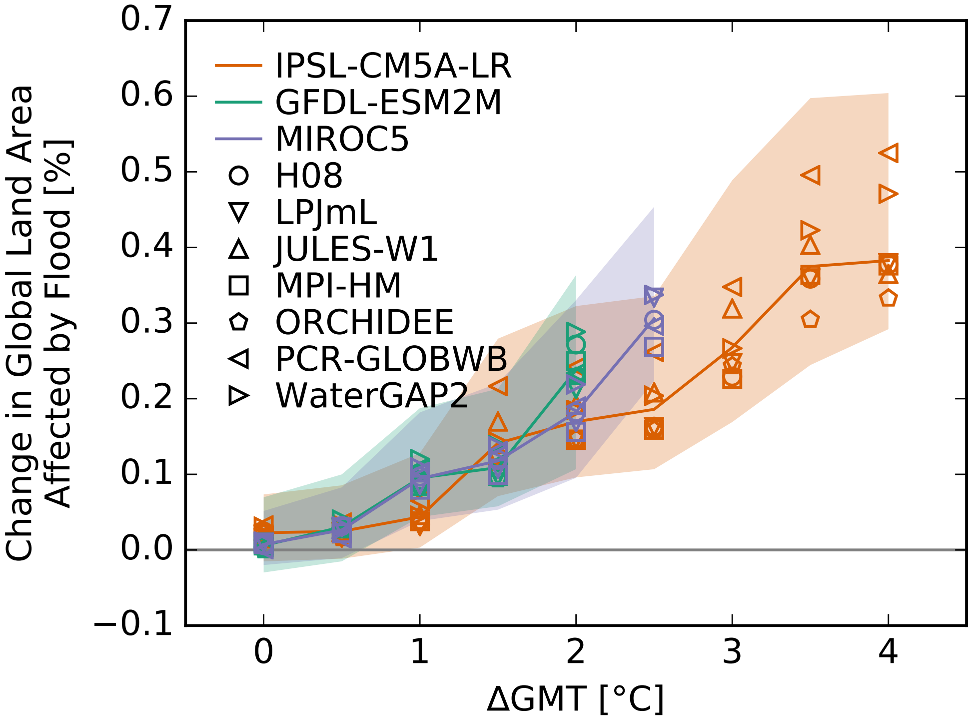

Figure S2: **Pure effect of climate change on global land area fraction affected by floods.** Absolute change in global land area fraction affected (AFA) by floods at different levels of global mean temperature (GMT) change relative to the long-term pre-industrial mean GMT as simulated by different impact models (symbols) driven by different GCMs (colors). Symbols indicate the impact model-GCM combination-specific median response to global warming (these are identical to the red solid lines in Panel D of Figures S24 . . . S41). Solid lines are the medians over all impact models per GCM. The shaded areas are the corresponding 20th-to-80th percentile ranges.

Since the GHMs provide grid-scale river discharge and runoff instead of flooded areas, it is necessary to apply the global river model CaMa-Flood [79, 80], which is forced only by the runoff simulations of each GHM. Simulated daily runoff are translated into annual maximum daily discharge by CaMa-Flood to estimate the fraction of each grid cell that has been affected by a flood event at least once in a considered year. CaMa-Flood has been shown to improve the reproduction of the multi-model ensemble mean of observed peak discharge in a majority of areas compared to the original routing schemes used within the GHMs, although individual GHM discharge might still fit better to observations [83]. The flood inundation scheme enables simulation of global gridded flooded area and depth, and the model is widely used to estimate global flood risk under climate change [40, 32, 50].

A grid cell is considered to be affected by flooding if the maximum annual discharge exceeds the 100-year return level derived from the pre-industrial simulations. While dams and levees are often effective measures to prevent flooding, flood defense in most developing regions are currently insufficient to prevent large floods with return periods longer than 100 years [61]. Assuming universal protection against floods with return periods shorter than 100 years is thus expected to underestimate flooded areas in developing countries, but overestimate the areas in some industrialized countries. Since regions with protection levels higher than 100-year return levels are small (see Figure S3), our default projections of areas affected by flooding are expected to be conservative.

Specifically, for each GCM-GHM combination and at every grid cell, a Generalized Extreme Value (GEV) distribution [37] is fitted to the distribution of annual maximum discharge (up to 639 years) using L-moment estimators [36]. The considered pre-industrial reference samples are much larger than the 30 historical years often considered in previous studies and allow for a more robust estimate of return periods. Since the climate forcing could still contain biases, the frequency distribution of annual maximum daily discharge, instead of flood depth and area directly simulated by CaMa-Flood, is used.

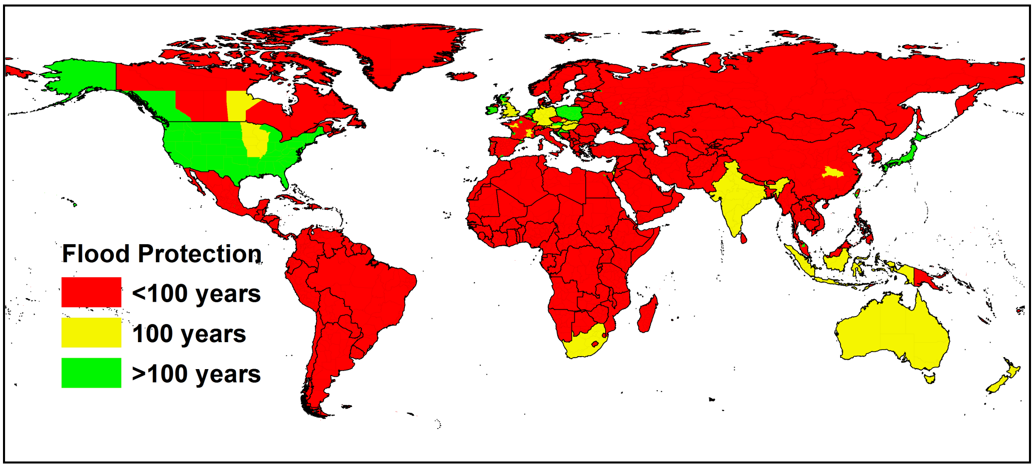

Figure S3: **Estimated present day protection levels against river floods expressed in return levels of discharge based on the FLOPROS database** [61]. Red areas: Flood protection is lower than the flood protection assumed in our default simulations. Yellow areas: Flood protection corresponds to the protection assumed in the default simulations. Green areas: Flood protection exceeds the level of protection considered in our default calculations.

Following the approach by [32], annual maximum daily discharge with a return period of more than 100 years is mapped to corresponding flood depth from a retrospective CaMa-Flood run with MATSIRO [69] runoff, driven by observed climate forcing. To estimate the fraction of the $0.5° \times 0.5°$ grid cell that is affected by the flood, the flood depth mapped to the retrospective MATSIRO run is then downscaled by CaMa-Flood based on high resolution topography data ($\sim 100\,\text{m}$ spatial resolution) to yield the annual maximum flood inundation area fraction on a $5' \times 5'$ grid.

Separation of pure effect of climate change from direct human influences Changing human water management and use in the historical period mostly affects river discharge (e.g. through water abstraction from rivers, lakes, and reservoir management) but only has a minor effect on gridded runoff. As CaMa-Flood uses the gridded daily runoff instead of routed discharge from the GHMs, the majority of human water management, such as dams and reservoirs (not simulated by CaMa-Flood), has a negligible effect on the derived areas affected by flooding. In those cases where water demand is satisfied from groundwater resources, a reasonable reduction of groundwater runoff (one component of runoff) can be expected. However, for flooded area this effect seems to be negligible (see preindustrial and future segments of the reference simulations shown in Panel A (gray dots) from multiple GHM-GCM combinations).

2.2 People exposed

For each cell we multiplied the annual inundated area by the cell population in the corresponding year. Before 1860 and after 2005, population data were held fixed at 1860 and 2005 levels, respectively. The estimates of exposed people on the $5' \times 5'$ grid were aggregated to the common ISIMIP2b $0.5° \times 0.5°$ grid.

Compared to the area fraction affected, the fraction of population exposed to flooding increases faster with increasing global warming levels. This suggests that floods with a return period of over 100 years increase more in areas with denser population (while change in population distribution in the historical period may play a role, it should not affect the change at higher warming levels where population is fixed at 2005 levels).

Separation of pure effect of climate change from direct human influences As shown in the previous section, direct human influences only have a minor influence on the extent of flooded areas derived by CaMaFlood. The additional effect of the historical changes in population patterns (1860–2005) on people exposed to flooding is minor, too (see pre-industrial and future segments of the

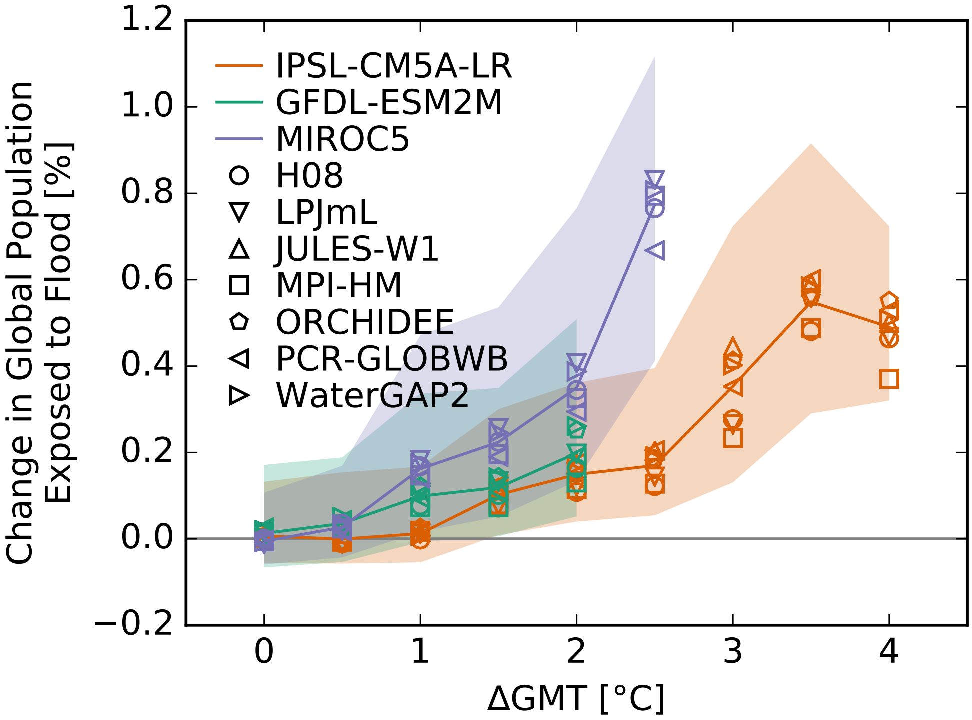

Figure S4: **Pure effect of climate change on global population fraction exposed to floods.** Absolute change in global population fraction exposed (PFE) to floods at different levels of global mean temperature (GMT) change relative to the long-term pre-industrial mean GMT as simulated by different impact models (symbols) driven by different GCMs (colors). Symbols indicate the impact model-GCM combination-specific median response to global warming (these are identical to the red solid lines in Panel D of Figures S42 . . . S59). Solid lines are the medians over all impact models per GCM. The shaded areas are the corresponding 20th-to-80th percentile ranges.

reference simulations shown in Panel A (median values for the gray dots), the differences shown in some individual GCM-GHM combinations are likely due difference in population patterns, although it is also possibly affected by different climate realizations).

In general the different GHMs closely agree regarding the projected relative changes in areas affected by flooding compared to the inter-impact model spread associated with the estimated relative change in areas affected by the other types of extremes. This suggests flood projections are mainly driven by high precipitation as provided by the climate projections and less dependent on e.g. the implementation of evapotranspiration in the GHMs. Thus, the inter-GHM spread in discharge under wet conditions is smaller than the overall spread of projections under dry conditions (see Figure S22).

2.3 Occurrence probability at grid scale

More than 66 % of the model combinations agree that annual maximum flood events with larger than 100 year return period will be more frequent with higher level of global warming in manyregions. The increase in its occurrence probability is largest in the tropical regions (most notably central Africa and southeast Asia) and east of boreal Eurasia, but also visible in boreal North America, and southeastern United States and China, Germany and Ireland. In a few regions the occurrence probability decreases, most notably in Central Europe. Most of the changes are already visible under 1.5 °C global warming and are further enhanced under 2 °C warming. This spatial pattern largely agrees with previous findings [32]. Note that the occurrence frequency is different from affected area, so while the eastern Boreal Eurasia shows the largest increase in flood occurrence, the actual flooded area may not contribute as much to global area affected by floods.

Differences in the spatial patterns mostly come from different GCMs: for IPSL-CM5A-LR and MIROC5, most of the changes occur under 1.5 °C warming, and the additional half degree warming has a limited enhancing effect especially for IPSL-CM5A-LR. For GFDL-ESM2M however, the impact

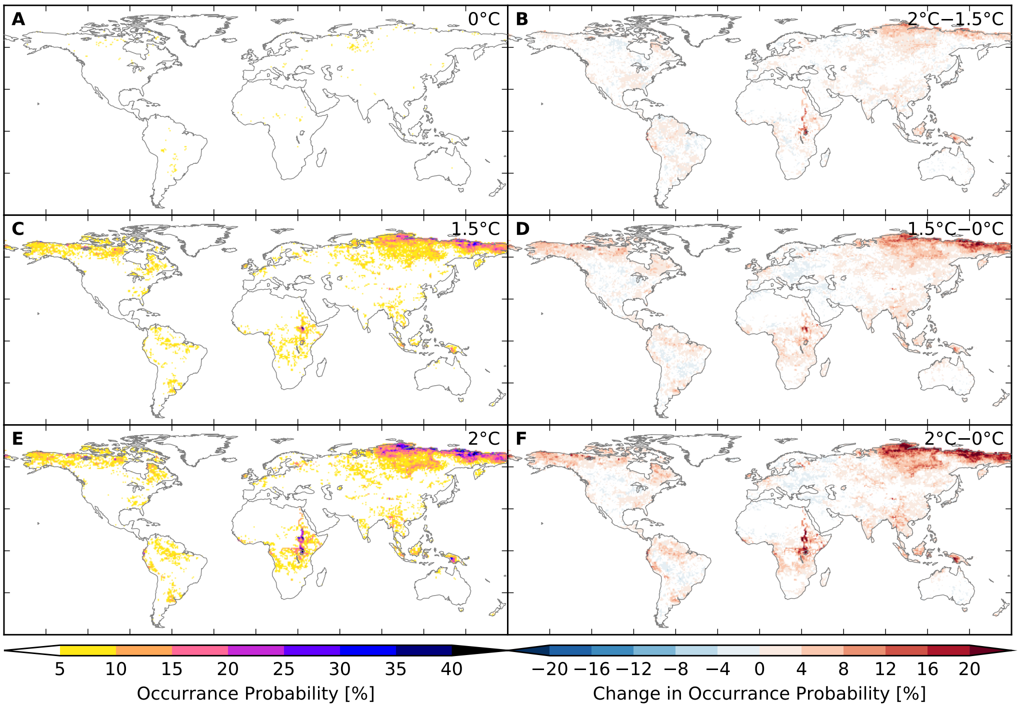

Figure S5: **Probability of occurrence of at least one flood event per year at different levels of global mean temperature.** Panels A, C, E: Probabilities at 0 °C, 1.5 °C, 2 °C, respectively. Panels B, D, F: Differences between probability at 2 °C and 1.5 °C, 1.5 °C and 0 °C, 2 °C and 0 °C, respectively. White in panels B, D, F indicates that less then 66 % of the impact model-GCM combinations agree on the sign of the difference. The impact model-GCM combination-specific occurrence probabilities are shown in Figures S175 . . . S192.

of an additional half degree warming changes the occurrence probability even more than the 1.5 °C warming compared to preindustrial conditions. Under the same GCM forcing, different GHMs show a similar pattern of the occurrence and its change, even though the area affected may differ.

3 Calculation of area affected by and people exposed to tropical cyclones

3.1 Areas affected

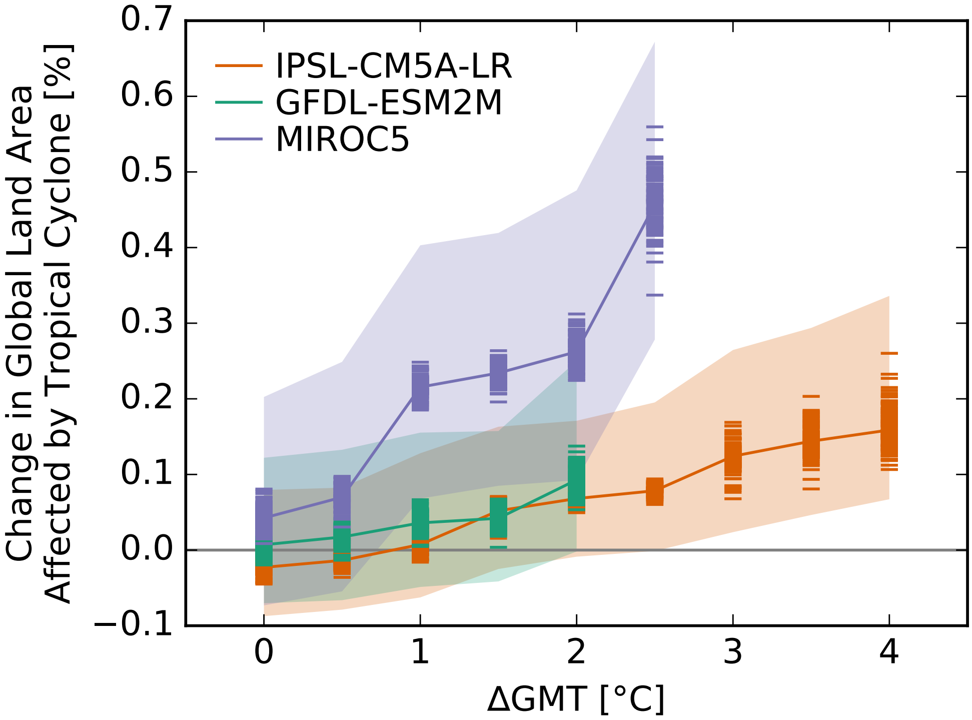

Figure S6: **Pure effect of climate change on global land area fraction affected by tropical cyclones.** Absolute change in global land area fraction affected (AFA) by tropical cyclones at different levels of global mean temperature (GMT) change relative to the long-term pre-industrial mean GMT as simulated by different model realizations (bars) driven by different GCMs (colors). Bars indicate the model realization-GCM combination-specific median response to global warming (these are identical to the red solid lines in Panel D of Figures S78 . . . S80). Solid lines are the medians over all model realizations per GCM. The shaded areas are the corresponding 20th-to-80th percentile ranges.

Land area affected by tropical cyclones (TCs) is defined as all grid cells subject to 1-minute sustained hurricane-force winds (wind speed larger or equal to 64 knots) at least once a year. Potential TC tracks are simulated using a dynamical tropical cyclone model [16] forced by GCM data. Affected areas are derived from a windfield model [33] providing bare track coordinates with a realistic extension of winds around the TC center, and implemented in the open-source climate risk modeling toolbox climada [11, 26, 24]. The dynamical downscaling approach [17] as well as the windfield model have been shown to realistically reproduce observational TC data [33, 24], and have been applied to project socio-economic TC impacts [44, 25].

Generation of 100 potential realizations of tropical cyclones for each year of the historical period and the RCP scenarios For each of the considered years a global total of 300 potential TCs per year and the expected number of cyclones for each year are provided. For the scenario runs, each underlying GCM year corresponds to the same year considered within all other sectors. To provide 100 sets of potential hurricane realizations for each year, we randomly draw the expected number of tracks from the sample of 300 tracks provided for each year. Each set of tracks is referred to as one realization in the following.

Generation of 100 potential realizations of tropical cyclones for each year of the pre-industrial reference scenario The pre-industrial control simulations only comprise 100 TCs tracks per year. In addition, the underlying GCM years do not necessarily match the years considered within all other sectors as the downscaling is partly forced by other segments of the pre-industrial GCM runs. To generate a sample of 100 potential realizations of cyclone tracks that correspond to the individual year considered within the other sectors, we select at least three years of cyclone simulations that match a considered year in the other sectors in terms of the low frequency variability of global mean temperature (21-year running-mean) and the 3-month running-mean of the Equatorial Southern Oscillation Index (as defined by NOAA's Climate Prediction Center http://www.cpc.ncep.noaa.gov/data/indices/). The algorithm initially sets a very strong threshold of similarity and iteratively and alternatively for GMT and ESOI lowers the threshold until at least three years have been selected. In this way we create a sample of at least 300 TCs we can draw from. The expected number of TCs to draw is randomly selected from the expected numbers of cyclones associated with the years contributing to the sample. As both GMT and ESOI (or variants thereof) have been shown to significantly modulate the occurrence of climate extremes, see e.g. Ref. [21, 76], we thereby account for relevant regional climate extreme patterns within this sector and across sectors.

For each year and each realization of tracks a binary map of affected land area with hurricane-force winds is generated with $0.1^\circ \times 0.1^\circ$ spatial resolution. This map is then aggregated to a grid with 0.5° spatial resolution and the area fraction affected of the larger grid cell is then saved and compared to the other climate extremes.

Discussion of Results The absolute change in global land area fraction affected (AFA) by TCs shows an increase across all models with increasing GMT, see S6. Two GCMs (GFDL-ESM2M and IPSL-CM5A-LR) show a comparable result with less than 0.1 % rise in AFA for 2 °C of warming, while for MIROC5 a tripling of AFA is obtained to almost 0.3 %. Naturally, TCs only affect a small portion of global land mass. Translated to relative quantities, however, these changes correspond to a more than 50 % rise in TC-affected areas for MIROC5.

The difference in AFA changes for different GCMs can be explained by how TC characteristics change in different models and ocean basins. While GFDL-ESM2M and IPSL-CM5A-LR predict large changes in annual TC frequency with rising GMT (see S8 and S9), MIROC5 additionally predicts large changes in annual maximum TC intensities (see S7). Both, changes in frequency and intensity result in rising AFA as more events can potentially cause more landfalls and more intense events cause higher wind speeds that can exceed the here-applied threshold of 64 knots over land.

Across all GCMs and all basins we observe similar changes in TC frequency and intensity with rising GMT across both RCP scenarios, indicating that GMT is sufficient to explain most changes in TC-specific impacts under global warming.

3.2 People exposed

On the high resolution grid ($0.1^\circ \times 0.1^\circ$) all people living in a grid cell affected by hurricane-force winds are considered to be exposed to the respective tropical cyclone. The number of people living in these grid cells is taken from the SSP2-based population distribution on the 0.1° grid provided within ISIMIP2b. The high resolution maps of people exposed are then spatially aggregated to obtain the PFA by TCs on the 0.5° grid.

Discussion of Results For PFA we obtain similar findings as for AFA, see S10. Across all GCMs we see increases in the number of exposed people with rising GMT, with MIROC5 again exposing about threefold as many people than GFDL-ESM2M and IPSL-CM5A-LR. Changes for PFA are somewhat larger than changes in AFA which can be explained by the fact that a large fraction of global population resides close to the coast. Hence, an additional unit of coastal AFA hosts overproportionally more people than a non-coastal area, and thus small changes in AFA can cause larger changes in PFA.

For PFA we also find larger uncertainties associated with each GCM than for AFA (shaded regions in S10). This fact is related to the stochastic nature of TC occurrence, as underlined by the large annual variability shown in thin lines in S7-S9. This stochasticity also affects the specific landfall location and the associated number of people exposed: whether a major city is directly hit or barely missed contributes significantly to the underlying uncertainty.

3.3 Occurrence probability at grid scale

More than 66 % of the model combinations agree that annual occurrence of TCs will increase with higher level of global warming in many regions, see Figure S11. Here, a 10 % probability of occurrence corresponds to one event in 10 years affecting this specific grid cell on average. The increase in occurrence probability is mostly but not exclusively confined to certain hot-spot regions, namely the Eastern Pacific coast of Mexico, the South-East coast of Africa, in particular Madagascar, Northern Australia, South-East Asia, in particular the Philippines and the Chinese coast, and to some extent India and the Bay of Bengal. Most of the changes are already visible under 1.5 °C global warming (Panel D) and are further enhanced under 2 °C warming (Panel F). There exists a discernible difference between a 1.5 °C and a 2.0 °C world, in particular for Madagascar but also for the East African, the Northern Australian, and the Chinese coast (Panel B). Note that the occurrence frequency is different from exposed population, so while Madagascar shows the largest increase in TC occurrence, the actual exposed population may not contribute as much to globally exposed population as e.g. the Chinese coast.

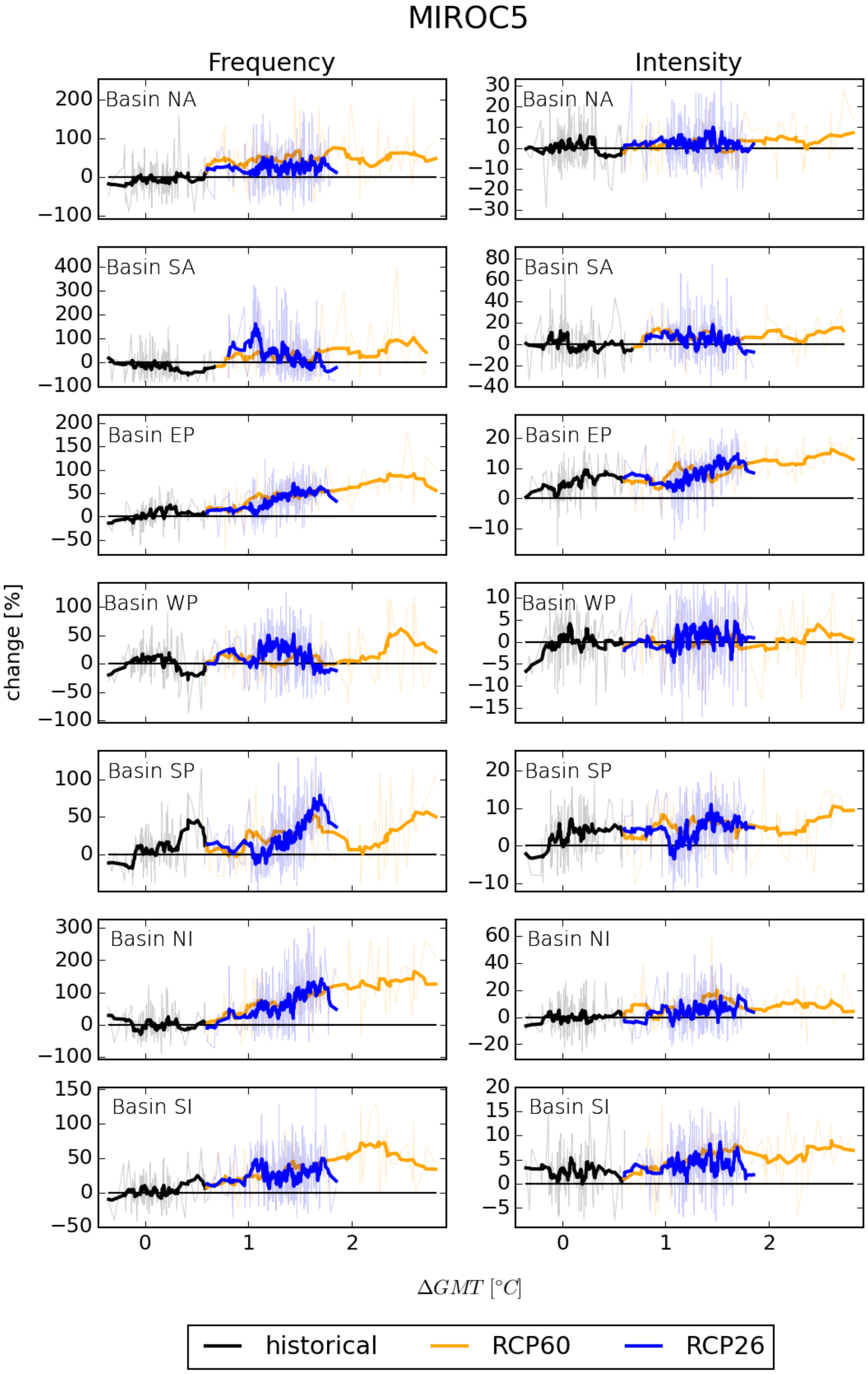

Figure S7: **Changes in annual ocean basin-specific TC frequency and intensity for different levels of global mean temperature for GCM MIROC5.** Per-cent changes relative to the long-term pre-industrial mean in ocean basin-specific annual TC frequency (left column) and mean annual maximum TC intensity (right column) analyzed over all simulated TCs for each year. Annual changes (thin colored lines) are overlaid with 11-year running-mean changes (thick colored lines) for the historical period (black), and the RCP26 (blue) and RCP60 (orange) scenarios. Basin abbreviations are as follows: NA – North Atlantic Ocean, SA – South Atlantic Ocean, EP – East Pacific Ocean, WP – West Pacific Ocean, SP – South Pacific Ocean, NI – North Indian Ocean, SI – South Indian Ocean. The line of zero change is marked with a thin black line.

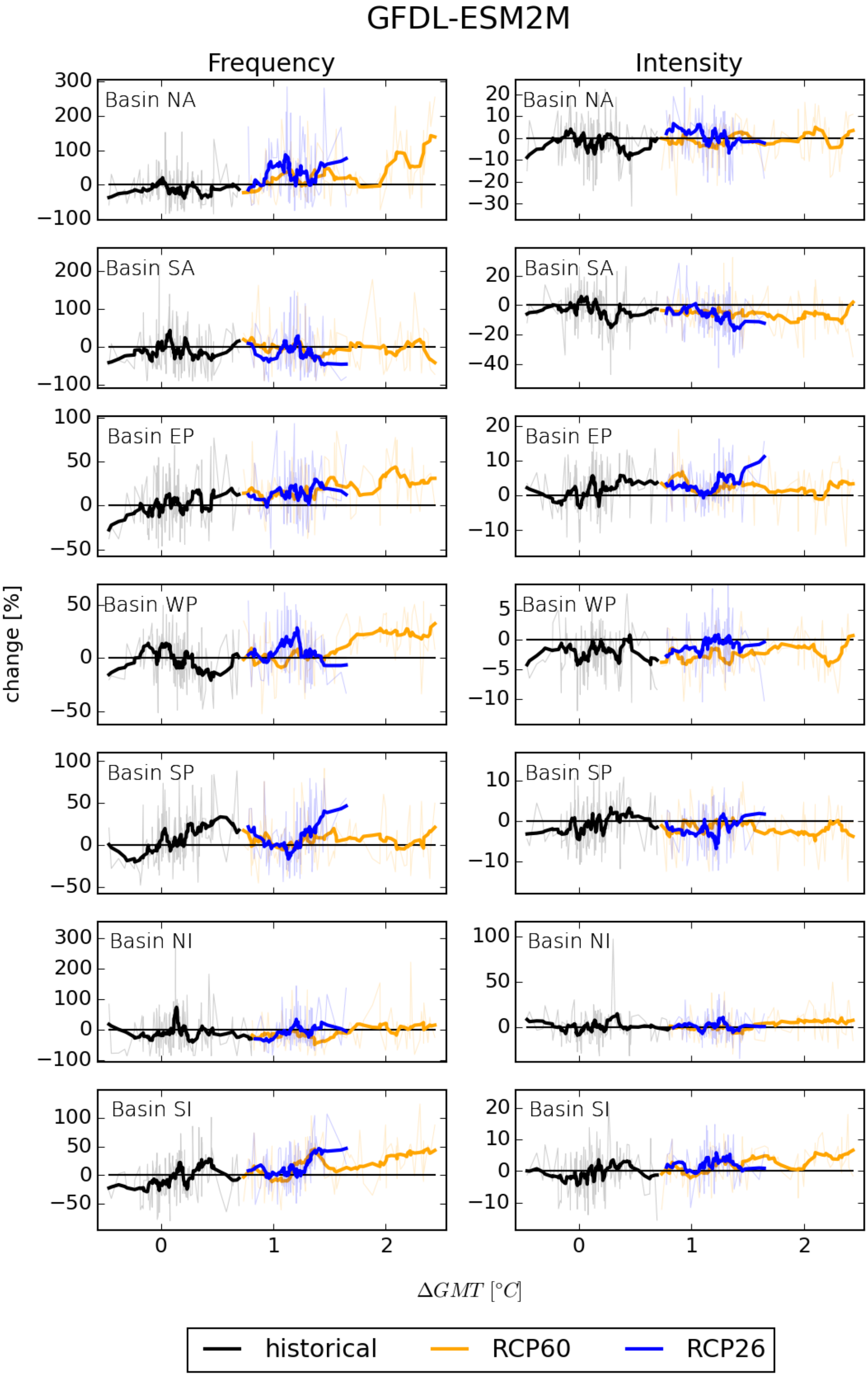

Figure S8: **Changes in annual ocean basin-specific TC frequency and intensity for different levels of global mean temperature for GCM GFDL-ESM2M.** Similar to S7 but for GCM GFDL-ESM2M.

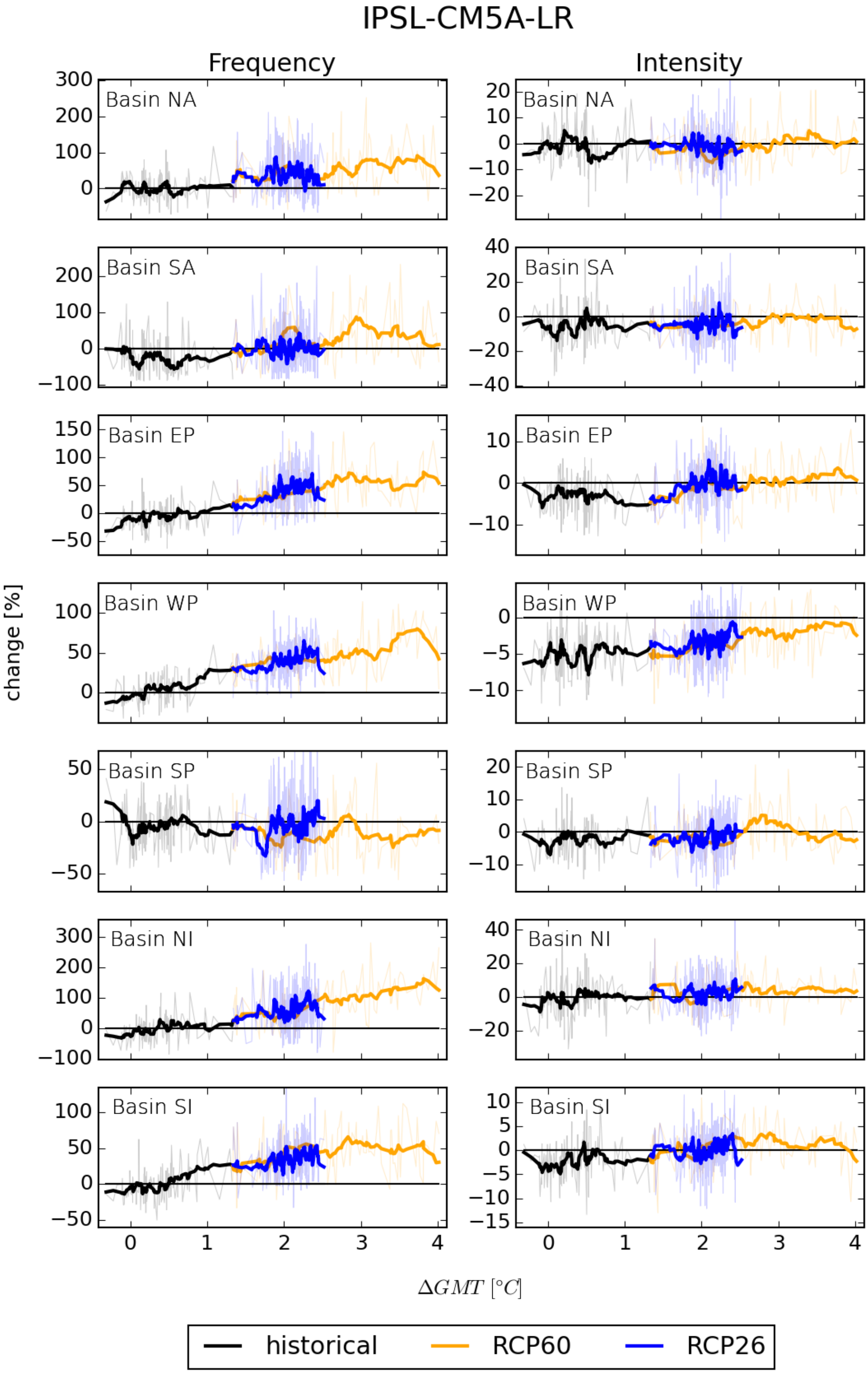

Figure S9: **Changes in annual ocean basin-specific TC frequency and intensity for different levels of global mean temperature for GCM IPSL-CM5A-LR.** Similar to S7 but for GCM IPSL-CM5A-LR.

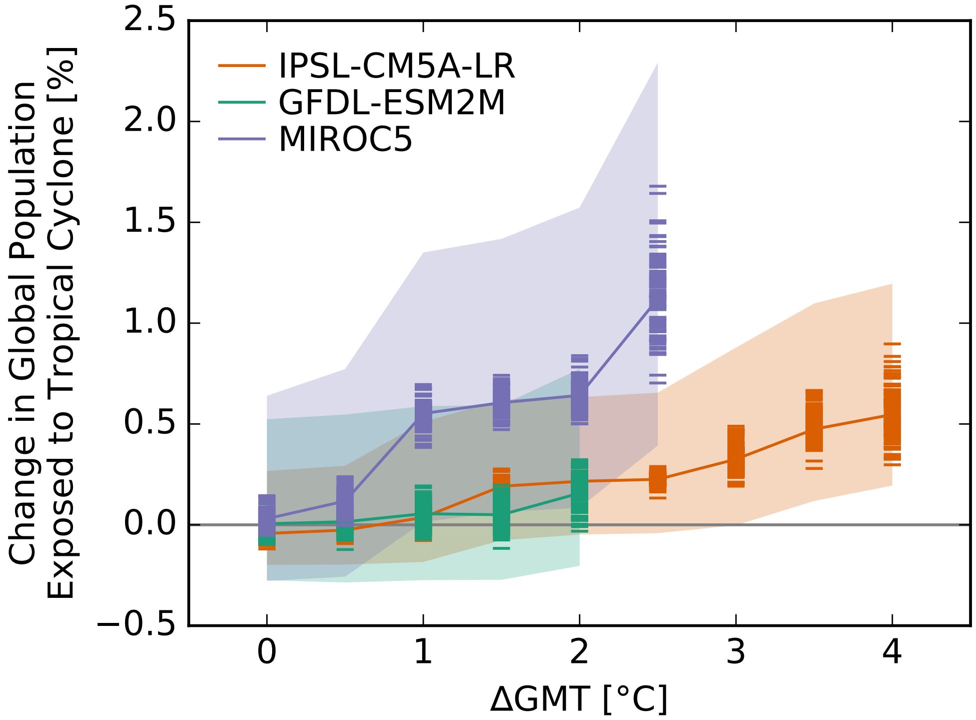

Figure S10: **Pure effect of climate change on global population fraction exposed to tropical cyclones.** Absolute change in global population fraction exposed (PFE) to tropical cyclones at different levels of global mean temperature (GMT) change relative to the long-term pre-industrial mean GMT as simulated by different model realizations (bars) driven by different GCMs (colors). Bars indicate the model realization-GCM combination-specific median response to global warming (these are identical to the red solid lines in Panel D of Figures S81 . . . S83). Solid lines are the medians over all model realizations per GCM. The shaded areas are the corresponding 20th-to-80th percentile ranges.

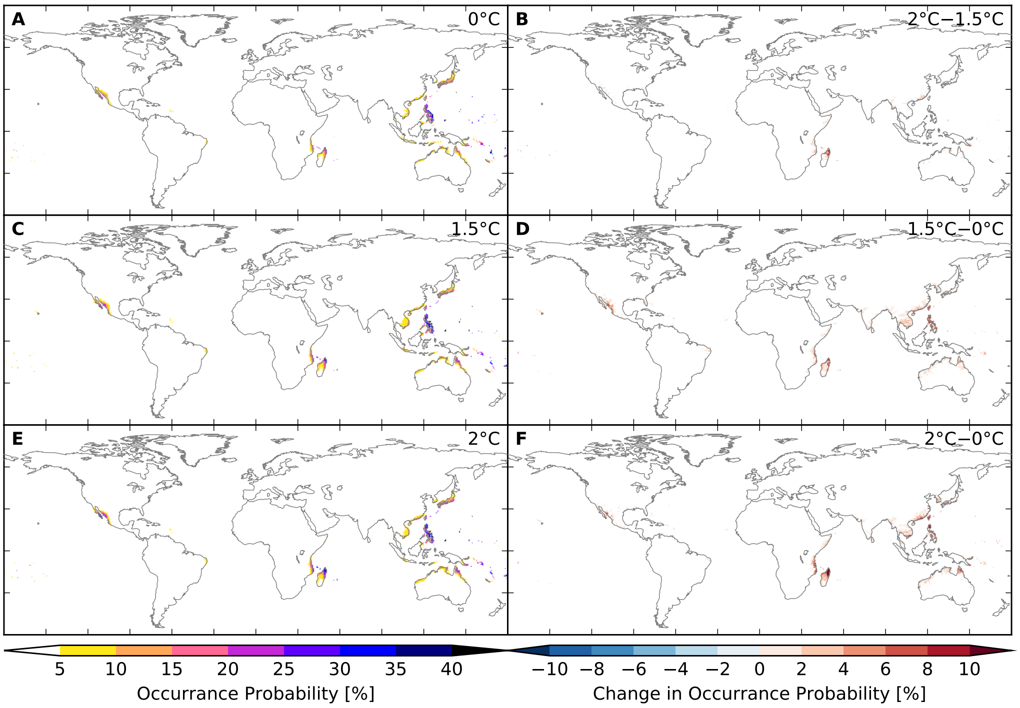

Figure S11: **Probability of occurrence of at least one tropical cyclone event per year at different levels of global mean temperature.** Panels A, C, E: Probabilities at 0 °C, 1.5 °C, 2 °C, respectively. Panels B, D, F: Differences between probability at 2 °C and 1.5 °C, 1.5 °C and 0 °C, 2 °C and 0 °C, respectively. White in panels B, D, F indicates that less then 66 % of the model realizations-GCM combinations agree on the sign of the difference. The impact model-GCM combination-specific occurrence probabilities are shown in Figures S84 . . . S86.

4 Calculation of area affected by and people exposed to crop failure

Crop failure is derived from three process-based crop models (GEPIC, LPJmL and PEPIC, see Table S5 for their basic characteristics) providing yields [t/ha] of wheat, maize, rice and soy on the ISIMIP2b 0.5° grid. The original simulations do not account for land use patterns. Instead, models provide pure crop runs assuming that each crop grows everywhere. For each crop, the individual modeling groups provide simulations assuming fully irrigated conditions, ignoring potential constraints on water availability and a separate set of simulations assuming purely rainfed management conditions everywhere. In this way LU patterns can be applied in post-processing ensuring maximum flexibility. Here, we apply historical land use and irrigation patterns for 5 crop classes [23] that have been downscaled to maize, rice, and soy [22]. The ISIMIP2b LU patterns only provide grid cell fractions for "temperate cereals" without considering wheat separately. The wheat patterns considered within this study are derived from the "annual C3 crops" category in LUH2 assuming constant wheat shares according to [45]. Before 1860 and after 2005 land use and irrigation patterns were held constant. Model simulations do not account for water constraints but assume that crops are fully irrigated on irrigated areas. All models provide 2005soc simulations according to the ISIMIP2b protocol, i.e. they do not account for historical or future management changes or technological progress but assume a fixed management setting described in Table S5. Yields are provided as annual output, assuming one single cropping cycle per crop and year. All considered crop models account for the CO_2 fertilization effects (See Table S5).

Table S5: Basic characteristics of the considered global gridded crop models. More detailed information on model setups are provided in [18] and [47]

Global Gridded Crop Model	CO_2 fertilization	Representation of human management	Calibration
GEPIC [42, 43, 78]	RUE, TE	No representation of historical changes in management (2005soc simulations according to the ISIMIP2b protocol): Representation of nutrient constraints:N application based on HYDE3.2 [38] dataset provided within ISIMIP2b. 1/3 of total dose applied at planting, 2/3 about 40 days after germination Implementation of growing seasons: Planting dates are based on the data provided within the global gridded crop model intercomparison project [15]; total heat units to reach maturity remain constant over time but vary spatially according to reported growing seasons for the recent historic period. Winter and spring wheat are distributed according to Stehfest et al (2007): Winter wheat is planted in grid cells with a minimum temperature in the coldest month of the year of $> -10\,°C$ and $< 5\,°C$ based on decadal monthly means during the recent historic time period and kept constant over time.	The model is not calibrated explicitly but has been evaluated in detail as [19] Maize cultivars are distributed based on the human development index (HDI) with high-yielding cultivars in countries with HDI¿80 and low-yielding in all others. Soils were pre-conditioned in a spin-up run as described in [19]. Subsequently, soils were treated statically in the model with an annual re-initialization of all soil properties except soil humidity and mineral N.
LPJmL [9]	LLP, CC	No representation of historical changes in management (2005soc simulations according to the ISIMIP2b protocol): Representation of nutrient constraints: soil nutrient limiting factors are not accounted for Implementation of growing seasons: Planting dates are based on the data provided within the global gridded crop model intercomparison project [15]; total heat units to reach maturity remain constant over time but vary spatially according to reported growing seasons for the recent historic period.	present day Leaf Area Index (LAI), Harvest Index (HI), and a scaling factor that scales leaf-level photosynthesis to stand level are adjusted to reproduce observed yields on country levels (1996-2000)

Table S5: Basic characteristics of the considered global gridded crop models, continued . . .

Global Gridded Crop Model	CO_2 fertilization	Representation of human management	Calibration
PEPIC [42, 43, 78]	RUE, TE	No representation of historical changes in management (2005soc simulations according to the ISIMIP2b protocol): Representation of nutrient constraints: flexible N application based on N stress $> 10\,\%$ with a maximum value according to the isimip2b input data; phosphorus deficiency was not considered. Implementation of growing seasons: fixed sowing dates [57] potential heat units to reach maturity based on average growing season temperature between 1980 and 2010, i.e. they vary spatially but stay constant over time.	present day Model parameters are adjusted to reproduce average (1998-2002) reported yields (FAO) on national level.

Crop failure at each grid cell and for irrigated and rainfed yields is defined of simulated yields falling below the 2.5th percentile of the associated reference distribution based on the model simulations forced by pre-industrial climate. As the crop models do not account for management changes the entire time series of reference simulations has been used.

4.1 Areas affected

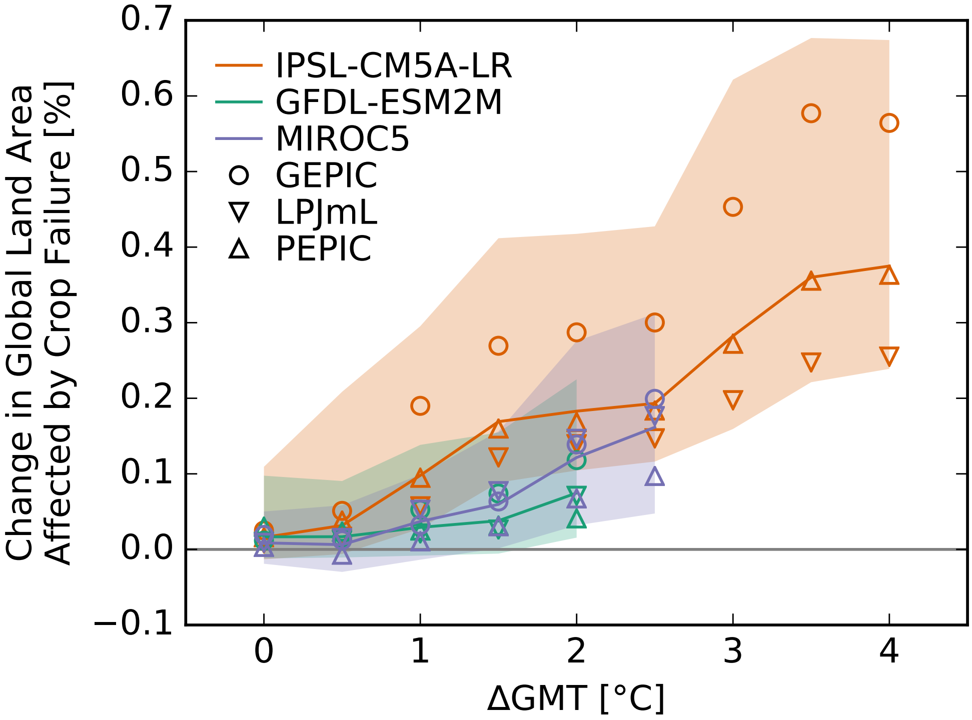

Figure S12: **Pure effect of climate change on global land area fraction affected by crop failures.** Absolute change in global land area fraction affected (AFA) by crop failures at different levels of global mean temperature (GMT) change relative to the long-term pre-industrial mean GMT as simulated by different impact models (symbols) driven by different GCMs (colors). Symbols indicate the impact model-GCM combination-specific median response to global warming (these are identical to the red solid lines in Panel D of Figures S87 . . . S95). Solid lines are the medians over all impact models per GCM. The shaded areas are the corresponding 20th-to-80th percentile ranges.

To estimate the area affected by crop failure we assume that it only affects the fraction of the grid cell where the crop is grown under irrigated and rainfed conditions, respectively. To estimate the total area affected the individual affected areas are added up across the different crops and irrigation settings.

Historical expansion of cropland alone lead to an increase in areas affected by crop failure (as a fraction of the global land area) simply because more land is used for cropping activities and all cropland is subject to crop failure (2.5 percentile). This is visible in the results of the crop models assuming pre-industrial climate (see gray dots in panel A of Figures S87 . . . S95). In addition, the annual variability of the global land area affected by crop failure increases with the expansion of global cropland. On top of this increase in variability that is driven by the expansion of cropland, we find that climate change drives further increases in crop failure. In spite of the CO_2 fertilization effect all models show an increase in areas affected by crop failure with increasing levels of global warming (see dots with color of black, yellow, and blue in Figures S87 . . . S95). This increase in areas affected is robust across all GCMs and GGCMs, even though the uncertainty between different climate scenarios and crop models is substantial. For the climate scenarios, this is mainly due to how spatial and temporal patterns of climate change overlap with cropland and growing seasons, whereas the differences between GGCMs stem from different assumptions in crop management systems and model-specific differences [18, 47]. There is no evident difference between the impacts of the concentration pathways RCP2.6

and 6.0 for a given change in GMT (Figures S87 ... S95). An exception is MIROC5, where impacts are often stronger for RCP2.6 in the +1 °C to +2 °C bin than for RCP 6.0 (Figures S89, S92, S95).

4.2 People exposed

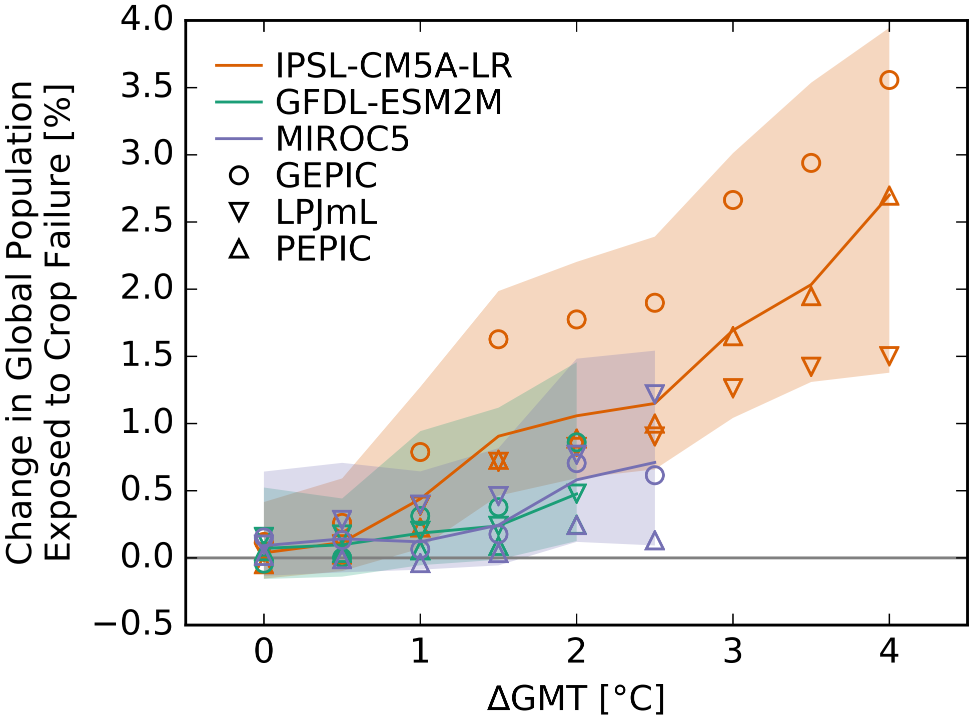

Figure S13: **Pure effect of climate change on global population fraction exposed to crop failures.** Absolute change in global population fraction exposed (PFE) to crop failures at different levels of global mean temperature (GMT) change relative to the long-term pre-industrial mean GMT as simulated by different impact models (symbols) driven by different GCMs (colors). Symbols indicate the impact model-GCM combination-specific median response to global warming (these are identical to the red solid lines in Panel D of Figures S96 ... S104). Solid lines are the medians over all impact models per GCM. The shaded areas are the corresponding 20th-to-80th percentile ranges.

When calculating the number of people exposed to crop failure we only account for local effects on people working in agriculture. Crop failure is expected to have widespread effects on global crop prices and the risk of hunger. However, these effects are not captured by our analysis. If fraction A_{failure} of the land area of a grid cell is affected by crop failure, then the fraction P of the population of that grid cell that is exposed to that crop failure is calculated as

$$P = F \frac{A_{\text{failure}}}{A_{\text{agriculture}}},$$

where F is a national estimate of the fraction of the total population working in agriculture, and $A_{\text{agriculture}}$ is the area fraction of the grid cell used for agriculture. The factor $A_{\text{failure}}/A_{\text{agriculture}}$ is supposed to estimate the fraction of the local population working in agriculture that is exposed to the crop failure. This factor is smaller than one in cases where not all of the crops grown in the grid cell failed. Gaps in the national time series of employment in agriculture have been filled by linear interpolation and the fraction is assumed to stay constant before the first and the last available data point at the first and last available value, respectively. In contrast to the area affected, the historical reduction in employment in agriculture leads to decreasing numbers of people directly (see definition above) exposed to crop failure under pre-industrial climate conditions over the historical period according to the applied definition (see gray dots in Panel A of Figures S96 ... S104). In addition the inter-annual variability of the numbers also decreases. However, the number of people exposed to crop failure is consistently increasing with global warming, which is mainly due to expanded areas affected despite population reduction in employment in agriculture.

4.3 Occurrence probability at grid scale

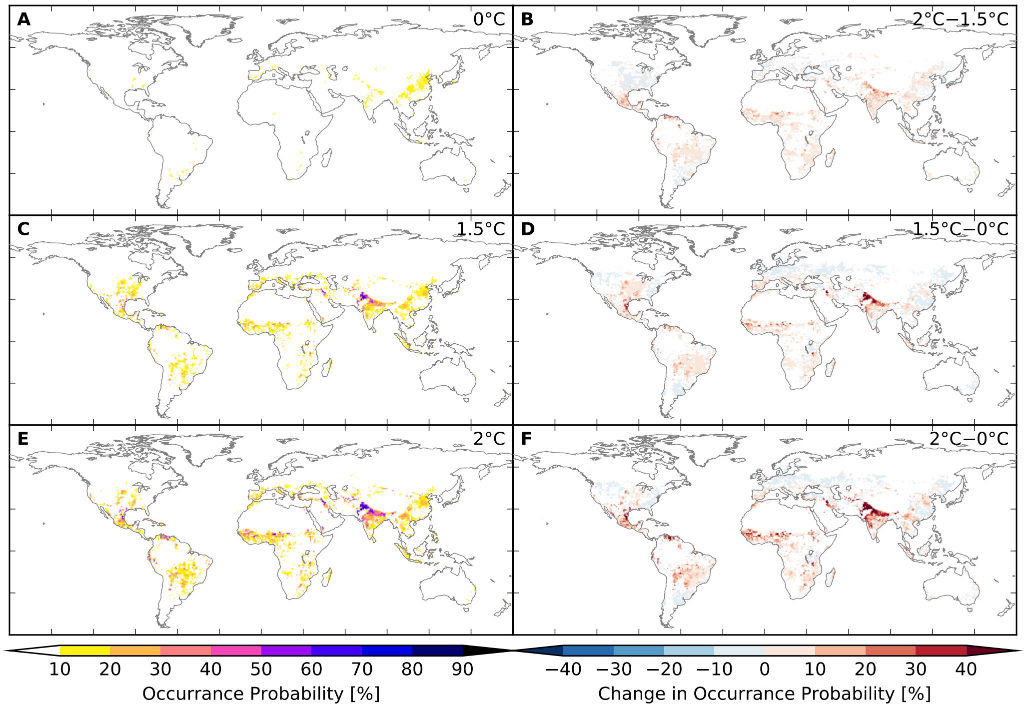

Figure S14: **Probability of occurrence of at least one crop failure event per year at different levels of global mean temperature.** Panels A, C, E: Probabilities at 0 °C, 1.5 °C, 2 °C, respectively. Panels B, D, F: Differences between probability at 2 °C and 1.5 °C, 1.5 °C and 0 °C, 2 °C and 0 °C, respectively. White in panels B, D, F indicates that less then 66 % of the impact model-GCM combinations agree on the sign of the difference. The impact model-GCM combination-specific occurrence probabilities are shown in Figures S105 . . . S113.

The occurrence of crop failure at the grid-cell level is a function of the actual distribution of crops in these grid cells as well as their climate-induced variability causing yields to be lower than the predefined yield threshold (2.5 percentile per crop and irrigation system and pixel under pre-industrial conditions). As such, regions where multiple crops are being cultivated are more likely to experience crop failures than regions with only a single crop, as e.g. western Australia, where basically only rainfed wheat is cultivated (of the four crops considered here).

At 0 °C warming (pre-industrial conditions), the highest probability of crop failures occurs for temperate and tropic regions, foremost in South and East Asia (Figure S14 panel A). Similar to earlier findings [53, 12], tropical regions see an increase in the probability of crop failure at both 1.5 °C and 2 °C warming (Figure S14 panels C–F). Both the highest occurrence probabilities and highest increases in probabilities are expected in presently semi-arid regions or tropical and temperate regions that are prone to crop failure also at 0 °C warming. Hotspots are the Indo-Gangetic Plain, Sudano-Sahelian belt and Central America. At 2 °C warming, spatial patterns remain similar to impacts at 1.5 °C but exhibit higher magnitudes (Figure S14 panels B,E,F). Decreases in crop failure occurrence probabilities with global temperature increase are foremost found for presently temperate and cold regions. The aforementioned hotspot regions of adverse impacts are also the locations in which most crop model-GCM combinations agree on the sign of the impact (Figures S105 . . . S113). Noticeable differences in impact estimates among crop model-GCM combinations occur e.g. for Central to Southern Africa and North America, which is - depending on the corp - in agreement with an earlier crop model intercomparison study [53].

5 Calculation of area affected by and people exposed to wildfires

Wildfire areas are derived from five Global Vegetation Models (GVM) (see Table SX). All GVMs are forced by bias-corrected daily climate data provided within ISIMIP2b [22]. With the exception of ORCHIDEE, all GVMs have been run on a 0.5° grid resolution. ORCHIDEE has been run on a 1° grid resolution because of computational constraints. All GVMs assume fixed socioeconomic conditions (e.g. changes in land use patterns) before 1860 (1860soc for 1661–1860 according to the ISIMIP2b protocol) and account for land-use changes and nitrogen deposition during the historical period (histsoc for 1861–2005 according to the ISIMIP2b protocol). After 2005 socio-economic conditions are held constant at present-day levels (2005soc for 2005–2100 or 2005–2300, respectively, according to the ISIMIP2b protocol).

The main elements of the fire modules used in the DVMs are described in Table S6. All GVMs assume that fires burn only natural vegetation and all GVMs simulate dynamic vegetation distribution over time (with the exception of VISIT).

Table S6: Main characteristics of the GVM fire models.

	Random ignition?[1]	Ignition factors?[2]	Human influences?[3]	Fire spread/extent?[4]
CARAIB [14]	yes	• availability of fuel • combustibility of fuel (soil moisture) • presence of ignition source	no	• function of soil moisture and wind speed
LPJ-GUESS [65]	yes	• soil moisture threshold for available litter associated with plant productivity	no	• empirical relationship between the length of the fire season and the annual area burned where the length of the fire season is derived from the number of fires initialized in the considered
LPJmL [71, 9, 59]	no	• availability of fuel • combustibility of fuel (soil moisture)	no	• empirical relationship between the length of the fire season and the annual area burned where the length of the fire season is derived from the number of fires initialized in the considered year

Table S6: Main characteristics of the GVM fire models, continued…

	Random ignition?[1]	Ignition factors?[2]	Human influences?[3]	Fire spread/extent?[4]
ORCHIDEE [70, 81, 82]	yes	• availability of fuel • combustibility of fuel (soil moisture) • presence of ignition source	both human ignitions and suppression are implicitly included in a single equation based on population density	• function of fuel load, fuel compact status, fire intensity and wind speed -final fire extent is determined by an assumed mean fire size derived from fire spread rate and duration, and the number of effective ignitions
VISIT [35, 34]	no	• fuel load (litter) • fuel combustibility (moisture content of upper soil layer)	no	• fire extent is an empirical function of soil moisture and fuel load

---

[1] Random fire ignition as a random process?
[2] What are the factors influencing ignition?
[3] Are there human influences on fire ignition?
[4] How is fire spread/extent modeled?

5.1 Areas affected

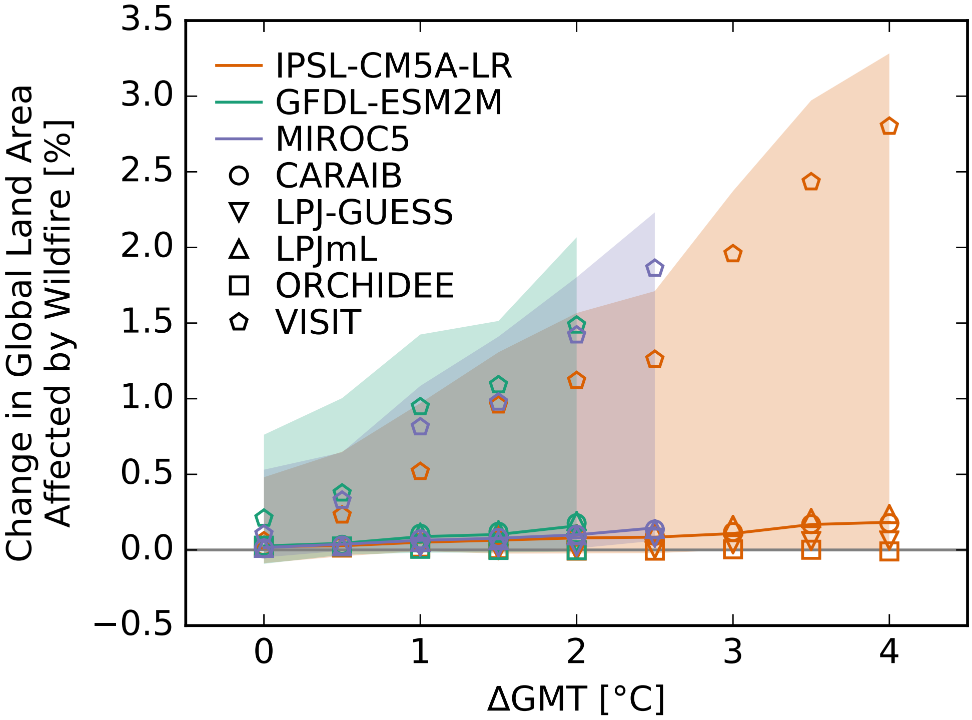

Figure S15: **Pure effect of climate change on global land area fraction affected by wildfires.** Absolute change in global land area fraction affected (AFA) by wildfires at different levels of global mean temperature (GMT) change relative to the long-term pre-industrial mean GMT as simulated by different impact models (symbols) driven by different GCMs (colors). Symbols indicate the impact model-GCM combination-specific median response to global warming (these are identical to the red solid lines in Panel D of Figures S114 . . . S127). Solid lines are the medians over all impact models per GCM. The shaded areas are the corresponding 20th-to-80th percentile ranges.

The global land area fraction affected by wildfire is directly derived from the monthly data of burnt areas provided by the considered GVMs. The annual area fraction affected by wildfire is calculated as the sum of these monthly values, assuming that an area that has burnt during one month of a year is very unlikely to burn again during another month of the same year because there will not be enough fuel left for a subsequent fire. This assumptions holds true for most of the globe [6]. Fire return intervals may only be smaller than one year in strongly fire-dominated ecosystems such as in Sub Saharan Africa [5]. Instead, we expect that two other factors neglected by the GVMs will lead to an underestimation of the simulated global area affected by wildfire: the GVMs do not account for fire being intentionally or unintentionally used to clear natural vegetation as part of land-use changes. Correspondingly, the GVMs simulate a global area affected by wildfire in the 20th century ranging from 0.05–1.2 % per year with the exception of VISIT for which the global area affected by wildfire in the 20th century reaches about 5.5 % per year for some years. Hence, most GVMs underestimate the global area affected by wildfire reconstructed from a wide array of sources over the same period of about 4 % per year [46]. Just like the GVMs, this reconstruction does not account for burning of agricultural wastes, nor for prescribed burning as part of landscape clearing or deforestation [46]. Overall, It does however account for a wider range of fires than considered by the GVM such as fires escaping from agricultural lands and land clearing as reported by firefighters. One reason why VISIT is overestimating the global burned area, might be that VISIT is the only GVM in or ensemble that does not simulate dynamic vegetation which might lead to increasing maladaptation of regrowing vegetation after a fire to further climate changes.

Separation of pure effect of climate change from direct human influences
While CARAIB and LPJmL show a clear decrease of the global area affected by wildfire in the

historical period that is driven by changing land use only, ORCHIDEE, VISIT and LPJ-GUESS only show minor changes partly even increasing the global area affected by wildfire (see gray dots in panels A of Figures S114 … S127). This effect of land use change also dominates the historical simulations of CARAIB and LPJmL where burnt areas substantially decrease. The pure climatic effect during the historical period is weak but slightly increases global area affected by wildfire (black dots in panel C). The pure climatic effect during the future time periods leads to a clear increase in the global area affected by wildfire for CARAIB, VISIT and LPJmL (blue and yellow dots in panel C). For LPJ-GUESS and ORCHIDEE, the direct climatic effect in the future time period is less clear: under RCP6.0 the median global area affected by wildfire increases, while for RCP2.6 the global area affected by wildfire decreases or increases. Generally, increasing GMT leads to an increase in global area affected by wildfires beyond the pre-industrial and historical levels in all considered GVMs except for ORCHIDEE (blue and yellow dots in panel D). For ORCHIDEE, the effects of increasing CO_2 on plant water relations might increase soil moisture and hence reduce combustibility of the fuel leading to decreasing global area affected by wildfire. These patterns of decreasing global area affected by wildfire with increasing land-use change in CARAIB and LPJmL seem counter-intuitive at a first glance because historically fire has been a key tool to clear natural vegetation [10]. However, as noted above, the considered GVMs do neither capture the application of fire as a way to clear land nor the associated risk of burning adjacent natural vegetation unintendedly through escaping fires. The decrease of global area affected by wildfire with changing land use in the historical period is due to a reduction in area covered by natural vegetation which reduces the overall area available to burn as the considered biomes models only allow for wildfires in natural vegetation. This mimics historical tendencies to suppress fires on agricultural and other human-dominated lands [51, 39]. It however also means that, because the pure climatic effect is increasing the global area affected by wildfire and because concomitantly the area available to burn is decreasing, the fire risk for the remaining natural vegetation is increasing.

5.2 People exposed

We assume that the fraction of the population of a grid cell that is exposed to a wildfire occurring in that grid cell scales with the grid cell's area fraction affected by the wildfire. Therefore, the fraction of the population exposed to wildfire is set equal to the fraction of the grid cell area affected by wildfire at the 0.5° grid level. Before 1860 and after 2005, population data were held fixed at 1860 and 2005 levels, respectively. Compared to the global land area fraction affected by wildfire, the fraction of population exposed to wildfire is slightly higher throughout all GVMs and GCM combinations ranging between 2–12 % per year for VISIT and between 0–1.2 % per year for all other models. This suggests that an area affected by wildfire houses slightly more people than an average area.

Separation of pure effect of climate change from direct human influences LPJmL, ORCHIDEE, CARAIB and VISIT (the latter two only when driven by MIROC5) show a decrease of the global population affected by wildfire in the historical period that is driven by changing land use only, LPJ-GUESS, CARAIB and VISIT (the latter two when driven by GFDL-ESM2M and IPSL-CM5A-LR) only show minor changes partly increasing the global population affected by wildfire (see gray dots in panels A of Figures S128 … S141). Whenever effects of land use change occur, they are also visible in the historical simulations. The pure climatic effect during the historical period is rather weak but slightly increases global population affected by wildfire in most GVM-GCM combinations (black dots in panel C). The pure climatic effect during the future time periods leads to a clear increase in the global population affected by wildfire for CARAIB, VISIT and LPJmL (blue and yellow dots in panel C). For LPJ-GUESS and ORCHIDEE, the direct climatic effect in the future time period is less clear: for LPJ-GUESS under RCP6.0 the median global population affected by wildfire increases, while for RCP2.6 the global population affected by wildfire decreases or increases depending on the GCM. For ORCHIDEE, the direct climatic effects are small but clearly decrease global population affected by wildfire. Generally, increasing GMT leads to an increase in global population affected by wildfire beyond the pre-industrial and historical levels in all considered GVM except for ORCHIDEE (blue and yellow dots in panel D) mirroring the effects of climate change on the global area affected

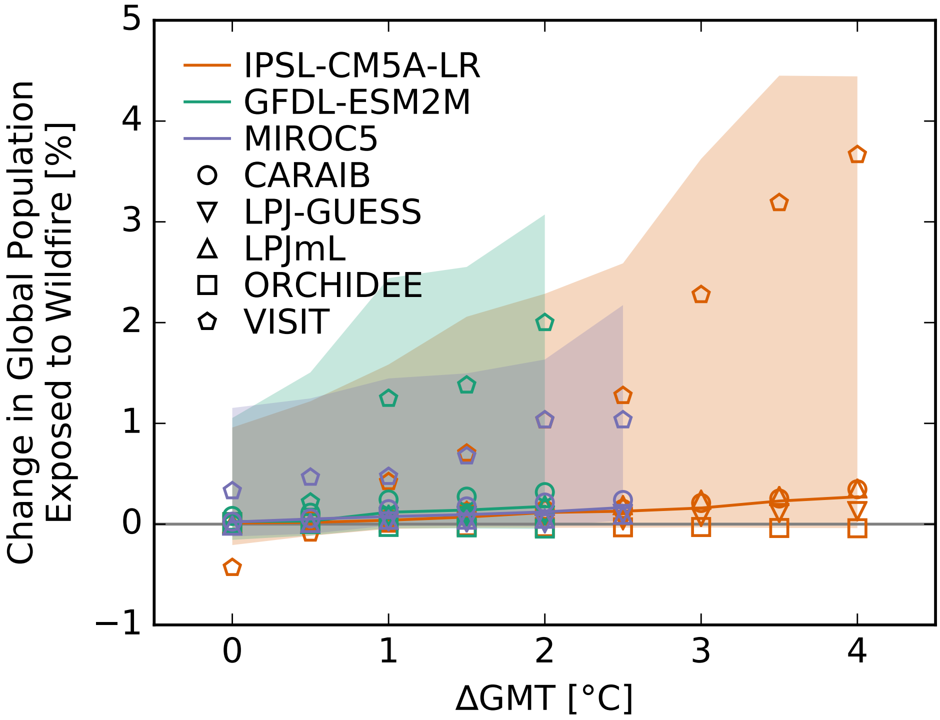

Figure S16: **Pure effect of climate change on global population fraction exposed to wildfires.** Absolute change in global population fraction exposed (PFE) to wildfires at different levels of global mean temperature (GMT) change relative to the long-term pre-industrial mean GMT as simulated by different impact models (symbols) driven by different GCMs (colors). Symbols indicate the impact model-GCM combination-specific median response to global warming (these are identical to the red solid lines in Panel D of Figures S128 . . . S141). Solid lines are the medians over all impact models per GCM. The shaded areas are the corresponding 20th-to-80th percentile ranges.

by wildfire described above.

5.3 Occurrence probability at grid scale

To calculate the occurrence probability of extre at grid scale, a grid cell is considered to be affected by wildfires if the burned area exceeds the 97.5th percentile of the pre-industrial reference distribution. Such focus on fires considered to be large relative to their given spatio-temporal context aligns well with recent criticism to classify mega-fires simply on a global threshold such as an areal extent of $> 10\,000$ ha [68]. However, our definition excludes recent claims to classify mega-fires based on their impact on society and not their area extent [68, 77].

Figures S142 . . . S155 show that fires which were extremely rare without climate change (panel A) are covering large parts of the Earth's vegetated land under 1.5 °C warming (Panel C) with occurrence probabilities ranging mostly between 5–25 %. This increase in extreme fire probability further intensifies under 2 °C warming (Panel E) but quite uniformly around the globe and by less than 10 % (Panel B). The regions with the highest fire activity in the recent past, Sub Saharan Africa and Northern Australia [6], seem to be already characterized by such large fires and short intervals between fires that our analysis does not reveal further increases in extreme fire occurrence probability.

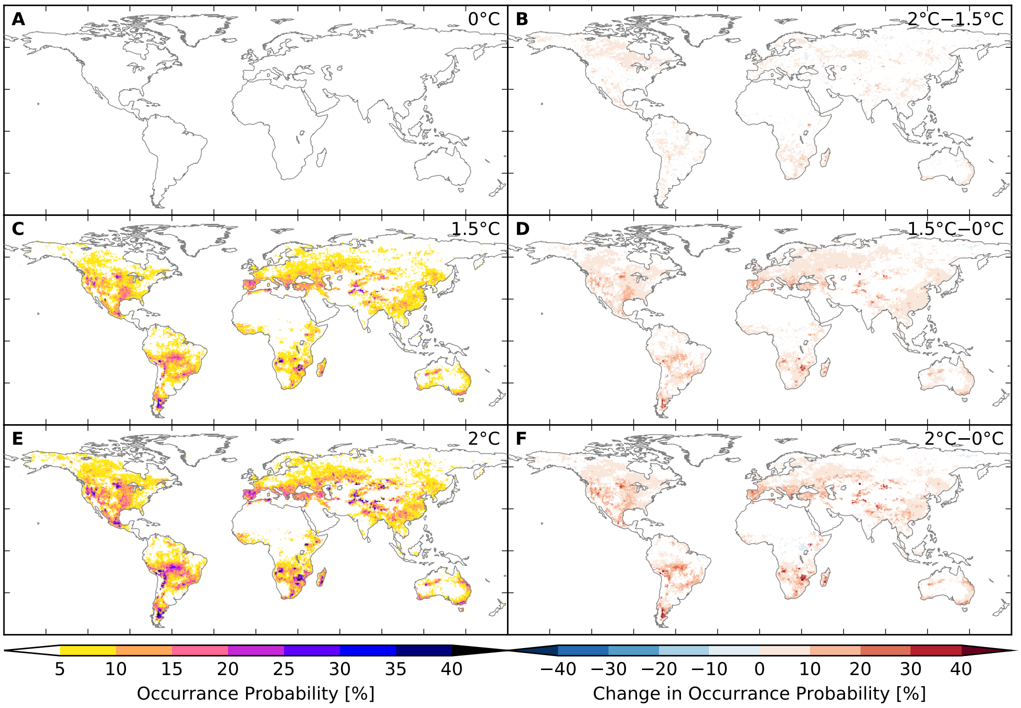

Figure S17: **Probability of occurrence of at least one wildfire event per year at different levels of global mean temperature.** Panels A, C, E: Probabilities at 0 °C, 1.5 °C, 2 °C, respectively. Panels B, D, F: Differences between probability at 2 °C and 1.5 °C, 1.5 °C and 0 °C, 2 °C and 0 °C, respectively. White in panels B, D, F indicates that less then 66 % of the impact model-GCM combinations agree on the sign of the difference. The impact model-GCM combination-specific occurrence probabilities are shown in Figures S142 . . . S155.

6 Calculation of area affected by and people exposed to droughts

Severe drought conditions are defined by monthly soil moisture [13, 63] falling below the 2.5th percentile variable monthly threshold, based on using of the pre-industrial reference distribution (1661–1859), for at least 7 consecutive months [62]. Moisture in the top meter of soil shows the combined effects of processes like precipitation, soil evaporation, plant transpiration, infiltration, runoff, snow accumulation and melt, and is therefore a good indicator for drought conditions [64]. The monthly soil moisture information used in this study that was provided by the individual hydrological models refers to soil layers of different thicknesses (see Table S4). Here we use root moisture as directly provided by H08, MPI-HM, and WaterGAP2. To approximate this variable we integrated soil moisture across the first three layers considered in JULES-W1 (up to a depth of 1 m), the first three layers of LPJmL (up to a depth of 1m), and the first 9 layers of ORCHIDEE (up to a depth of 75 cm). Further propertief of the models are shown in Table S4.

The variable monthly threshold level method [72, 2, 49, 31, 73] was applied here to distinguish periods of soil moisture drought from periods of no drought. The use of a variable monthly threshold accounts for seasonal climatology [64, 31], which is relevant for the management of water resources.

For each month individually we identified per model and climatological forcing combination the 2.5th percentile soil moisture value at the grid-level, using the pre-industrial scenario as reference period. Using these spatially and monthly explicit threshold-levels we, subsequently, evaluated for the different scenarios applied how often the soil moisture conditions fall below this threshold. Subsequently, we applied a six-month threshold to distinguish the longer, prolonged drought events from the short, incidental ones [63]. Only these prolonged droughts were taken into account when evaluating the land area and population exposed to drought conditions at the yearly scale. In doing so, we checked for each year whether a grid-cell was exposed to at least one of a period of prolonged droughts (i.e. drought conditions that last longer than 6 months). In case the grid-cell was exposed this cell was accounted as ‘being exposed to drought’ for that respective year, in case the grid-cell was not exposed to drought conditions or only to relatively short drought conditions, the grid-cell was classified as ‘not exposed to drought’ for that respective year.

To evaluate the impacts of human actions and climate change on the occurrence and spatial extent of droughts we superimpose the critical drought thresholds that were defined for the pre-industrial reference period over the scenarios that represent the historical (including human actions) and/or climate change conditions (including both human actions and climate change impacts). Hence, the difference in exposure between these scenarios give indication to the attribution of climate change and human activities to droughts. It must be said, though, that with such an approach we only evaluate the attribution of climate change and human activities to the increase in the exposure of drought events in time and place. Any changes in the severity of drought conditions, nor in the duration or of frequency (if consistently lower or higher than 6 months) of drought events at sub-yearly scales were not accounted for in this evaluation.

6.1 Areas affected

To estimate the area affected by drought, we sum the grid cells with a fraction of the grid cell suffering drought. To estimate the total area affected the individual affected areas are added up.

For pre-industrial climate conditions and 1860/2005 socio-economic conditions, the distribution of the annual global land area fraction affected (AFA) remains almost constant for all model and GCM combinations. Such ranges vary depending on the model and GCM combination, but are mostly within the 2 % and never go beyond the 5 %.

For historical climate conditions, the pure effect of climate change in AFA by drought for H08 and WaterGAP2 is small, as the differences between the annual AFA by drought and the median of the simulations assuming pre-industrial climate conditions are of at most 2 %. For JULES-W1, PCR-GLOBWB, ORCHIDEE, MPI-HM and LPJmL, the change in AFA by drought increases over time, and such ranges depend on the model and GCM, but in general reach the 4 %. These results are in line with Dai [13], who showed an increasing trend in drought exposure between 1950 and 2010 using a Palmer Drought Severity Index (PDSI) based drought indicator. According to Dai [13], the

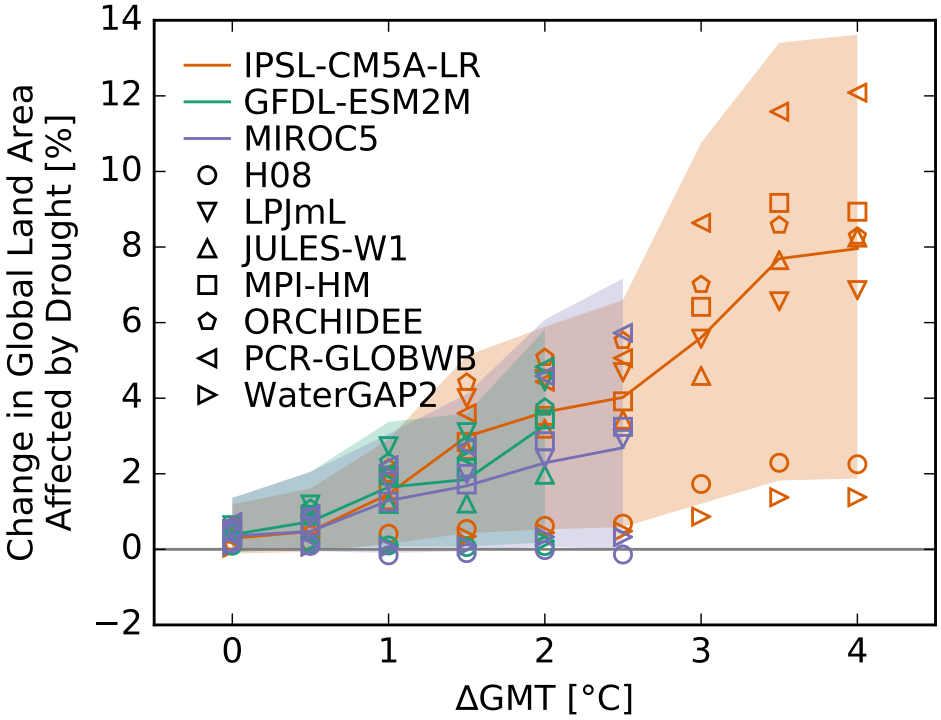

Figure S18: **Pure effect of climate change on global land area fraction affected by drought.** Absolute change in global land area fraction affected (AFA) by drought at different levels of global mean temperature (GMT) change relative to the long-term pre-industrial mean GMT as simulated by different impact models (symbols) driven by different GCMs (colors). Symbols indicate the impact model-GCM combination-specific median response to global warming (these are identical to the red solid lines in Panel D of Figures S156 . . . S174). Solid lines are the medians over all impact models per GCM. The shaded areas are the corresponding 20th-to-80th percentile ranges.

global land area affected by drought has an initial increase of around 0.5 % by 1950, which grows up to 5 % by 2010. Dai [13] showed that increasing global temperatures since the 1980s have contributed significantly to the increase in land areas exposed to drought globally (+8 %), mainly as a result of increased evaporation.

The increase in AFA by drought starting in the historical period highlights the effects of human forcing. WaterGAP2 and H08 models show little increase in the AFA by drought, while other models show significantly larger effects. All models include human impacts, but they do so in a different way. Methods of human impact parameterization may give rise to the differences in the observed impacts and it would be worth to analyze this further.

For RCP2.6 climate conditions, the change in AFA by drought for H08 and WaterGAP2 follows the same behavior as for the historical climate conditions. For all other models, the change in AFA by drought increases in time, reaching up to 8 %. For RCP6.0 climate conditions, the change in AFA by drought increases over time for all models. Such change is small for H08 and WaterGAP2, where the largest change occurs for H08 + IPSL-CM5A-LR, reaching the 8 %, but remains under 2 % for all other cases. For all other models and GCMs, the change is larger, reaching up to 15 % for PCR-GLOBWB + IPSL-CM5A-LR. All of Dai [13], Lehner et al. [41] and Sheffield & Wood [63] support our observations of increases in drought exposure under climate change. Dai [13] suggest that severe and widespread droughts will occur in the next decades over many land areas as a result of either decreased precipitation and/or increased evapotranspiration. The results of Lehner et al. [41] indicate for many global land areas a widespread drying under both 1.5 °C and 2.0 °C degree climates, for example in the Mediterranean, central Europe, the Amazon, and southern Africa. Sheffield & Wood [63] show that most models show decreases in soil moisture globally under future projections which results in a doubling of the area exposed to severe soil moisture deficits and the frequency of short term soil moisture droughts. Longer, prolonged droughts triple under the scenarios applied by Sheffield

& Wood [63], although model results vary.

6.2 People exposed

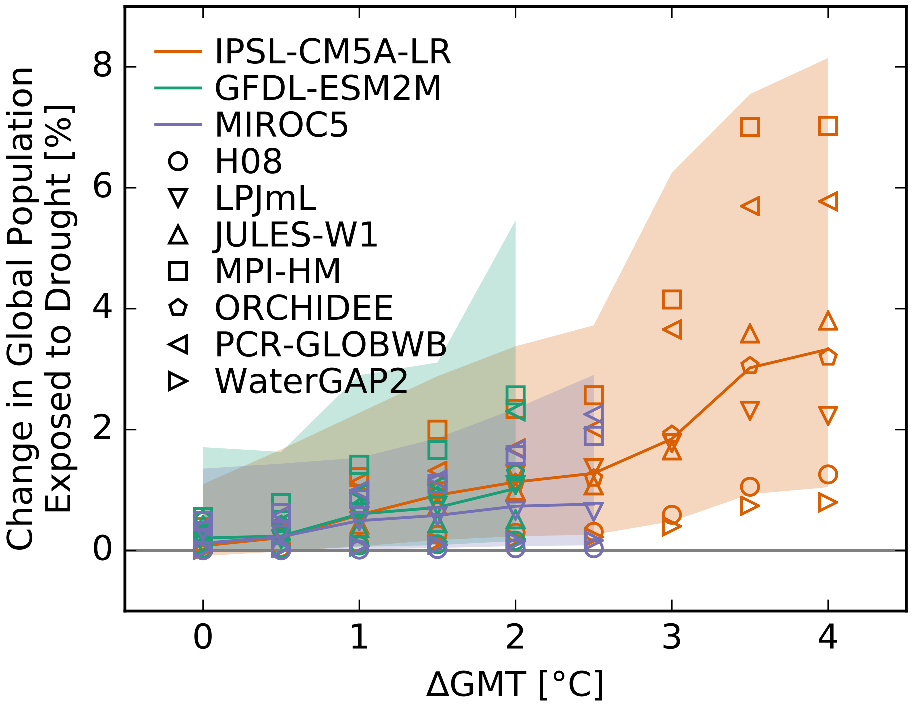

Figure S19: **Pure effect of climate change on global population fraction exposed to drought.** Absolute change in global population fraction exposed (PFE) to drought at different levels of global mean temperature (GMT) change relative to the long-term pre-industrial mean GMT as simulated by different impact models (symbols) driven by different GCMs (colors). Symbols indicate the impact model-GCM combination-specific median response to global warming (these are identical to the red solid lines in Panel D of Figures S193 . . . S211). Solid lines are the medians over all impact models per GCM. The shaded areas are the corresponding 20th-to-80th percentile ranges.

The fraction of the population of a grid cell exposed to drought scales with the area of the grid cell affected by drought at the 0.5° grid level. Before 1860, the population is fixed at 1860 levels, and after 2005, the population is fixed at 2005 levels.

The behavior of the time series of annual global population fraction exposed (PFE) to drought is very similar to the one seen in the AFA by drought. The difference is in the percentage of change due to the pure effect of climate change in PFE, which is considerably smaller.

For pre-industrial climate conditions, the percentage of the global population exposed to drought ranges for all models between 0.2 % and 5 %, being H08 and WaterGAP2 the models with smaller percentages of PFE, up to 2 %. The change of PFE due to historical climate conditions shows a small increase over time for all models, being IPSL-CM5A-LR + MPI-HM the one with the largest change over time, from 3 % to 6 %. For RCP2.6 and RCP6.0 climate conditions we see consistent increments in the PFE to drought over time, being the largest changes under the IPSL-CM5A-LR GCM, which reaches up to 10 % change for PCR-GLOBWB and 12 % for MPI-HM.

Despite the similar behavior in trends for the AFA and PFE to drought, the lower percentages found in the pure effect of climate change may be due to the population being unequally distributed, which introduces changes in exposure of to soil moisture.

An interesting feature of these results is the decrease in the PFE to drought for historical climate conditions for most models, being the decrease more significant for LPJmL and PCR-GLOBWB, two models considering reservoir storage and detailed land-use classification [66]. This finding also suggests a strong effect of the population density, growth and distribution, which should be considered for further analysis.

It is also worth mentioning that the exposure to this drought calculation does not take into account vulnerability, i.e. how much water one would need to accommodate its daily needs [27]. This, being a relative threshold on a specific hydrological condition, does not consider the absolute water availability. Therefore, exposure to drought should not be confused with exposure to water scarcity (water-demand versus water-supply).

6.3 Occurrence probability at grid scale

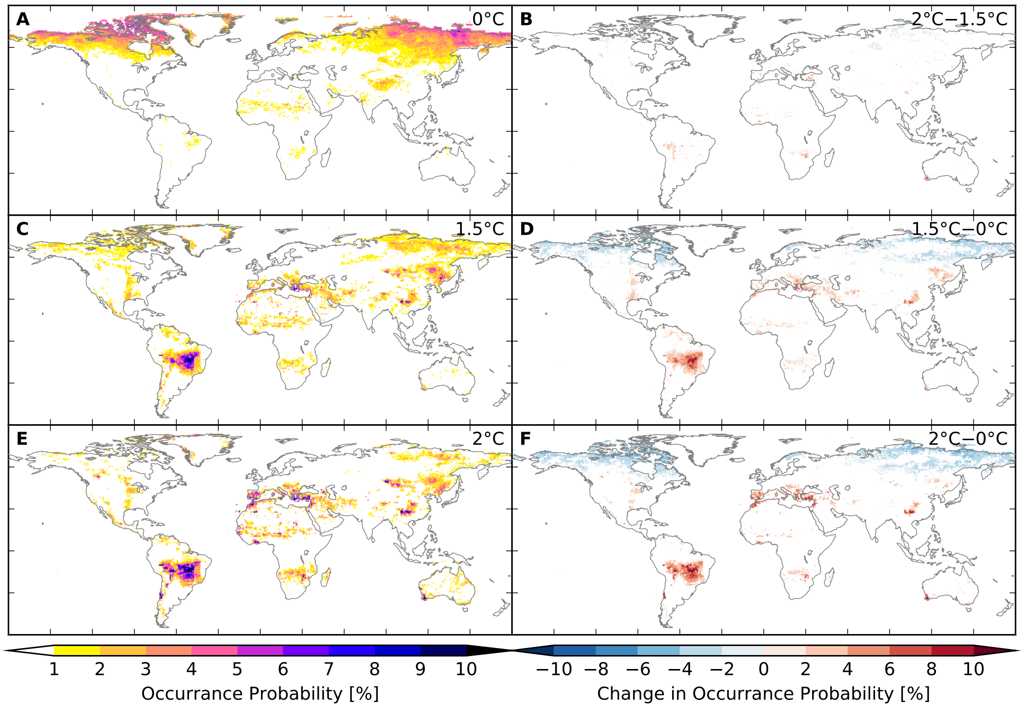

Figure S20: **Probability of occurrence of at least one drought event per year at different levels of global mean temperature.** Panels A, C, E: Probabilities at 0 °C, 1.5 °C, 2 °C, respectively. Panels B, D, F: Differences between probability at 2 °C and 1.5 °C, 1.5 °C and 0 °C, 2 °C and 0 °C, respectively. White in panels B, D, F indicates that less then 66 % of the impact model-GCM combinations agree on the sign of the difference. The impact model-GCM combination-specific occurrence probabilities are shown in Figures S212 . . . S230.

To calculate the occurrence of drought at the 0.5° grid-cell level, a cell is considered affected by drought if it falls below its 2.5th percentile variable monthly threshold, based on the pre-industrial reference distribution for at least 6 consecutive months.

We observe three different behaviors in the occurrence probability of drought at grid scale, with the spatial distribution depending mainly in the model and the intensity on the GCM.

Models H08 and WaterGAP2 are the ones with lower occurrence probabilities, localized mainly in the Amazon and Central Africa. Models JULES-W1 and LPJmL show larger and well localized regions of occurrence probability, both focused in North Africa, Middle East. Both of these models focus on vegetation. JULES-W1 also shows higher occurrence probability in the East part of the US and LPJmL in Central Australia. Finally, MPI-HM, ORCHIDEE and PCR-GLOBWB show wide non-well localized regions with high occurrence probability of drought all over the globe, but mainly in Central Africa, Central Asia, the Amazon and North America.

In comparison with other models, these regions are partially in agreement with [13], who shows increases in drought exposure due to increased warming to be largest over northern mid-high latitudes, and increases in drought conditions in Africa, southeast Asia, eastern Australia and Europe predominantly due to decreases in precipitation.

Lehner et al. [41] show widespread drought under 1.5 °C and 2 °C climates, with significantly more drying at 2 °C compared to 1.5 °C. They show significant drying in the Mediterranean, central Europe, the Amazon, southern Africa, and southern Australia at 1.5 °C and 2 °C, and insignificant changes in the United States of America. Southwest, Central Plains, and Southeast Asia.

There are significant differences between the areas with higher occurrence probability between the models. This, however, is a normal consequence of the definitions of our drought indicator and the characteristics of each of these models, as drought indices can result in somewhat different change patterns, especially on small scales.

7 Calculation of area affected by and people exposed to heat waves

7.1 Areas affected

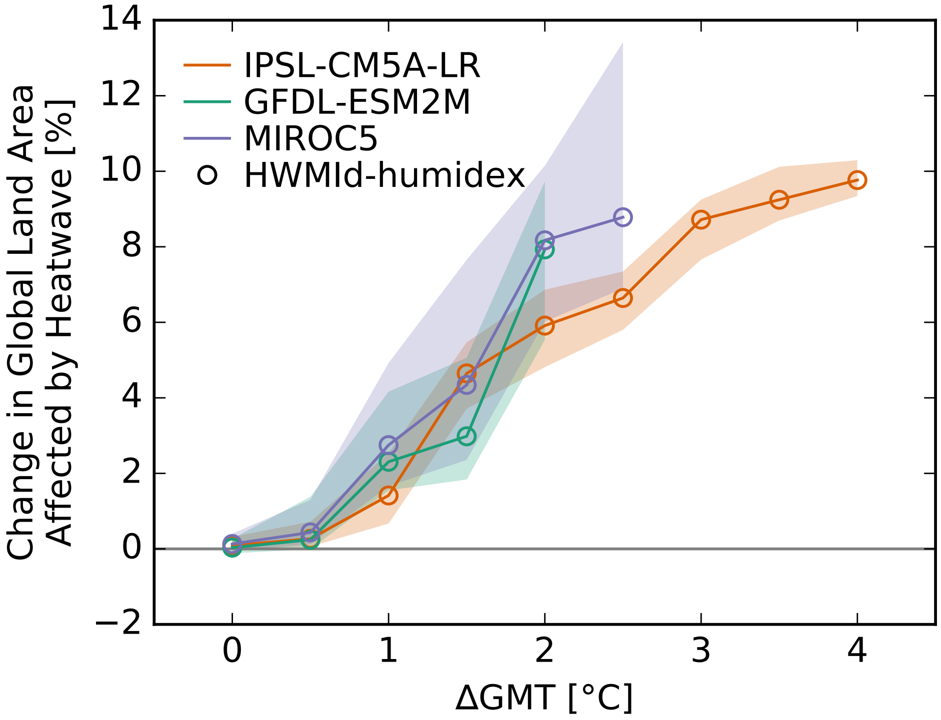

Figure S21: **Pure effect of climate change on global land area fraction affected by heatwaves.** Absolute change in global land area fraction affected (AFA) by heatwaves at different levels of global mean temperature (GMT) change relative to the long-term pre-industrial mean GMT as simulated by different impact models (symbols) driven by different GCMs (colors). Symbols indicate the impact model-GCM combination-specific median response to global warming (these are identical to the red solid lines in Panel D of Figures S231 ... S233). Solid lines are the medians over all impact models per GCM. The shaded areas are the corresponding 20th-to-80th percentile ranges.

Heatwaves are defined based on GCM output of daily mean relative humidity and daily mean and maximum temperature. A grid cell is considered to be affected by a heatwave in a given year if (i) the Heat Wave Magnitude Index daily (HWMId, 55, 56) of that year exceeds the 97.5th percentile of the HWMId distribution under pre-industrial climate conditions of that grid cell, and if (ii) the humidex exceeds 45 on all days of heatwave period corresponding to the HWMId. If both criteria are fulfilled then the area fraction affected by heatwave of the grid cell in that year is set to one, otherwise it is set to zero.

Our heatwave definition combines a relative criterion, which assesses the magnitude of a heatwave relative to magnitudes that are normal under pre-industrial climate conditions, with an absolute criterion that is to prevent us from labeling a period that would be considered exceptionally warm under pre-industrial climate conditions as a heatwave even though the period is not hot enough in an absolute sense to have a negative impact on human health. In the following we describe how HWMId and humidex are defined and computed here.

The HWMId is defined as the maximum magnitude of all hot periods occurring in a year, where a hot period is a period of at least 3 consecutive days with daily maximum temperature exceeding a threshold value T_{pi90} which is defined as the 90th percentile of daily maximum temperatures under pre-industrial climate conditions, centered on a 31-day window. The magnitude of each hot period in a year is the sum of the daily magnitudes on the consecutive days composing the hot period, with daily magnitude calculated according to $M_{\mathrm{d}}(T_{\mathrm{d}}) = 0$ if $T_{\mathrm{d}} \leq T_{\mathrm{pi25}}$ else $(T_{\mathrm{d}} - T_{\mathrm{pi25}})/(T_{\mathrm{pi75}} - T_{\mathrm{pi25}})$ where T_{d} is the daily maximum temperature on day d of the hot period, and T_{pi25} and T_{pi75} are the 25th and 75th percentile, respectively, of the annual maximum of the daily maximum temperature under pre-industrial climate conditions. In order to estimate T_{pi90}, T_{pi25} and T_{pi75}, we use more than 400 years of daily maximum temperature data of 0.5° spatial resolution representing pre-industrial climate conditions as available from the ISIMIP2b climate input data set. Based on these more than 400 years of temperature data we then derive $M_{\mathrm{pi97.5}}$, the 97.5th percentile of the HWMId distribution under pre-industrial climate conditions.

The humidex [1] was developed to capture the experienced effects of hot weather on the human body by combining temperature and relative humidity via the dew point to an effective temperature:

$$\text{Humidex} = T_{\max} + 0.5555 \left[6.11\, e^{5417.7530 \left(\frac{1}{273.16} - \frac{1}{273.15 + T_{\mathrm{dew}}} \right)} - 10 \right].$$

We calculate the humidex at the time of maximum daily temperature using the above formula, the daily maximum temperature for $T_{\max}$, and the daily mean temperature and relative humidity to approximately compute the dew point temperature T_{dew} at the time of maximum daily temperature, exploiting that the dew point does usually not vary much over the course of a day [52, 60]. The Canadian Center for Occupational Health and Safety links the humidex to human stress as follows [20].

20–29	comfortable
30–39	some discomfort
40–45	great discomfort, avoid exertion
above 45	dangerous, heat stroke possible

The resulting probabilities of occurrence are very low under pre-industrial climate conditions, with less than 1 % of the global land area being affected by heatwaves annually. This area fraction rises to about 7 % at 2 °C of global warming, and to about 10 % at 4 °C of global warming. The emissions scenario-dependence of the relationship between global mean temperature change and global land area affected by heatwave is low as are differences between GCMs.

7.2 People exposed

It is assumed that if a grid cell is struck by a heatwave, then all people living in that grid cell are affected by that heatwave. Therefore, the population fraction exposed to heatwave is set equal to the area fraction affected by heatwave at the 0.5° grid level. Less than 1 % of the global population is exposed to heatwaves annually under pre-industrial climate conditions. This fraction rises to about 12 % at 2 °C of global warming, and to 24 % at 4 °C of global warming. The emissions scenario-dependence of the relationship between global mean temperature change and heatwave exposure of the global population is low as are differences between GCMs.

7.3 Occurrence probability at grid scale

Owing to the relative criterion used here to define heatwaves, under pre-industrial climate conditions, the probability of occurrence of a heatwave is less than 2.5 % annually everywhere on the globe. With increasing global mean temperature, an increase in the probability of occurrence of heatwaves over the tropics and subtropics is found for all three GCMs. Already at 2 °C of global warming, various regions are affected by heatwaves every second year or more often. For GFDL-ESM2M and MIROC5, these regions are parts of Latin America, Central America and the Southern USA, Central, East and North Africa, North India and the Persian Gulf region. For IPSL-CM5A-LR, less pronounced probability increases are found in North Africa and around the Persian Gulf and more pronounced probability increases are found in South-East Asia and North Australia.

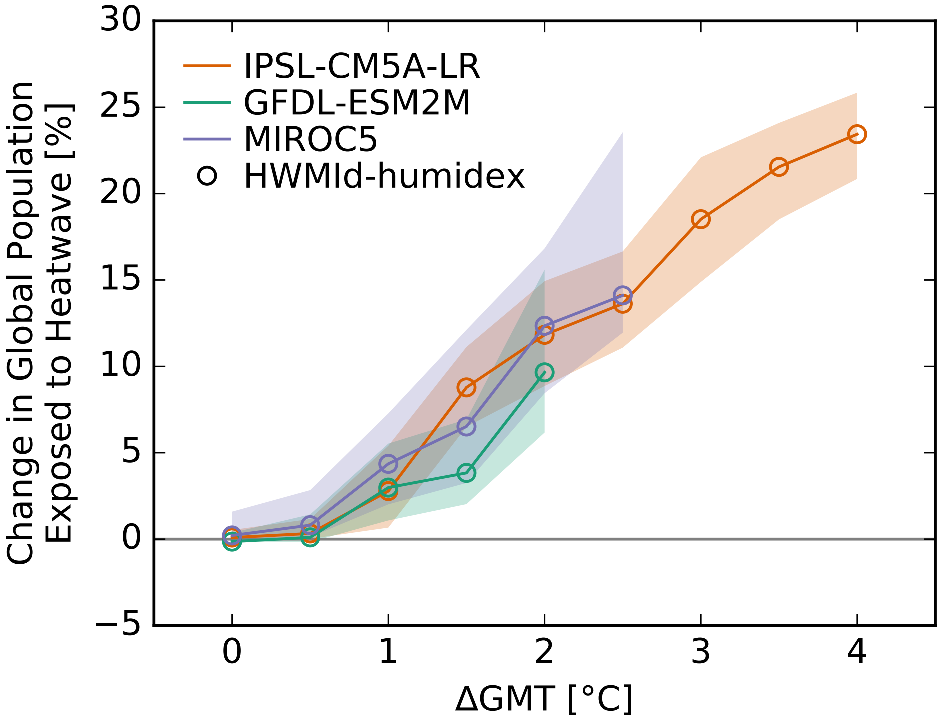

Figure S22: **Pure effect of climate change on global population fraction exposed to heatwaves.** Absolute change in global population fraction exposed (PFE) to heatwaves at different levels of global mean temperature (GMT) change relative to the long-term pre-industrial mean GMT as simulated by different impact models (symbols) driven by different GCMs (colors). Symbols indicate the impact model-GCM combination-specific median response to global warming (these are identical to the red solid lines in Panel D of Figures S234 . . . S236). Solid lines are the medians over all impact models per GCM. The shaded areas are the corresponding 20th-to-80th percentile ranges.

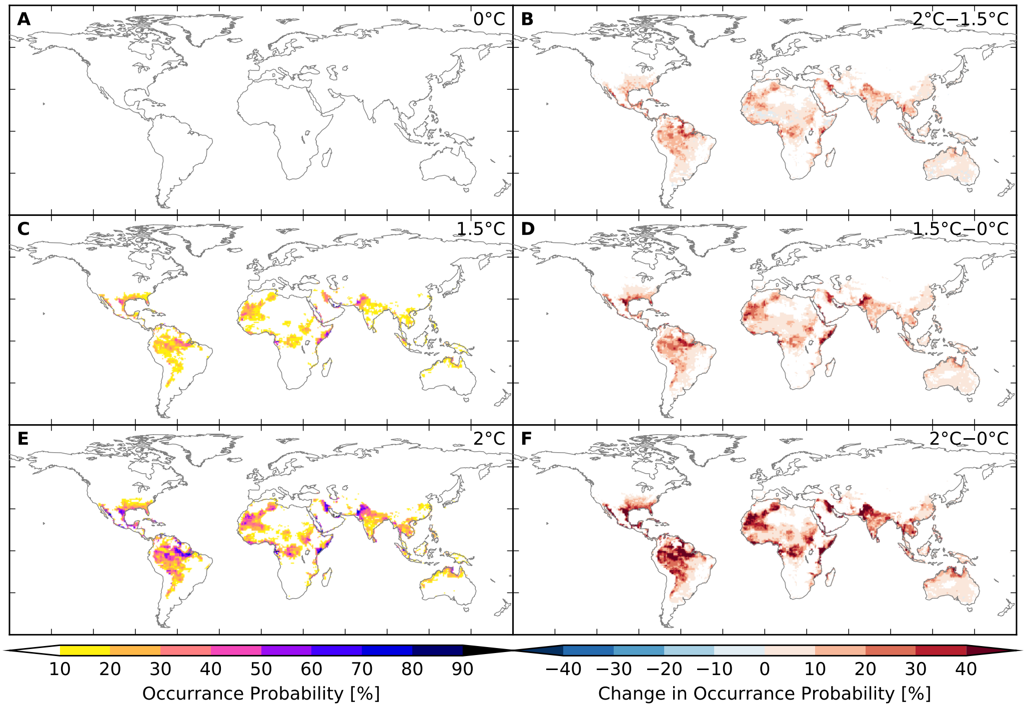

Figure S23: **Probability of occurrence of at least one heatwave event per year at different levels of global mean temperature.** Panels A, C, E: Probabilities at 0 °C, 1.5 °C, 2 °C, respectively. Panels B, D, F: Differences between probability at 2 °C and 1.5 °C, 1.5 °C and 0 °C, 2 °C and 0 °C, respectively. White in panels B, D, F indicates that less then 66 % of the impact model-GCM combinations agree on the sign of the difference. The impact model-GCM combination-specific occurrence probabilities are shown in Figures S237 . . . S239.

8 Model specific results

8.1 Floods

Areas affected

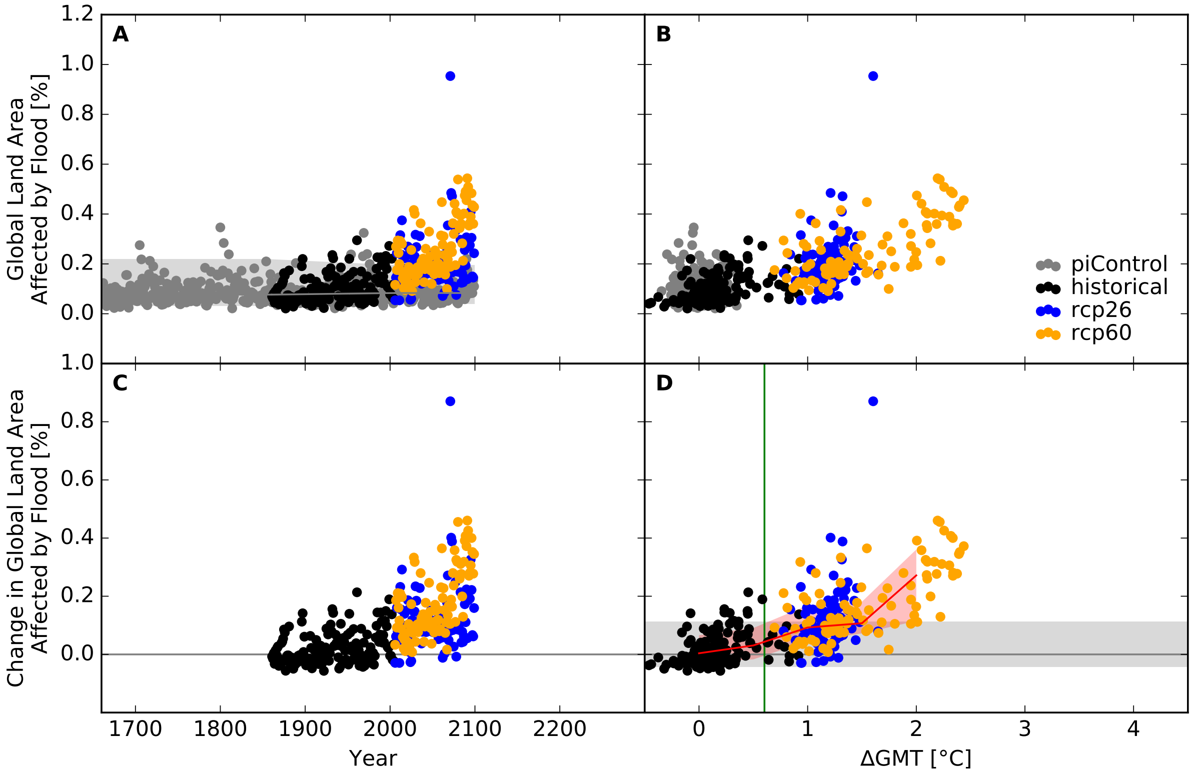

Figure S24: **Derivation of the pure effect of climate change on global land area fraction affected by flood events (GFDL-ESM2M + H08).** Panel A: Time series of annual global land area fraction affected (AFA) by flood events for pre-industrial climate (grey dots), historical climate (black dots), climate projections for RCP2.6 (blue dots), and RCP6.0 (orange dots). In all simulations, socio-economic conditions are varied according to the historically observed development between 1860 and 2005, and held fixed at 1860 conditions before 1860 and at 2005 conditions after 2005. Shaded areas before 1860/after 2005 represent the range from the 2nd to the 98th percentile of the distribution of the annual AFA under pre-industrial climate conditions in combination with 1860/2005 socio-economic conditions; the solid gray lines represent the respective median values; the shaded areas and solid gray line between 1860 and 2005 are linear interpolations of the respective values before 1860 and after 2005. Panel B: Data shown in Panel A plotted against the associated GCM-specific annual global mean temperature (GMT) change relative to the long-term pre-industrial mean. Panel C: Pure effect of climate change on AFA, calculated as the difference between the annual data shown in Panel A and the median of the simulations assuming pre-industrial climate conditions (solid gray line in Panel A). Panel D: Pure effect of climate change on AFA in terms of global mean temperature change, with distributions of the annual data estimated for each 1°C-wide bin of global mean temperature change that contains at least five data points, at least one data point above and at least one data point below the bin center. Areas shaded in red represent the range from the 20th to the 80th percentile around the median (solid red line) of these distributions. Areas shaded in gray represent the range from the 2nd to the 98th percentile of the zero-centered distribution of the annual AFA under pre-industrial climate and 2005 socio-economic conditions (cf. Panel A). The green vertical line represents the detection level defined as the global warming level at which a 1-in-50-years event under pre-industrial climate and 2005 socio-economic conditions becomes a 1-in-5-years event under changing climate and 2005 socio-economic conditions.

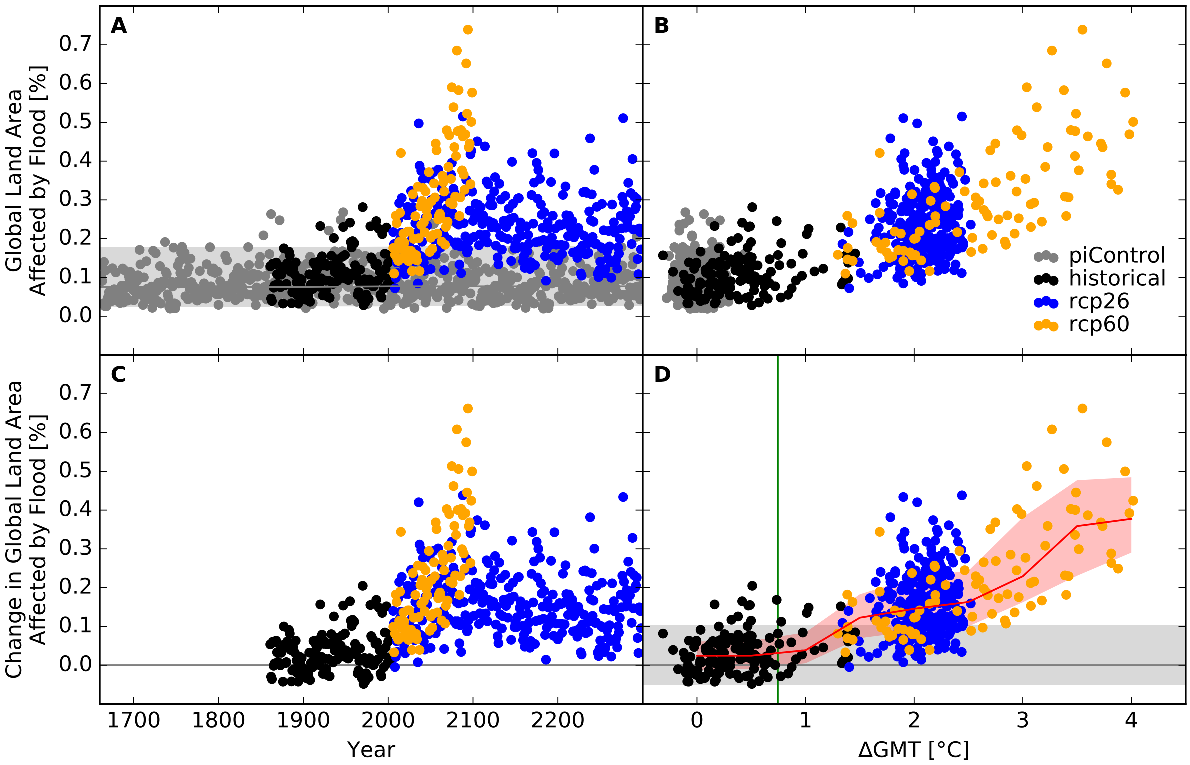

Figure S25: **Derivation of the pure effect of climate change on global land area fraction affected by flood events (IPSL-CM5A-LR + H08).** Analogous to Figure S24.

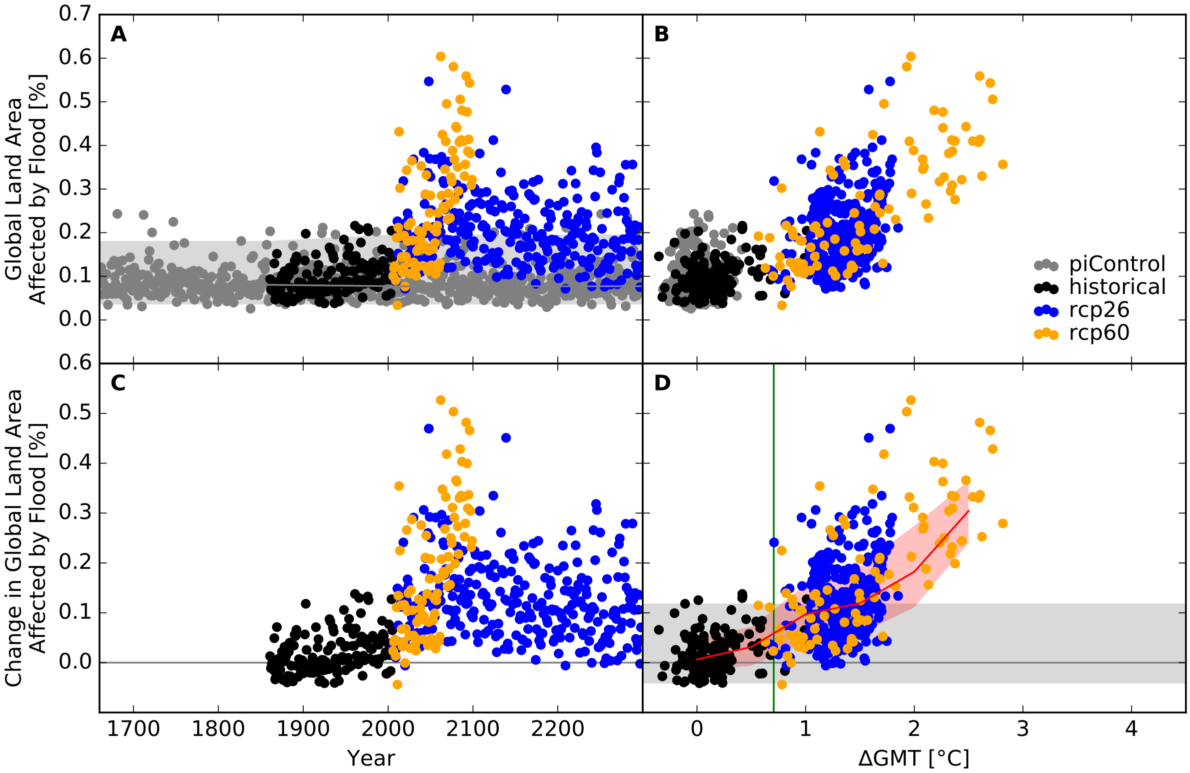

Figure S26: **Derivation of the pure effect of climate change on global land area fraction affected by flood events (MIROC5 + H08).** Analogous to Figure S24.

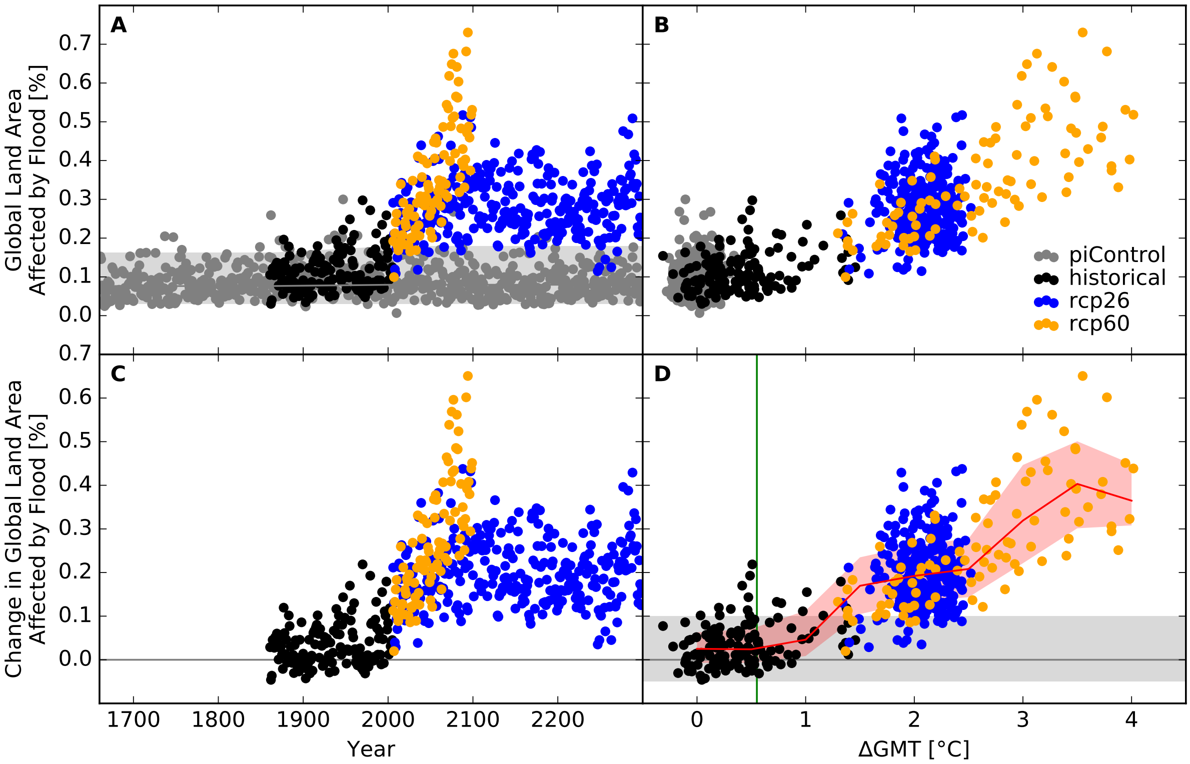

Figure S27: **Derivation of the pure effect of climate change on global land area fraction affected by flood events (IPSL-CM5A-LR + JULES-W1).** Analogous to Figure S24.

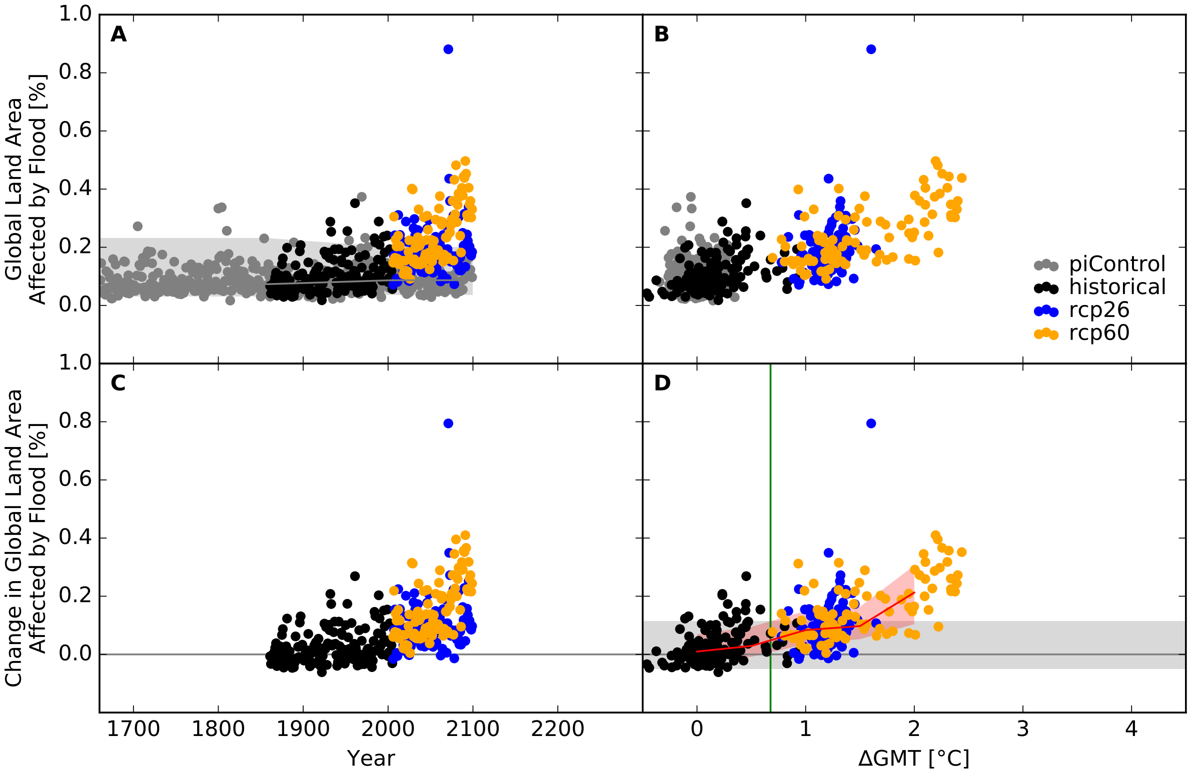

Figure S28: **Derivation of the pure effect of climate change on global land area fraction affected by flood events (GFDL-ESM2M + LPJmL).** Analogous to Figure S24.

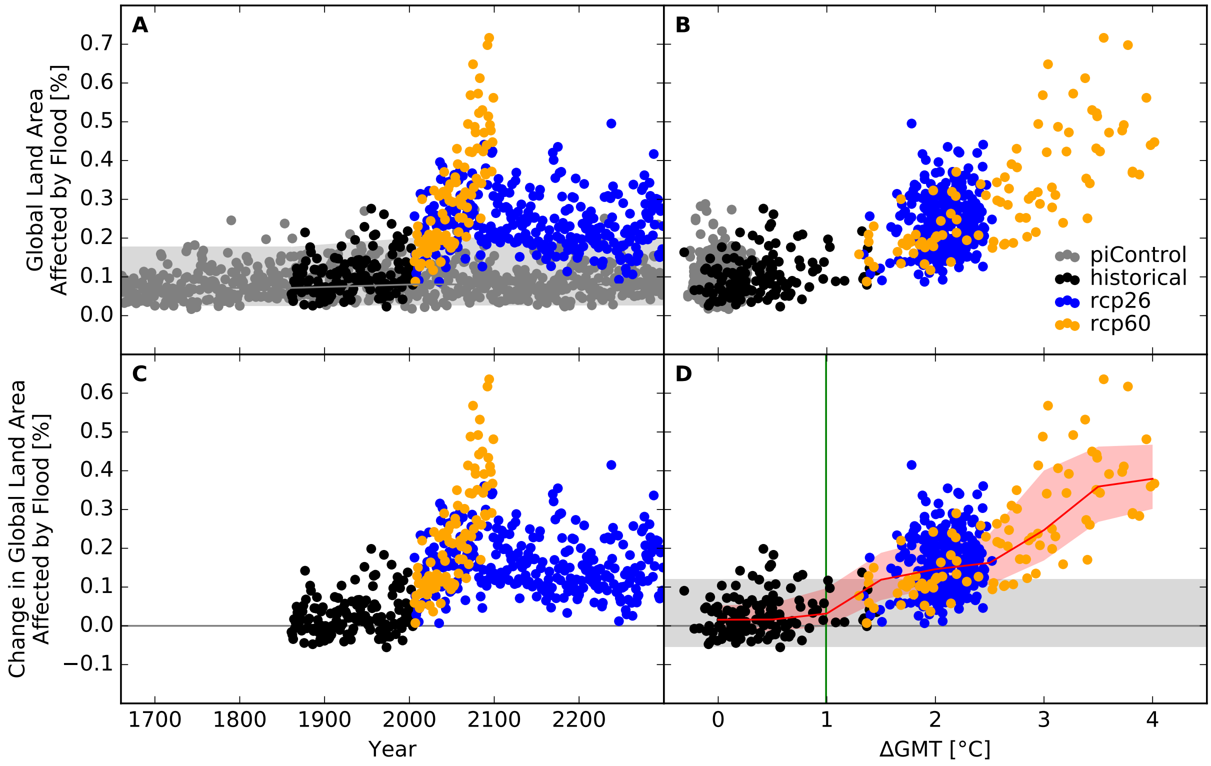

Figure S29: **Derivation of the pure effect of climate change on global land area fraction affected by flood events (IPSL-CM5A-LR + LPJmL).** Analogous to Figure S24.

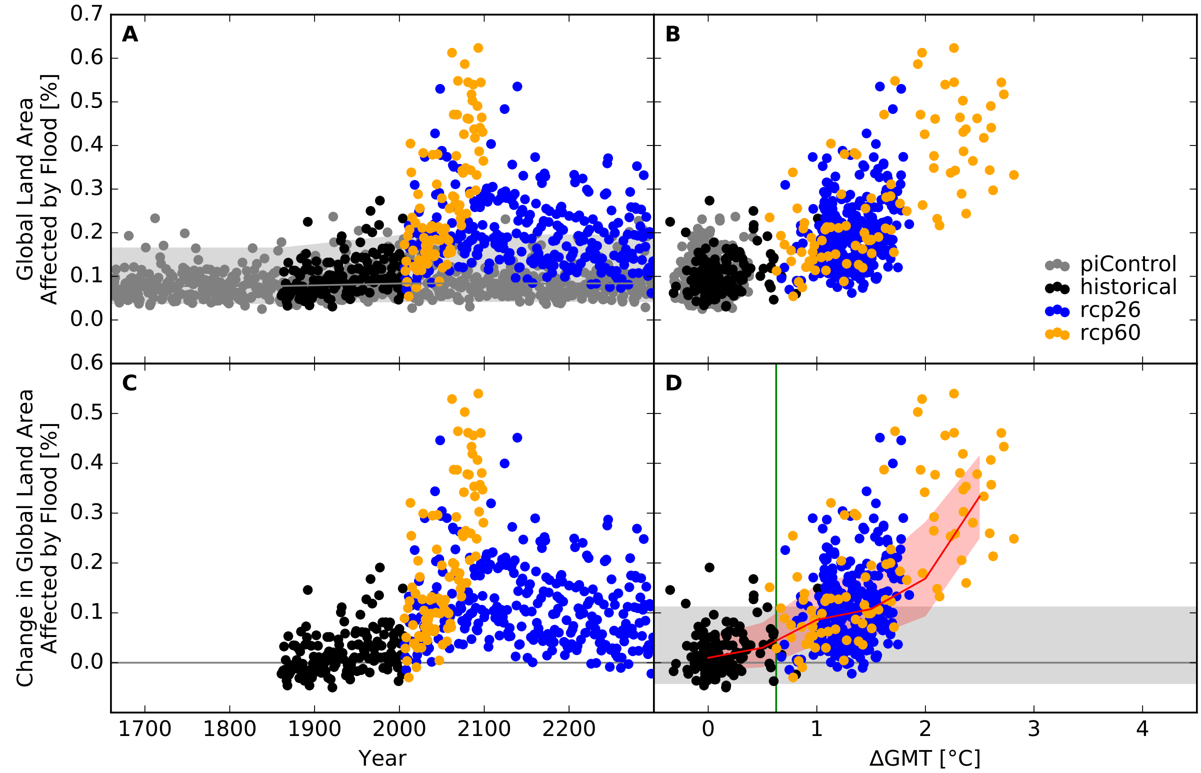

Figure S30: **Derivation of the pure effect of climate change on global land area fraction affected by flood events (MIROC5 + LPJmL).** Analogous to Figure S24.

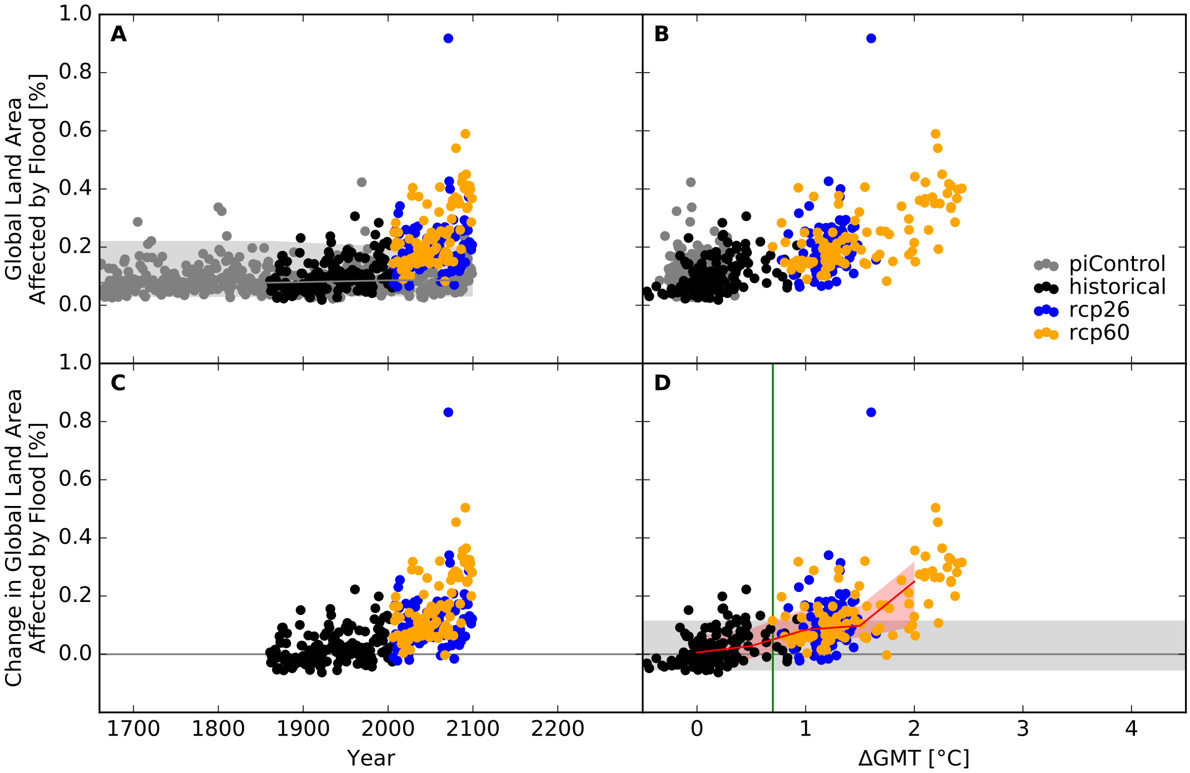

Figure S31: **Derivation of the pure effect of climate change on global land area fraction affected by flood events (GFDL-ESM2M + MPI-HM).** Analogous to Figure S24.

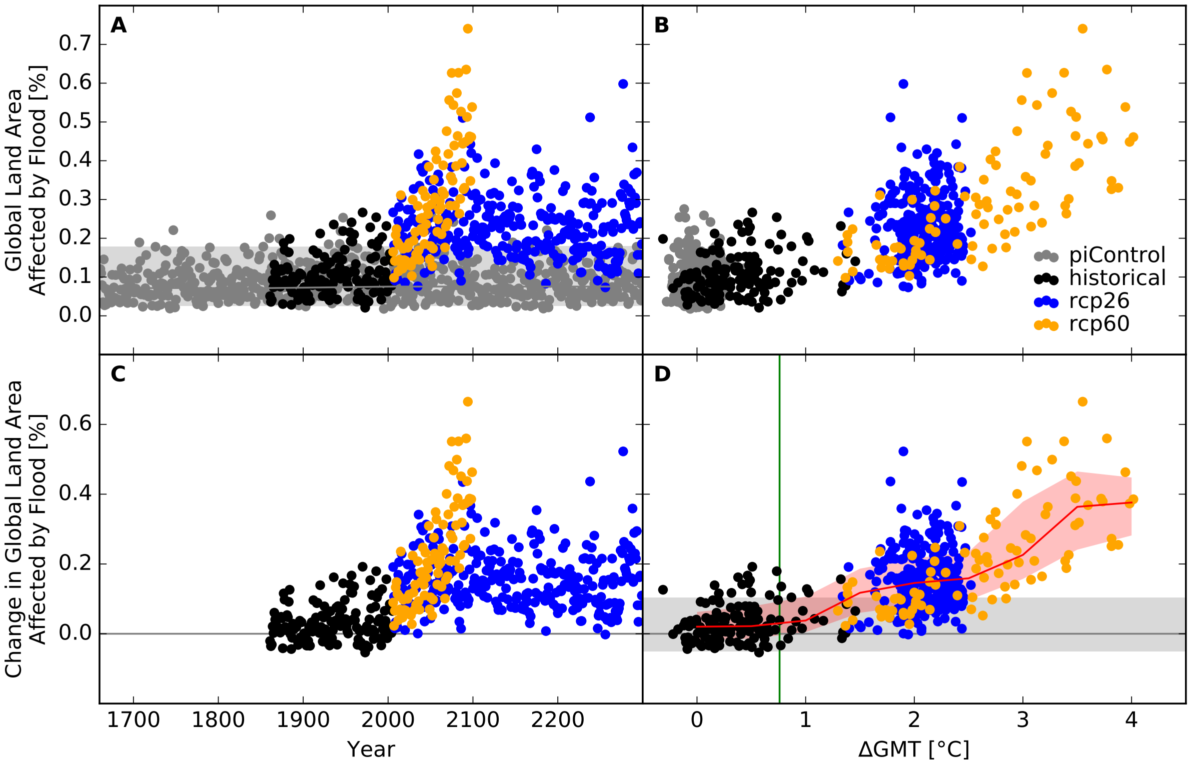

Figure S32: **Derivation of the pure effect of climate change on global land area fraction affected by flood events (IPSL-CM5A-LR + MPI-HM).** Analogous to Figure S24.

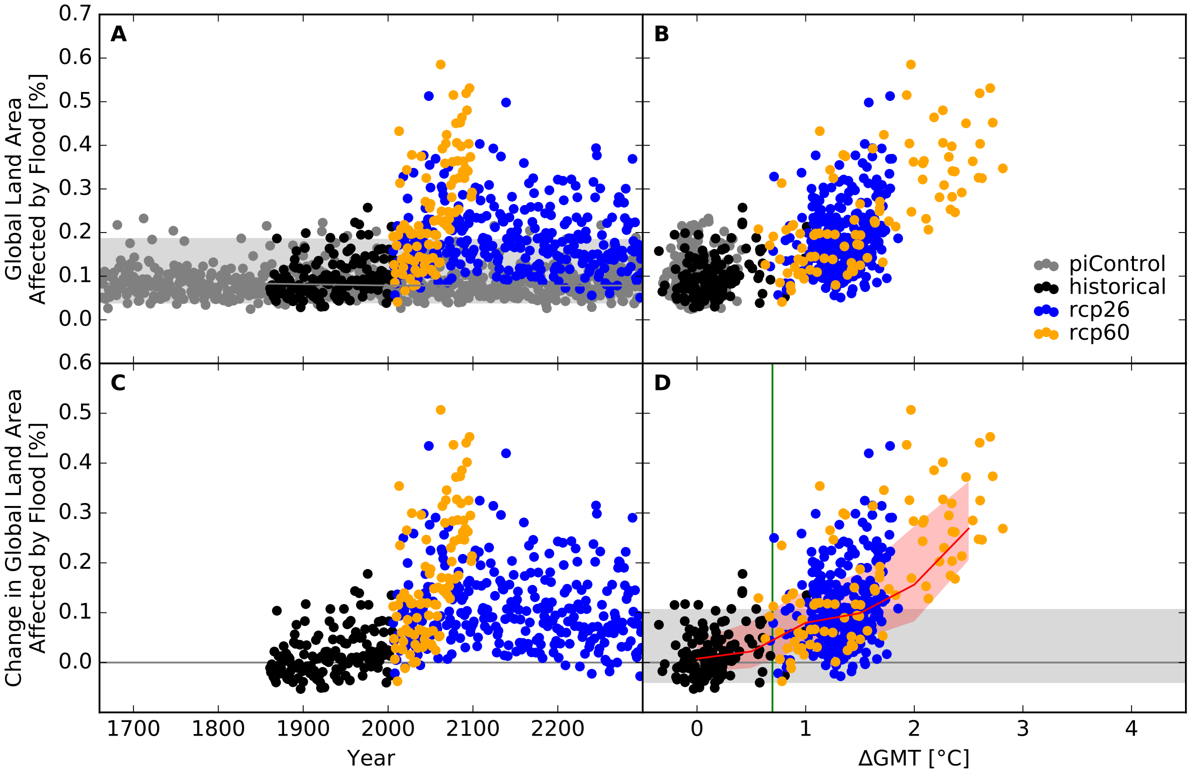

Figure S33: **Derivation of the pure effect of climate change on global land area fraction affected by flood events (MIROC5 + MPI-HM).** Analogous to Figure S24.

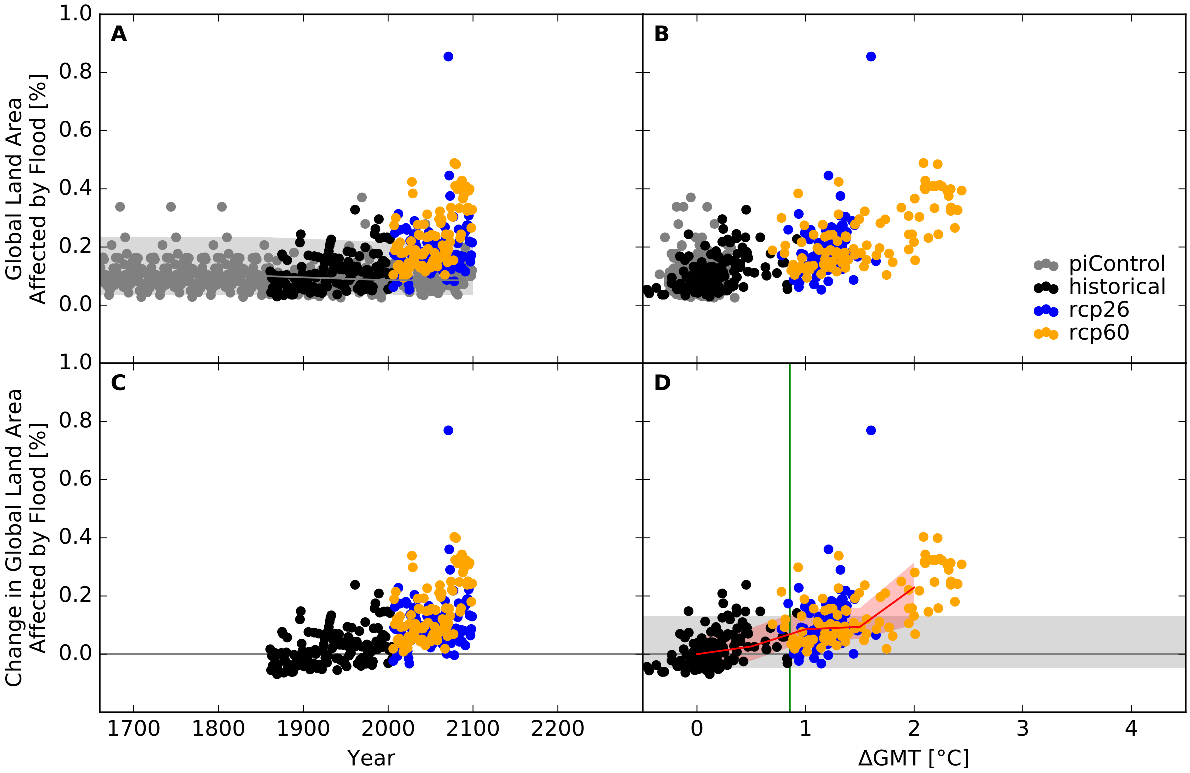

Figure S34: **Derivation of the pure effect of climate change on global land area fraction affected by flood events (GFDL-ESM2M + ORCHIDEE).** Analogous to Figure S24.

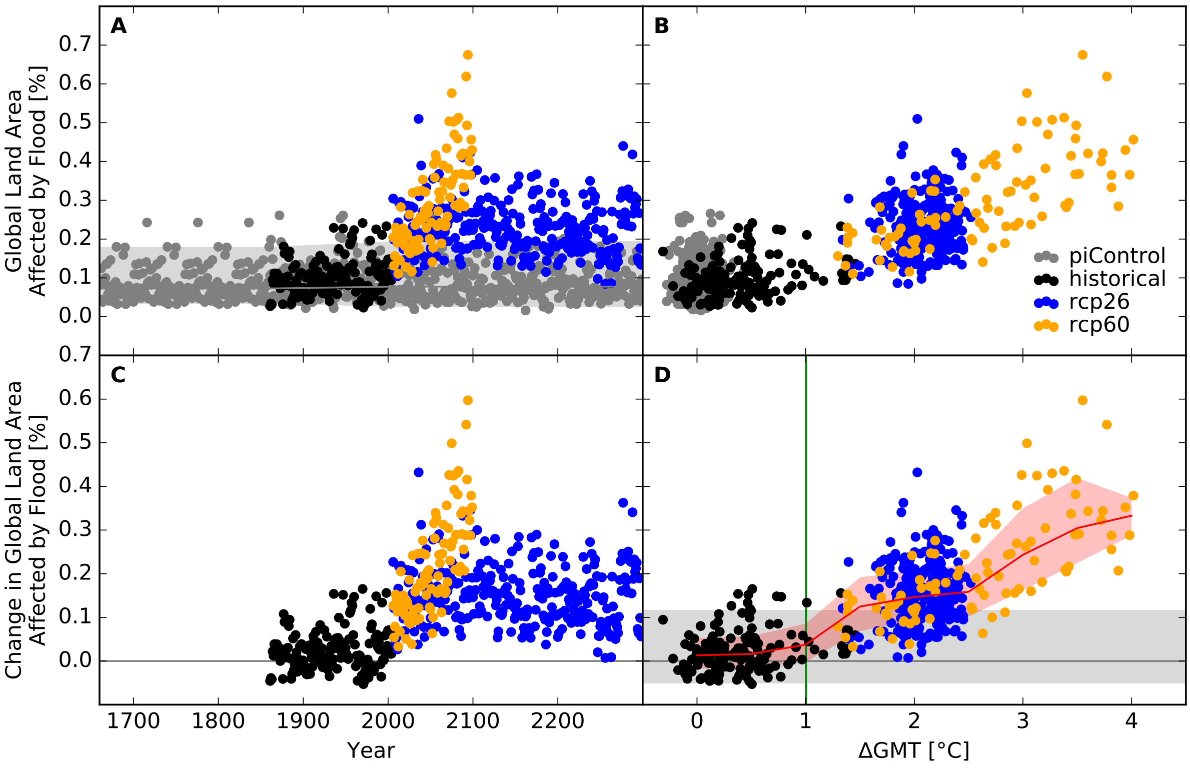

Figure S35: **Derivation of the pure effect of climate change on global land area fraction affected by flood events (IPSL-CM5A-LR + ORCHIDEE).** Analogous to Figure S24.

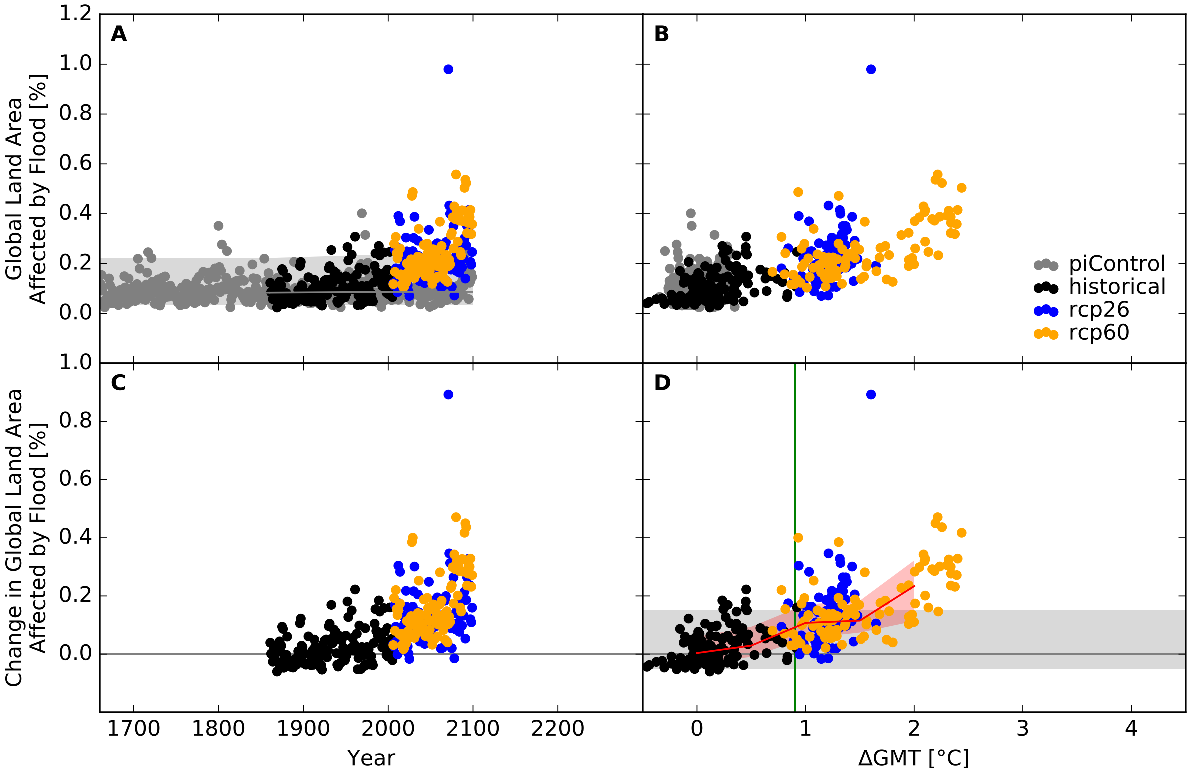

Figure S36: **Derivation of the pure effect of climate change on global land area fraction affected by flood events (GFDL-ESM2M + PCR-GLOBWB).** Analogous to Figure S24.

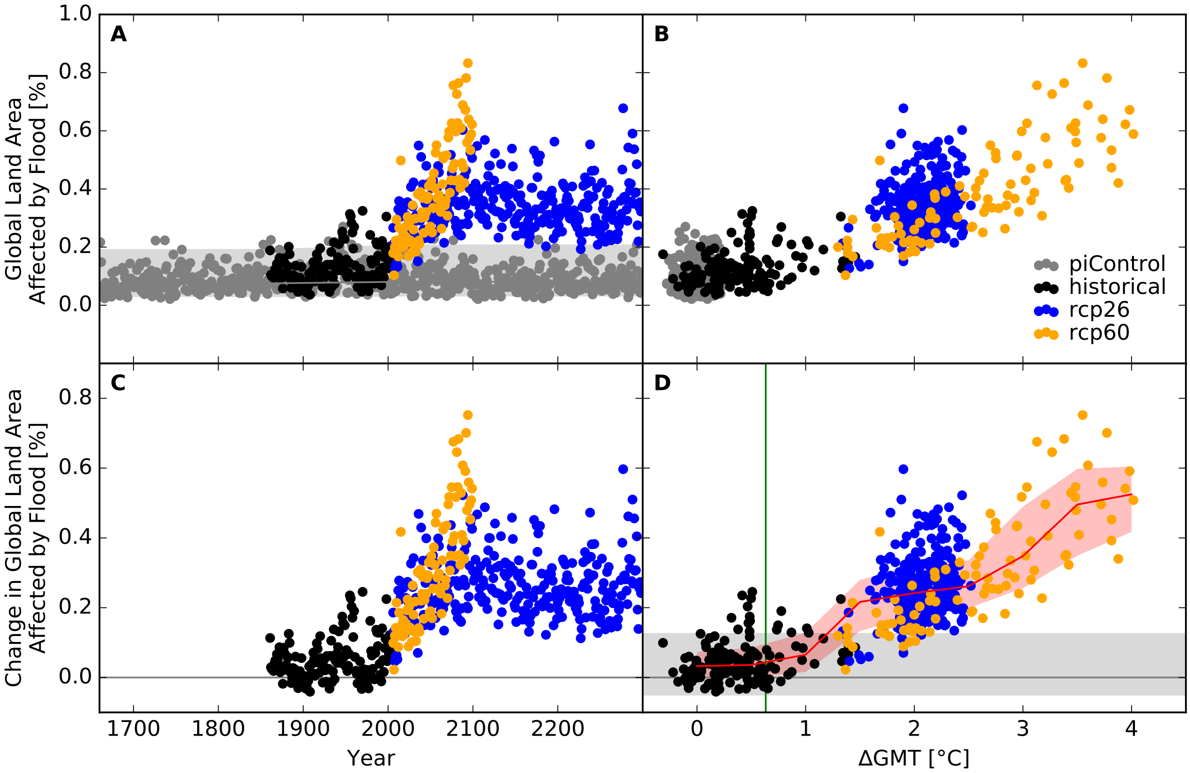

Figure S37: **Derivation of the pure effect of climate change on global land area fraction affected by flood events (IPSL-CM5A-LR + PCR-GLOBWB).** Analogous to Figure S24.

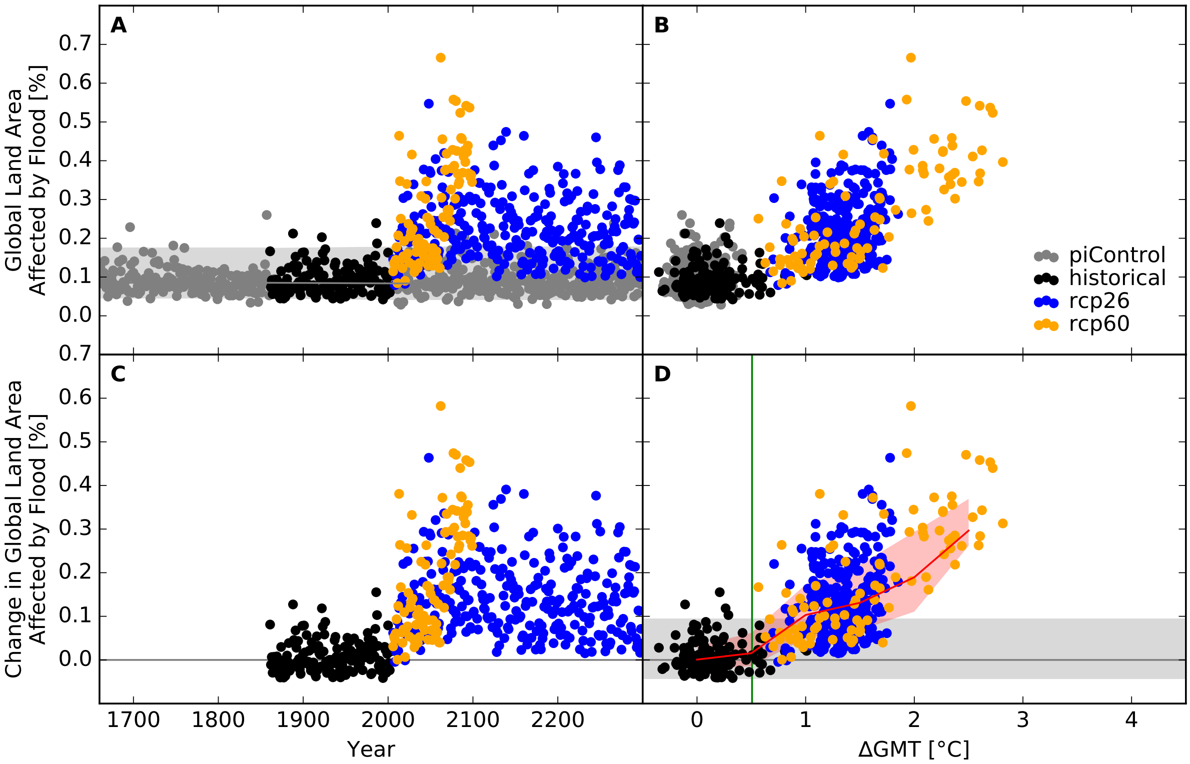

Figure S38: **Derivation of the pure effect of climate change on global land area fraction affected by flood events (MIROC5 + PCR-GLOBWB).** Analogous to Figure S24.

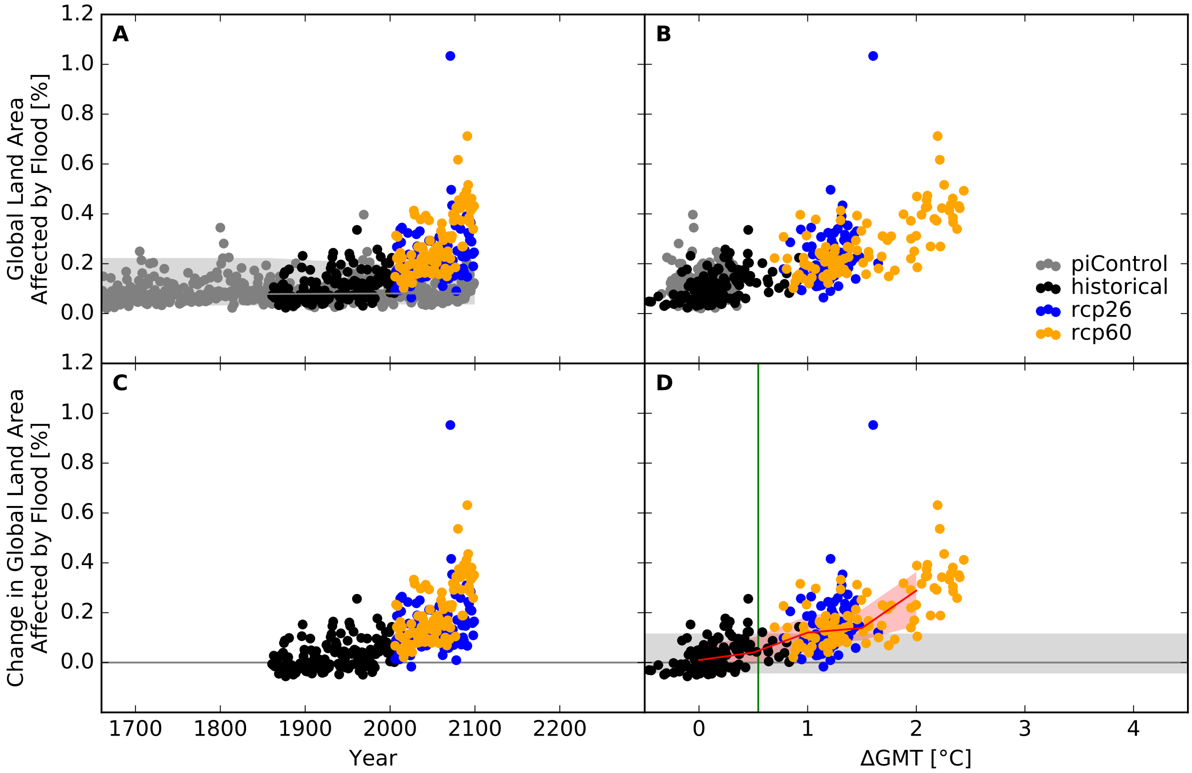

Figure S39: **Derivation of the pure effect of climate change on global land area fraction affected by flood events (GFDL-ESM2M + WaterGAP2).** Analogous to Figure S24.

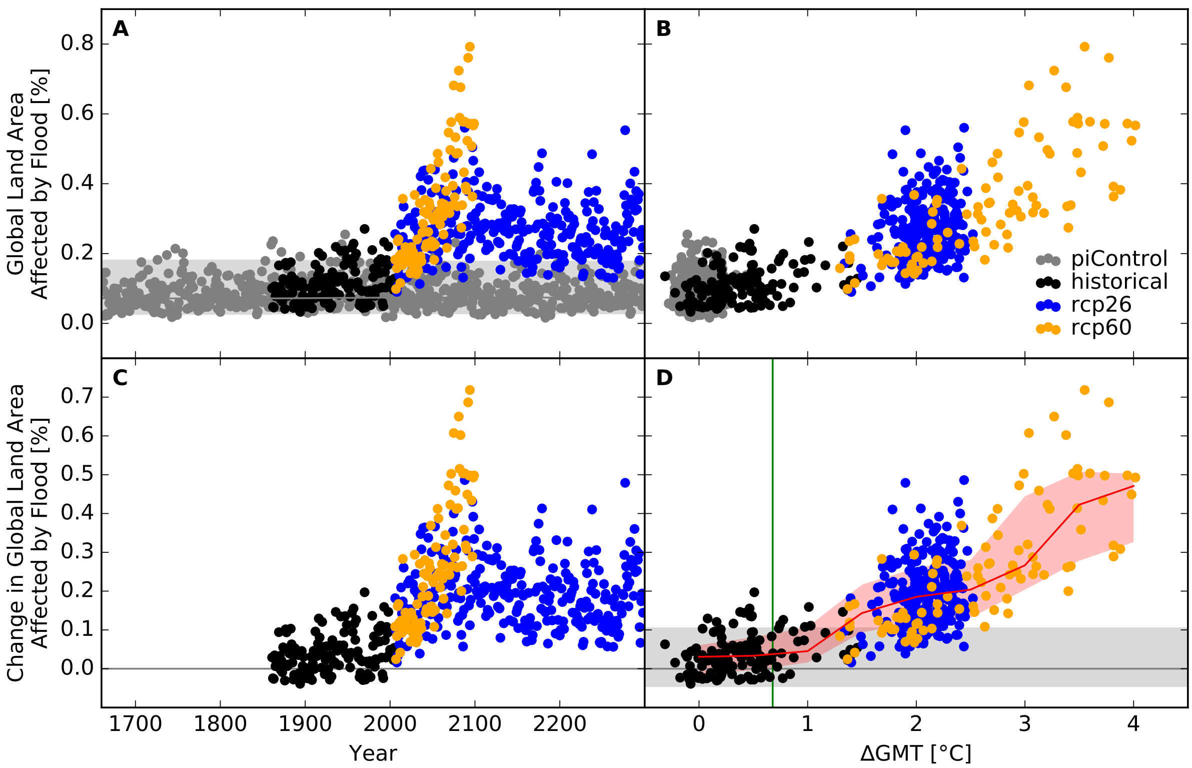

Figure S40: **Derivation of the pure effect of climate change on global land area fraction affected by flood events (IPSL-CM5A-LR + WaterGAP2).** Analogous to Figure S24.

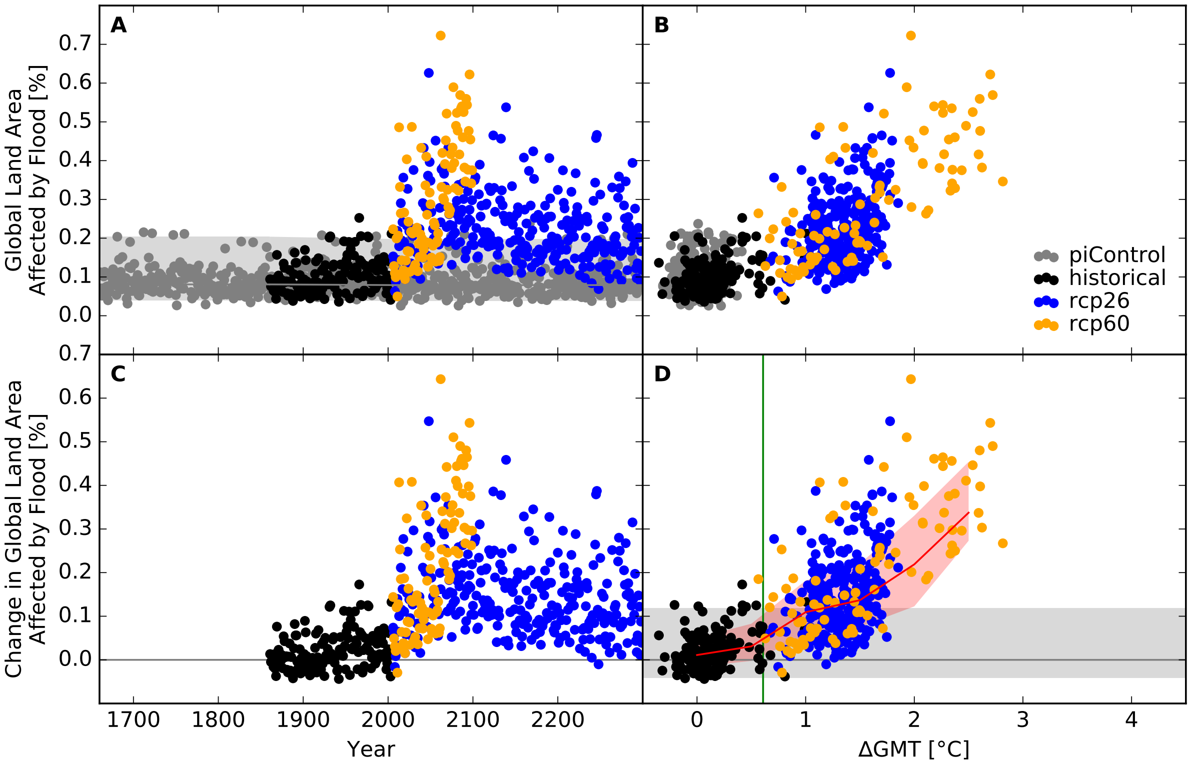

Figure S41: **Derivation of the pure effect of climate change on global land area fraction affected by flood events (MIROC5 + WaterGAP2).** Analogous to Figure S24.

People exposed

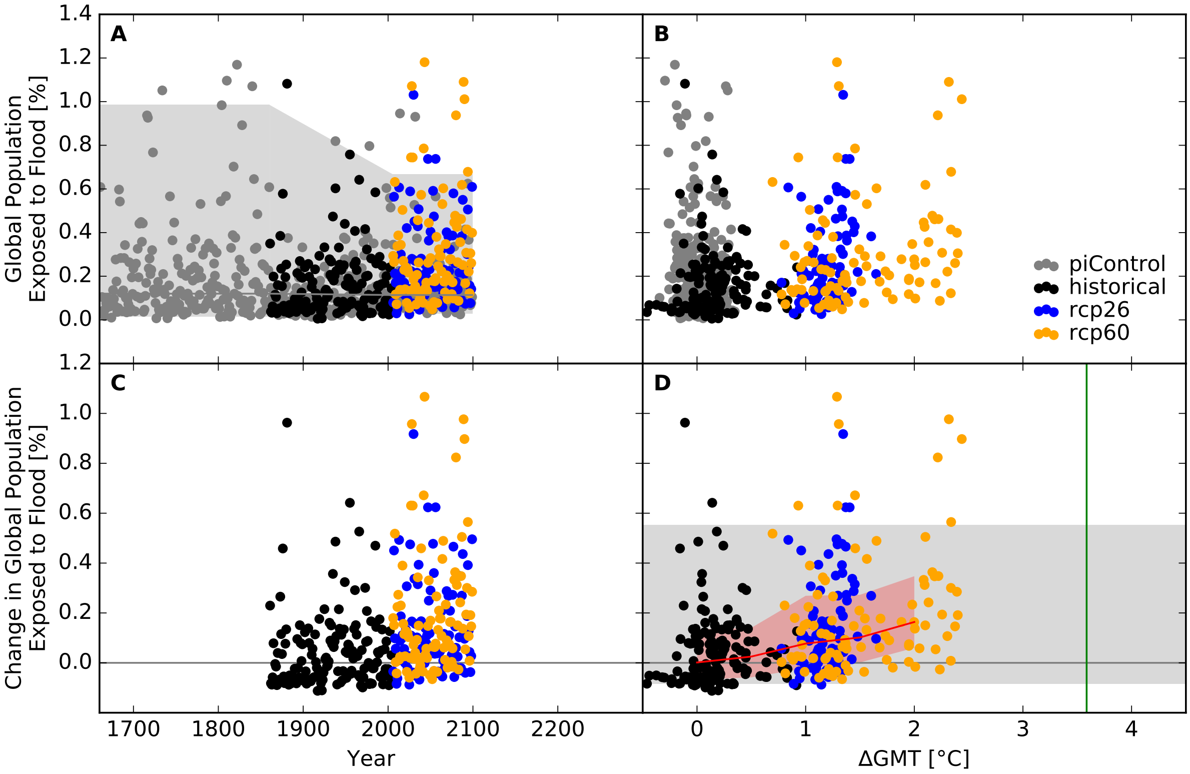

Figure S42: **Derivation of the pure effect of climate change on global population fraction affected by flood events (GFDL-ESM2M + H08).** Panel A: Time series of annual global population fraction affected (PFA) by flood events for pre-industrial climate (grey dots), historical climate (black dots), climate projections for RCP2.6 (blue dots), and RCP6.0 (orange dots). In all simulations, socio-economic conditions are varied according to the historically observed development between 1860 and 2005, and held fixed at 1860 conditions before 1860 and at 2005 conditions after 2005. Shaded areas before 1860/after 2005 represent the range from the 2nd to the 98th percentile of the distribution of the annual PFA under pre-industrial climate conditions in combination with 1860/2005 socio-economic conditions; the solid gray lines represent the respective median values; the shaded areas and solid gray line between 1860 and 2005 are linear interpolations of the respective values before 1860 and after 2005. Panel B: Data shown in Panel A plotted against the associated GCM-specific annual global mean temperature (GMT) change relative to the long-term pre-industrial mean. Panel C: Pure effect of climate change on PFA, calculated as the difference between the annual data shown in Panel A and the median of the simulations assuming pre-industrial climate conditions (solid gray line in Panel A). Panel D: Pure effect of climate change on PFA in terms of global mean temperature change, with distributions of the annual data estimated for each 1°C-wide bin of global mean temperature change that contains at least five data points, at least one data point above and at least one data point below the bin center. Areas shaded in red represent the range from the 20th to the 80th percentile around the median (solid red line) of these distributions. Areas shaded in gray represent the range from the 2nd to the 98th percentile of the zero-centered distribution of the annual PFA under pre-industrial climate and 2005 socio-economic conditions (cf. Panel A). The green vertical line represents the detection level defined as the global warming level at which a 1-in-50-years event under pre-industrial climate and 2005 socio-economic conditions becomes a 1-in-5-years event under changing climate and 2005 socio-economic conditions.

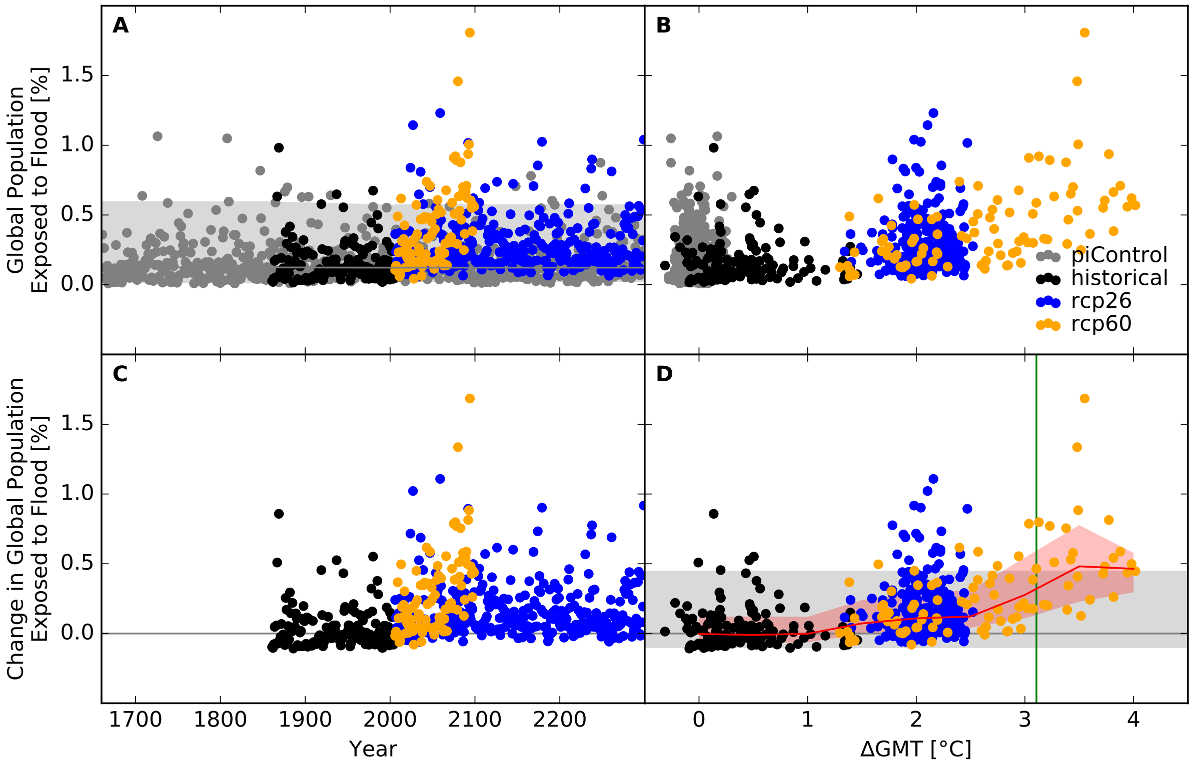

Figure S43: **Derivation of the pure effect of climate change on global population fraction affected by flood events (IPSL-CM5A-LR + H08).** Analogous to Figure S42.

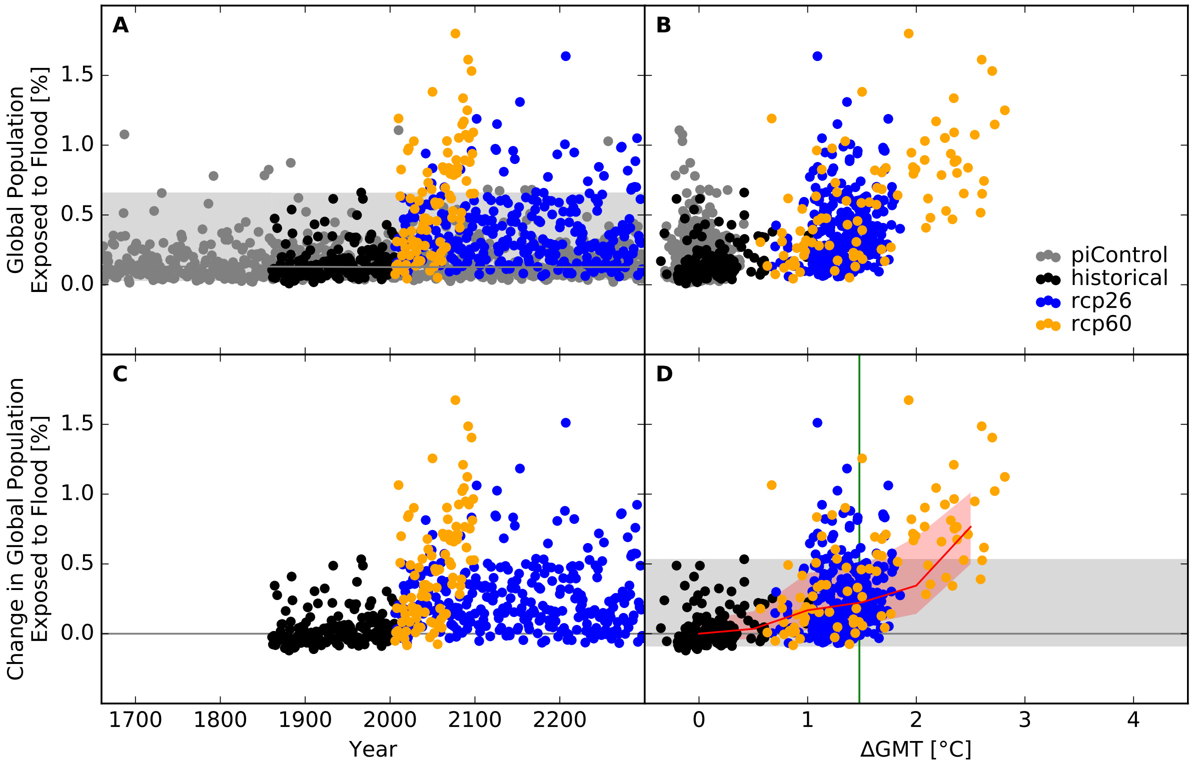

Figure S44: **Derivation of the pure effect of climate change on global population fraction affected by flood events (MIROC5 + H08).** Analogous to Figure S42.

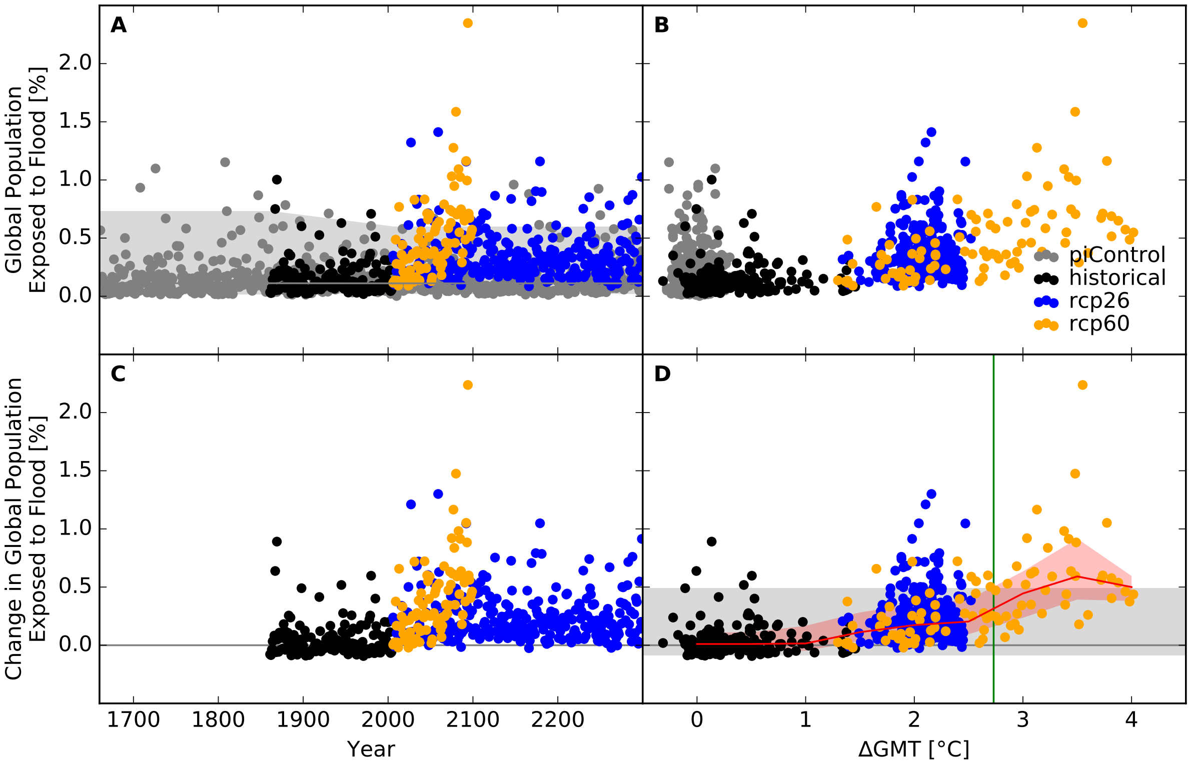

Figure S45: **Derivation of the pure effect of climate change on global population fraction affected by flood events (IPSL-CM5A-LR + JULES-W1).** Analogous to Figure S42.

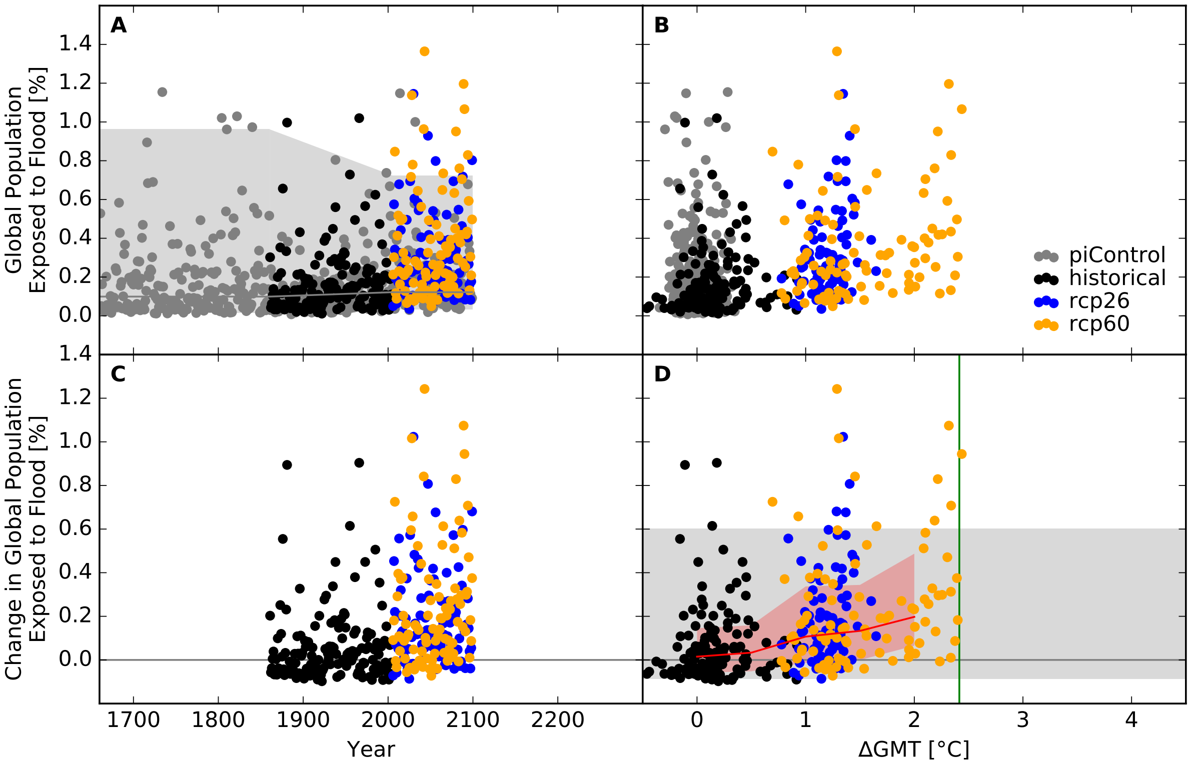

Figure S46: **Derivation of the pure effect of climate change on global population fraction affected by flood events (GFDL-ESM2M + LPJmL).** Analogous to Figure S42.

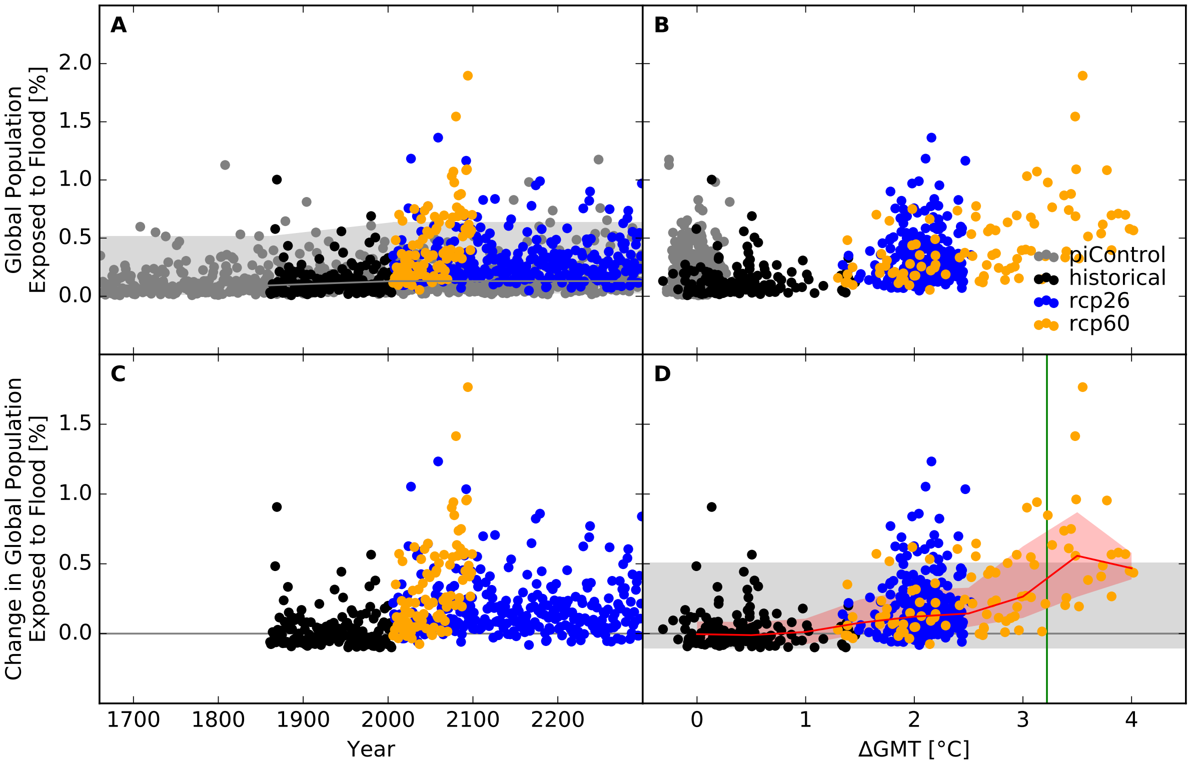

Figure S47: **Derivation of the pure effect of climate change on global population fraction affected by flood events (IPSL-CM5A-LR + LPJmL).** Analogous to Figure S42.

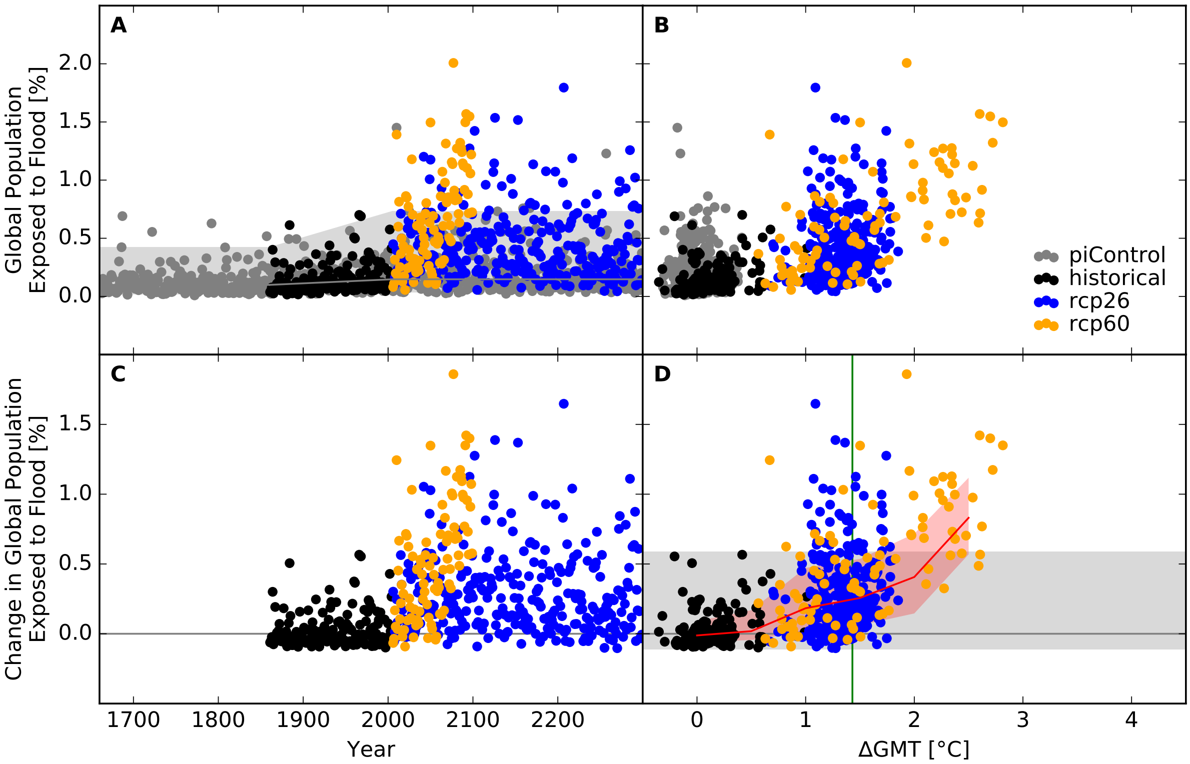

Figure S48: **Derivation of the pure effect of climate change on global population fraction affected by flood events (MIROC5 + LPJmL).** Analogous to Figure S42.

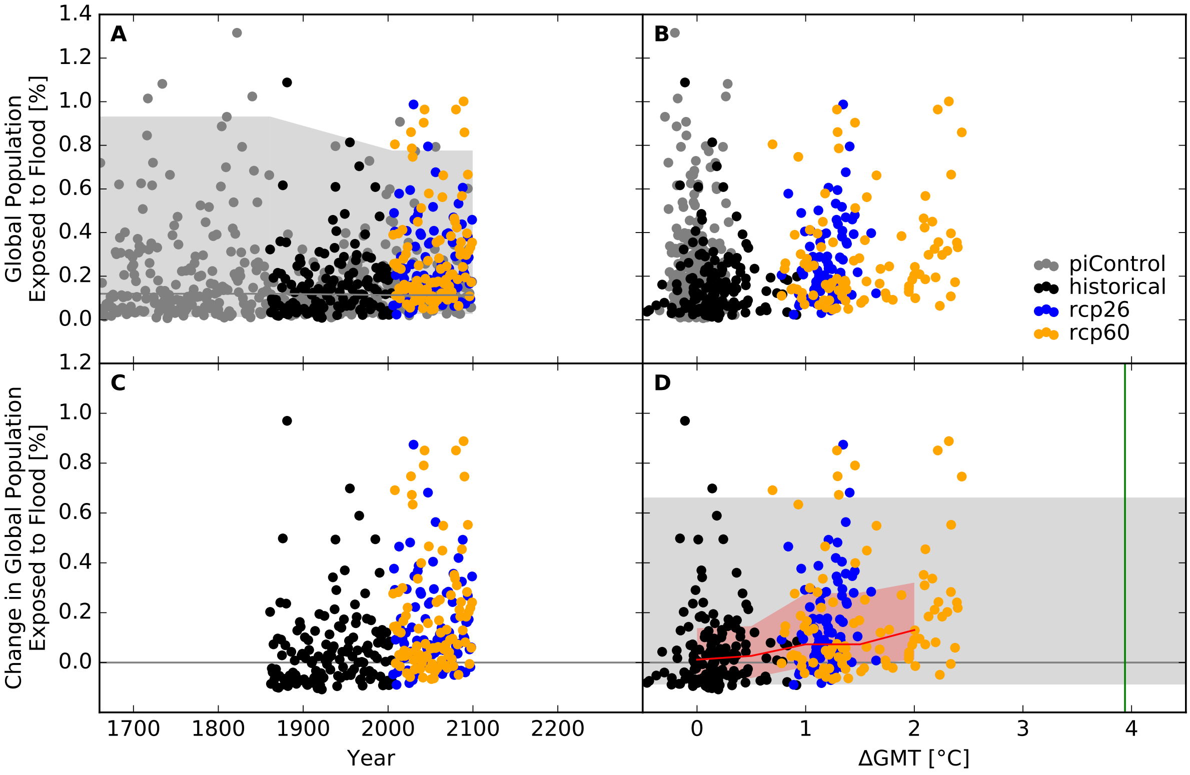

Figure S49: **Derivation of the pure effect of climate change on global population fraction affected by flood events (GFDL-ESM2M + MPI-HM).** Analogous to Figure S42.

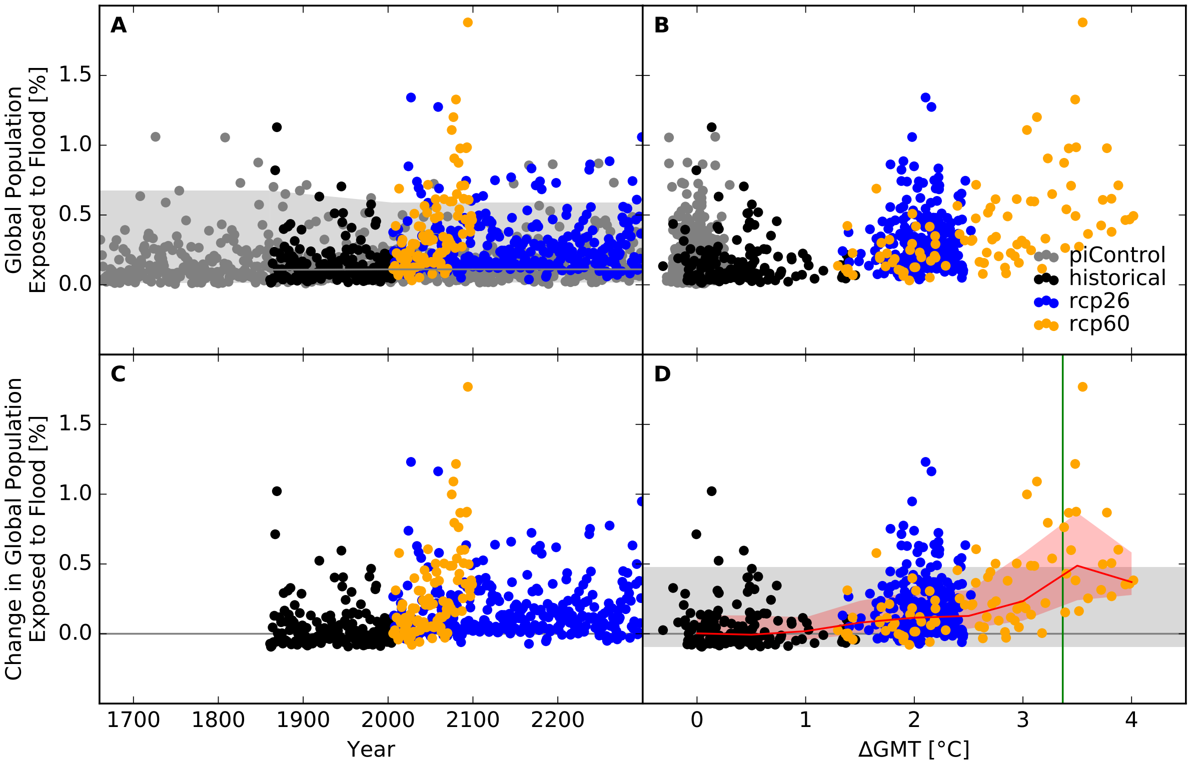

Figure S50: **Derivation of the pure effect of climate change on global population fraction affected by flood events (IPSL-CM5A-LR + MPI-HM).** Analogous to Figure S42.

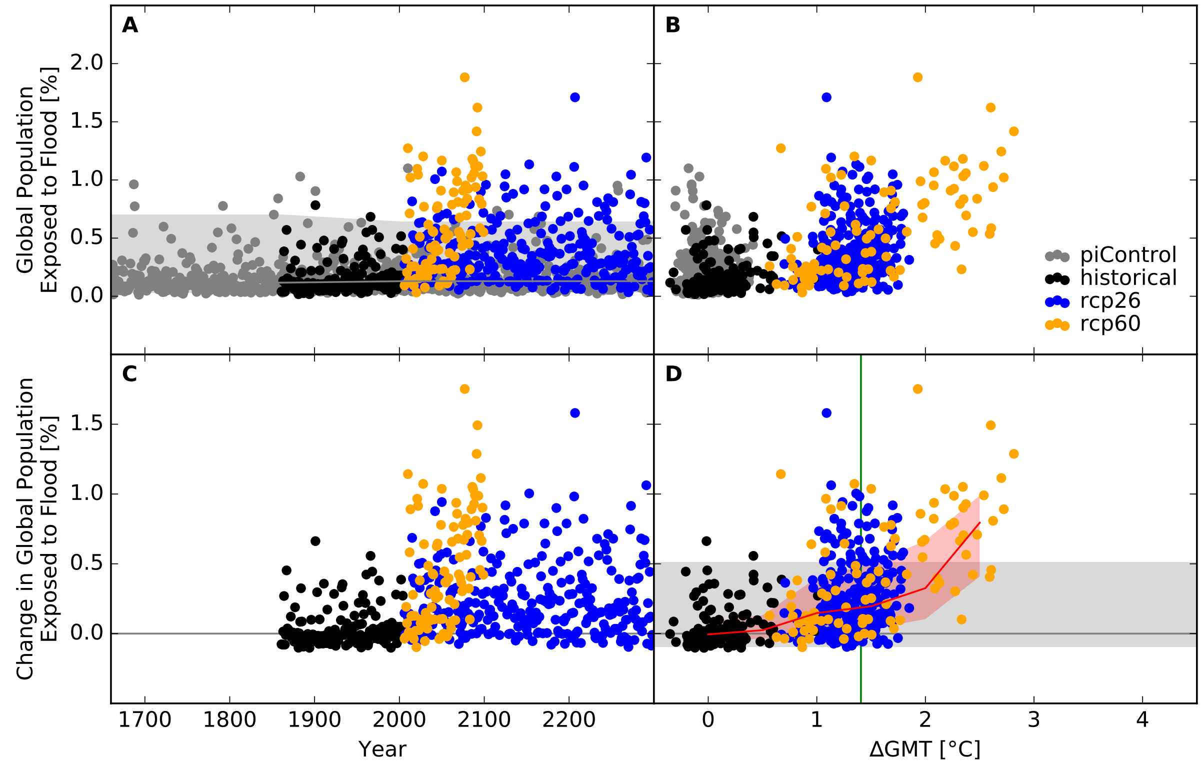

Figure S51: **Derivation of the pure effect of climate change on global population fraction affected by flood events (MIROC5 + MPI-HM).** Analogous to Figure S42.

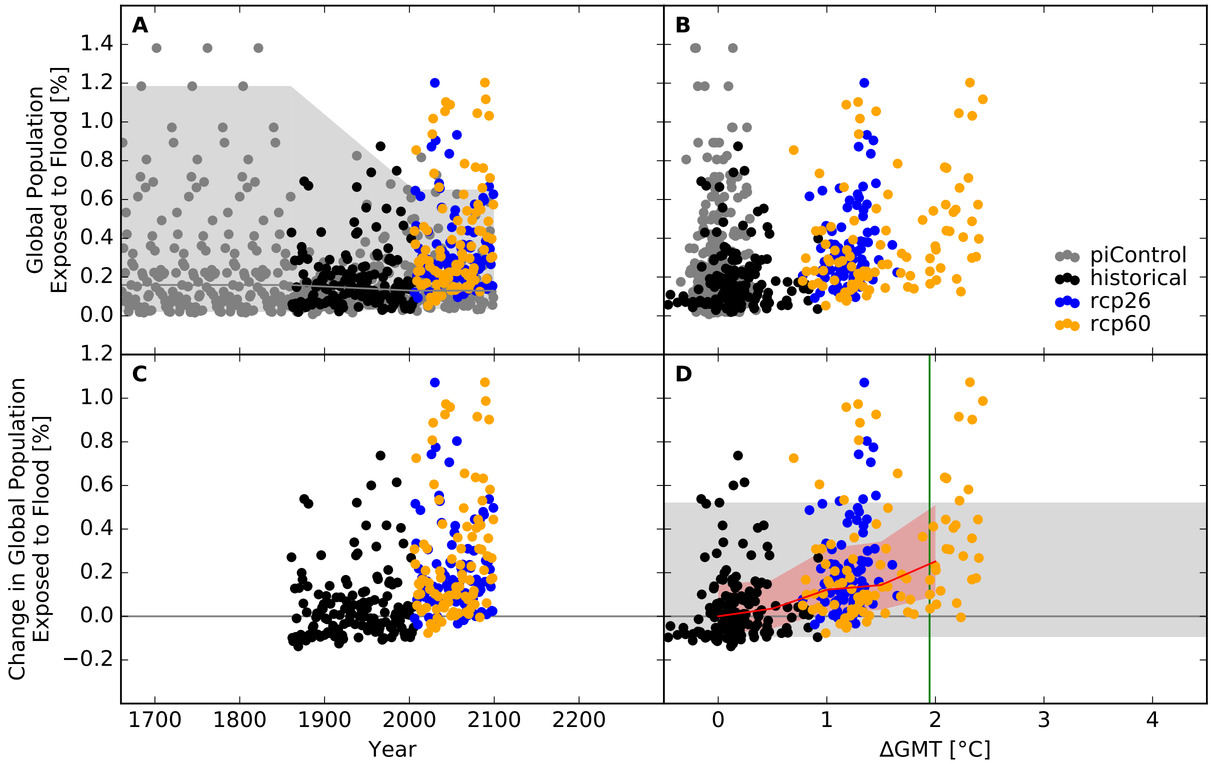

Figure S52: **Derivation of the pure effect of climate change on global population fraction affected by flood events (GFDL-ESM2M + ORCHIDEE).** Analogous to Figure S42.

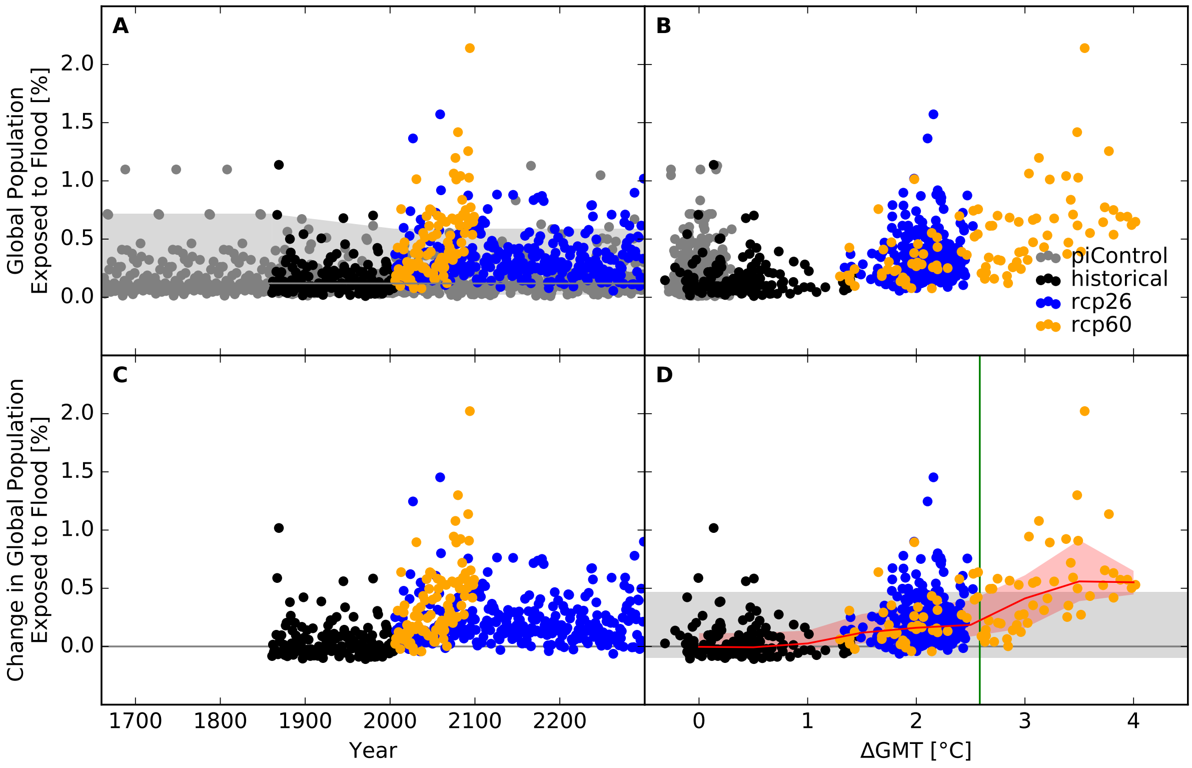

Figure S53: **Derivation of the pure effect of climate change on global population fraction affected by flood events (IPSL-CM5A-LR + ORCHIDEE).** Analogous to Figure S42.

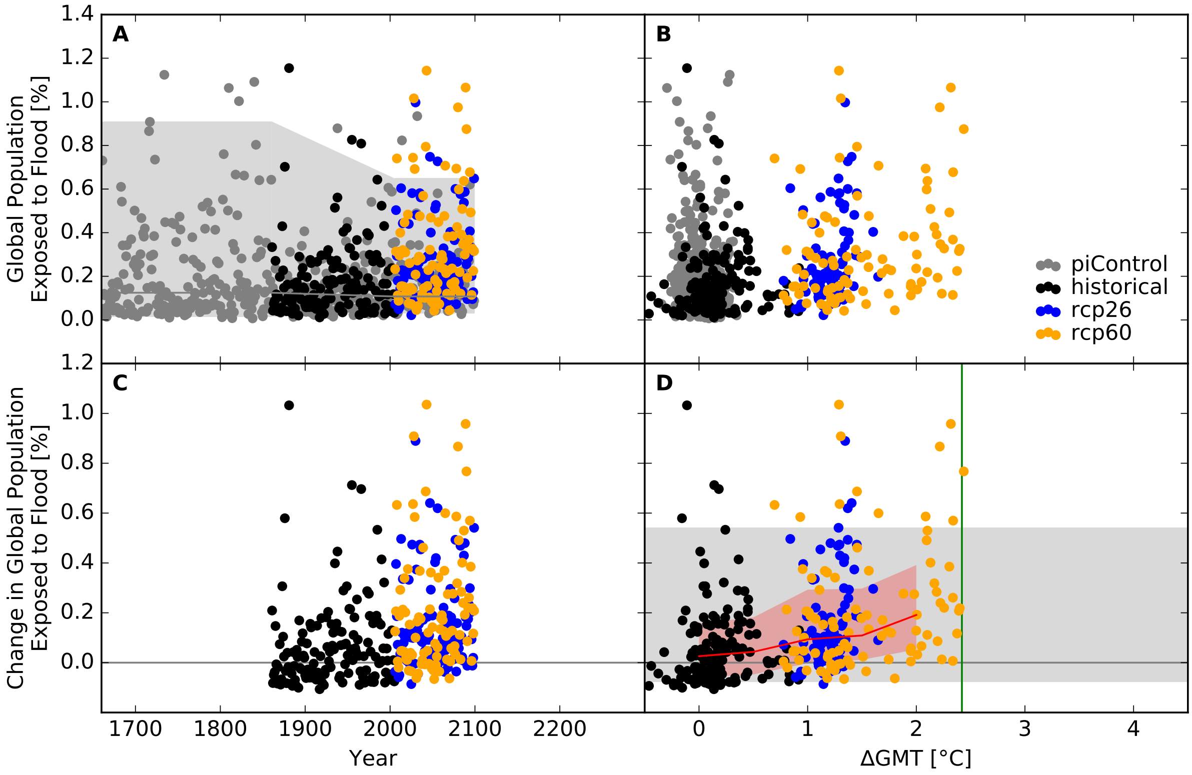

Figure S54: **Derivation of the pure effect of climate change on global population fraction affected by flood events (GFDL-ESM2M + PCR-GLOBWB).** Analogous to Figure S42.

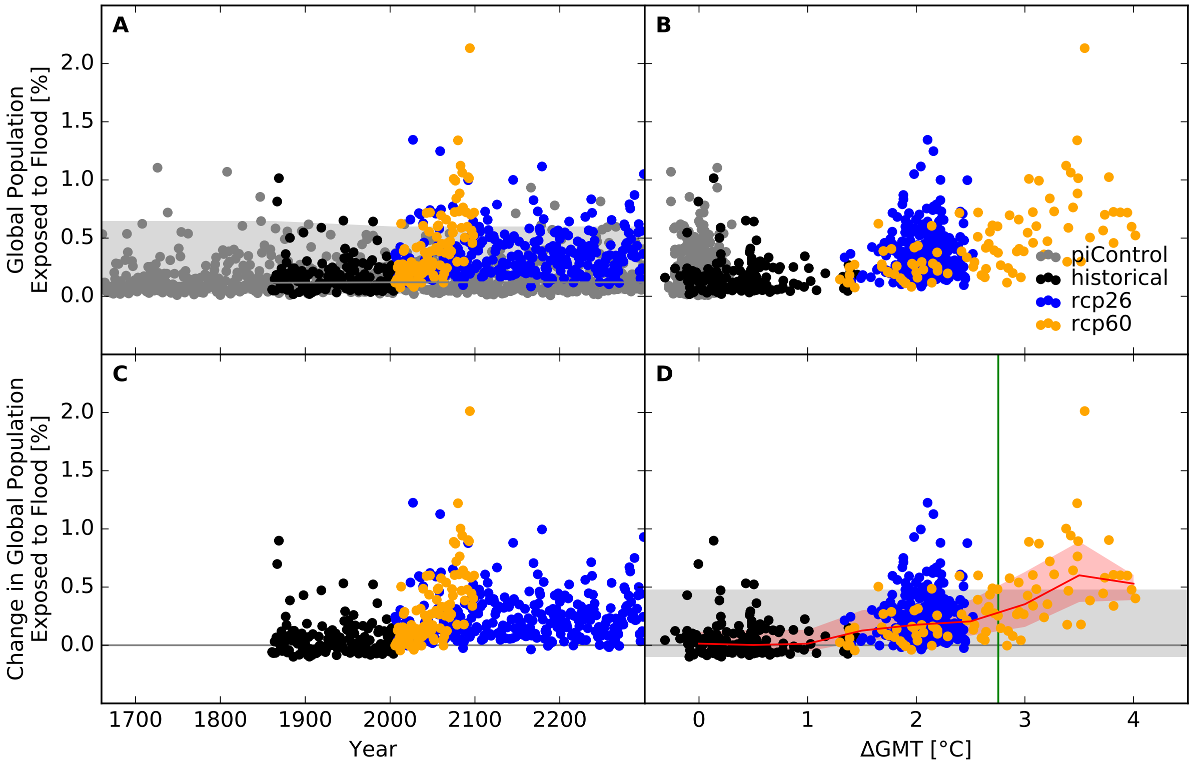

Figure S55: **Derivation of the pure effect of climate change on global population fraction affected by flood events (IPSL-CM5A-LR + PCR-GLOBWB).** Analogous to Figure S42.

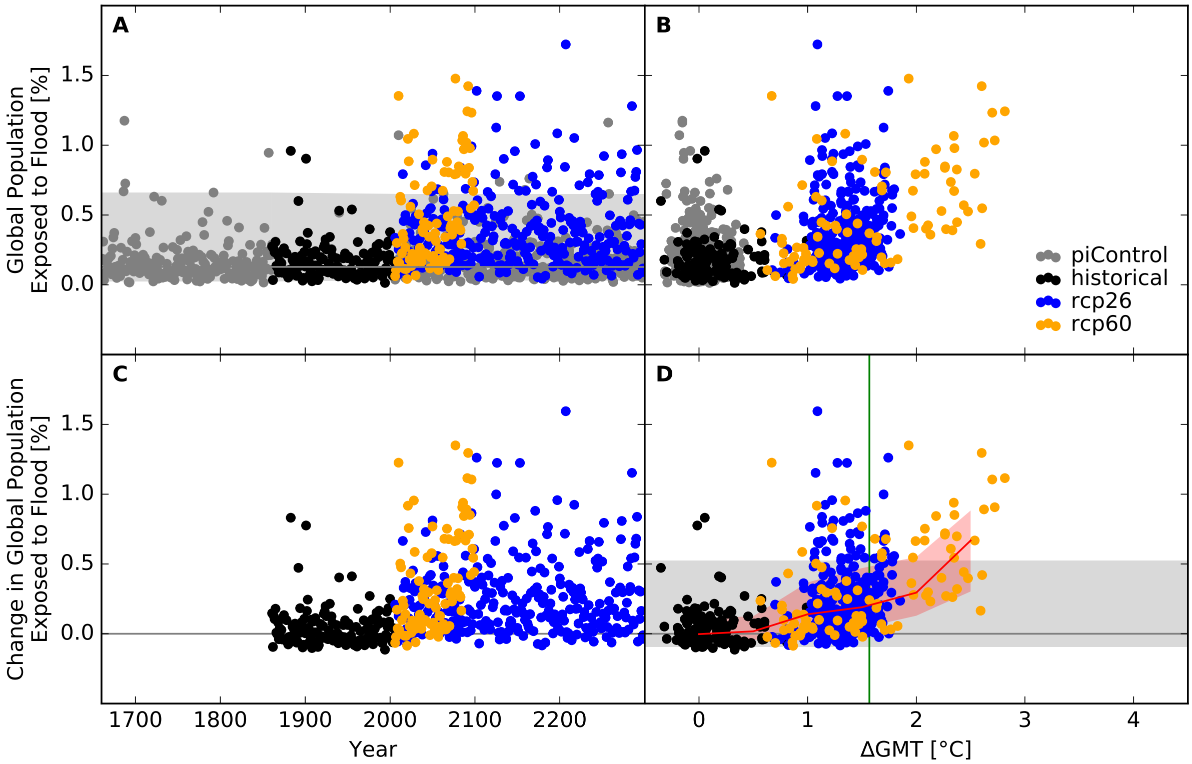

Figure S56: **Derivation of the pure effect of climate change on global population fraction affected by flood events (MIROC5 + PCR-GLOBWB).** Analogous to Figure S42.

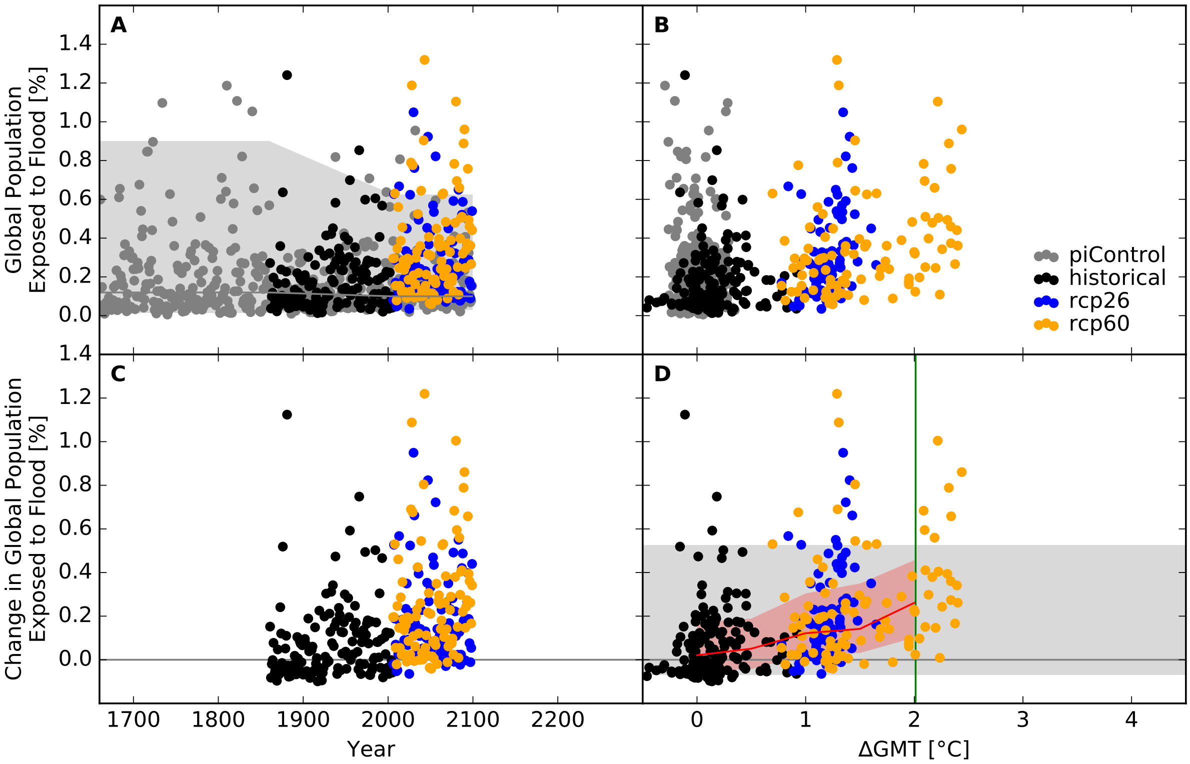

Figure S57: **Derivation of the pure effect of climate change on global population fraction affected by flood events (GFDL-ESM2M + WaterGAP2).** Analogous to Figure S42.

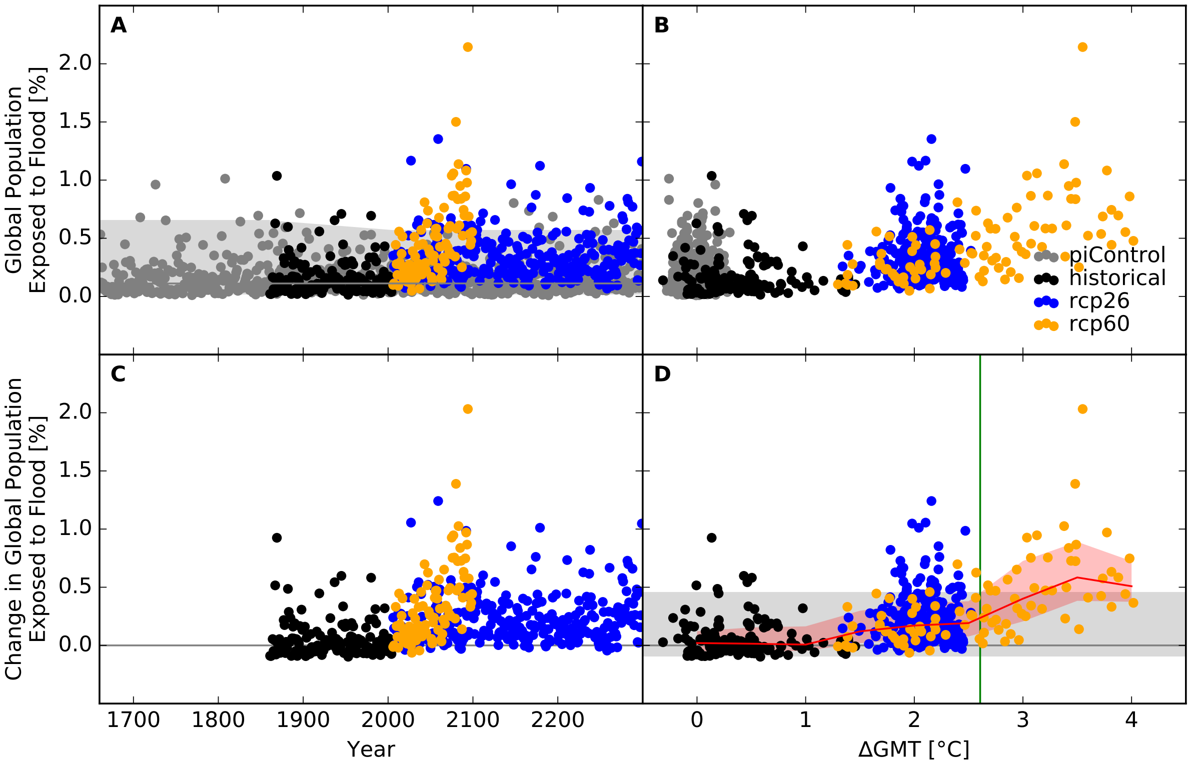

Figure S58: **Derivation of the pure effect of climate change on global population fraction affected by flood events (IPSL-CM5A-LR + WaterGAP2).** Analogous to Figure S42.

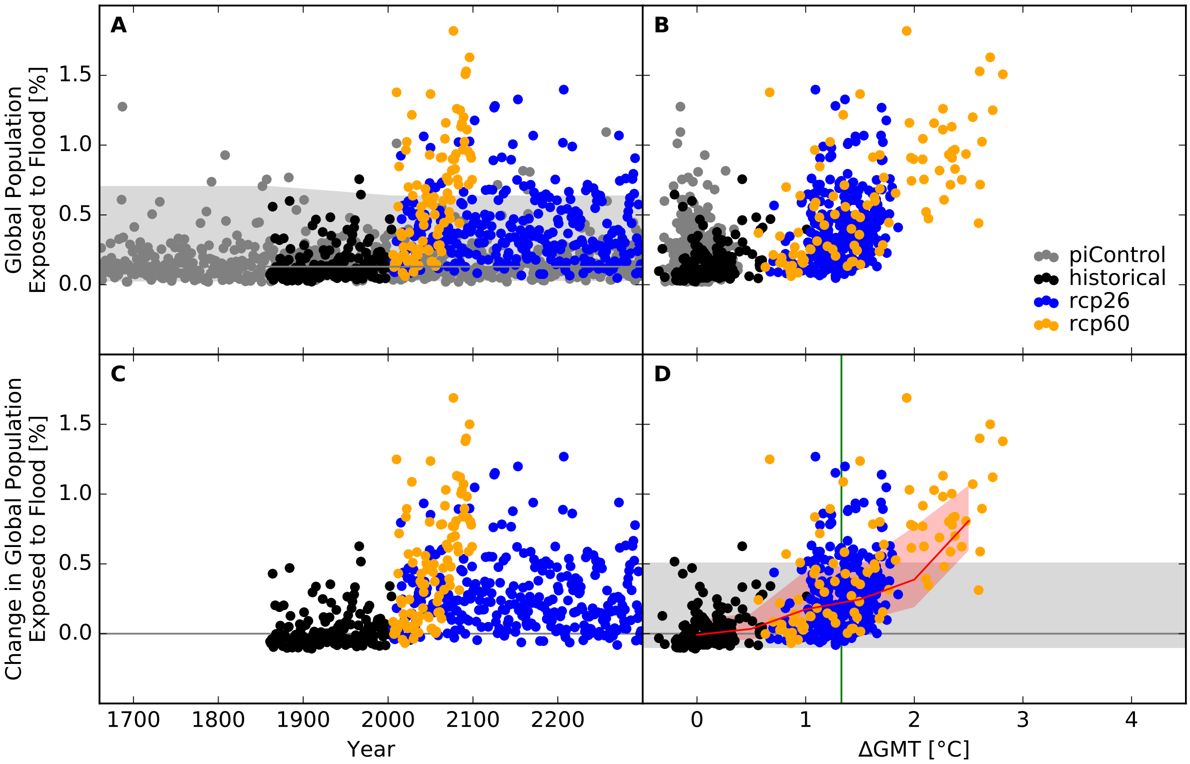

Figure S59: **Derivation of the pure effect of climate change on global population fraction affected by flood events (MIROC5 + WaterGAP2).** Analogous to Figure S42.

Occurrence probability at grid scale

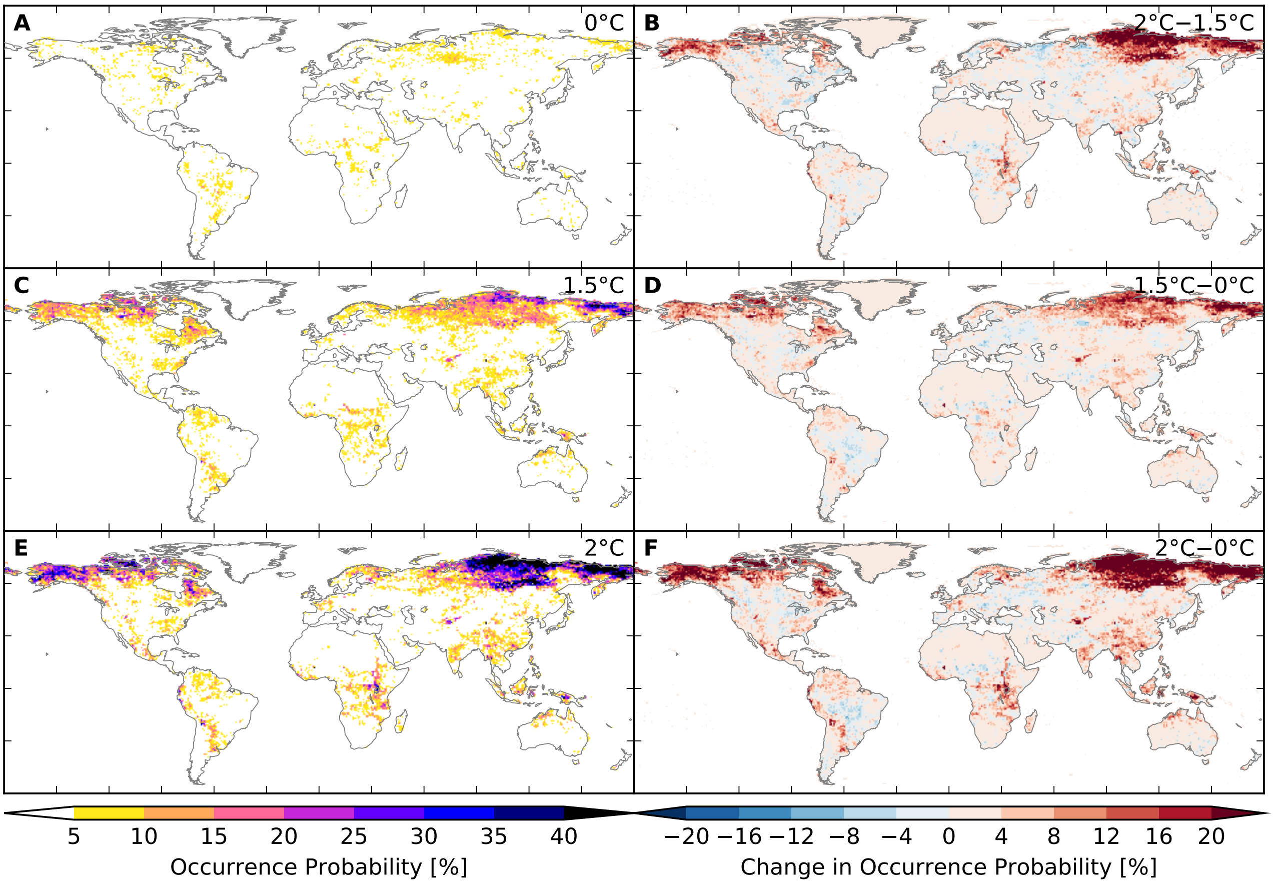

Figure S60: **Probability of occurrence of at least one flood event per year at different global warming levels (GFDL-ESM2M + H08).** Panels A, C, E: Probabilities at 0°C, 1.5°C, 2°C global mean temperature (GMT) change relative to the long-term pre-industrial mean GMT, respectively. Panels B, D, F: Differences between probabilities at GMT change levels of 2°C and 1.5°C, 1.5°C and 0°C, 2°C and 0°C, respectively.

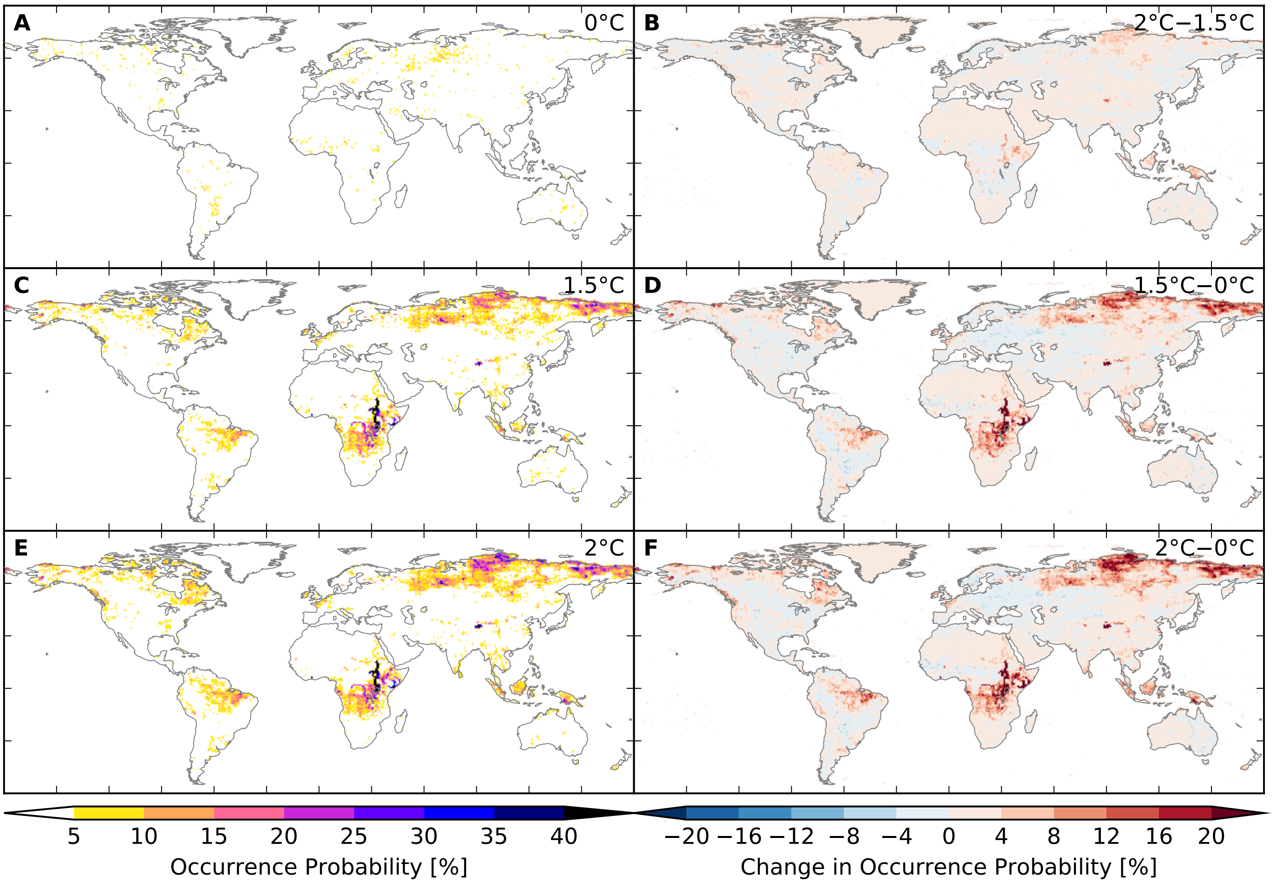

Figure S61: **Probability of occurrence of at least one flood event per year at different global warming levels (IPSL-CM5A-LR + H08).** Analogous to Figure S175.

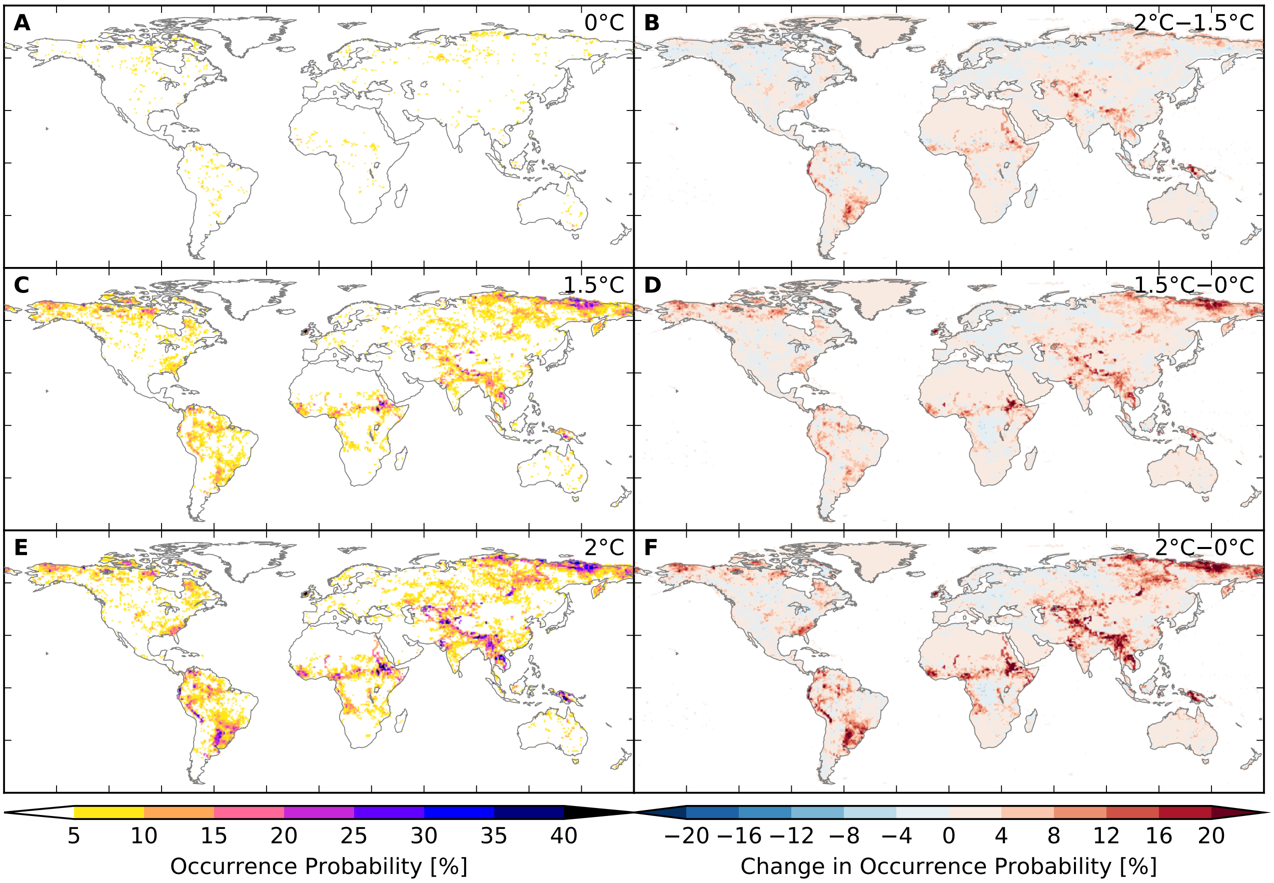

Figure S62: **Probability of occurrence of at least one flood event per year at different global warming levels (MIROC5 + H08).** Analogous to Figure S175.

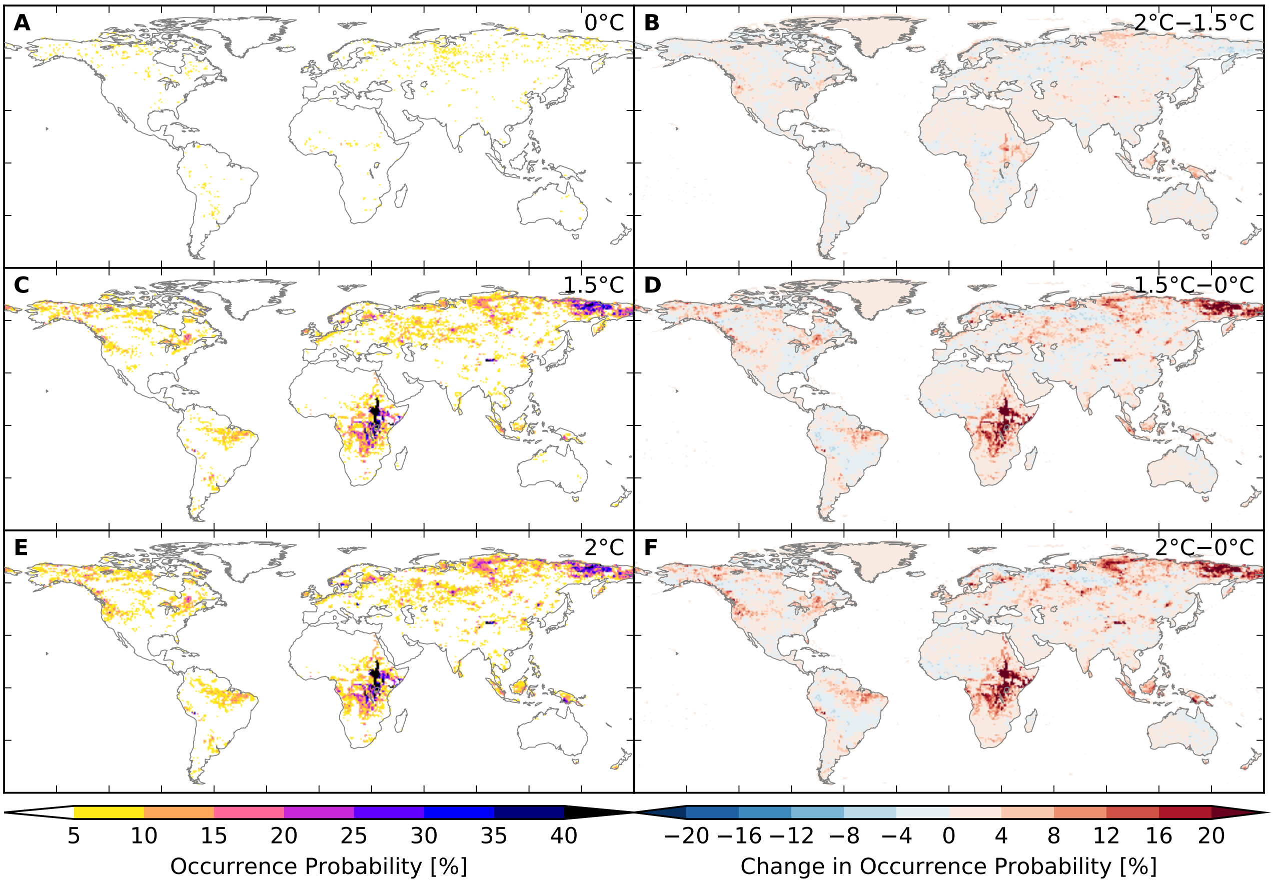

Figure S63: **Probability of occurrence of at least one flood event per year at different global warming levels (IPSL-CM5A-LR + JULES-W1).** Analogous to Figure S175.

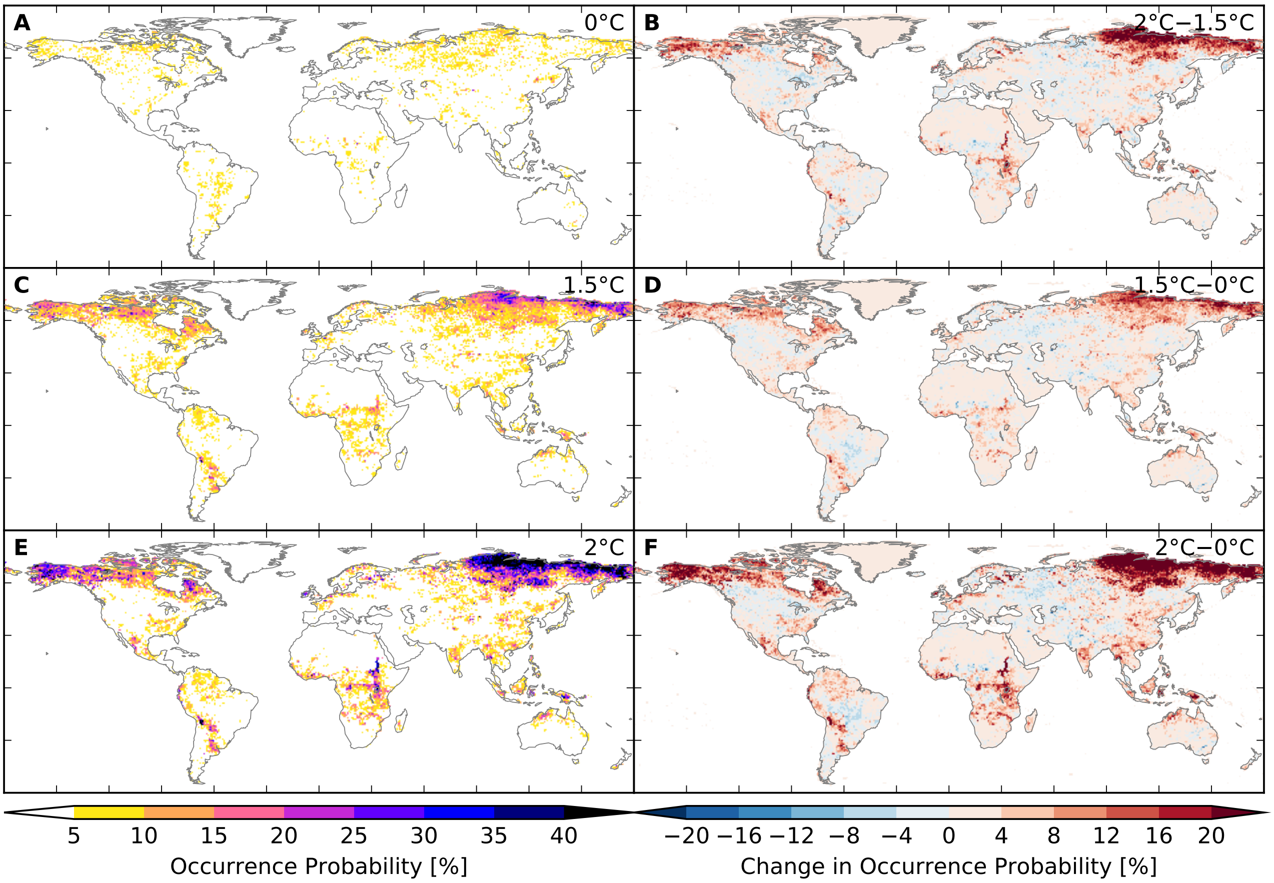

Figure S64: **Probability of occurrence of at least one flood event per year at different global warming levels (GFDL-ESM2M + LPJmL).** Analogous to Figure S175.

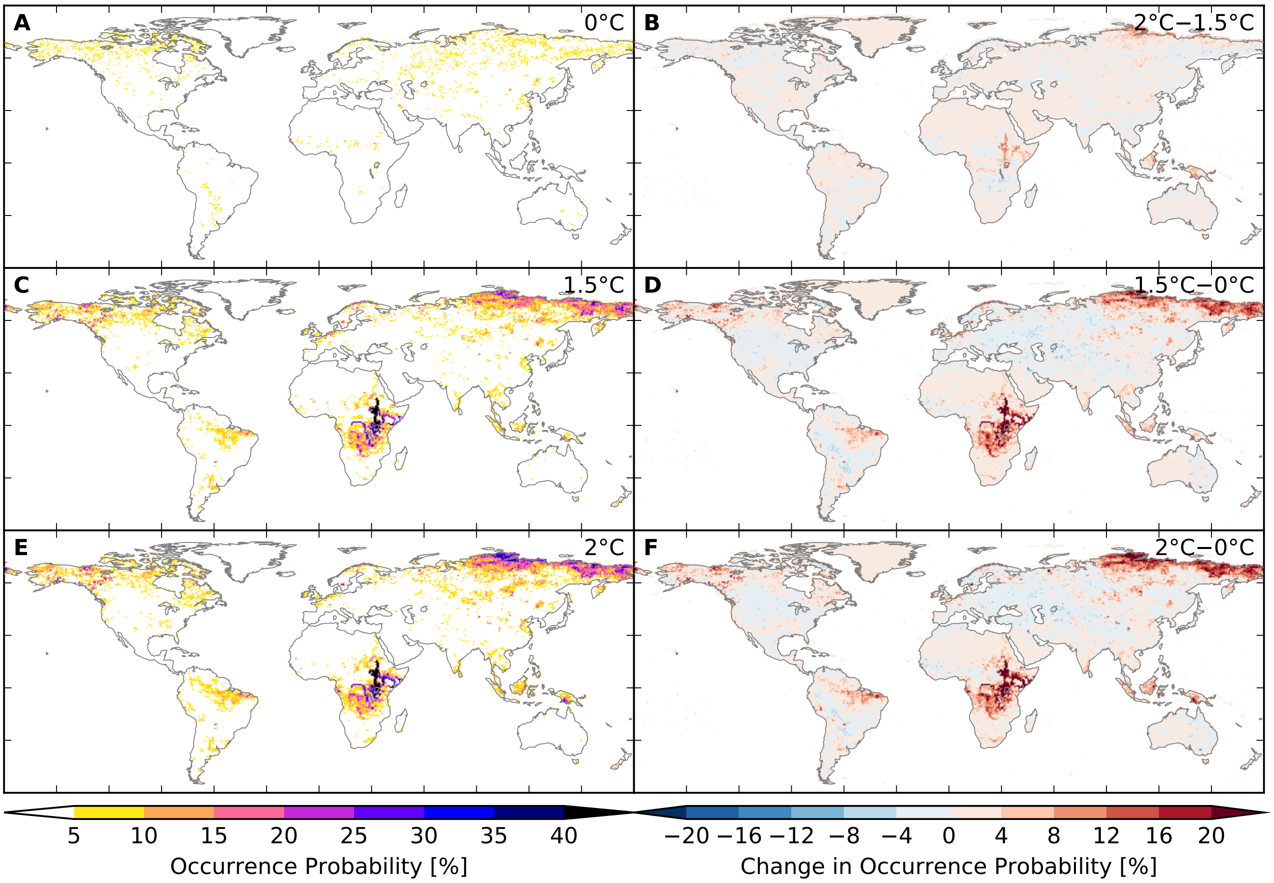

Figure S65: **Probability of occurrence of at least one flood event per year at different global warming levels (IPSL-CM5A-LR + LPJmL).** Analogous to Figure S175.

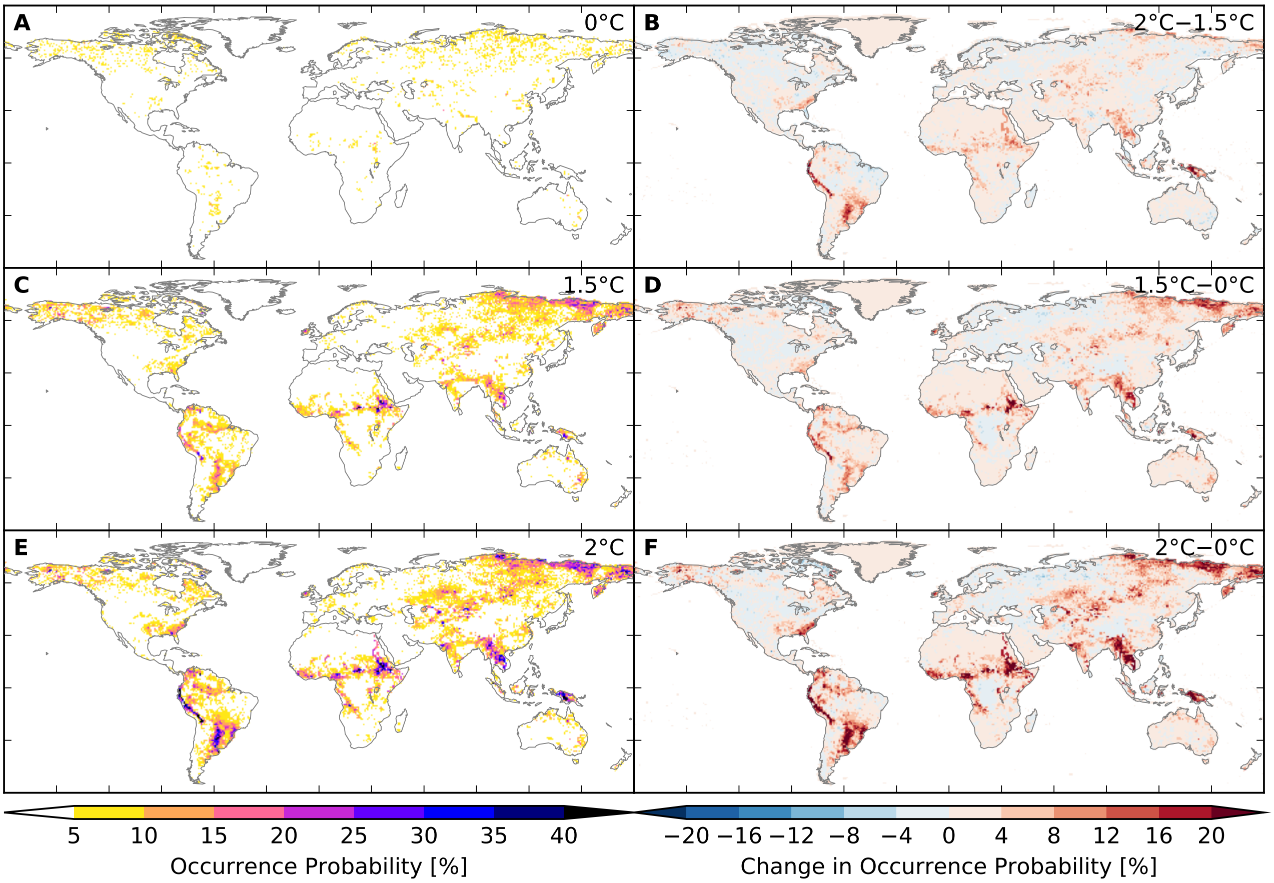

Figure S66: **Probability of occurrence of at least one flood event per year at different global warming levels (MIROC5 + LPJmL).** Analogous to Figure S175.

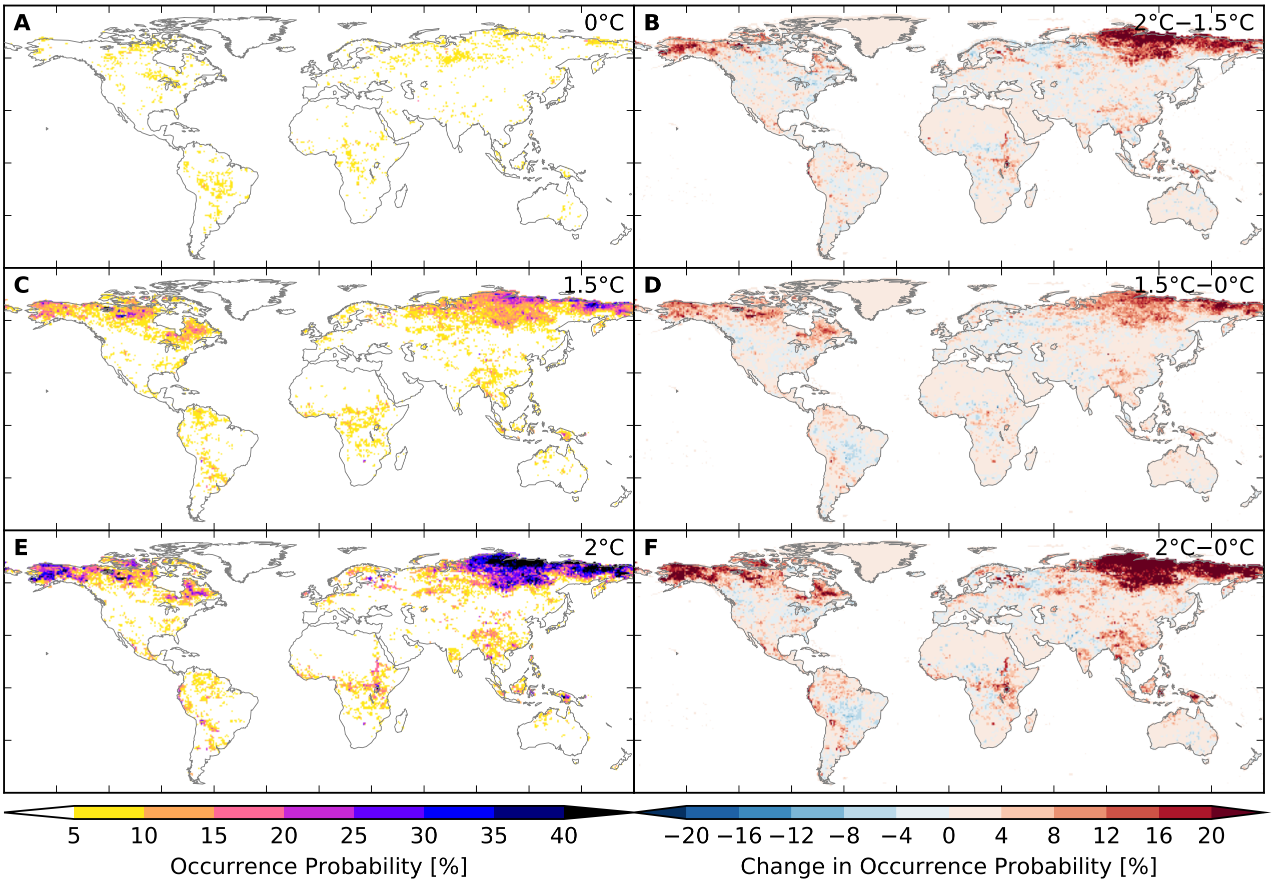

Figure S67: **Probability of occurrence of at least one flood event per year at different global warming levels (GFDL-ESM2M + MPI-HM).** Analogous to Figure S175.

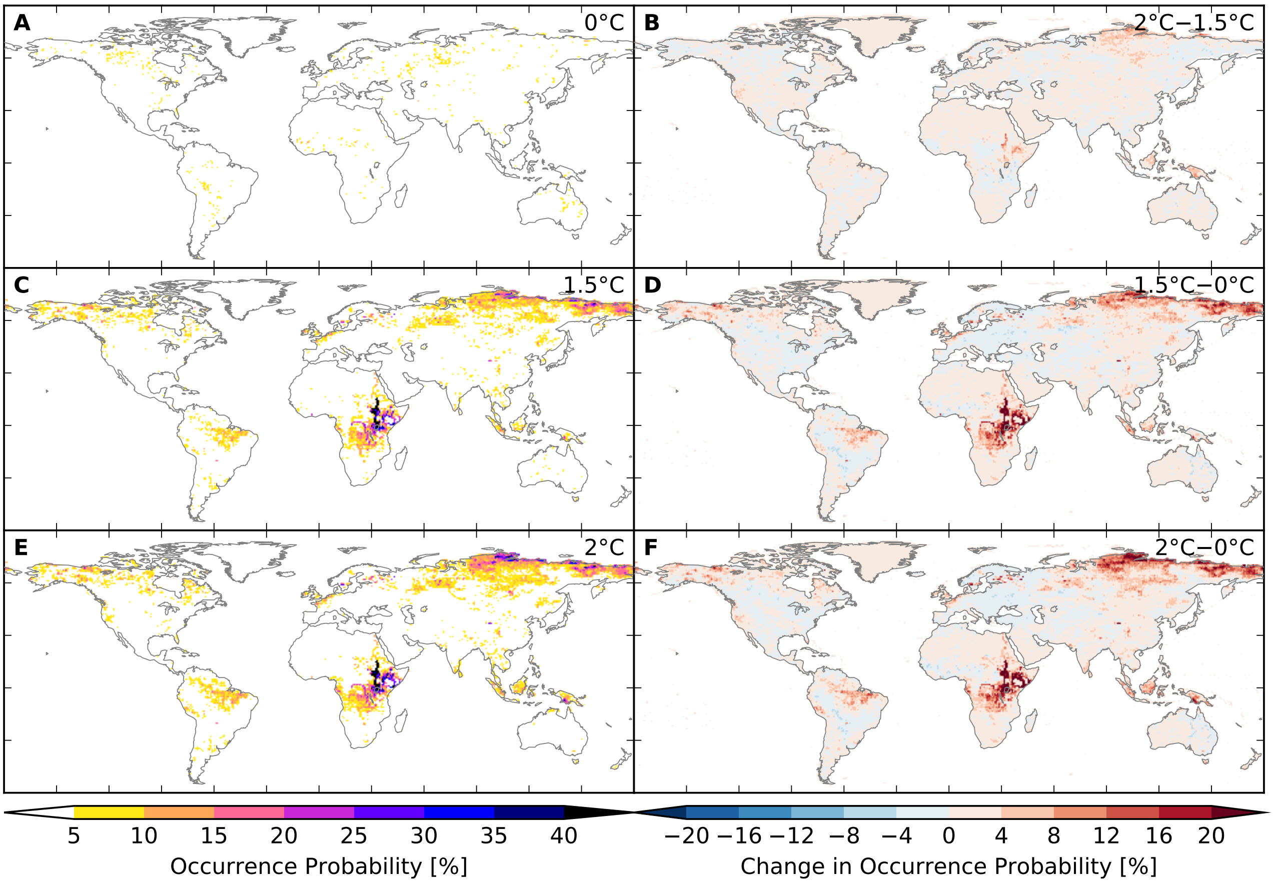

Figure S68: **Probability of occurrence of at least one flood event per year at different global warming levels (IPSL-CM5A-LR + MPI-HM).** Analogous to Figure S175.

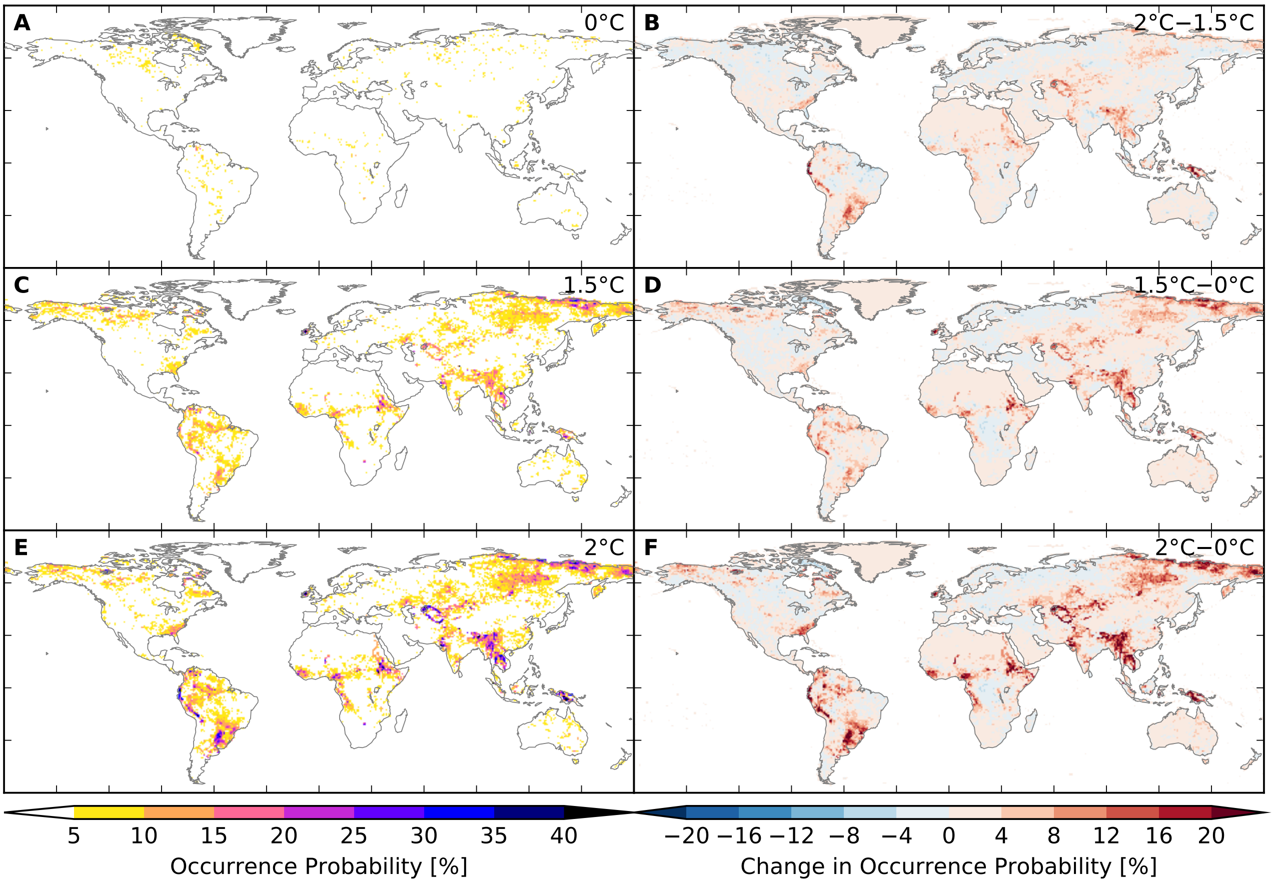

Figure S69: **Probability of occurrence of at least one flood event per year at different global warming levels (MIROC5 + MPI-HM).** Analogous to Figure S175.

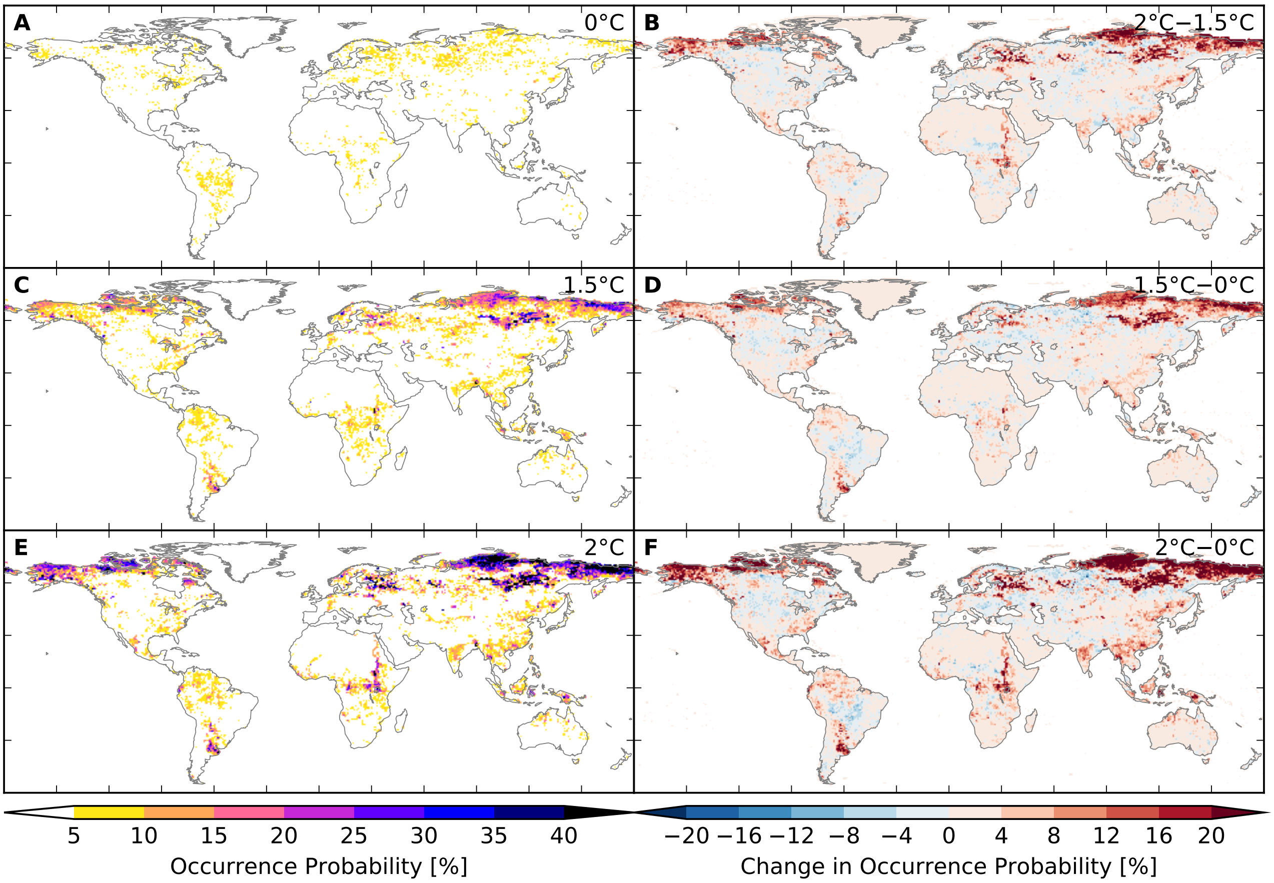

Figure S70: **Probability of occurrence of at least one flood event per year at different global warming levels (GFDL-ESM2M + ORCHIDEE).** Analogous to Figure S175.

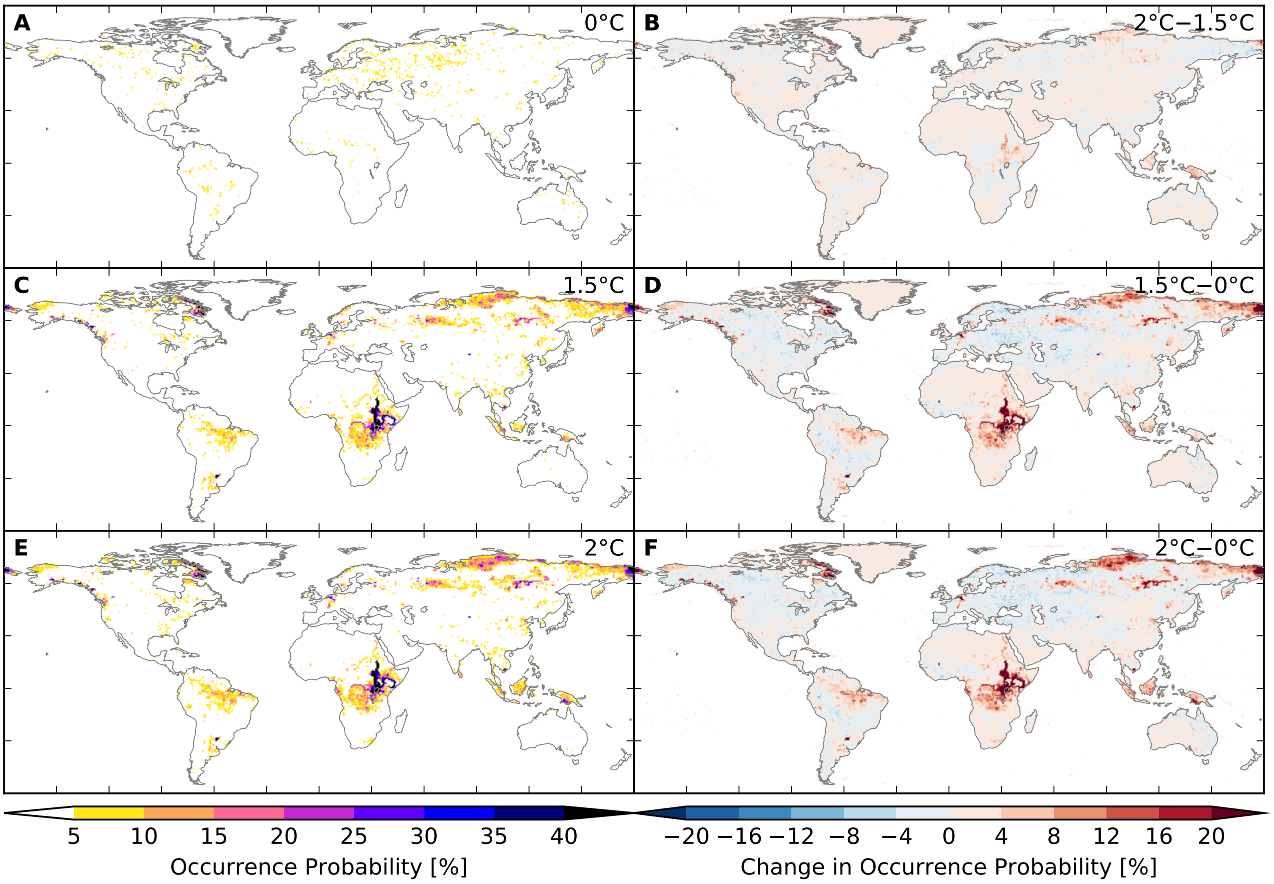

Figure S71: **Probability of occurrence of at least one flood event per year at different global warming levels (IPSL-CM5A-LR + ORCHIDEE).** Analogous to Figure S175.

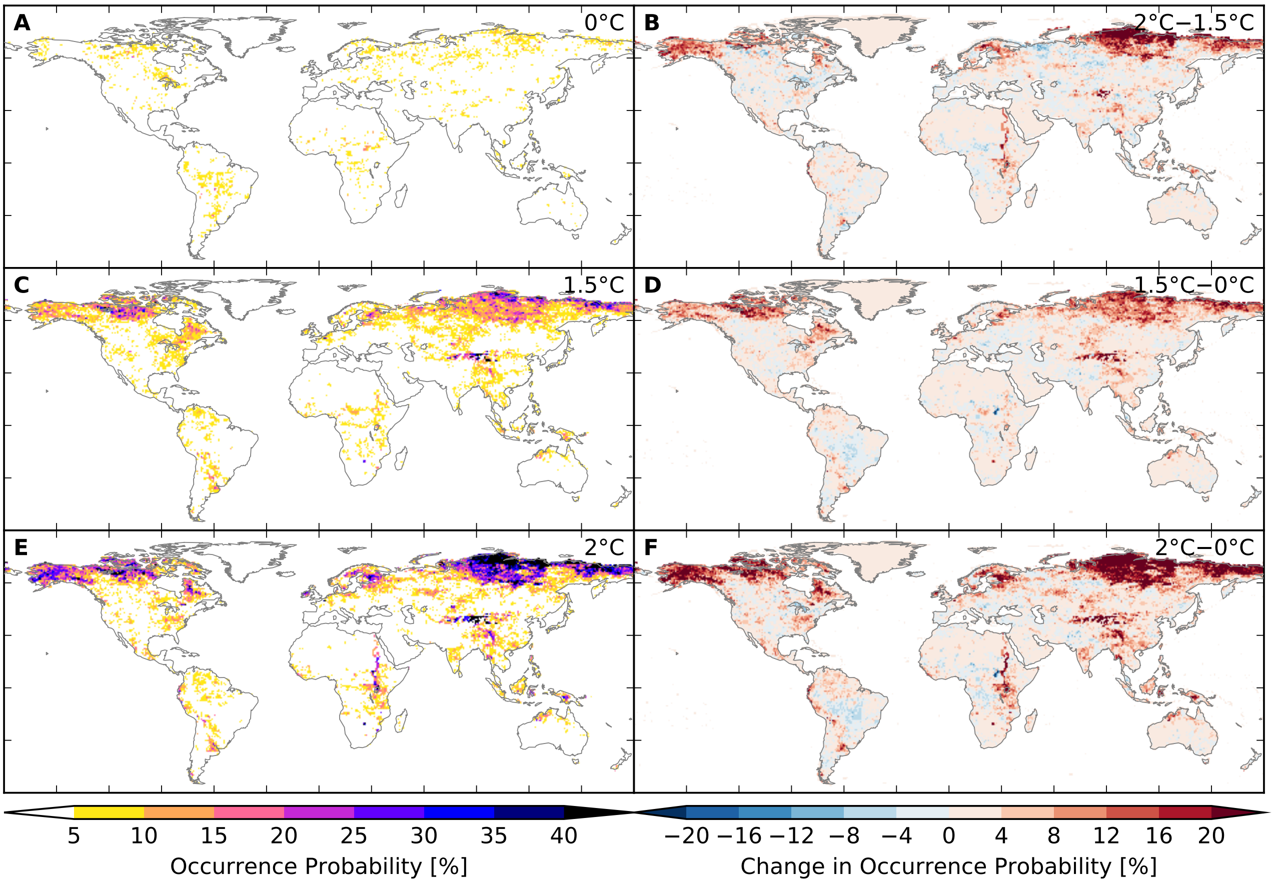

Figure S72: **Probability of occurrence of at least one flood event per year at different global warming levels (GFDL-ESM2M + PCR-GLOBWB).** Analogous to Figure S175.

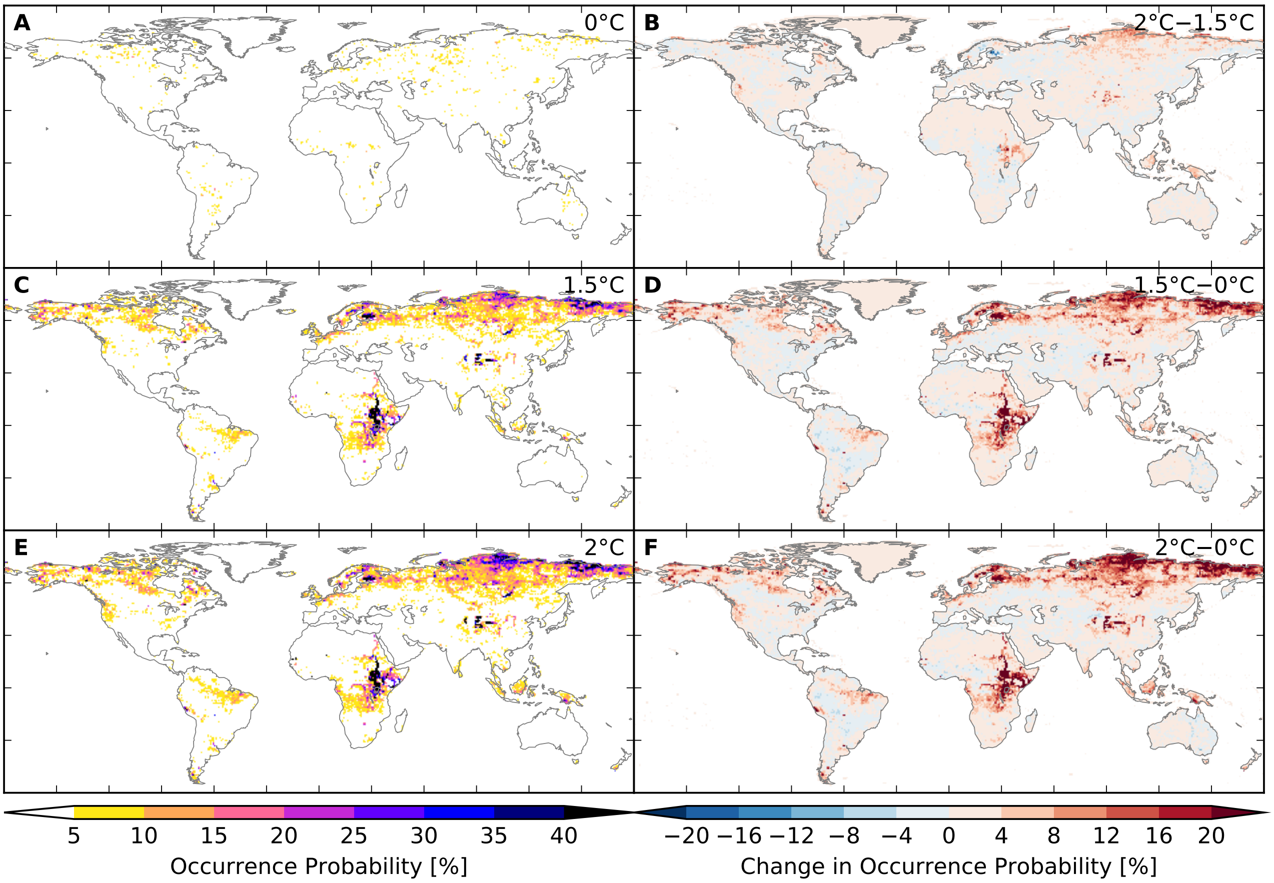

Figure S73: **Probability of occurrence of at least one flood event per year at different global warming levels (IPSL-CM5A-LR + PCR-GLOBWB).** Analogous to Figure S175.

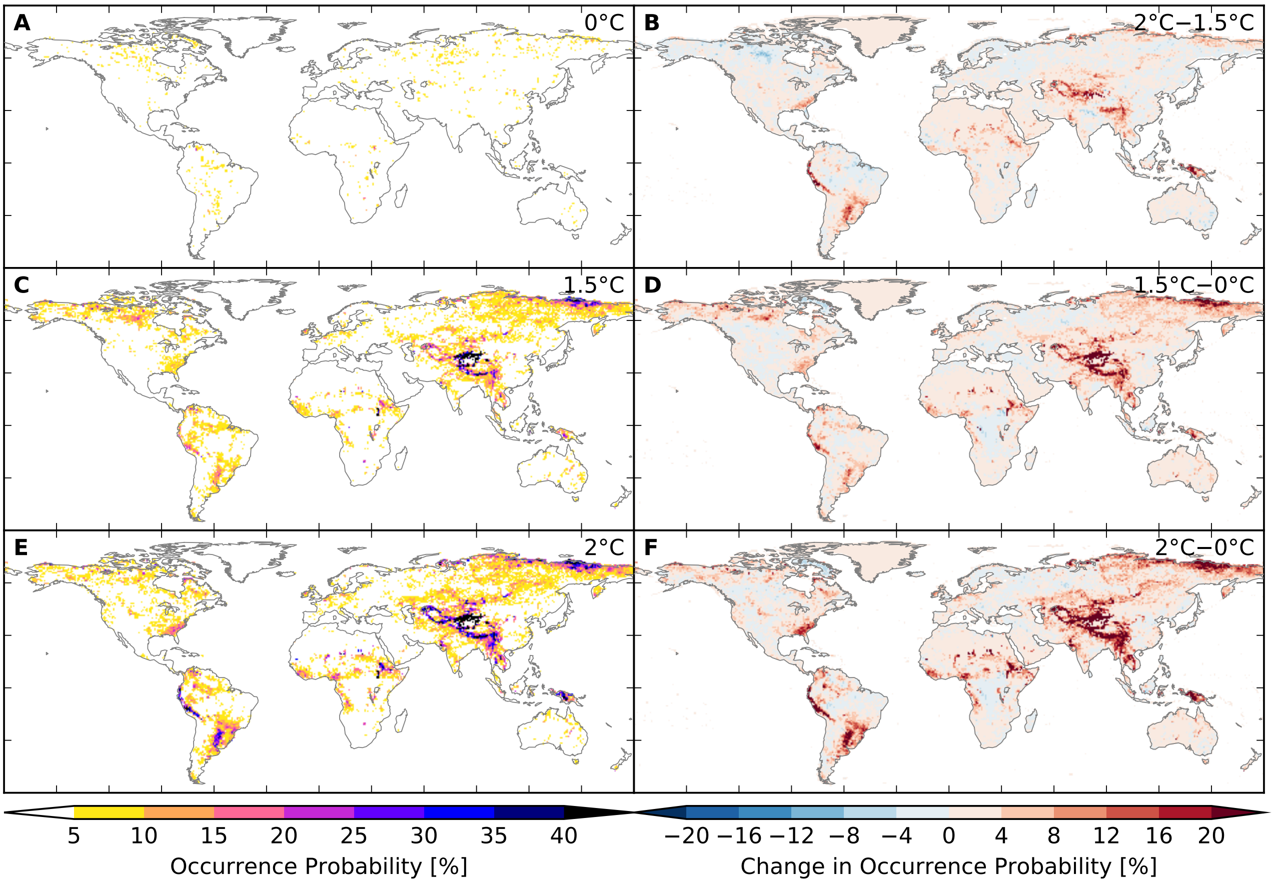

Figure S74: **Probability of occurrence of at least one flood event per year at different global warming levels (MIROC5 + PCR-GLOBWB).** Analogous to Figure S175.

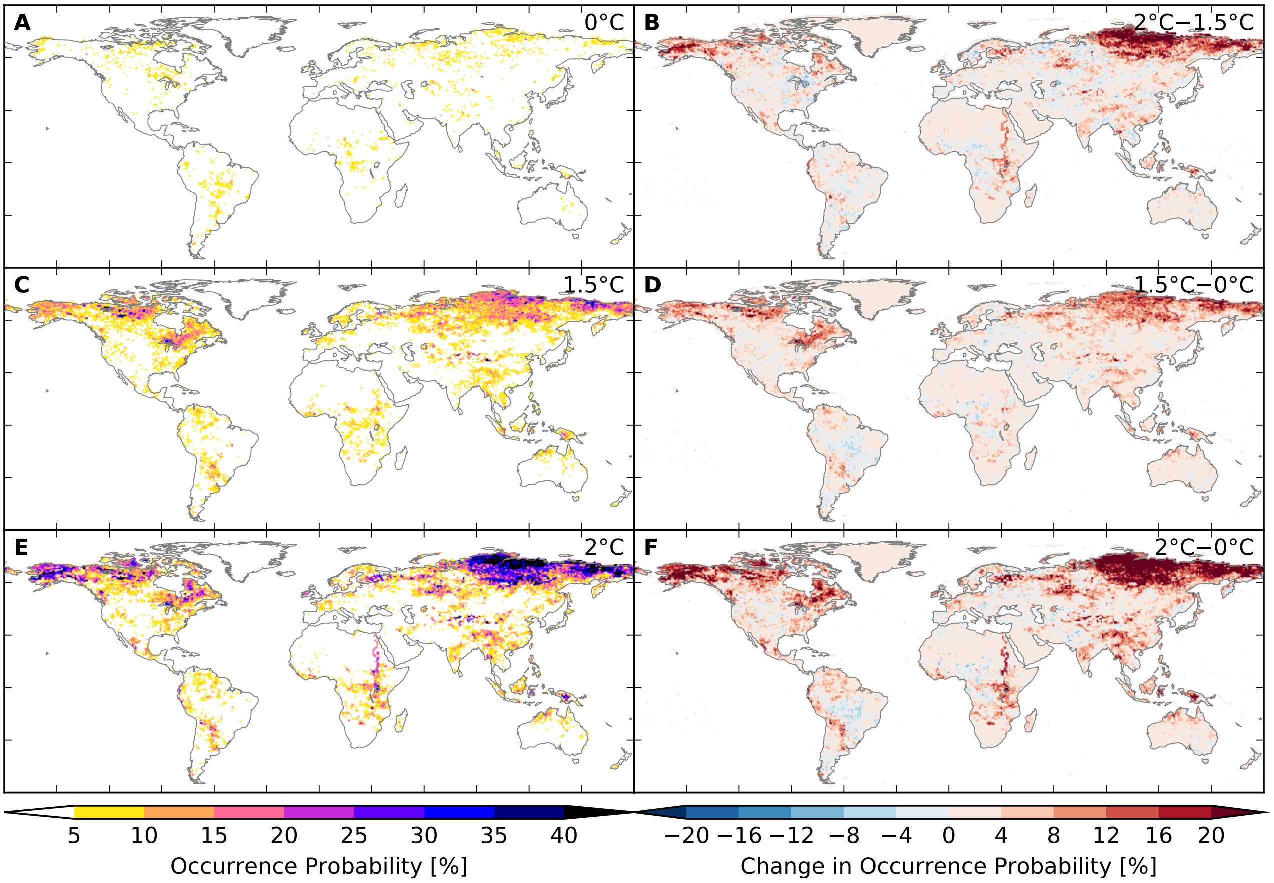

Figure S75: **Probability of occurrence of at least one flood event per year at different global warming levels (GFDL-ESM2M + WaterGAP2).** Analogous to Figure S175.

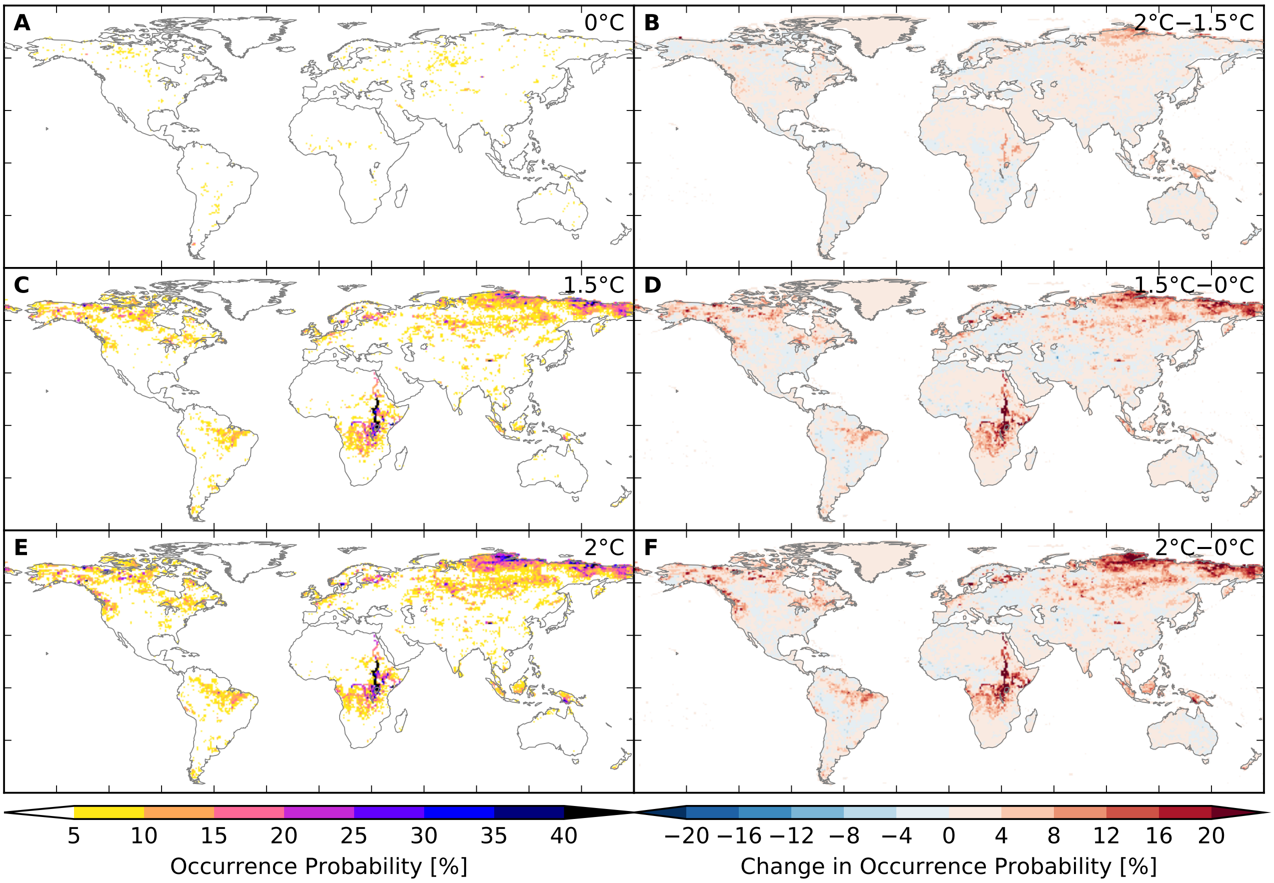

Figure S76: **Probability of occurrence of at least one flood event per year at different global warming levels (IPSL-CM5A-LR + WaterGAP2).** Analogous to Figure S175.

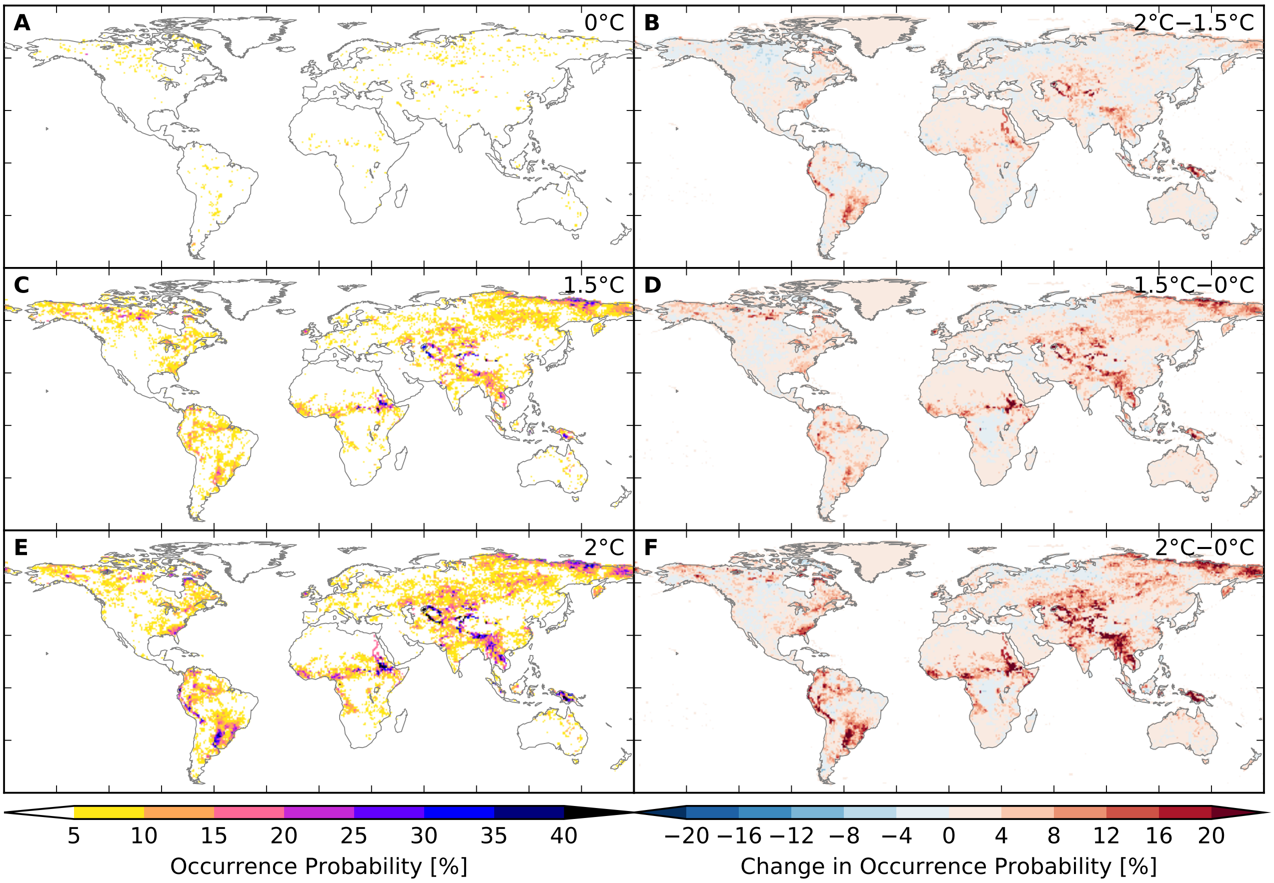

Figure S77: **Probability of occurrence of at least one flood event per year at different global warming levels (MIROC5 + WaterGAP2).** Analogous to Figure S175.

8.2 Tropical Cyclones

For tropical cyclones we provide 100 model realizations of the same model. Here we show one example, i.e. one realization for each GCM. Despite slight differences between different realizations, that account for the stochasticity of tropical cyclone impacts, we do not observe relevant realization-specific deviations that require a detailed discussion. All model realizations-GCM combinations are available on request.

Areas affected

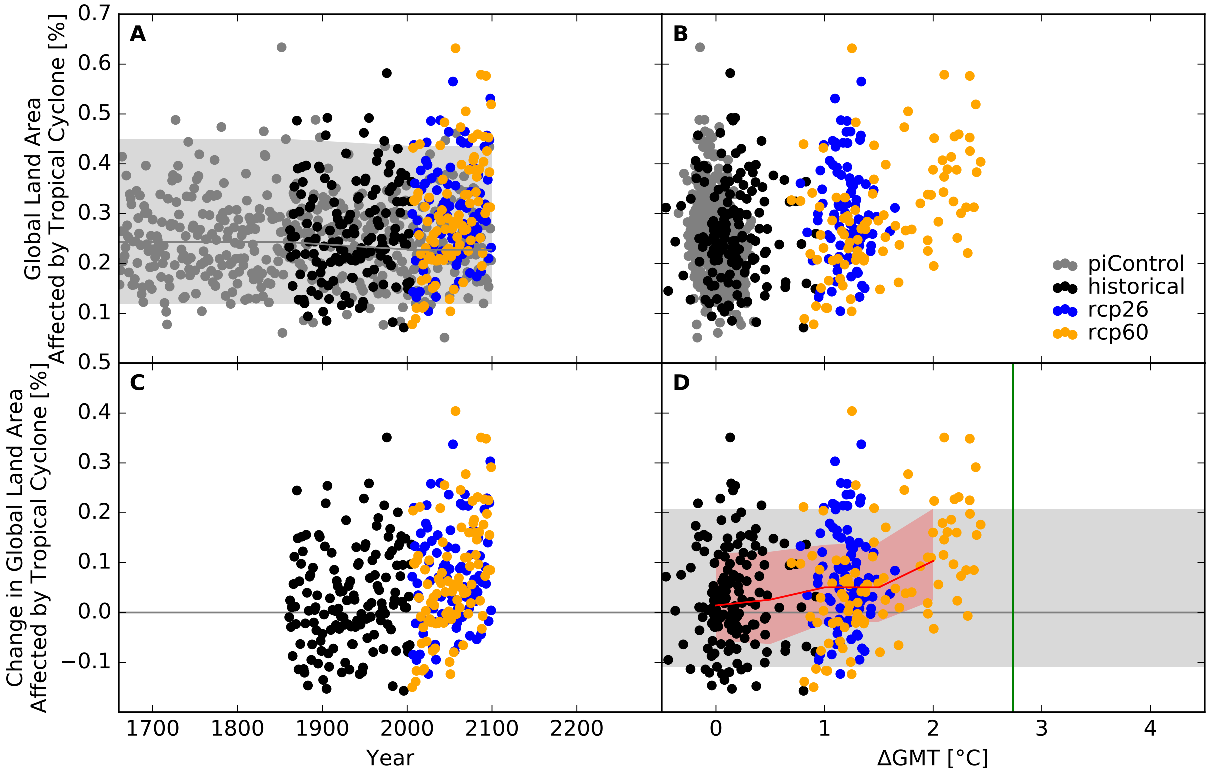

Figure S78: **Derivation of the pure effect of climate change on global land area fraction affected by tropical cyclone events (GFDL-ESM2M + KE-TG-001).** Panel A: Time series of annual global land area fraction affected (AFA) by tropical cyclone events for pre-industrial climate (grey dots), historical climate (black dots), climate projections for RCP2.6 (blue dots), and RCP6.0 (orange dots). In all simulations, socio-economic conditions are varied according to the historically observed development between 1860 and 2005, and held fixed at 1860 conditions before 1860 and at 2005 conditions after 2005. Shaded areas before 1860/after 2005 represent the range from the 2nd to the 98th percentile of the distribution of the annual AFA under pre-industrial climate conditions in combination with 1860/2005 socio-economic conditions; the solid gray lines represent the respective median values; the shaded areas and solid gray line between 1860 and 2005 are linear interpolations of the respective values before 1860 and after 2005. Panel B: Data shown in Panel A plotted against the associated GCM-specific annual global mean temperature (GMT) change relative to the long-term pre-industrial mean. Panel C: Pure effect of climate change on AFA, calculated as the difference between the annual data shown in Panel A and the median of the simulations assuming pre-industrial climate conditions (solid gray line in Panel A). Panel D: Pure effect of climate change on AFA in terms of global mean temperature change, with distributions of the annual data estimated for each 1°C-wide bin of global mean temperature change that contains at least five data points, at least one data point above and at least one data point below the bin center. Areas shaded in red represent the range from the 20th to the 80th percentile around the median (solid red line) of these distributions. Areas shaded in gray represent the range from the 2nd to the 98th percentile of the zero-centered distribution of the annual AFA under pre-industrial climate and 2005 socio-economic conditions (cf. Panel A). The green vertical line represents the detection level defined as the global warming level at which a 1-in-50-years event under pre-industrial climate and 2005 socio-economic conditions becomes a 1-in-5-years event under changing climate and 2005 socio-economic conditions.

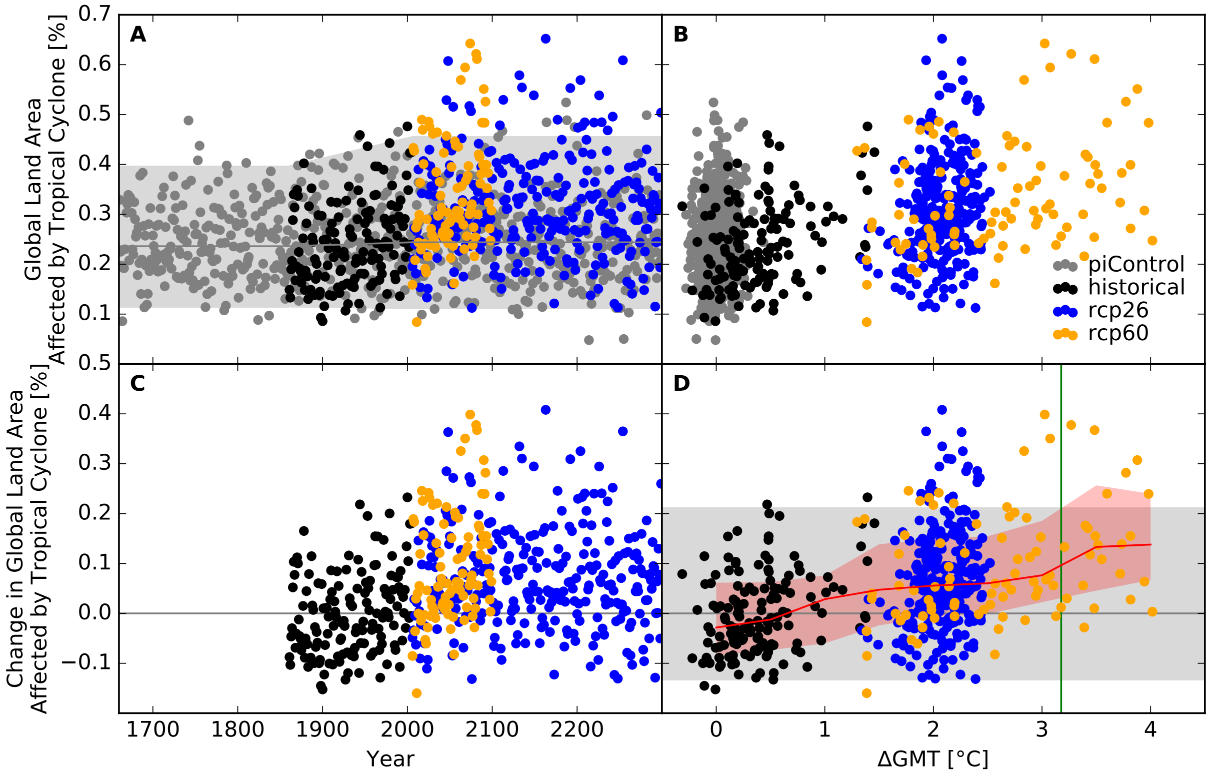

Figure S79: **Derivation of the pure effect of climate change on global land area fraction affected by tropical cyclone events (IPSL-CM5A-LR + KE-TG-001).** Analogous to Figure S78.

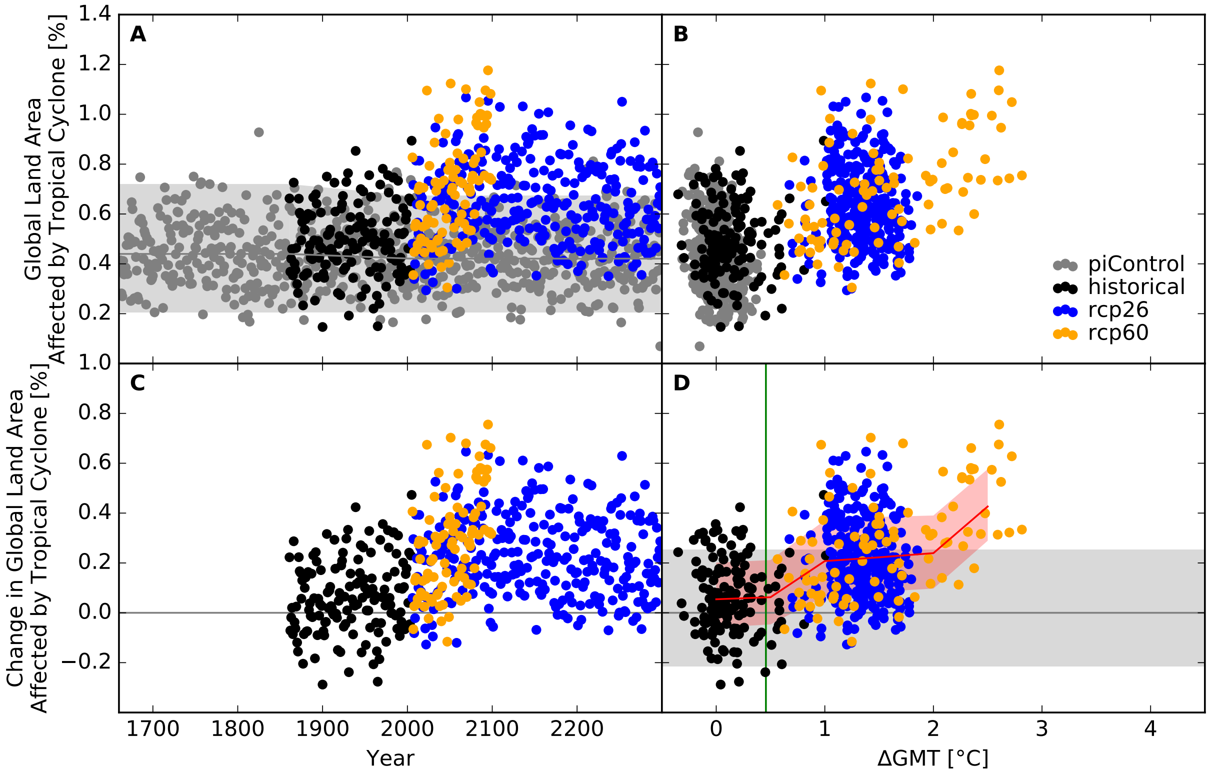

Figure S80: **Derivation of the pure effect of climate change on global land area fraction affected by tropical cyclone events (MIROC5 + KE-TG-001).** Analogous to Figure S78.

People exposed

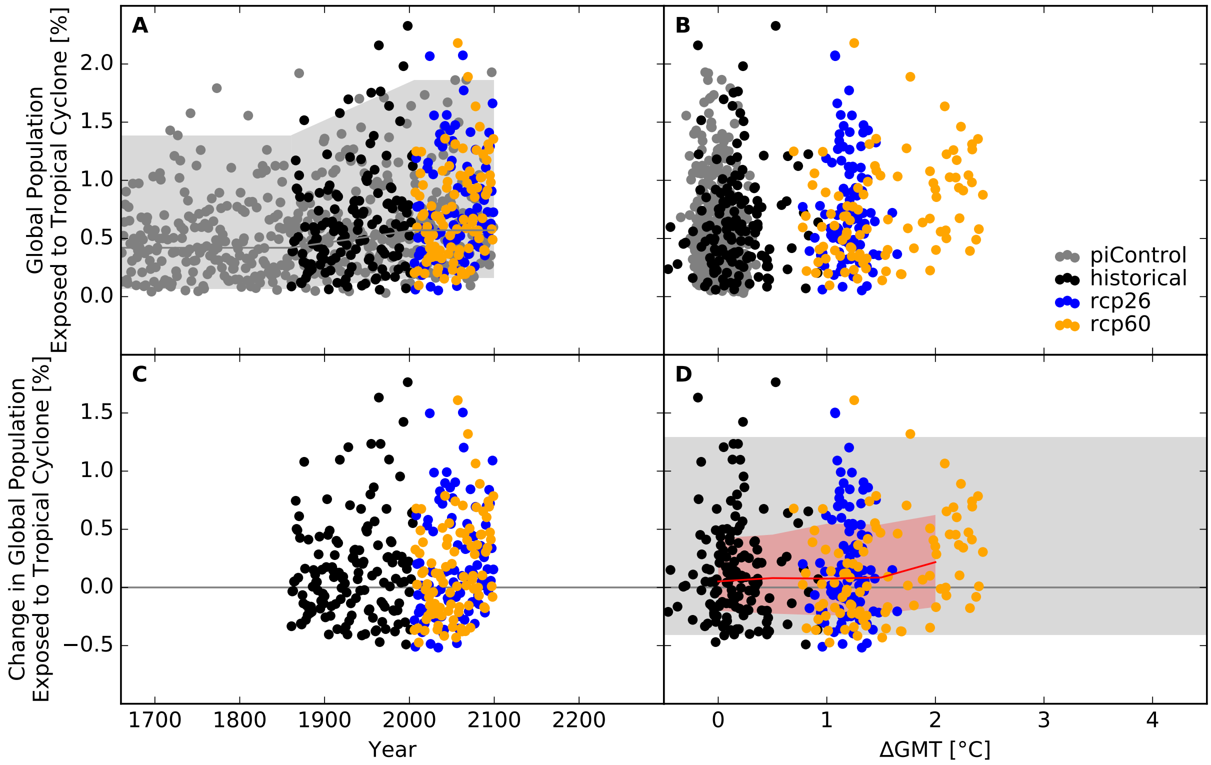

Figure S81: **Derivation of the pure effect of climate change on global population fraction affected by tropical cyclone events (GFDL-ESM2M + KE-TG-001).** Panel A: Time series of annual global population fraction affected (PFA) by tropical cyclone events for pre-industrial climate (grey dots), historical climate (black dots), climate projections for RCP2.6 (blue dots), and RCP6.0 (orange dots). In all simulations, socio-economic conditions are varied according to the historically observed development between 1860 and 2005, and held fixed at 1860 conditions before 1860 and at 2005 conditions after 2005. Shaded areas before 1860/after 2005 represent the range from the 2nd to the 98th percentile of the distribution of the annual PFA under pre-industrial climate conditions in combination with 1860/2005 socio-economic conditions; the solid gray lines represent the respective median values; the shaded areas and solid gray line between 1860 and 2005 are linear interpolations of the respective values before 1860 and after 2005. Panel B: Data shown in Panel A plotted against the associated GCM-specific annual global mean temperature (GMT) change relative to the long-term pre-industrial mean. Panel C: Pure effect of climate change on PFA, calculated as the difference between the annual data shown in Panel A and the median of the simulations assuming pre-industrial climate conditions (solid gray line in Panel A). Panel D: Pure effect of climate change on PFA in terms of global mean temperature change, with distributions of the annual data estimated for each 1°C-wide bin of global mean temperature change that contains at least five data points, at least one data point above and at least one data point below the bin center. Areas shaded in red represent the range from the 20th to the 80th percentile around the median (solid red line) of these distributions. Areas shaded in gray represent the range from the 2nd to the 98th percentile of the zero-centered distribution of the annual PFA under pre-industrial climate and 2005 socio-economic conditions (cf. Panel A). The green vertical line represents the detection level defined as the global warming level at which a 1-in-50-years event under pre-industrial climate and 2005 socio-economic conditions becomes a 1-in-5-years event under changing climate and 2005 socio-economic conditions.

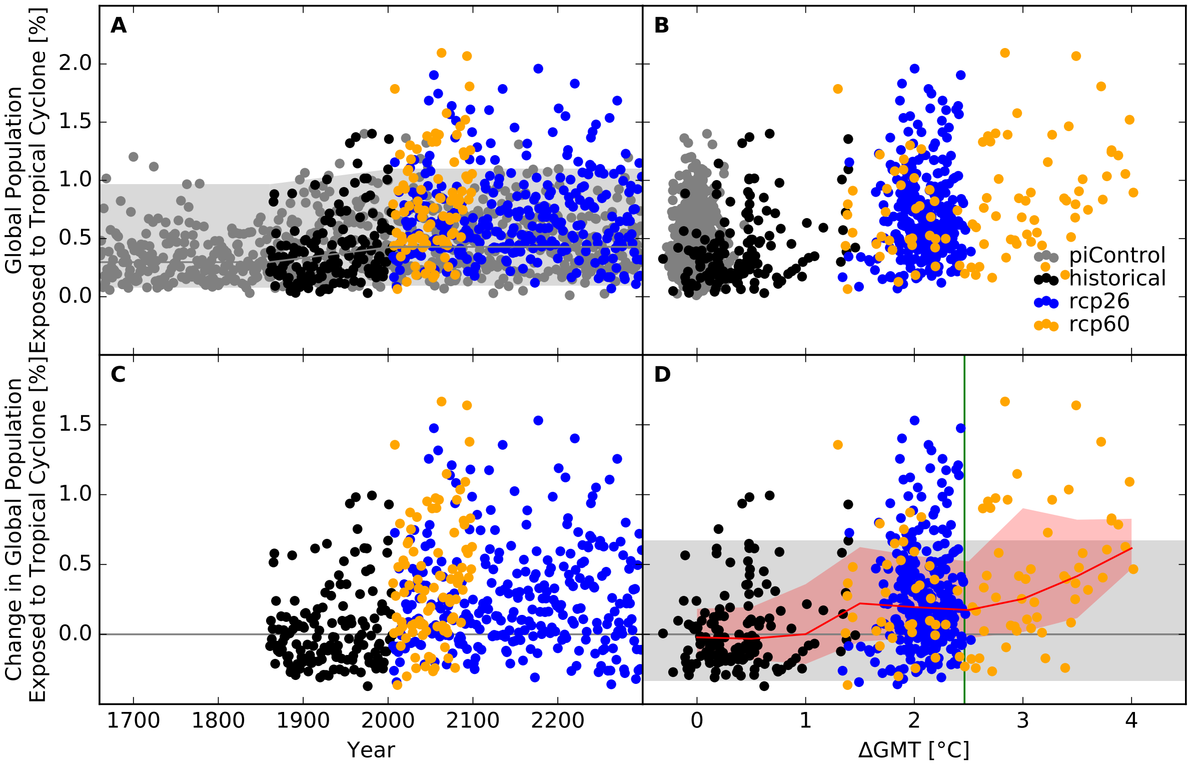

Figure S82: **Derivation of the pure effect of climate change on global population fraction affected by tropical cyclone events (IPSL-CM5A-LR + KE-TG-001).** Analogous to Figure S81.

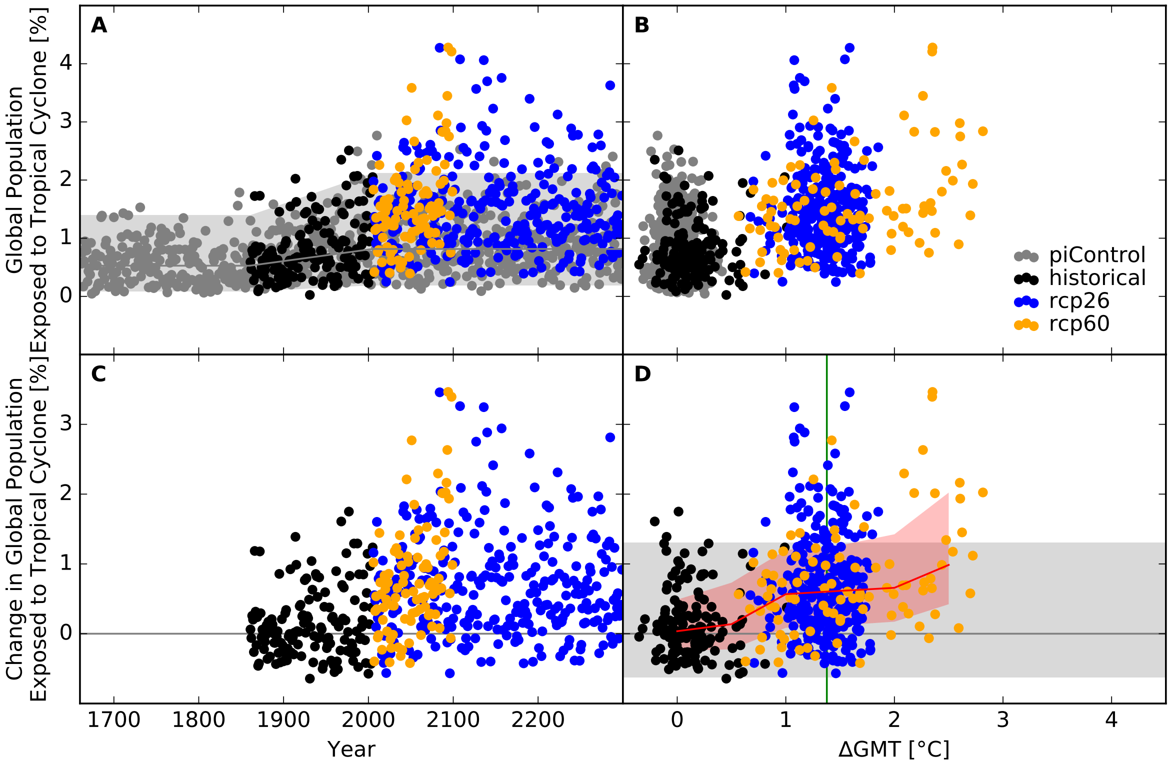

Figure S83: **Derivation of the pure effect of climate change on global population fraction affected by tropical cyclone events (MIROC5 + KE-TG-001).** Analogous to Figure S81.

Occurrence probability at grid scale

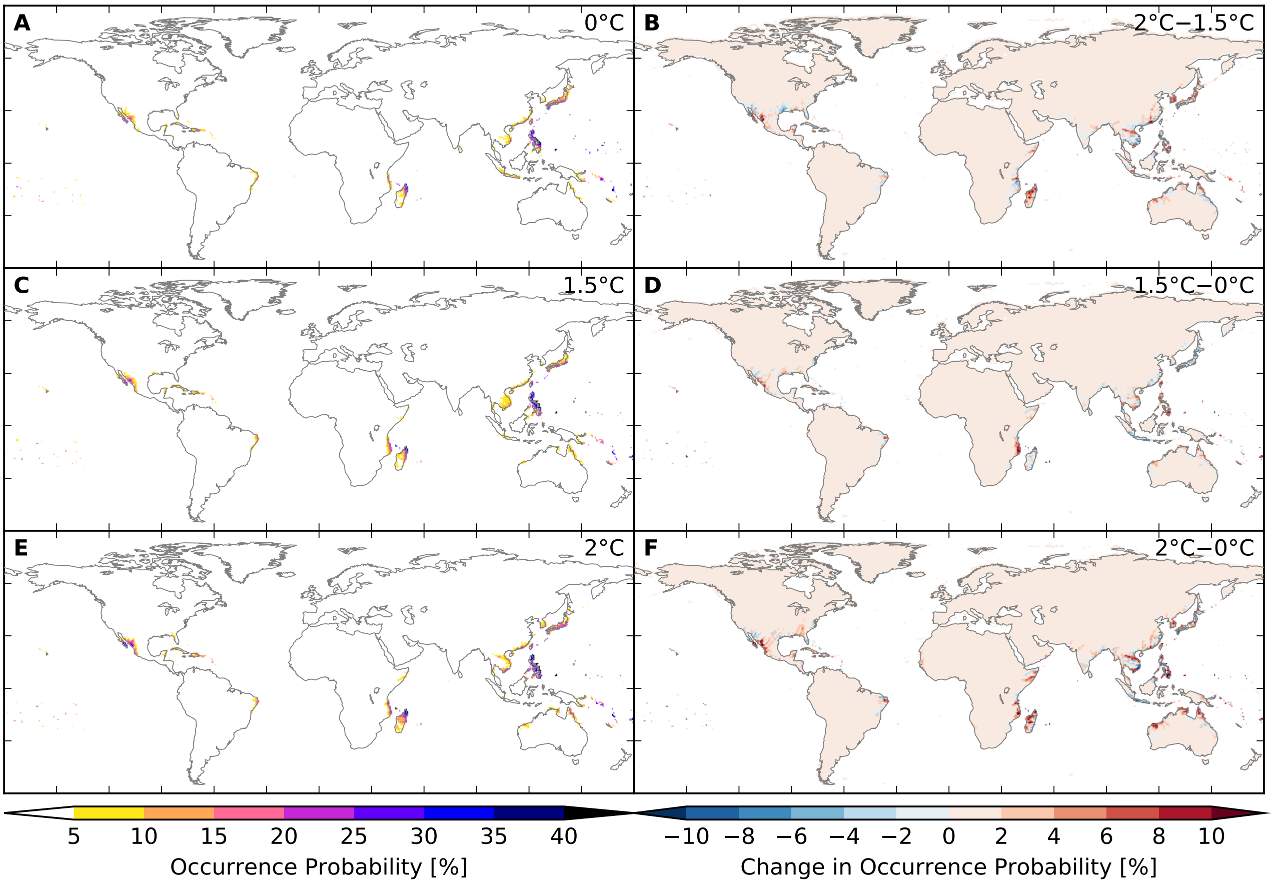

Figure S84: **Probability of occurrence of at least one tropical cyclone event per year at different global warming levels (GFDL-ESM2M + KE-TG-001).** Panels A, C, E: Probabilities at 0°C, 1.5°C, 2°C global mean temperature (GMT) change relative to the long-term pre-industrial mean GMT, respectively. Panels B, D, F: Differences between probabilities at GMT change levels of 2°C and 1.5°C, 1.5°C and 0°C, 2°C and 0°C, respectively.

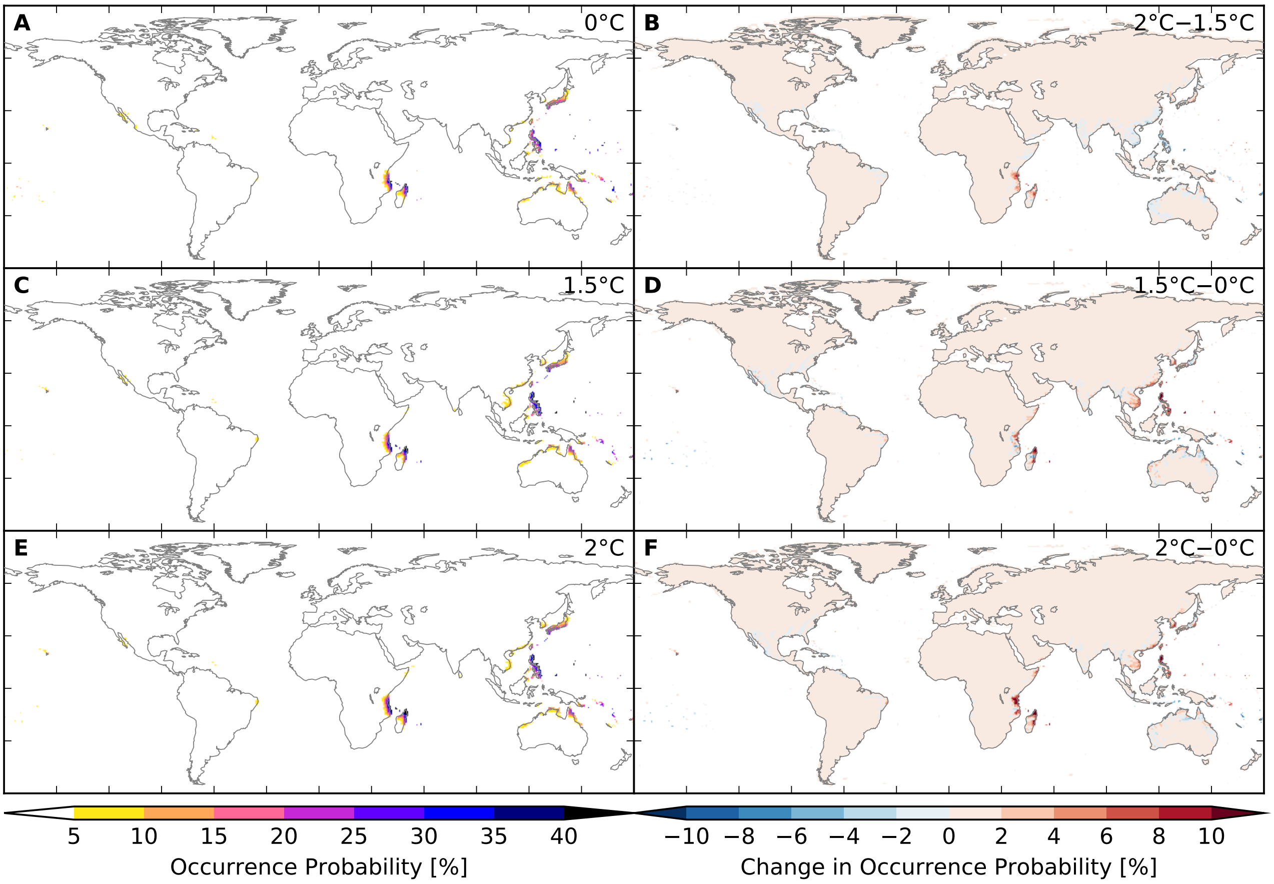

Figure S85: **Probability of occurrence of at least one tropical cyclone event per year at different global warming levels (IPSL-CM5A-LR + KE-TG-001).** Analogous to Figure S84.

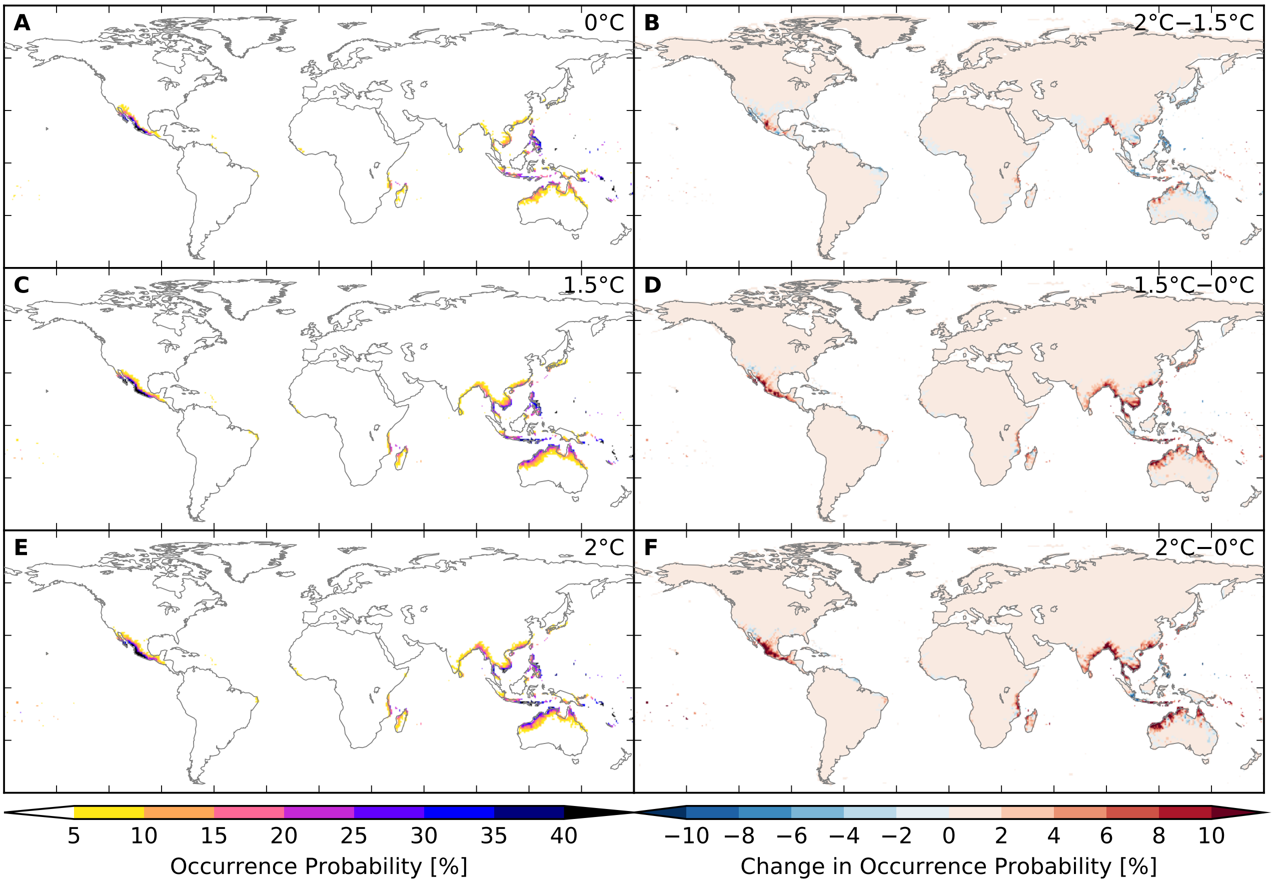

Figure S86: **Probability of occurrence of at least one tropical cyclone event per year at different global warming levels (MIROC5 + KE-TG-001).** Analogous to Figure S84.

8.3 Crop failures

Areas affected

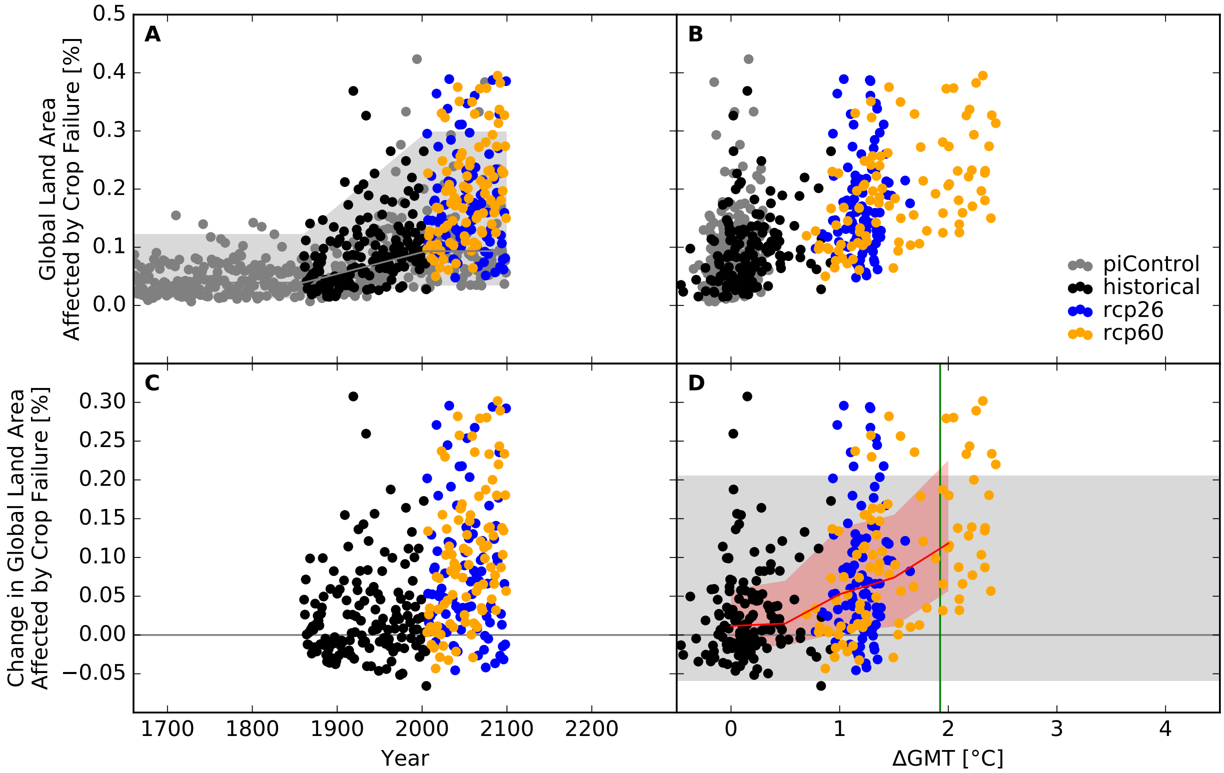

Figure S87: **Derivation of the pure effect of climate change on global land area fraction affected by crop failure events (GFDL-ESM2M + GEPIC).** Panel A: Time series of annual global land area fraction affected (AFA) by crop failure events for pre-industrial climate (grey dots), historical climate (black dots), climate projections for RCP2.6 (blue dots), and RCP6.0 (orange dots). In all simulations, socio-economic conditions are varied according to the historically observed development between 1860 and 2005, and held fixed at 1860 conditions before 1860 and at 2005 conditions after 2005. Shaded areas before 1860/after 2005 represent the range from the 2nd to the 98th percentile of the distribution of the annual AFA under pre-industrial climate conditions in combination with 1860/2005 socio-economic conditions; the solid gray lines represent the respective median values; the shaded areas and solid gray line between 1860 and 2005 are linear interpolations of the respective values before 1860 and after 2005. Panel B: Data shown in Panel A plotted against the associated GCM-specific annual global mean temperature (GMT) change relative to the long-term pre-industrial mean. Panel C: Pure effect of climate change on AFA, calculated as the difference between the annual data shown in Panel A and the median of the simulations assuming pre-industrial climate conditions (solid gray line in Panel A). Panel D: Pure effect of climate change on AFA in terms of global mean temperature change, with distributions of the annual data estimated for each 1°C-wide bin of global mean temperature change that contains at least five data points, at least one data point above and at least one data point below the bin center. Areas shaded in red represent the range from the 20th to the 80th percentile around the median (solid red line) of these distributions. Areas shaded in gray represent the range from the 2nd to the 98th percentile of the zero-centered distribution of the annual AFA under pre-industrial climate and 2005 socio-economic conditions (cf. Panel A). The green vertical line represents the detection level defined as the global warming level at which a 1-in-50-years event under pre-industrial climate and 2005 socio-economic conditions becomes a 1-in-5-years event under changing climate and 2005 socio-economic conditions.

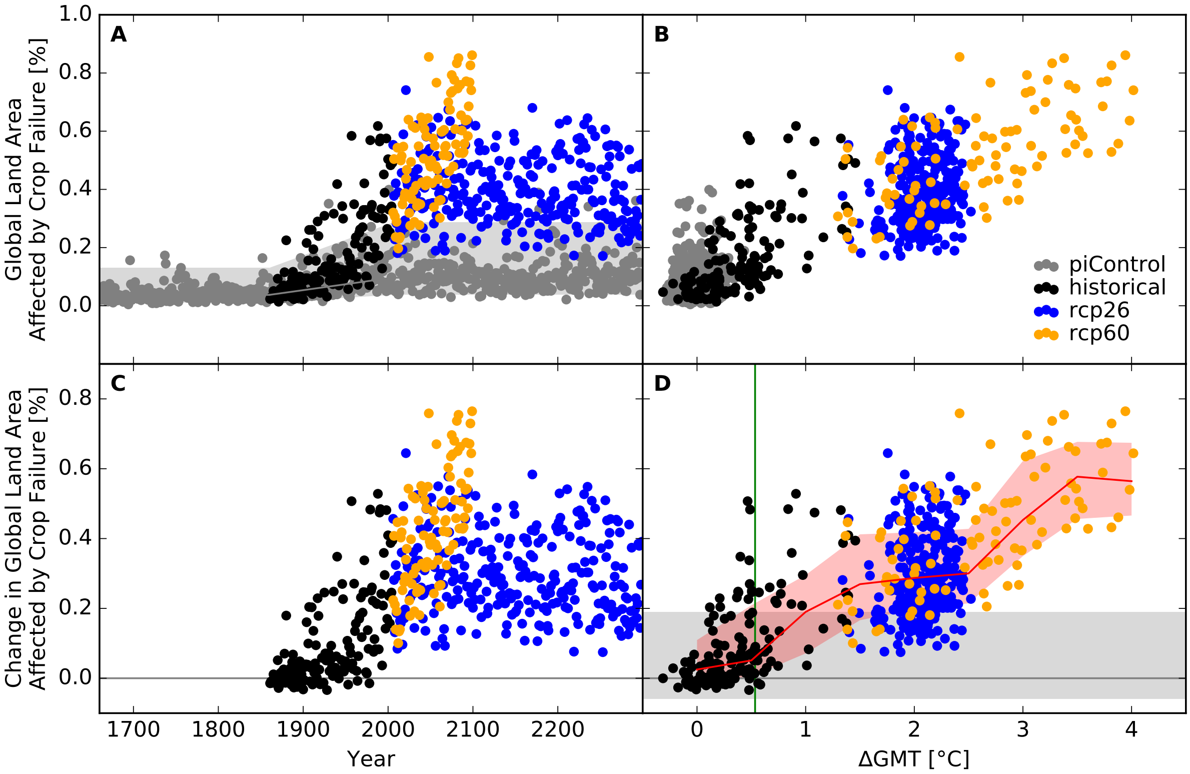

Figure S88: **Derivation of the pure effect of climate change on global land area fraction affected by crop failure events (IPSL-CM5A-LR + GEPIC).** Analogous to Figure S87.

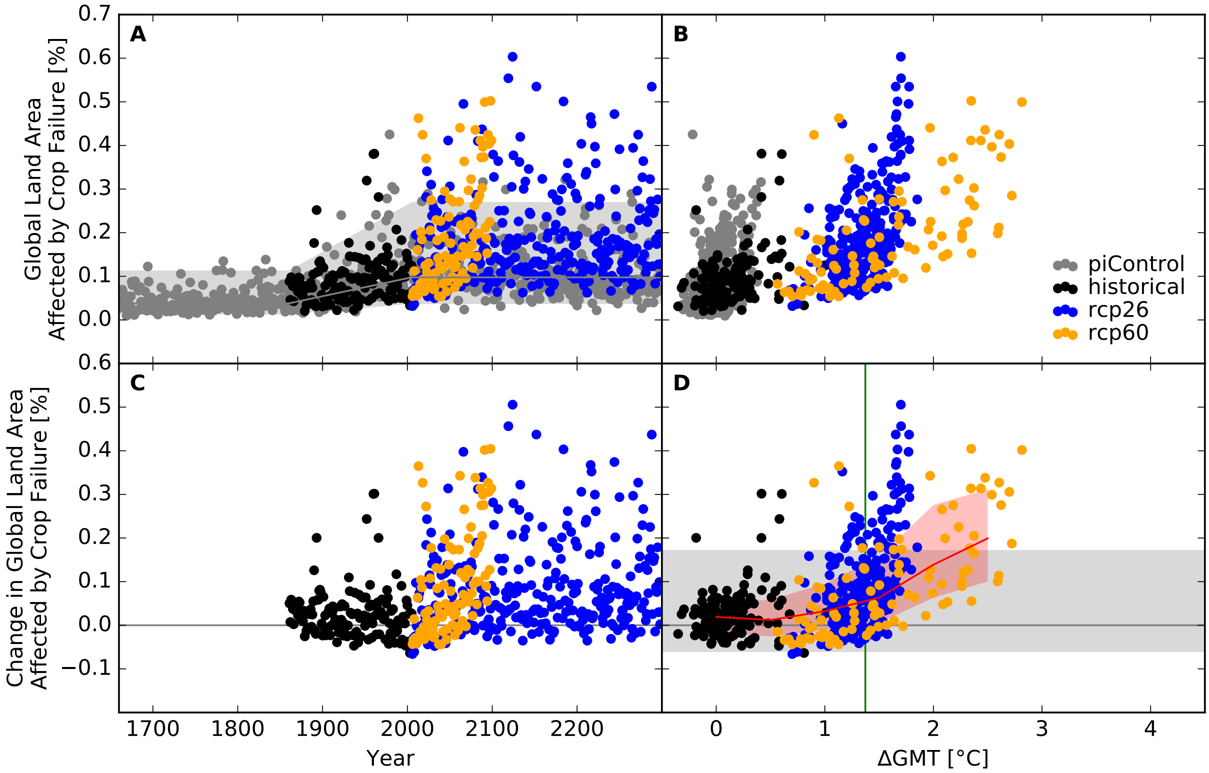

Figure S89: **Derivation of the pure effect of climate change on global land area fraction affected by crop failure events (MIROC5 + GEPIC).** Analogous to Figure S87.

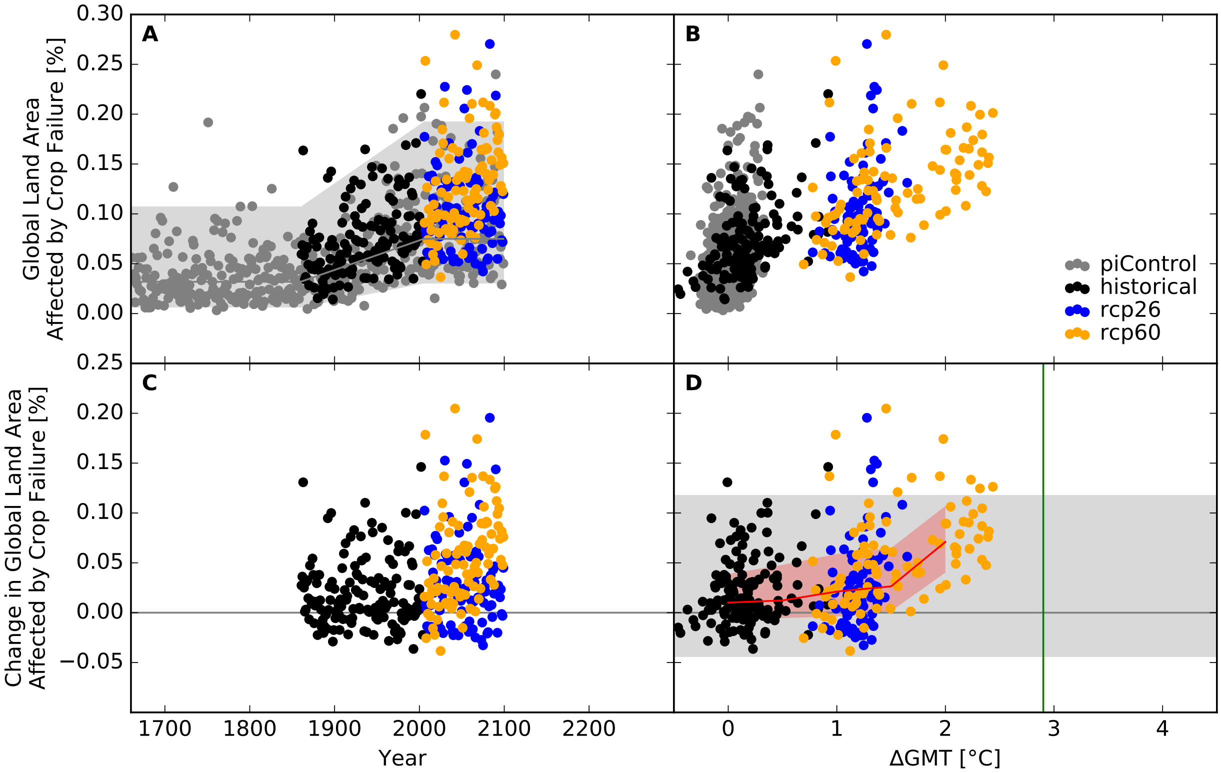

Figure S90: **Derivation of the pure effect of climate change on global land area fraction affected by crop failure events (GFDL-ESM2M + LPJmL).** Analogous to Figure S87.

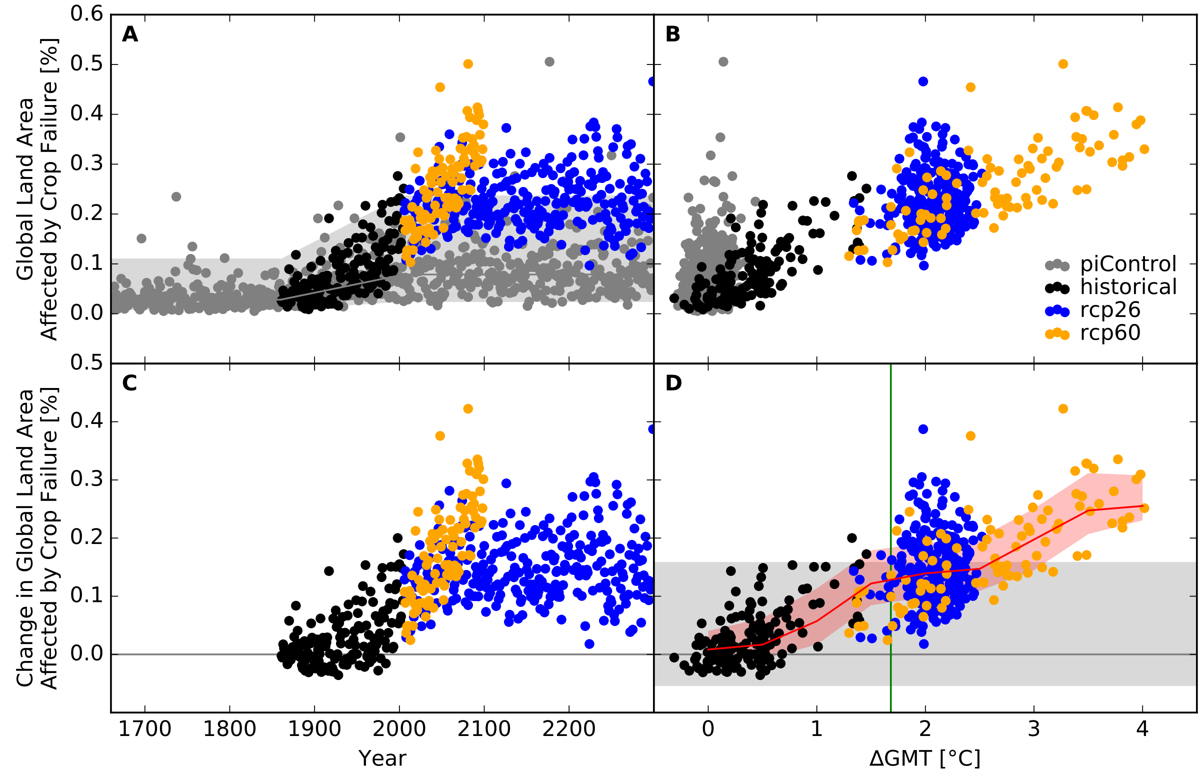

Figure S91: **Derivation of the pure effect of climate change on global land area fraction affected by crop failure events (IPSL-CM5A-LR + LPJmL).** Analogous to Figure S87.

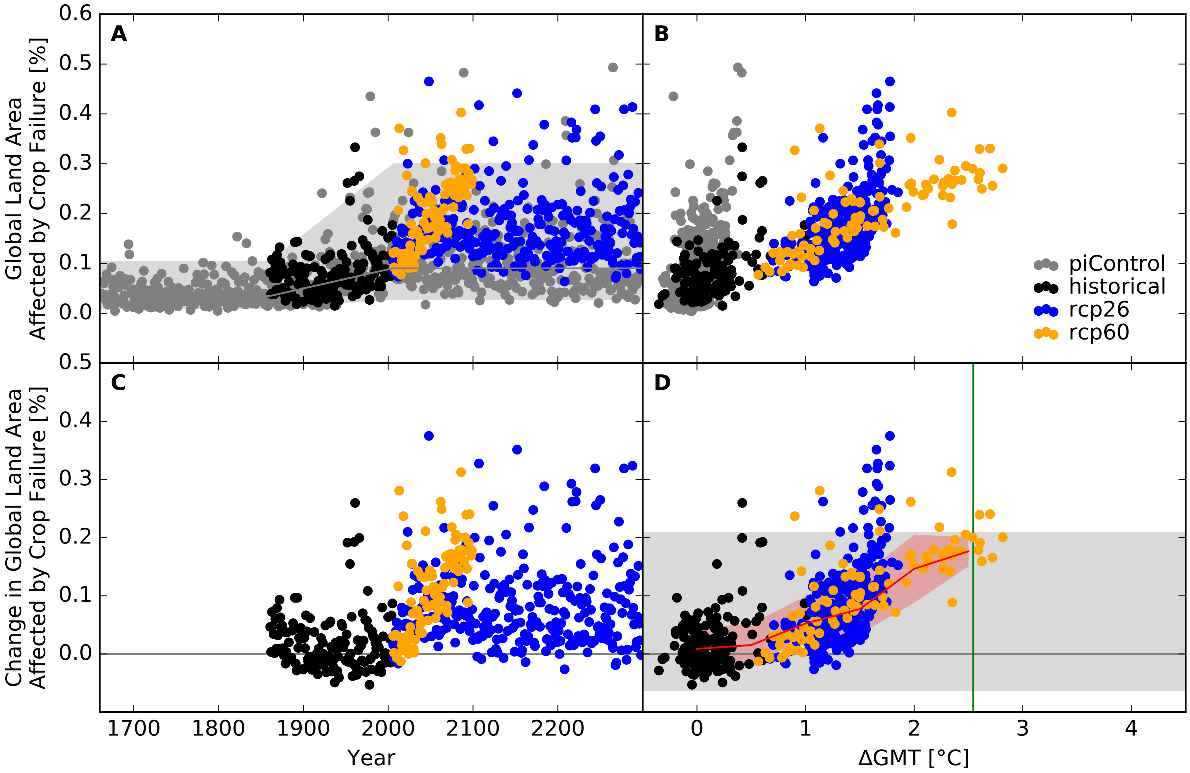

Figure S92: **Derivation of the pure effect of climate change on global land area fraction affected by crop failure events (MIROC5 + LPJmL).** Analogous to Figure S87.

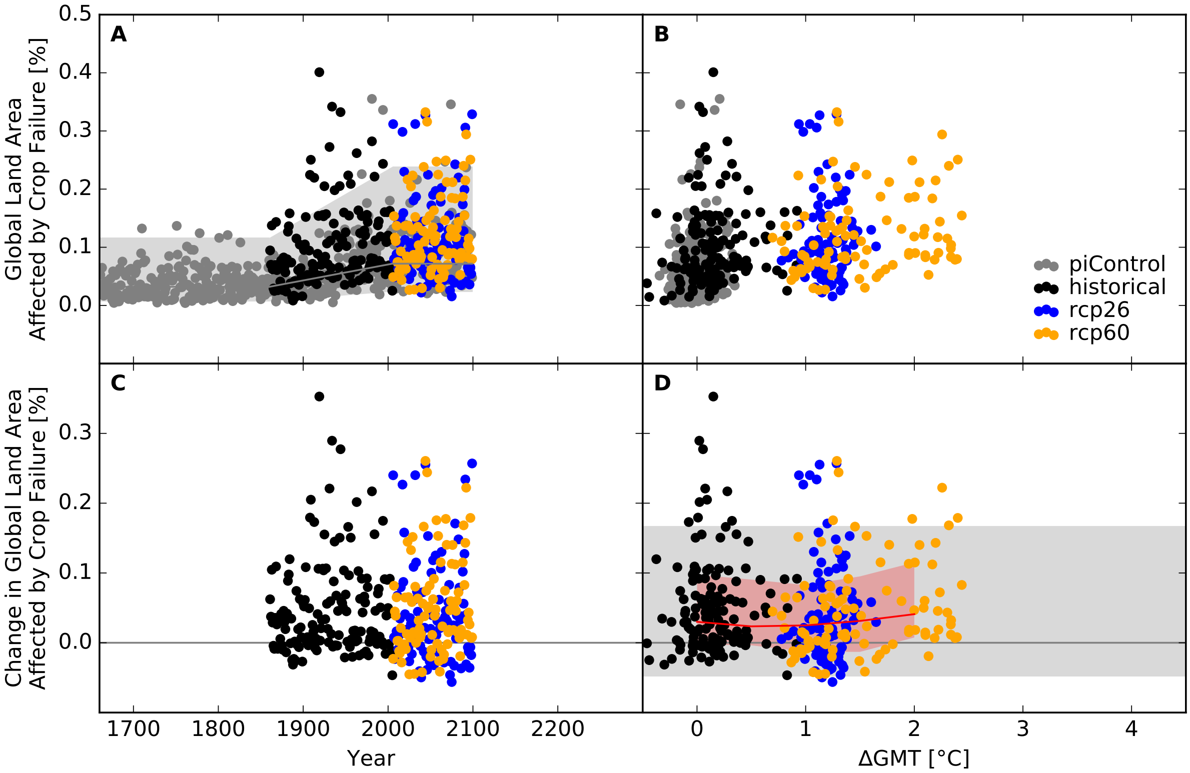

Figure S93: **Derivation of the pure effect of climate change on global land area fraction affected by crop failure events (GFDL-ESM2M + PEPIC).** Analogous to Figure S87.

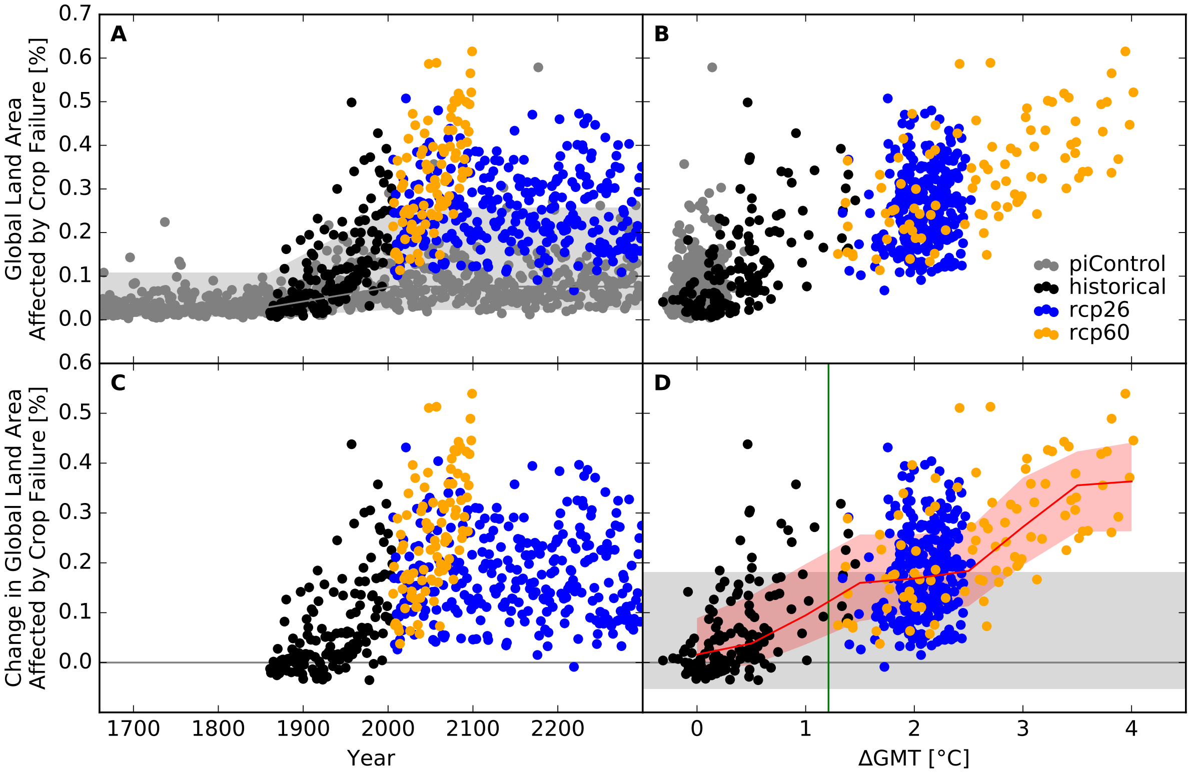

Figure S94: **Derivation of the pure effect of climate change on global land area fraction affected by crop failure events (IPSL-CM5A-LR + PEPIC).** Analogous to Figure S87.

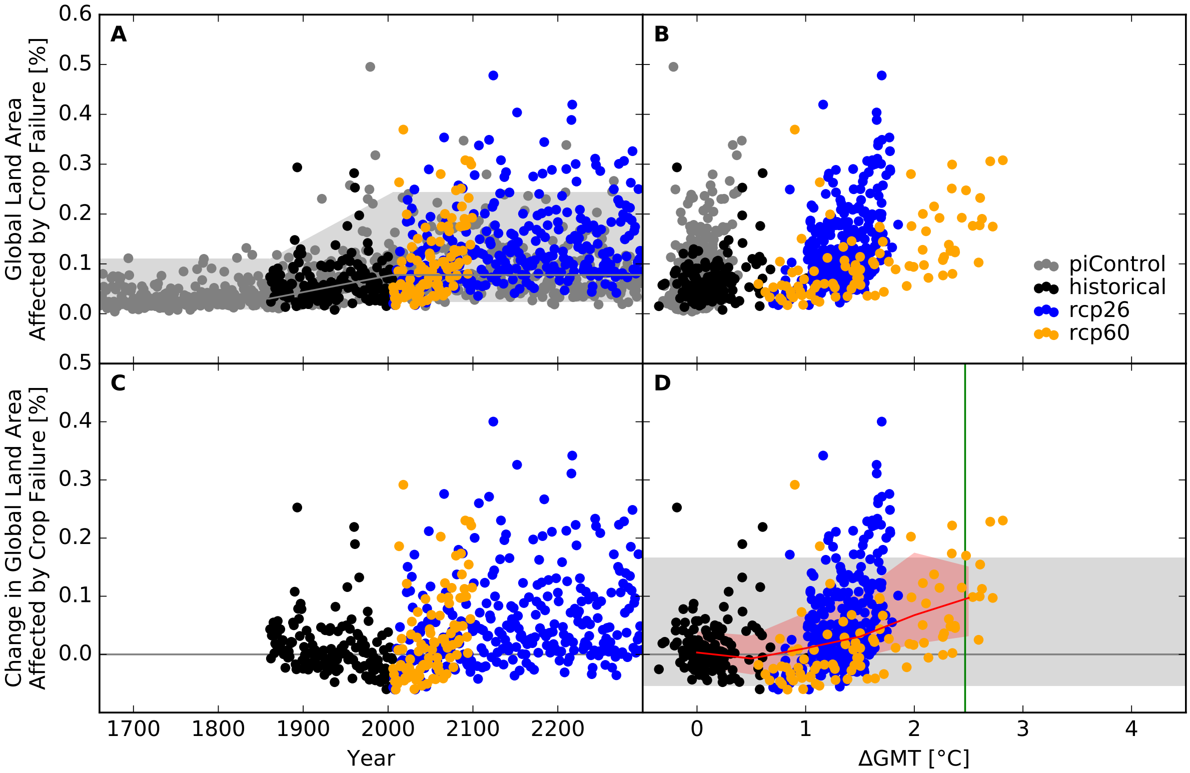

Figure S95: **Derivation of the pure effect of climate change on global land area fraction affected by crop failure events (MIROC5 + PEPIC).** Analogous to Figure S87.

People exposed

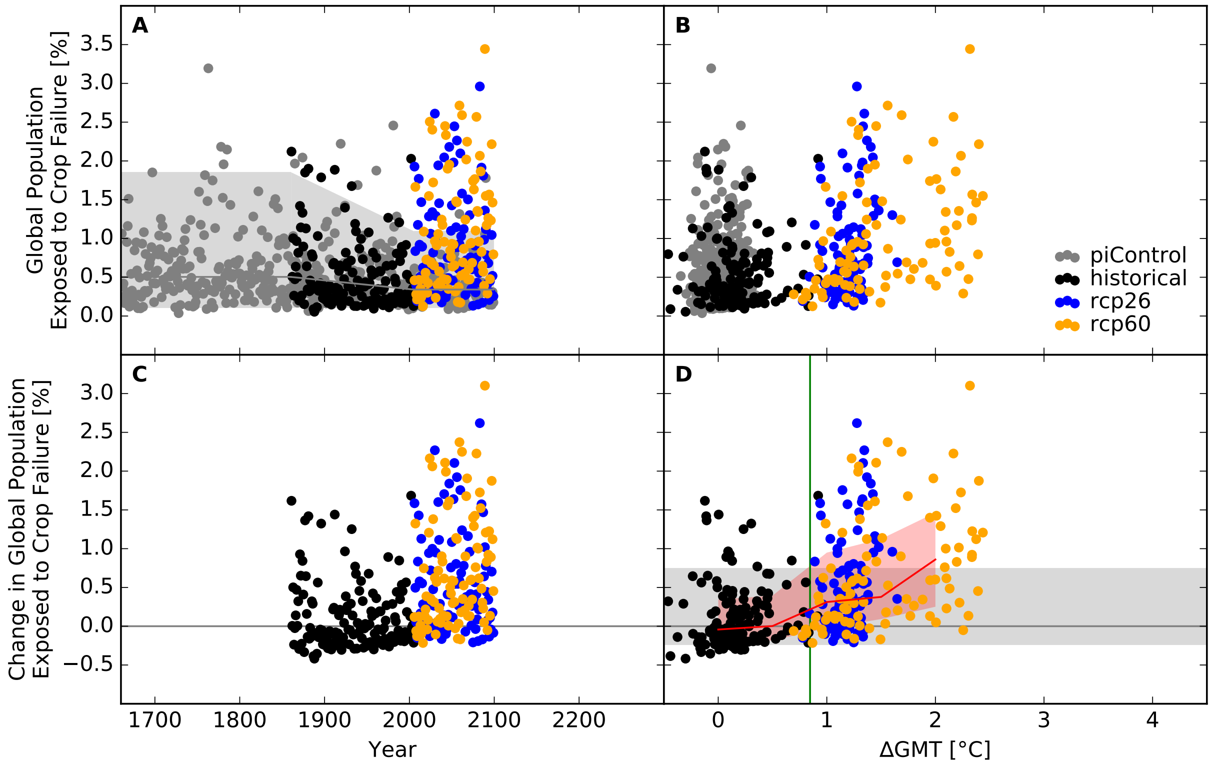

Figure S96: **Derivation of the pure effect of climate change on global population fraction affected by crop failure events (GFDL-ESM2M + GEPIC).** Panel A: Time series of annual global population fraction affected (PFA) by crop failure events for pre-industrial climate (grey dots), historical climate (black dots), climate projections for RCP2.6 (blue dots), and RCP6.0 (orange dots). In all simulations, socio-economic conditions are varied according to the historically observed development between 1860 and 2005, and held fixed at 1860 conditions before 1860 and at 2005 conditions after 2005. Shaded areas before 1860/after 2005 represent the range from the 2nd to the 98th percentile of the distribution of the annual PFA under pre-industrial climate conditions in combination with 1860/2005 socio-economic conditions; the solid gray lines represent the respective median values; the shaded areas and solid gray line between 1860 and 2005 are linear interpolations of the respective values before 1860 and after 2005. Panel B: Data shown in Panel A plotted against the associated GCM-specific annual global mean temperature (GMT) change relative to the long-term pre-industrial mean. Panel C: Pure effect of climate change on PFA, calculated as the difference between the annual data shown in Panel A and the median of the simulations assuming pre-industrial climate conditions (solid gray line in Panel A). Panel D: Pure effect of climate change on PFA in terms of global mean temperature change, with distributions of the annual data estimated for each 1°C-wide bin of global mean temperature change that contains at least five data points, at least one data point above and at least one data point below the bin center. Areas shaded in red represent the range from the 20th to the 80th percentile around the median (solid red line) of these distributions. Areas shaded in gray represent the range from the 2nd to the 98th percentile of the zero-centered distribution of the annual PFA under pre-industrial climate and 2005 socio-economic conditions (cf. Panel A). The green vertical line represents the detection level defined as the global warming level at which a 1-in-50-years event under pre-industrial climate and 2005 socio-economic conditions becomes a 1-in-5-years event under changing climate and 2005 socio-economic conditions.

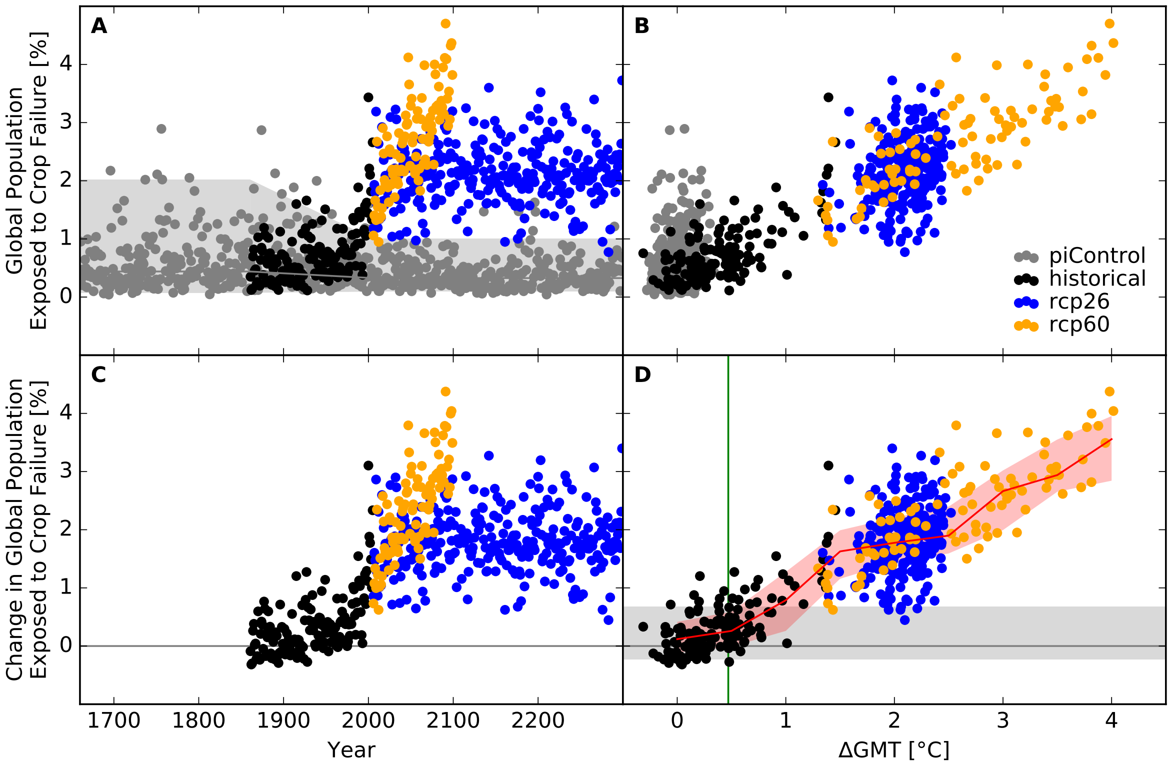

Figure S97: **Derivation of the pure effect of climate change on global population fraction affected by crop failure events (IPSL-CM5A-LR + GEPIC).** Analogous to Figure S96.

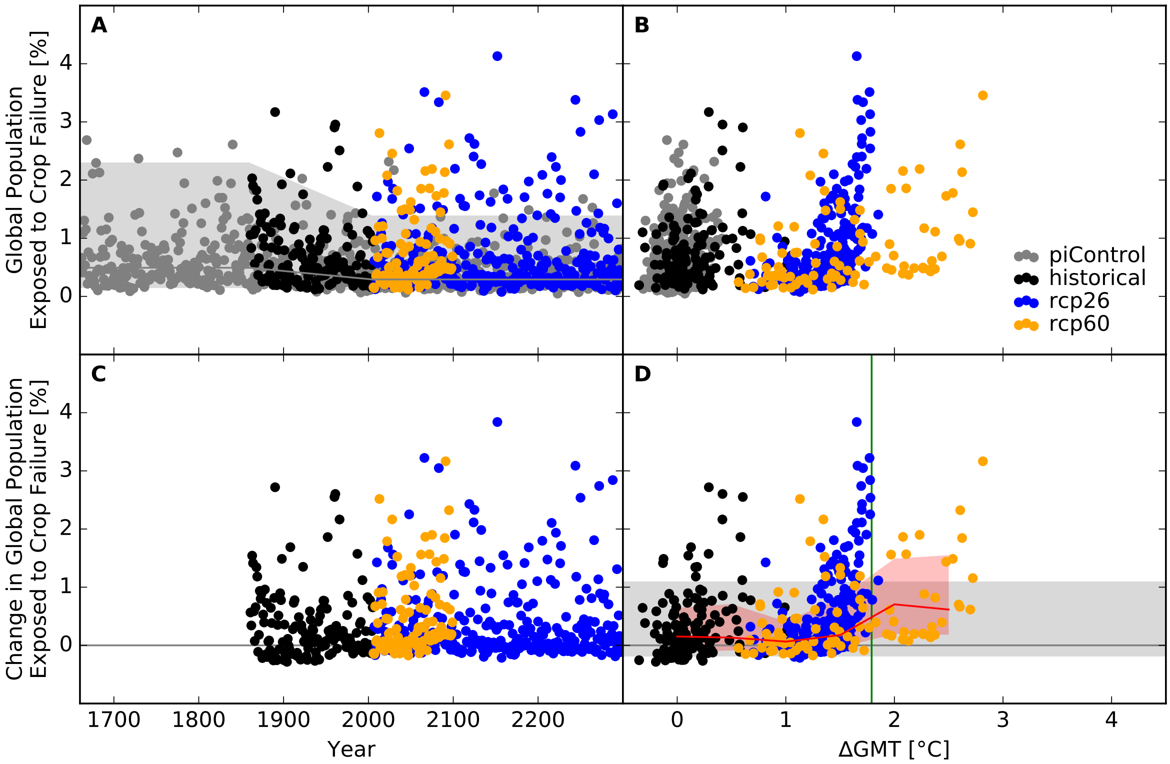

Figure S98: **Derivation of the pure effect of climate change on global population fraction affected by crop failure events (MIROC5 + GEPIC).** Analogous to Figure S96.

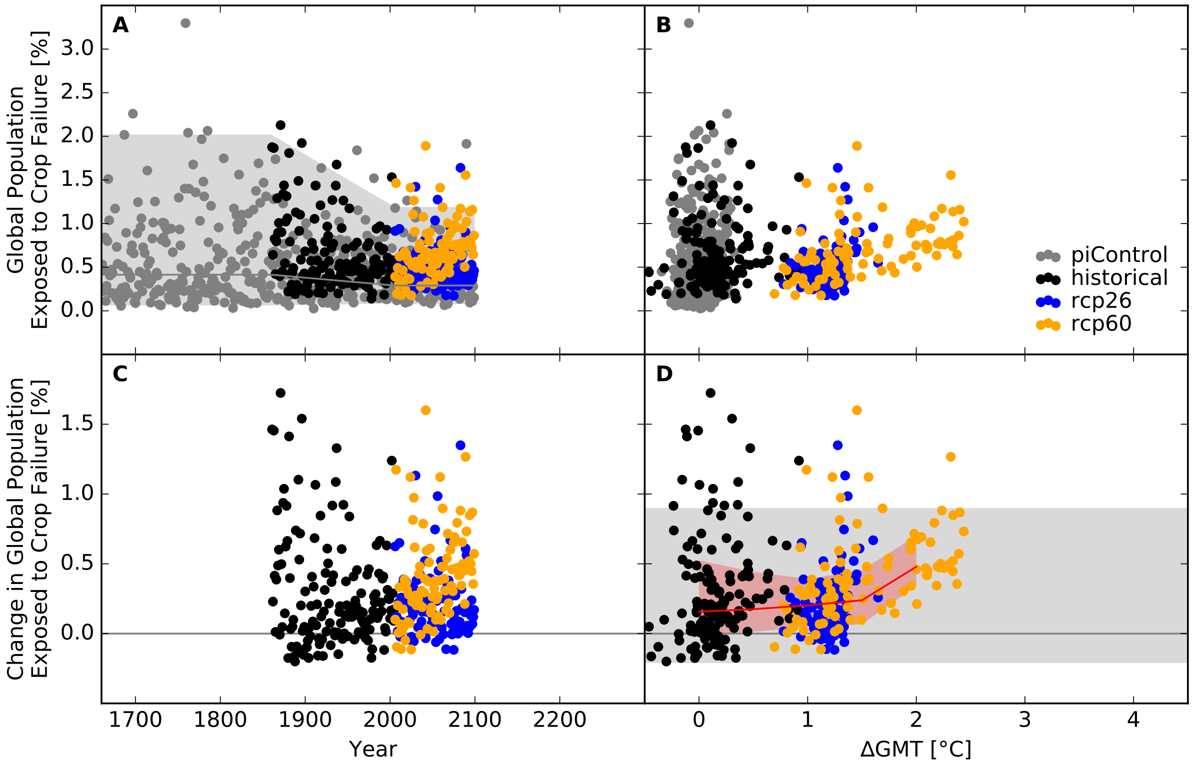

Figure S99: **Derivation of the pure effect of climate change on global population fraction affected by crop failure events (GFDL-ESM2M + LPJmL).** Analogous to Figure S96.

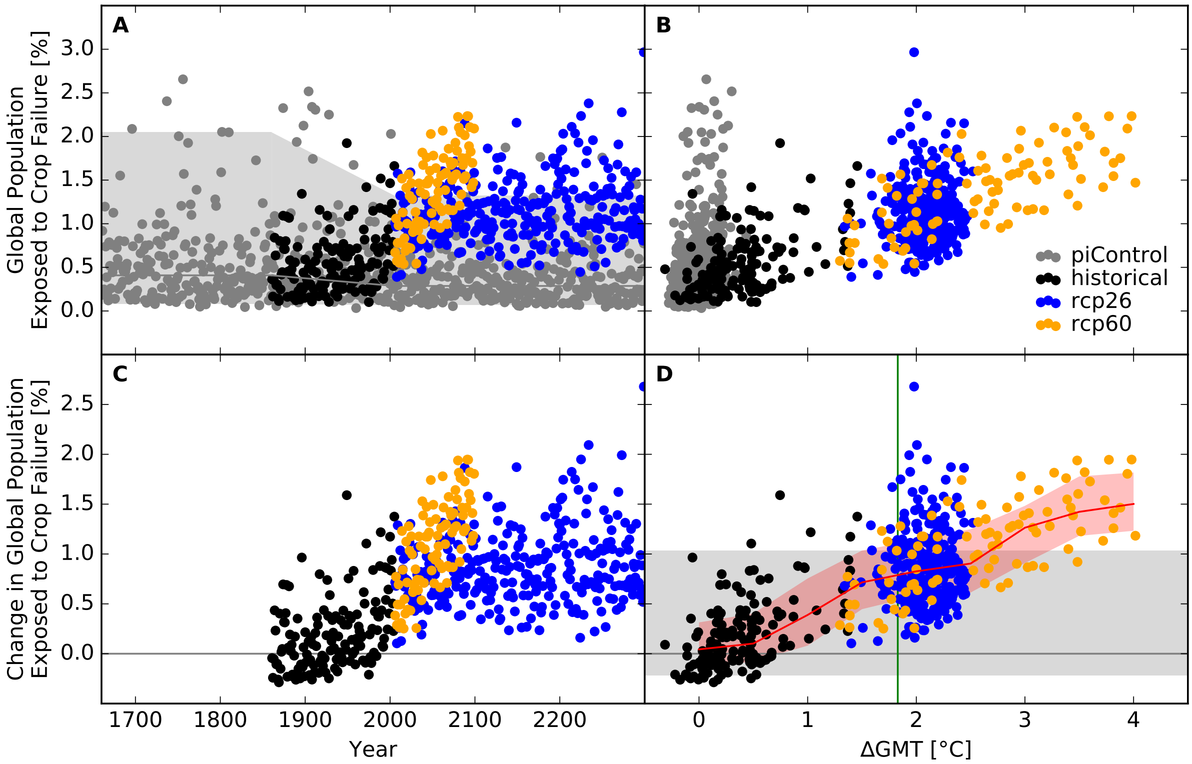

Figure S100: **Derivation of the pure effect of climate change on global population fraction affected by crop failure events (IPSL-CM5A-LR + LPJmL).** Analogous to Figure S96.

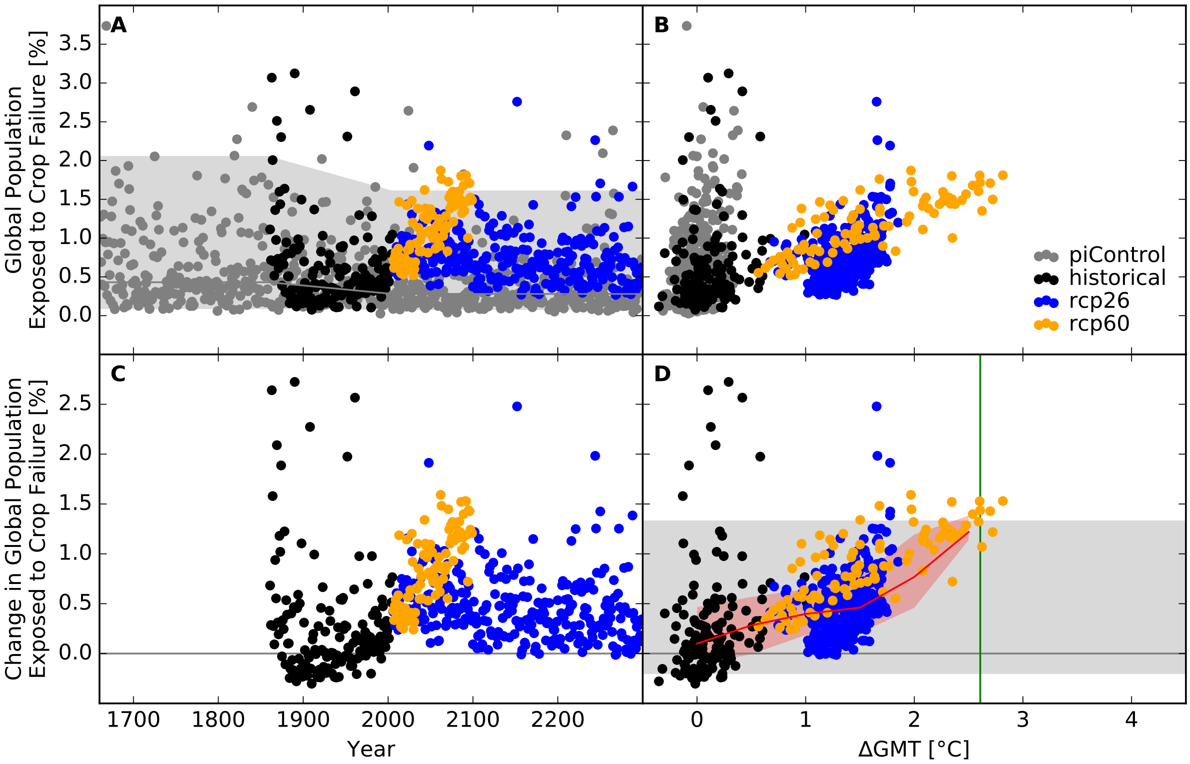

Figure S101: **Derivation of the pure effect of climate change on global population fraction affected by crop failure events (MIROC5 + LPJmL).** Analogous to Figure S96.

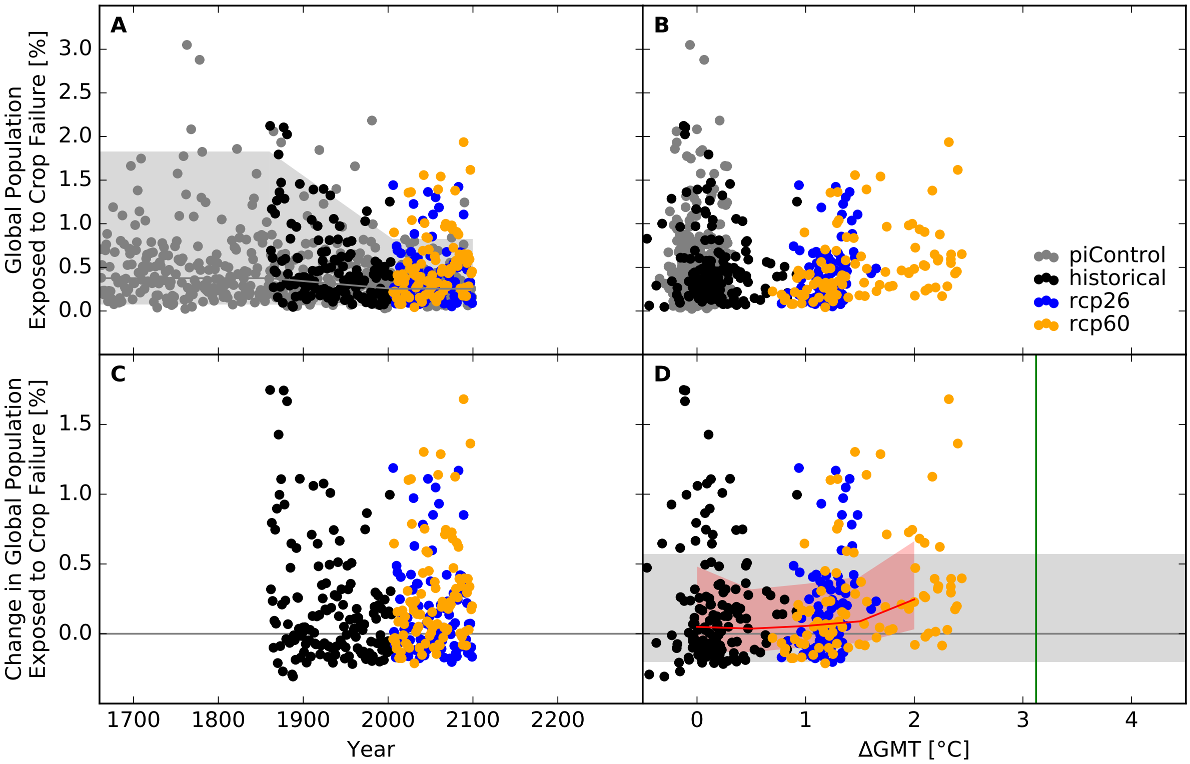

Figure S102: **Derivation of the pure effect of climate change on global population fraction affected by crop failure events (GFDL-ESM2M + PEPIC).** Analogous to Figure S96.

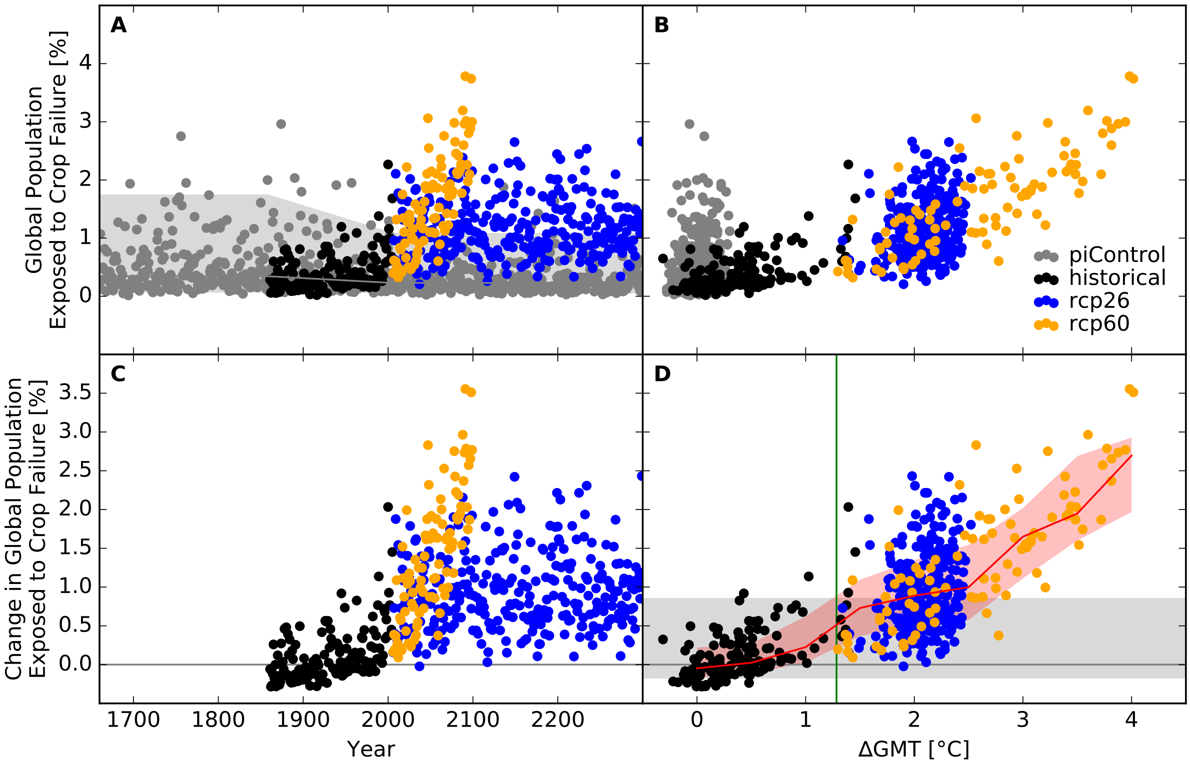

Figure S103: **Derivation of the pure effect of climate change on global population fraction affected by crop failure events (IPSL-CM5A-LR + PEPIC).** Analogous to Figure S96.

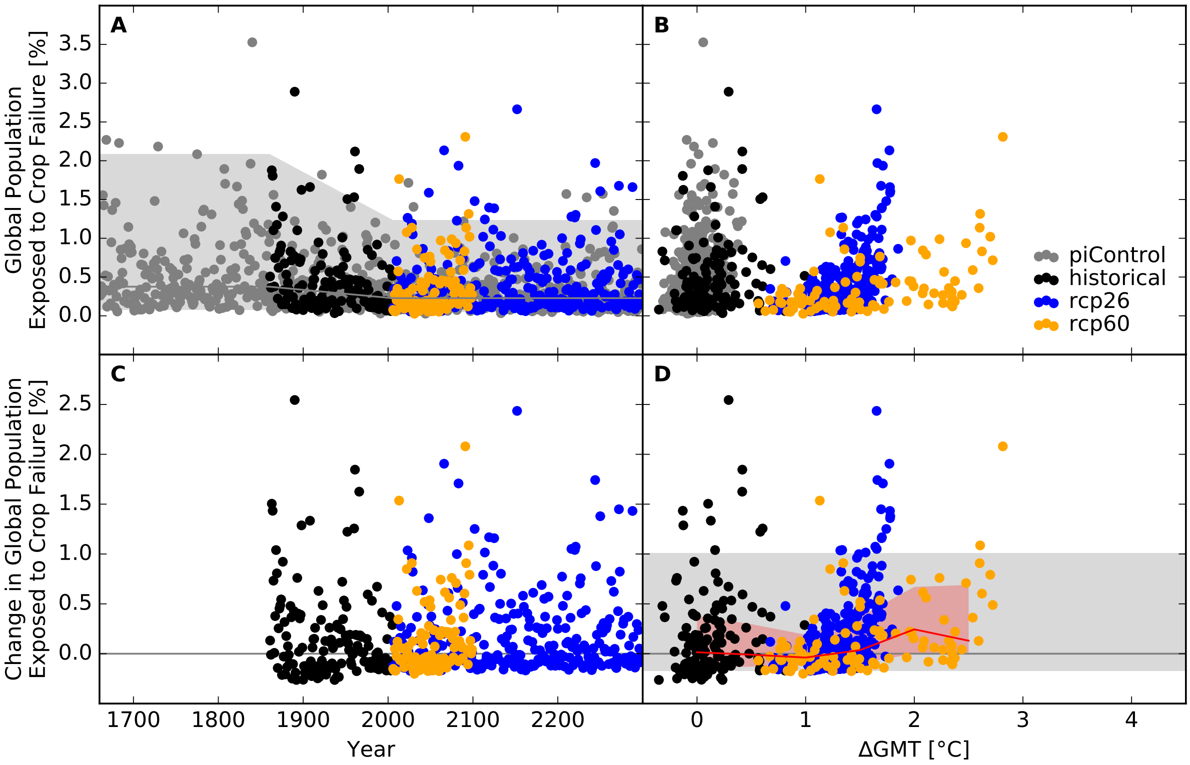

Figure S104: **Derivation of the pure effect of climate change on global population fraction affected by crop failure events (MIROC5 + PEPIC).** Analogous to Figure S96.

Occurrence probability at grid scale

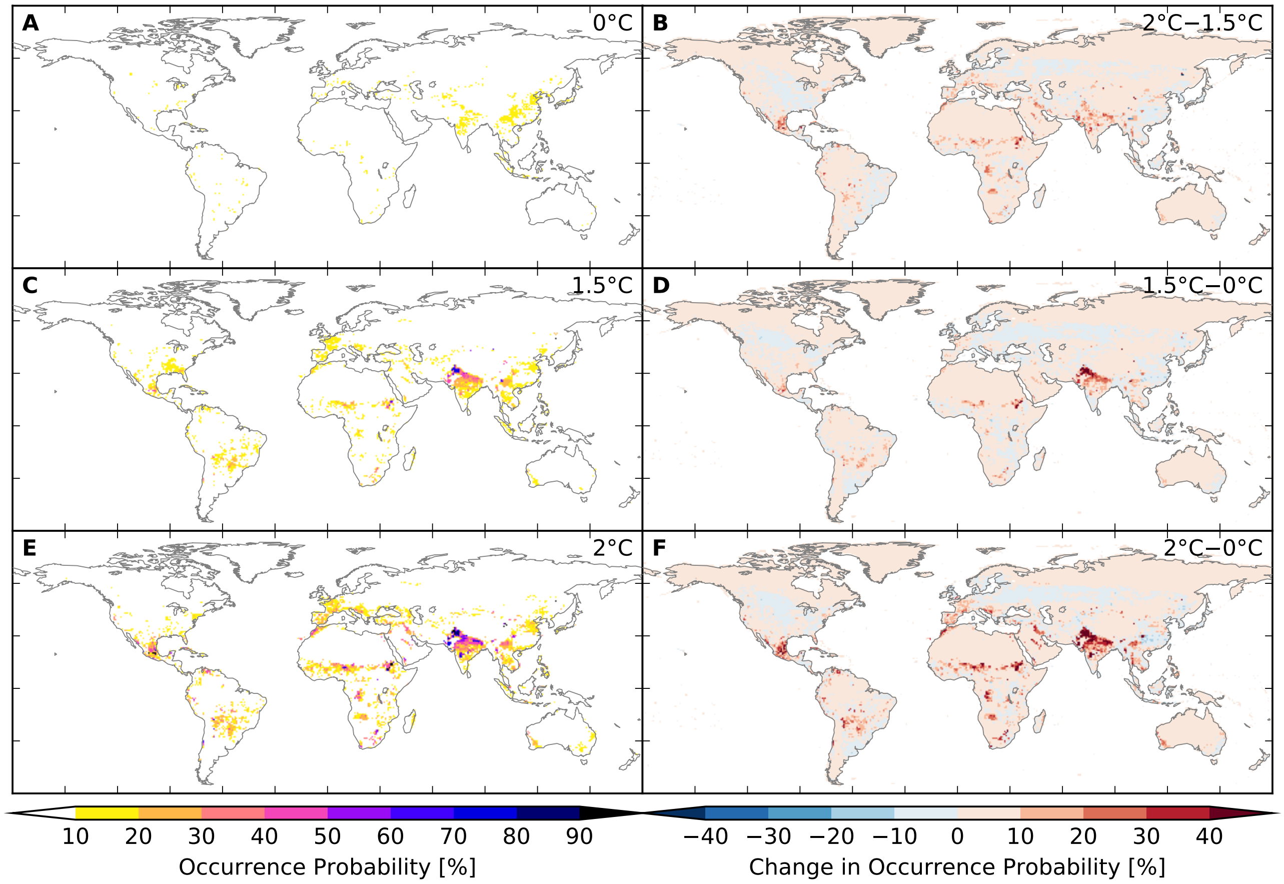

Figure S105: **Probability of occurrence of at least one crop failure event per year at different global warming levels (GFDL-ESM2M + GEPIC).** Panels A, C, E: Probabilities at 0°C, 1.5°C, 2°C global mean temperature (GMT) change relative to the long-term pre-industrial mean GMT, respectively. Panels B, D, F: Differences between probabilities at GMT change levels of 2°C and 1.5°C, 1.5°C and 0°C, 2°C and 0°C, respectively.

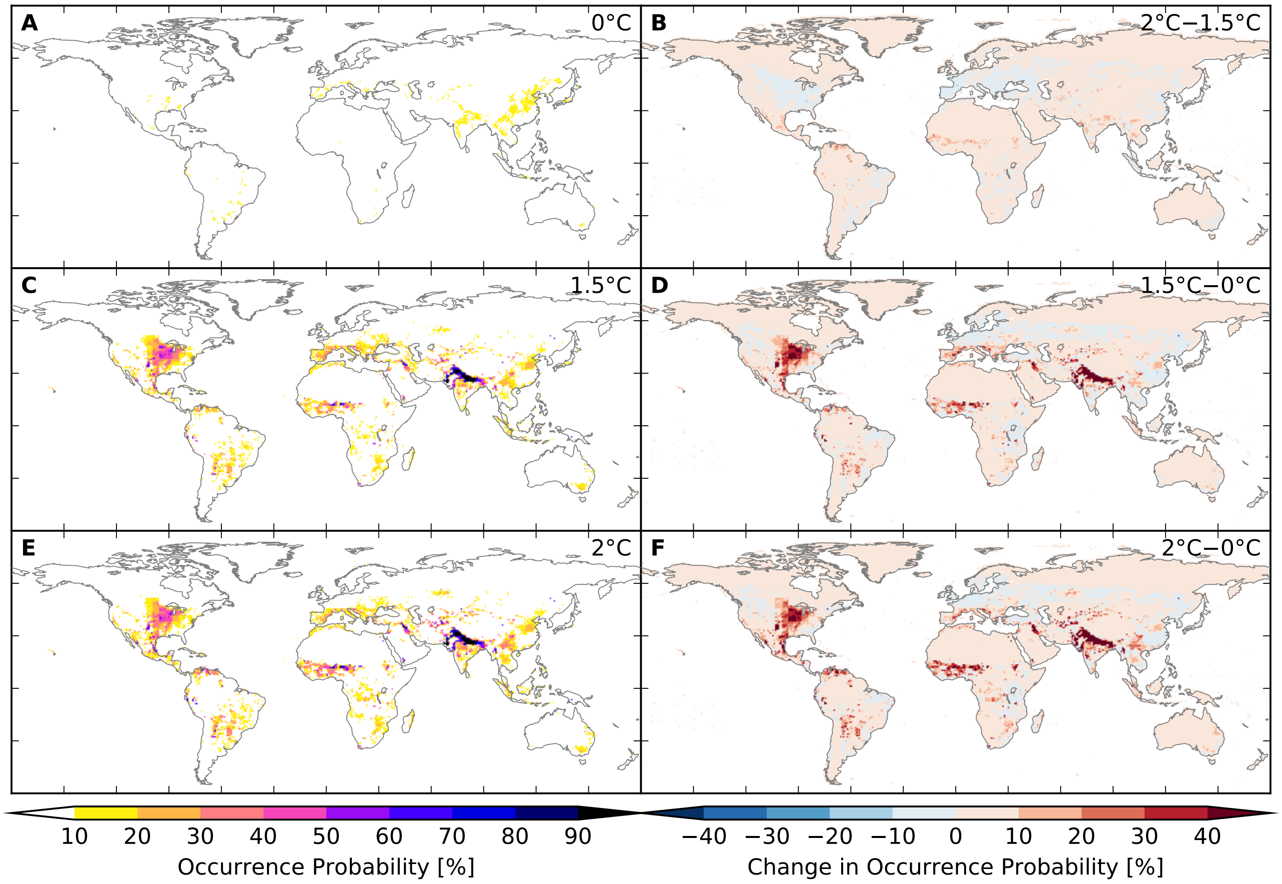

Figure S106: **Probability of occurrence of at least one crop failure event per year at different global warming levels (IPSL-CM5A-LR + GEPIC).** Analogous to Figure S105.

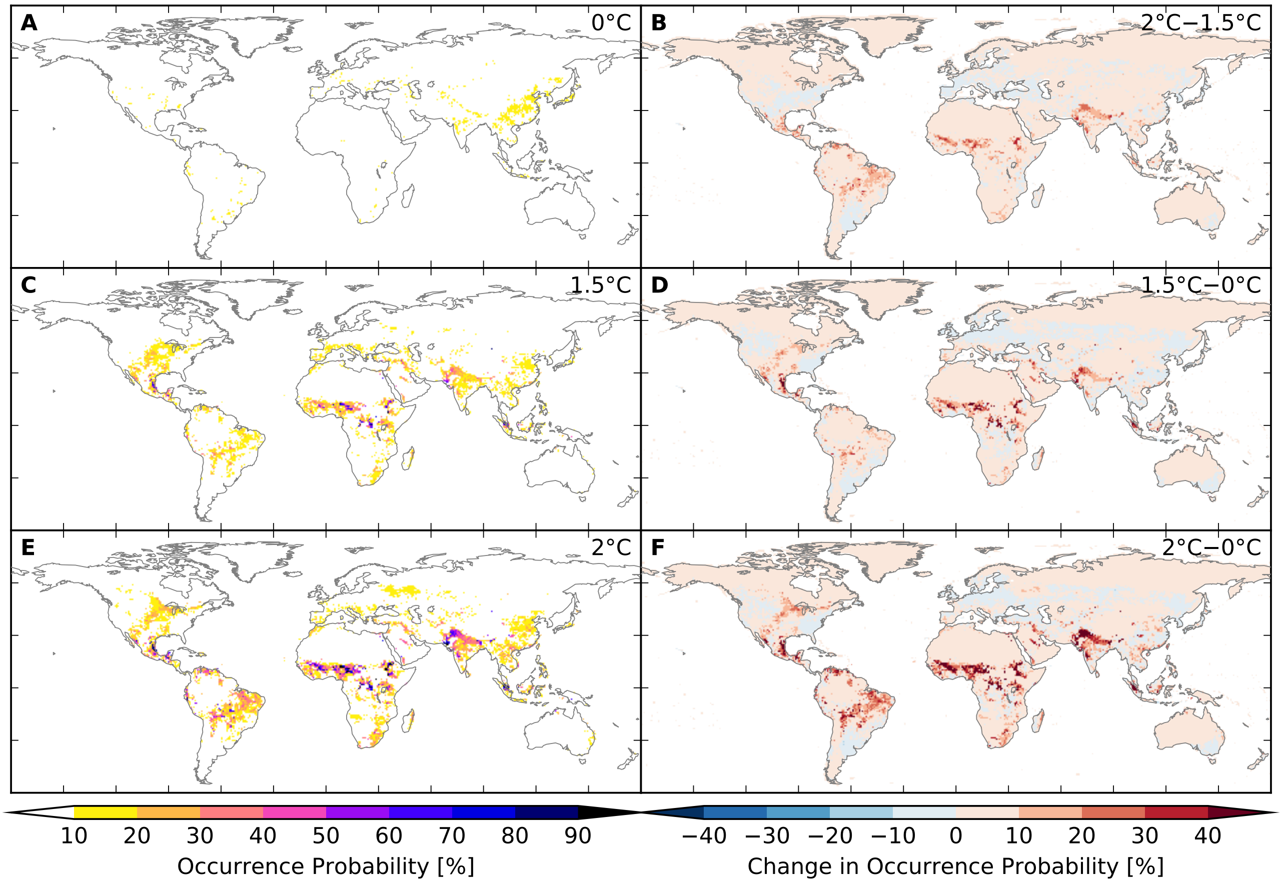

Figure S107: **Probability of occurrence of at least one crop failure event per year at different global warming levels (MIROC5 + GEPIC).** Analogous to Figure S105.

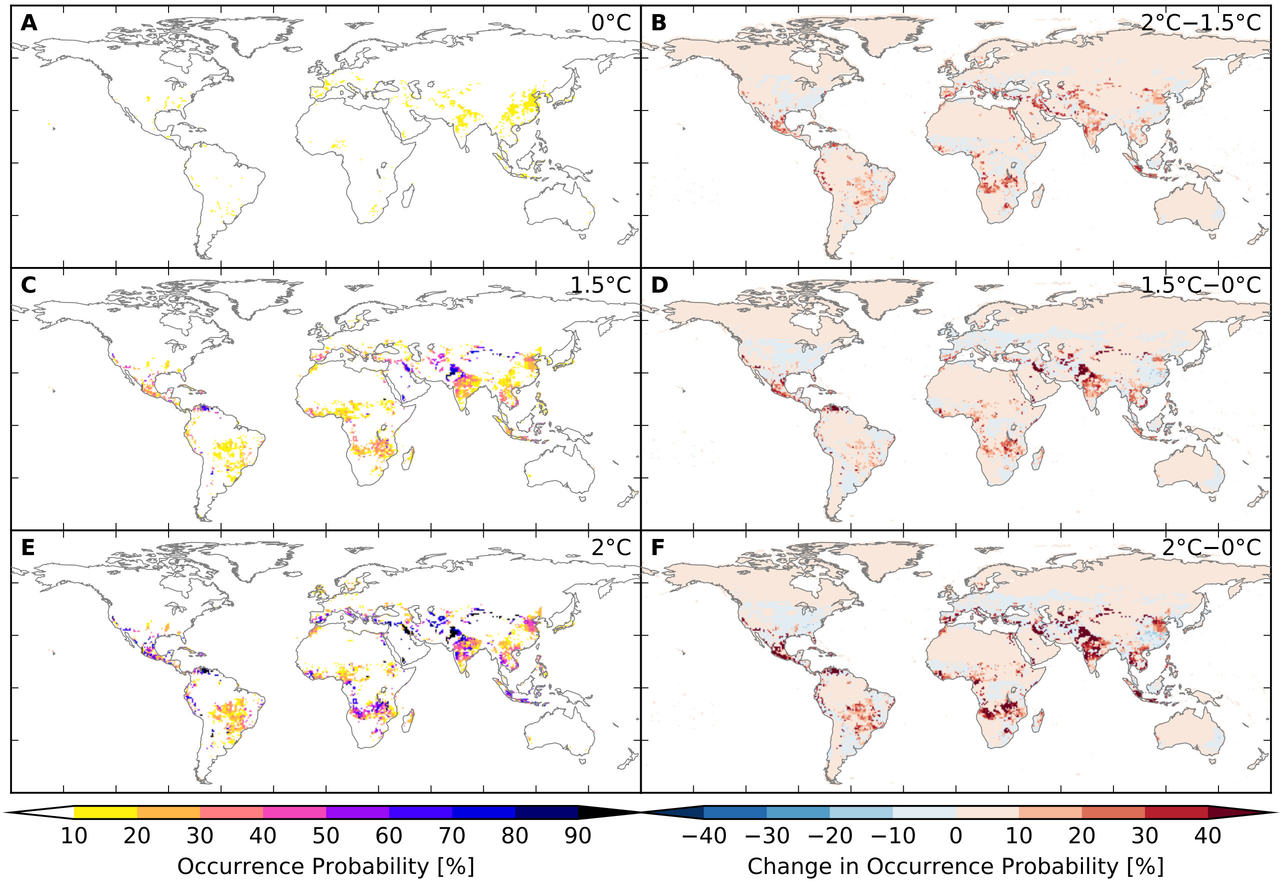

Figure S108: **Probability of occurrence of at least one crop failure event per year at different global warming levels (GFDL-ESM2M + LPJmL).** Analogous to Figure S105.

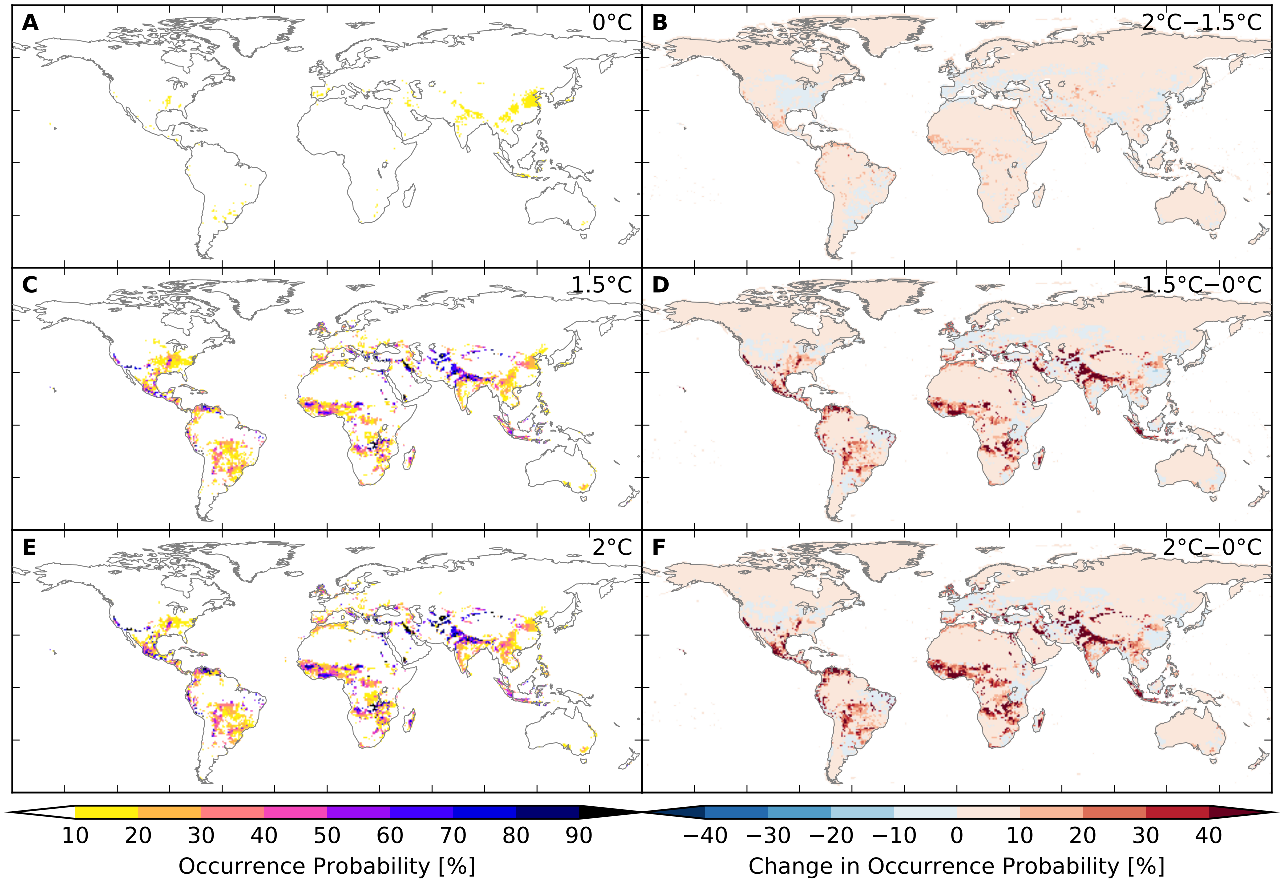

Figure S109: **Probability of occurrence of at least one crop failure event per year at different global warming levels (IPSL-CM5A-LR + LPJmL).** Analogous to Figure S105.

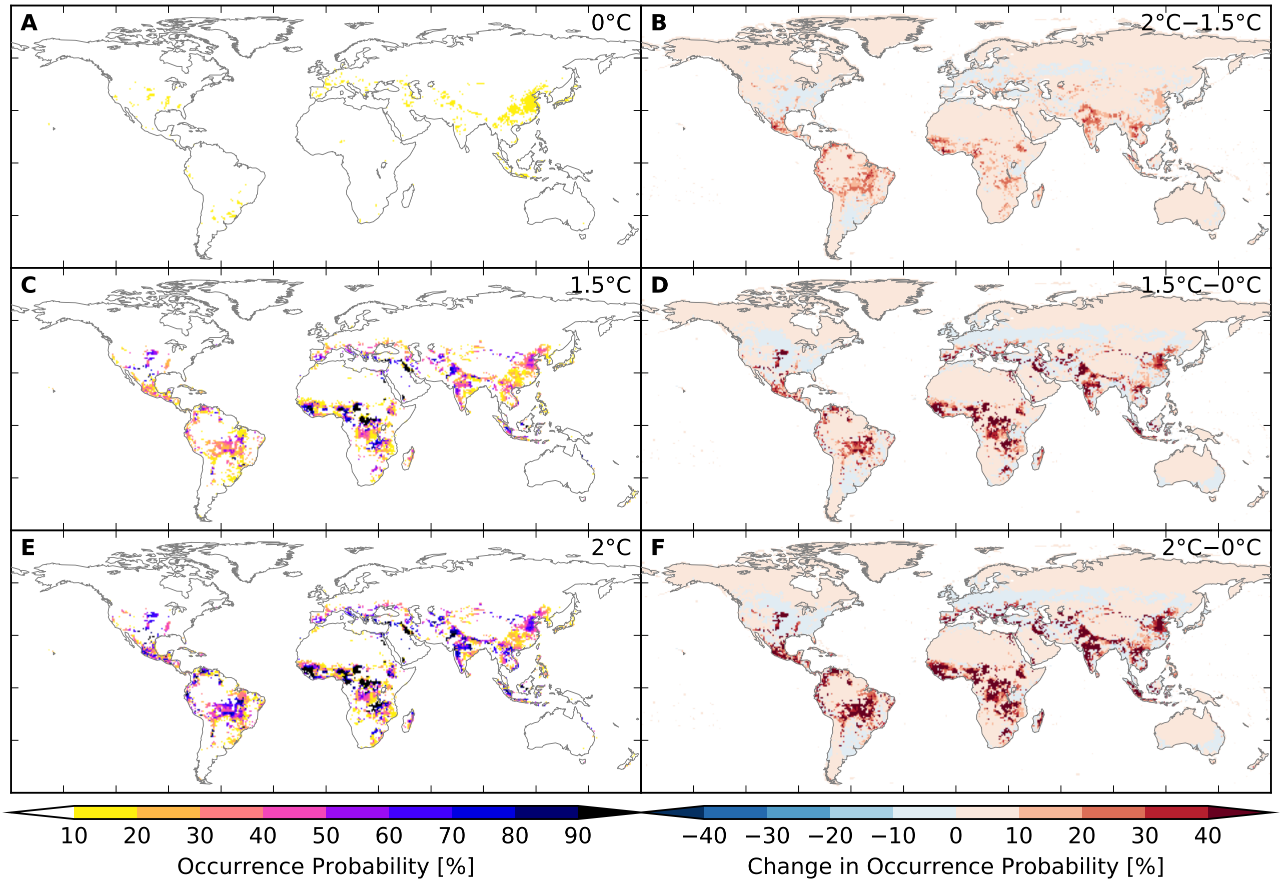

Figure S110: **Probability of occurrence of at least one crop failure event per year at different global warming levels (MIROC5 + LPJmL).** Analogous to Figure S105.

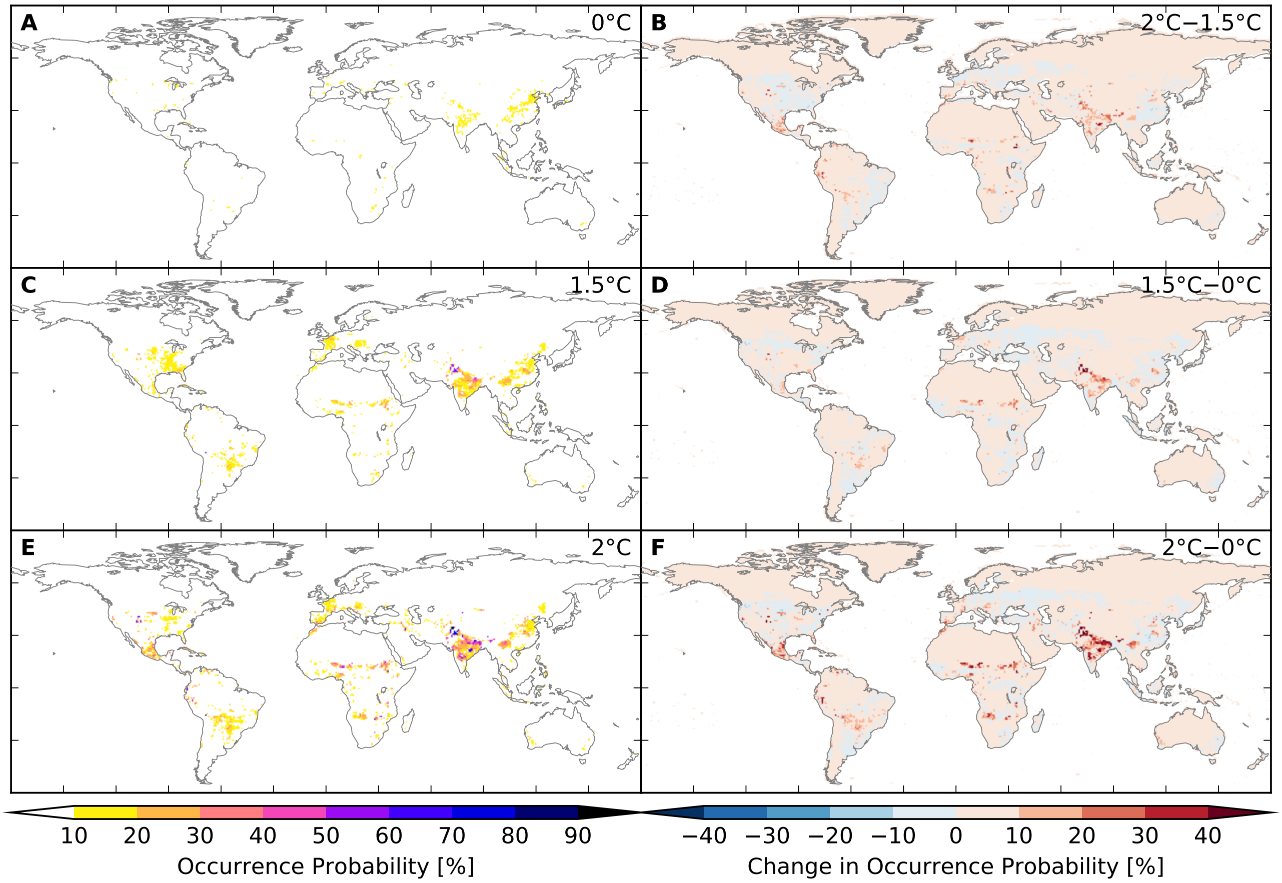

Figure S111: **Probability of occurrence of at least one crop failure event per year at different global warming levels (GFDL-ESM2M + PEPIC).** Analogous to Figure S105.

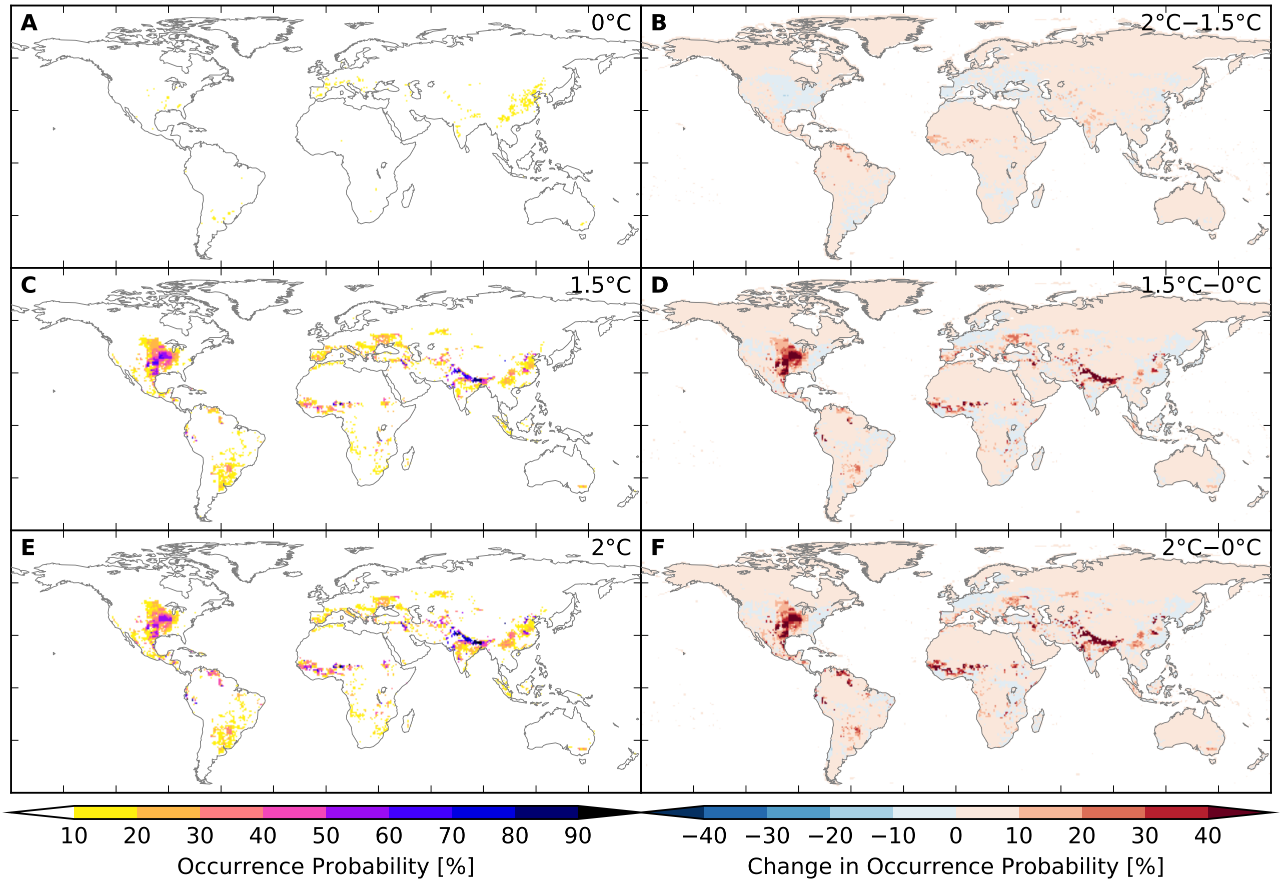

Figure S112: **Probability of occurrence of at least one crop failure event per year at different global warming levels (IPSL-CM5A-LR + PEPIC).** Analogous to Figure S105.

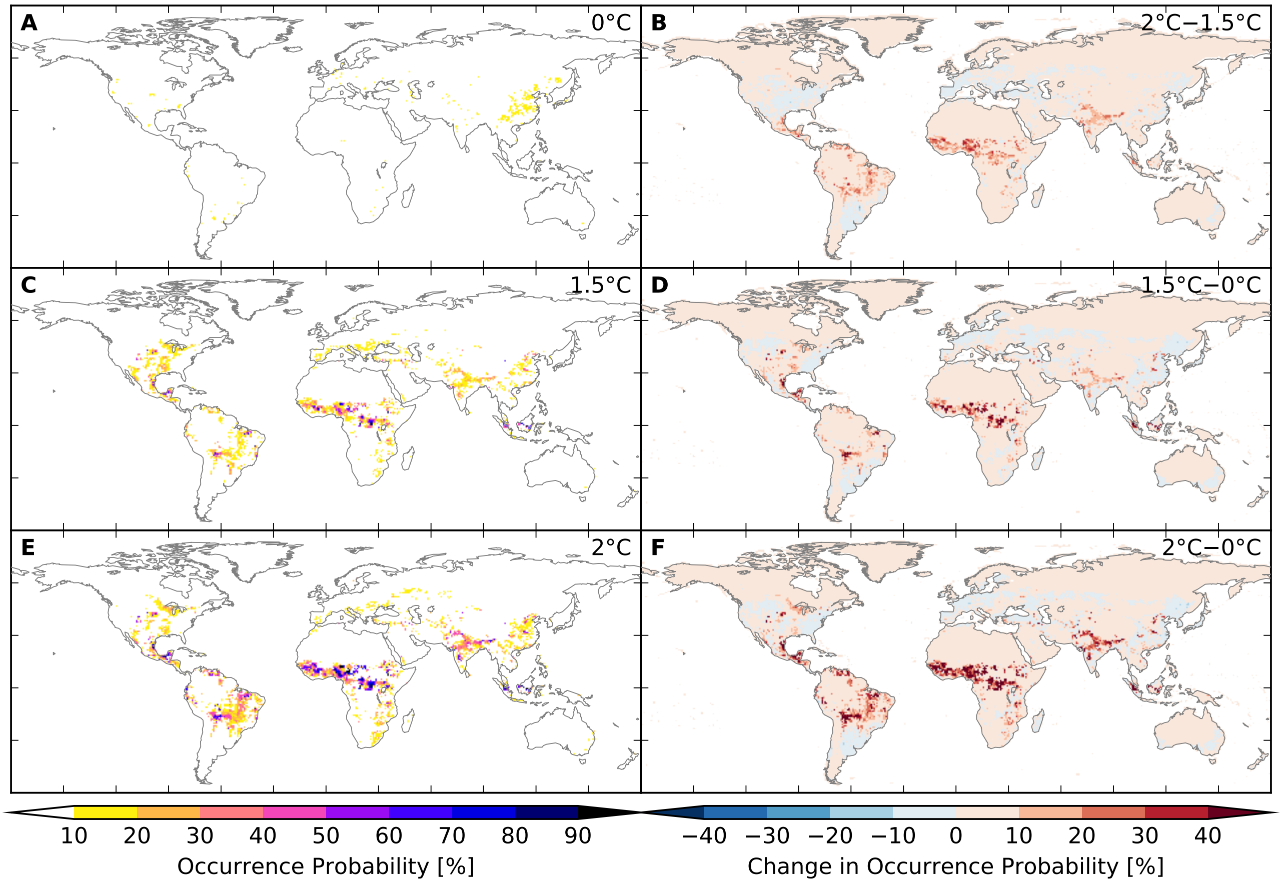

Figure S113: **Probability of occurrence of at least one crop failure event per year at different global warming levels (MIROC5 + PEPIC).** Analogous to Figure S105.

8.4 Wildfires

Areas affected

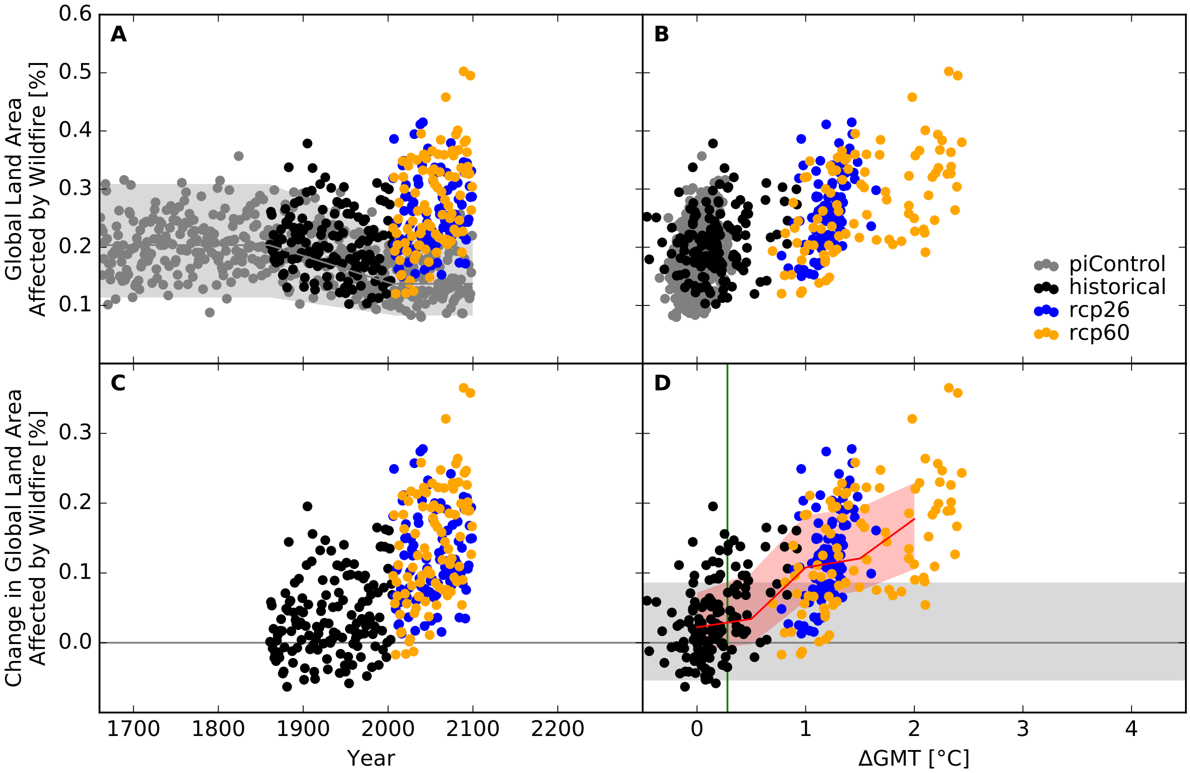

Figure S114: **Derivation of the pure effect of climate change on global land area fraction affected by wildfire events (GFDL-ESM2M + CARAIB).** Panel A: Time series of annual global land area fraction affected (AFA) by wildfire events for pre-industrial climate (grey dots), historical climate (black dots), climate projections for RCP2.6 (blue dots), and RCP6.0 (orange dots). In all simulations, socio-economic conditions are varied according to the historically observed development between 1860 and 2005, and held fixed at 1860 conditions before 1860 and at 2005 conditions after 2005. Shaded areas before 1860/after 2005 represent the range from the 2nd to the 98th percentile of the distribution of the annual AFA under pre-industrial climate conditions in combination with 1860/2005 socio-economic conditions; the solid gray lines represent the respective median values; the shaded areas and solid gray line between 1860 and 2005 are linear interpolations of the respective values before 1860 and after 2005. Panel B: Data shown in Panel A plotted against the associated GCM-specific annual global mean temperature (GMT) change relative to the long-term pre-industrial mean. Panel C: Pure effect of climate change on AFA, calculated as the difference between the annual data shown in Panel A and the median of the simulations assuming pre-industrial climate conditions (solid gray line in Panel A). Panel D: Pure effect of climate change on AFA in terms of global mean temperature change, with distributions of the annual data estimated for each 1°C-wide bin of global mean temperature change that contains at least five data points, at least one data point above and at least one data point below the bin center. Areas shaded in red represent the range from the 20th to the 80th percentile around the median (solid red line) of these distributions. Areas shaded in gray represent the range from the 2nd to the 98th percentile of the zero-centered distribution of the annual AFA under pre-industrial climate and 2005 socio-economic conditions (cf. Panel A). The green vertical line represents the detection level defined as the global warming level at which a 1-in-50-years event under pre-industrial climate and 2005 socio-economic conditions becomes a 1-in-5-years event under changing climate and 2005 socio-economic conditions.

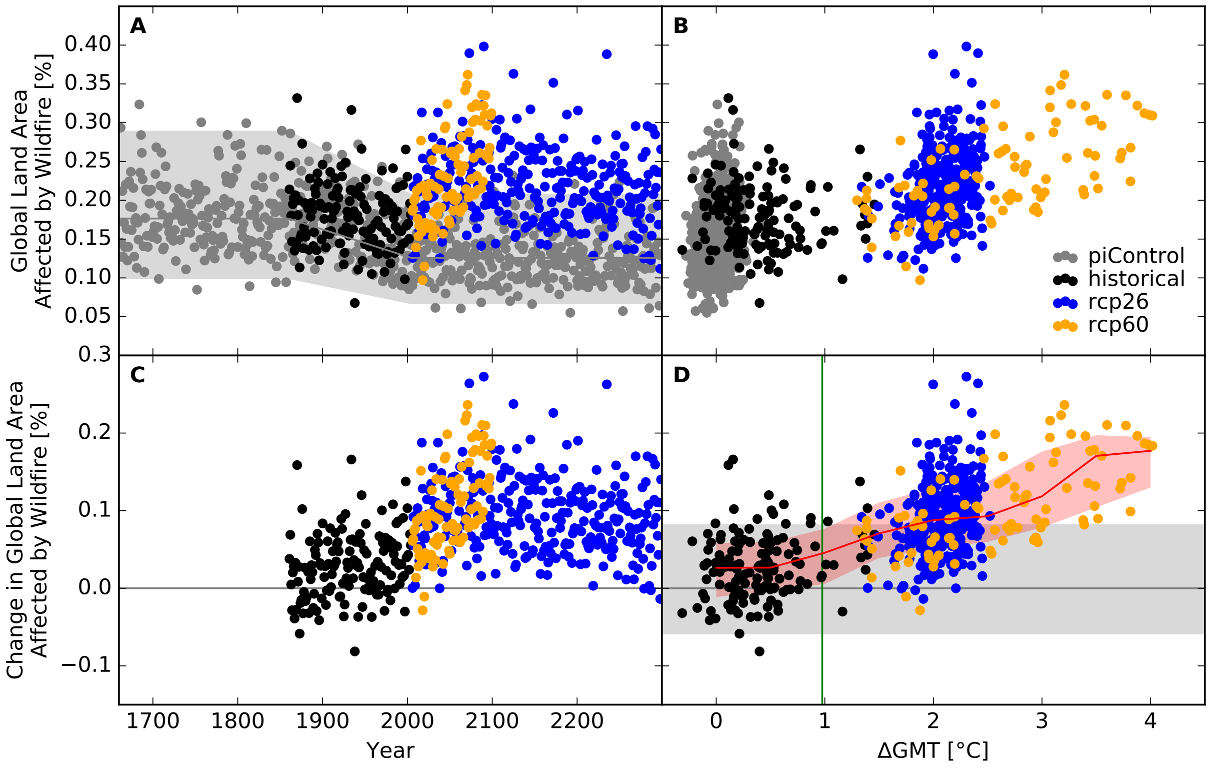

Figure S115: **Derivation of the pure effect of climate change on global land area fraction affected by wildfire events (IPSL-CM5A-LR + CARAIB).** Analogous to Figure S114.

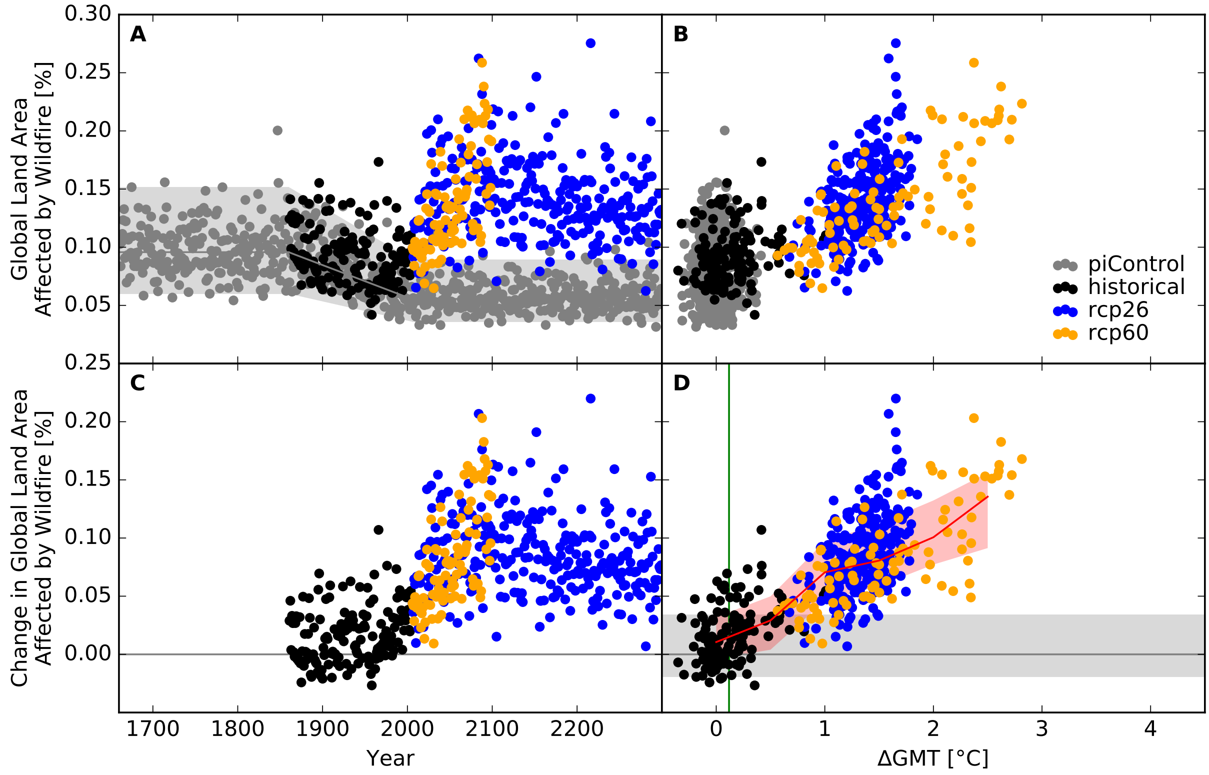

Figure S116: **Derivation of the pure effect of climate change on global land area fraction affected by wildfire events (MIROC5 + CARAIB).** Analogous to Figure S114.

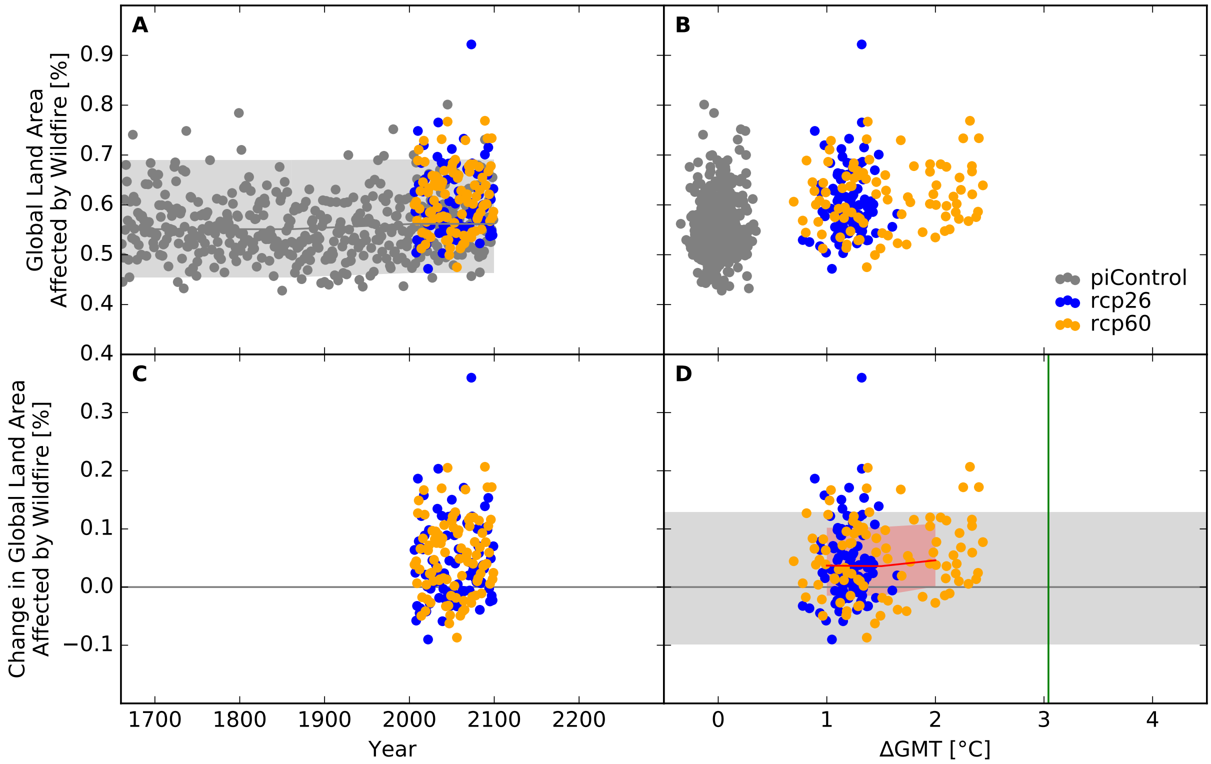

Figure S117: **Derivation of the pure effect of climate change on global land area fraction affected by wildfire events (GFDL-ESM2M + LPJ-GUESS).** Analogous to Figure S114.

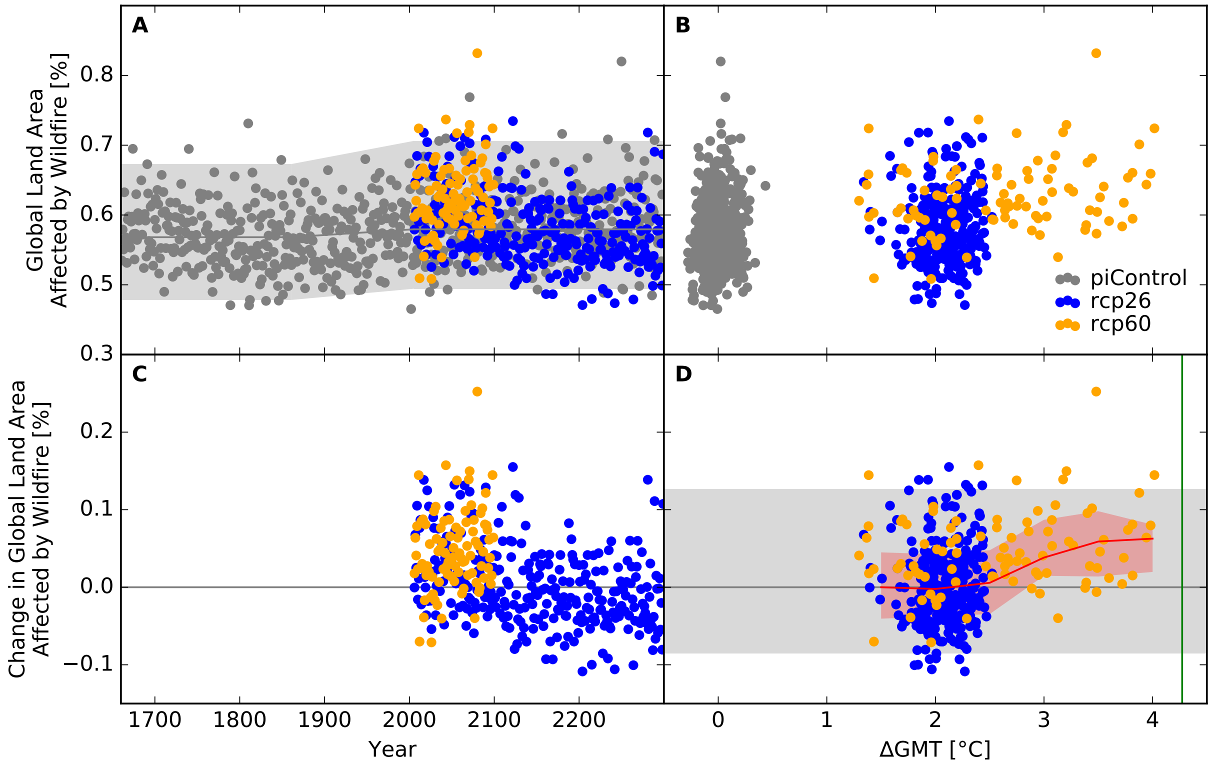

Figure S118: **Derivation of the pure effect of climate change on global land area fraction affected by wildfire events (IPSL-CM5A-LR + LPJ-GUESS).** Analogous to Figure S114.

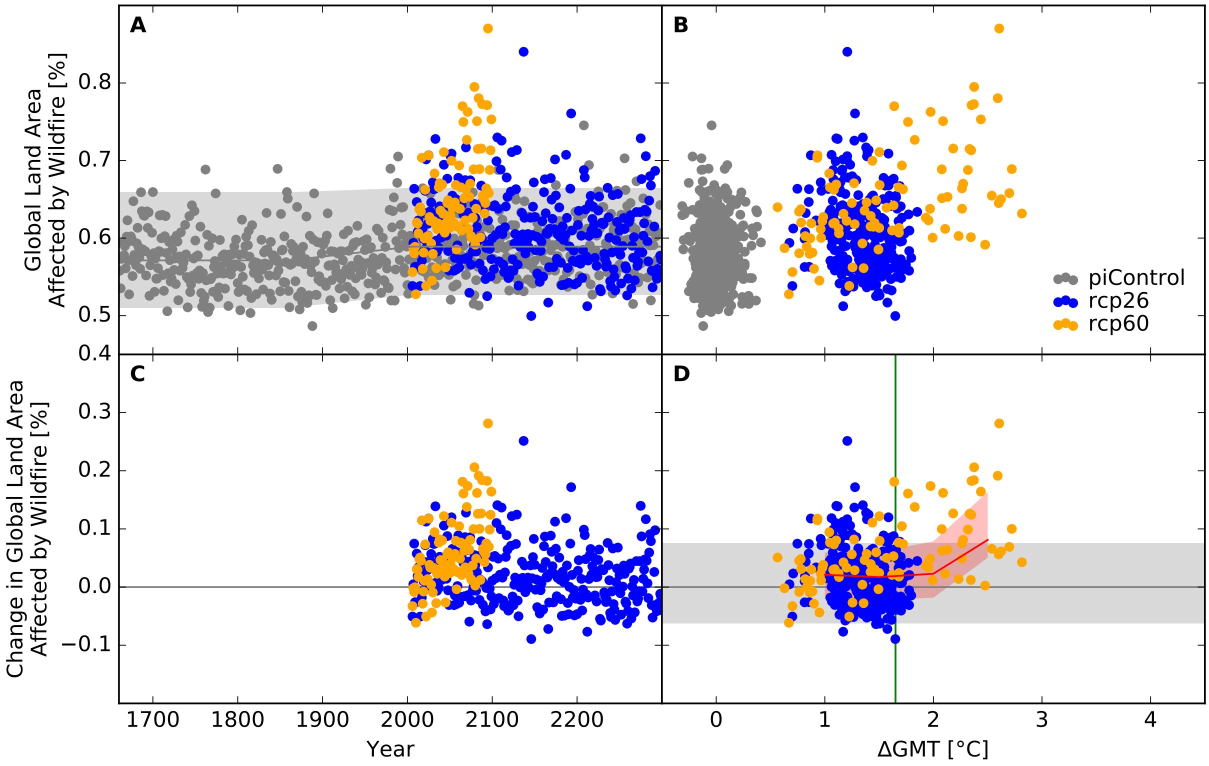

Figure S119: **Derivation of the pure effect of climate change on global land area fraction affected by wildfire events (MIROC5 + LPJ-GUESS).** Analogous to Figure S114.

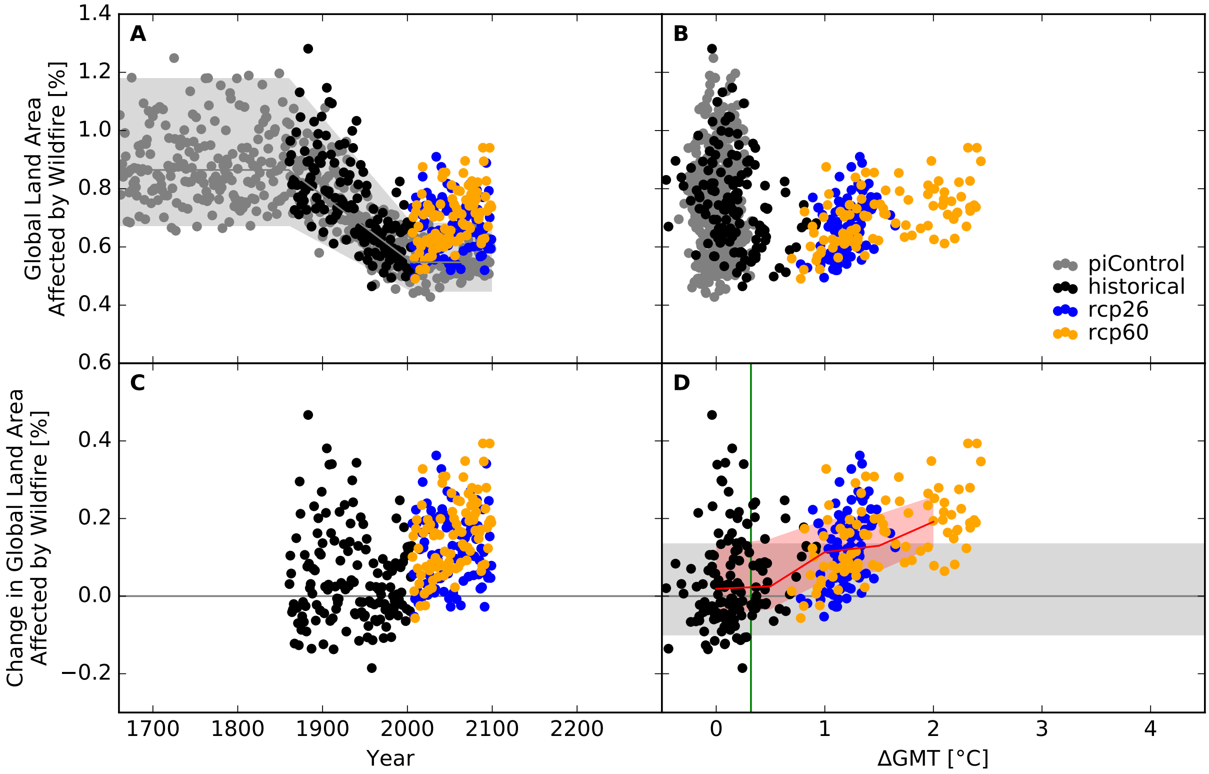

Figure S120: **Derivation of the pure effect of climate change on global land area fraction affected by wildfire events (GFDL-ESM2M + LPJmL).** Analogous to Figure S114.

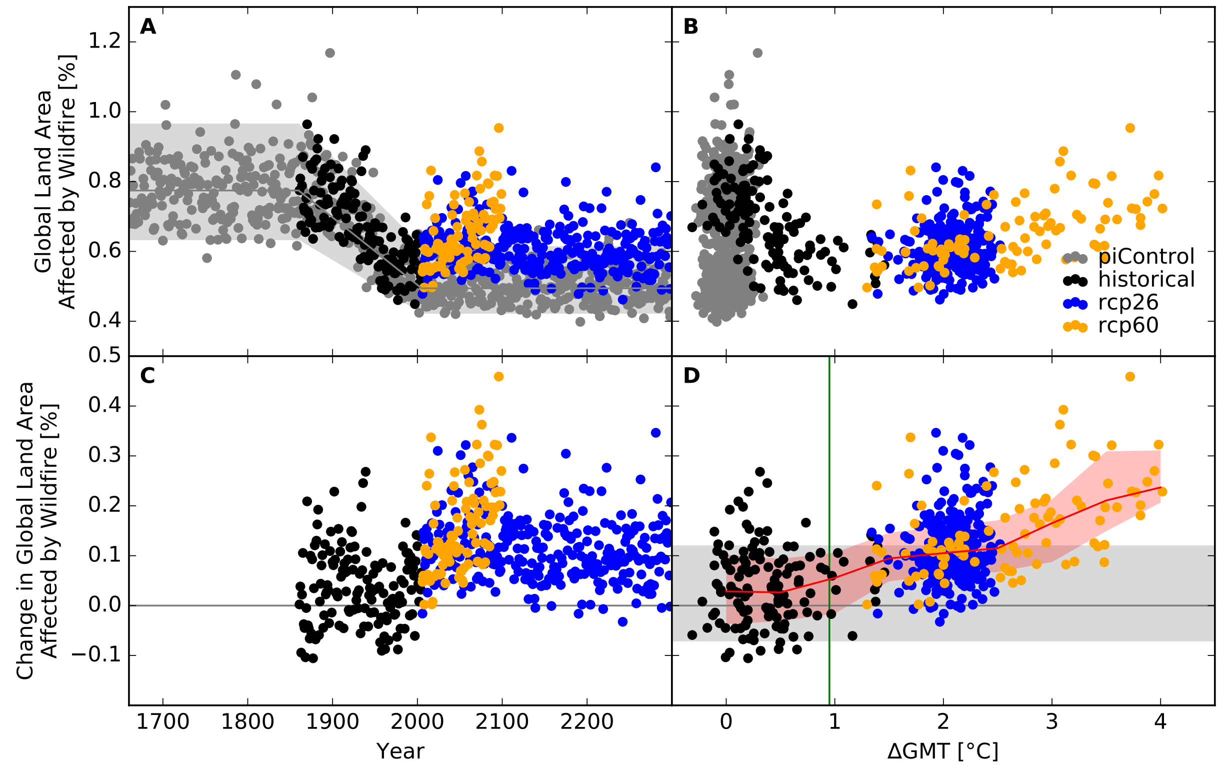

Figure S121: **Derivation of the pure effect of climate change on global land area fraction affected by wildfire events (IPSL-CM5A-LR + LPJmL).** Analogous to Figure S114.

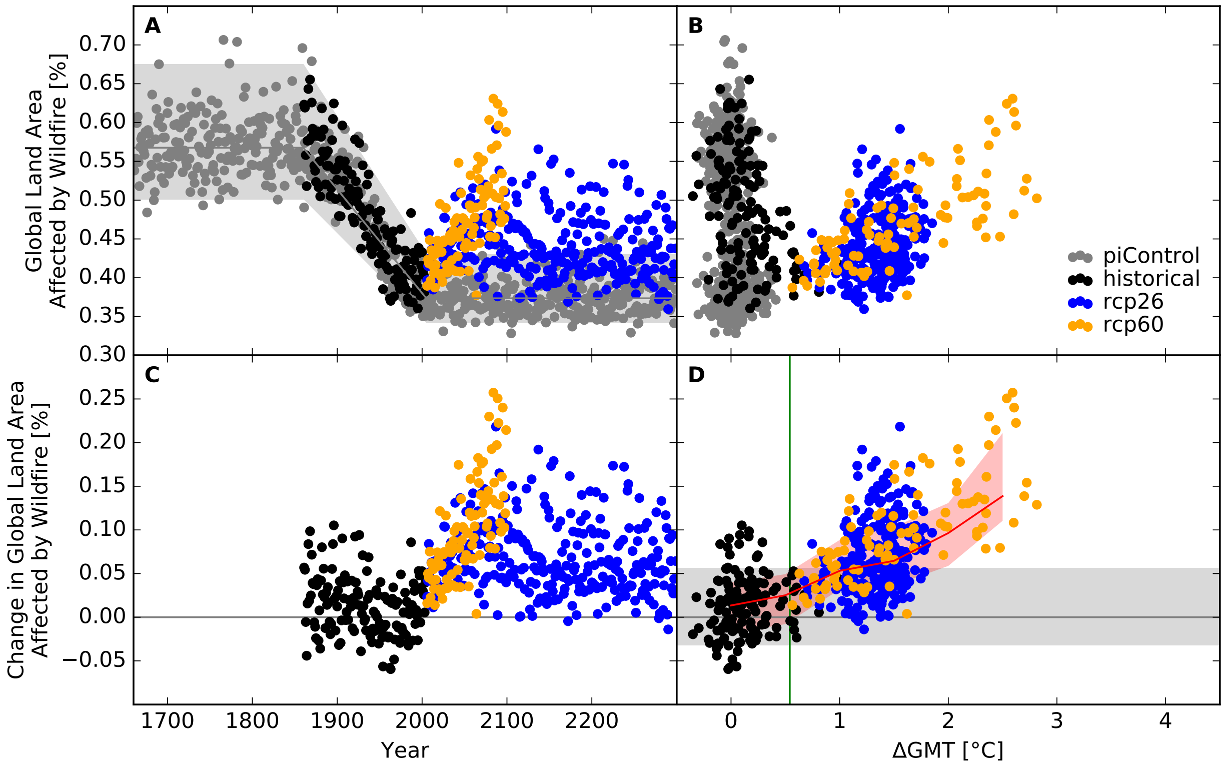

Figure S122: **Derivation of the pure effect of climate change on global land area fraction affected by wildfire events (MIROC5 + LPJmL).** Analogous to Figure S114.

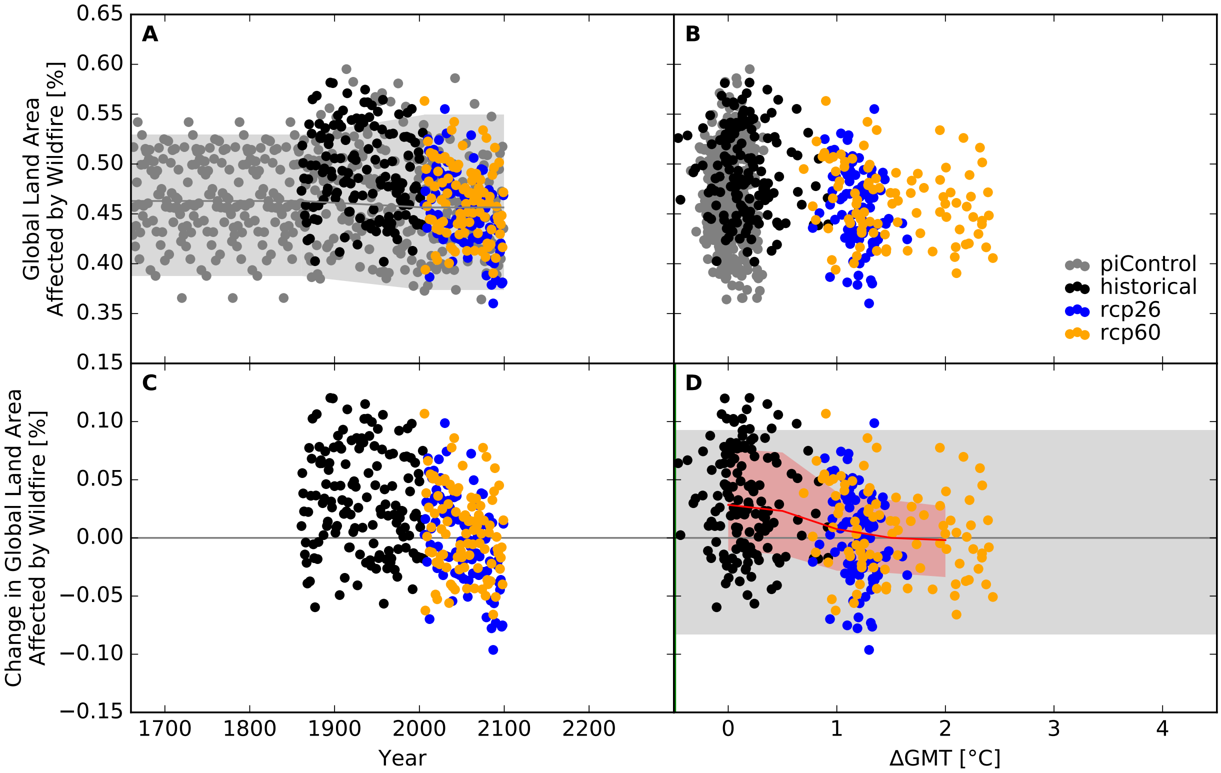

Figure S123: **Derivation of the pure effect of climate change on global land area fraction affected by wildfire events (GFDL-ESM2M + ORCHIDEE).** Analogous to Figure S114.

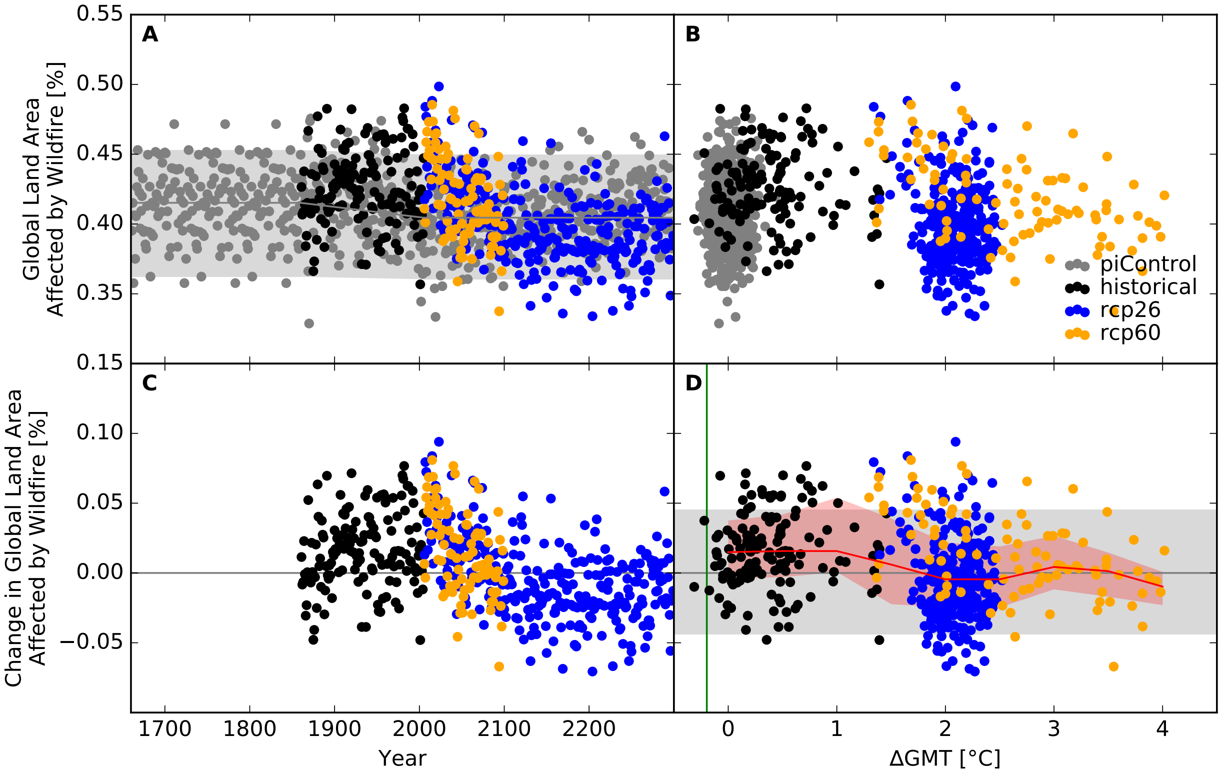

Figure S124: **Derivation of the pure effect of climate change on global land area fraction affected by wildfire events (IPSL-CM5A-LR + ORCHIDEE).** Analogous to Figure S114.

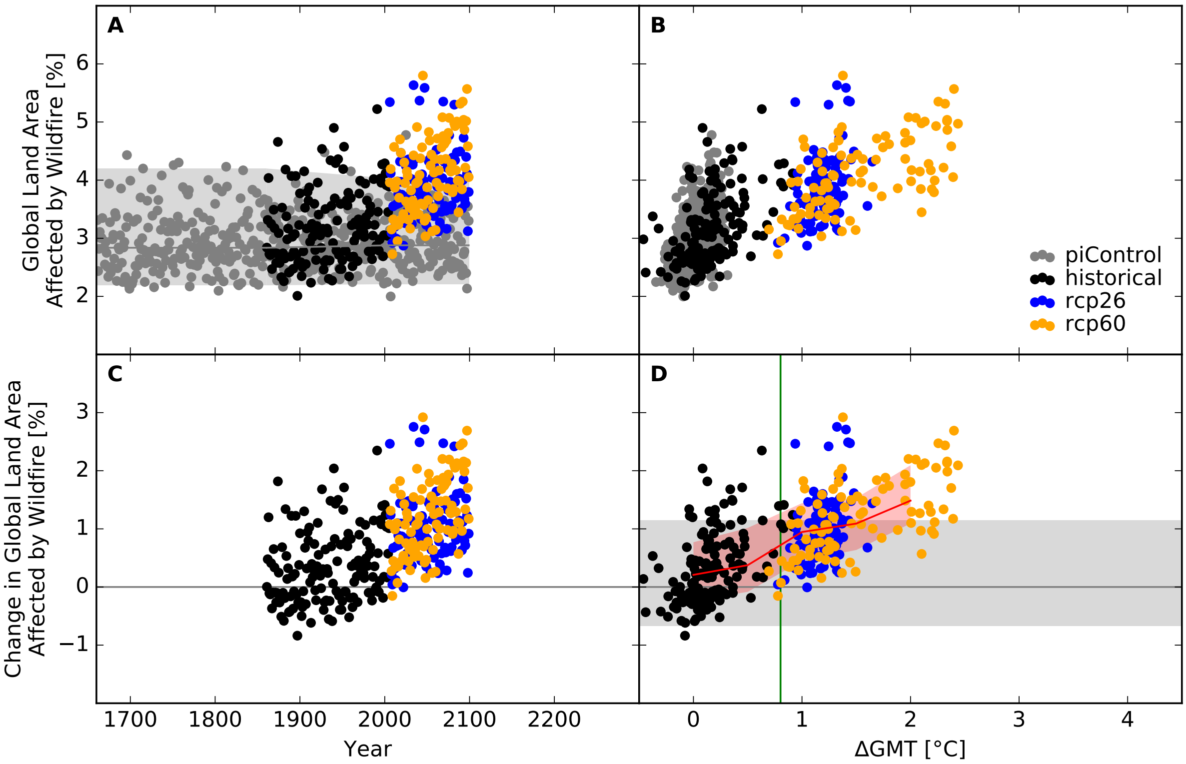

Figure S125: **Derivation of the pure effect of climate change on global land area fraction affected by wildfire events (GFDL-ESM2M + VISIT).** Analogous to Figure S114.

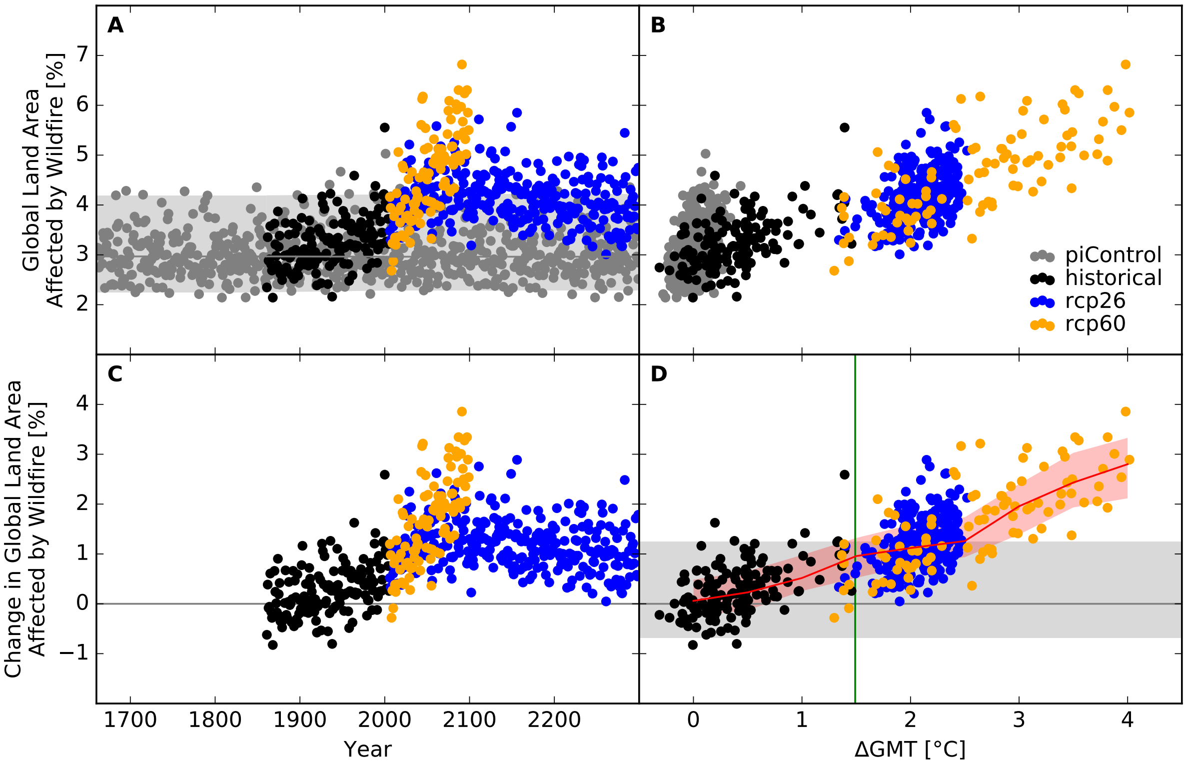

Figure S126: **Derivation of the pure effect of climate change on global land area fraction affected by wildfire events (IPSL-CM5A-LR + VISIT).** Analogous to Figure S114.

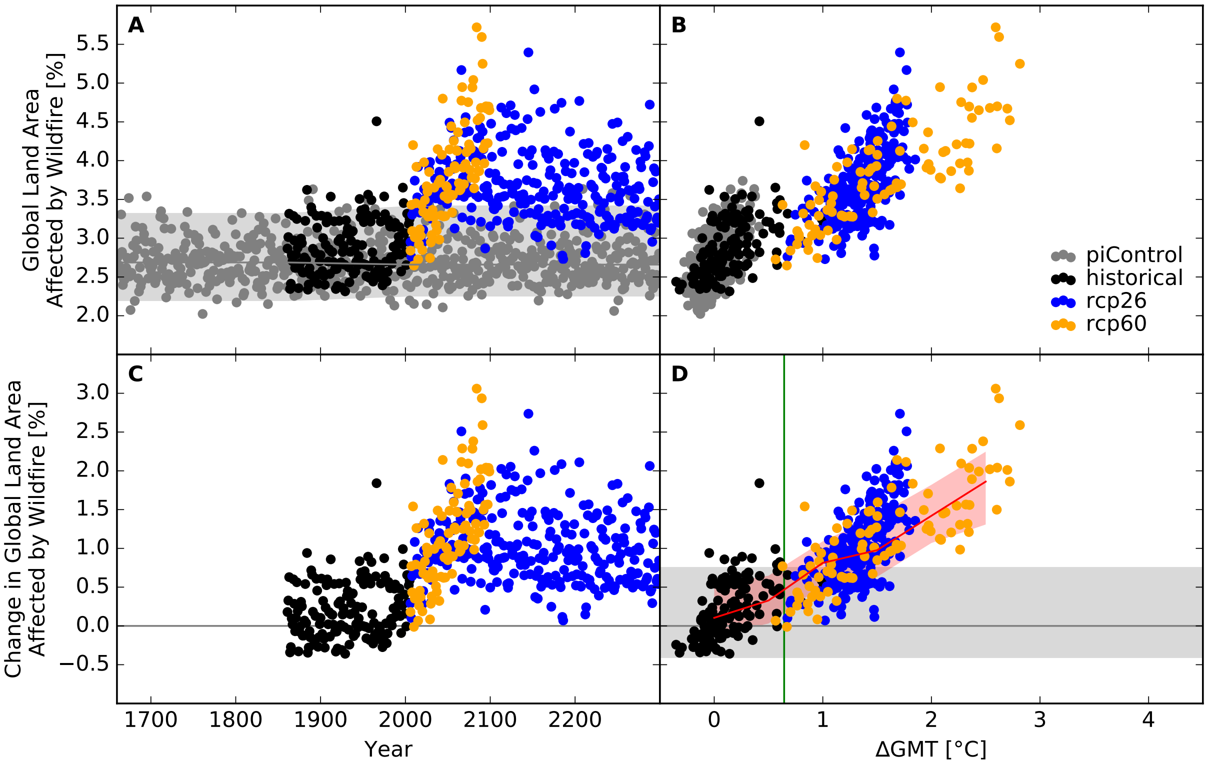

Figure S127: **Derivation of the pure effect of climate change on global land area fraction affected by wildfire events (MIROC5 + VISIT).** Analogous to Figure S114.

People exposed

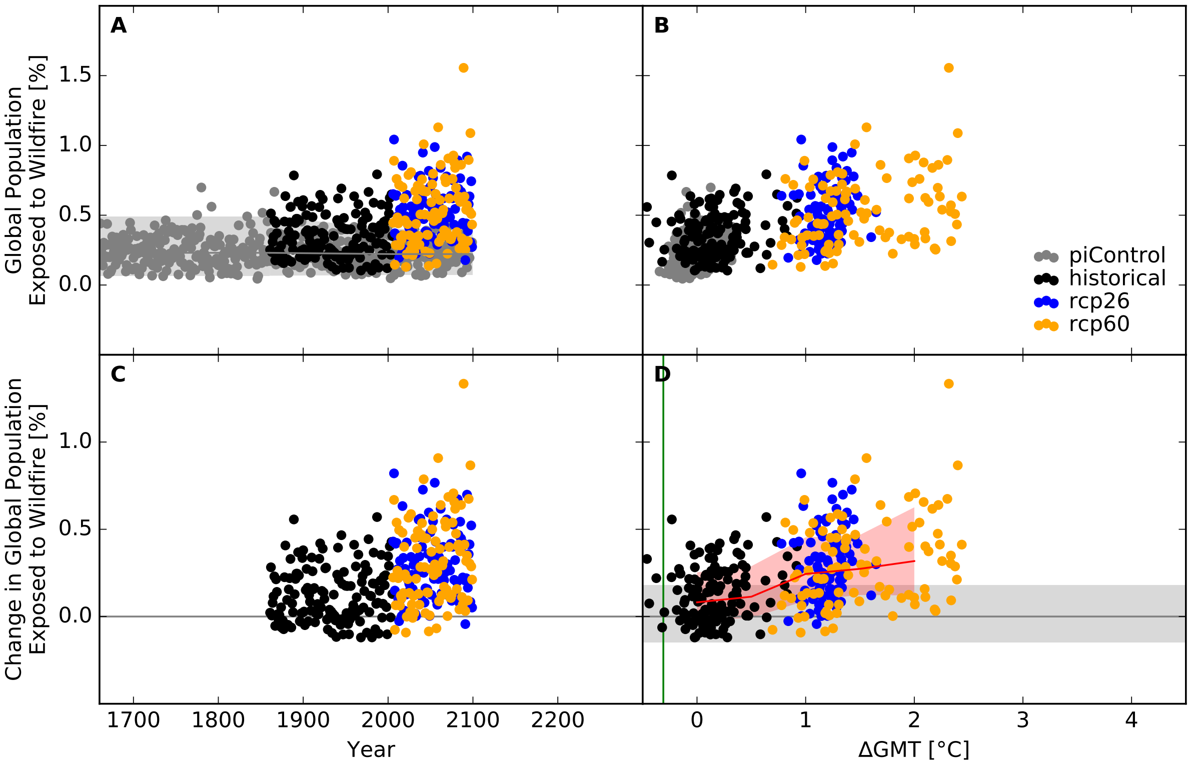

Figure S128: **Derivation of the pure effect of climate change on global population fraction affected by wildfire events (GFDL-ESM2M + CARAIB).** Panel A: Time series of annual global population fraction affected (PFA) by wildfire events for pre-industrial climate (grey dots), historical climate (black dots), climate projections for RCP2.6 (blue dots), and RCP6.0 (orange dots). In all simulations, socio-economic conditions are varied according to the historically observed development between 1860 and 2005, and held fixed at 1860 conditions before 1860 and at 2005 conditions after 2005. Shaded areas before 1860/after 2005 represent the range from the 2nd to the 98th percentile of the distribution of the annual PFA under pre-industrial climate conditions in combination with 1860/2005 socio-economic conditions; the solid gray lines represent the respective median values; the shaded areas and solid gray line between 1860 and 2005 are linear interpolations of the respective values before 1860 and after 2005. Panel B: Data shown in Panel A plotted against the associated GCM-specific annual global mean temperature (GMT) change relative to the long-term pre-industrial mean. Panel C: Pure effect of climate change on PFA, calculated as the difference between the annual data shown in Panel A and the median of the simulations assuming pre-industrial climate conditions (solid gray line in Panel A). Panel D: Pure effect of climate change on PFA in terms of global mean temperature change, with distributions of the annual data estimated for each 1°C-wide bin of global mean temperature change that contains at least five data points, at least one data point above and at least one data point below the bin center. Areas shaded in red represent the range from the 20th to the 80th percentile around the median (solid red line) of these distributions. Areas shaded in gray represent the range from the 2nd to the 98th percentile of the zero-centered distribution of the annual PFA under pre-industrial climate and 2005 socio-economic conditions (cf. Panel A). The green vertical line represents the detection level defined as the global warming level at which a 1-in-50-years event under pre-industrial climate and 2005 socio-economic conditions becomes a 1-in-5-years event under changing climate and 2005 socio-economic conditions.

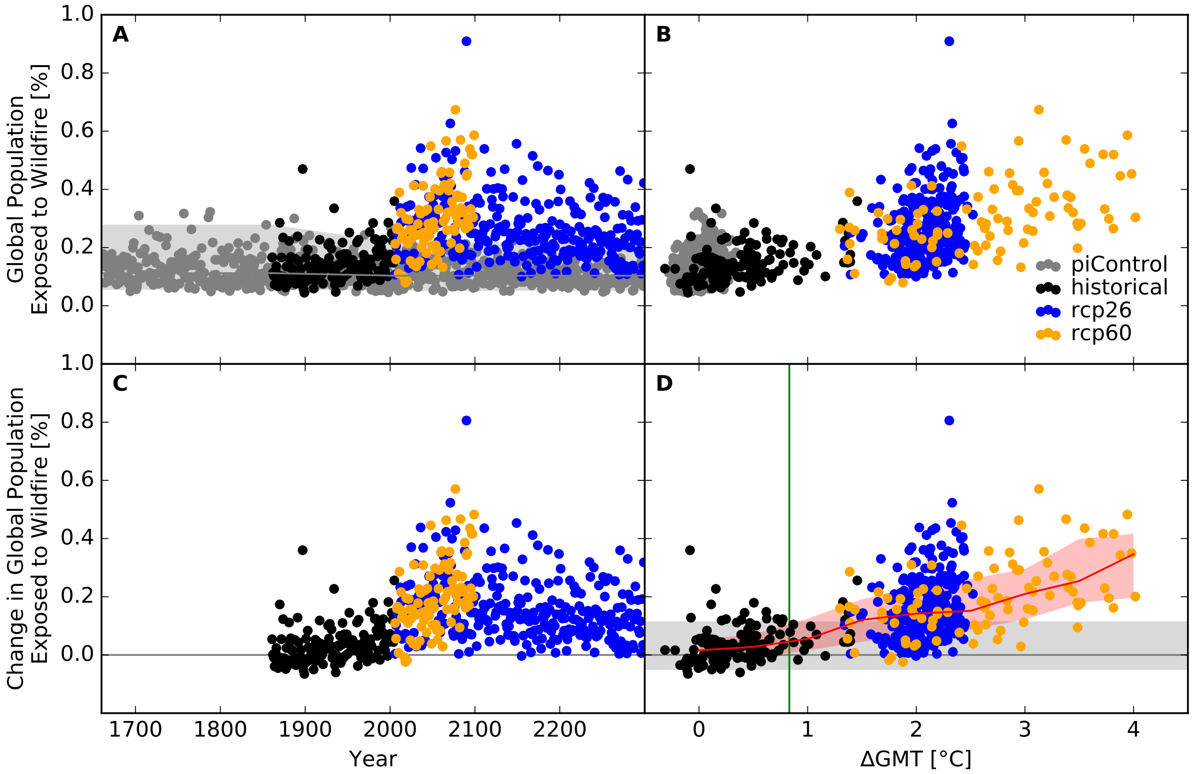

Figure S129: **Derivation of the pure effect of climate change on global population fraction affected by wildfire events (IPSL-CM5A-LR + CARAIB).** Analogous to Figure S128.

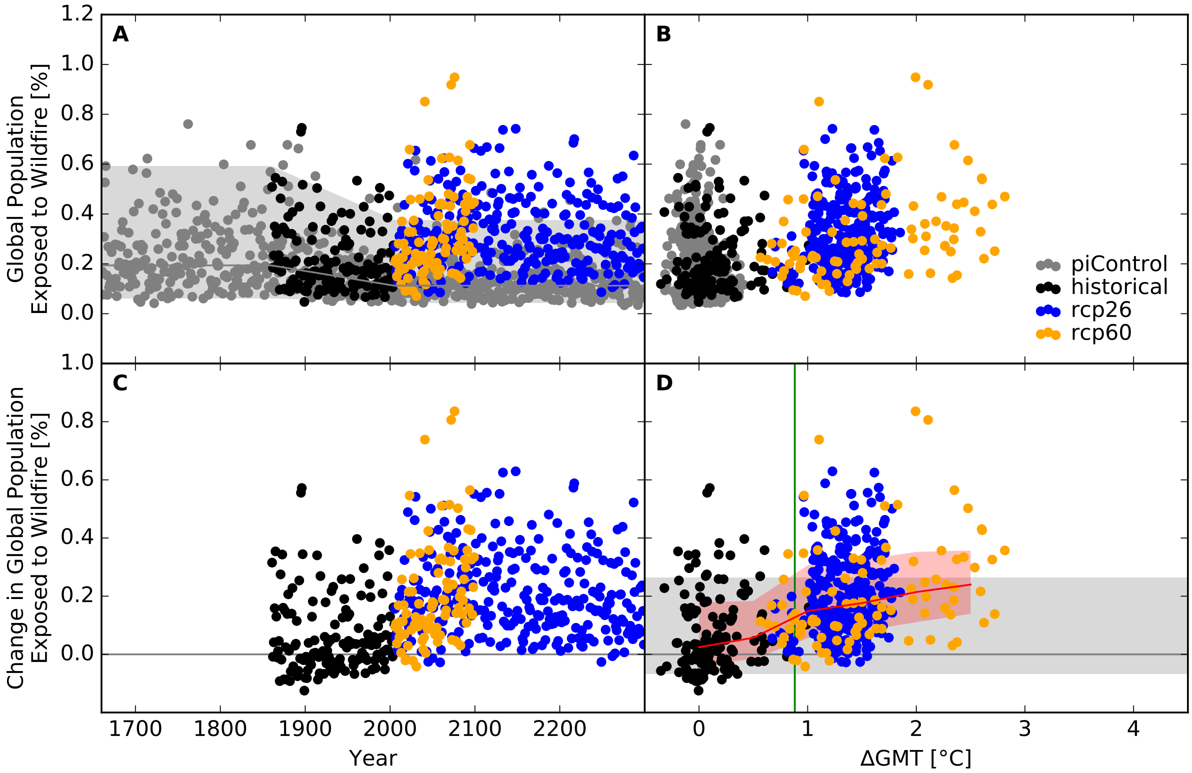

Figure S130: **Derivation of the pure effect of climate change on global population fraction affected by wildfire events (MIROC5 + CARAIB).** Analogous to Figure S128.

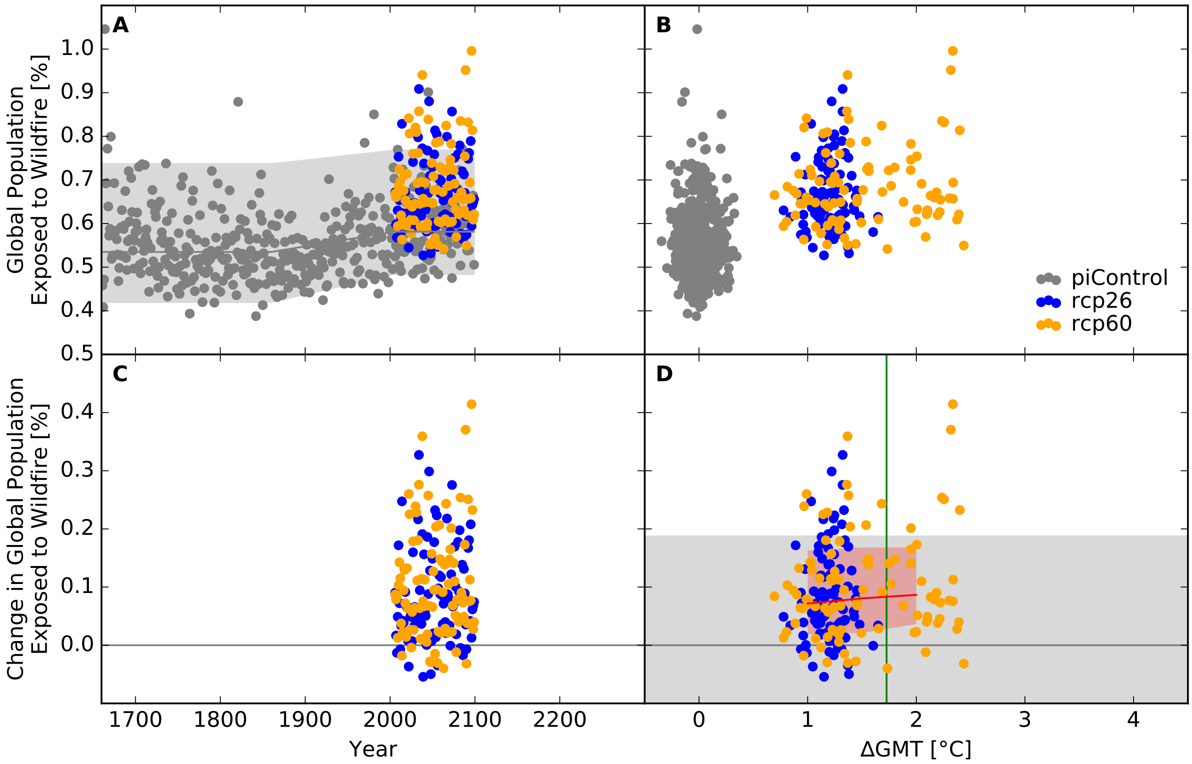

Figure S131: **Derivation of the pure effect of climate change on global population fraction affected by wildfire events (GFDL-ESM2M + LPJ-GUESS).** Analogous to Figure S128.

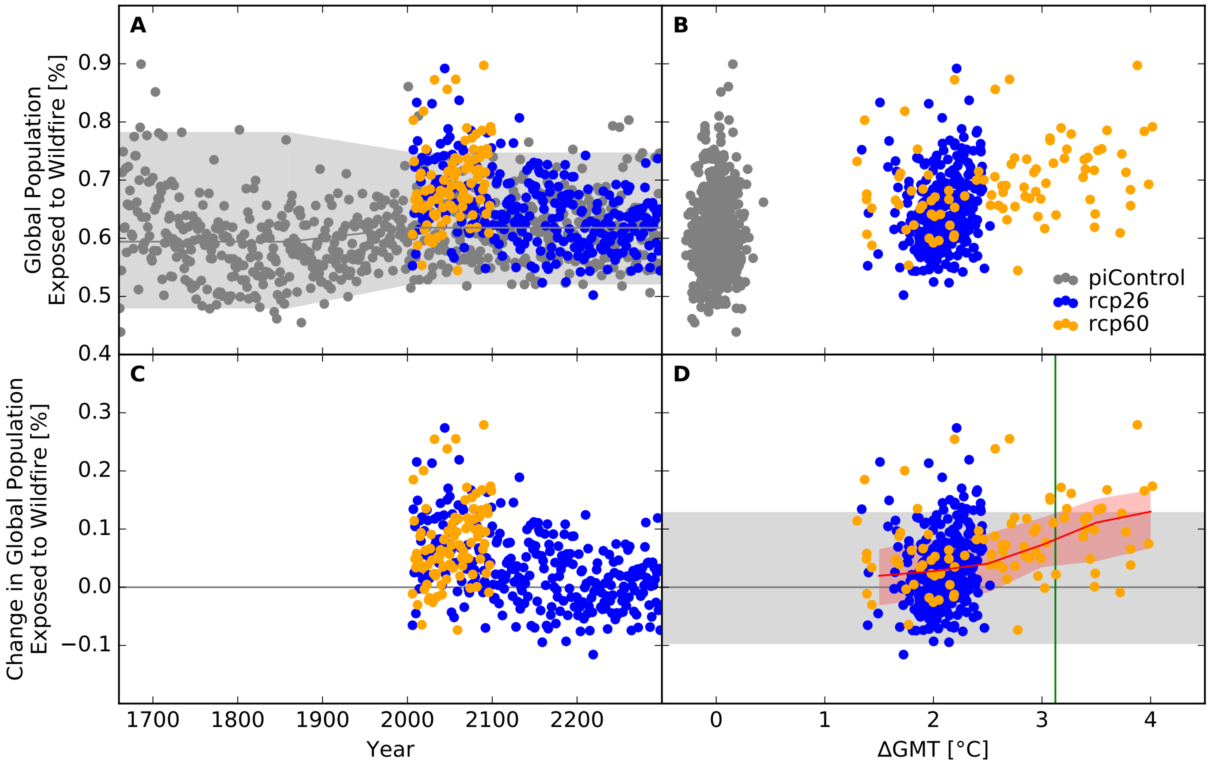

Figure S132: **Derivation of the pure effect of climate change on global population fraction affected by wildfire events (IPSL-CM5A-LR + LPJ-GUESS).** Analogous to Figure S128.

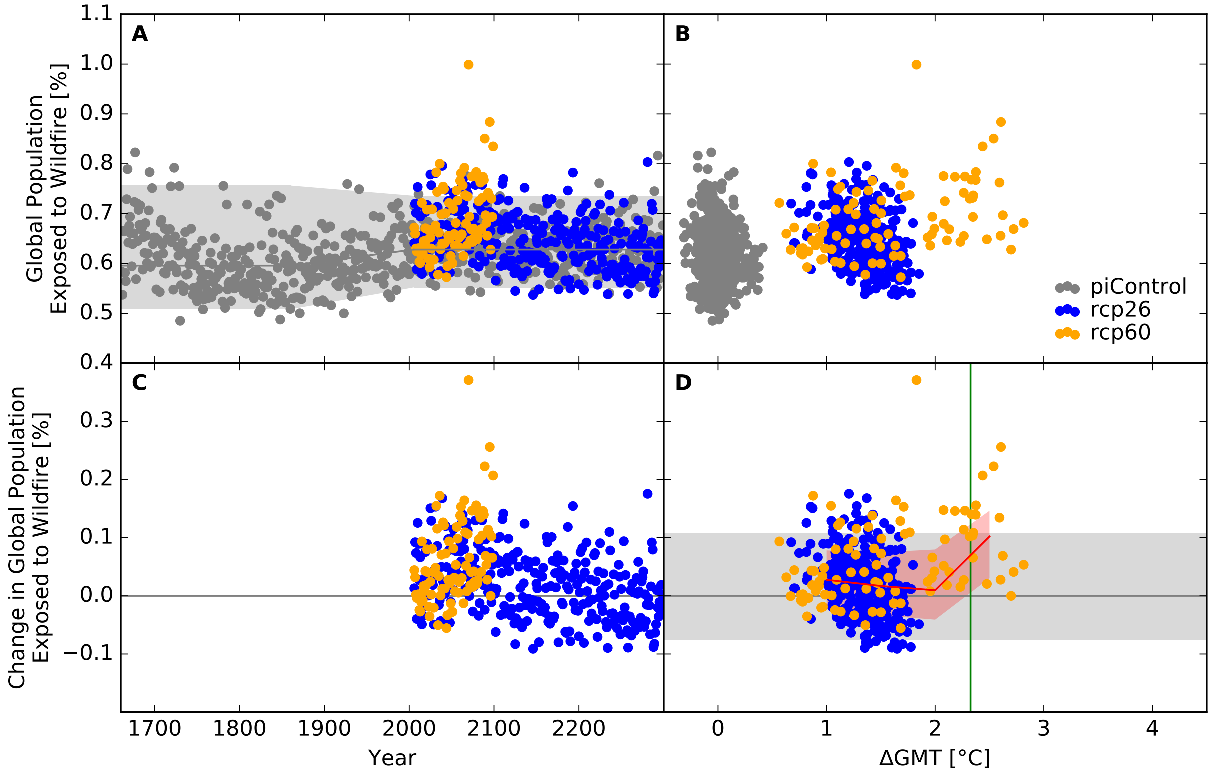

Figure S133: **Derivation of the pure effect of climate change on global population fraction affected by wildfire events (MIROC5 + LPJ-GUESS).** Analogous to Figure S128.

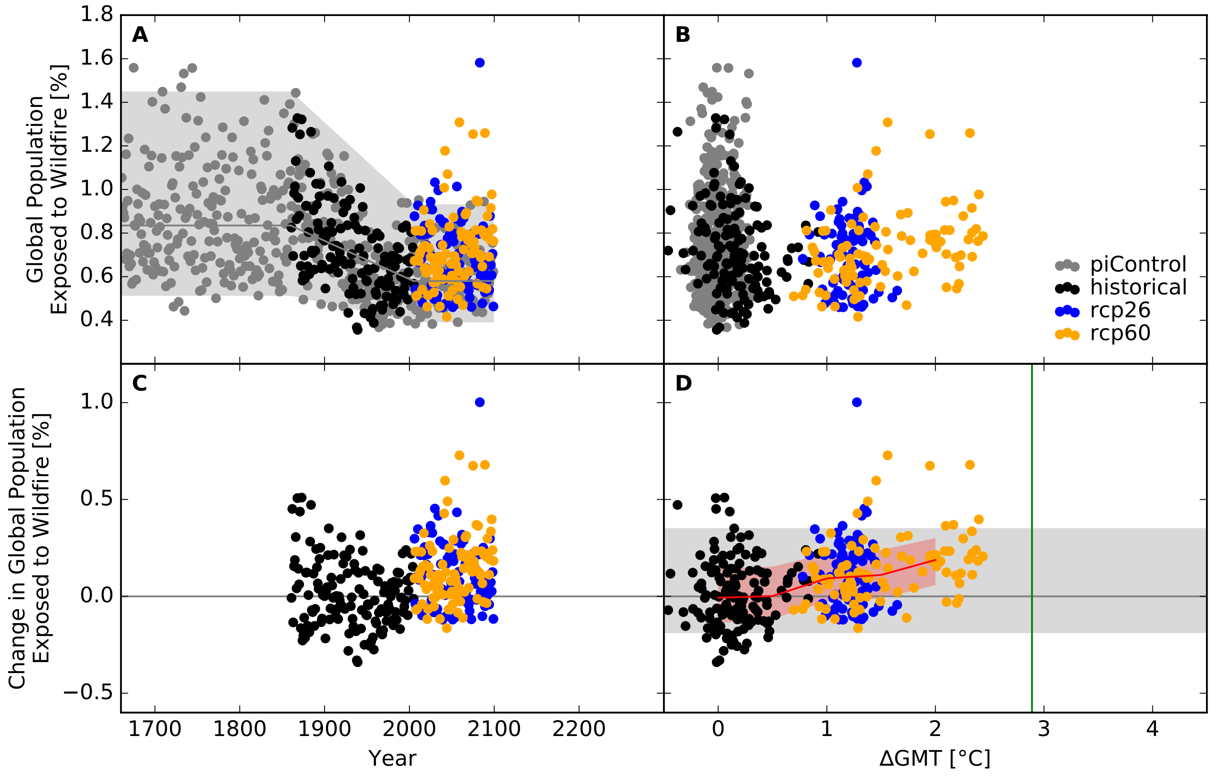

Figure S134: **Derivation of the pure effect of climate change on global population fraction affected by wildfire events (GFDL-ESM2M + LPJmL).** Analogous to Figure S128.

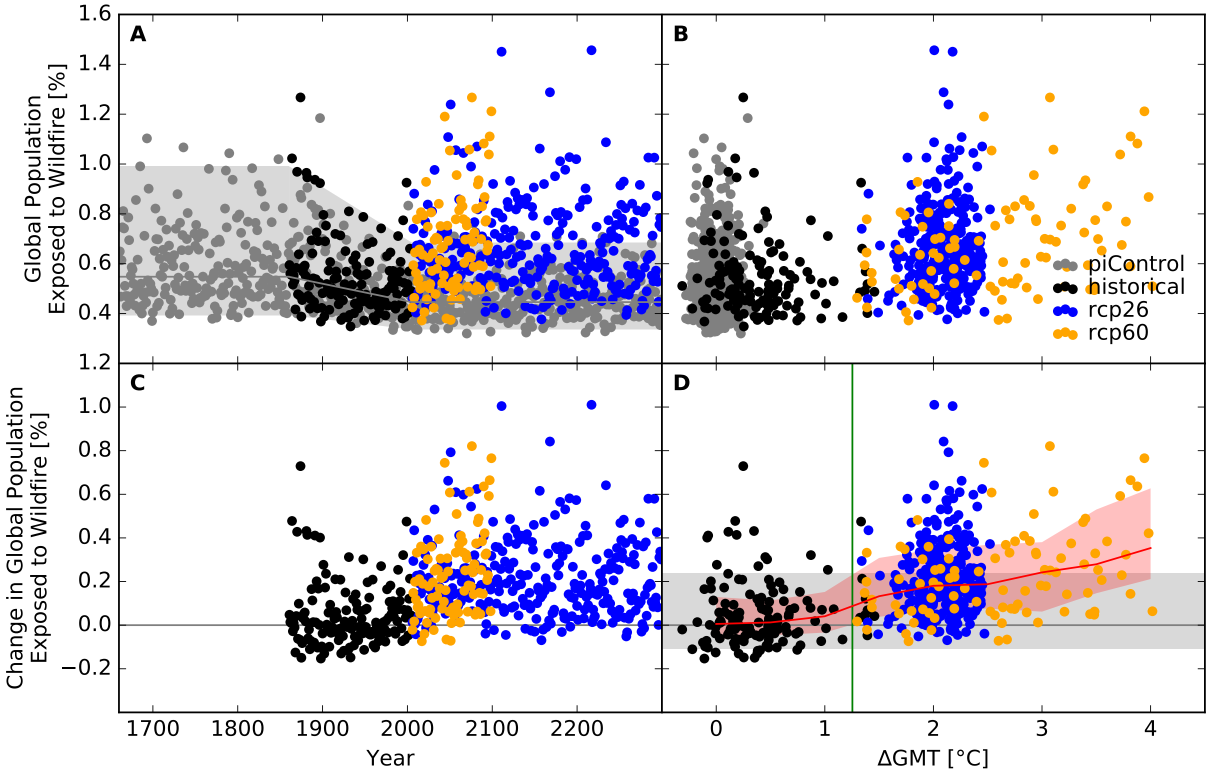

Figure S135: **Derivation of the pure effect of climate change on global population fraction affected by wildfire events (IPSL-CM5A-LR + LPJmL).** Analogous to Figure S128.

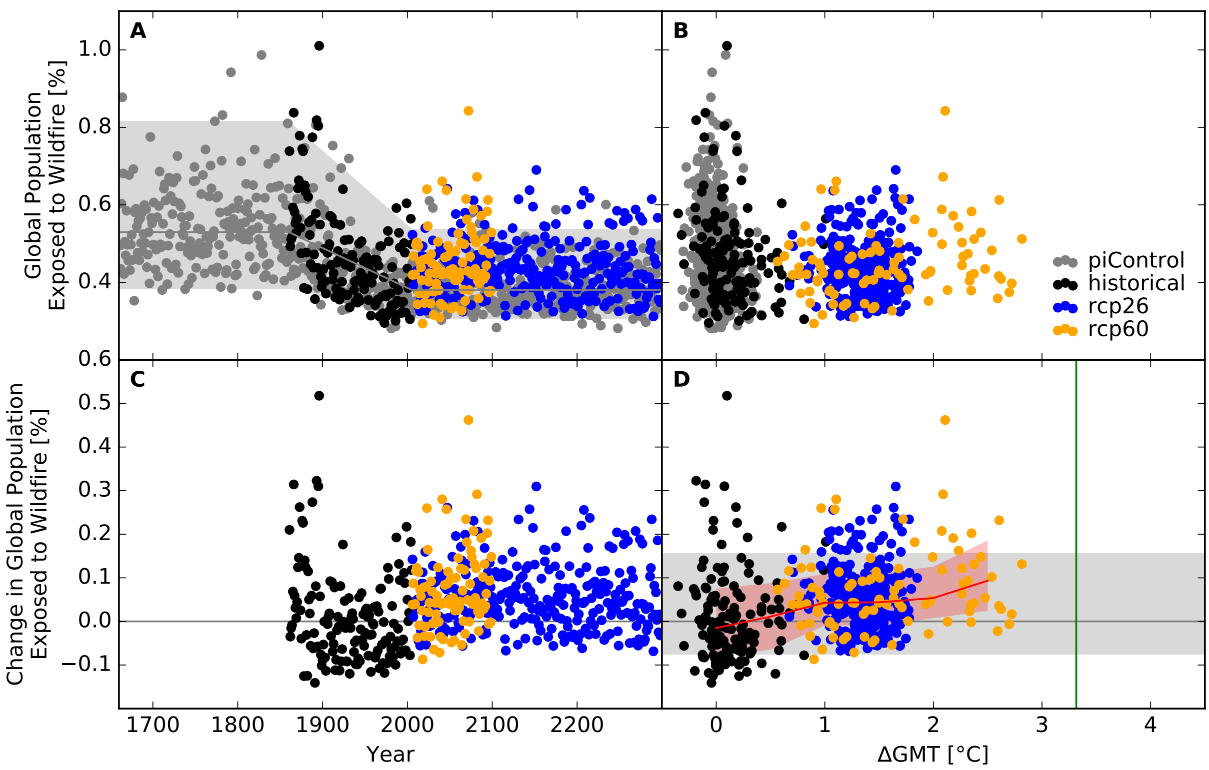

Figure S136: **Derivation of the pure effect of climate change on global population fraction affected by wildfire events (MIROC5 + LPJmL).** Analogous to Figure S128.

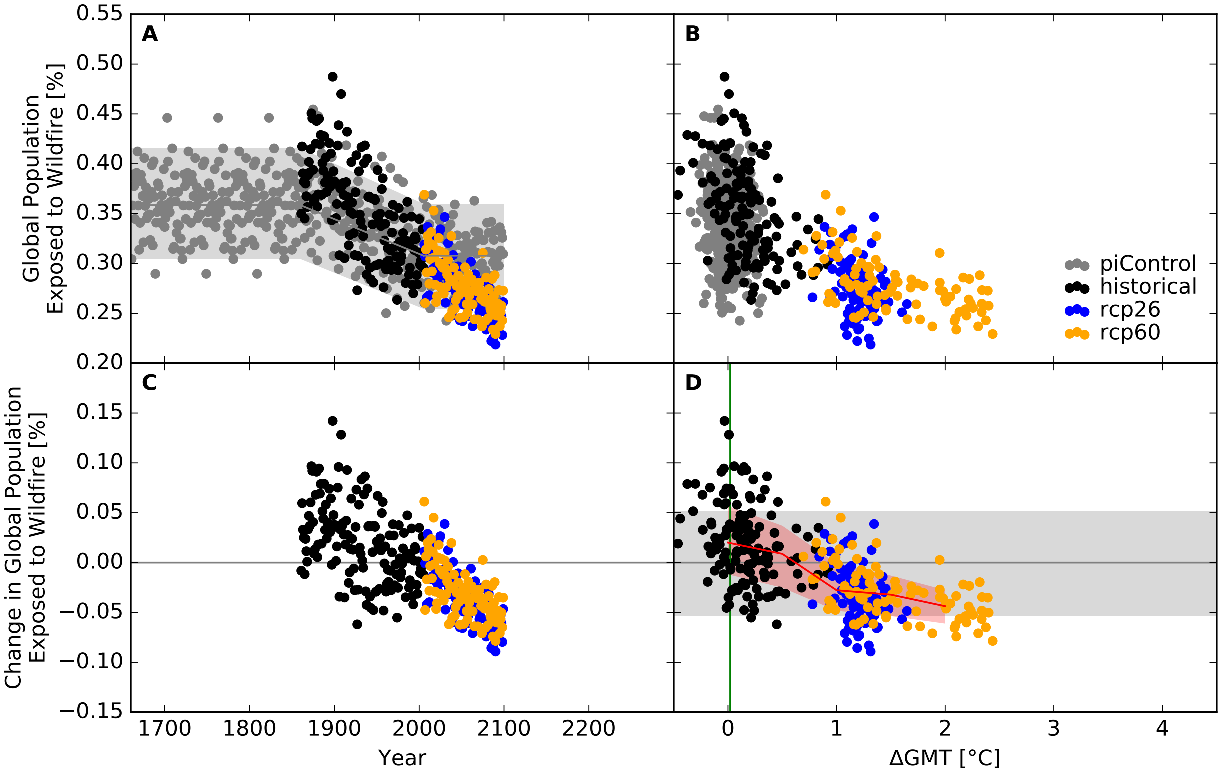

Figure S137: **Derivation of the pure effect of climate change on global population fraction affected by wildfire events (GFDL-ESM2M + ORCHIDEE).** Analogous to Figure S128.

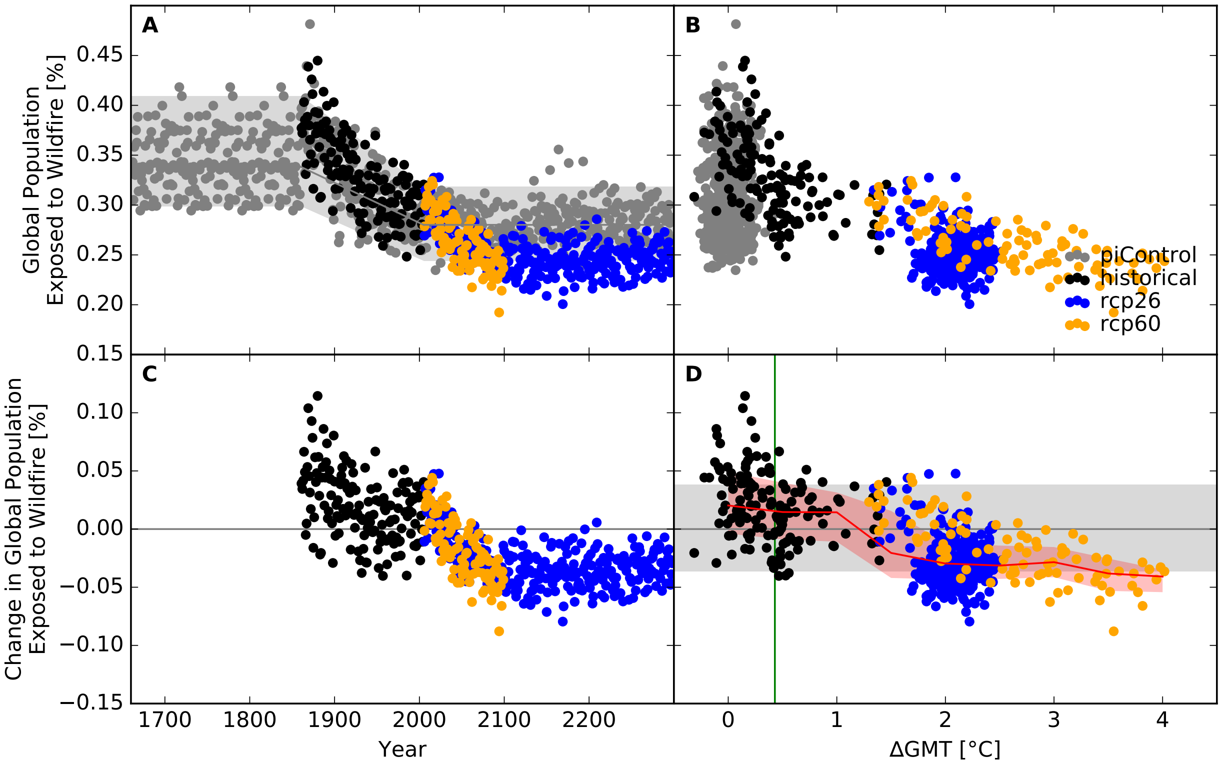

Figure S138: **Derivation of the pure effect of climate change on global population fraction affected by wildfire events (IPSL-CM5A-LR + ORCHIDEE).** Analogous to Figure S128.

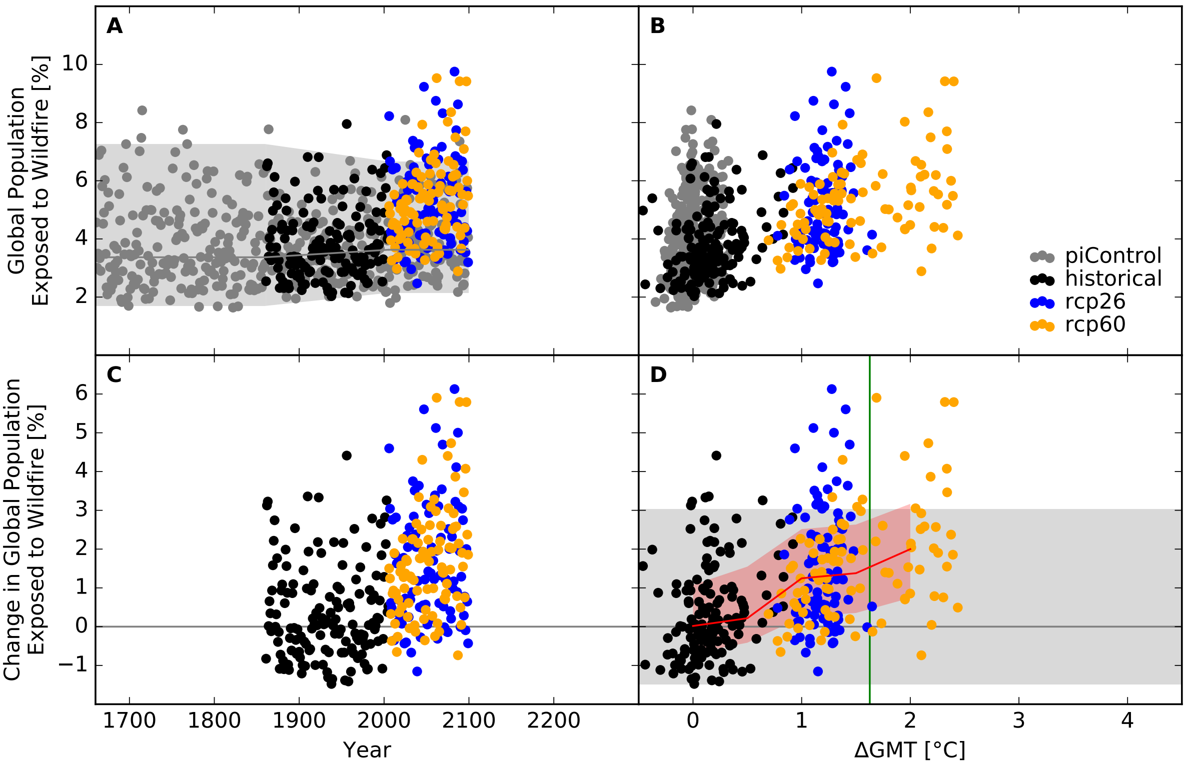

Figure S139: **Derivation of the pure effect of climate change on global population fraction affected by wildfire events (GFDL-ESM2M + VISIT).** Analogous to Figure S128.

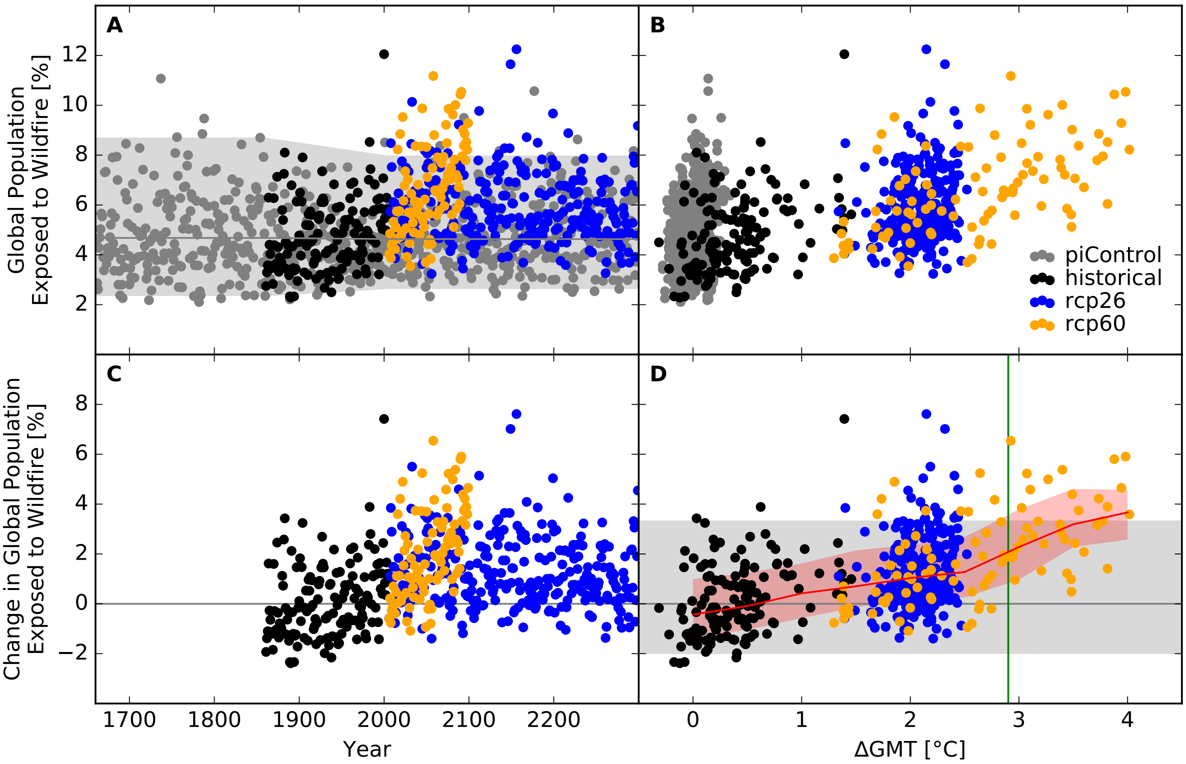

Figure S140: **Derivation of the pure effect of climate change on global population fraction affected by wildfire events (IPSL-CM5A-LR + VISIT).** Analogous to Figure S128.

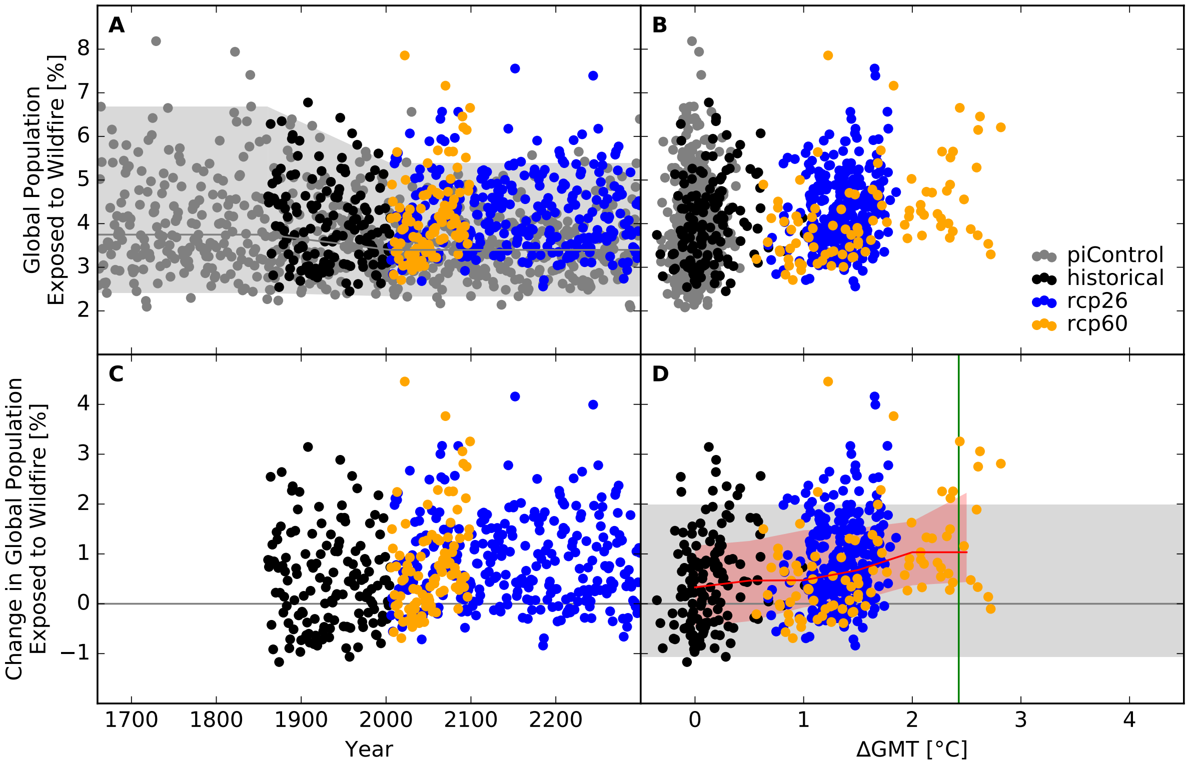

Figure S141: **Derivation of the pure effect of climate change on global population fraction affected by wildfire events (MIROC5 + VISIT).** Analogous to Figure S128.

Occurrence probability at grid scale

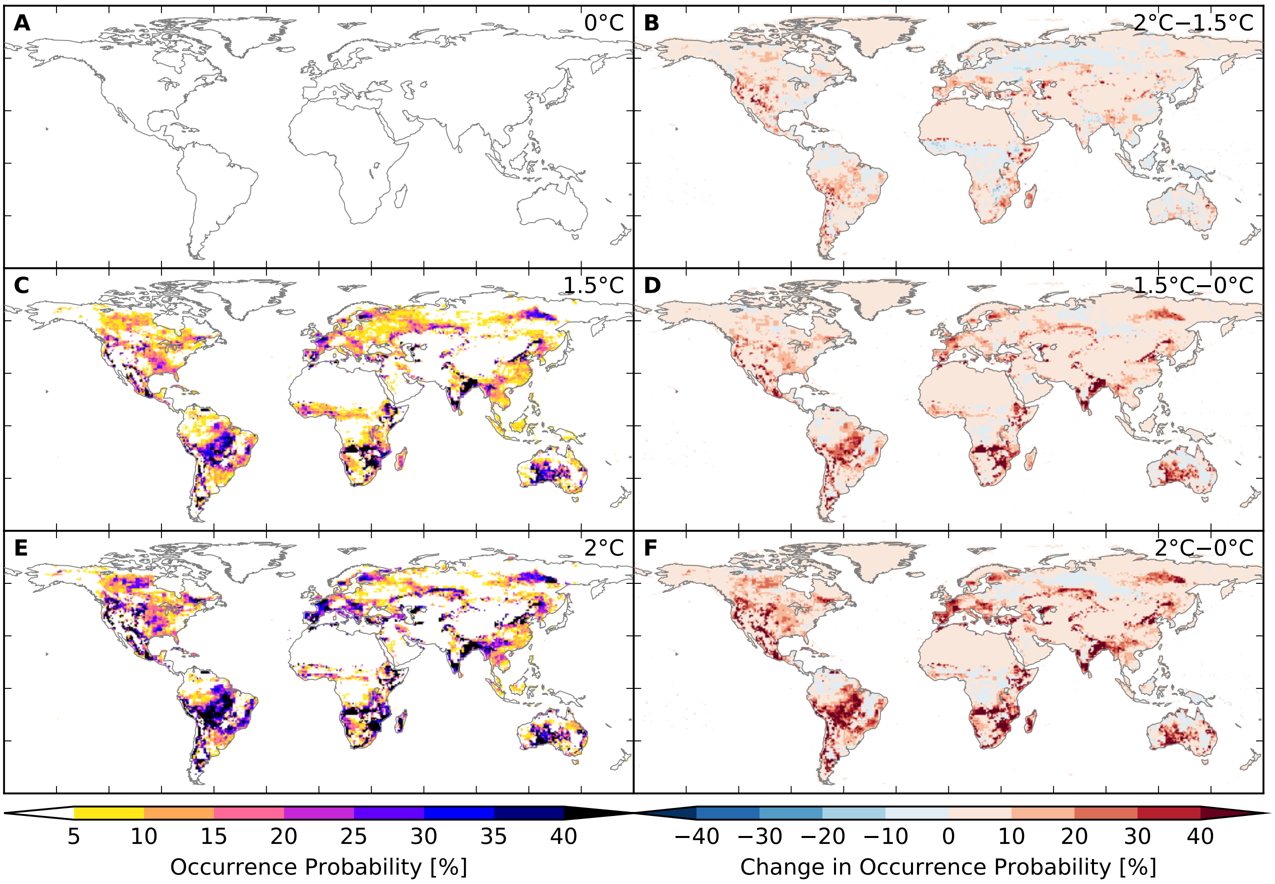

Figure S142: **Probability of occurrence of at least one wildfire event per year at different global warming levels (GFDL-ESM2M + CARAIB).** Panels A, C, E: Probabilities at 0°C, 1.5°C, 2°C global mean temperature (GMT) change relative to the long-term pre-industrial mean GMT, respectively. Panels B, D, F: Differences between probabilities at GMT change levels of 2°C and 1.5°C, 1.5°C and 0°C, 2°C and 0°C, respectively.

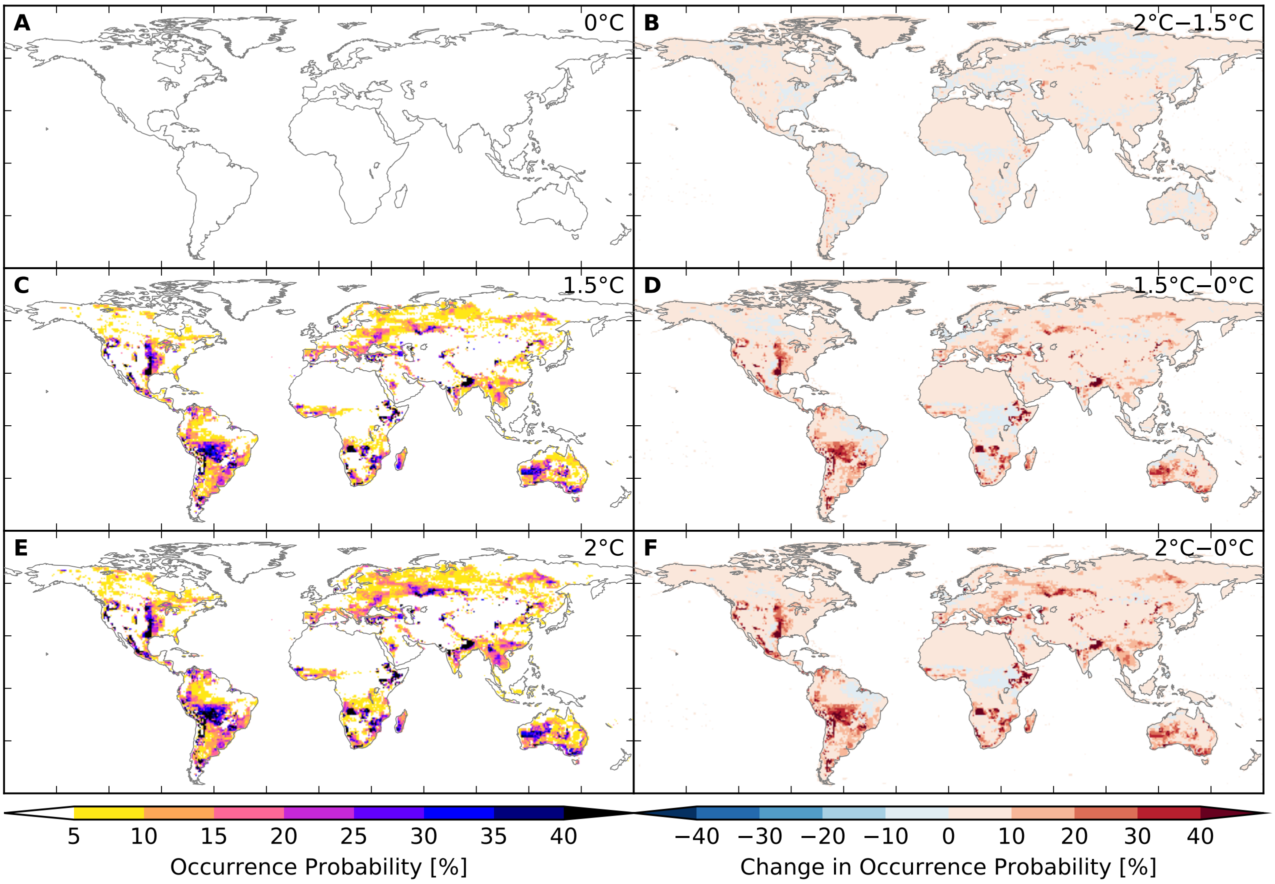

Figure S143: **Probability of occurrence of at least one wildfire event per year at different global warming levels (IPSL-CM5A-LR + CARAIB).** Analogous to Figure S142.

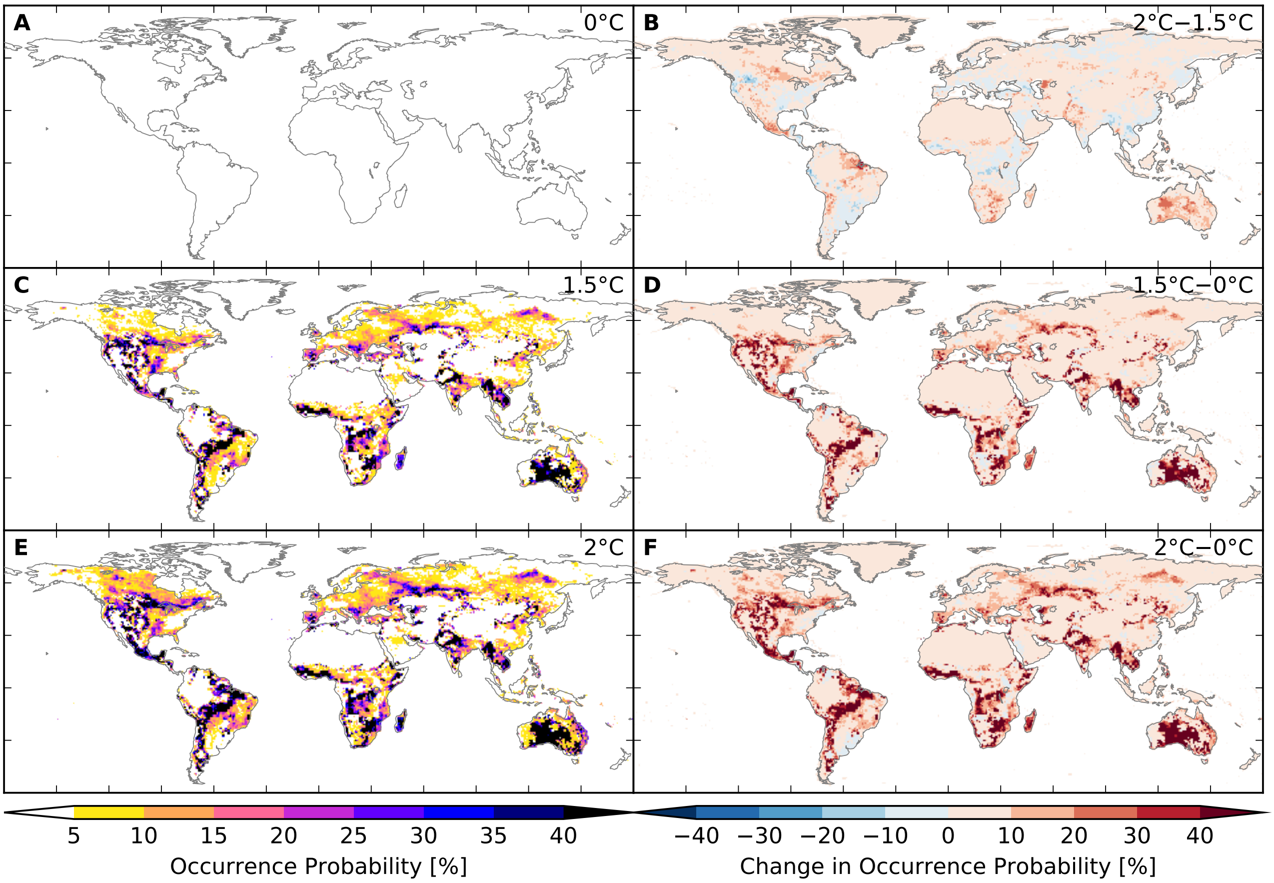

Figure S144: **Probability of occurrence of at least one wildfire event per year at different global warming levels (MIROC5 + CARAIB).** Analogous to Figure S142.

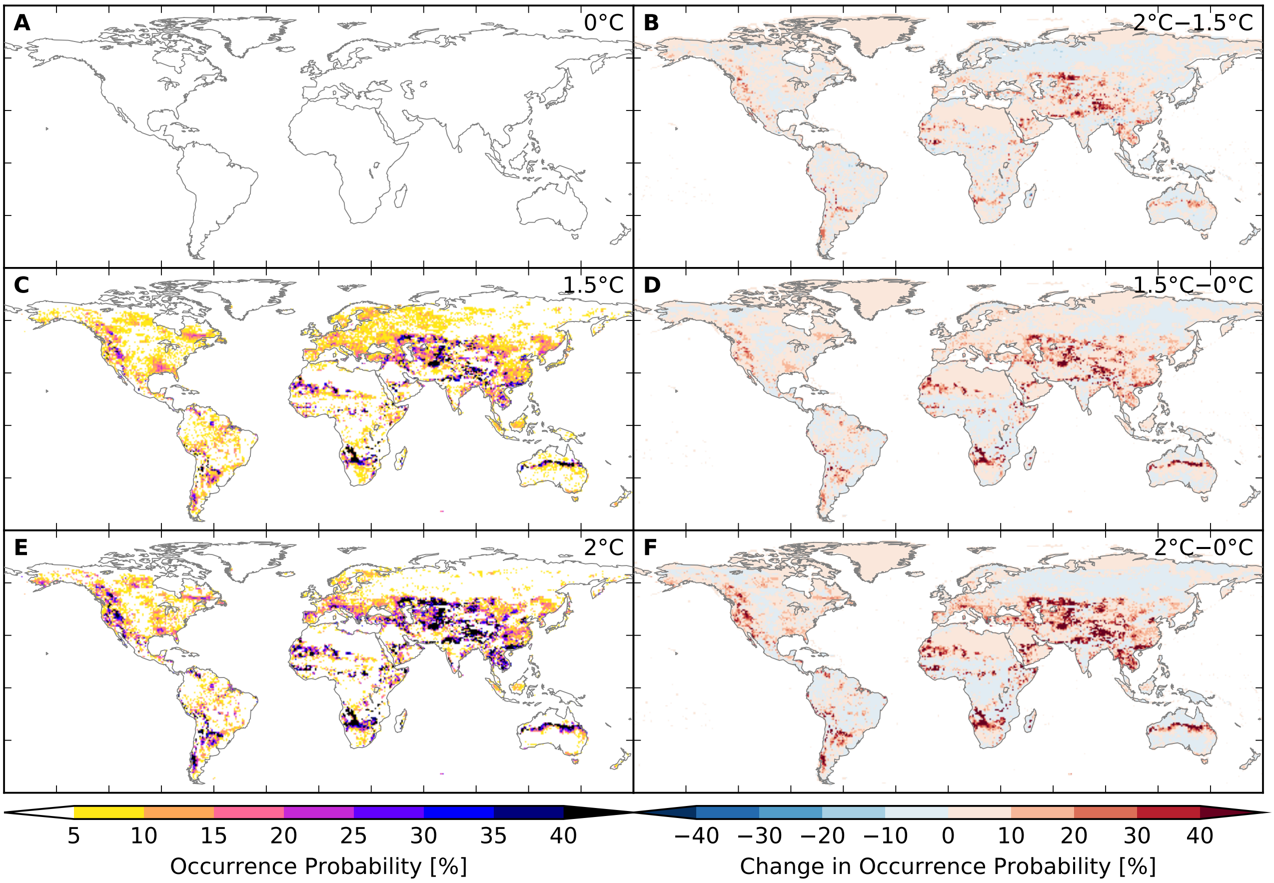

Figure S145: **Probability of occurrence of at least one wildfire event per year at different global warming levels (GFDL-ESM2M + LPJ-GUESS).** Analogous to Figure S142.

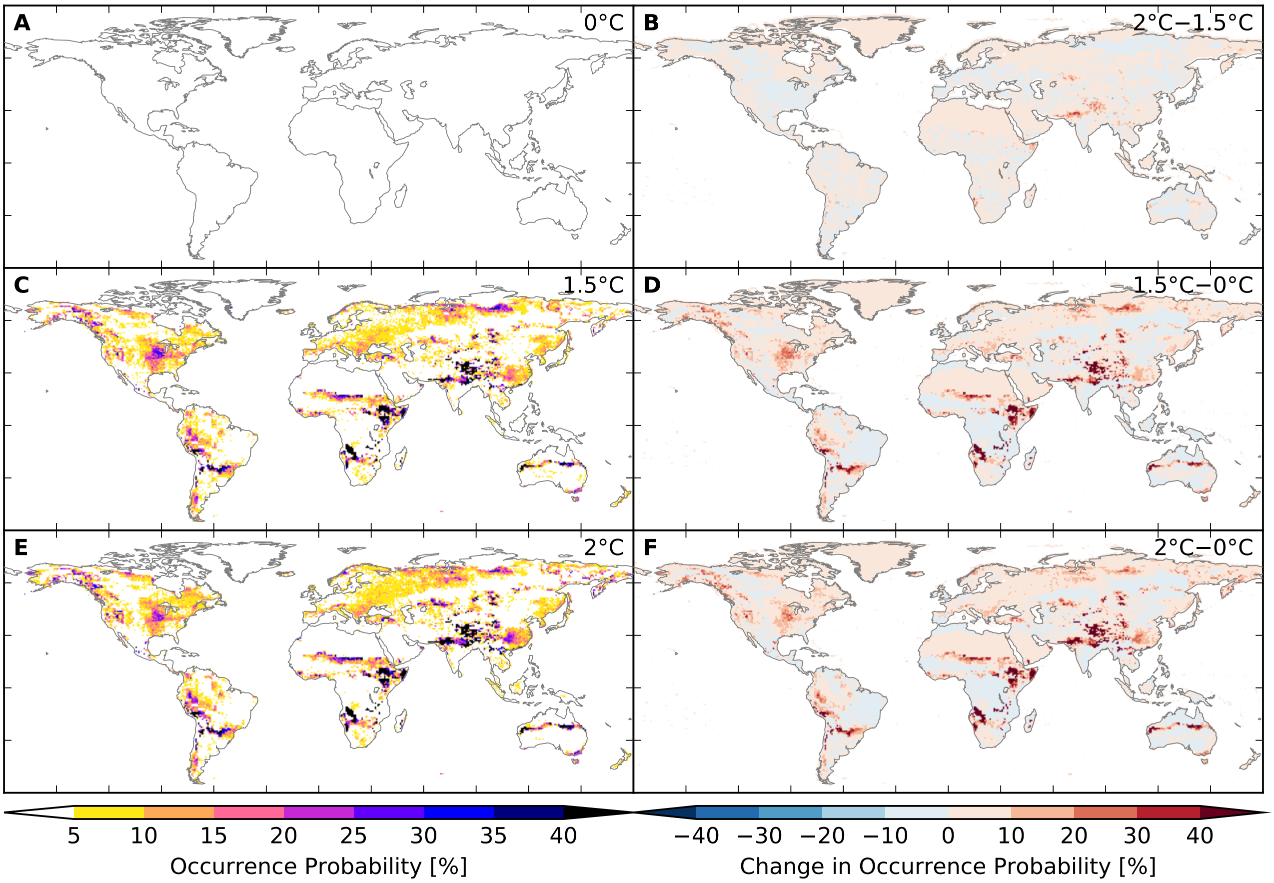

Figure S146: **Probability of occurrence of at least one wildfire event per year at different global warming levels (IPSL-CM5A-LR + LPJ-GUESS).** Analogous to Figure S142.

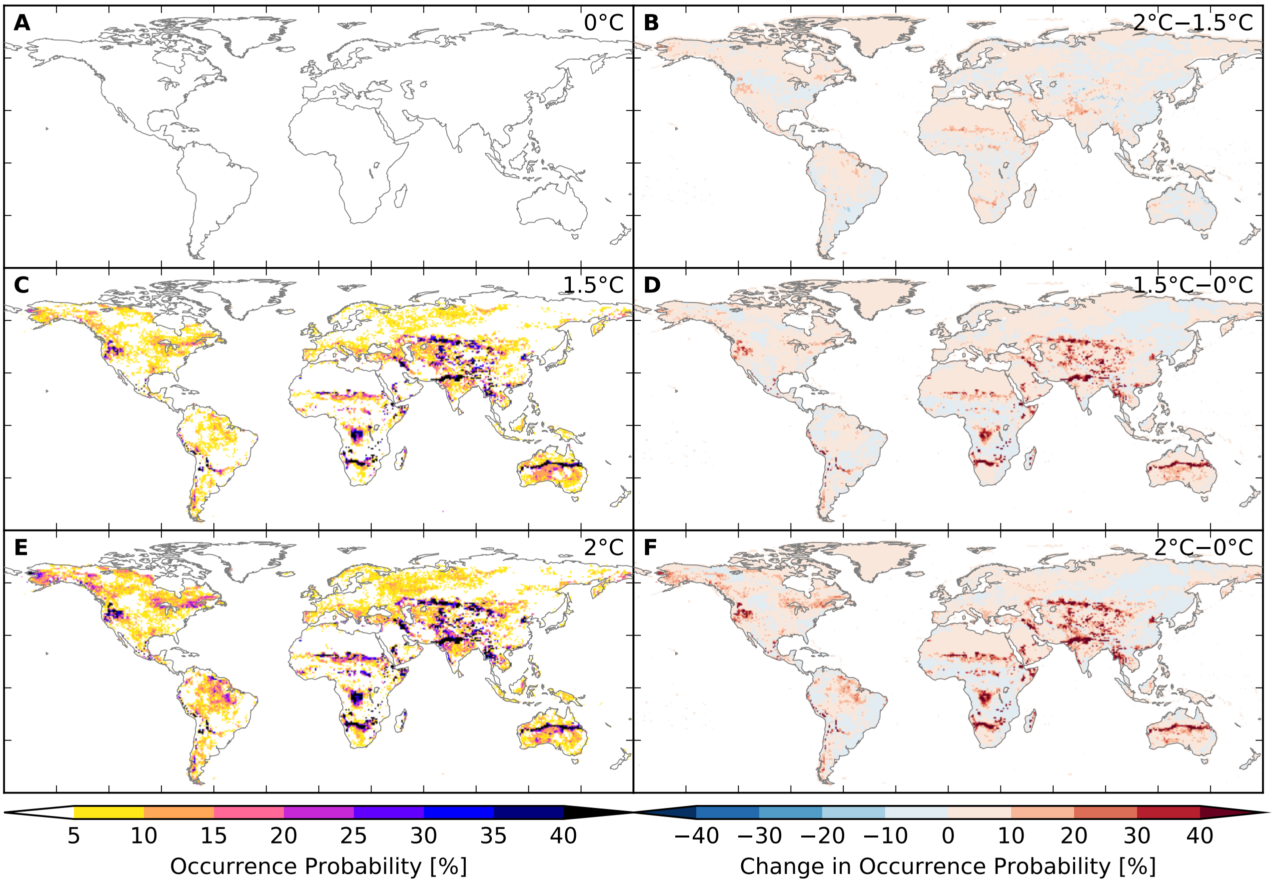

Figure S147: **Probability of occurrence of at least one wildfire event per year at different global warming levels (MIROC5 + LPJ-GUESS).** Analogous to Figure S142.

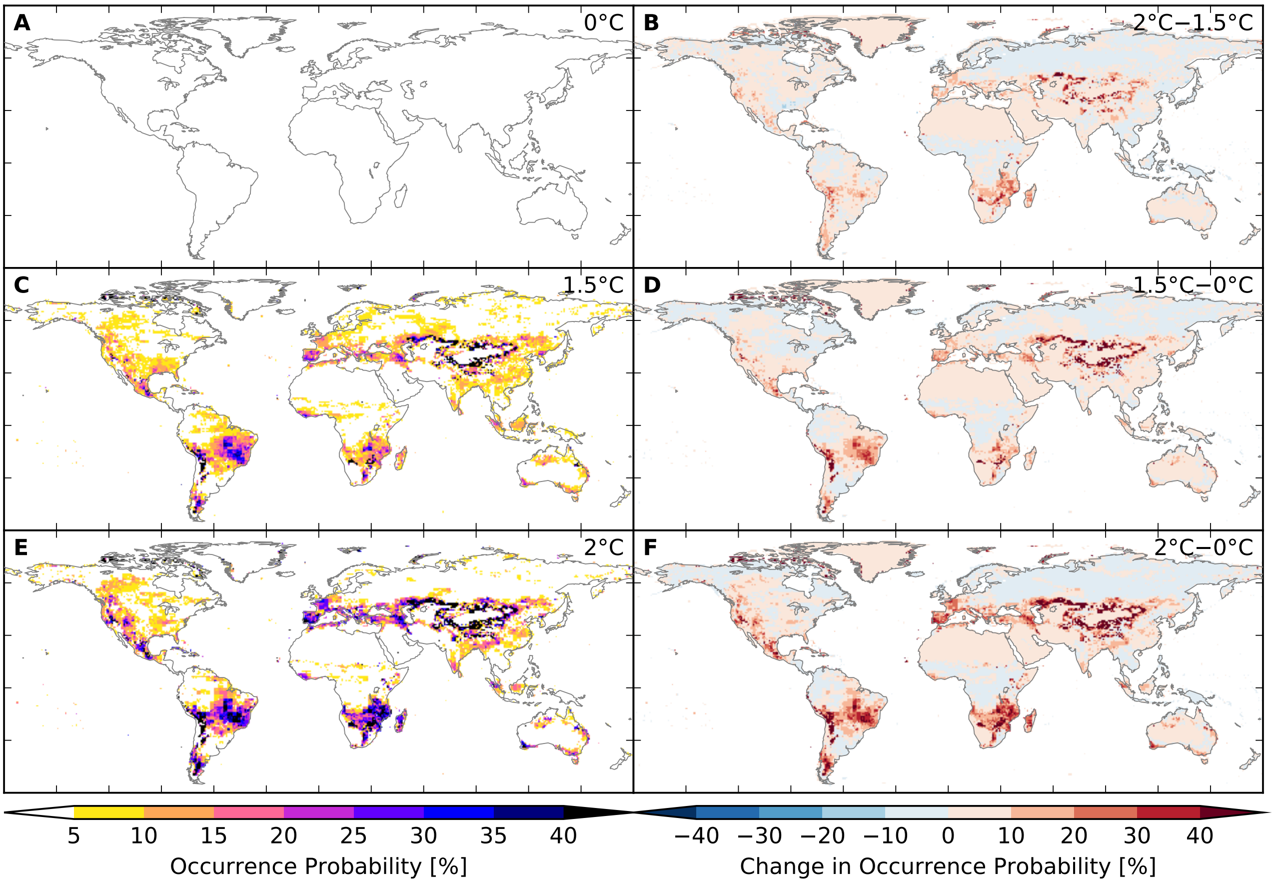

Figure S148: **Probability of occurrence of at least one wildfire event per year at different global warming levels (GFDL-ESM2M + LPJmL).** Analogous to Figure S142.

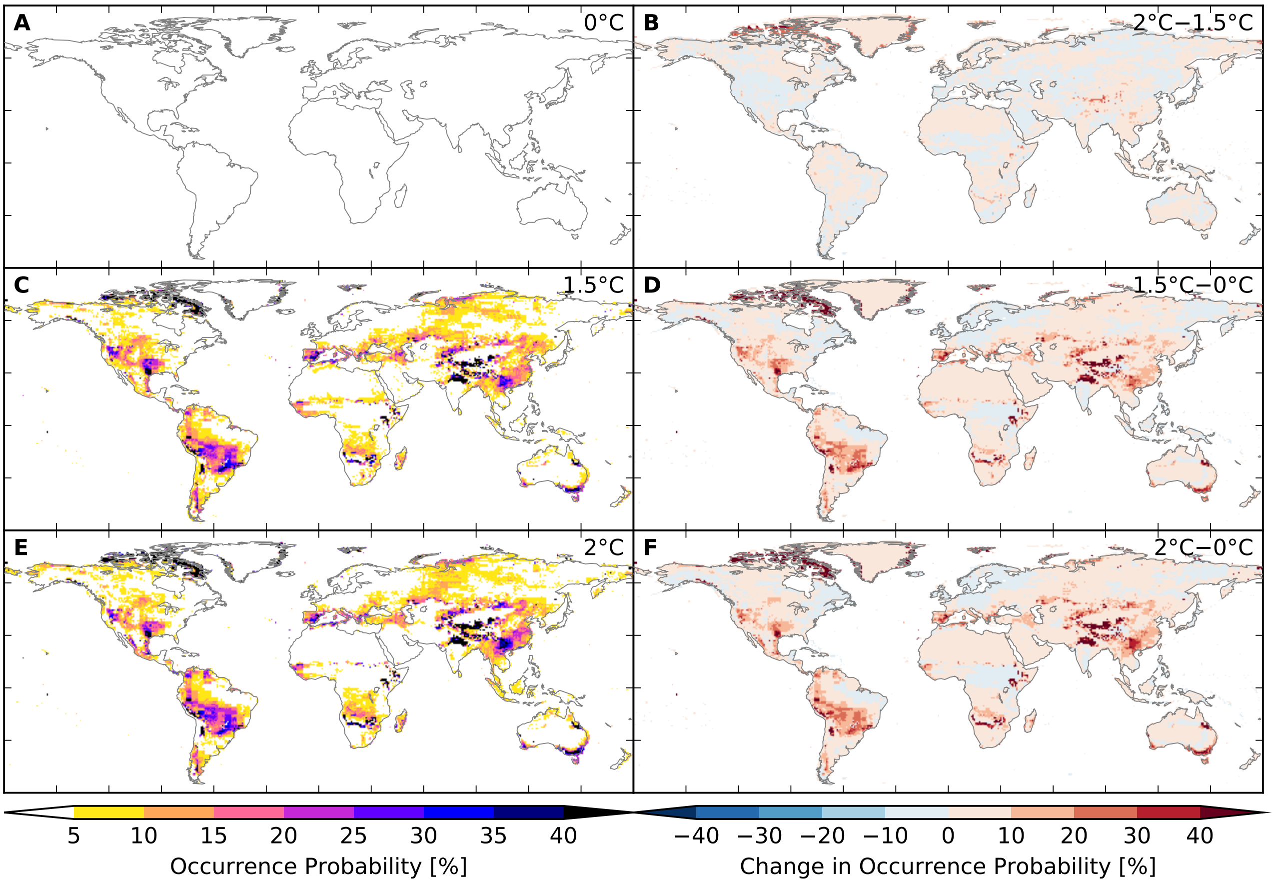

Figure S149: **Probability of occurrence of at least one wildfire event per year at different global warming levels (IPSL-CM5A-LR + LPJmL).** Analogous to Figure S142.

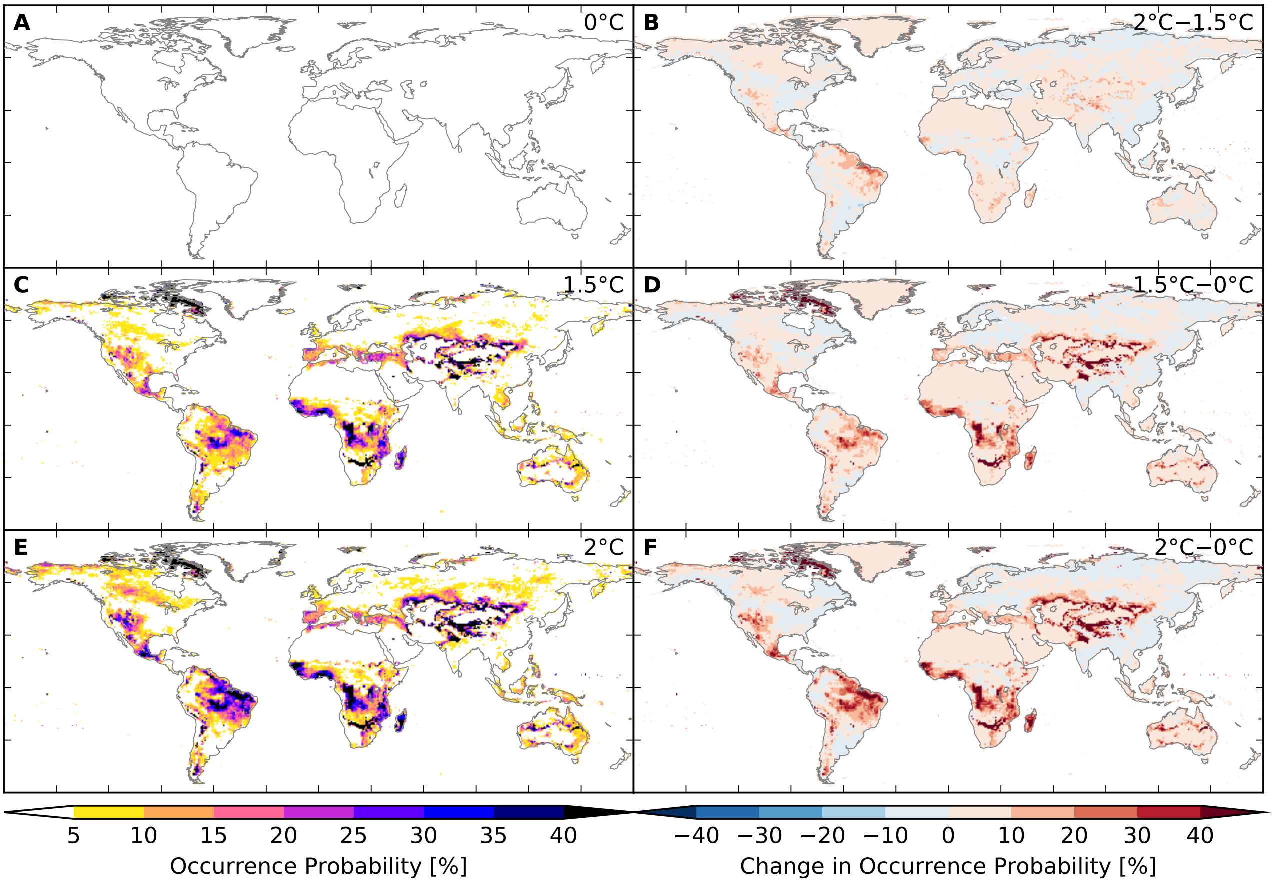

Figure S150: **Probability of occurrence of at least one wildfire event per year at different global warming levels (MIROC5 + LPJmL).** Analogous to Figure S142.

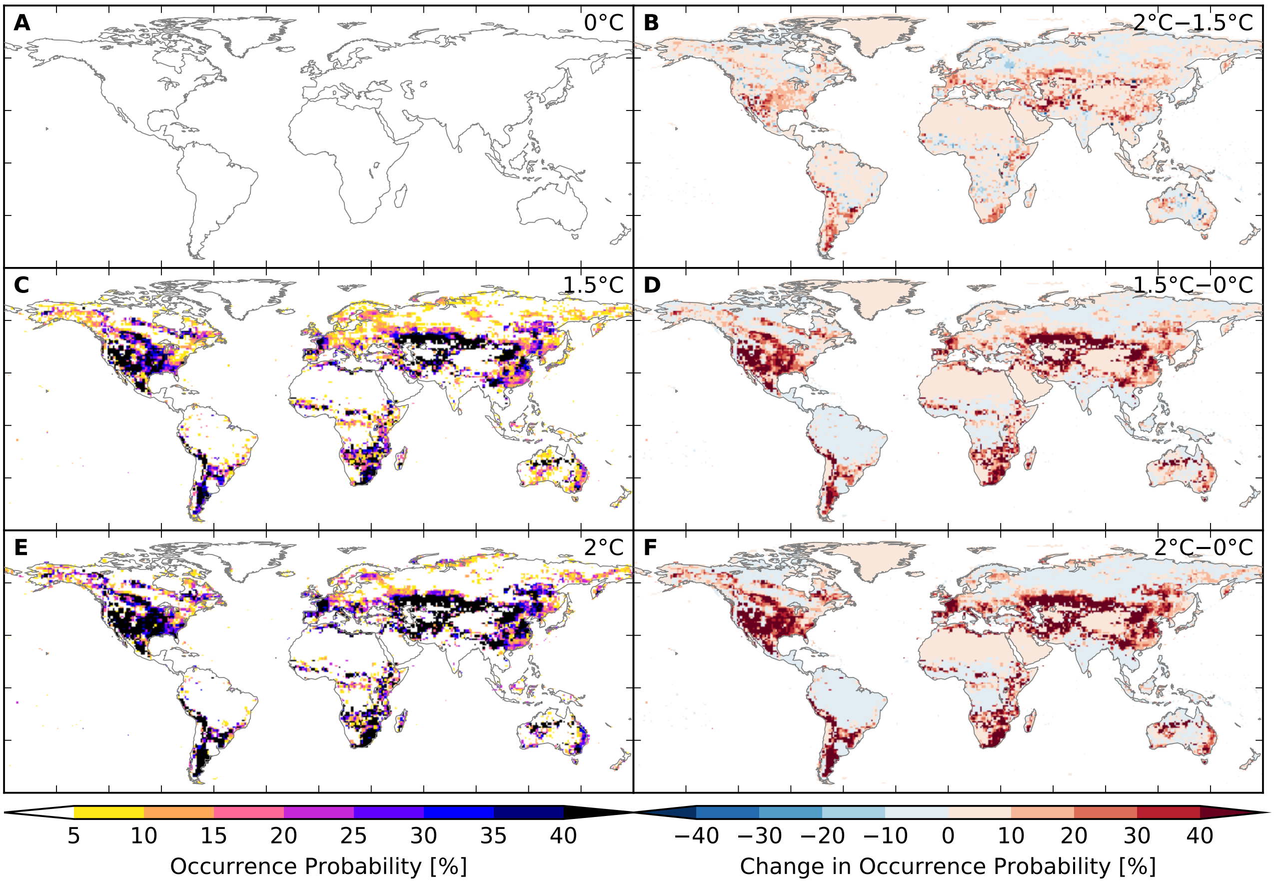

Figure S151: **Probability of occurrence of at least one wildfire event per year at different global warming levels (GFDL-ESM2M + ORCHIDEE).** Analogous to Figure S142.

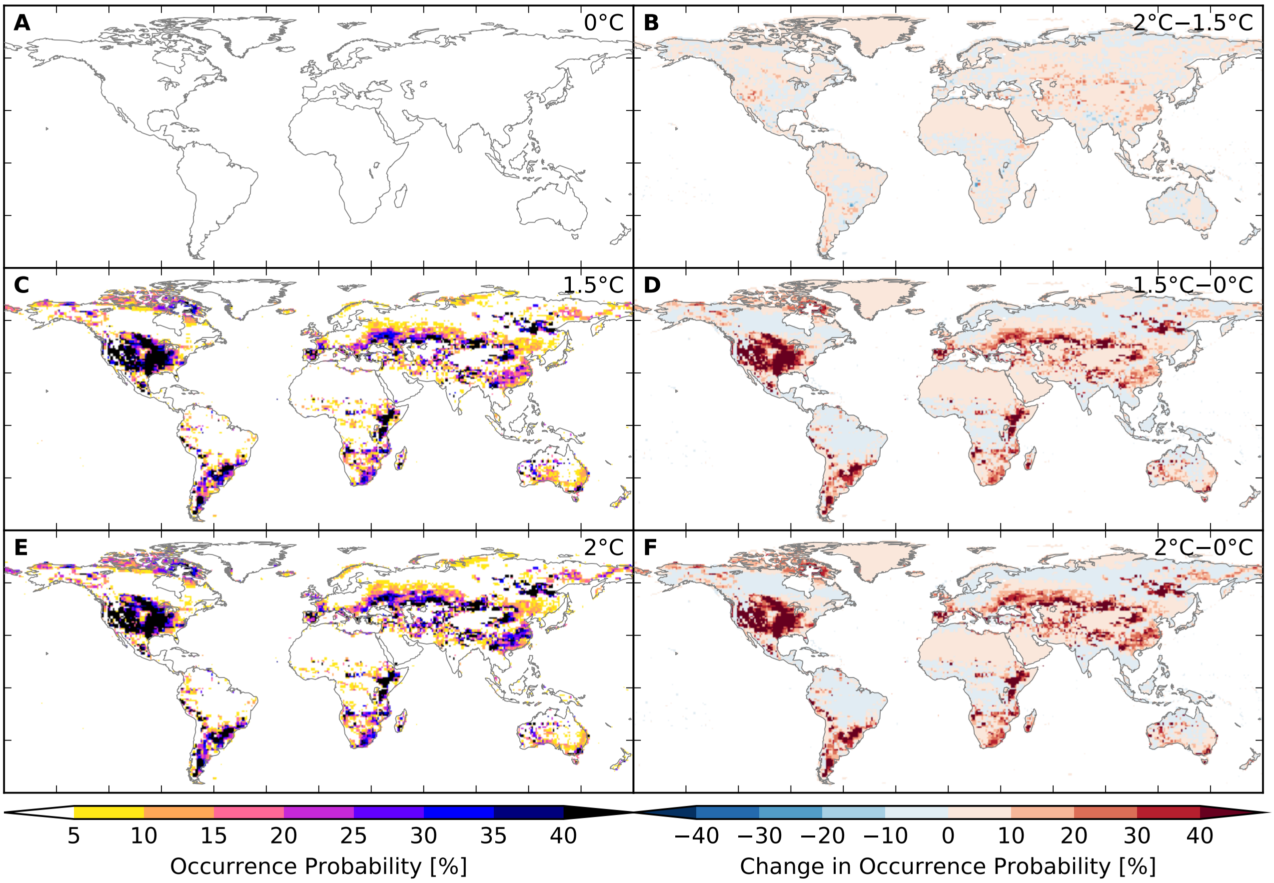

Figure S152: **Probability of occurrence of at least one wildfire event per year at different global warming levels (IPSL-CM5A-LR + ORCHIDEE).** Analogous to Figure S142.

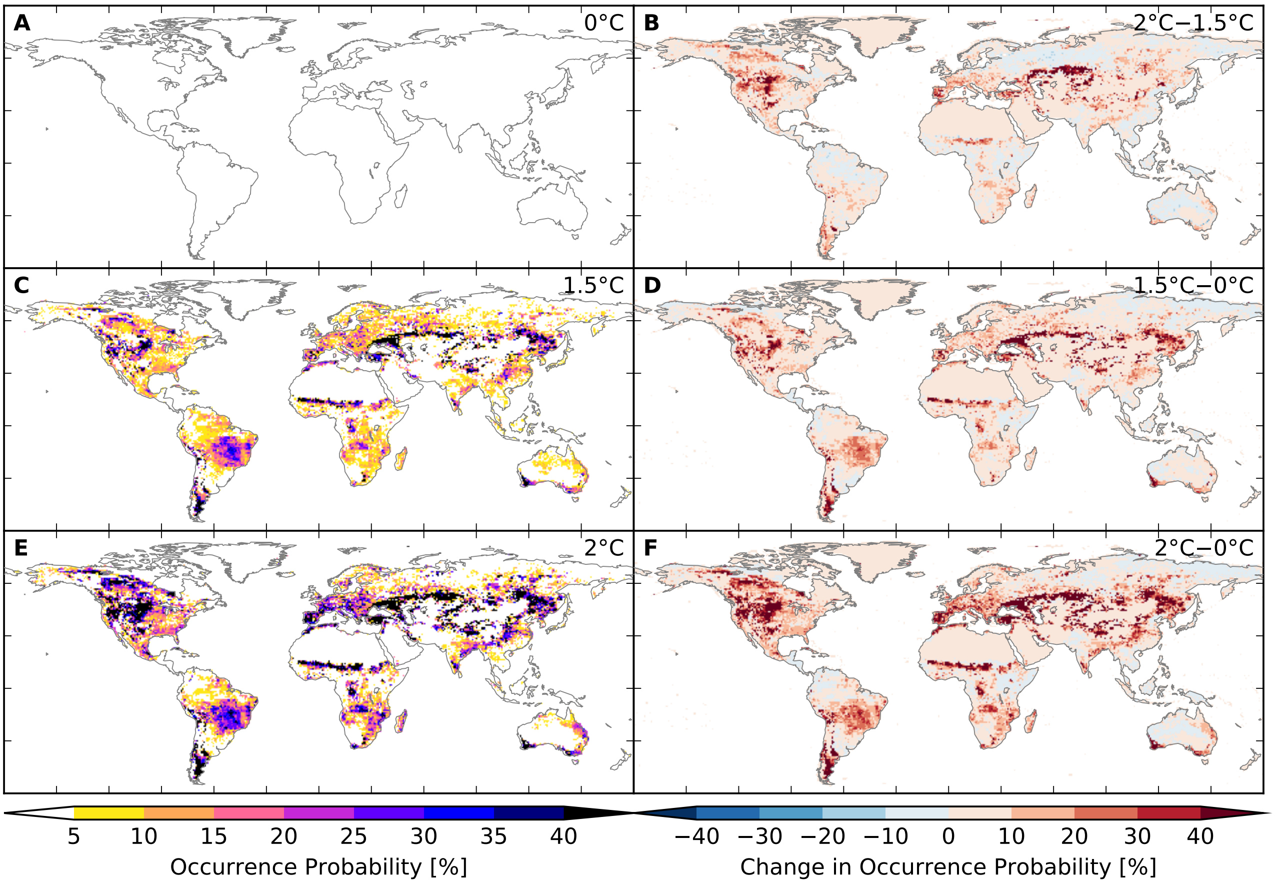

Figure S153: **Probability of occurrence of at least one wildfire event per year at different global warming levels (GFDL-ESM2M + VISIT).** Analogous to Figure S142.

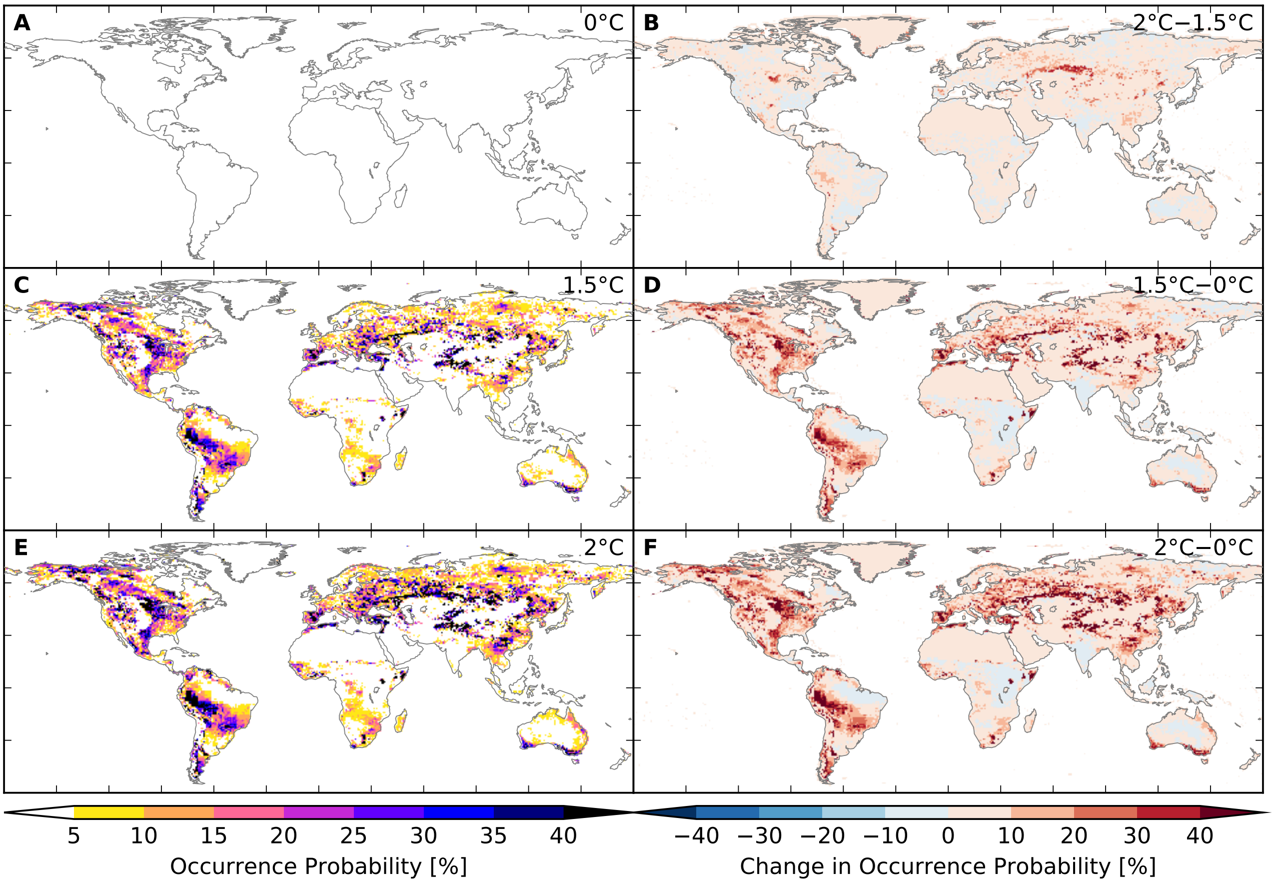

Figure S154: **Probability of occurrence of at least one wildfire event per year at different global warming levels (IPSL-CM5A-LR + VISIT).** Analogous to Figure S142.

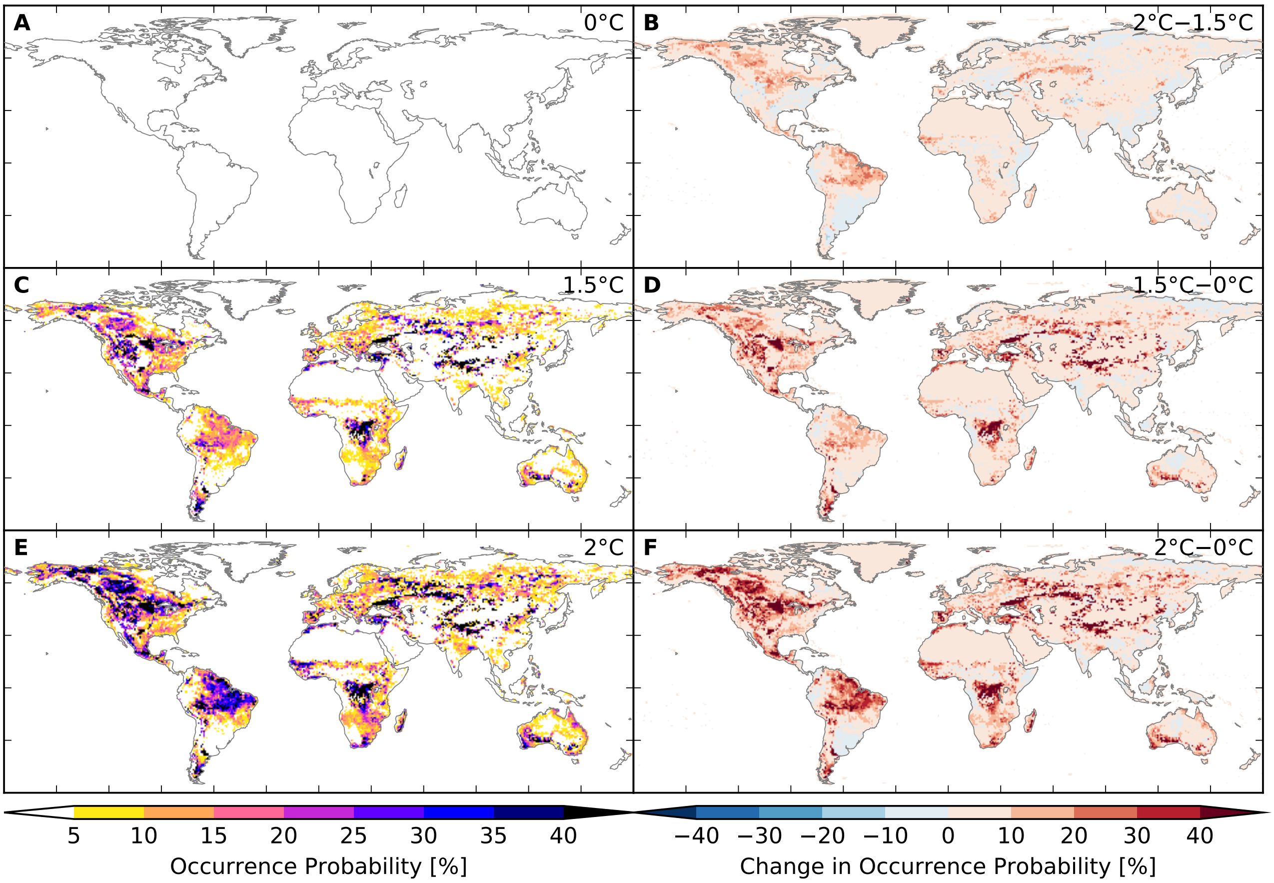

Figure S155: **Probability of occurrence of at least one wildfire event per year at different global warming levels (MIROC5 + VISIT).** Analogous to Figure S142.

8.5 Droughts

Areas affected

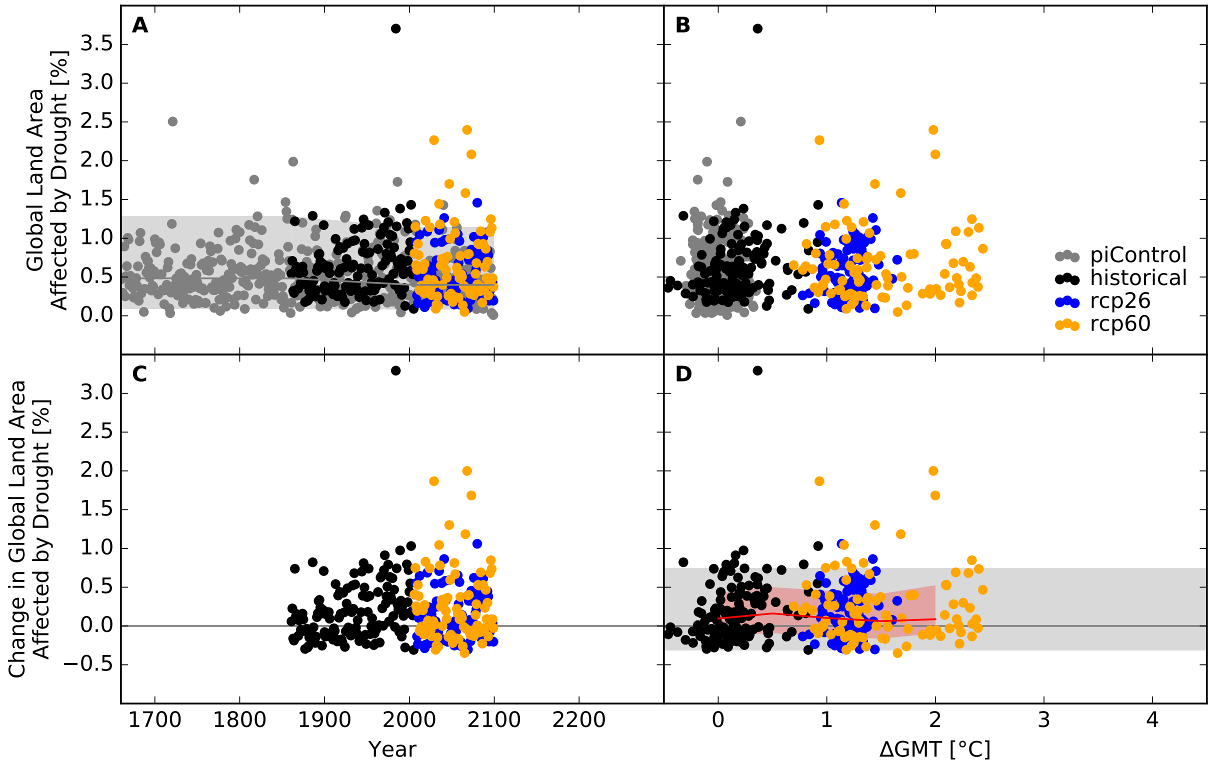

Figure S156: **Derivation of the pure effect of climate change on global land area fraction affected by drought events (GFDL-ESM2M + H08).** Panel A: Time series of annual global land area fraction affected (AFA) by drought events for pre-industrial climate (grey dots), historical climate (black dots), climate projections for RCP2.6 (blue dots), and RCP6.0 (orange dots). In all simulations, socio-economic conditions are varied according to the historically observed development between 1860 and 2005, and held fixed at 1860 conditions before 1860 and at 2005 conditions after 2005. Shaded areas before 1860/after 2005 represent the range from the 2nd to the 98th percentile of the distribution of the annual AFA under pre-industrial climate conditions in combination with 1860/2005 socio-economic conditions; the solid gray lines represent the respective median values; the shaded areas and solid gray line between 1860 and 2005 are linear interpolations of the respective values before 1860 and after 2005. Panel B: Data shown in Panel A plotted against the associated GCM-specific annual global mean temperature (GMT) change relative to the long-term pre-industrial mean. Panel C: Pure effect of climate change on AFA, calculated as the difference between the annual data shown in Panel A and the median of the simulations assuming pre-industrial climate conditions (solid gray line in Panel A). Panel D: Pure effect of climate change on AFA in terms of global mean temperature change, with distributions of the annual data estimated for each 1°C-wide bin of global mean temperature change that contains at least five data points, at least one data point above and at least one data point below the bin center. Areas shaded in red represent the range from the 20th to the 80th percentile around the median (solid red line) of these distributions. Areas shaded in gray represent the range from the 2nd to the 98th percentile of the zero-centered distribution of the annual AFA under pre-industrial climate and 2005 socio-economic conditions (cf. Panel A). The green vertical line represents the detection level defined as the global warming level at which a 1-in-50-years event under pre-industrial climate and 2005 socio-economic conditions becomes a 1-in-5-years event under changing climate and 2005 socio-economic conditions.

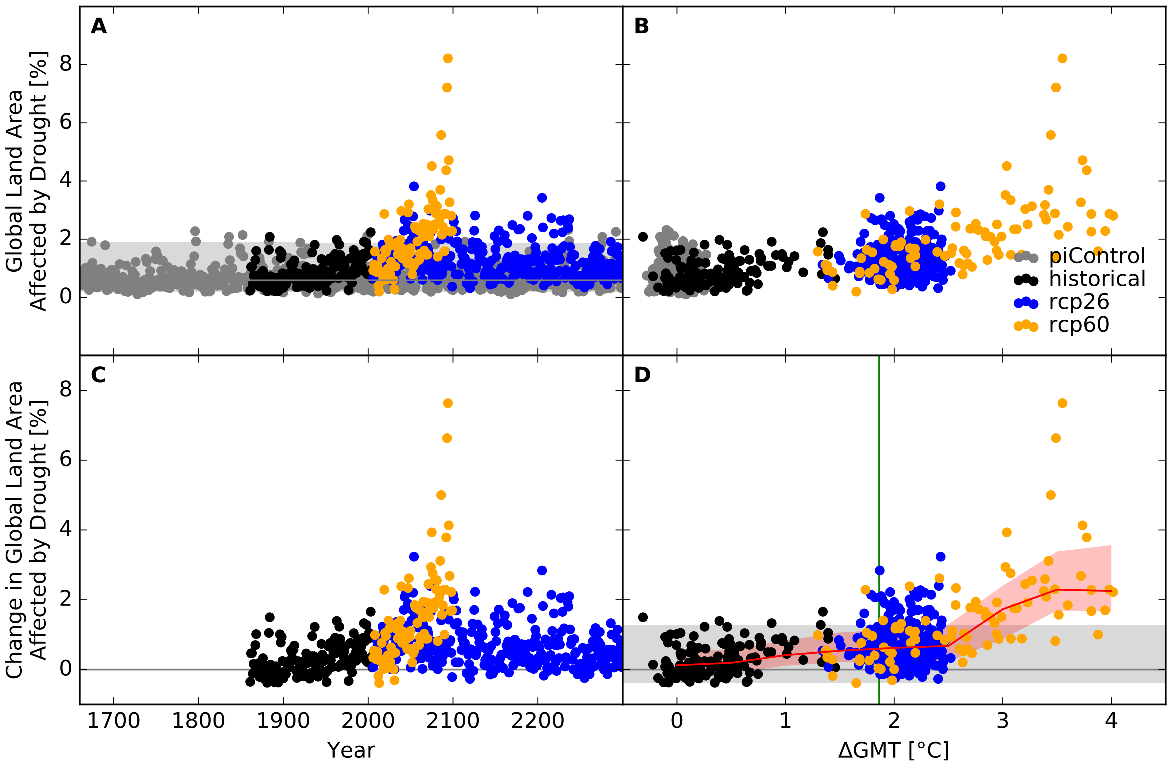

Figure S157: **Derivation of the pure effect of climate change on global land area fraction affected by drought events (IPSL-CM5A-LR + H08).** Analogous to Figure S156.

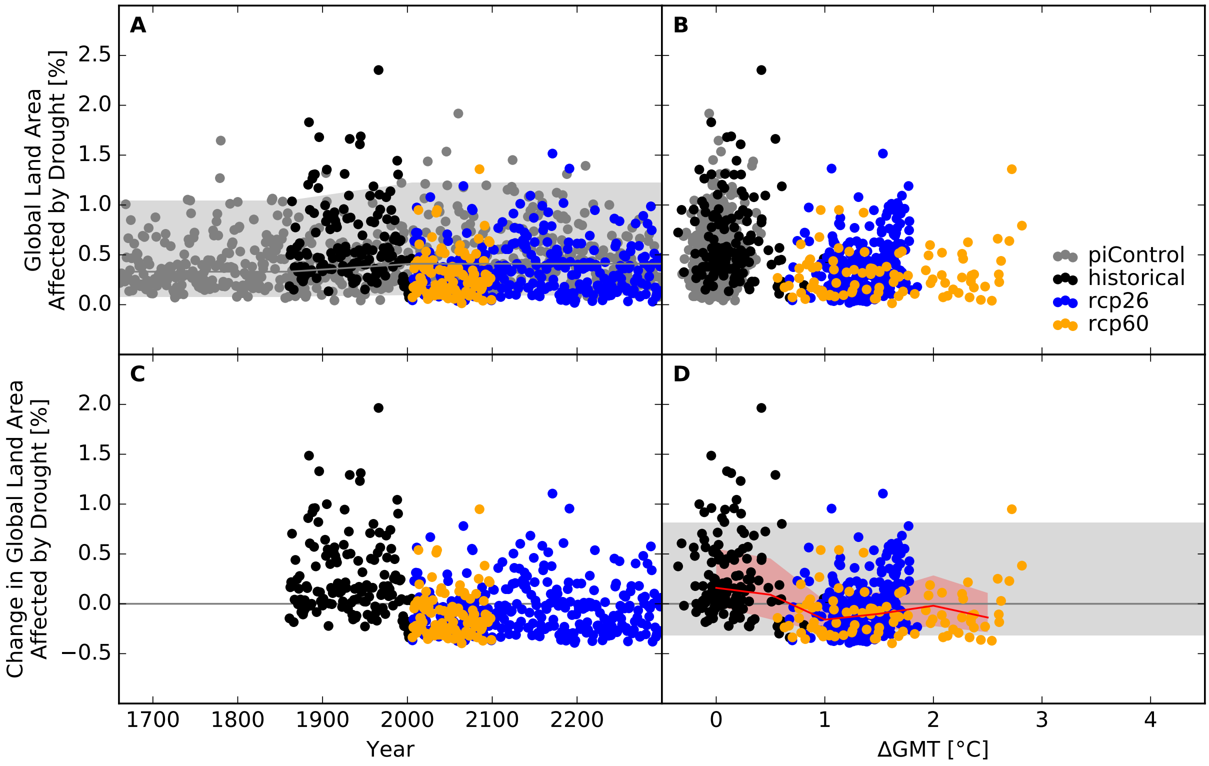

Figure S158: **Derivation of the pure effect of climate change on global land area fraction affected by drought events (MIROC5 + H08).** Analogous to Figure S156.

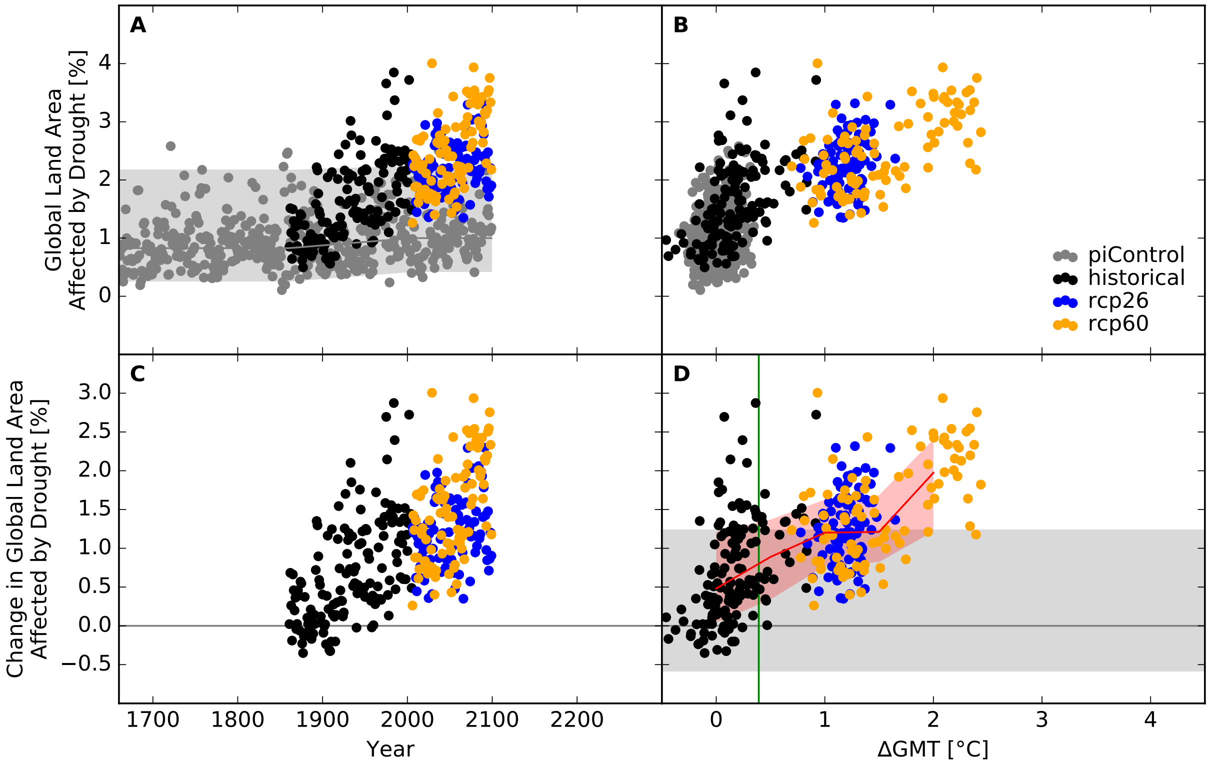

Figure S159: **Derivation of the pure effect of climate change on global land area fraction affected by drought events (GFDL-ESM2M + JULES-W1).** Analogous to Figure S156.

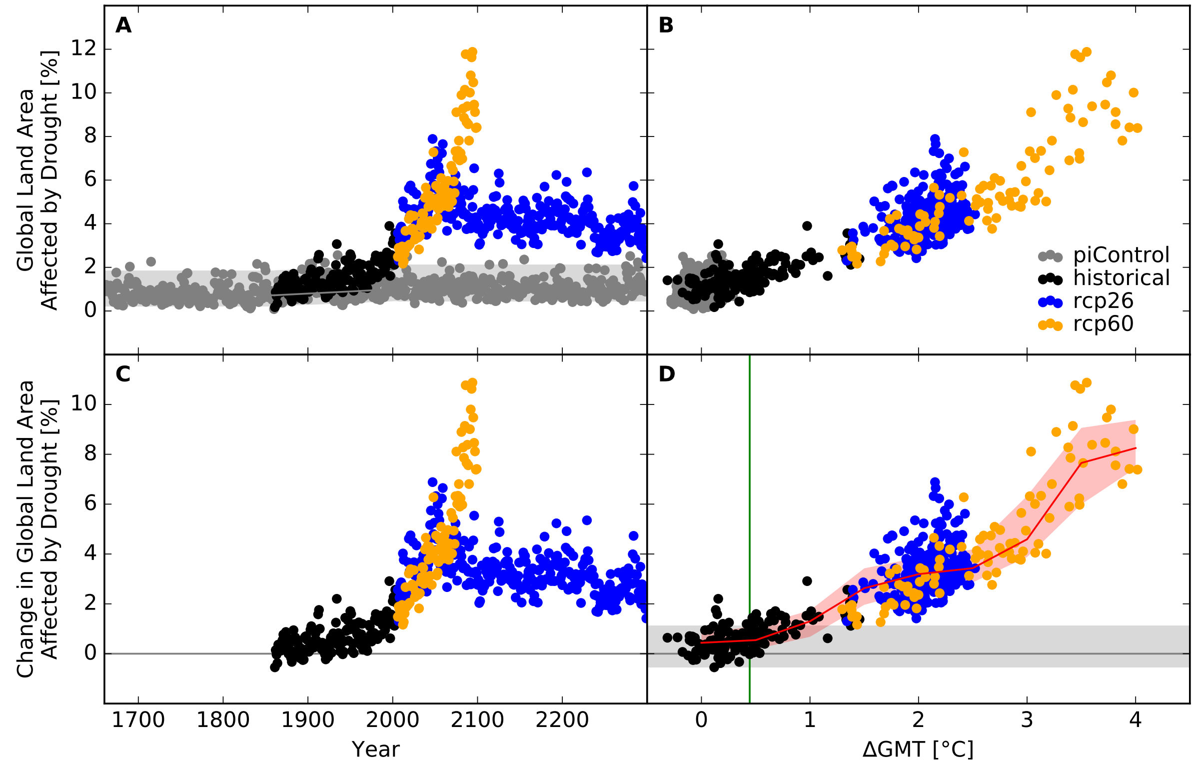

Figure S160: **Derivation of the pure effect of climate change on global land area fraction affected by drought events (IPSL-CM5A-LR + JULES-W1).** Analogous to Figure S156.

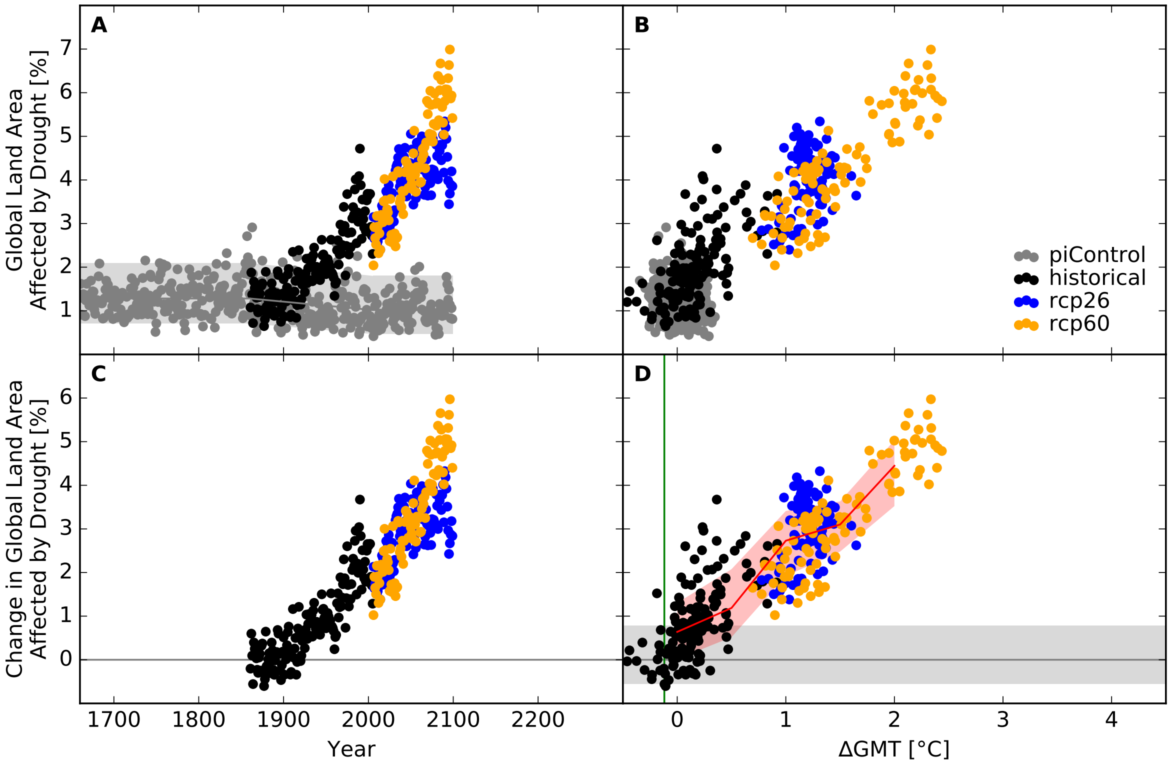

Figure S161: **Derivation of the pure effect of climate change on global land area fraction affected by drought events (GFDL-ESM2M + LPJmL).** Analogous to Figure S156.

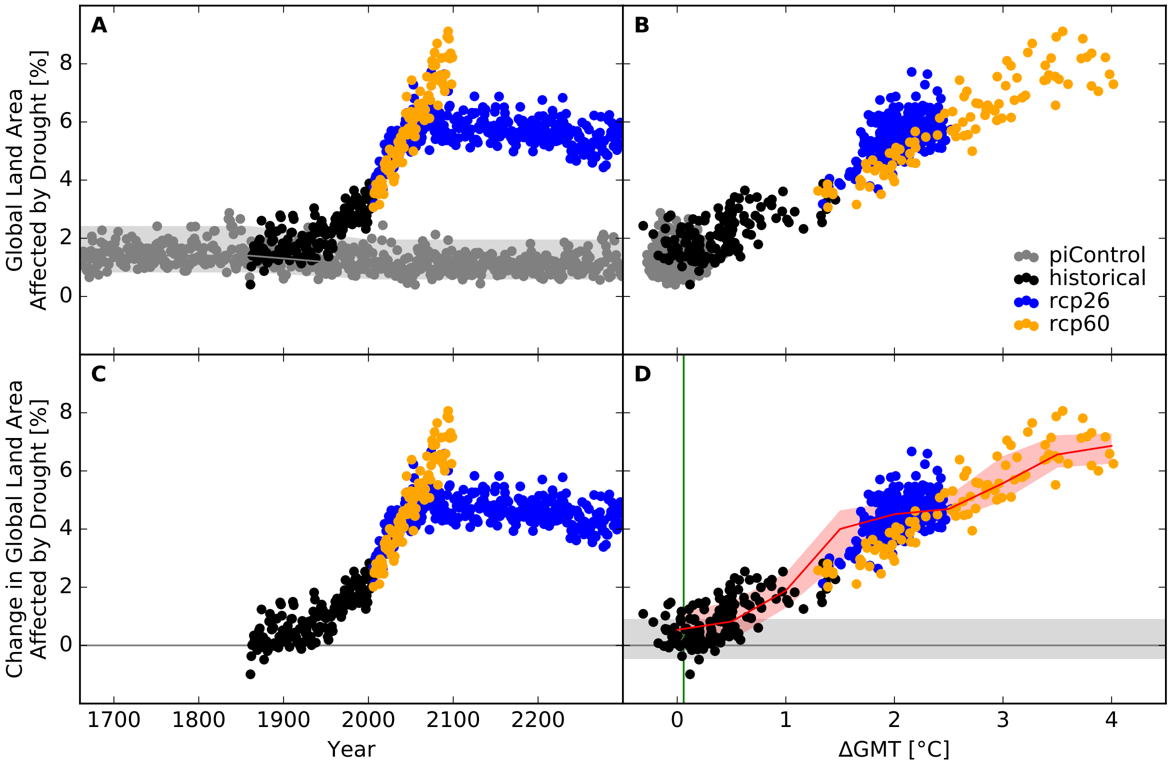

Figure S162: **Derivation of the pure effect of climate change on global land area fraction affected by drought events (IPSL-CM5A-LR + LPJmL).** Analogous to Figure S156.

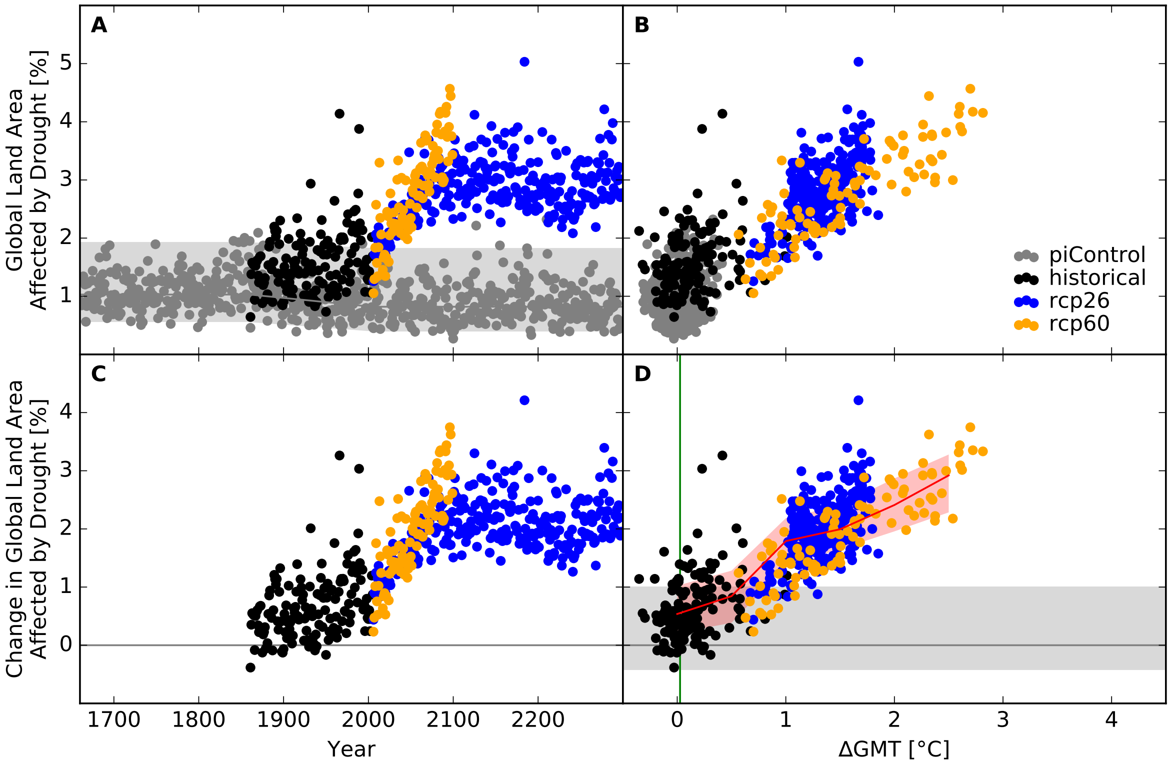

Figure S163: **Derivation of the pure effect of climate change on global land area fraction affected by drought events (MIROC5 + LPJmL).** Analogous to Figure S156.

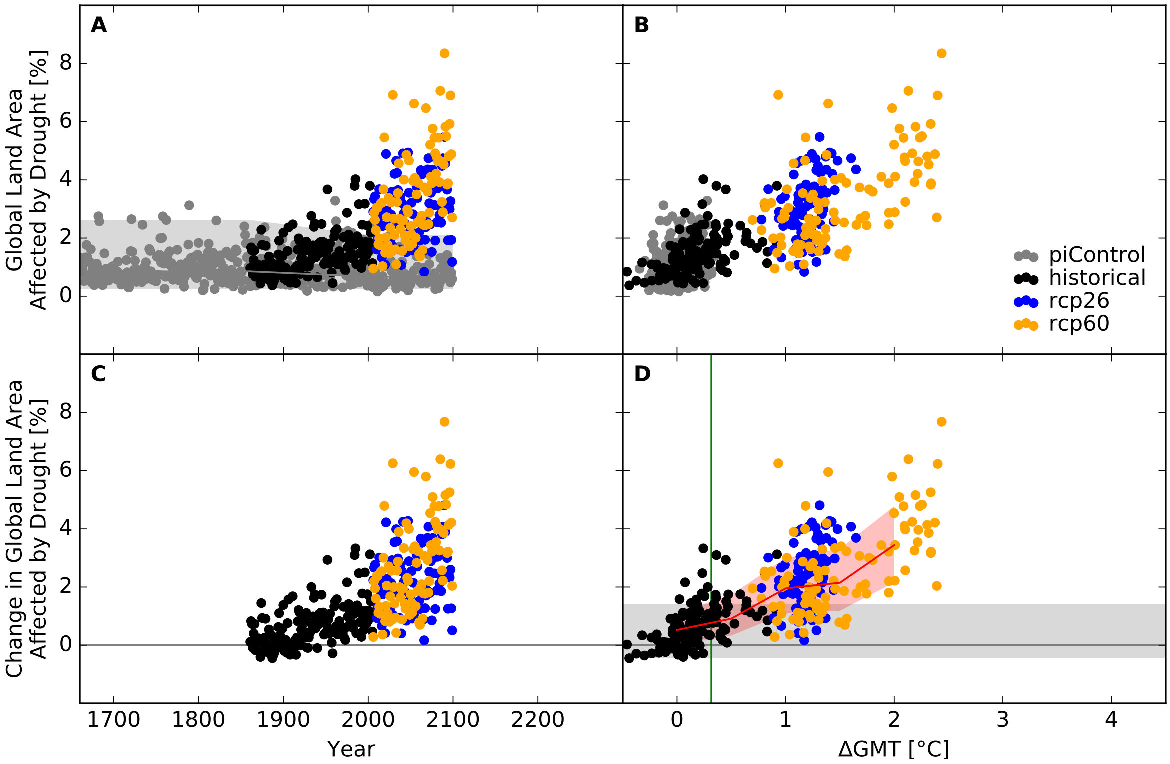

Figure S164: **Derivation of the pure effect of climate change on global land area fraction affected by drought events (GFDL-ESM2M + MPI-HM).** Analogous to Figure S156.

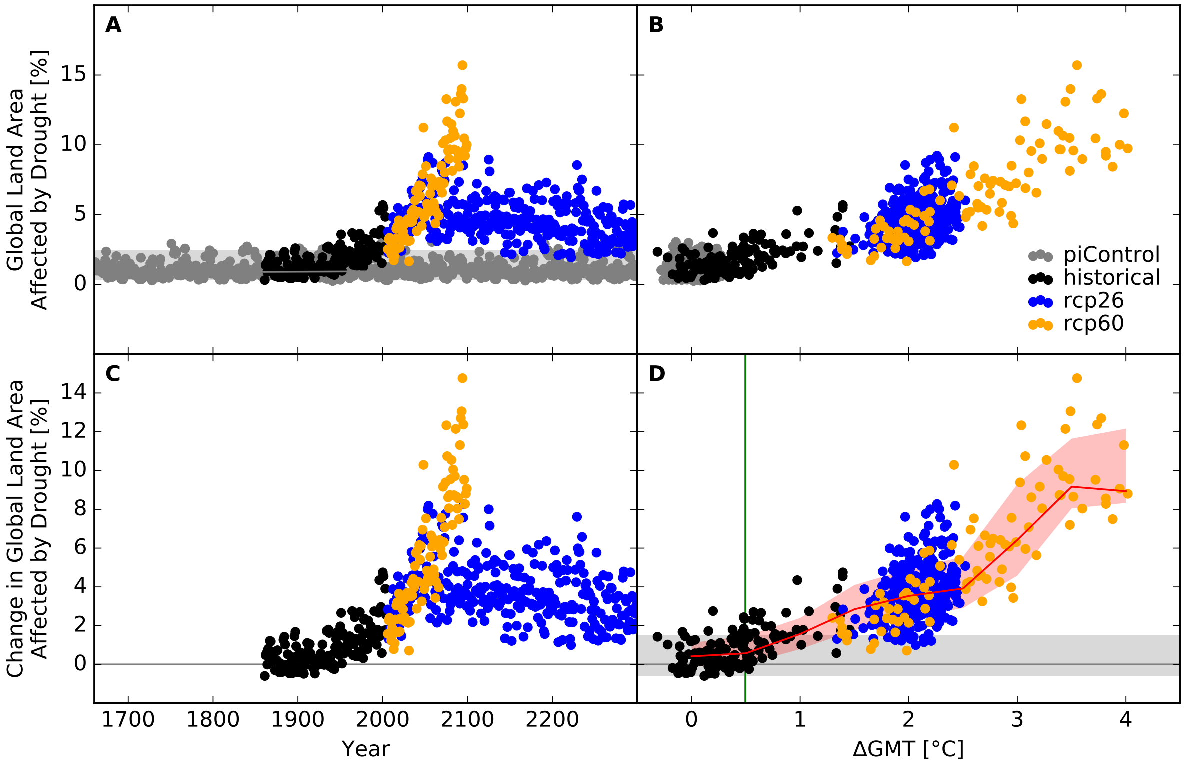

Figure S165: **Derivation of the pure effect of climate change on global land area fraction affected by drought events (IPSL-CM5A-LR + MPI-HM).** Analogous to Figure S156.

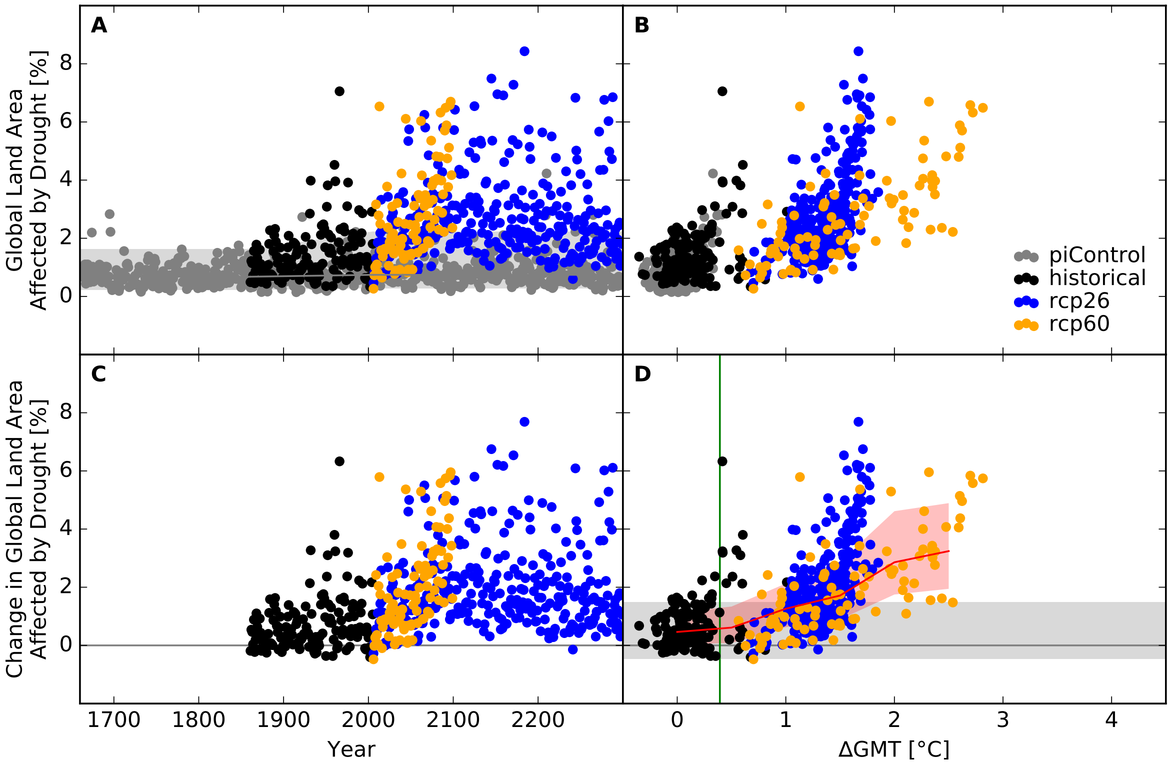

Figure S166: **Derivation of the pure effect of climate change on global land area fraction affected by drought events (MIROC5 + MPI-HM).** Analogous to Figure S156.

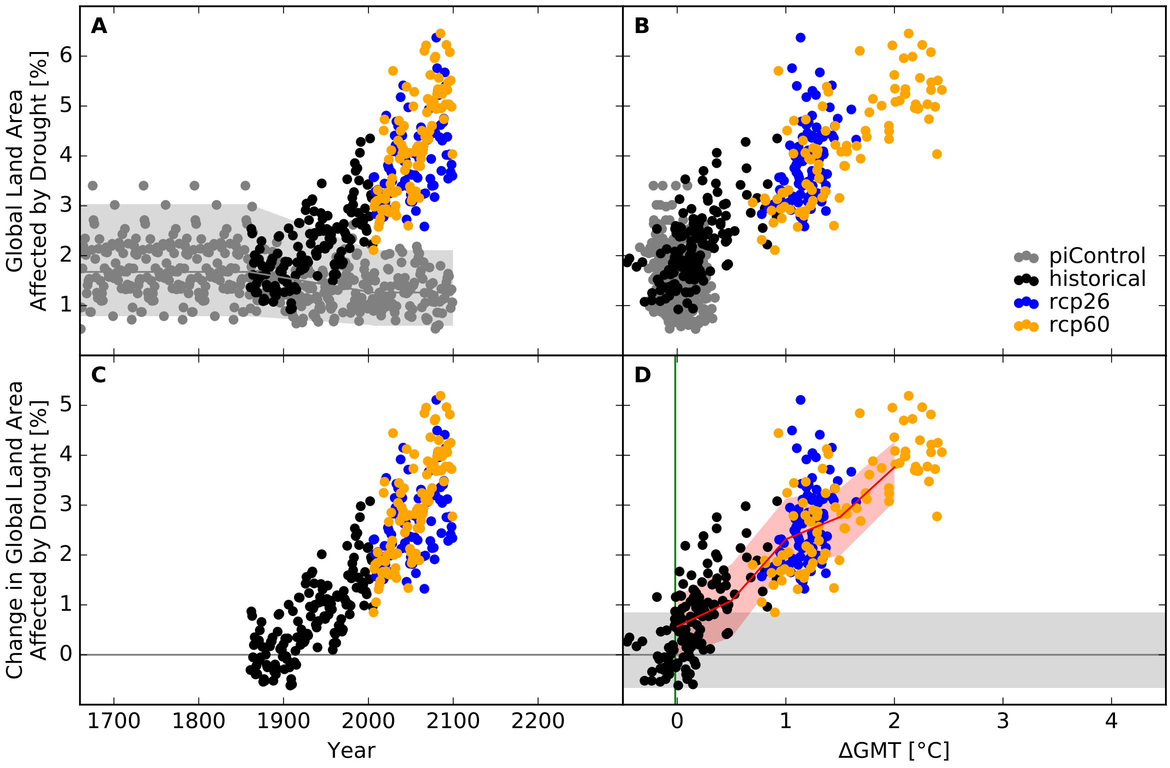

Figure S167: **Derivation of the pure effect of climate change on global land area fraction affected by drought events (GFDL-ESM2M + ORCHIDEE).** Analogous to Figure S156.

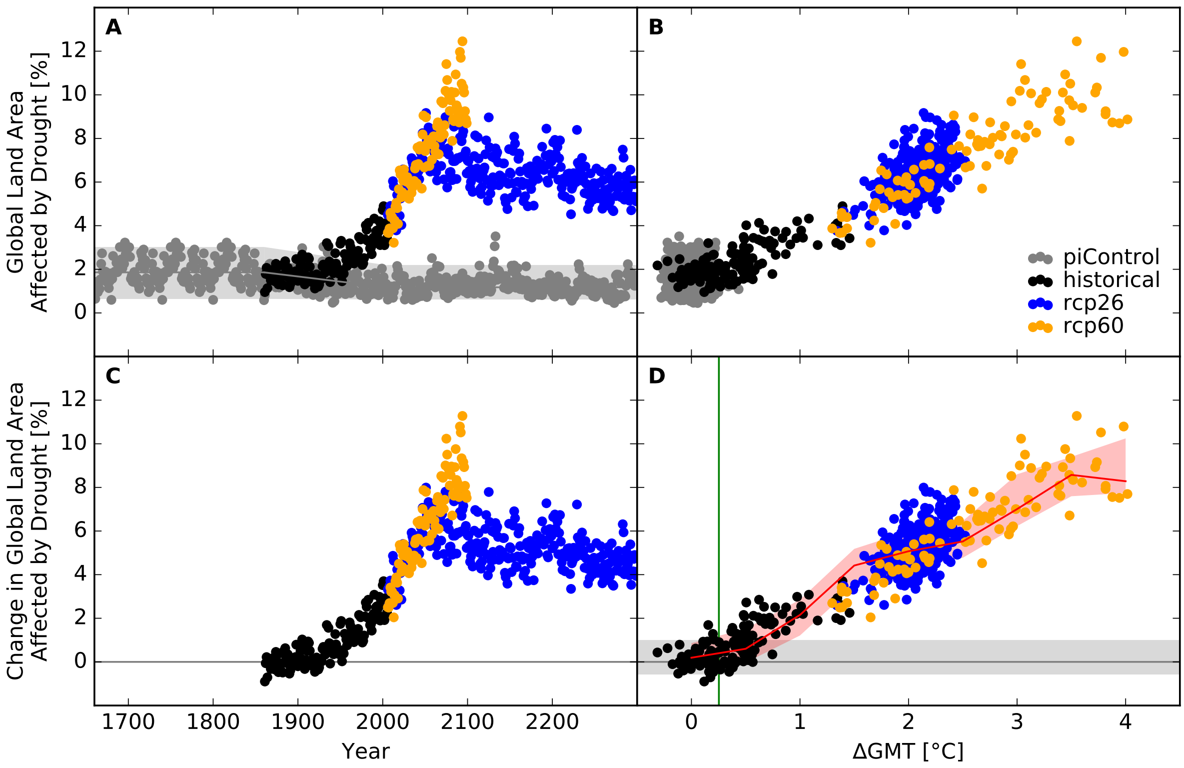

Figure S168: **Derivation of the pure effect of climate change on global land area fraction affected by drought events (IPSL-CM5A-LR + ORCHIDEE).** Analogous to Figure S156.

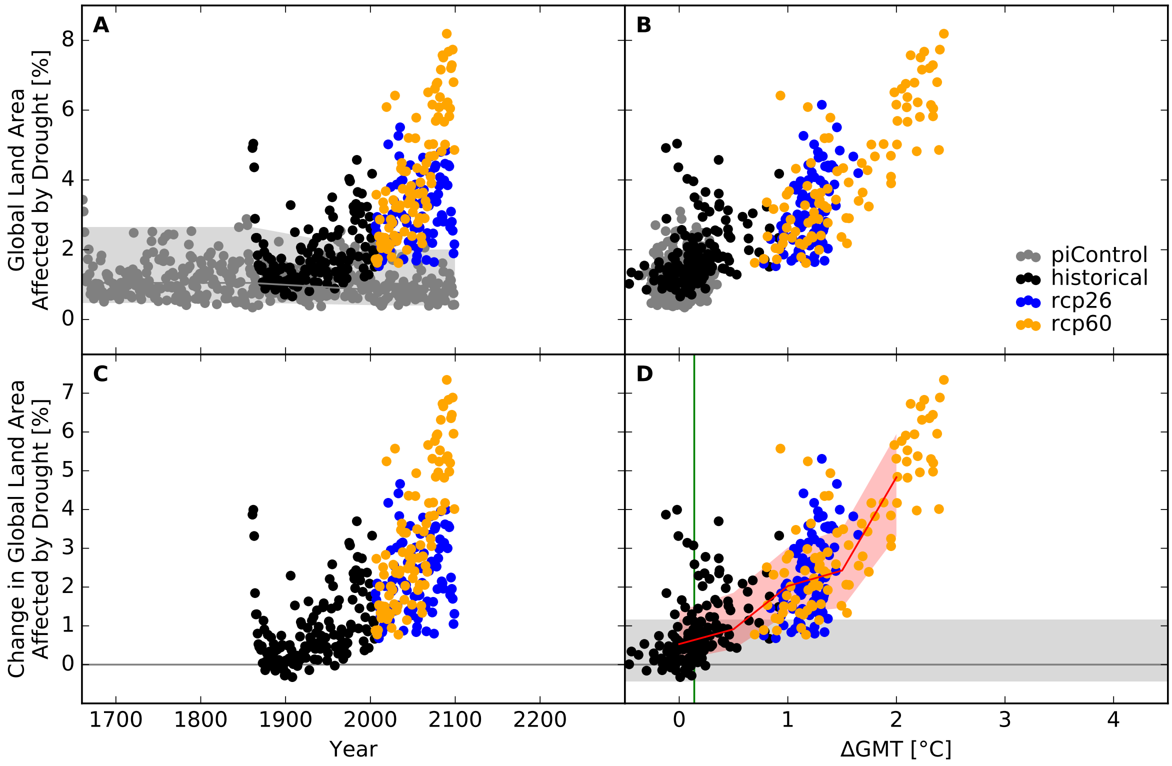

Figure S169: **Derivation of the pure effect of climate change on global land area fraction affected by drought events (GFDL-ESM2M + PCR-GLOBWB).** Analogous to Figure S156.

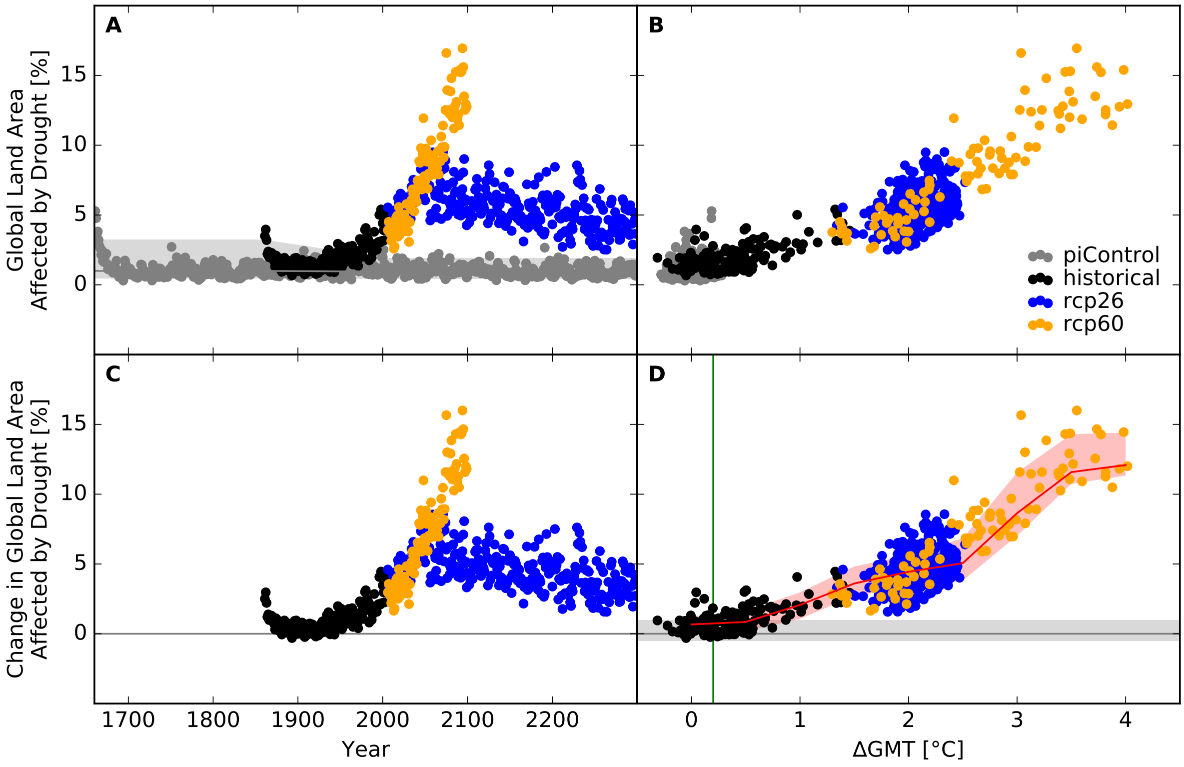

Figure S170: **Derivation of the pure effect of climate change on global land area fraction affected by drought events (IPSL-CM5A-LR + PCR-GLOBWB).** Analogous to Figure S156.

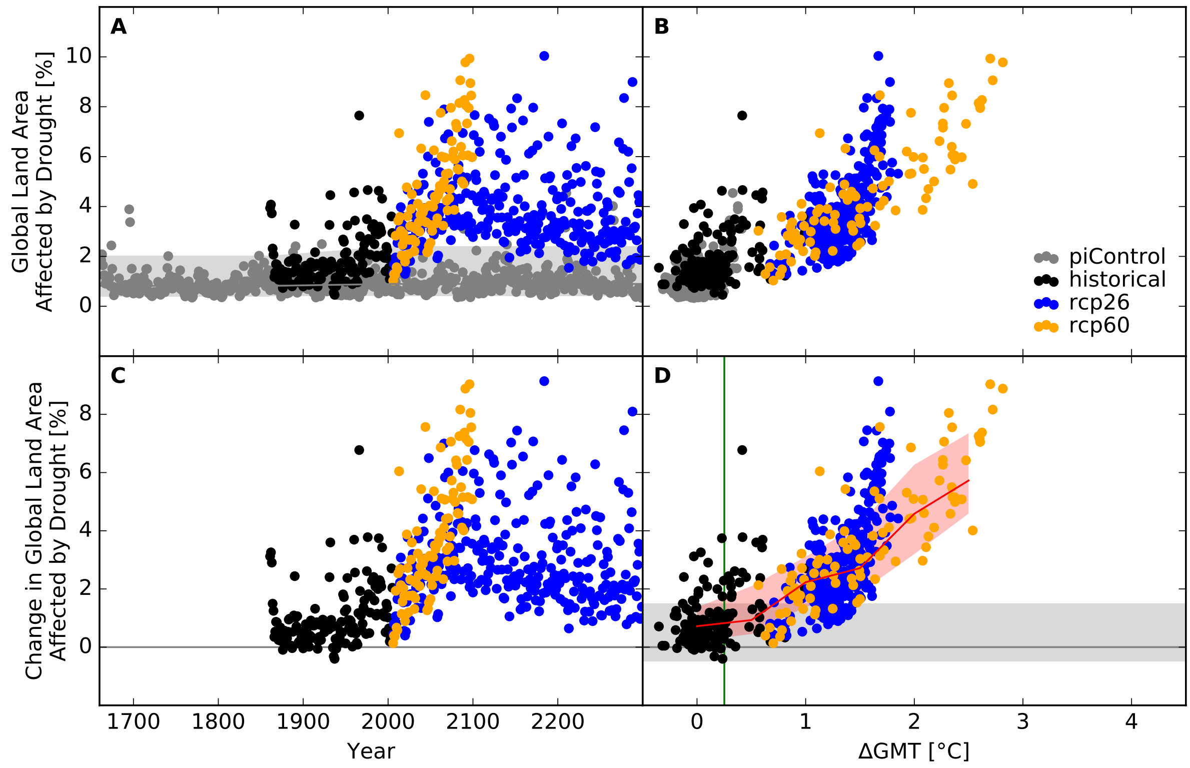

Figure S171: **Derivation of the pure effect of climate change on global land area fraction affected by drought events (MIROC5 + PCR-GLOBWB).** Analogous to Figure S156.

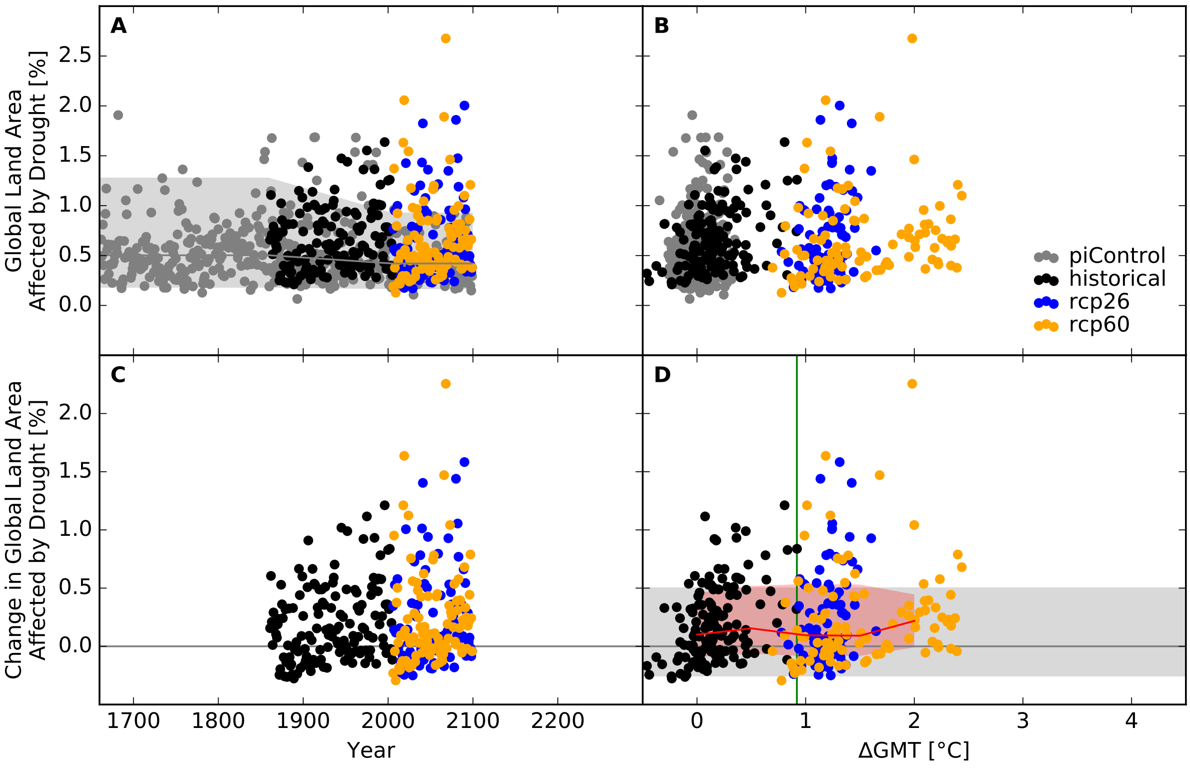

Figure S172: **Derivation of the pure effect of climate change on global land area fraction affected by drought events (GFDL-ESM2M + WaterGAP2).** Analogous to Figure S156.

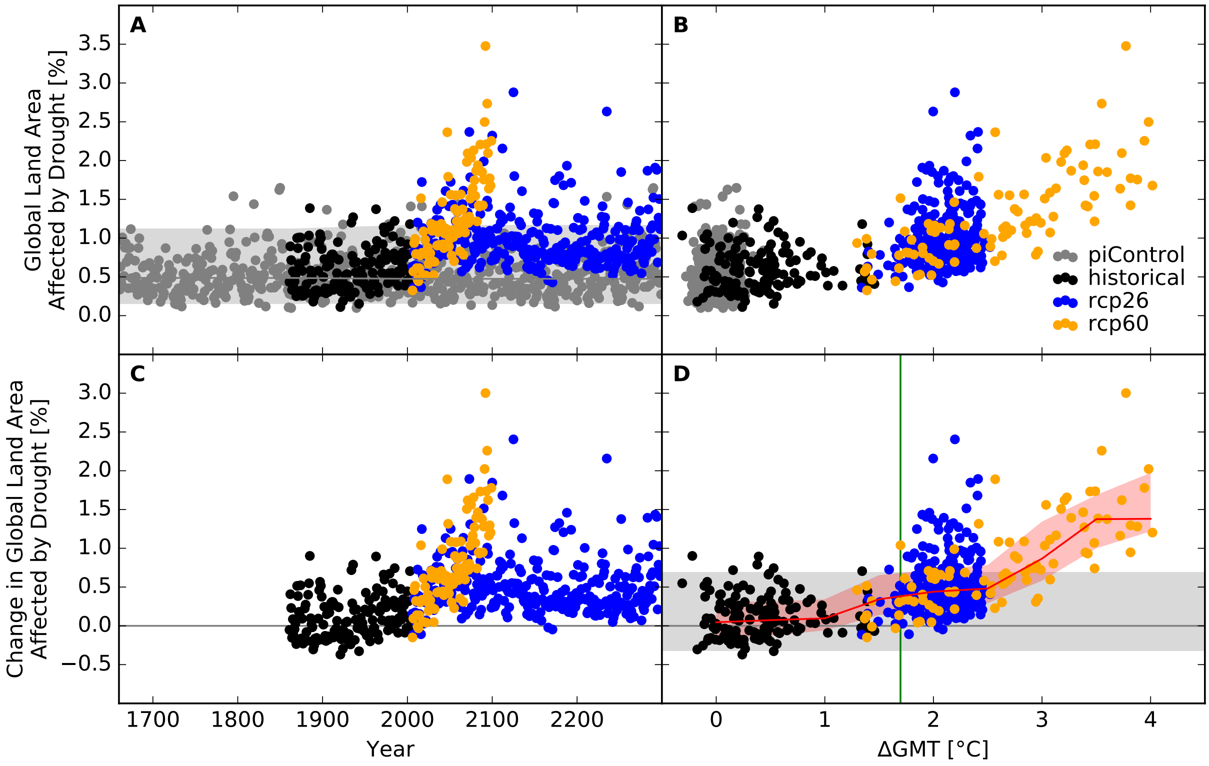

Figure S173: **Derivation of the pure effect of climate change on global land area fraction affected by drought events (IPSL-CM5A-LR + WaterGAP2).** Analogous to Figure S156.

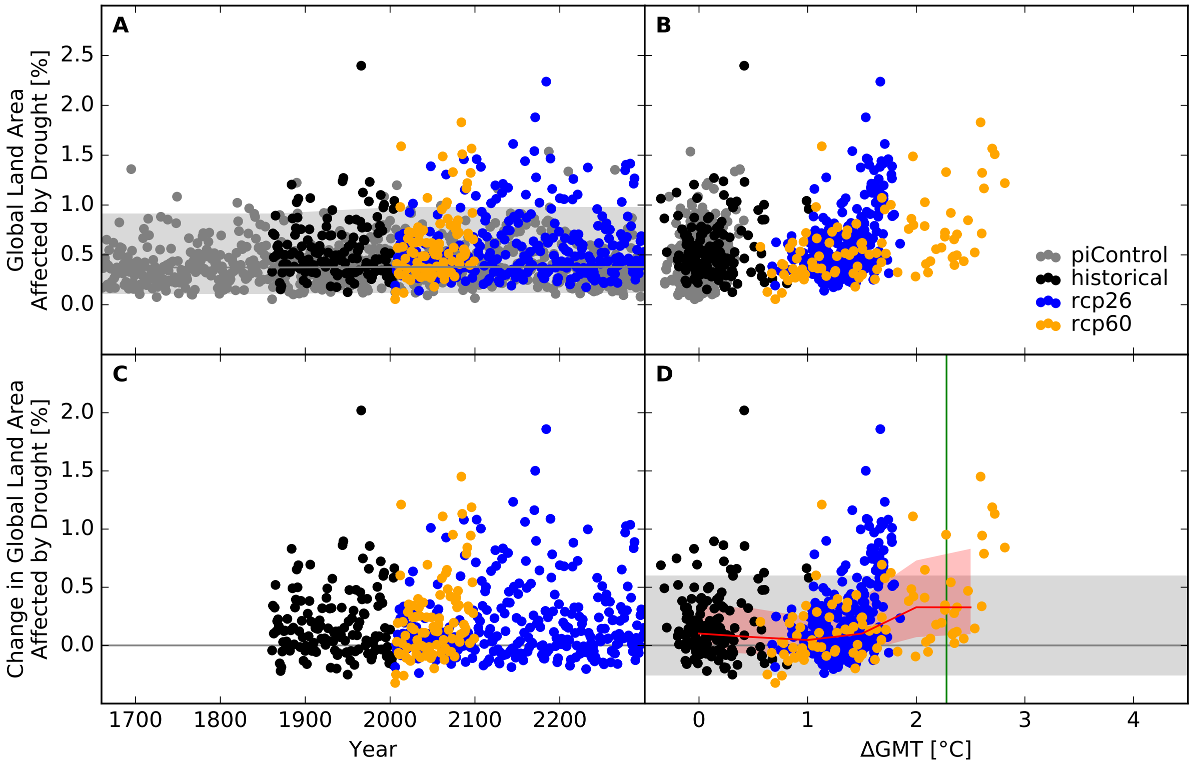

Figure S174: **Derivation of the pure effect of climate change on global land area fraction affected by drought events (MIROC5 + WaterGAP2).** Analogous to Figure S156.

Occurrence probability at grid scale

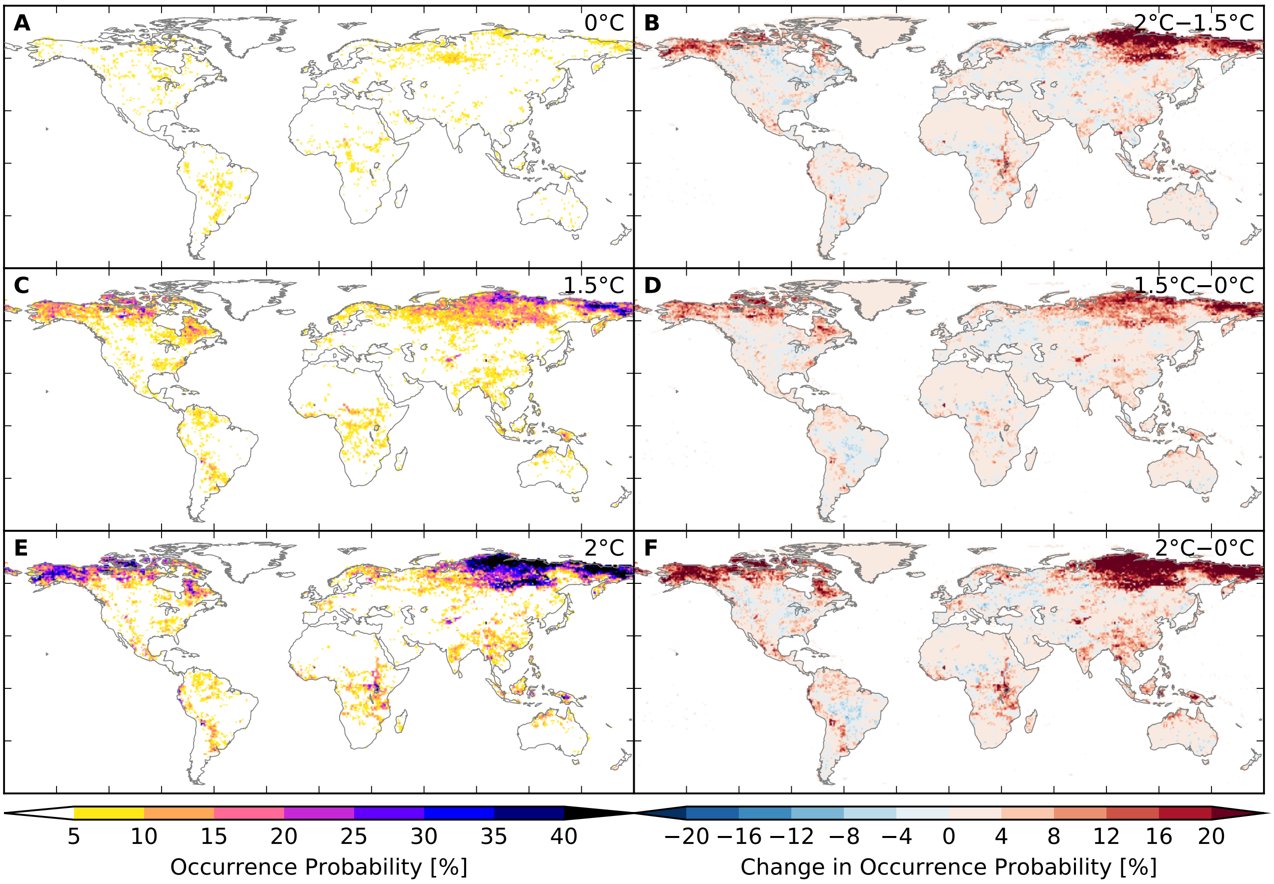

Figure S175: **Probability of occurrence of at least one flood event per year at different global warming levels (GFDL-ESM2M + H08).** Panels A, C, E: Probabilities at 0°C, 1.5°C, 2°C global mean temperature (GMT) change relative to the long-term pre-industrial mean GMT, respectively. Panels B, D, F: Differences between probabilities at GMT change levels of 2°C and 1.5°C, 1.5°C and 0°C, 2°C and 0°C, respectively.

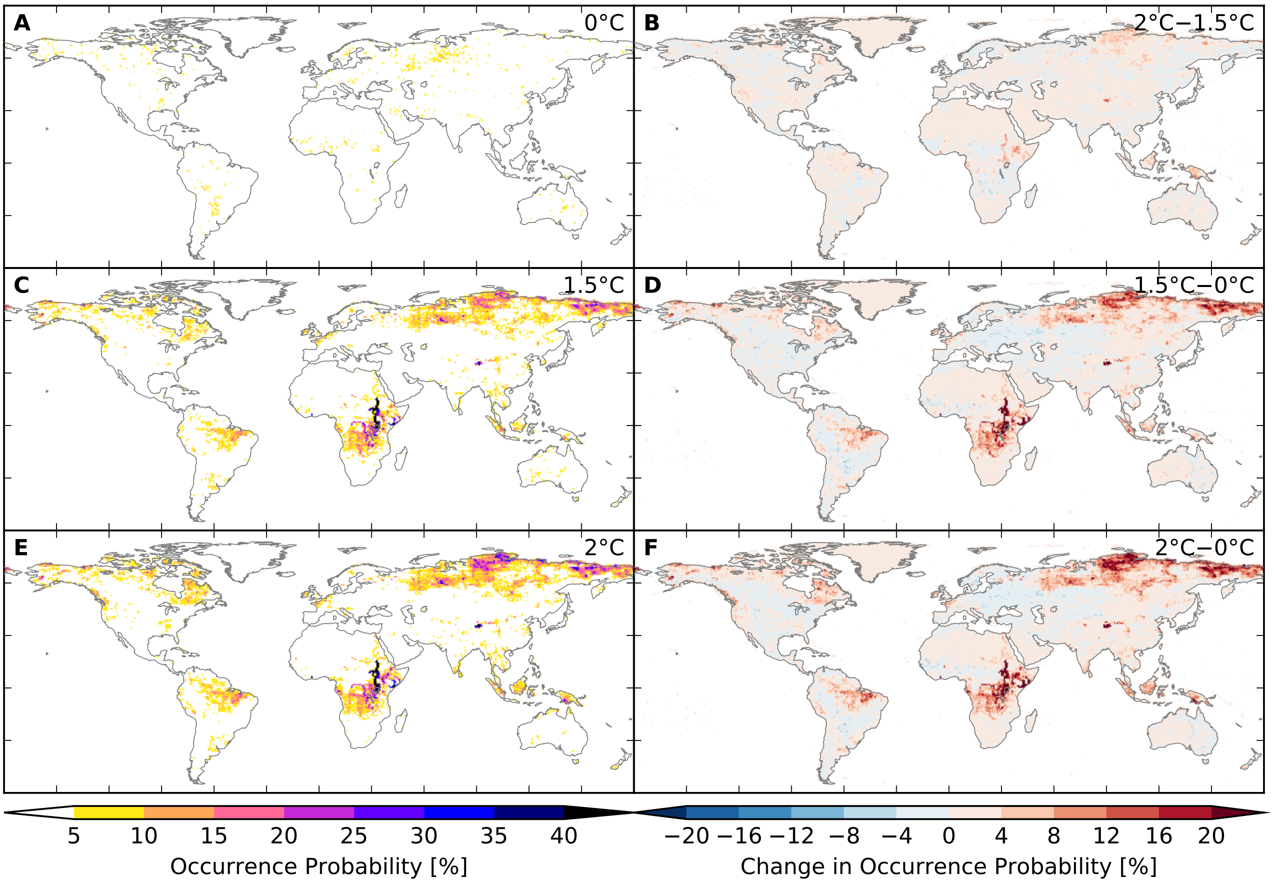

Figure S176: **Probability of occurrence of at least one flood event per year at different global warming levels (IPSL-CM5A-LR + H08).** Analogous to Figure S175.

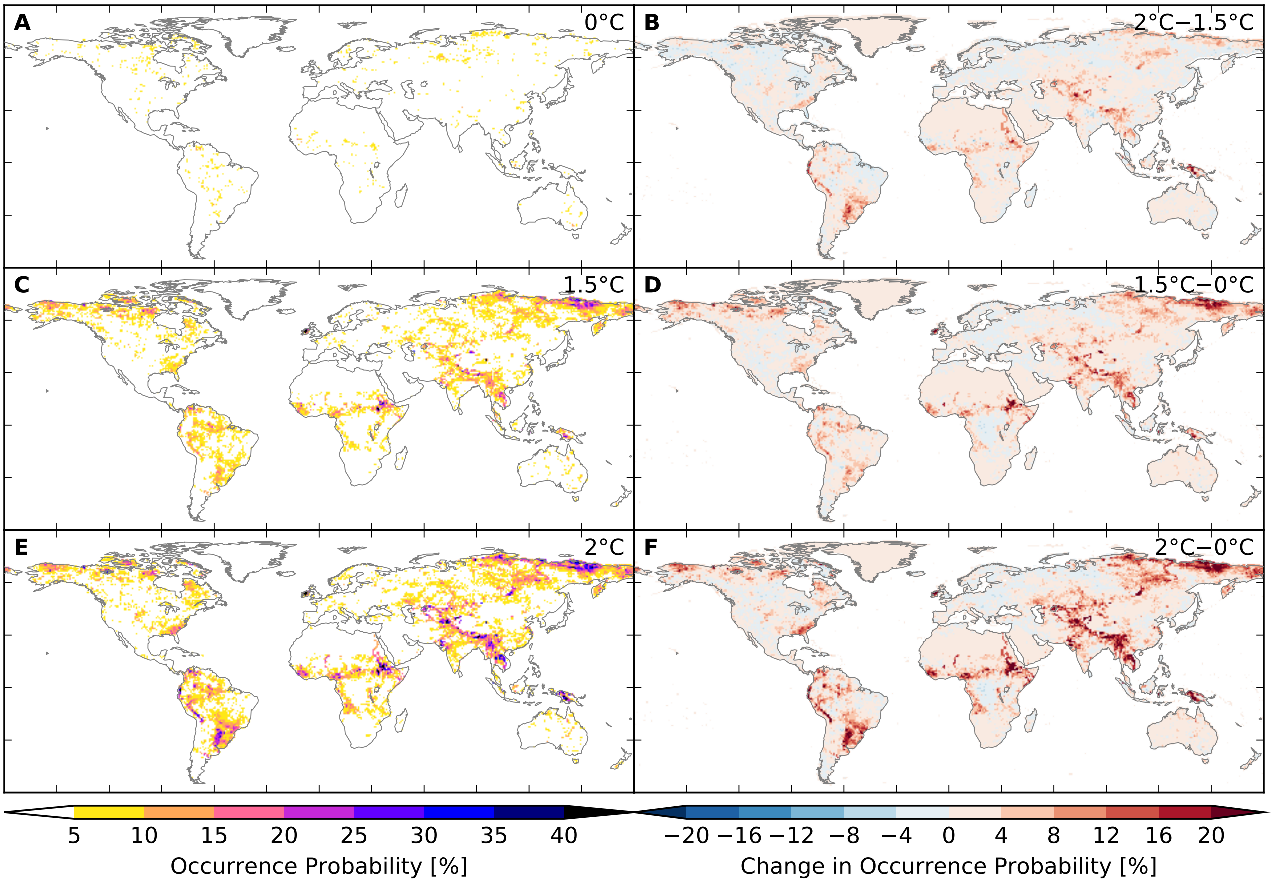

Figure S177: **Probability of occurrence of at least one flood event per year at different global warming levels (MIROC5 + H08).** Analogous to Figure S175.

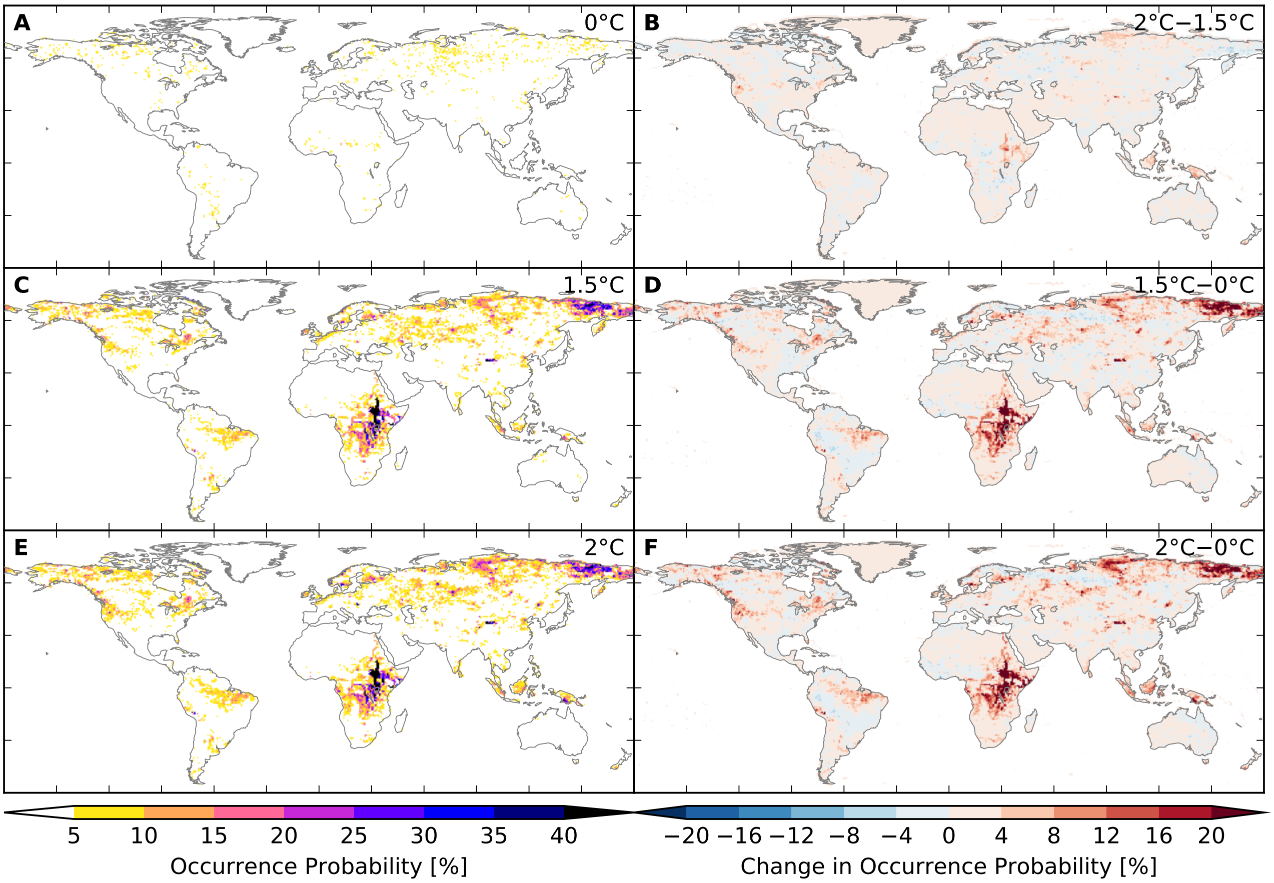

Figure S178: **Probability of occurrence of at least one flood event per year at different global warming levels (IPSL-CM5A-LR + JULES-W1).** Analogous to Figure S175.

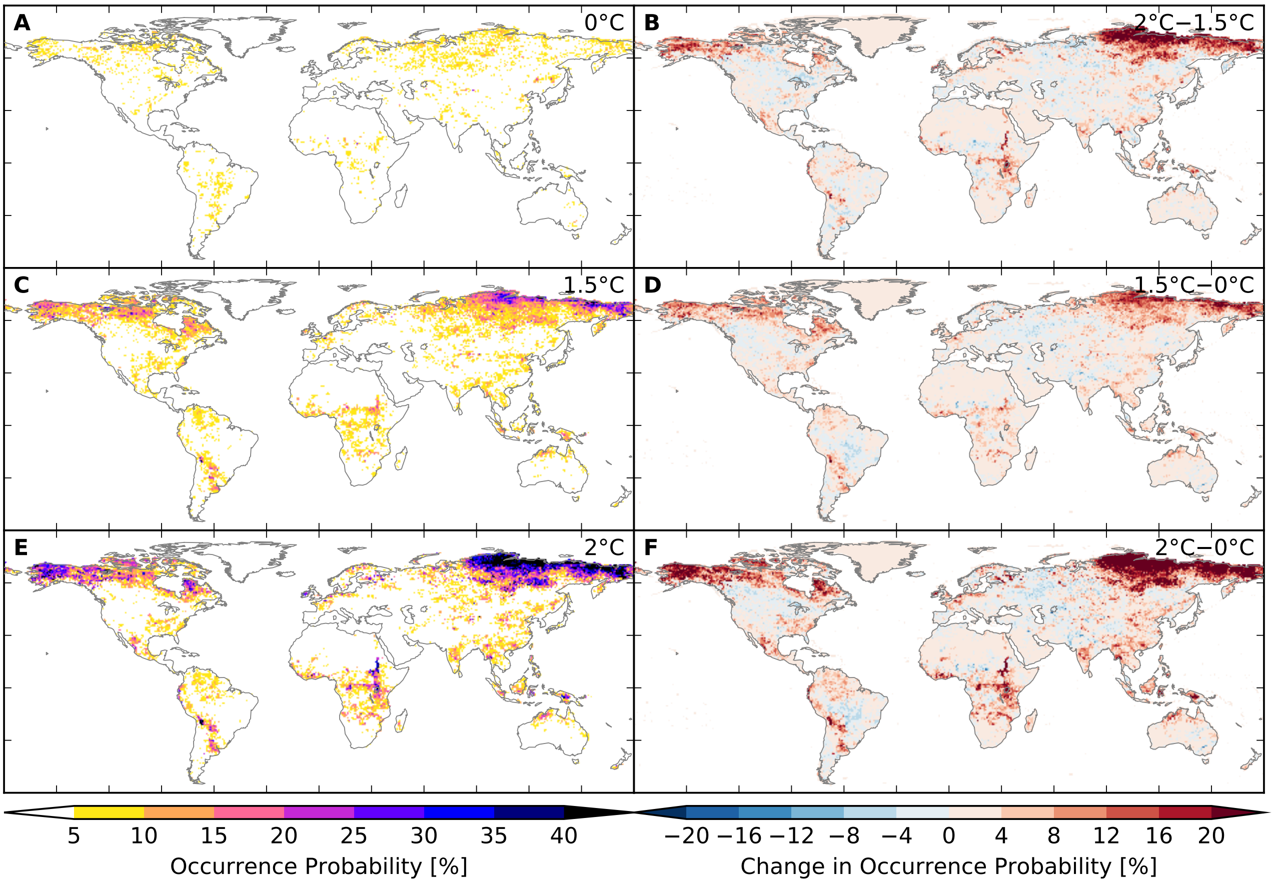

Figure S179: **Probability of occurrence of at least one flood event per year at different global warming levels (GFDL-ESM2M + LPJmL).** Analogous to Figure S175.

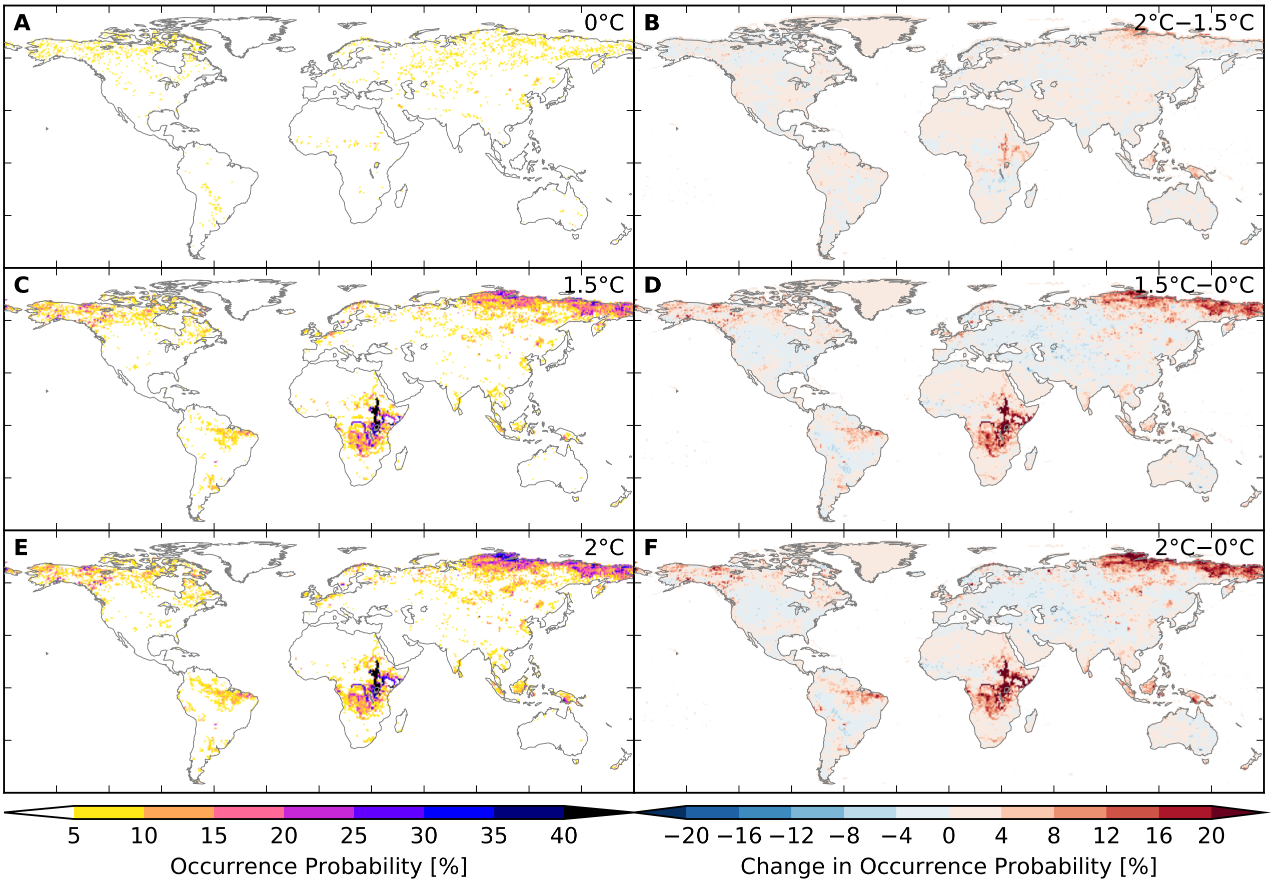

Figure S180: **Probability of occurrence of at least one flood event per year at different global warming levels (IPSL-CM5A-LR + LPJmL).** Analogous to Figure S175.

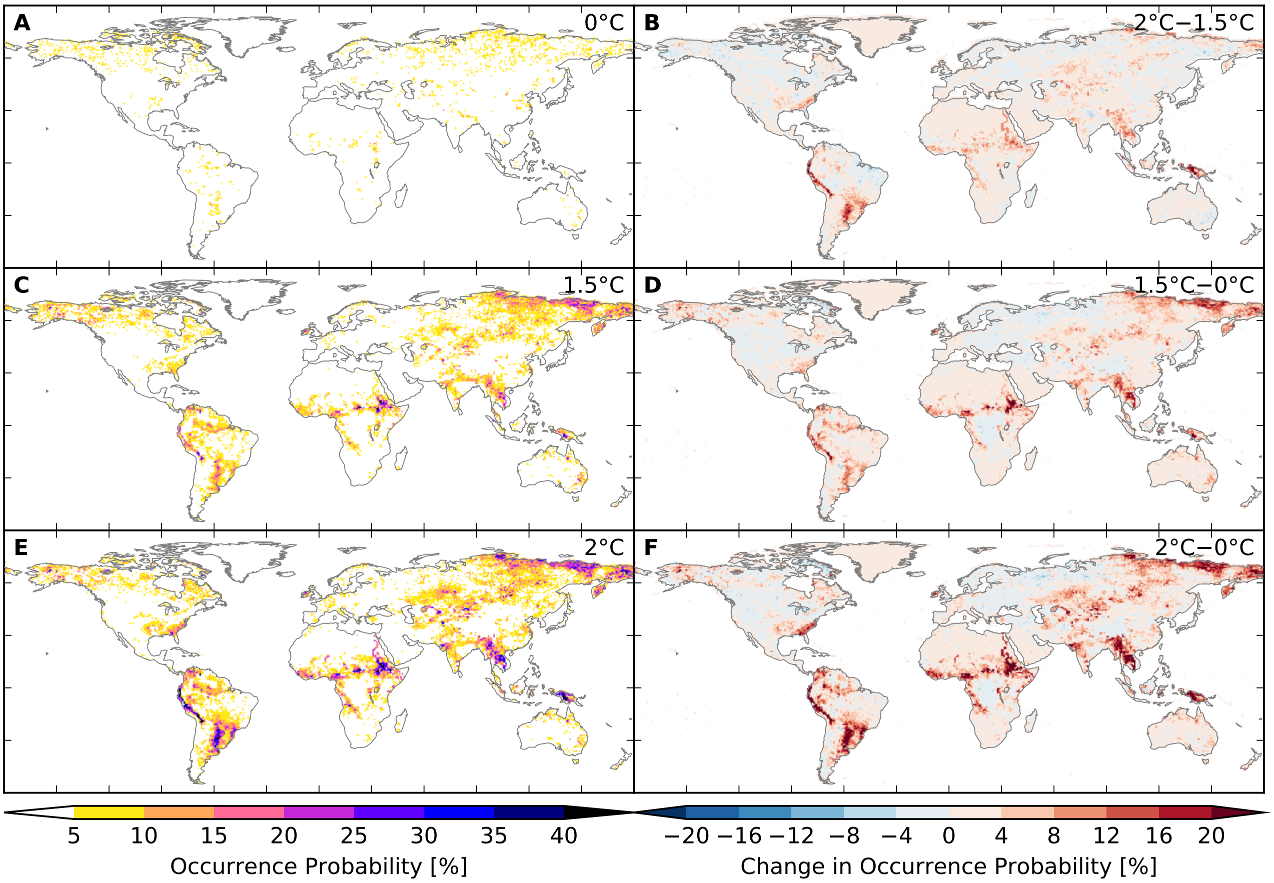

Figure S181: **Probability of occurrence of at least one flood event per year at different global warming levels (MIROC5 + LPJmL).** Analogous to Figure S175.

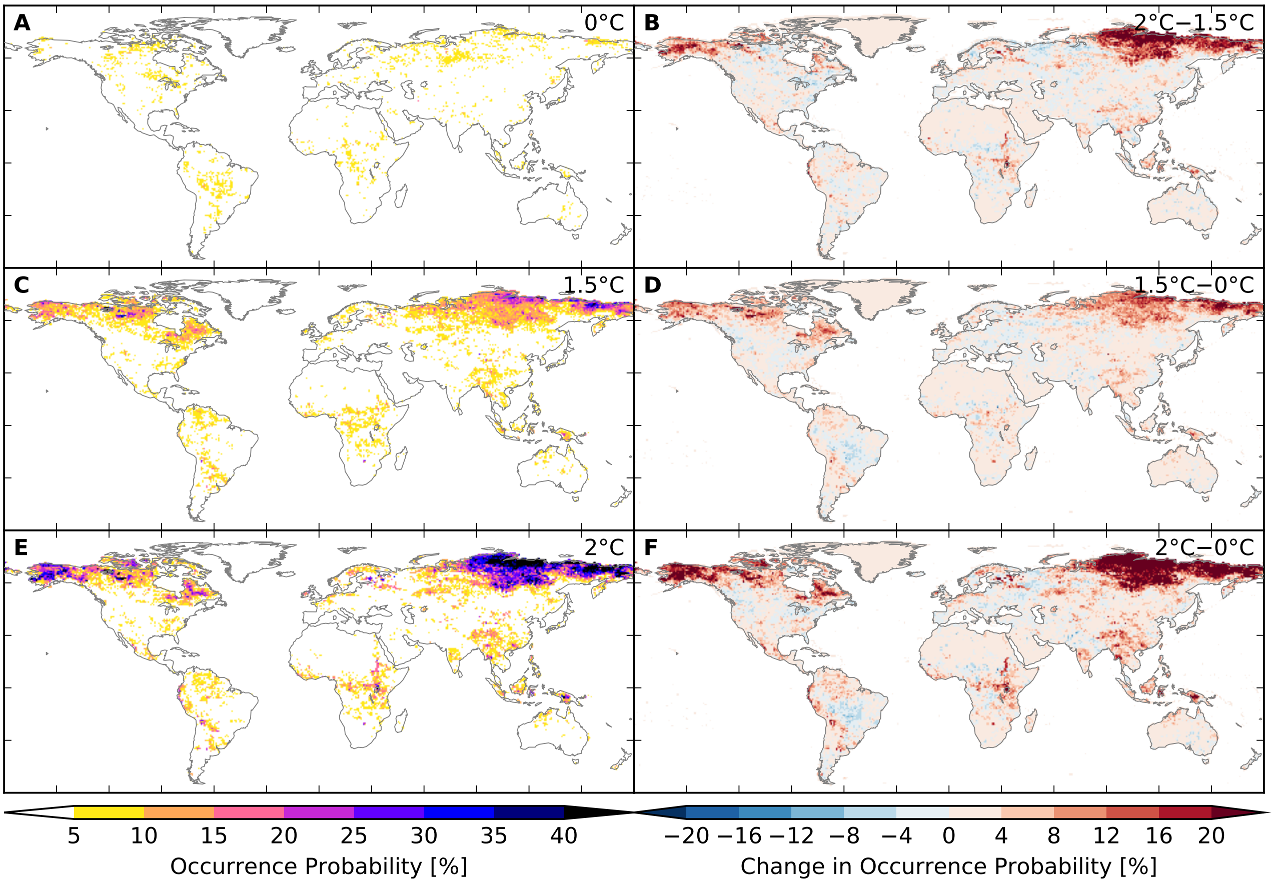

Figure S182: **Probability of occurrence of at least one flood event per year at different global warming levels (GFDL-ESM2M + MPI-HM).** Analogous to Figure S175.

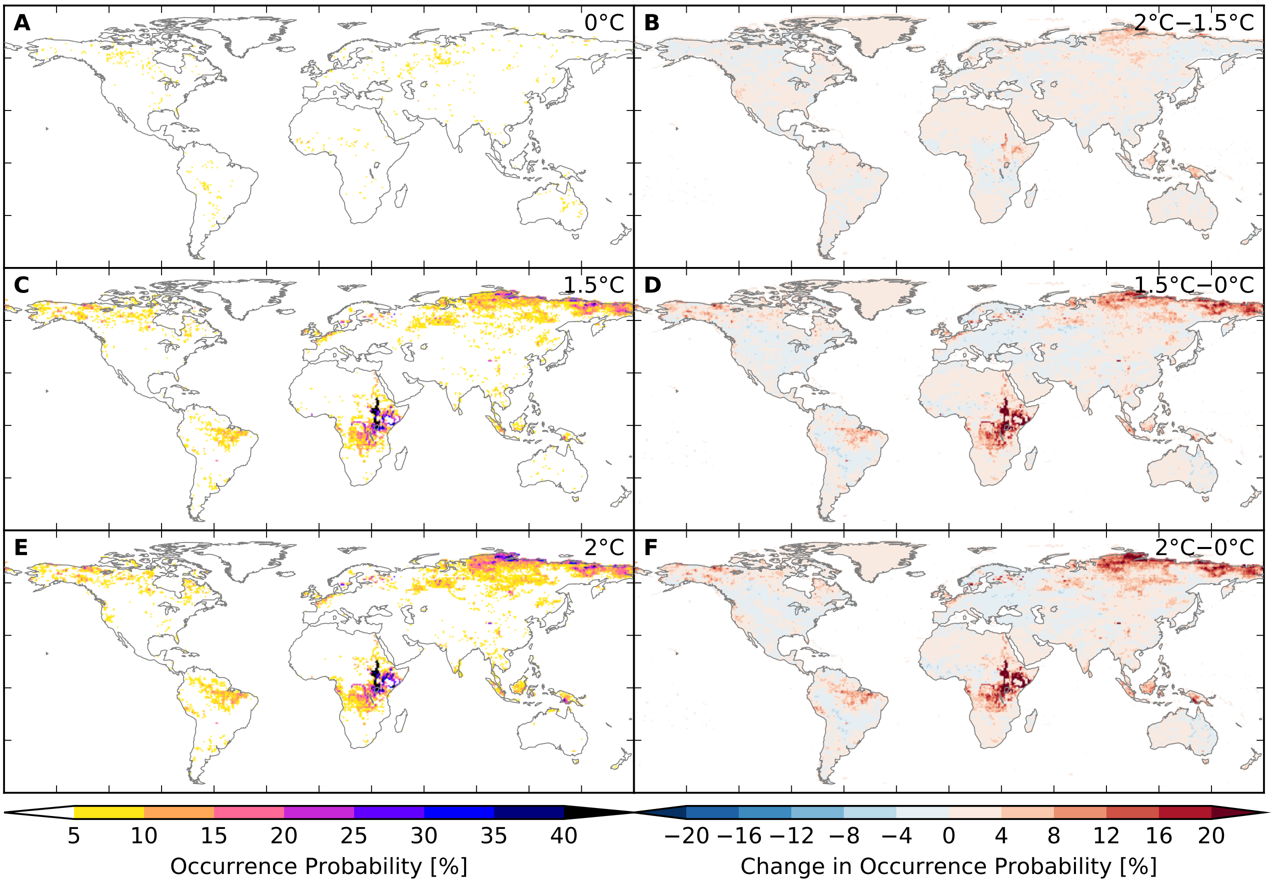

Figure S183: **Probability of occurrence of at least one flood event per year at different global warming levels (IPSL-CM5A-LR + MPI-HM).** Analogous to Figure S175.

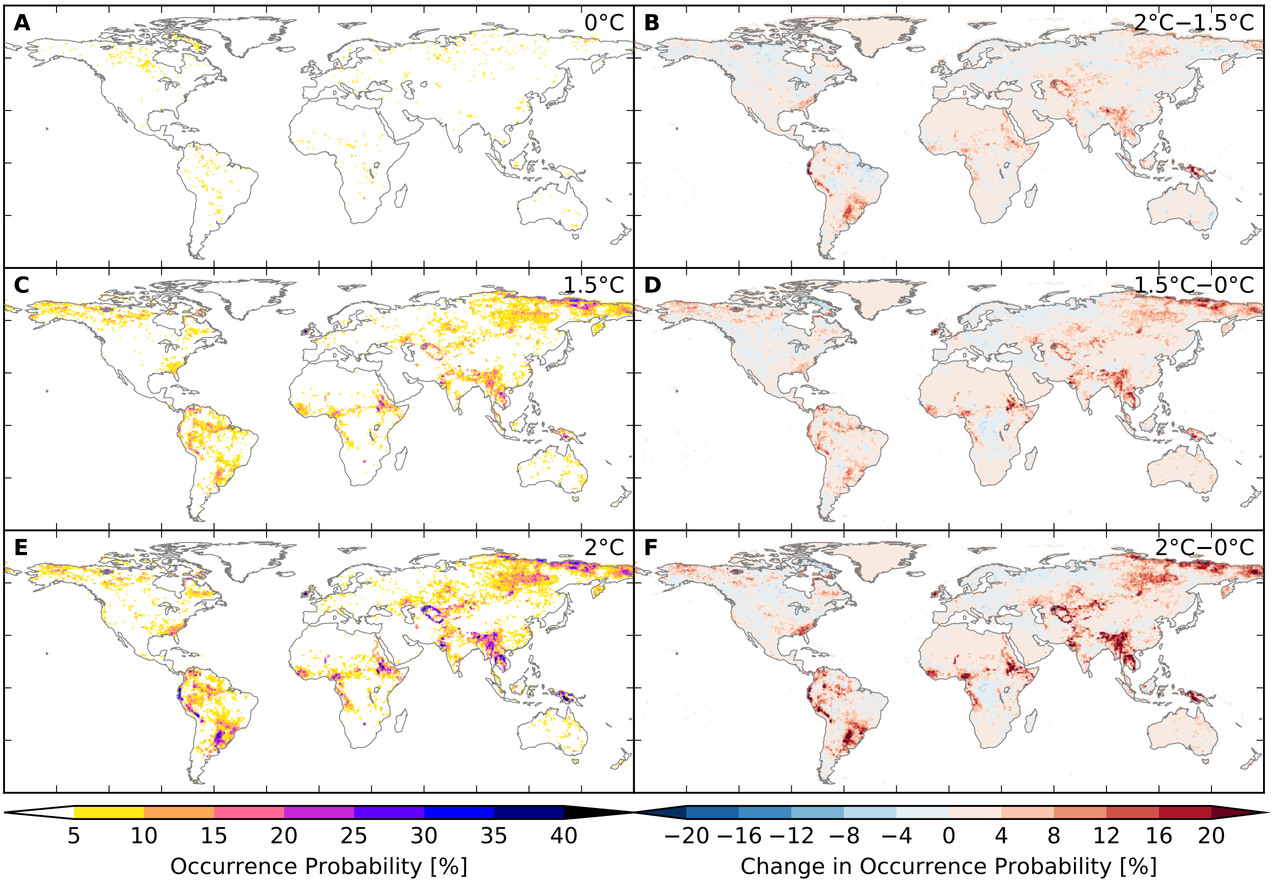

Figure S184: **Probability of occurrence of at least one flood event per year at different global warming levels (MIROC5 + MPI-HM).** Analogous to Figure S175.

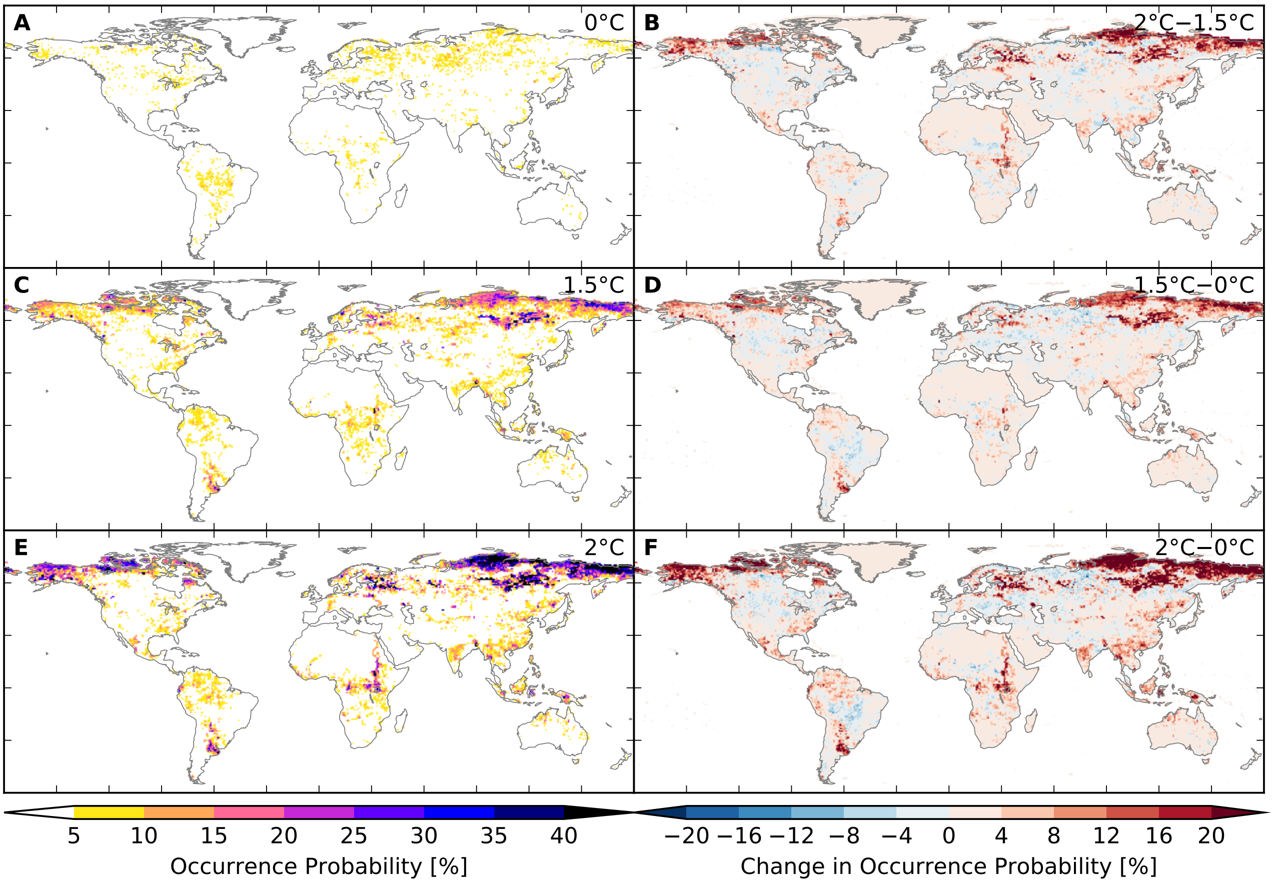

Figure S185: **Probability of occurrence of at least one flood event per year at different global warming levels (GFDL-ESM2M + ORCHIDEE).** Analogous to Figure S175.

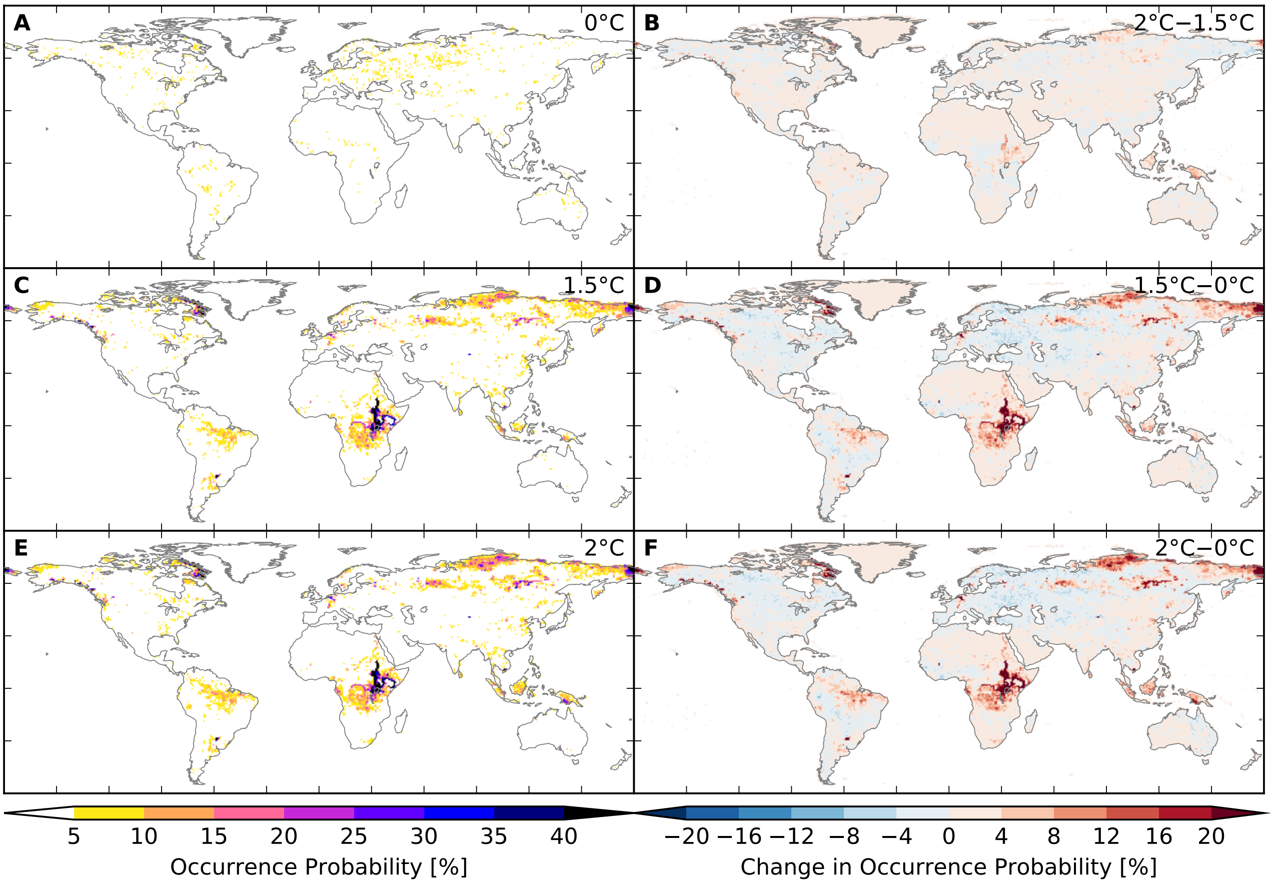

Figure S186: **Probability of occurrence of at least one flood event per year at different global warming levels (IPSL-CM5A-LR + ORCHIDEE).** Analogous to Figure S175.

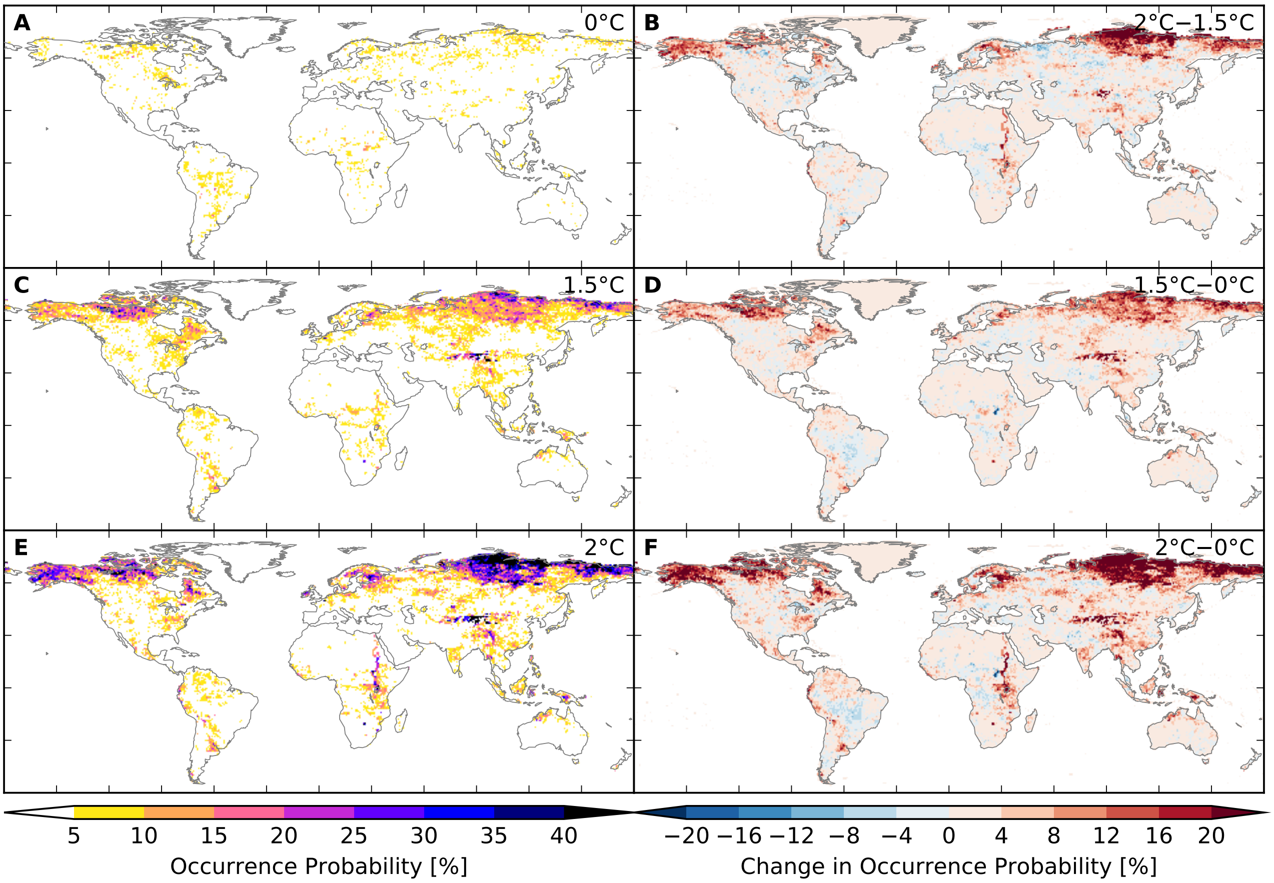

Figure S187: **Probability of occurrence of at least one flood event per year at different global warming levels (GFDL-ESM2M + PCR-GLOBWB).** Analogous to Figure S175.

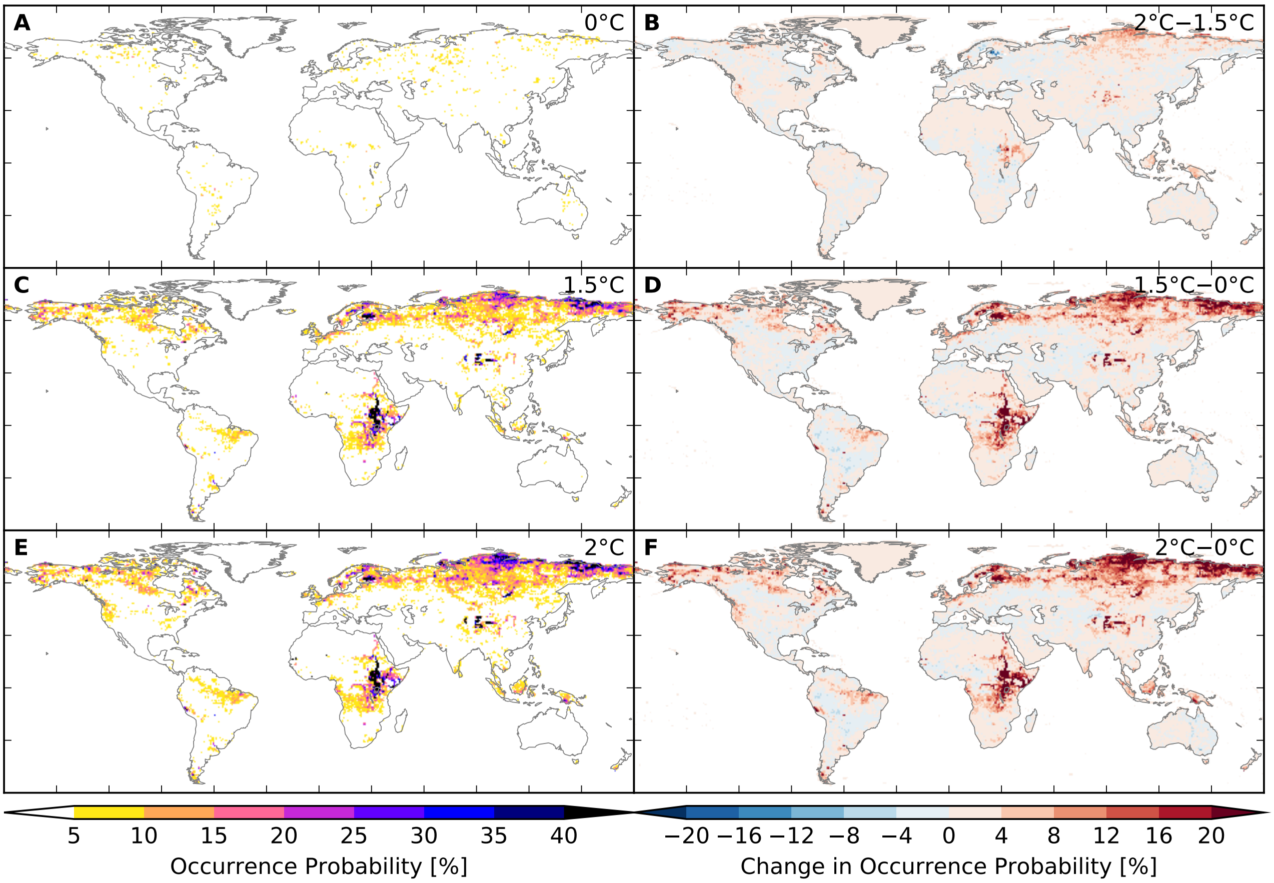

Figure S188: **Probability of occurrence of at least one flood event per year at different global warming levels (IPSL-CM5A-LR + PCR-GLOBWB).** Analogous to Figure S175.

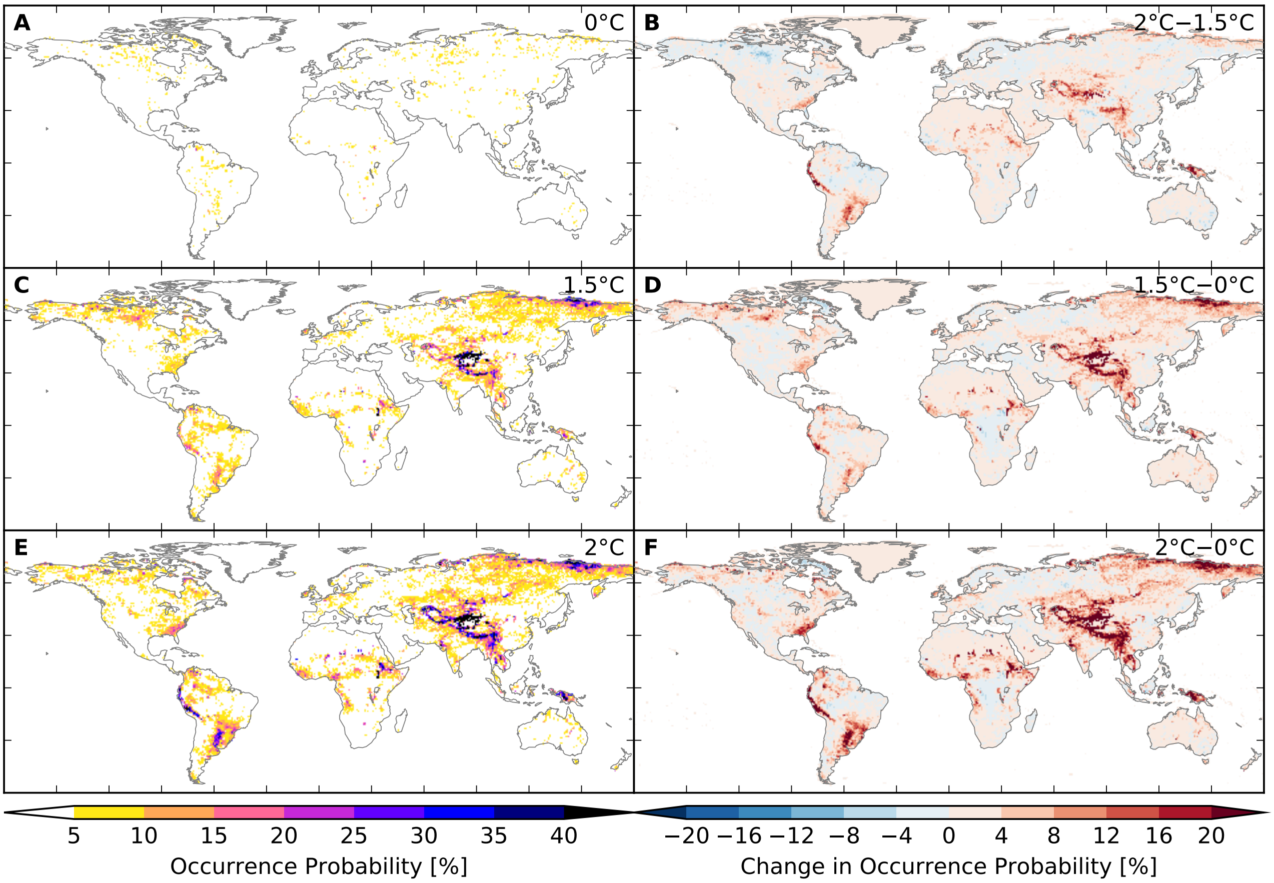

Figure S189: **Probability of occurrence of at least one flood event per year at different global warming levels (MIROC5 + PCR-GLOBWB).** Analogous to Figure S175.

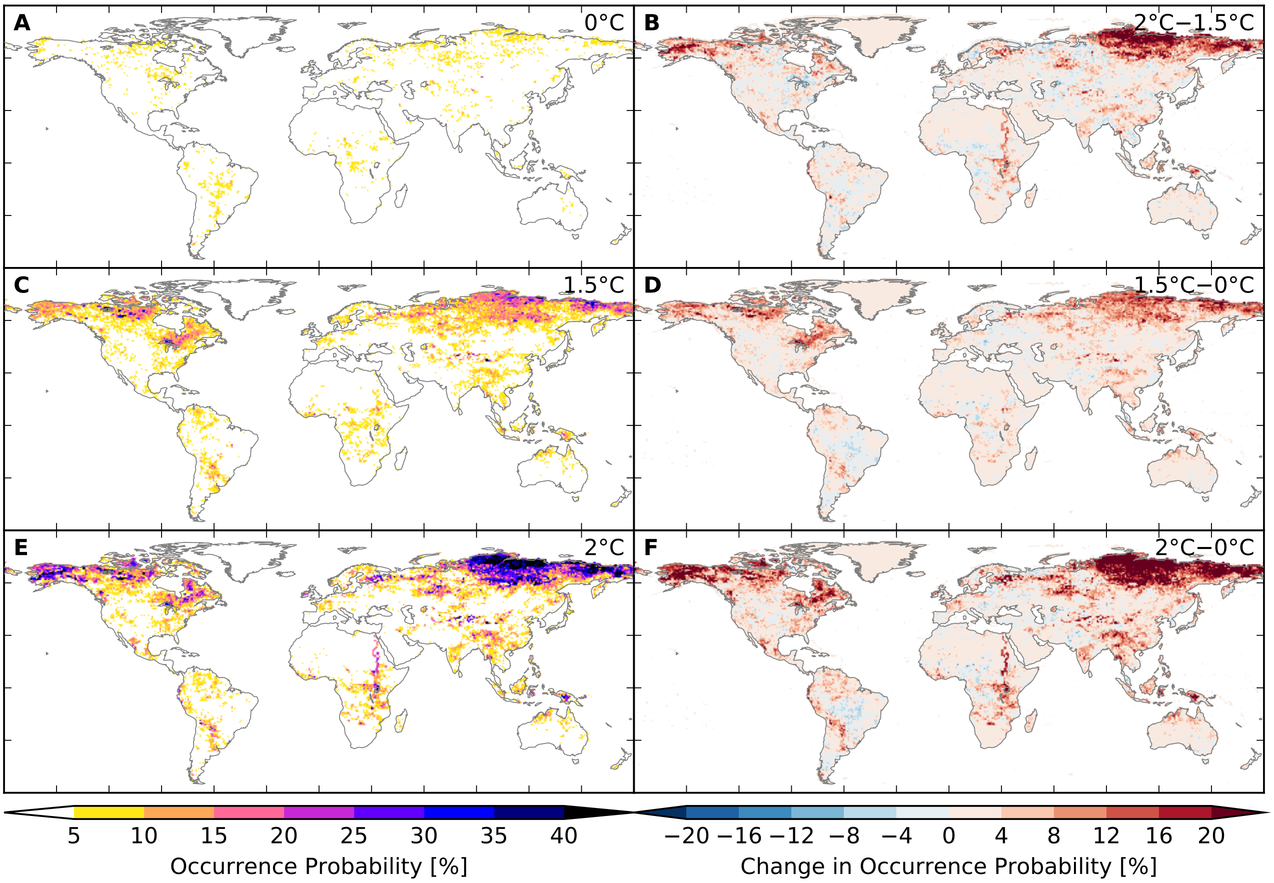

Figure S190: **Probability of occurrence of at least one flood event per year at different global warming levels (GFDL-ESM2M + WaterGAP2).** Analogous to Figure S175.

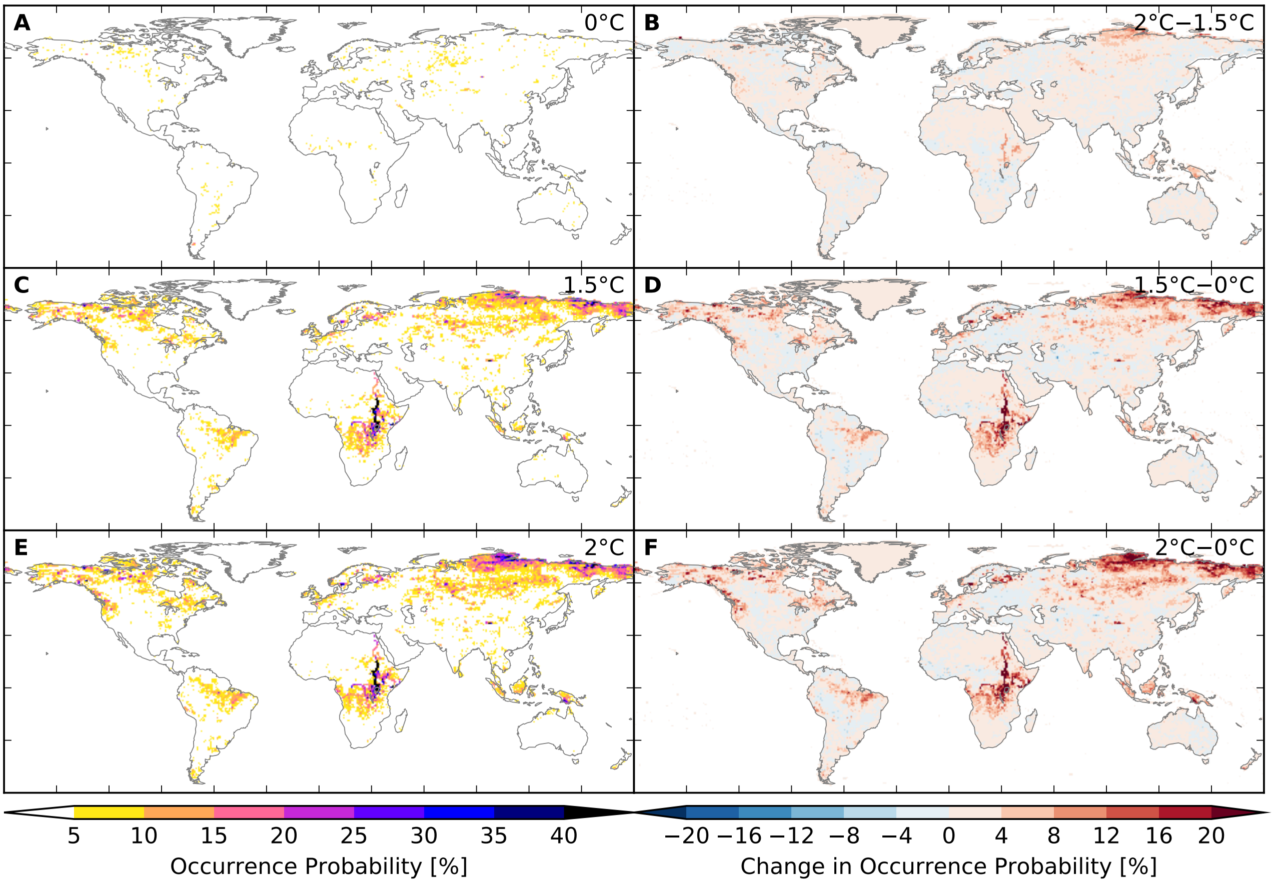

Figure S191: **Probability of occurrence of at least one flood event per year at different global warming levels (IPSL-CM5A-LR + WaterGAP2).** Analogous to Figure S175.

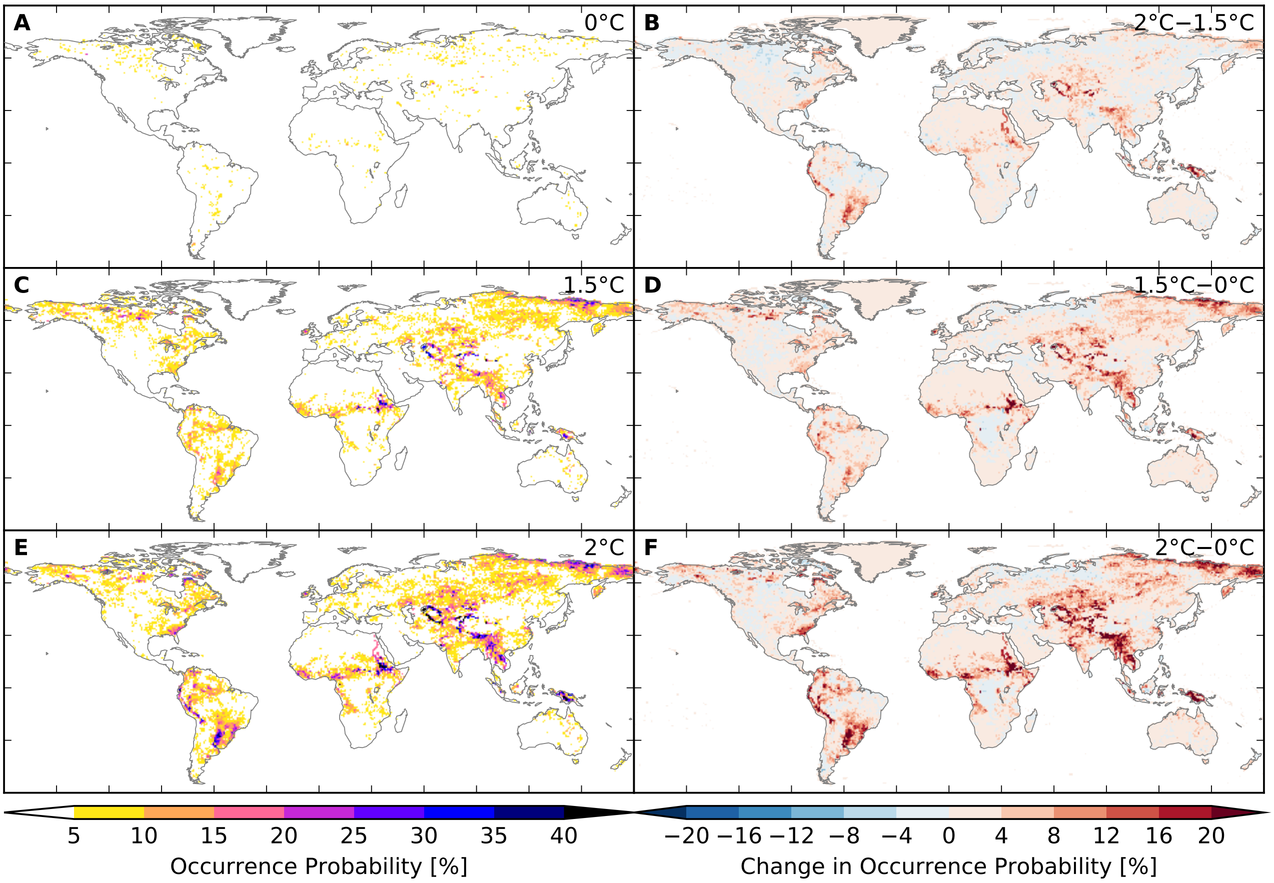

Figure S192: **Probability of occurrence of at least one flood event per year at different global warming levels (MIROC5 + WaterGAP2).** Analogous to Figure S175.

People exposed

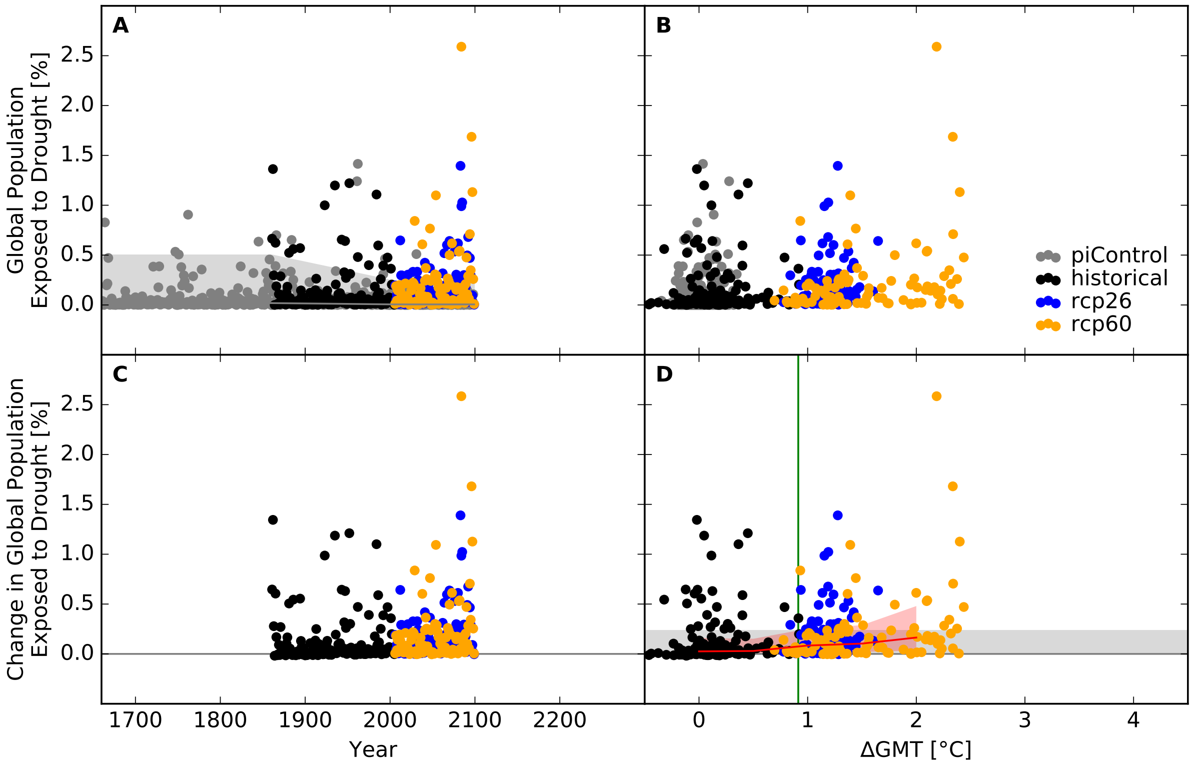

Figure S193: **Derivation of the pure effect of climate change on global population fraction affected by drought events (GFDL-ESM2M + H08).** Panel A: Time series of annual global population fraction affected (PFA) by drought events for pre-industrial climate (grey dots), historical climate (black dots), climate projections for RCP2.6 (blue dots), and RCP6.0 (orange dots). In all simulations, socio-economic conditions are varied according to the historically observed development between 1860 and 2005, and held fixed at 1860 conditions before 1860 and at 2005 conditions after 2005. Shaded areas before 1860/after 2005 represent the range from the 2nd to the 98th percentile of the distribution of the annual PFA under pre-industrial climate conditions in combination with 1860/2005 socio-economic conditions; the solid gray lines represent the respective median values; the shaded areas and solid gray line between 1860 and 2005 are linear interpolations of the respective values before 1860 and after 2005. Panel B: Data shown in Panel A plotted against the associated GCM-specific annual global mean temperature (GMT) change relative to the long-term pre-industrial mean. Panel C: Pure effect of climate change on PFA, calculated as the difference between the annual data shown in Panel A and the median of the simulations assuming pre-industrial climate conditions (solid gray line in Panel A). Panel D: Pure effect of climate change on PFA in terms of global mean temperature change, with distributions of the annual data estimated for each 1°C-wide bin of global mean temperature change that contains at least five data points, at least one data point above and at least one data point below the bin center. Areas shaded in red represent the range from the 20th to the 80th percentile around the median (solid red line) of these distributions. Areas shaded in gray represent the range from the 2nd to the 98th percentile of the zero-centered distribution of the annual PFA under pre-industrial climate and 2005 socio-economic conditions (cf. Panel A). The green vertical line represents the detection level defined as the global warming level at which a 1-in-50-years event under pre-industrial climate and 2005 socio-economic conditions becomes a 1-in-5-years event under changing climate and 2005 socio-economic conditions.

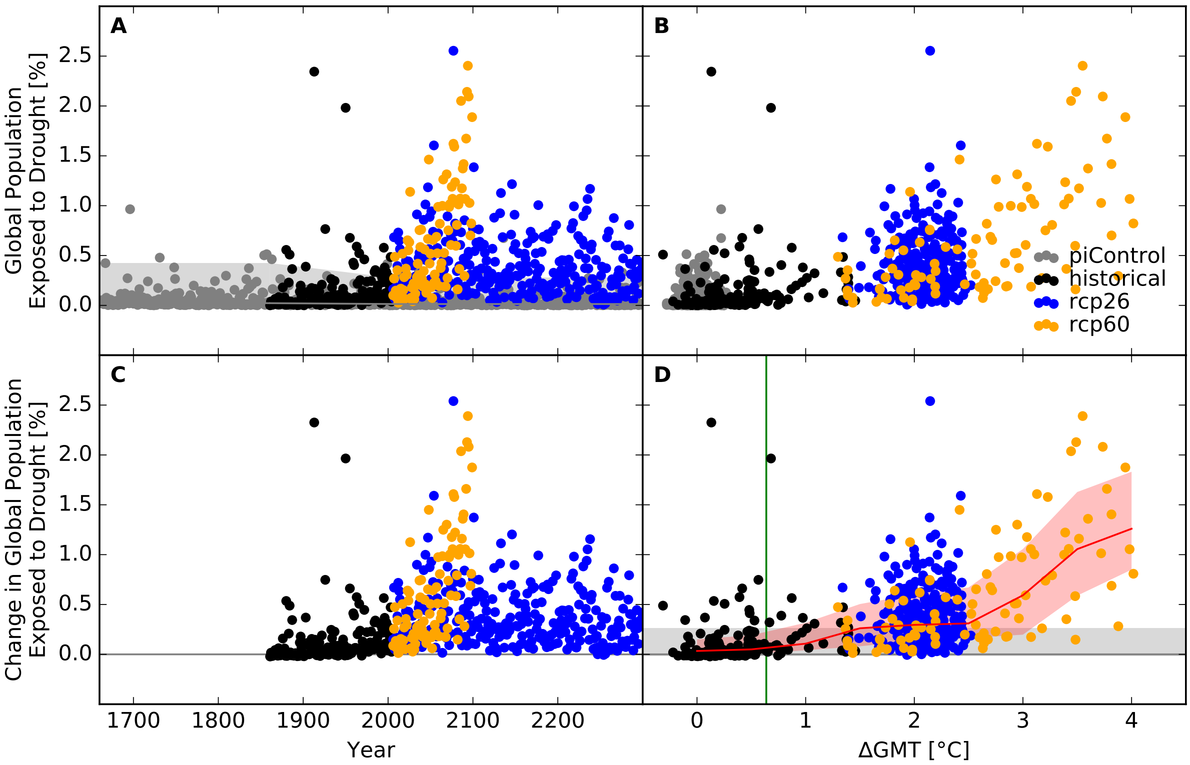

Figure S194: **Derivation of the pure effect of climate change on global population fraction affected by drought events (IPSL-CM5A-LR + H08).** Analogous to Figure S193.

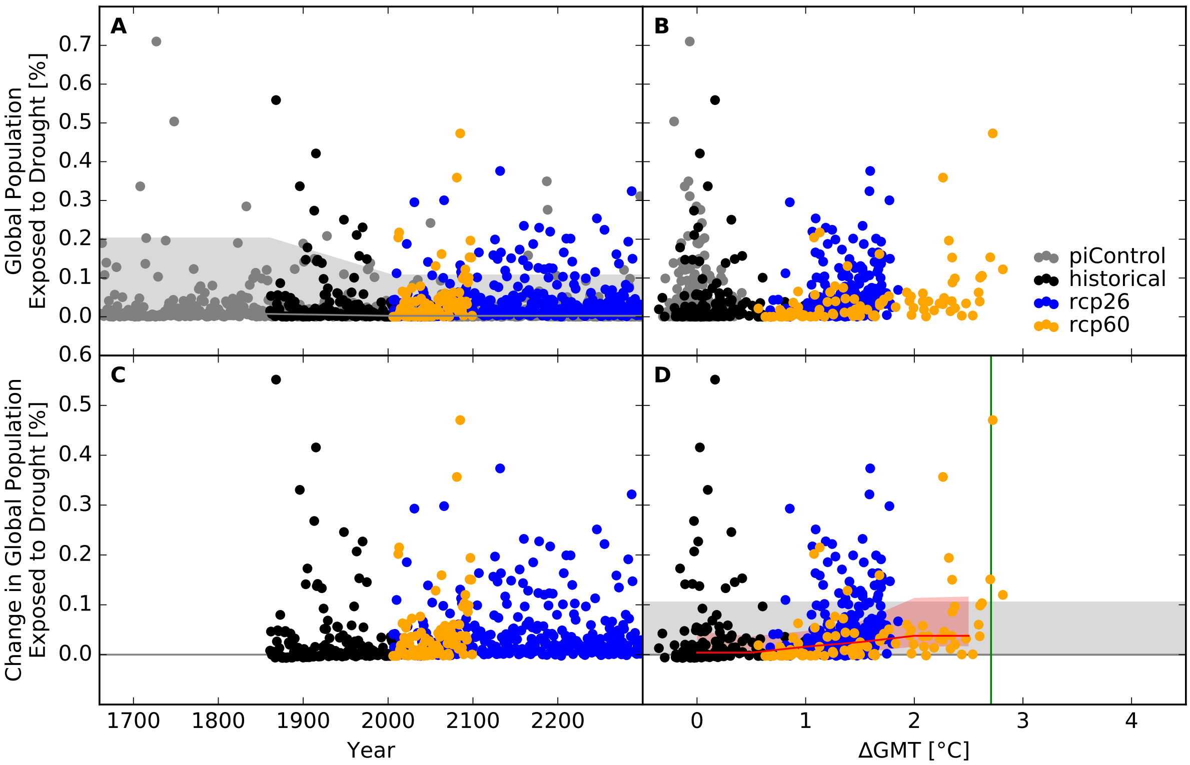

Figure S195: **Derivation of the pure effect of climate change on global population fraction affected by drought events (MIROC5 + H08).** Analogous to Figure S193.

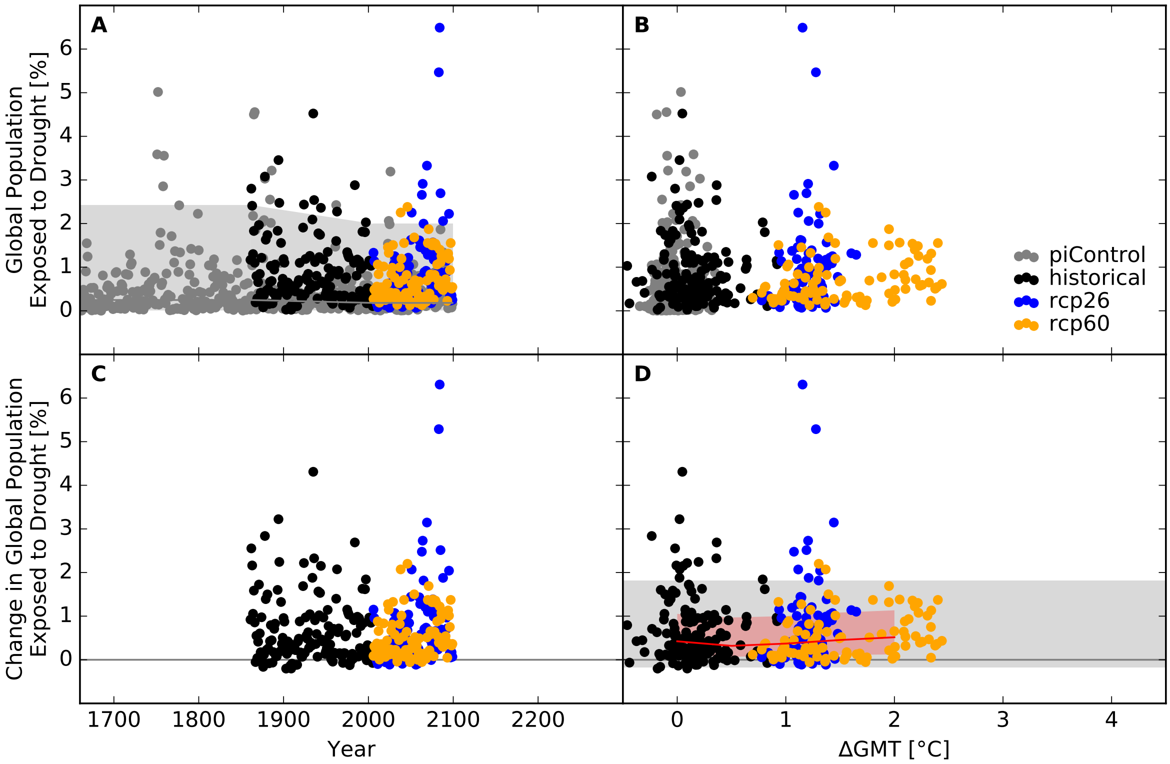

Figure S196: **Derivation of the pure effect of climate change on global population fraction affected by drought events (GFDL-ESM2M + JULES-W1).** Analogous to Figure S193.

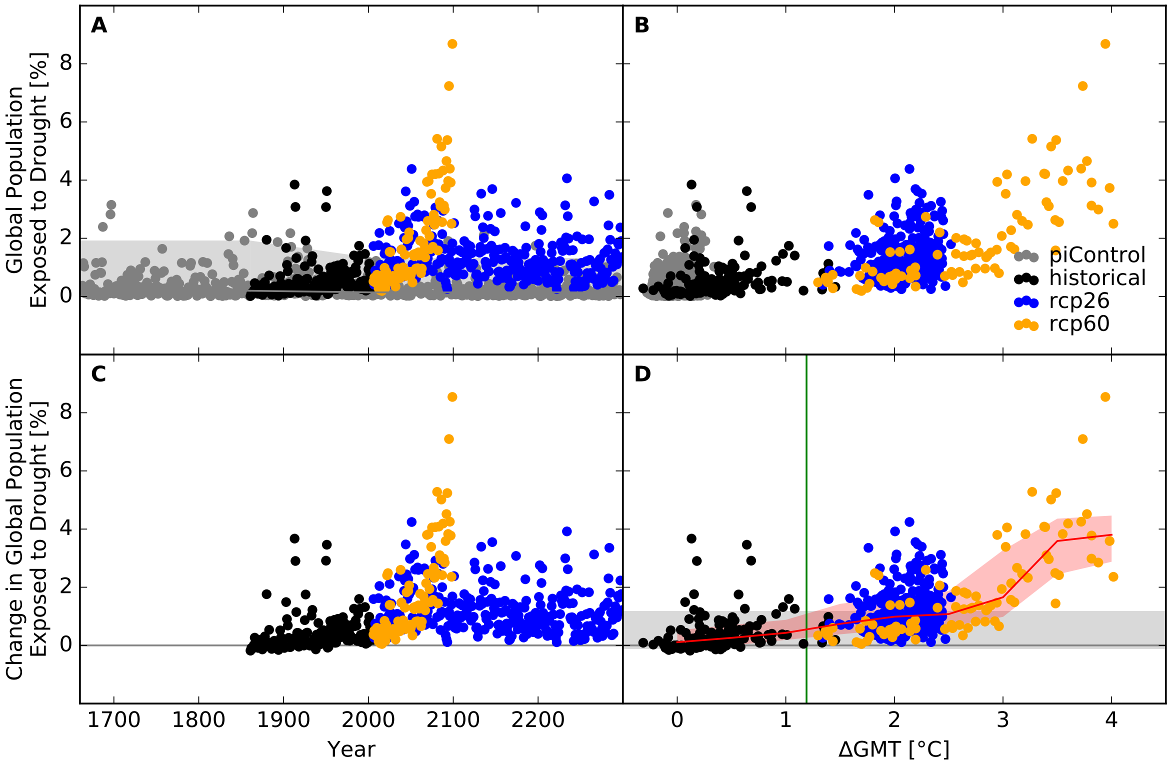

Figure S197: **Derivation of the pure effect of climate change on global population fraction affected by drought events (IPSL-CM5A-LR + JULES-W1).** Analogous to Figure S193.

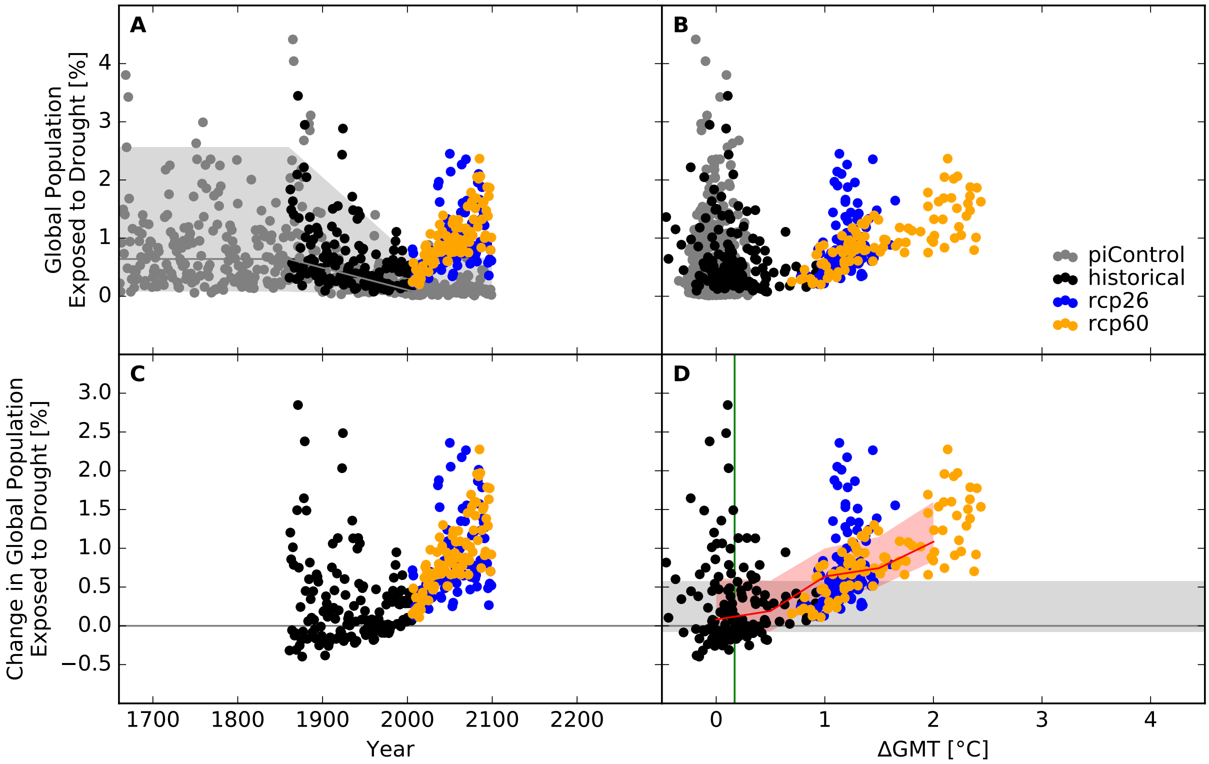

Figure S198: **Derivation of the pure effect of climate change on global population fraction affected by drought events (GFDL-ESM2M + LPJmL).** Analogous to Figure S193.

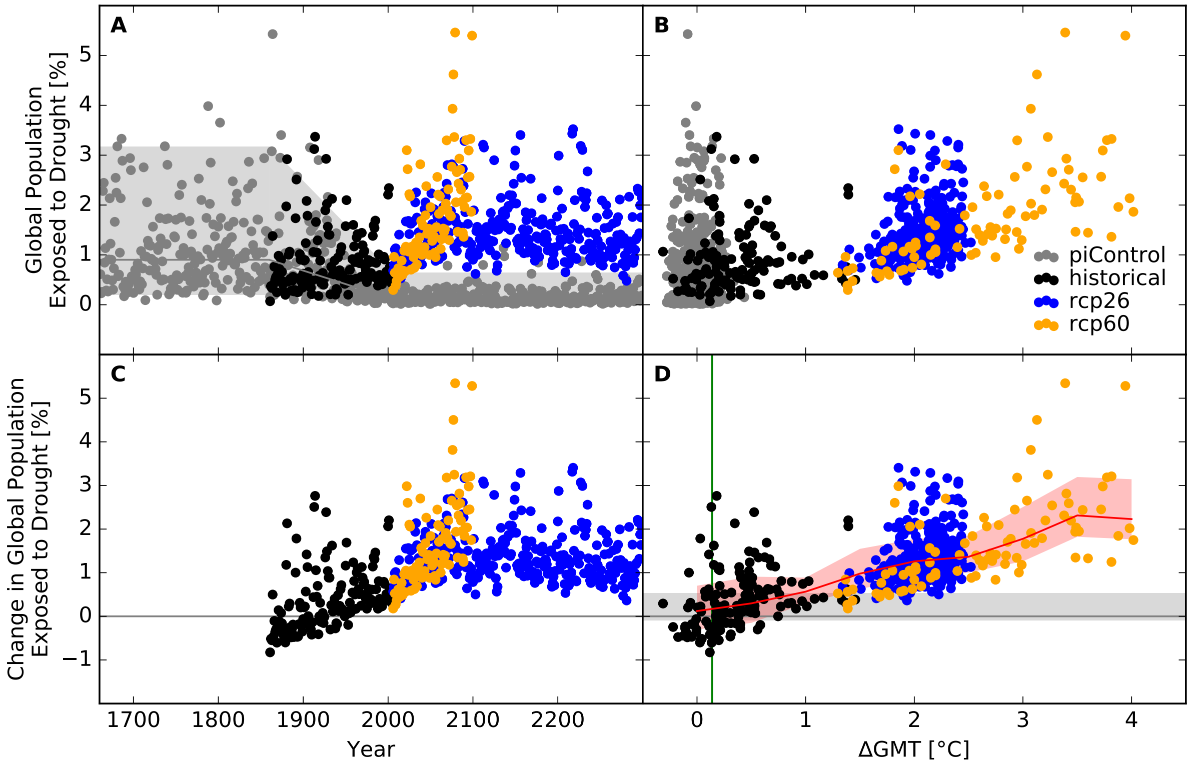

Figure S199: **Derivation of the pure effect of climate change on global population fraction affected by drought events (IPSL-CM5A-LR + LPJmL).** Analogous to Figure S193.

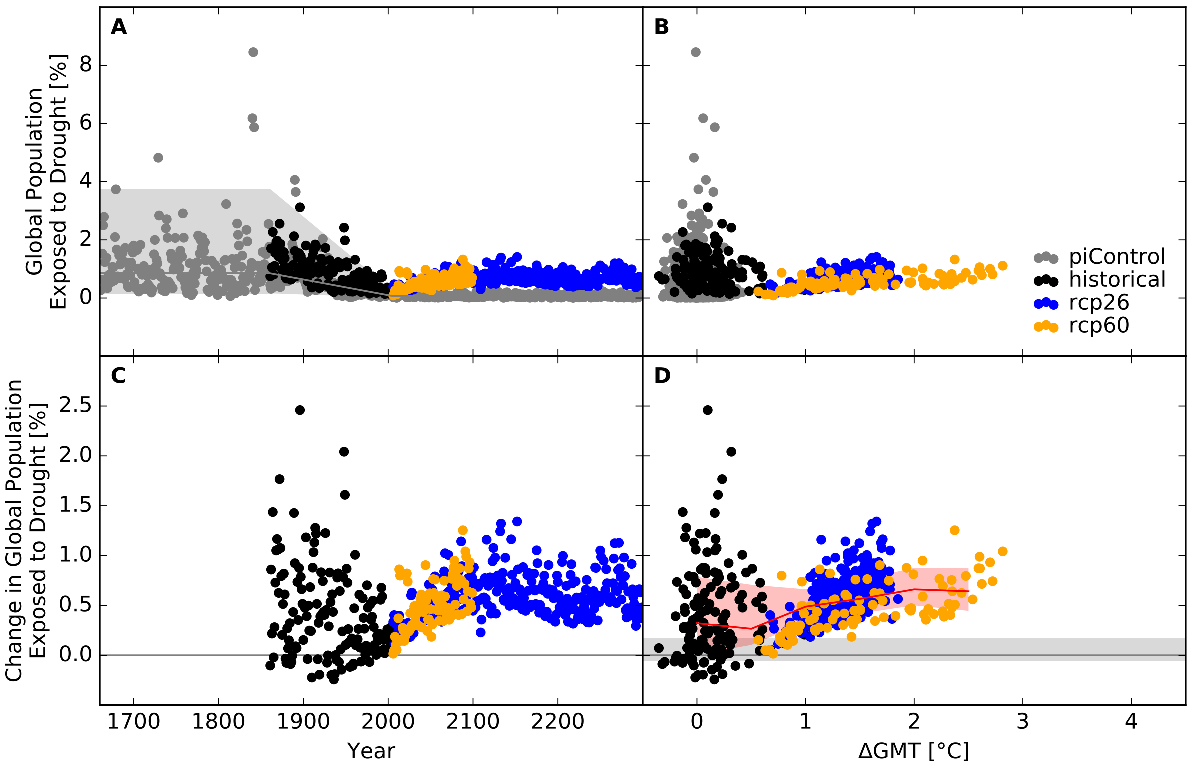

Figure S200: **Derivation of the pure effect of climate change on global population fraction affected by drought events (MIROC5 + LPJmL).** Analogous to Figure S193.

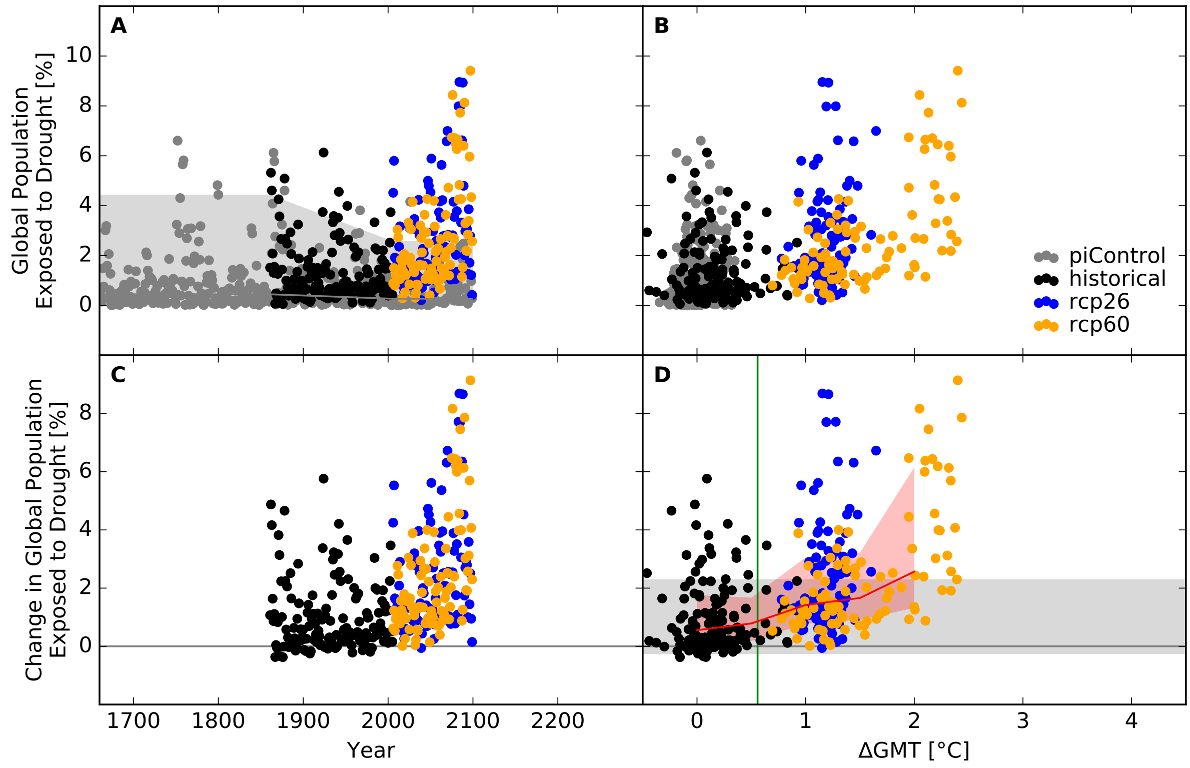

Figure S201: **Derivation of the pure effect of climate change on global population fraction affected by drought events (GFDL-ESM2M + MPI-HM).** Analogous to Figure S193.

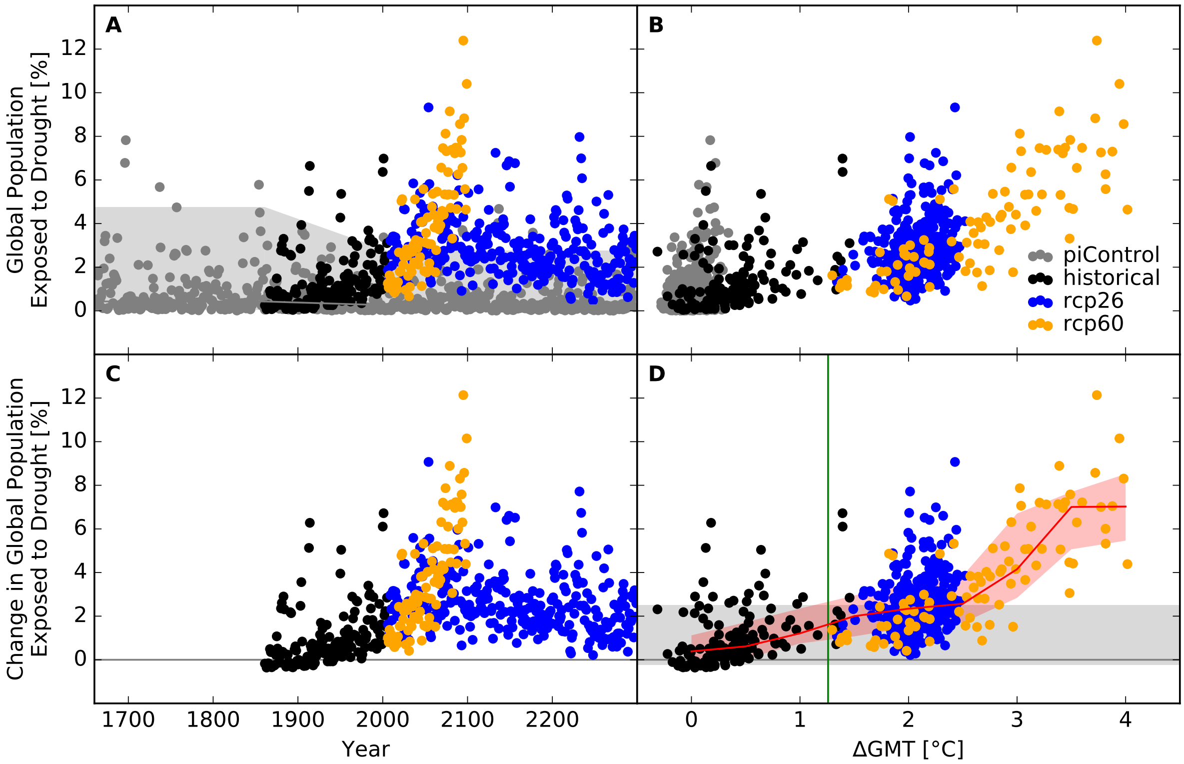

Figure S202: **Derivation of the pure effect of climate change on global population fraction affected by drought events (IPSL-CM5A-LR + MPI-HM).** Analogous to Figure S193.

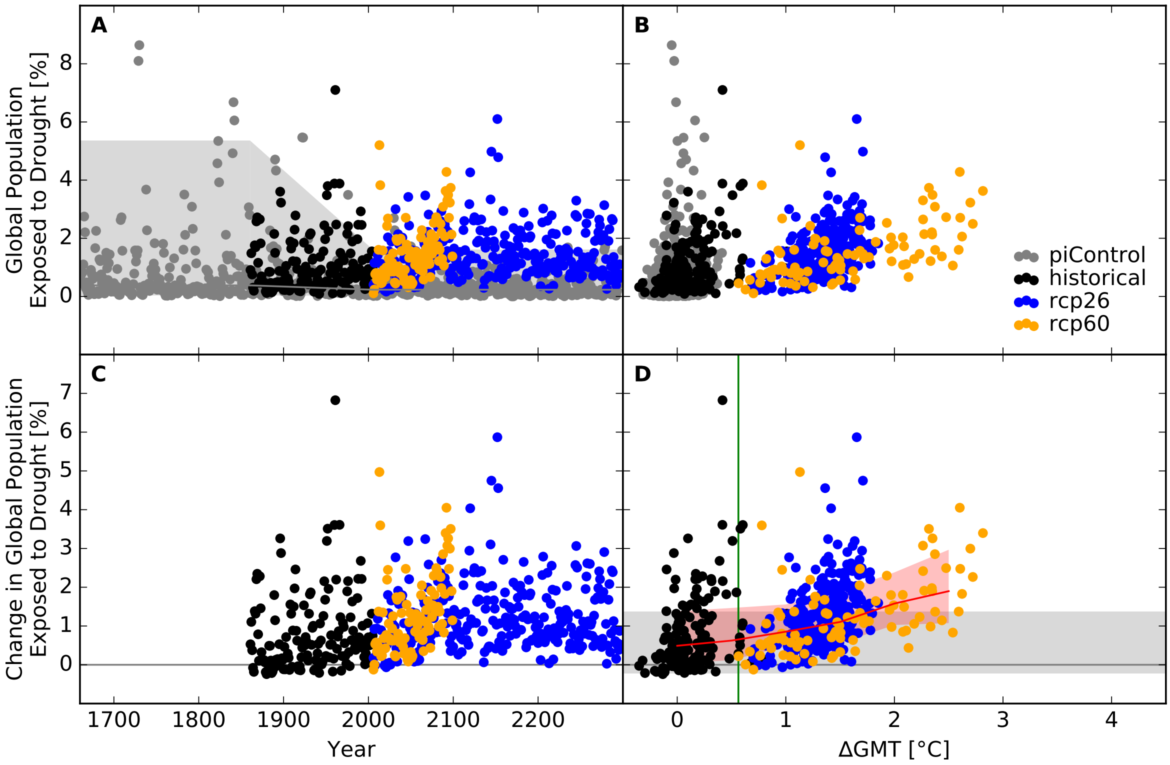

Figure S203: **Derivation of the pure effect of climate change on global population fraction affected by drought events (MIROC5 + MPI-HM).** Analogous to Figure S193.

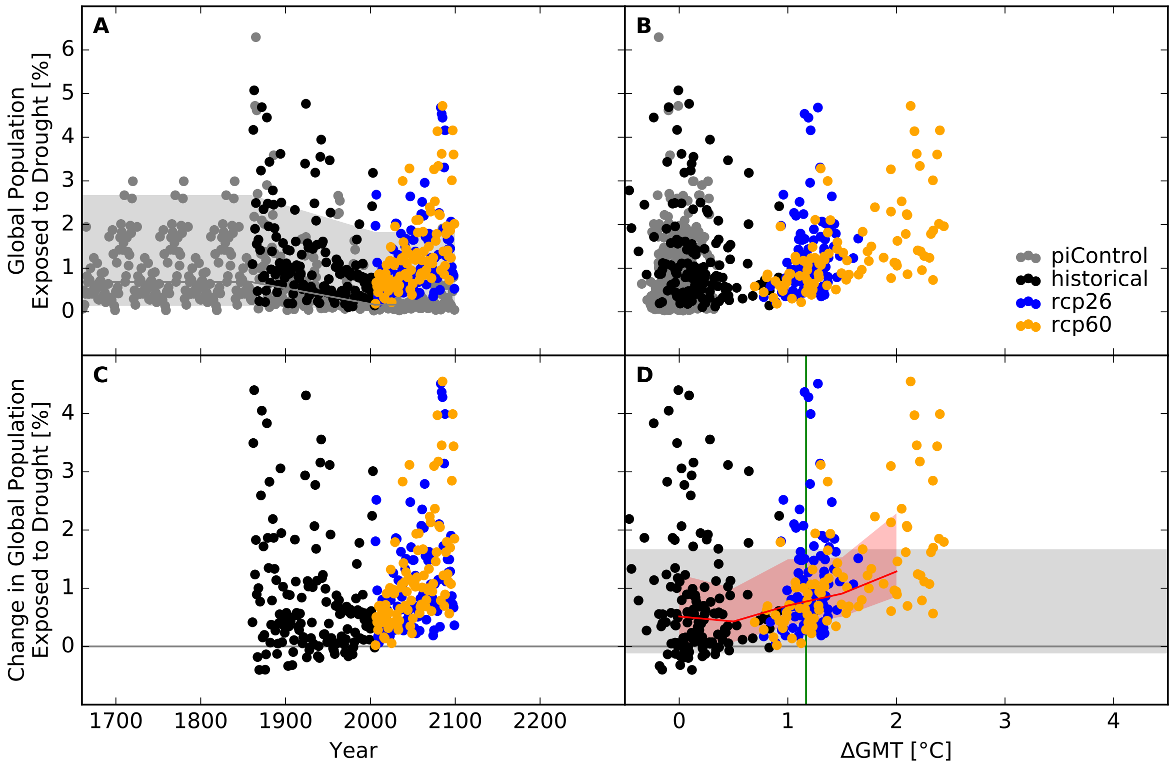

Figure S204: **Derivation of the pure effect of climate change on global population fraction affected by drought events (GFDL-ESM2M + ORCHIDEE).** Analogous to Figure S193.

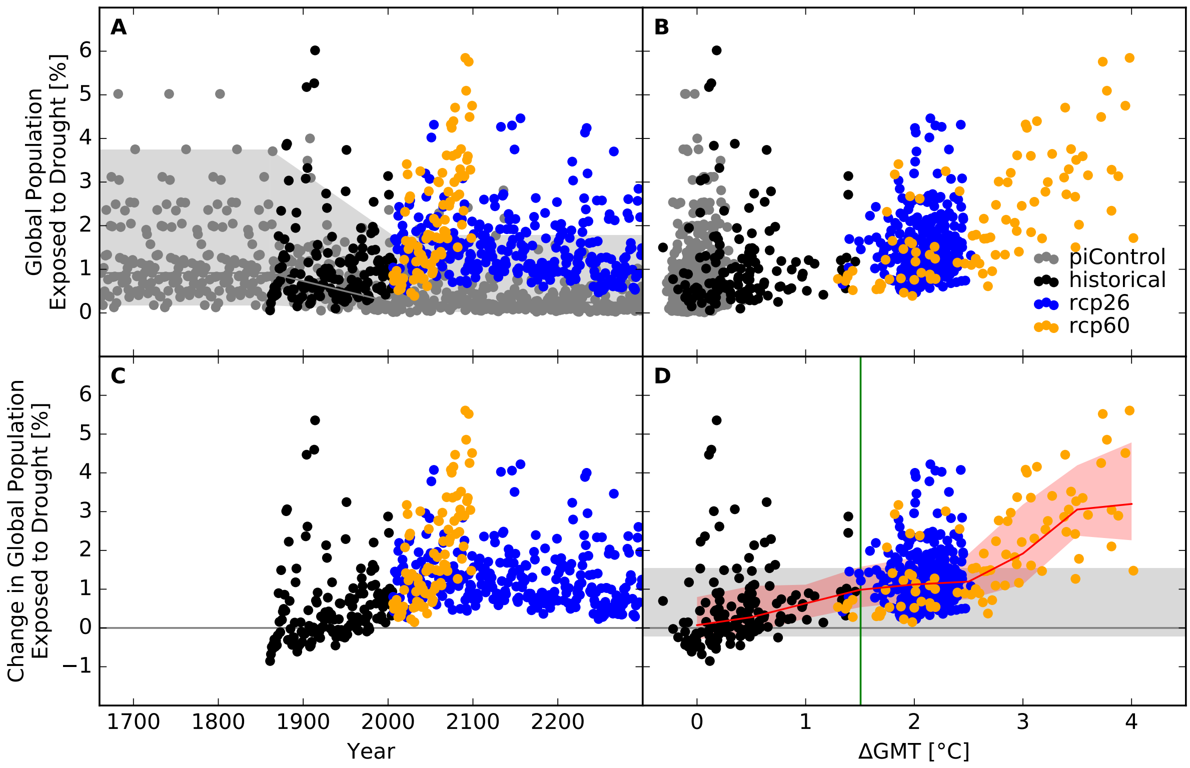

Figure S205: **Derivation of the pure effect of climate change on global population fraction affected by drought events (IPSL-CM5A-LR + ORCHIDEE).** Analogous to Figure S193.

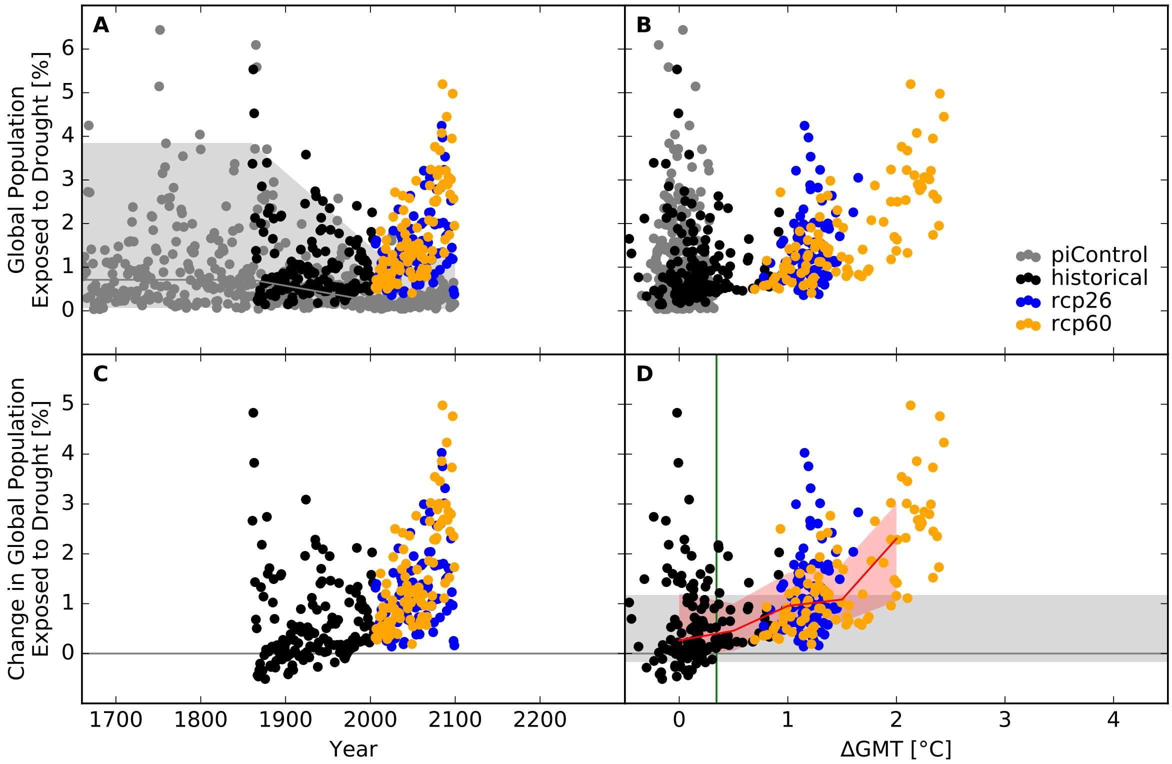

Figure S206: **Derivation of the pure effect of climate change on global population fraction affected by drought events (GFDL-ESM2M + PCR-GLOBWB).** Analogous to Figure S193.

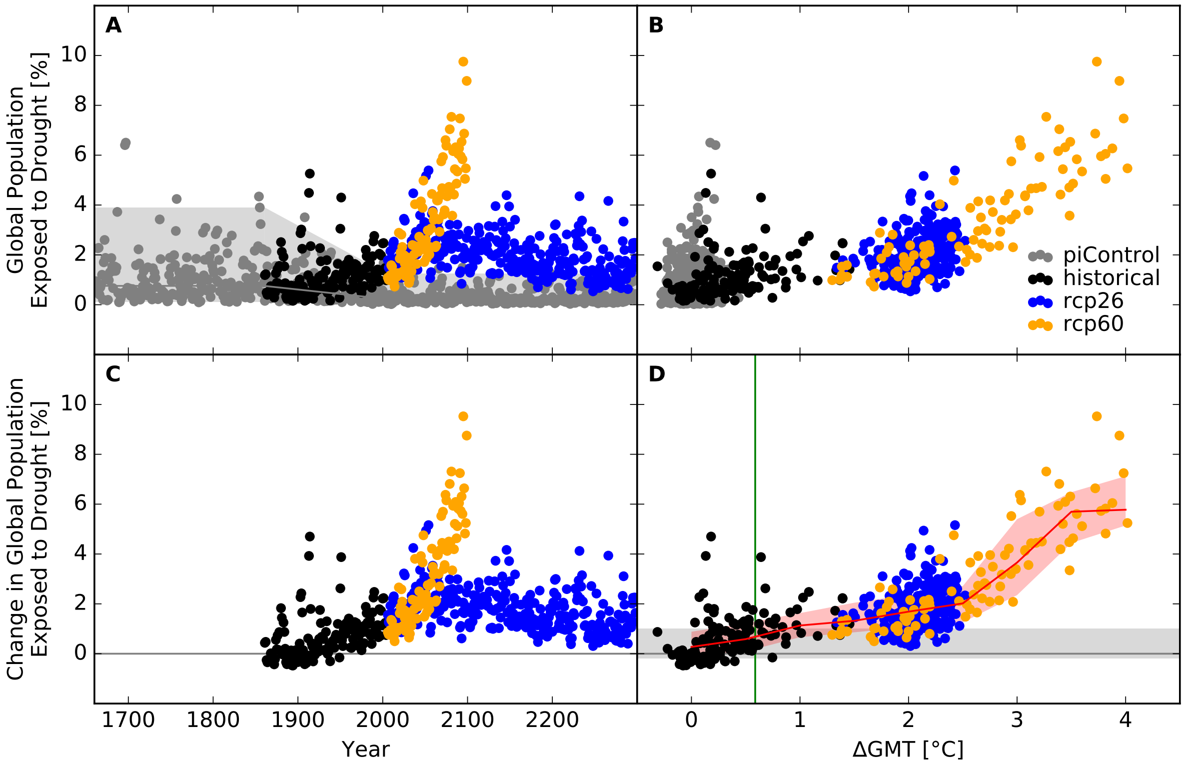

Figure S207: **Derivation of the pure effect of climate change on global population fraction affected by drought events (IPSL-CM5A-LR + PCR-GLOBWB).** Analogous to Figure S193.

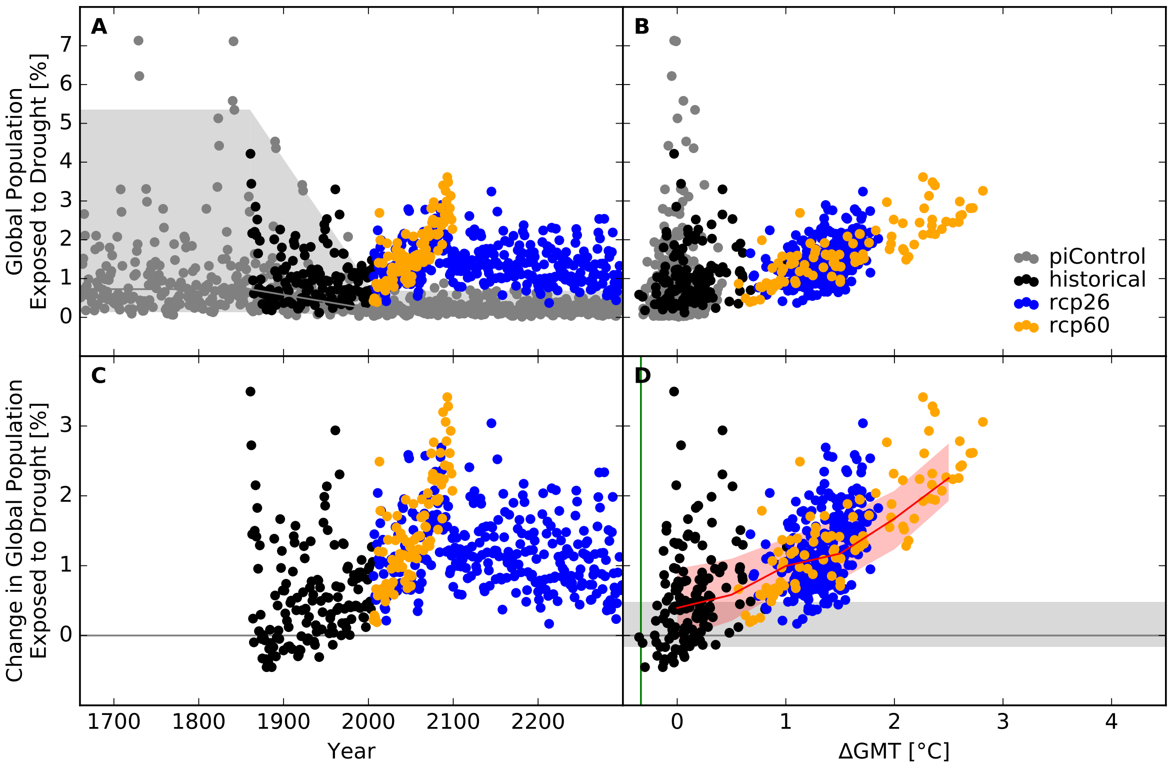

Figure S208: **Derivation of the pure effect of climate change on global population fraction affected by drought events (MIROC5 + PCR-GLOBWB).** Analogous to Figure S193.

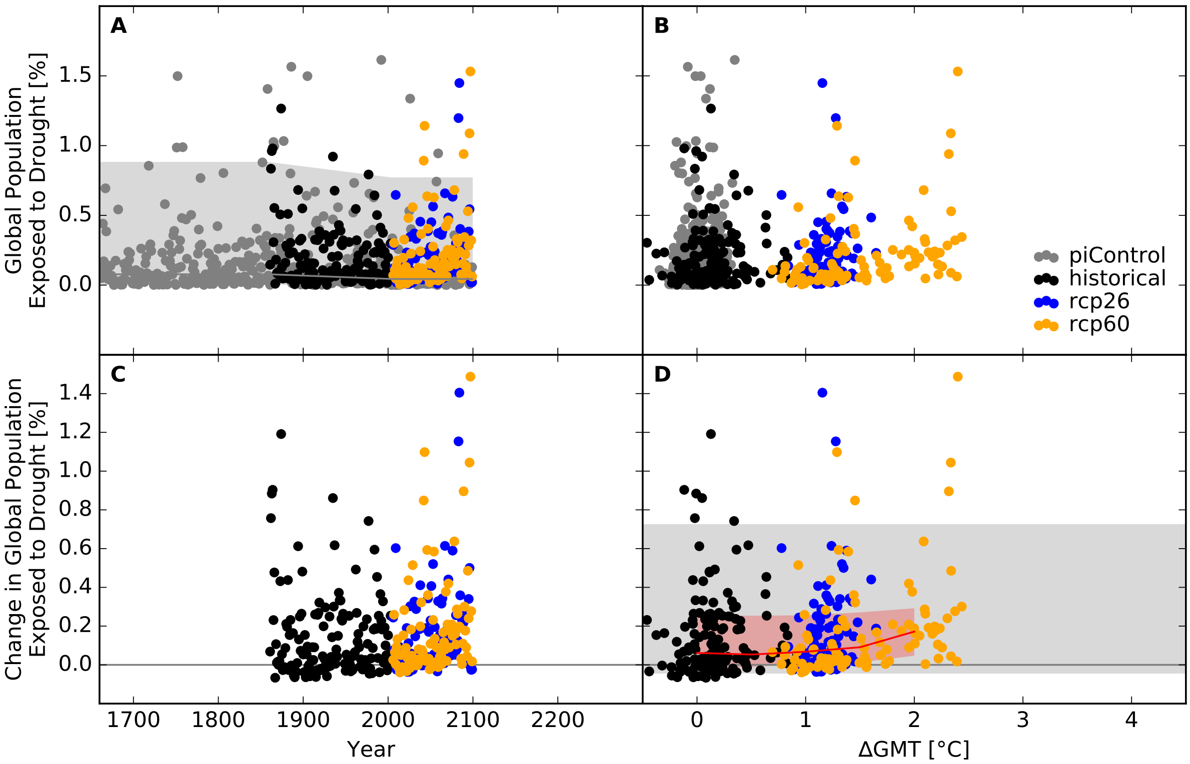

Figure S209: **Derivation of the pure effect of climate change on global population fraction affected by drought events (GFDL-ESM2M + WaterGAP2).** Analogous to Figure S193.

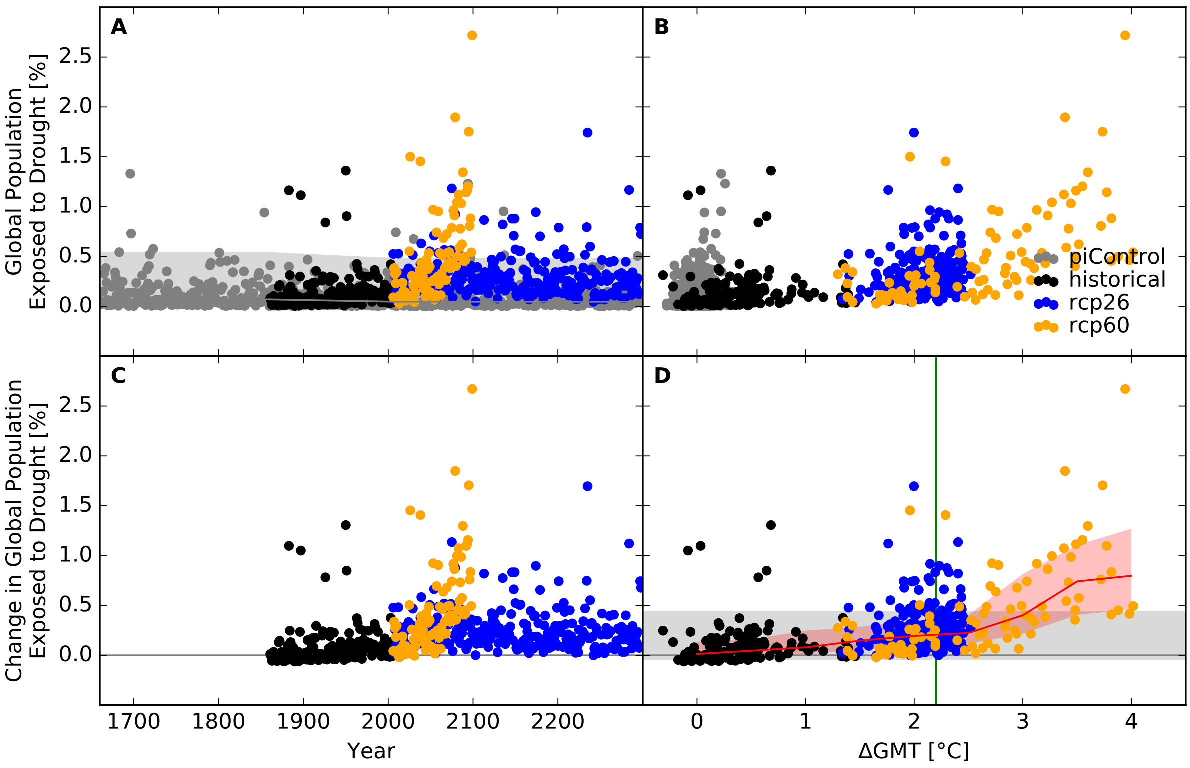

Figure S210: **Derivation of the pure effect of climate change on global population fraction affected by drought events (IPSL-CM5A-LR + WaterGAP2).** Analogous to Figure S193.

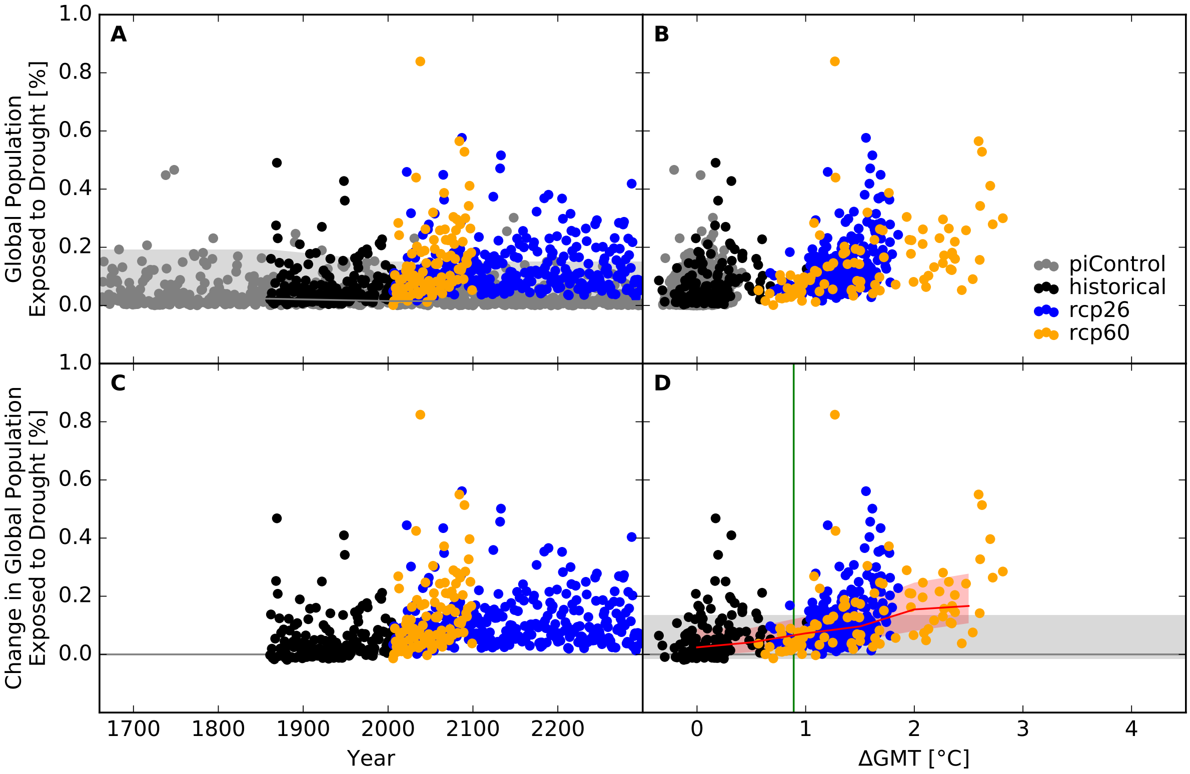

Figure S211: **Derivation of the pure effect of climate change on global population fraction affected by drought events (MIROC5 + WaterGAP2).** Analogous to Figure S193.

Occurrence probability at grid scale

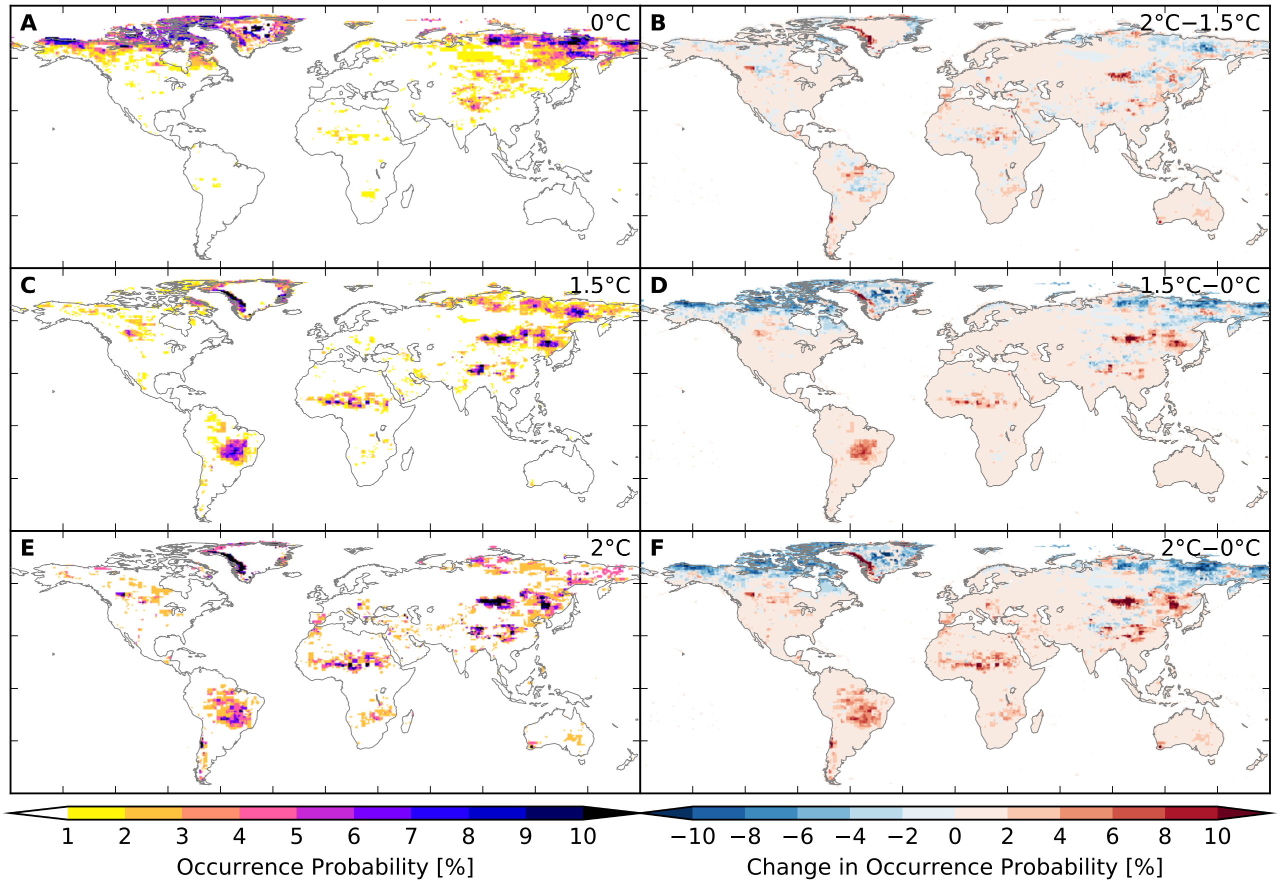

Figure S212: **Probability of occurrence of at least one drought event per year at different global warming levels (GFDL-ESM2M + H08).** Panels A, C, E: Probabilities at 0°C, 1.5°C, 2°C global mean temperature (GMT) change relative to the long-term pre-industrial mean GMT, respectively. Panels B, D, F: Differences between probabilities at GMT change levels of 2°C and 1.5°C, 1.5°C and 0°C, 2°C and 0°C, respectively.

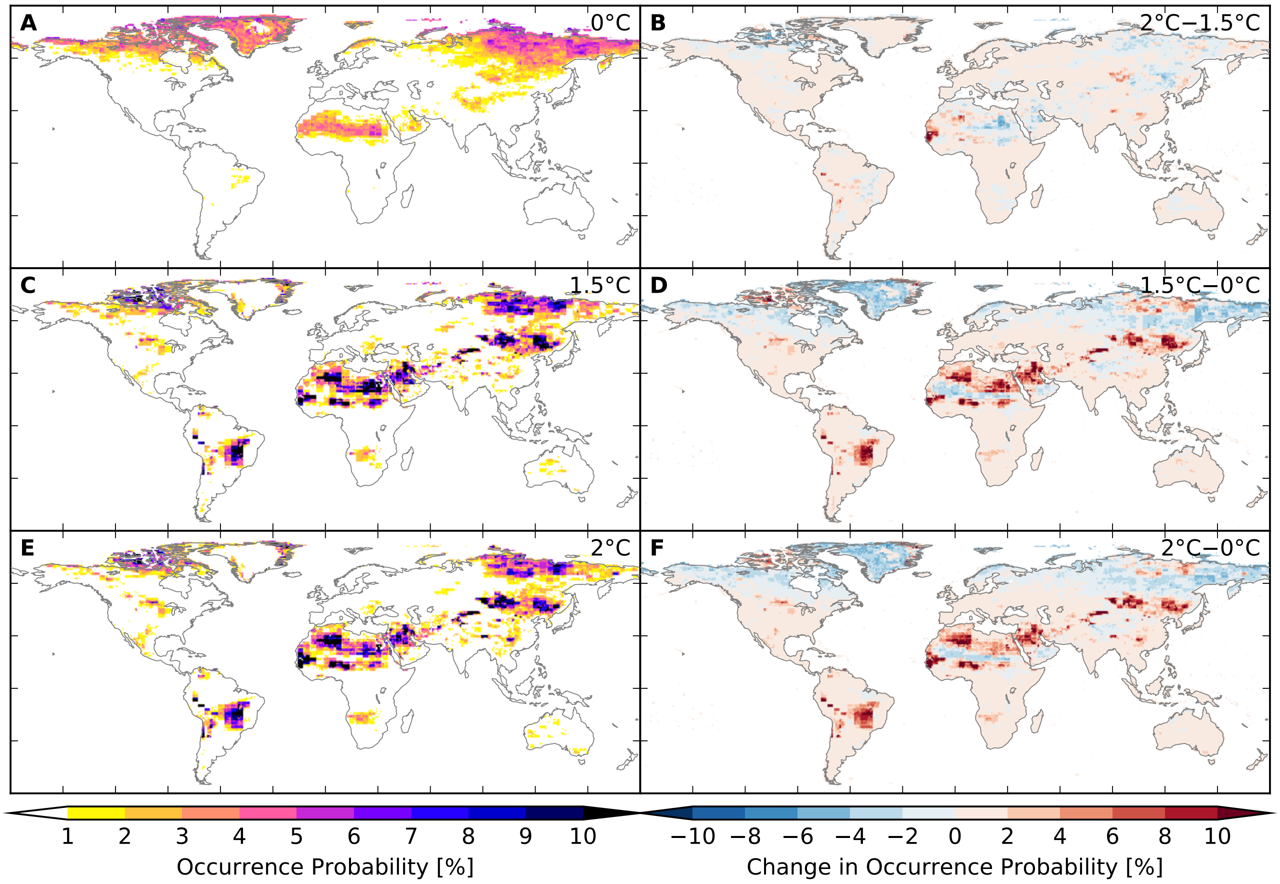

Figure S213: **Probability of occurrence of at least one drought event per year at different global warming levels (IPSL-CM5A-LR + H08).** Analogous to Figure S212.

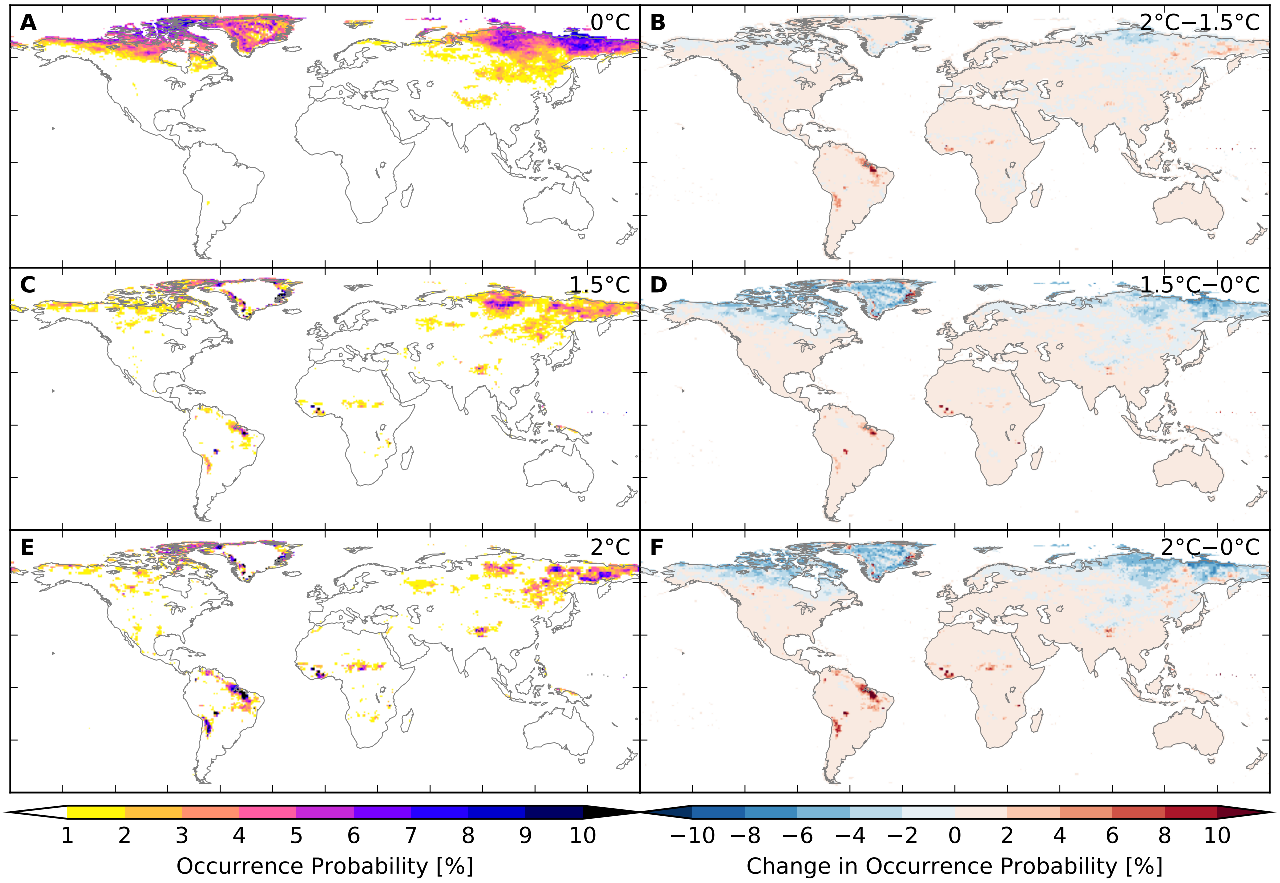

Figure S214: **Probability of occurrence of at least one drought event per year at different global warming levels (MIROC5 + H08).** Analogous to Figure S212.

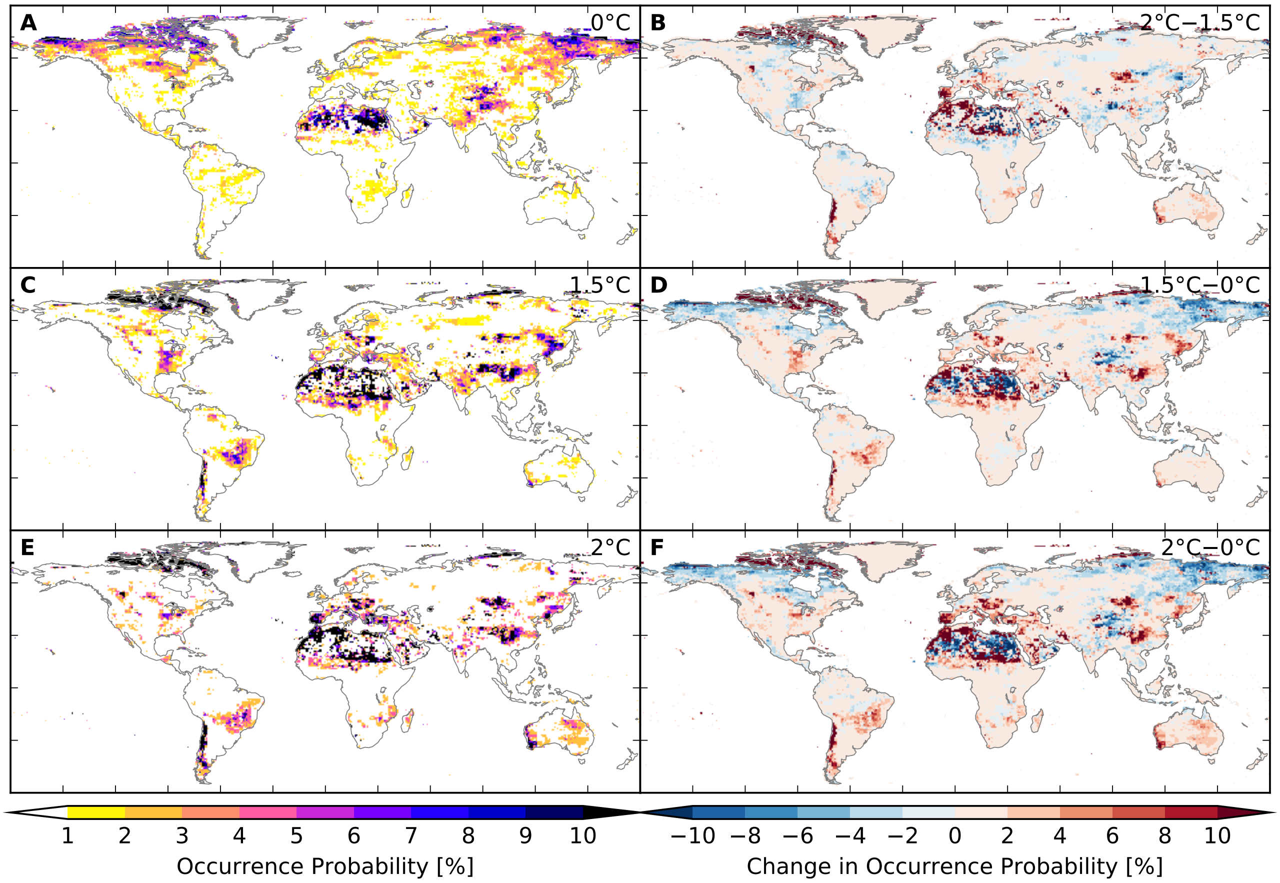

Figure S215: **Probability of occurrence of at least one drought event per year at different global warming levels (GFDL-ESM2M + JULES-W1).** Analogous to Figure S212.

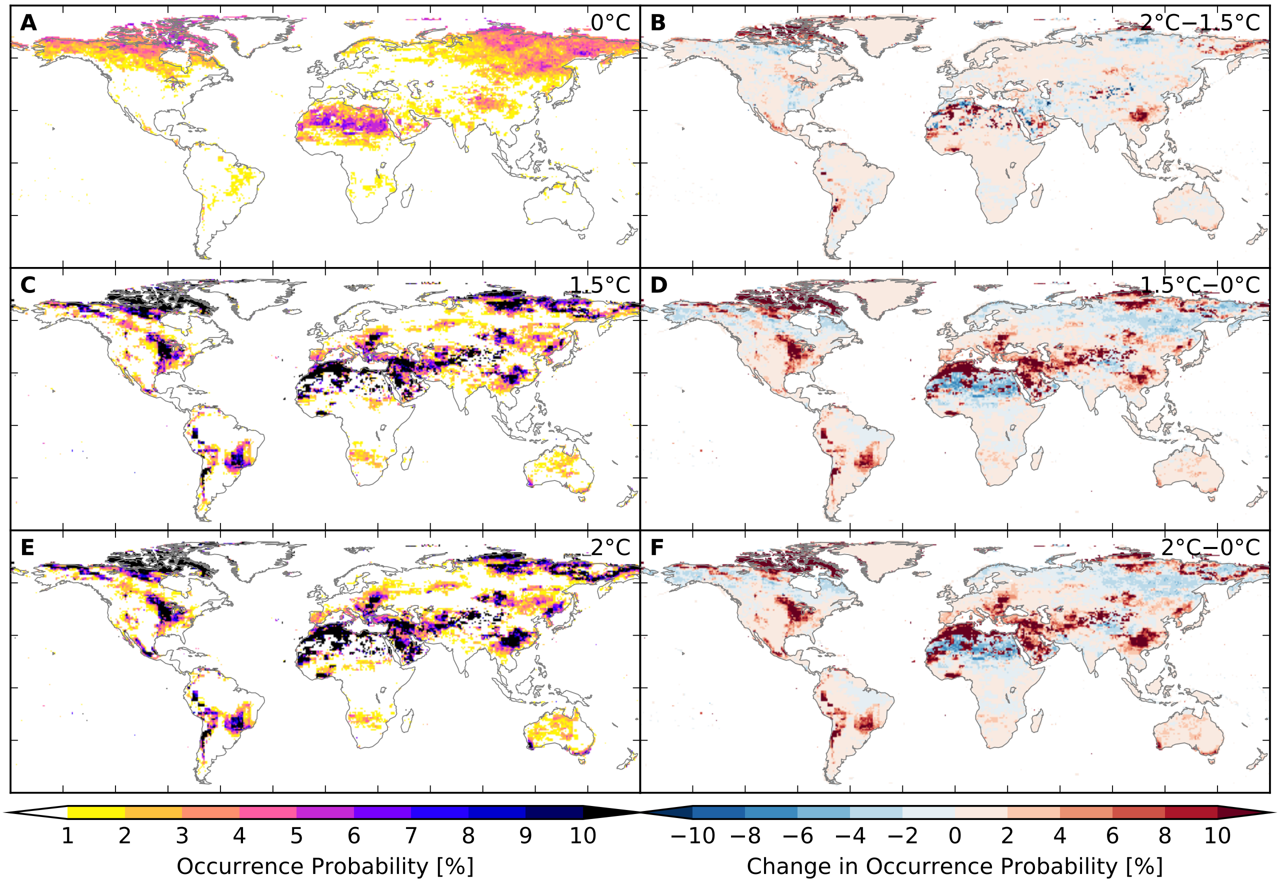

Figure S216: **Probability of occurrence of at least one drought event per year at different global warming levels (IPSL-CM5A-LR + JULES-W1).** Analogous to Figure S212.

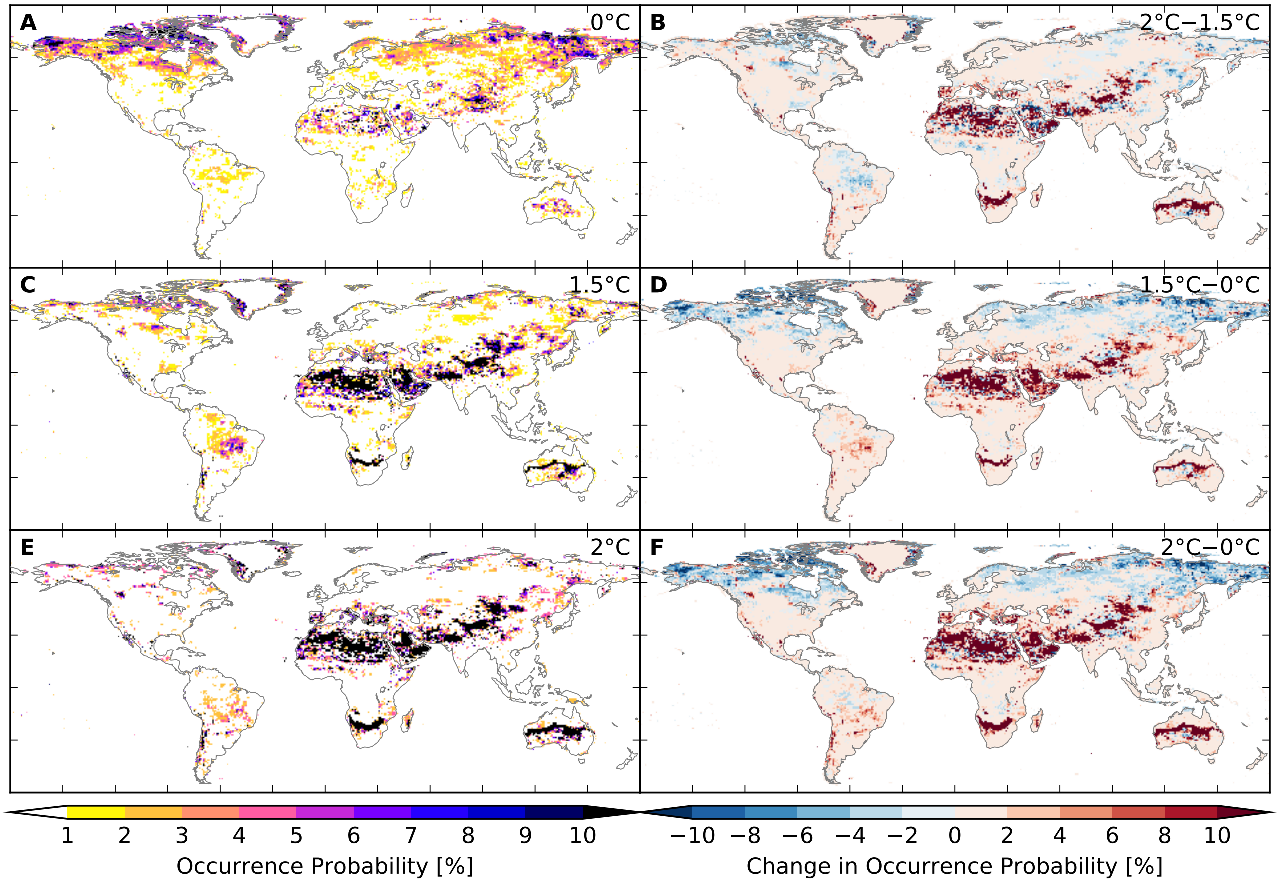

Figure S217: **Probability of occurrence of at least one drought event per year at different global warming levels (GFDL-ESM2M + LPJmL).** Analogous to Figure S212.

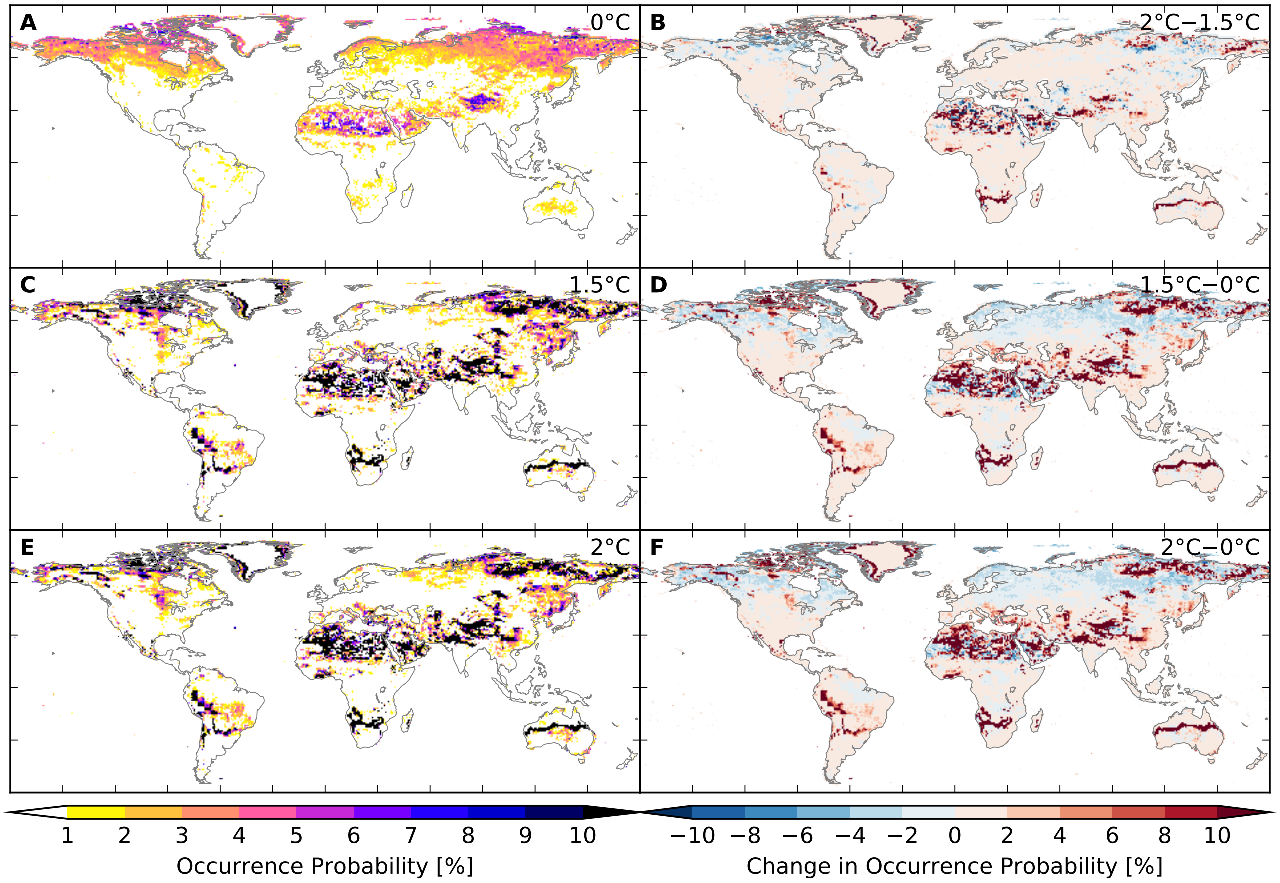

Figure S218: **Probability of occurrence of at least one drought event per year at different global warming levels (IPSL-CM5A-LR + LPJmL).** Analogous to Figure S212.

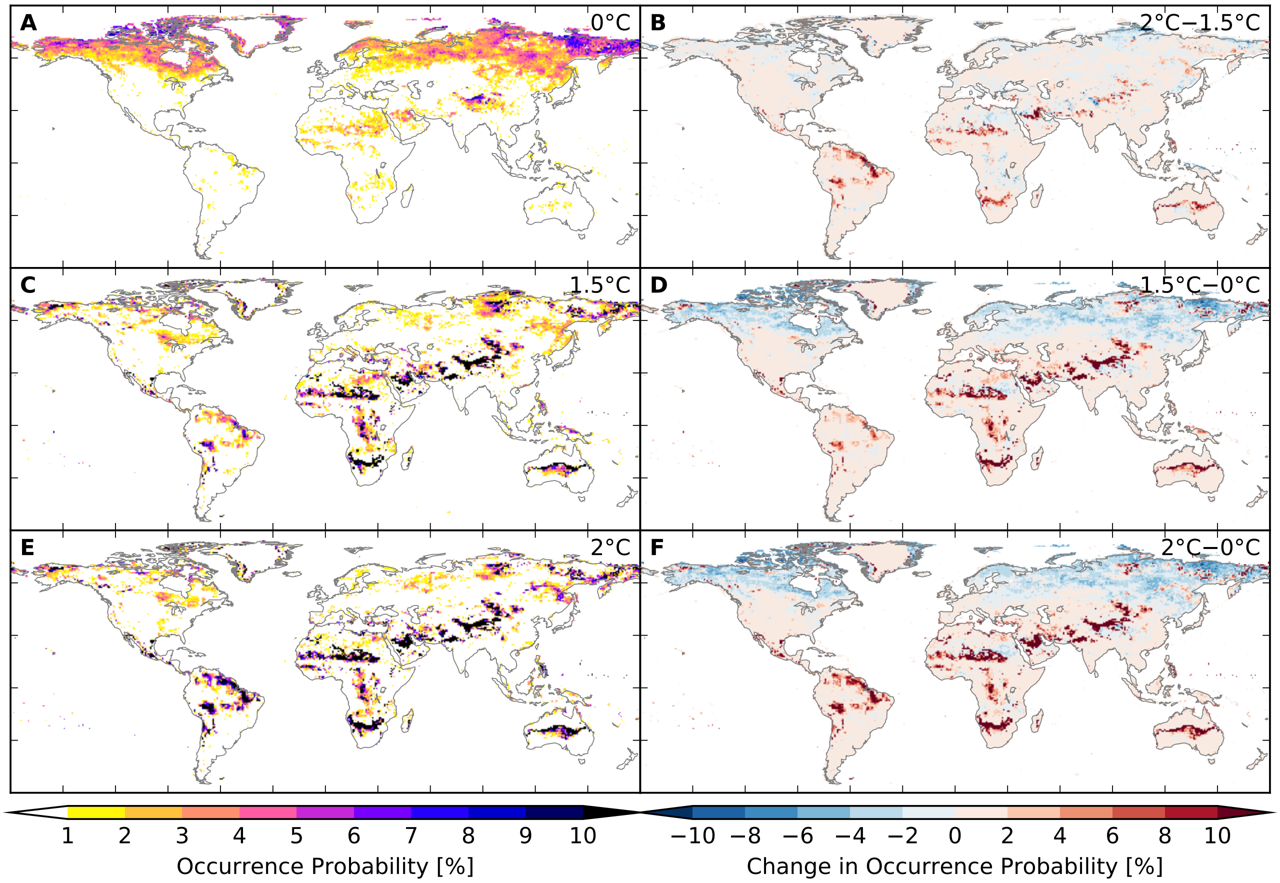

Figure S219: **Probability of occurrence of at least one drought event per year at different global warming levels (MIROC5 + LPJmL).** Analogous to Figure S212.

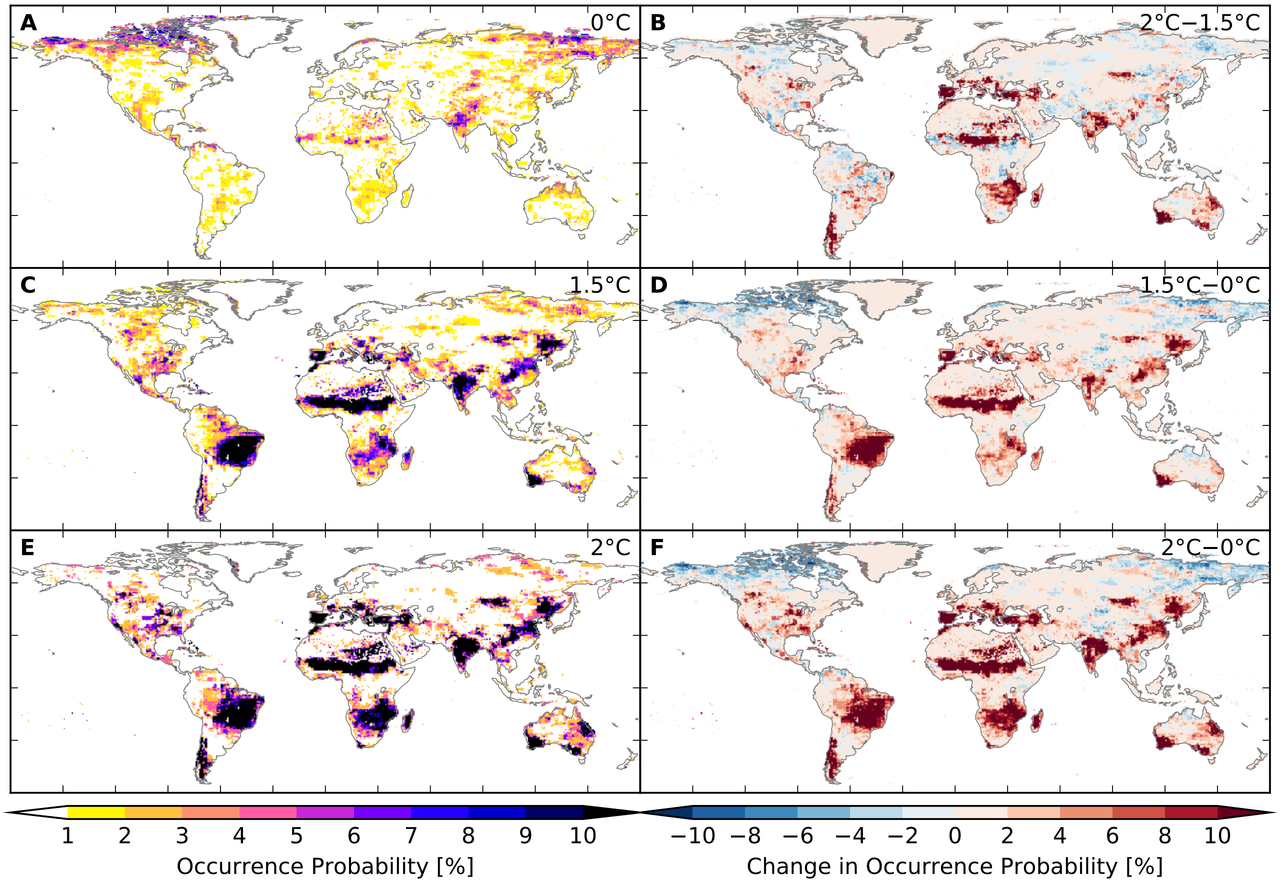

Figure S220: **Probability of occurrence of at least one drought event per year at different global warming levels (GFDL-ESM2M + MPI-HM).** Analogous to Figure S212.

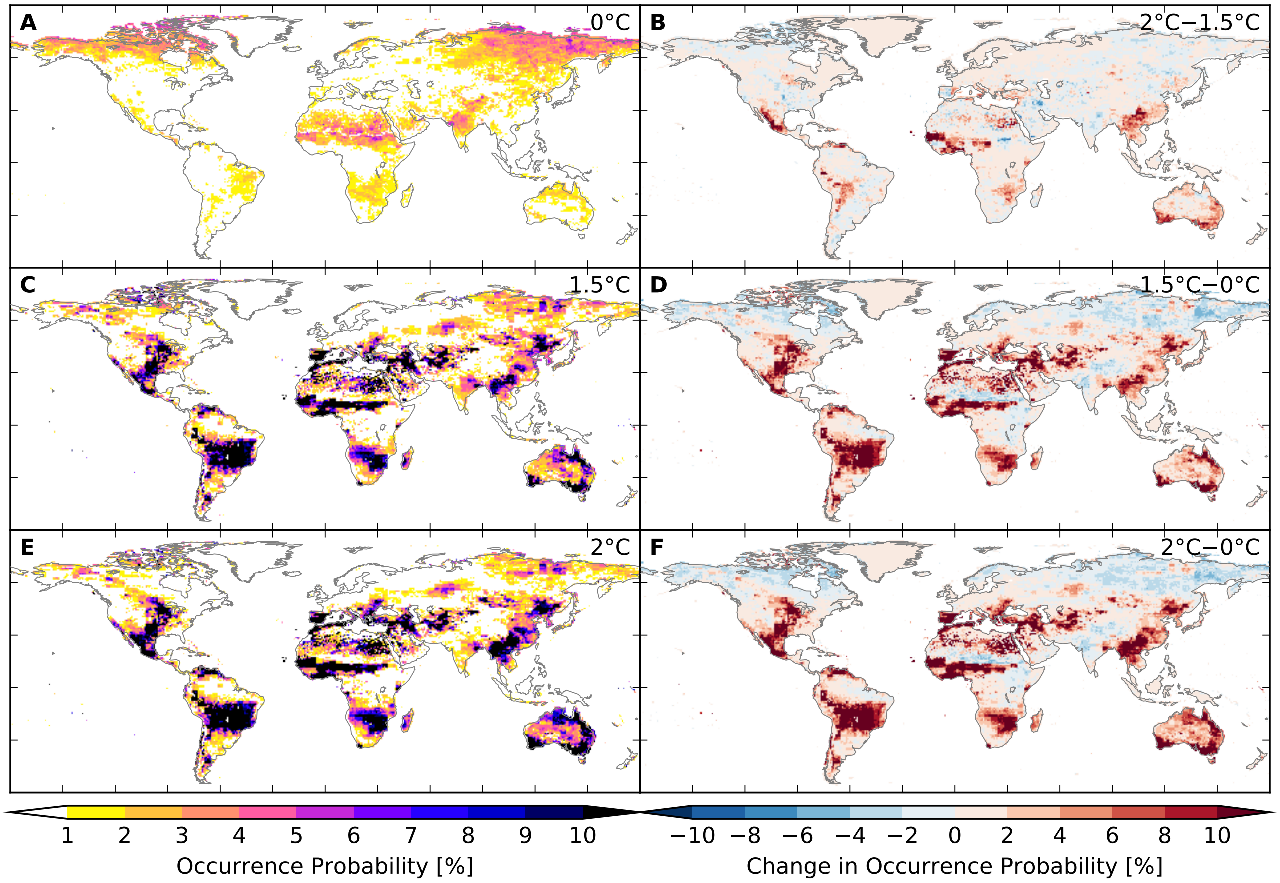

Figure S221: **Probability of occurrence of at least one drought event per year at different global warming levels (IPSL-CM5A-LR + MPI-HM).** Analogous to Figure S212.

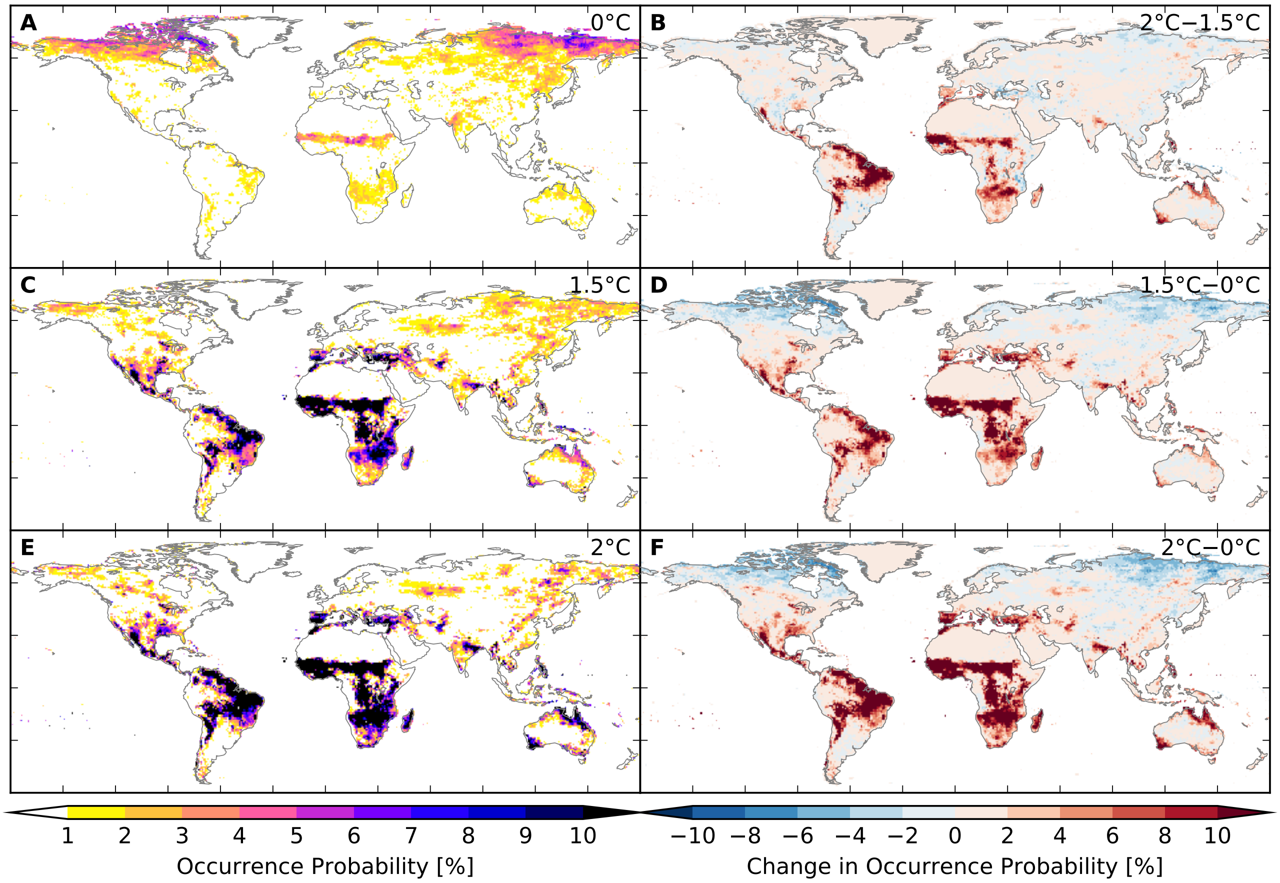

Figure S222: **Probability of occurrence of at least one drought event per year at different global warming levels (MIROC5 + MPI-HM).** Analogous to Figure S212.

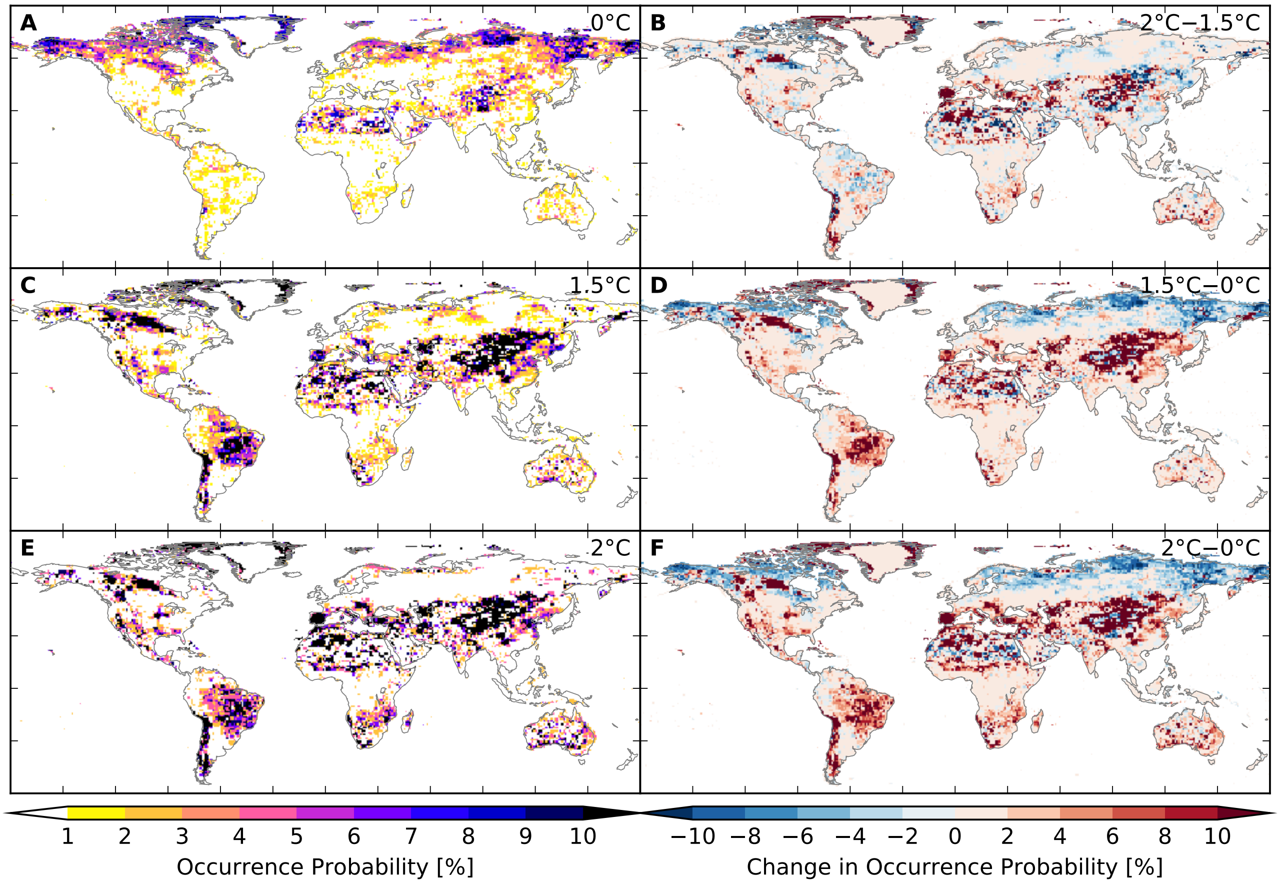

Figure S223: **Probability of occurrence of at least one drought event per year at different global warming levels (GFDL-ESM2M + ORCHIDEE).** Analogous to Figure S212.

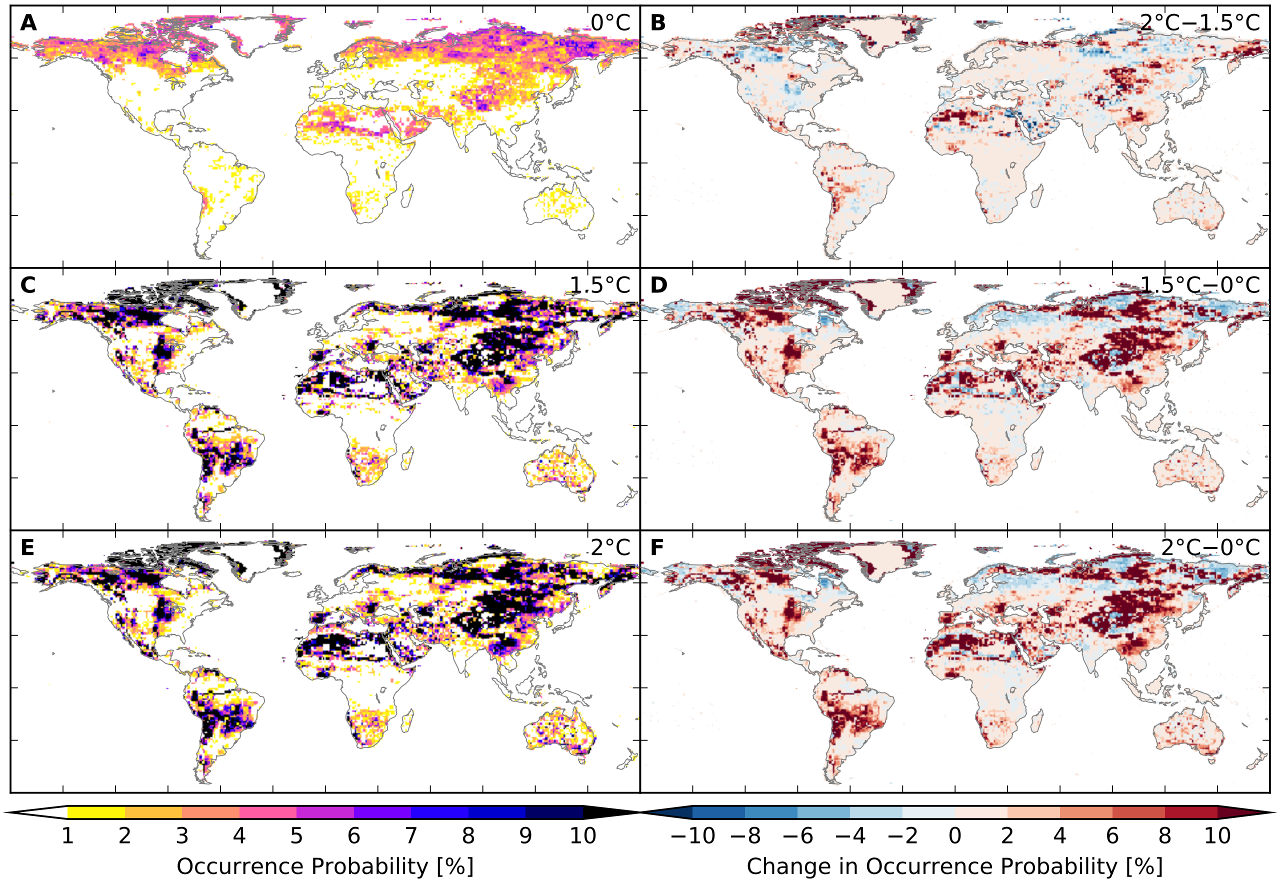

Figure S224: **Probability of occurrence of at least one drought event per year at different global warming levels (IPSL-CM5A-LR + ORCHIDEE).** Analogous to Figure S212.

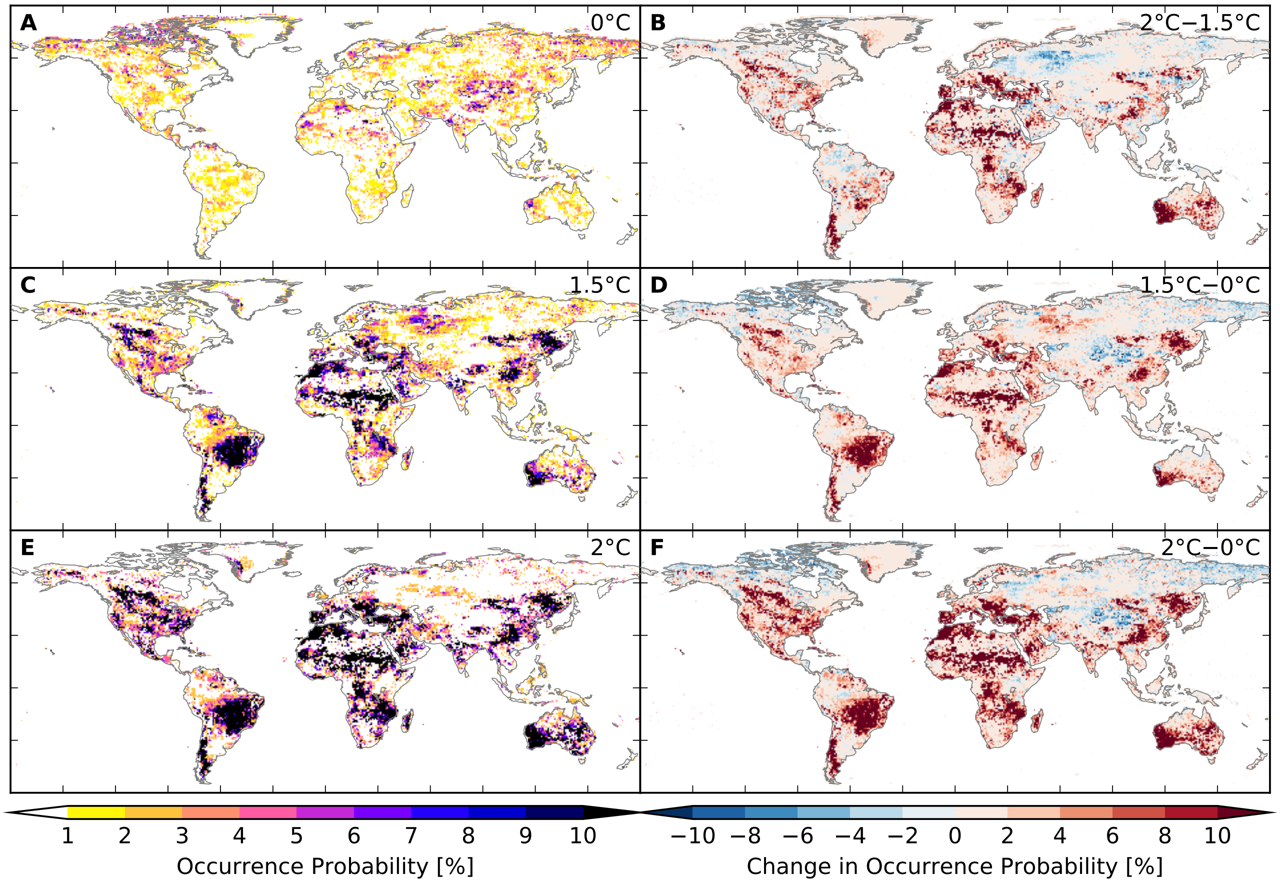

Figure S225: **Probability of occurrence of at least one drought event per year at different global warming levels (GFDL-ESM2M + PCR-GLOBWB).** Analogous to Figure S212.

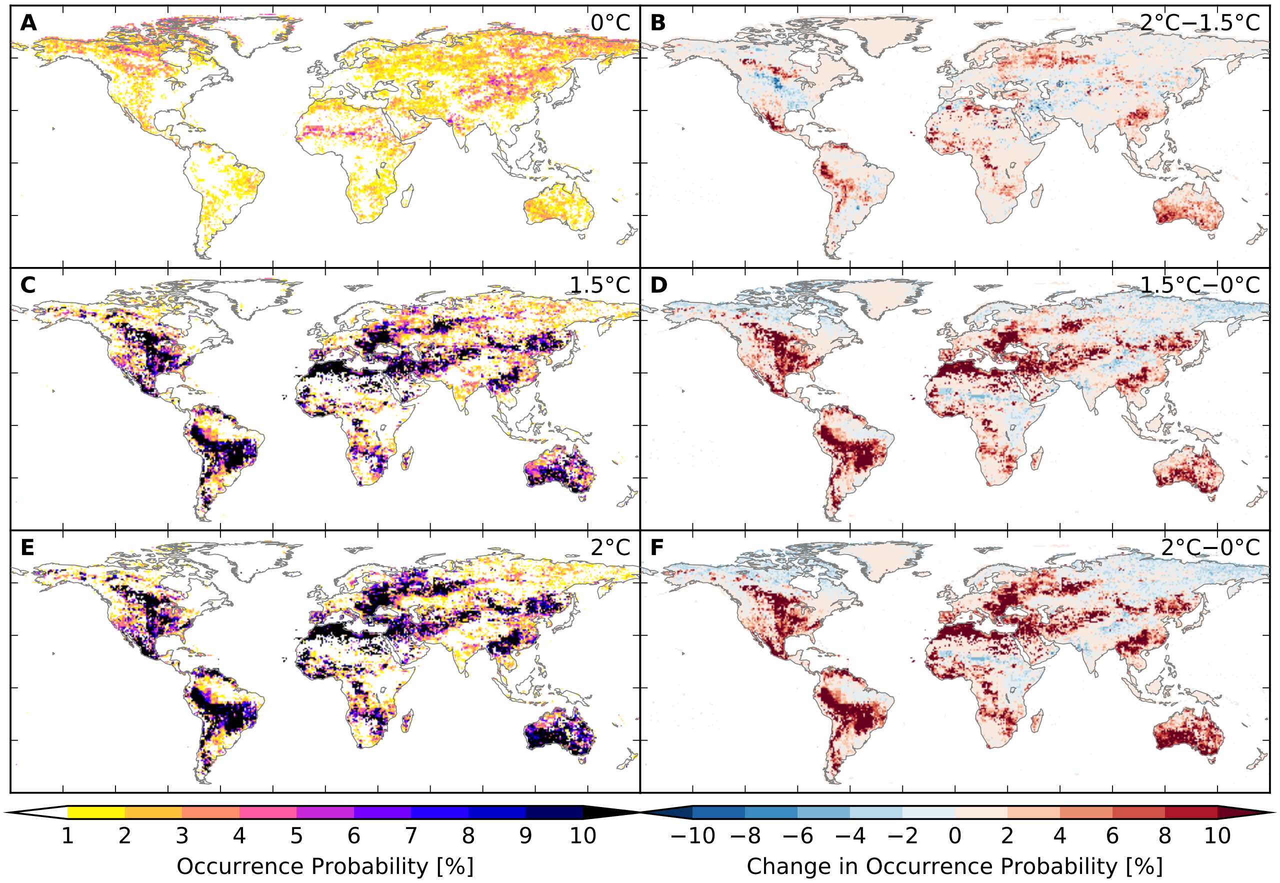

Figure S226: **Probability of occurrence of at least one drought event per year at different global warming levels (IPSL-CM5A-LR + PCR-GLOBWB).** Analogous to Figure S212.

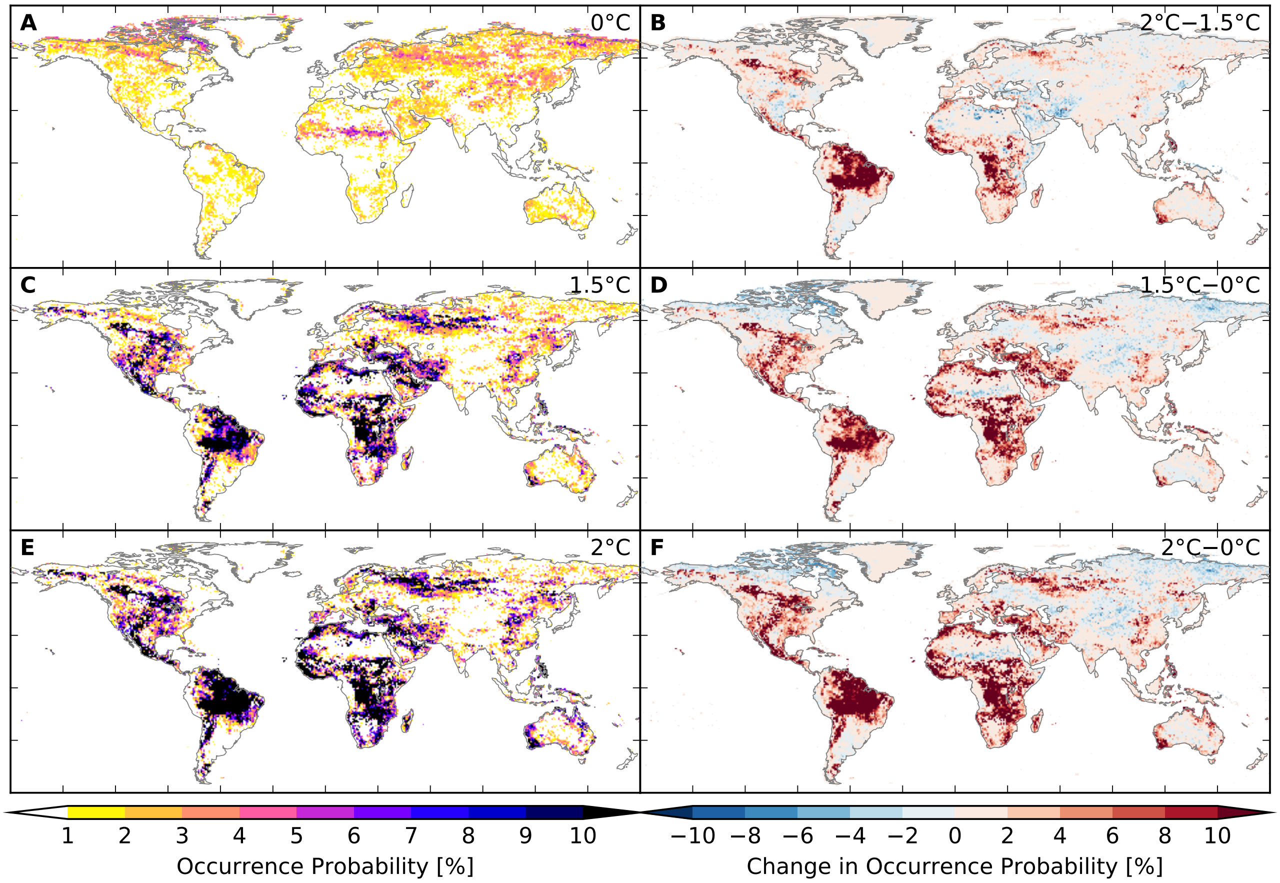

Figure S227: **Probability of occurrence of at least one drought event per year at different global warming levels (MIROC5 + PCR-GLOBWB).** Analogous to Figure S212.

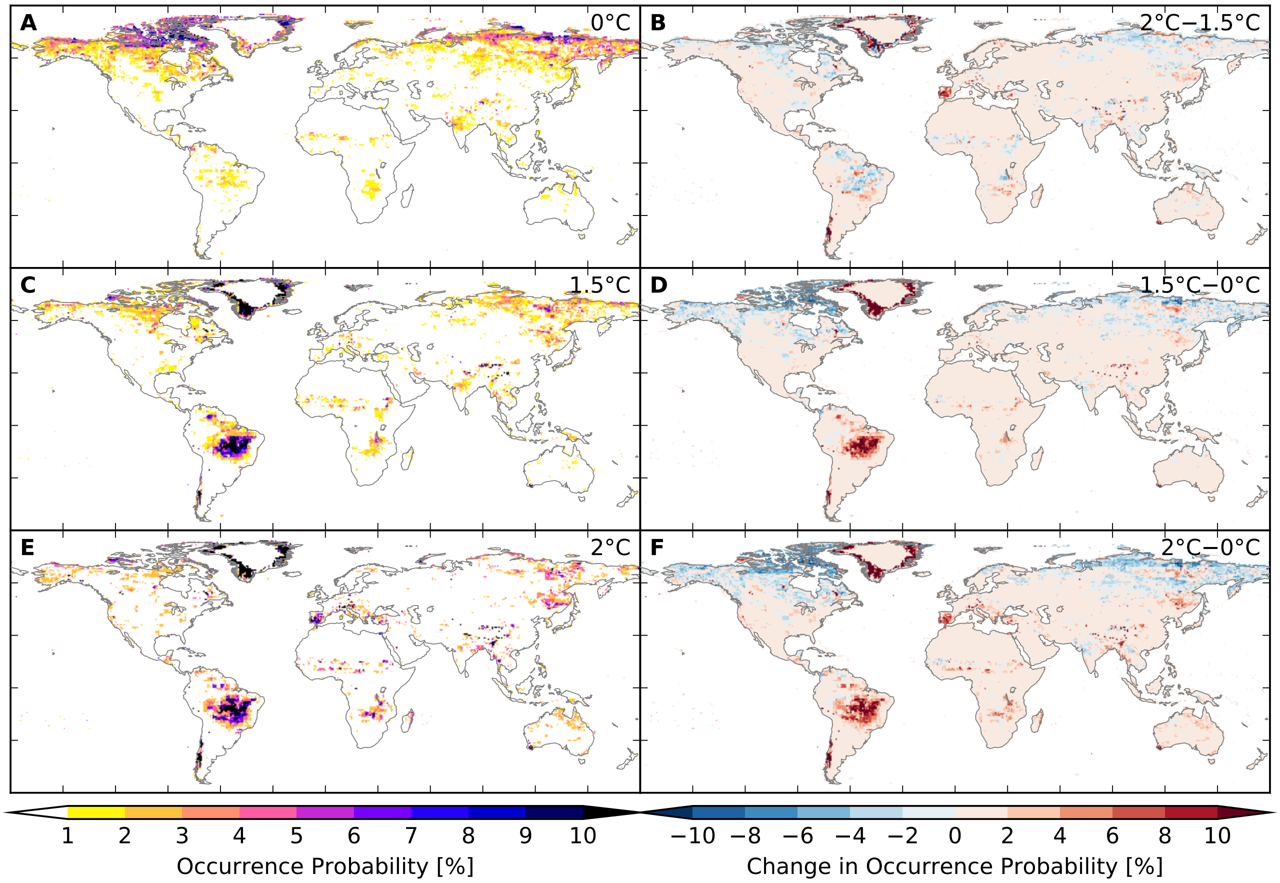

Figure S228: **Probability of occurrence of at least one drought event per year at different global warming levels (GFDL-ESM2M + WaterGAP2).** Analogous to Figure S212.

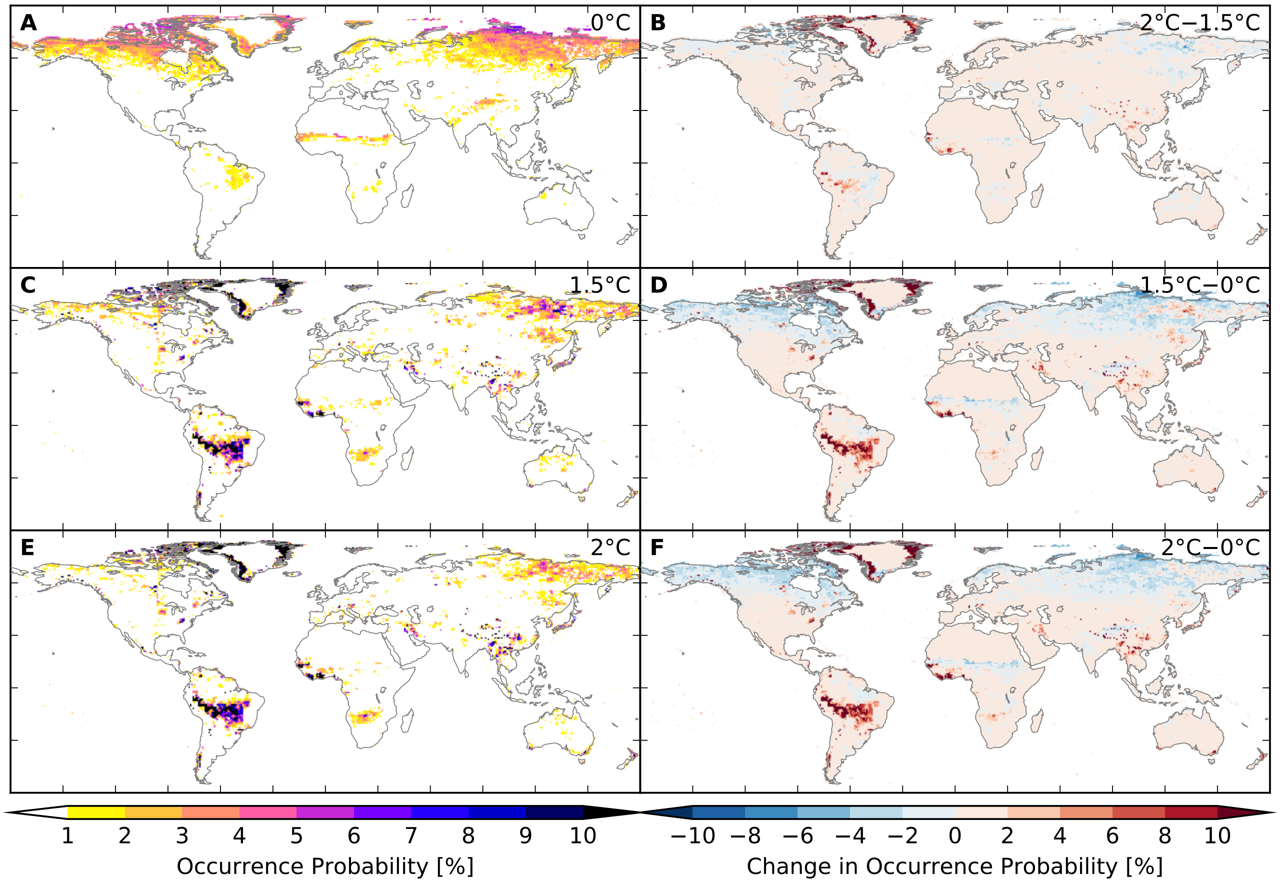

Figure S229: **Probability of occurrence of at least one drought event per year at different global warming levels (IPSL-CM5A-LR + WaterGAP2).** Analogous to Figure S212.

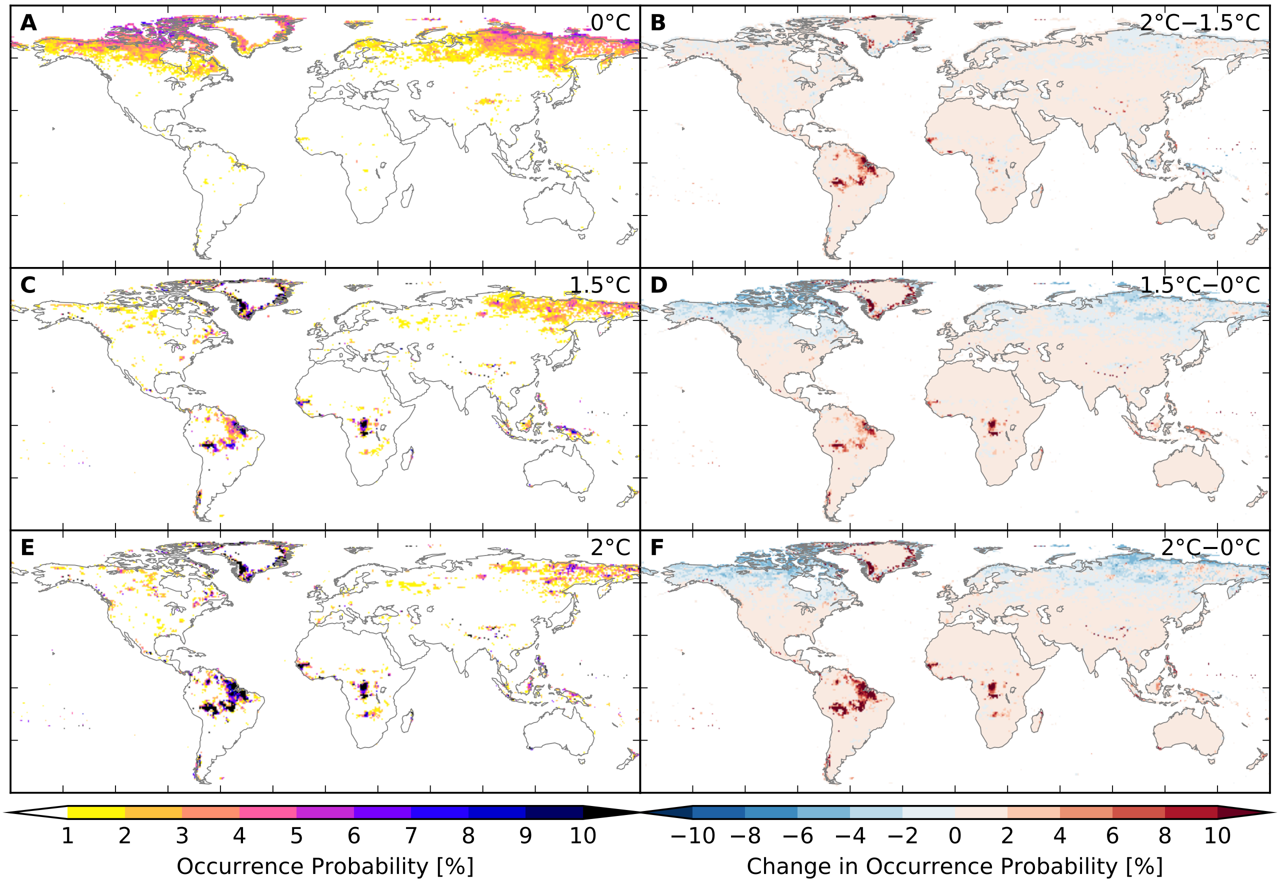

Figure S230: **Probability of occurrence of at least one drought event per year at different global warming levels (MIROC5 + WaterGAP2).** Analogous to Figure S212.

8.6 Heatwaves

Areas affected

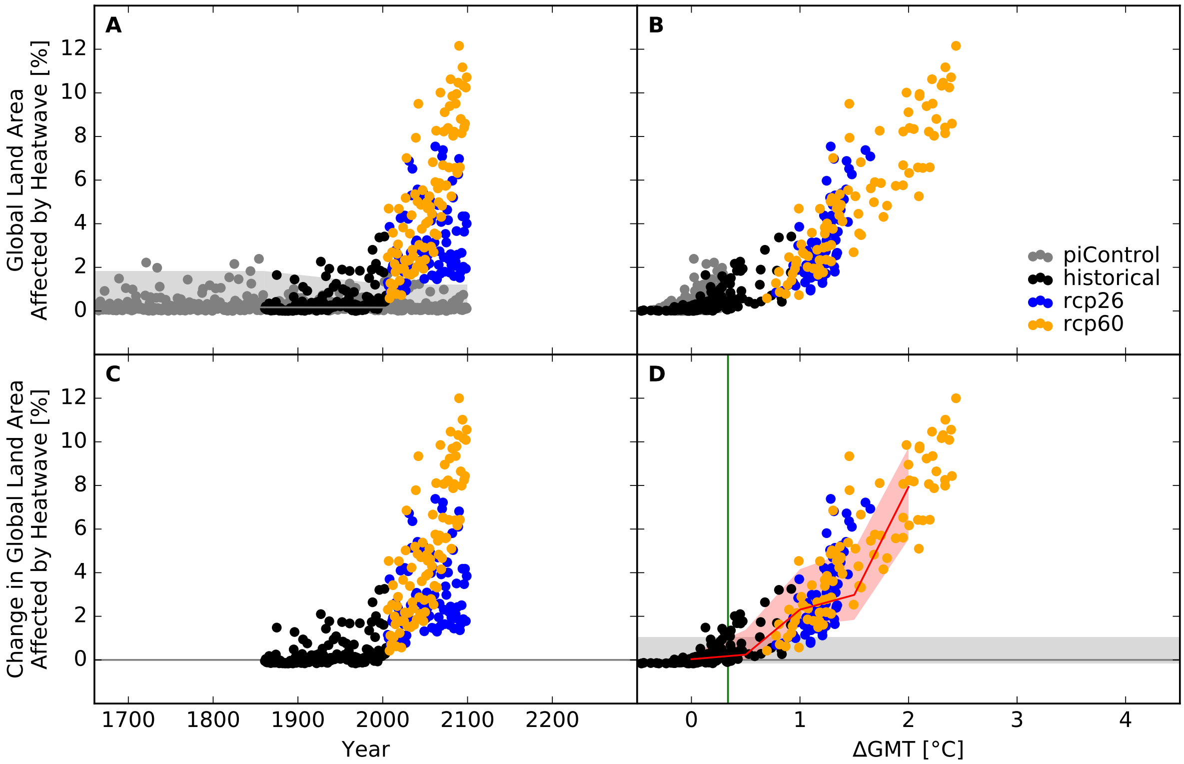

Figure S231: **Derivation of the pure effect of climate change on global land area fraction affected by heatwave events (GFDL-ESM2M + HWMId-humidex).** Panel A: Time series of annual global land area fraction affected (AFA) by heatwave events for pre-industrial climate (grey dots), historical climate (black dots), climate projections for RCP2.6 (blue dots), and RCP6.0 (orange dots). In all simulations, socio-economic conditions are varied according to the historically observed development between 1860 and 2005, and held fixed at 1860 conditions before 1860 and at 2005 conditions after 2005. Shaded areas before 1860/after 2005 represent the range from the 2nd to the 98th percentile of the distribution of the annual AFA under pre-industrial climate conditions in combination with 1860/2005 socio-economic conditions; the solid gray lines represent the respective median values; the shaded areas and solid gray line between 1860 and 2005 are linear interpolations of the respective values before 1860 and after 2005. Panel B: Data shown in Panel A plotted against the associated GCM-specific annual global mean temperature (GMT) change relative to the long-term pre-industrial mean. Panel C: Pure effect of climate change on AFA, calculated as the difference between the annual data shown in Panel A and the median of the simulations assuming pre-industrial climate conditions (solid gray line in Panel A). Panel D: Pure effect of climate change on AFA in terms of global mean temperature change, with distributions of the annual data estimated for each 1°C-wide bin of global mean temperature change that contains at least five data points, at least one data point above and at least one data point below the bin center. Areas shaded in red represent the range from the 20th to the 80th percentile around the median (solid red line) of these distributions. Areas shaded in gray represent the range from the 2nd to the 98th percentile of the zero-centered distribution of the annual AFA under pre-industrial climate and 2005 socio-economic conditions (cf. Panel A). The green vertical line represents the detection level defined as the global warming level at which a 1-in-50-years event under pre-industrial climate and 2005 socio-economic conditions becomes a 1-in-5-years event under changing climate and 2005 socio-economic conditions.

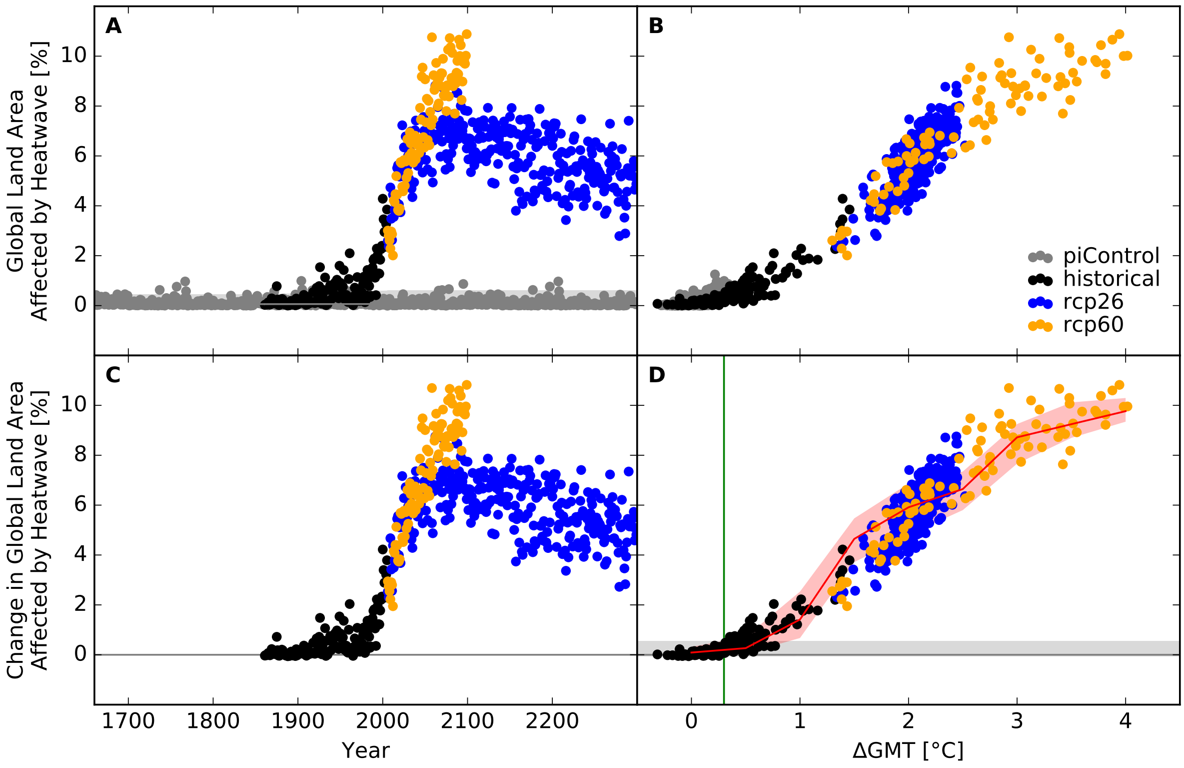

Figure S232: **Derivation of the pure effect of climate change on global land area fraction affected by heatwave events (IPSL-CM5A-LR + HWMId-humidex).** Analogous to Figure S231.

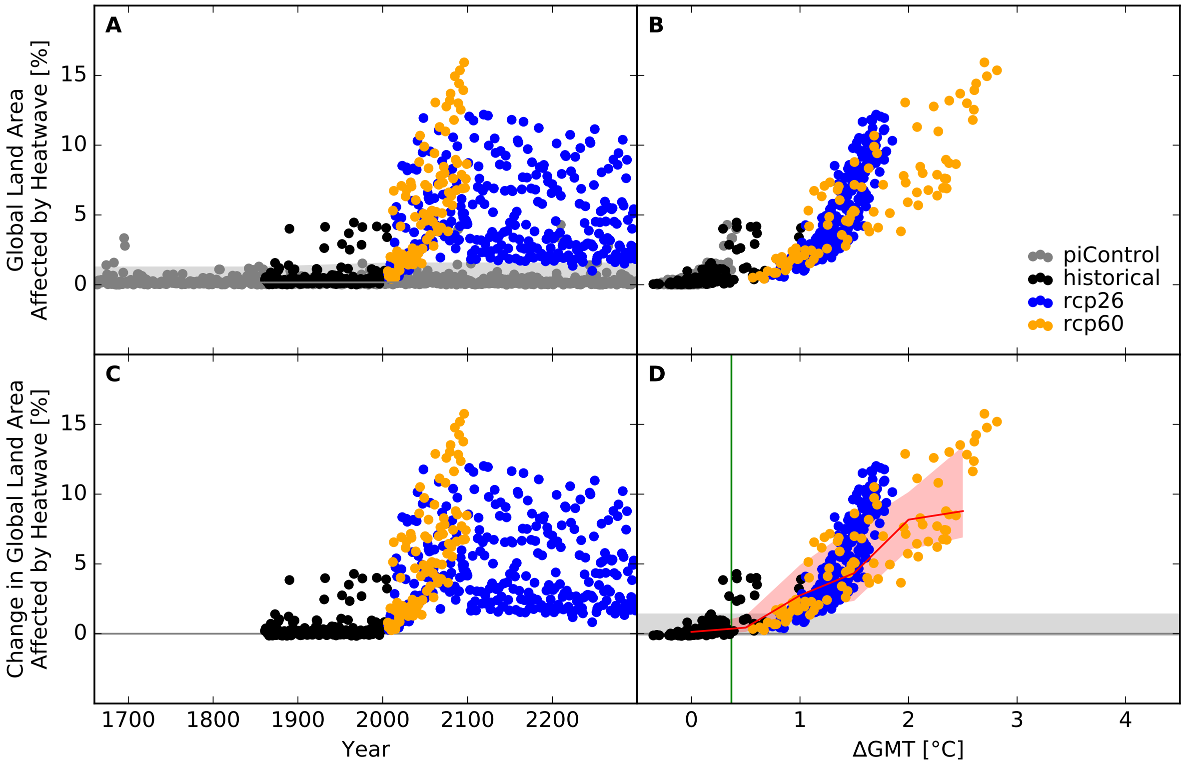

Figure S233: **Derivation of the pure effect of climate change on global land area fraction affected by heatwave events (MIROC5 + HWMId-humidex).** Analogous to Figure S231.

People exposed

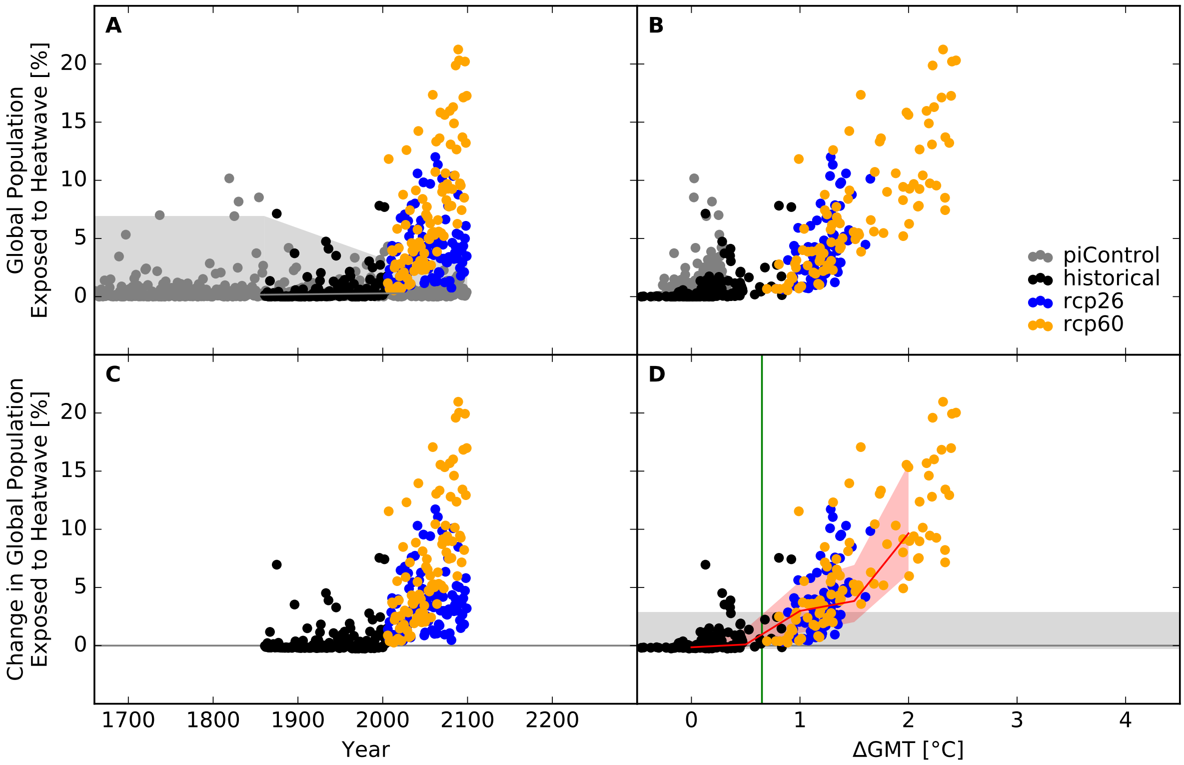

Figure S234: **Derivation of the pure effect of climate change on global population fraction affected by heatwave events (GFDL-ESM2M + HWMId-humidex).** Panel A: Time series of annual global population fraction affected (PFA) by heatwave events for pre-industrial climate (grey dots), historical climate (black dots), climate projections for RCP2.6 (blue dots), and RCP6.0 (orange dots). In all simulations, socio-economic conditions are varied according to the historically observed development between 1860 and 2005, and held fixed at 1860 conditions before 1860 and at 2005 conditions after 2005. Shaded areas before 1860/after 2005 represent the range from the 2nd to the 98th percentile of the distribution of the annual PFA under pre-industrial climate conditions in combination with 1860/2005 socio-economic conditions; the solid gray lines represent the respective median values; the shaded areas and solid gray line between 1860 and 2005 are linear interpolations of the respective values before 1860 and after 2005. Panel B: Data shown in Panel A plotted against the associated GCM-specific annual global mean temperature (GMT) change relative to the long-term pre-industrial mean. Panel C: Pure effect of climate change on PFA, calculated as the difference between the annual data shown in Panel A and the median of the simulations assuming pre-industrial climate conditions (solid gray line in Panel A). Panel D: Pure effect of climate change on PFA in terms of global mean temperature change, with distributions of the annual data estimated for each 1°C-wide bin of global mean temperature change that contains at least five data points, at least one data point above and at least one data point below the bin center. Areas shaded in red represent the range from the 20th to the 80th percentile around the median (solid red line) of these distributions. Areas shaded in gray represent the range from the 2nd to the 98th percentile of the zero-centered distribution of the annual PFA under pre-industrial climate and 2005 socio-economic conditions (cf. Panel A). The green vertical line represents the detection level defined as the global warming level at which a 1-in-50-years event under pre-industrial climate and 2005 socio-economic conditions becomes a 1-in-5-years event under changing climate and 2005 socio-economic conditions.

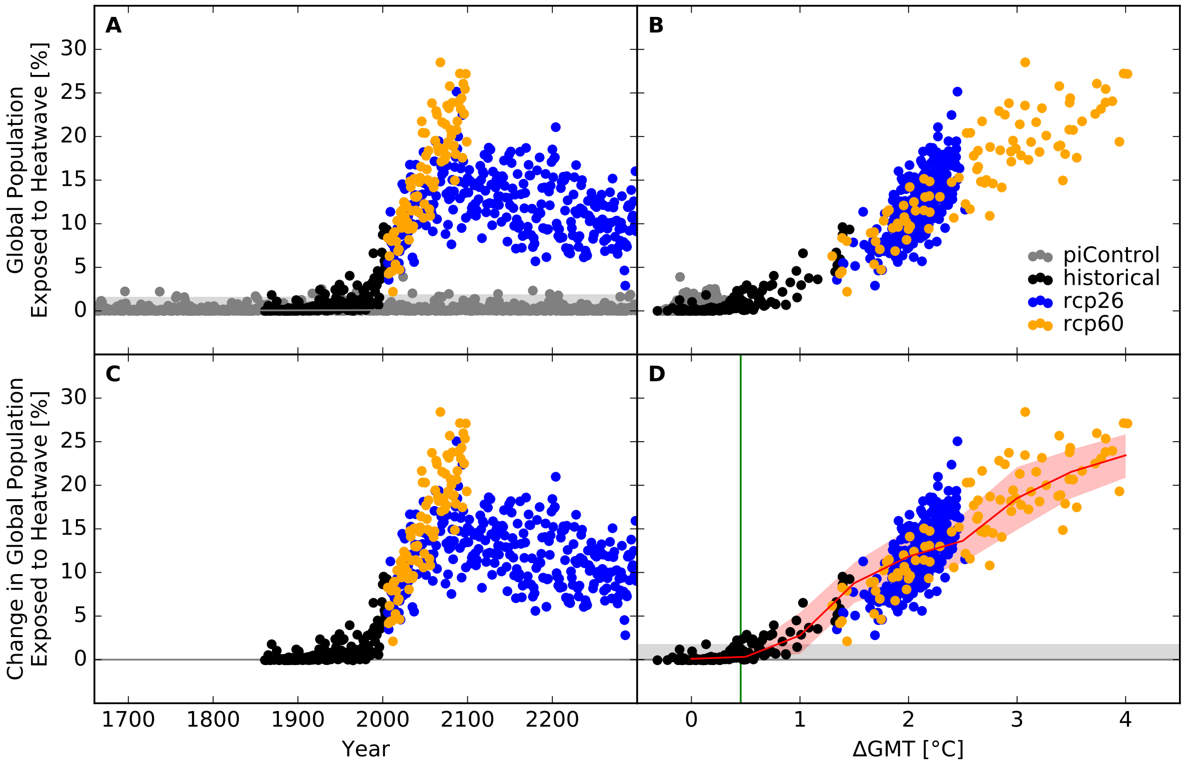

Figure S235: **Derivation of the pure effect of climate change on global population fraction affected by heatwave events (IPSL-CM5A-LR + HWMId-humidex).** Analogous to Figure S234.

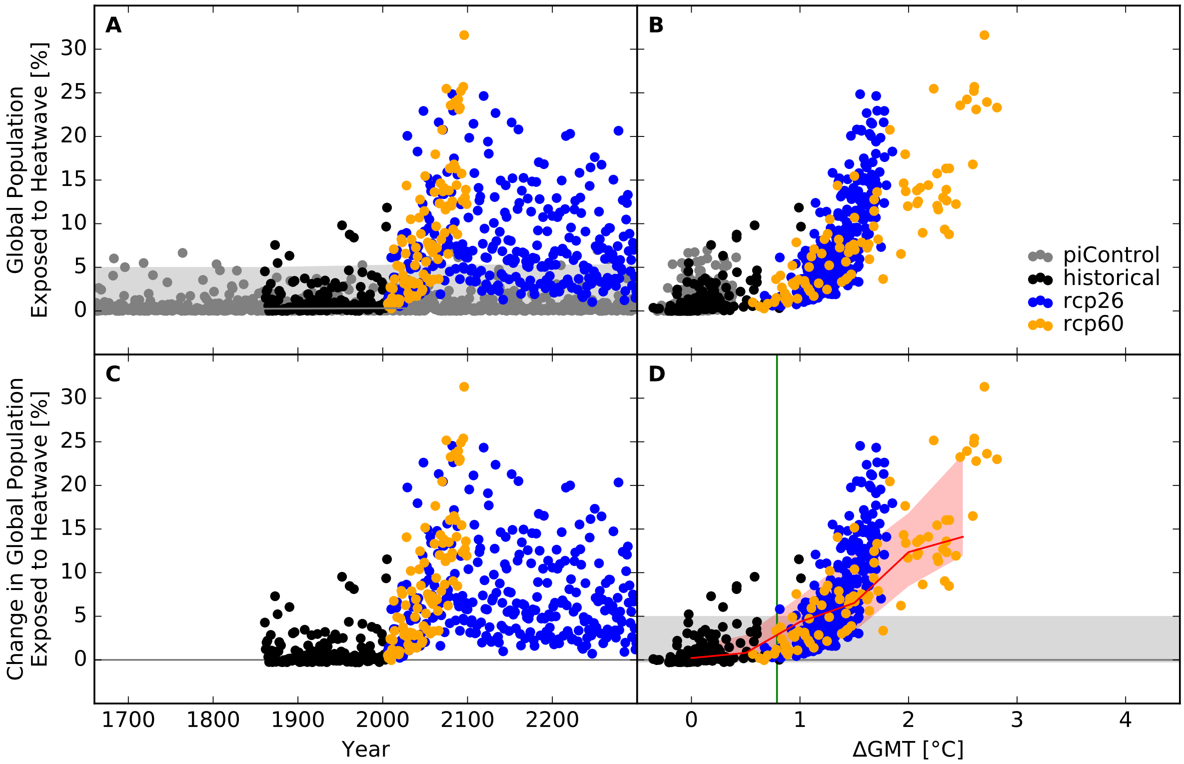

Figure S236: **Derivation of the pure effect of climate change on global population fraction affected by heatwave events (MIROC5 + HWMId-humidex).** Analogous to Figure S234.

Occurrence probability at grid scale

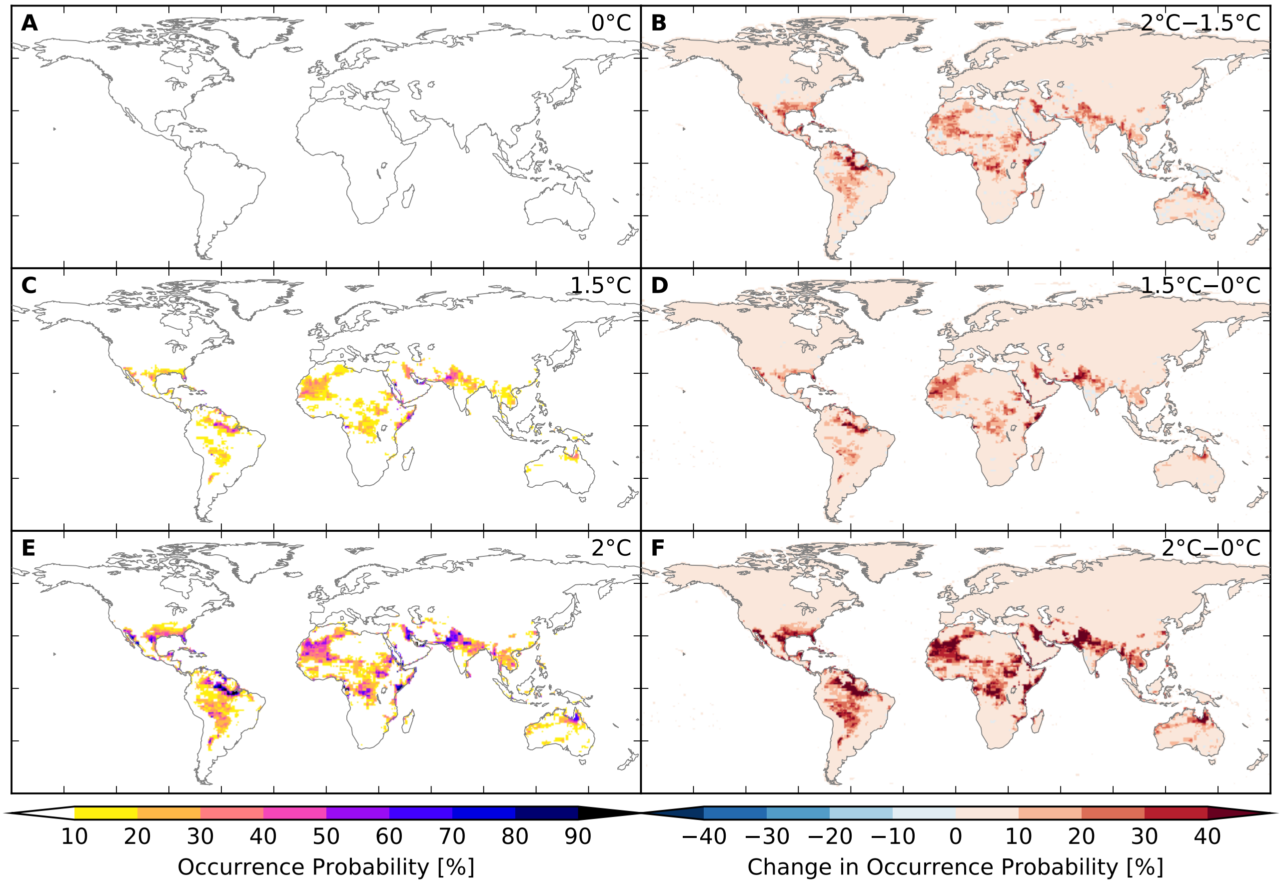

Figure S237: **Probability of occurrence of at least one heatwave event per year at different global warming levels (GFDL-ESM2M + HWMId-humidex).** Panels A, C, E: Probabilities at 0°C, 1.5°C, 2°C global mean temperature (GMT) change relative to the long-term pre-industrial mean GMT, respectively. Panels B, D, F: Differences between probabilities at GMT change levels of 2°C and 1.5°C, 1.5°C and 0°C, 2°C and 0°C, respectively.

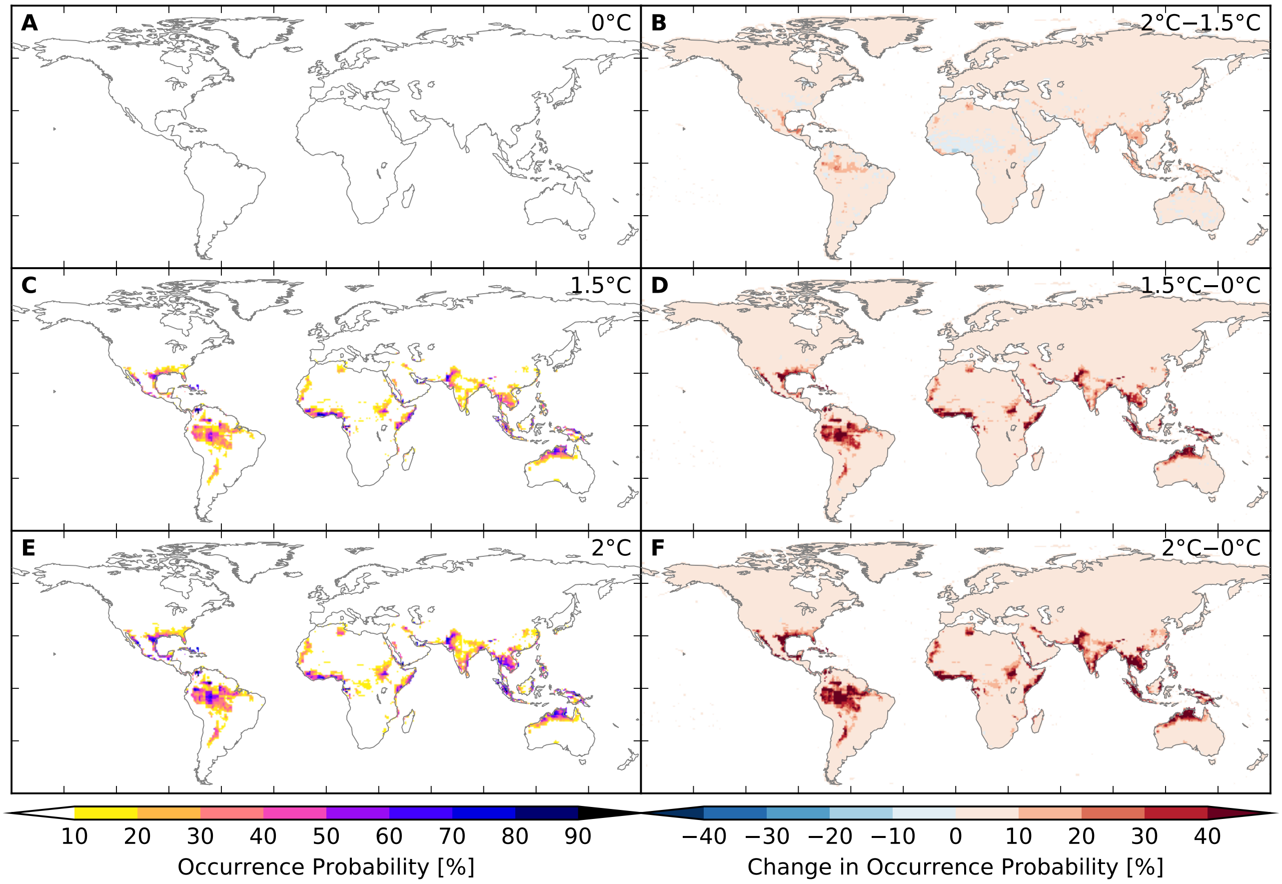

Figure S238: **Probability of occurrence of at least one heatwave event per year at different global warming levels (IPSL-CM5A-LR + HWMId-humidex).** Analogous to Figure S237.

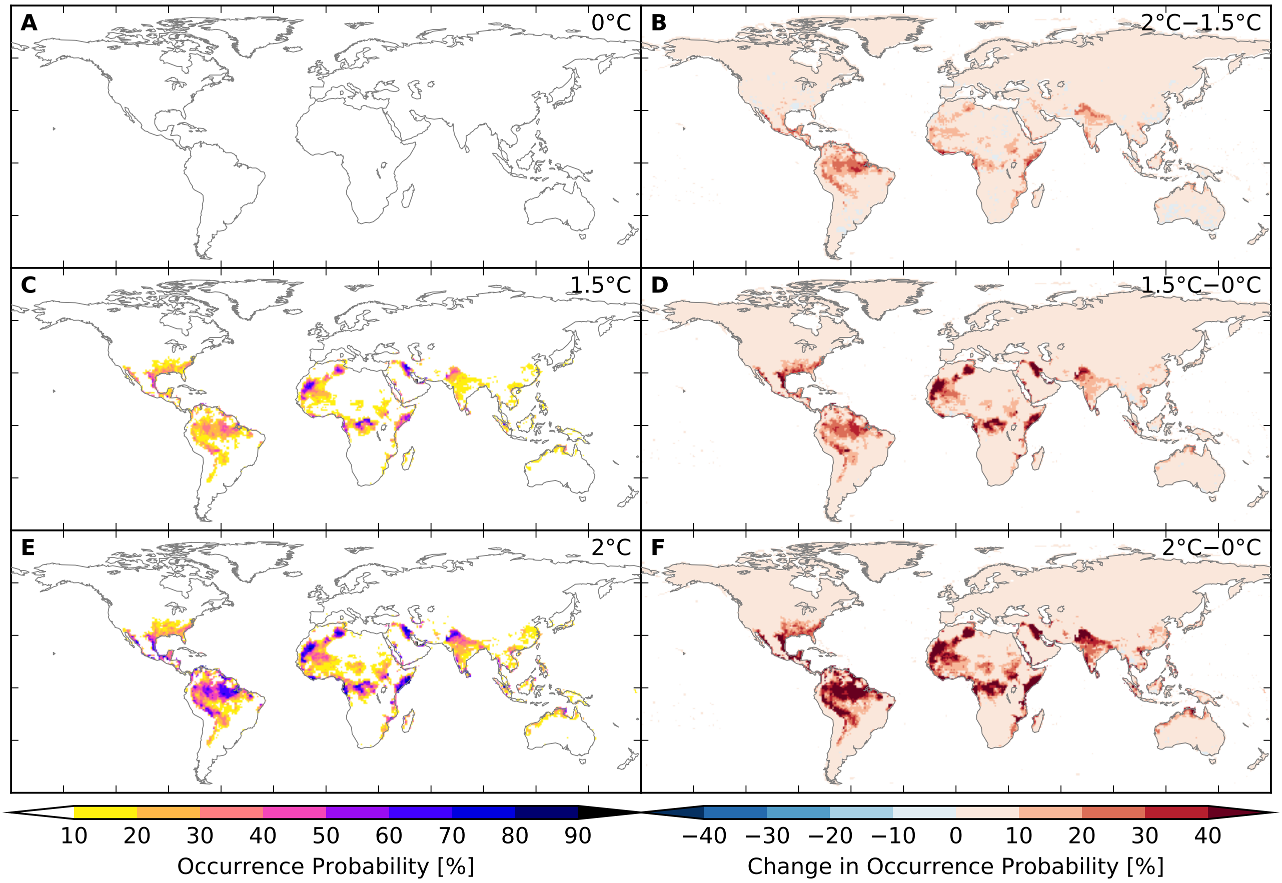

Figure S239: **Probability of occurrence of at least one heatwave event per year at different global warming levels (MIROC5 + HWMId-humidex).** Analogous to Figure S237.

References

[1] *Humidex: A Method of Quantifying Human Discomfort Due to Excessive Heat and Humidity.* Environment Canada.

[2] *Hydrological drought—a study across Europe.* PhD thesis, Albert- Ludwigs-Universität, Freiburg, Germany, year = 2001, doi = https://doi.org/10.1016/j.pce.2004.09.018, url = http://www.sciencedirect.com/science/article/pii/S1474706504001676, author = Stahl K., type = PhD dissertation,.

[3] The effect of GCM biases on global runoff simulations of a land surface model. *Hydrology and Earth System Sciences Discussions*, (April):1–43, 2017.

[4] Hannes Müller Schmied, Linda Adam, Stephanie Eisner, Gabriel Fink, Martina Florke, Hyungjun Kim, Taikan Oki, Felix Theodor Portmann, Robert Reinecke, Claudia Riedel, Qi Song, Jing Zhang, and Petra Doll. Variations of global and continental water balance components as impacted by climate forcing uncertainty and human water use. *Hydrology and Earth System Sciences*, 20(7):2877–2898, 2016.

[5] S. Archibald, R.J. Scholes, D.P. Roy, G. Roberts, and L. Boschetti. Southern african fire regimes as revealed by remote sensing, 2010.

[6] Sally Archibald, Caroline E. R. Lehmann, Jose L. Gómez-Dans, and Ross A. Bradstock. Defining pyromes and global syndromes of fire regimes. *Proceedings of the National Academy of Sciences*, 110(16):6442–6447, 2013.

[7] Douglas Bates, Martin Mächler, Ben Bolker, and Steve Walker. Fitting linear mixed-effects models using lme4. *Journal of Statistical Software*, 67(1):1–48, 2015.

[8] M. J. Best, M. Pryor, D. B. Clark, G. G. Rooney, R .L. H. Essery, C. B. Ménard, J. M. Edwards, M. A. Hendry, A. Porson, N. Gedney, L. M. Mercado, S. Sitch, E. Blyth, O. Boucher, P. M. Cox, C. S. B. Grimmond, and R. J. Harding. The Joint UK Land Environment Simulator (JULES), model description – Part 1: Energy and water fluxes. *Geoscientific Model Development*, 4(3):677–699, sep 2011.

[9] Alberte Bondeau, Pascalle c. Smith, Sönke Zaehle, Sibyll Schaphoff, Wolfgang Lucht, Wolfgang Cramer, Dieter Gerten, Hermann Lotze-Campen, Christoph Müller, Markus Reichstein, and Benjamin Smith. Modelling the role of agriculture for the 20th century global terrestrial carbon balance. *Global Change Biology*, 13(3):679–706, 2007.

[10] David M. J. S. Bowman, Jennifer K. Balch, Paulo Artaxo, William J. Bond, Jean M. Carlson, Mark A. Cochrane, Carla M. D'Antonio, Ruth S. DeFries, John C. Doyle, Sandy P. Harrison, Fay H. Johnston, Jon E. Keeley, Meg A. Krawchuk, Christian A. Kull, J. Brad Marston, Max A. Moritz, I. Colin Prentice, Christopher I. Roos, Andrew C. Scott, Thomas W. Swetnam, Guido R. van der Werf, and Stephen J. Pyne. Fire in the earth system. *Science*, 324(5926):481–484, 2009.

[11] David N. Bresch. Shaping Climate Resilient Development: Economics of Climate Adaptation. In *Climate Change Adaptation Strategies – An Upstream-downstream Perspective*, pages 241–254. Springer International Publishing, Cham, 2016.

[12] A. J. Challinor, J. Watson, D. B. Lobell, S. M. Howden, D. R. Smith, and N. Chhetri. A meta-analysis of crop yield under climate change and adaptation. *Nature Clim. Change*, 4(4):287–291, 2014.

[13] Aiguo Dai. Increasing drought under global warming in observations and models. *Nature Clim. Change*, 3:52–58, 2013.

[14] Warnant P Henrot A Favre E Ouberdous M Dury M, Hambuckers A and François L. Responses of european forest ecosystems to 21st century climate: assessing changes in interannual variability and fire intensity. *iForest – Biogeosciences and Forestry*, (2):82–99, 2011.

[15] J. Elliott, C. Müller, D. Deryng, J. Chryssanthacopoulos, K. J. Boote, M. Büchner, I. Foster, M. Glotter, J. Heinke, T. Iizumi, R. C. Izaurralde, N. D. Mueller, D. K. Ray, C. Rosenzweig, A. C. Ruane, and J. Sheffield. The global gridded crop model intercomparison: data and modeling protocols for phase 1 (v1.0). *Geoscientific Model Development*, 8(2):261–277, 2015.

[16] Kerry Emanuel. Downscaling CMIP5 climate models shows increased tropical cyclone activity over the 21st century. *Proceedings of the National Academy of Sciences of the United States of America*, 110(30):12219–24, jul 2013.

[17] Kerry Emanuel, Ragoth Sundararajan, and John Williams. Hurricanes and Global Warming: Results from Downscaling IPCC AR4 Simulations. *Bulletin of the American Meteorological Society*, 89(3):347–367, mar 2008.

[18] C. Folberth, J. Elliott, C. Müller, J. Balkovic, J. Chryssanthacopoulos, R. C. Izaurralde, C. D. Jones, N. Khabarov, W. Liu, A. Reddy, E. Schmid, R. Skalský, H. Yang, A. Arneth, P. Ciais, D. Deryng, P. J. Lawrence, S. Olin, T. A. M. Pugh, A. C. Ruane, and X. Wang. Uncertainties in global crop model frameworks: effects of cultivar distribution, crop management and soil handling on crop yield estimates. *Biogeosciences Discussions*, 2016:1–30, 2016.

[19] Christian Folberth, Thomas Gaiser, Karim C. Abbaspour, Rainer Schulin, and Hong Yang. Regionalization of a large-scale crop growth model for sub-saharan africa: Model setup, evaluation, and estimation of maize yields. *Agriculture, Ecosystems & Environment*, 151(Supplement C):21 – 33, 2012.

[20] Canadian Center for Occupational Health and Safety. Humidex Rating and Work. `https://www.ccohs.ca/oshanswers/phys_agents/humidex.html`, 2017. [retrieved on 10/27/2017].

[21] William M. Frank, George S. Young, William M. Frank, and George S. Young. The Interannual Variability of Tropical Cyclones. *Monthly Weather Review*, 135(10):3587–3598, oct 2007.

[22] K Frieler, R Betts, E Burke, P Ciais, S Denvil, D Deryng, K Ebi, T Eddy, K Emanuel, J Elliot, E Galbraith, S Gosling, K Halladay, F Hatermann, T Hickler, J Hinkel, V Huber, C Jones, V Krysanova, S Lange, H Lotze, H Lotze-Campen, M Mengel, I Mouratiadou, H Müller Schmied, S Ostberg, F Piontek, A Popp, C Reyer, J Schewe, M Stevanovic, K Suzuki, T andThonicke, H Tian, D. T. Tittensor, R Vautard, M van Vliet, L Warszawski, and F Zhao. Assessing the impacts of 1.5°C global warming - simulation protocol of the Inter-Sectoral Model Intercomparison Project (ISIMIP2b). *Geoscientific Model Development*, (October):submitted, 2016.

[23] R. Sahajpal S. Frolking et al. G. Hurtt, L. Chini. Harmonization of global land-use change and management for the period 850-2100. *Geoscientific Model Development*, in prep.

[24] T. Geiger, K. Frieler, and D. N. Bresch. A global historical data set of tropical cyclone exposure (tce-dat). *Earth System Science Data Discussions*, 2017:1–15, 2017.

[25] Tobias Geiger, Katja Frieler, and Anders Levermann. High-income does not protect against hurricane losses. *Environmental Research Letters*, 11(8):084012, aug 2016.

[26] A. Gettelman, D. N. Bresch, C. C. Chen, J. E. Truesdale, and J. T. Bacmeister. Projections of future tropical cyclone damage with a high-resolution global climate model. *Climatic Change*, pages 1–11, 2017.

[27] Peter H. Gleick. Basic water requirements for human activities - meeting basic needs. *Water International*, 21(2):83–92, 1996.

[28] M Guimberteau, A Ducharne, P Ciais, J P Boisier, S Peng, M De Weirdt, H Verbeeck, and Environmental Biology. Testing conceptual and physically based soil hydrology schemes against observations for the Amazon Basin. *Geoscientific Model Development*, 7(3):1115–1136, 2014.

[29] S. Hagemann and L. Dümenil Gates. Improving a subgrid runoff parameterization scheme for climate models by the use of high resolution data derived from satellite observations. *Climate Dynamics*, 21(3-4):349–359, sep 2003.

[30] N. Hanasaki, S. Yoshikawa, Y. Pokhrel, and S. Kanae. A global hydrological simulation to specify the sources of water used by humans. *Hydrology and Earth System Sciences Discussions*, 2017:1–53, 2017.

[31] Yukiko Hirabayashi, Shinjiro Kanae, Seita Emori, Taikan Oki, and Masahide Kimoto. Global projections of changing risks of floods and droughts in a changing climate. *Hydrological Sciences Journal*, 53(4):754–772, 2008.

[32] Yukiko Hirabayashi, Roobavannan Mahendran, Sujan Koirala, Lisako Konoshima, Dai Yamazaki, Satoshi Watanabe, Hyungjun Kim, and Shinjiro Kanae. Global flood risk under climate change. *Nature Climate Change*, 3(9):816–821, 2013.

[33] Greg Holland. A Revised Hurricane Pressure–Wind Model. *Monthly Weather Review*, 136(9):3432–3445, 2008.

[34] Akihiko Ito and Motoko Inatomi. Water-use efficiency of the terrestrial biosphere: A model analysis focusing on interactions between the global carbon and water cycles. *Journal of Hydrometeorology*, 13(2):681–694, 2012.

[35] Akihiko Ito and Takehisa Oikawa. A simulation model of the carbon cycle in land ecosystems (sim-cycle): a description based on dry-matter production theory and plot-scale validation. *Ecological Modelling*, 151(2):143 – 176, 2002.

[36] J. R. Wallis J. R. M. Hosking. *Regional Frequency Analysis.* Cambridge University Press, 1997.

[37] A F Jenkinson. The frequency distribution of the annual maximum (or minimum) values of meteorological elements. *Q. J. R. Meteorol. Soc.*, 81:158–171, 1955.

[38] K. Klein Goldewijk, A. Beusen, J. Doelman, and E. Stehfest. New anthropogenic land use estimates for the holocene; hyde 3.2. *Earth System Science Data Discussions*, 2016:1–40, 2016.

[39] W. Knorr, A. Arneth, and L. Jiang. Demographic controls of future global fire risk. *Nature Climate Change*, 6:781–785, 2016.

[40] Sujan Koirala, Pat J F Yeh, Yukiko Hirabayashi, Shinjiro Kanae, and Taikan Oki. Global-scale land surface hydrologic modeling with the representation of water table dynamics. *Journal of Geophysical Research Atmospheres*, 119(1):75–89, 2014.

[41] Flavio Lehner, Sloan Coats, Thomas F. Stocker, Angeline G. Pendergrass, Benjamin M. Sanderson, Christoph C. Raible, and Jason E. Smerdon. Projected drought risk in 1.5°c and 2°c warmer climates. *Geophysical Research Letters*, 44(14):7419–7428, 2017. 2017GL074117.

[42] Wenfeng Liu, Hong Yang, Christian Folberth, Xiuying Wang, Qunying Luo, and Rainer Schulin. Global investigation of impacts of pet methods on simulating crop-water relations for maize. *Agricultural and Forest Meteorology*, 221(Supplement C):164 – 175, 2016.

[43] Wenfeng Liu, Hong Yang, Junguo Liu, Ligia B. Azevedo, Xiuying Wang, Zongxue Xu, Karim C. Abbaspour, and Rainer Schulin. Global assessment of nitrogen losses and trade-offs with yields from major crop cultivations. *Science of The Total Environment*, 572(Supplement C):526 – 537, 2016.

[44] Robert Mendelsohn, Kerry Emanuel, Shun Chonabayashi, and Laura Bakkensen. The impact of climate change on global tropical cyclone damage. *Nature Climate Change*, 2(3):205–209, jan 2012.

[45] Chad Monfreda, Navin Ramankutty, and Jonathan A. Foley. Farming the planet: 2. geographic distribution of crop areas, yields, physiological types, and net primary production in the year 2000. *Global Biogeochemical Cycles*, 22(1):n/a–n/a, 2008. GB1022.

[46] Florent Mouillot and Christopher B. Field. Fire history and the global carbon budget: a 1°× 1° fire history reconstruction for the 20thcentury. *Global Change Biology*, 11(3):398–420, 2005.

[47] C. Müller, J. Elliott, J. Chryssanthacopoulos, A. Arneth, J. Balkovic, P. Ciais, D. Deryng, C. Folberth, M. Glotter, S. Hoek, T. Iizumi, R. C. Izaurralde, C. Jones, N. Khabarov, P. Lawrence, W. Liu, S. Olin, T. A. M. Pugh, D. K. Ray, A. Reddy, C. Rosenzweig, A. C. Ruane, G. Sakurai, E. Schmid, R. Skalsky, C. X. Song, X. Wang, A. de Wit, and H. Yang. Global gridded crop model evaluation: benchmarking, skills, deficiencies and implications. *Geoscientific Model Development*, 10(4):1403–1422, 2017.

[48] H Müller Schmied, S. Eisner, D. Franz, M. Wattenbach, F. T. Portmann, M. Flörke, and P. Döll. Sensitivity of simulated global-scale freshwater fluxes and storages to input data, hydrological model structure, human water use and calibration. *Hydrology and Earth System Sciences*, 18(9):3511–3538, 2014.

[49] Washington R. Nyabeze. Estimating and interpreting hydrological drought indices using a selected catchment in zimbabwe. *Physics and Chemistry of the Earth, Parts A/B/C*, 29(15):1173–1180, 2004. Water, Science, Technology and Policy Convergence and Action by All (A Meeting Point for Action leading to Sustainable Development).

[50] F. Pappenberger, E. Dutra, F. Wetterhall, and H. L. Cloke. Deriving global flood hazard maps of fluvial floods through a physical model cascade. *Hydrology and Earth System Sciences*, 16(11):4143–4156, 2012.

[51] O. Pechony and D. T. Shindell. Driving forces of global wildfires over the past millennium and the forthcoming century. *Proceedings of the National Academy of Sciences*, 107(45):19167–19170, 2010.

[52] Leland T. Peirce. Diurnal variation in the dew-point temperature at asheville, n. c. *Monthly Weather Review*, 62(8):289–293, 1934.

[53] Cynthia Rosenzweig, Joshua Elliott, Delphine Deryng, Alex C. Ruane, Christoph Müller, Almut Arneth, Kenneth J. Boote, Christian Folberth, Michael Glotter, Nikolay Khabarov, Kathleen Neumann, Franziska Piontek, Thomas A. M. Pugh, Erwin Schmid, Elke Stehfest, Hong Yang, and James W. Jones. Assessing agricultural risks of climate change in the 21st century in a global gridded crop model intercomparison. *Proceedings of the National Academy of Sciences*, 111(9):3268–3273, 2014.

[54] Stefanie Rost, Dieter Gerten, Alberte Bondeau, Wolfgang Lucht, Janine Rohwer, and Sibyll Schaphoff. Agricultural green and blue water consumption and its influence on the global water system. *Water Resources Research*, 44(9):1–17, sep 2008.

[55] Simone Russo, Jana Sillmann, and Erich M Fischer. Top ten european heatwaves since 1950 and their occurrence in the coming decades. *Environmental Research Letters*, 10(12):124003, 2015.

[56] Simone Russo, Jana Sillmann, and Andreas Sterl. Humid heat waves at different warming levels. *Scientific Reports*, 7(1):7477, 2017.

[57] William J. Sacks, Delphine Deryng, Jonathan A. Foley, and Navin Ramankutty. Crop planting dates: an analysis of global patterns. *Global Ecology and Biogeography*, 19(5):607–620, 2010.

[58] Sibyll Schaphoff, Ursula Heyder, Sebastian Ostberg, Dieter Gerten, Jens Heinke, and Wolfgang Lucht. Contribution of permafrost soils to the global carbon budget. *Environmental Research Letters*, 8(1):014026, 2013.

[59] Sibyll Schaphoff, Ursula Heyder, Sebastian Ostberg, Dieter Gerten, Jens Heinke, and Wolfgang Lucht. Contribution of permafrost soils to the global carbon budget. *Environmental Research Letters*, 8(1):014026, 2013.

[60] Peter D. Schwartzman, Patrick J. Michaels, and Paul C. Knappenberger. Observed changes in the diurnal dewpoint cycles across north america. *Geophysical Research Letters*, 25(13):2265–2268, 1998.

[61] Paolo Scussolini, Jeroen C. J. H. Aerts, Brenden Jongman, Laurens M. Bouwer, Hessel C. Winsemius, Hans de Moel, Philip J. Ward, Hans de Moel, and Philip J. Ward. FLOPROS: an evolving global database of flood protection standards. *Natural Hazards and Earth System Sciences*, 16(5):1049–1061, may 2016.

[62] Sonia I. Seneviratne, Thierry Corti, Edouard L. Davin, Martin Hirschi, Eric B. Jaeger, Irene Lehner, Boris Orlowsky, and Adriaan J. Teuling. Investigating soil moisture–climate interactions in a changing climate: A review. *Earth-Science Reviews*, 99(3):125–161, 2010.

[63] J. Sheffield and E. F. Wood. Characteristics of global and regional drought, 1950–2000: Analysis of soil moisture data from off-line simulation of the terrestrial hydrologic cycle. *J. Geophys. Res.-Atmos.*, 112:D17115, 2007.

[64] Justin Sheffield and Eric F. Wood. Projected changes in drought occurrence under future global warming from multi-model, multi-scenario, ipcc ar4 simulations. *Climate Dynamics*, 31(1):79–105, 2008.

[65] B. Smith, D. Wårlind, A. Arneth, T. Hickler, P. Leadley, J. Siltberg, and S. Zaehle. Implications of incorporating n cycling and n limitations on primary production in an individual-based dynamic vegetation model. *Biogeosciences*, 11(7):2027–2054, 2014.

[66] Aditya Sood and Vladimir Smakhtin. Global hydrological models: a review. *Hydrological Sciences Journal*, 60(4):549–565, 2015.

[67] T Stacke and S Hagemann. Development and validation of a global dynamical wetlands extent scheme. *Hydrology and Earth System Sciences Discussions*, 9(1):405–440, 2012.

[68] Scott L Stephens, Neil Burrows, Alexander Buyantuyev, Robert W Gray, Robert E Keane, Rick Kubian, Shirong Liu, Francisco Seijo, Lifu Shu, Kevin G Tolhurst, and Jan W van Wagtendonk. Temperate and boreal forest mega-fires: characteristics and challenges. *Frontiers in Ecology and the Environment*, 12(2):115–122, 2014.

[69] Kumiko Takata, Seita Emori, and Tsutomu Watanabe. Development of the minimal advanced treatments of surface interaction and runoff. *Global and Planetary Change*, 38(1-2):209–222, jul 2003.

[70] K. Thonicke, A. Spessa, I. C. Prentice, S. P. Harrison, L. Dong, and C. Carmona-Moreno. The influence of vegetation, fire spread and fire behaviour on biomass burning and trace gas emissions: results from a process-based model. *Biogeosciences*, 7(6):1991–2011, 2010.

[71] Kirsten Thonicke, Sergey Venevsky, Stephen Sitch, and Wolfgang Cramer. The role of fire disturbance for global vegetation dynamics: coupling fire into a dynamic global vegetation model. *Global Ecology and Biogeography*, 10(6):661–677, 2001.

[72] Anne F. Van Loon. Hydrological drought explained. *Wiley Interdisciplinary Reviews: Water*, 2(4):359–392, 2015.

[73] J.P. Vidal, E. Martin, L. Franchistéguy, Florence Habets, Jean-Michel Soubeyroux, M. Blanchard, and M. Baillon. Multilevel and multiscale drought reanalysis over france with the safran-isba-modcou hydrometeorological suite. *Hydrol. Earth Syst. Sci.*, 14(3):459–478, 2010.

[74] Y. Wada, D. Wisser, and M. F P Bierkens. Global modeling of withdrawal, allocation and consumptive use of surface water and groundwater resources. *Earth System Dynamics*, 5(1):15–40, 2014.

[75] Yoshihide Wada, Inge E. M. de Graaf, and Ludovicus P. H. van Beek. High-resolutionmodeling of human and climate impacts on global water resources. *Journal of Advances in Modeling Earth Systems*, 8:735–763, 2016.

[76] P.J. Ward, B. Jongman, M. Kummu, M.D. Dettinger, F.C. Sperna Weiland, and H.C. Winsemius. Strong influence of El Niño Southern Oscillation on flood risk around the world. *Proceedings of the National Academy of Science of the USA*, pages 1–6, 2014.

[77] Jerry Williams. Exploring the onset of high-impact mega-fires through a forest land management prism. *Forest Ecology and Management*, 294(Supplement C):4 – 10, 2013. The Mega-fire reality.

[78] J.R. Williams. *The EPIC Model*, pages 909–1000. Water Resources Publications, Littleton, USA, 1995.

[79] Dai Yamazaki, Gustavo A M De Almeida, and Paul D. Bates. Improving computational efficiency in global river models by implementing the local inertial flow equation and a vector-based river network map. *Water Resources Research*, 49(11):7221–7235, 2013.

[80] Dai Yamazaki, Shinjiro Kanae, Hyungjun Kim, and Taikan Oki. A physically based description of floodplain inundation dynamics in a global river routing model. *Water Resources Research*, 47(4):1–21, 2011.

[81] C. Yue, P. Ciais, P. Cadule, K. Thonicke, S. Archibald, B. Poulter, W. M. Hao, S. Hantson, F. Mouillot, P. Friedlingstein, F. Maignan, and N. Viovy. Modelling the role of fires in the terrestrial carbon balance by incorporating spitfire into the global vegetation model orchidee – part 1: simulating historical global burned area and fire regimes. *Geoscientific Model Development*, 7(6):2747–2767, 2014.

[82] C. Yue, P. Ciais, P. Cadule, K. Thonicke, and T. T. van Leeuwen. Modelling the role of fires in the terrestrial carbon balance by incorporating spitfire into the global vegetation model orchidee – part 2: Carbon emissions and the role of fires in the global carbon balance. *Geoscientific Model Development*, 8(5):1321–1338, 2015.

[83] Fang Zhao, Ted I E Veldkamp, Katja Frieler, Jacob Schewe, Sebastian Ostberg, Sven Willner, Bernhard Schauberger, Simon N Gosling, Hannes Müller Schmied, Felix T Portmann, Guoyong Leng, Maoyi Huang, Xingcai Liu, Qiuhong Tang, Naota Hanasaki, Hester Biemans, Dieter Gerten, Yusuke Satoh, Yadu Pokhrel, Tobias Stacke, Philippe Ciais, Jinfeng Chang, Agnes Ducharne, Matthieu Guimberteau, Yoshihide Wada, Hyungjun Kim, and Dai Yamazaki. The critical role of the routing scheme in simulating peak river discharge in global hydrological models. *Environmental Research Letters*, 12(7):075003, jul 2017.